UNIVERSIDAD COMPLUTENSE DE MADRID

FACULTAD DE CIENCIAS QUÍMICAS

TESIS DOCTORAL

Dinámica estructural ultrarrápida de fotodisociación molecular resuelta en tiempo

Ultrafast studies on time-resolved structural dynamics of photodissociating molecules

MEMORIA PARA OPTAR AL GRADO DE DOCTOR

PRESENTADA POR

Marta Luisa Murillo Sánchez

DIRECTOR

Luis Bañares Morcillo

UNIVERSIDAD COMPLUTENSE DE MADRID
FACULTAD DE CIENCIAS QUÍMICAS
Departamento de Química Física

TESIS DOCTORAL

DINÁMICA ESTRUCTURAL ULTRARRÁPIDA DE FOTODISOCIACIÓN MOLECULAR RESUELTA EN TIEMPO

ULTRAFAST STUDIES ON TIME-RESOLVED STRUCTURAL DYNAMICS OF PHOTODISSOCIATING MOLECULES

Memoria para optar al grado de Doctor presentada por
MARTA LUISA MURILLO SÁNCHEZ

Director
LUIS BAÑARES MORCILLO

UNIVERSIDAD COMPLUTENSE DE MADRID
FACULTAD DE CIENCIAS QUÍMICAS
Departamento de Química Física

DOCTORAL THESIS

DINÁMICA ESTRUCTURAL ULTRARRÁPIDA DE FOTODISOCIACIÓN MOLECULAR RESUELTA EN TIEMPO

ULTRAFAST STUDIES ON TIME-RESOLVED STRUCTURAL DYNAMICS OF PHOTODISSOCIATING MOLECULES

A thesis submitted for the degree of Doctor of Philosophy by
MARTA LUISA MURILLO SÁNCHEZ

Supervisor
LUIS BAÑARES MORCILLO

A mi abuelo Paulino.

“Nothing in life is to be feared, it is only to be understood. Now is the time to understand more, so that we may fear less.”

Marie Curie

Acknowledgments

The research that led to the results collected in the present Doctoral Thesis was carried out between October 2016 and February 2020 in the department of Physical Chemistry at the faculty of Chemical Science of the Complutense University of Madrid under the supervision of Prof. Dr. Luis Bañares. The experiments were performed with the femtosecond laser and velocity map imaging setup at the Center for Ultrafast Lasers (CLUR).

The accomplishment of the present Doctoral Thesis was possible thanks to a grant for predoctoral contracts conceded by Complutense University of Madrid in association with Banco Santander in February 2017. As well, the Ministry of Economy and Competitiveness and the Ministry of Science and Innovation provided financial support through the projects "Procesos moleculares fotoinducidos y colisionales por medio de experimentos láser y métodos teóricos" (CTQ2015-65033-P) and "Dinámica de reacciones químicas y nanomateriales inducida por irradiación láser ultrarrápida" (PGC2018-096444-B-I00), respectively.

Part of the research presented in this Thesis is born from a collaboration with the Ultrafast XUV Physics research group (A2) directed by Dr. Oleg Kornilov. This group belongs to the Attosecond Physics division (Division A), directed by Prof. Dr. Marc J.J. Vrakking at the Max Born Institute (MBI) for Non-linear Optics and Short Pulse Spectroscopy (Berlin, Germany). This collaboration was possible thanks to three LaserLab Europe access projects: "In search of intramolecular coulombic decay in a polyatomic dissociating molecule" (MBI002647), "XUV/IR photodissociation dynamics of neutral and cationic water and acetonitrile molecules by Coulomb explosion velocity map imaging" (MBI002530) and "Reconstruction of attosecond beatings by interferences of two-photon transitions" (MBI002239), financed, in turn, by the European Unions' Horizon 2020 research and innovation program. Within the framework of this collaboration, a pre-doctoral stay of three months was carried out at the MBI between 25th August and 1st November of 2019, with additional funding from an Erasmus+ fellowship.

First, I would like to thank my thesis supervisor Dr. Luis Bañares for the opportunity he gave me to carry out the thesis in his research group. Thank you for your constant support and help in completing this training period. You have always managed to give me energy and motivation in the most challenging moments; thanks for listening to me and giving me your best advice.

Carrying out this Doctoral Thesis would not have been possible without the help of Dr. Sonia Marggi-Poullain. Without you, my experimental results would have never seen the light in different scientific contributions. Thanks for your endless help.

David, you have been an exceptional lab partner despite not working in the same experimental setup. You have always had an excellent disposition to help me and solve my doubts. Despite being very different, you have always helped me to find balance and calm. Thanks for being my adventure partner. What patience you have had with me!

Thanks to Dr. Rebeca de Nalda. You always know how to bring brilliant ideas and coherence. Thank you very much for your constant support; you know how much I appreciate you.

I also wanted to thank Dr. María Eugenia Corrales for her casual help in the laboratory and her ability to explain the most difficult concepts to me like no one else, and our friendship beyond the laboratory. Thanks for all shared moments.

To Hugo, I want to thank him for his help as a physicist to improve my optical setup, his willingness to solve my doubts about optics, but also his closeness and the fun times together.

Of course, I cannot forget other people with whom I have shared time in the laboratory, such as Dr. Jesús Gonzalez Izquierdo, with whom I have shared long conversations but also Pablo, Ignacio, Pedro and Garikoitz. I have had excellent colleagues and friends who have made my daily work much more enjoyable and fun. On the other hand, I want to thank Dr. Vincent Loriot and Dr. Gregory Gitzinger for their legacy in the laboratory, which has been indispensable for the conduction of the experiments.

I would also like to thank the senior members of the research team, especially Dr. Marta Menéndez and Dr. Enrique Verdasco. You have always made me feel very comfortable in the group.

The contribution of theorists has been essential for this work, especially that of Dr. Jesús Gonzalez-Vázquez, who has been involved in the entirety of my doctoral thesis. Your work has been exceptional and key in this thesis. Also, mention Dr. Alberto García Vela and Dr. Alexandre Zanchet, with whom I have also established a very good friendship through our shared coffee times. Thanks to Dr. Paulo Limão-Viera for his contribution to this Thesis and Dr. Raúl Ferreira de Pablo for his kind help with my mathematical doubts.

I would like to make a special mention to those who have contributed to the experimental development of this thesis. Among them, the mechanical workshop staff and especially its head, Rubén Ayuso, for his excellent disposition and kindness. Also, to Javier Rodríguez Azadeño for his electronics

works essential for conducting my experiments. My deepest thanks to the LASING team for always having the laser system ready, with special mention to Álvaro Guadaño and Fernando Allen-Perkins. However, I want to highlight the figure of Valentín Guadaño, the head of LASING. He is an unbeatable professional with an excellent disposition and training motivation. Thank you for those conversations and countless tips for both my professional and personal life.

Thanks to Dr. Oleg Kornilov from the Max Born Institute for Non-linear Optics and Short Pulse Spectroscopy in Berlin for hosting me in his research group during various scientific collaborations and the three-month stay. Also, to all the people involved in the experimental work there, Dr. Geert Reitsma, Dr. Lorenz Drescher and Dr. Tobbias Wittig. My stay in Berlin was an unforgettable experience, and it was due to the people I met there, such as Melisa and Laura, and to many others who made it very special. At this stage, my cousin Belén was essential. I have so much to thank you that it would not fit in this dedication. Thank you for your welcome in Berlin and for always giving me your unconditional love and support.

This thesis would not have been possible without the support of my friends. Ana, my longtime friend from school. Sandra and Laura, “mis flores”, with whom I shared unforgettable and great moments. Maria, thank you for being there from the real scientific beginning. Thank you for our shared laughs, the cinema times, and for always giving me strength and the best and most valuable advice. Miriam, thank you for that great connection and for being with me through good and bad times. Iker, whom I met by chance in my first year of thesis during a congress, you have been one of the best things I have gotten out of this period. Despite the distance, you have always given me your constant support. Thank you for our special friendship and complicity. A special mention must be made to my friends from the department with whom I have shared an unforgettable moment, Ana, Laura, Mac, Guillermo, and Olivia. I cannot forget my “físicas transatlánticas” Mila and Ana and my Cambridge girls, Gunel and Shahad.

I am sure I am leaving someone out of these acknowledgments; therefore, this one goes to all those people who in one way or another have been part of this.

Last but not least, I would like to thank my family for their unconditional love and support despite not really understanding what I was doing with the molecules. Your pride has been one of the best motivations. I know my grandparents would have been eternally proud of everything I have achieved. The most significant acknowledgment goes to my parents for being the fundamental key in my life; your constant love and support I cannot express how grateful I am. They know how to guide me and give me the necessary energy and motivation. Álvaro, my brother, I have no words to express how much I appreciate your love and unconditionality. You are my all-time partner in crime.

Contents

List of abbreviations and acronyms

AMFI ..... atomic mean-field integral
ANO-RCC ..... relativistic contracted atomic natural orbitals
AOM ..... acousto-optical modulator
AOPDF ..... acousto-optic programmable dispersive filter device
APT ..... attosecond pulse train
ATI ..... above-threshold ionization
BAGEL ..... Brilliantly Advanced General Electronic-structure Library
BASEX ..... basis set expansion
BBO ..... beta barium borate
BI ..... Binding energy
CASSCF ..... complete active space self-consistent field
CC ..... concave
CCD ..... charge-coupled device
CF ..... ConFlat
CIS ..... configuration interaction singles
CM ..... center of mass
COLTRIMS ..... Cold Target Recoil Ion Momentum Spectroscopy
CPA ..... chirped pulse amplification
CW ..... continuous wave
CX ..... convex
DC ..... direct current
DDG ..... digital delay generator
DEA ..... dissociative electron attachment
DFG ..... difference frequency generation
DZVP ..... contracted to a doble zeta polarized
ECP ..... effective core potential
ESDIAD ..... electron stimulated ion desorption ion angular distributions
FEL ..... free-electron laser
FFT ..... fast Fourier transform
FHG ..... fourth-harmonic generation

FROG ..... frequency-resolved optical gating
FTL ..... Fourier-transform-limited
FTS ..... femtosecond transition state spectroscopy, Fourier Transform Spectrometer
GAMESS ..... General atomic and molecular electronic structure system
GVD ..... group velocity dispersion
HOMO ..... highest occupied molecular orbital
HV ..... high voltage
IAP ..... isolated attosecond pulse
IP ..... ionization potential
IR ..... infrared
IRC ..... intrinsic reaction coordinate
ISO ..... International Organization for Standardization
KDP ..... monopotassium phosphate
KER ..... kinetic energy release
LBO ..... lithium triborate
LIF ..... laser-induced fluorescence
MCD ..... magnetic circular dichroism
MCP ..... microchannel plate
MEP ..... minimum energy path
MP2 ..... second-order Møller-Plesset perturbation theory
MPI ..... multiphoton ionization
MRCI ..... multireference configuration interaction
MRCISD ..... multireference configuration interaction method with singles and doubles
MS-CASPT2 ..... multistate complete active-space second-order perturbation theory
NIR ..... near-infrared
NRT ..... non-radiative transition
OPA ..... optical parametric amplifier
OPG ..... optical parametric generation
pBASEX ..... basis set expansion in polar coordinates
PEISI ..... Post Extraction Inversion Slice Imaging
PEPICO ..... photoelectron photoion coincidence spectroscopy
PES ..... photoelectron spectroscopy
PImMS ..... pixel imaging mass spectrometry
PIMS ..... photoionization mass spectrometry
PM-CASSCF ..... perturbation modified complete active space self-consistent field
PT ..... perturbation theory
PTS ..... photofragment translational spectroscopy

QMS ..... quadrupolar mass spectrometer
RABBITT ..... reconstruction of attosecond interference by beating of two-photon transitions
REMPI ..... resonance-enhanced multiphoton ionization
RF ..... radio frequency
RTOF-MS ..... reflection time-of-flight mass spectrometry
SA ..... state average
SFA ..... strong field approximation
SFG ..... sum-frequency generation
SHARC ..... surface hopping including arbitrary couplings
SHG ..... second-harmonic generation
SMI ..... spatial map imaging
SO-MCQDPT ..... spin-orbit multi configurational quasi degenerated perturbation theory
SPIDER ..... spectral phase interferometry for direct electric-field reconstruction
SPM ..... self-phase modulation
SSHHG ..... solid surface high harmonic generation
SSI ..... spectral shearing interferometry
TA ..... transient absorption
TDM ..... transition dipole moment
THG ..... third-harmonic generation
TOD ..... third-order dispersion
TOF ..... time-of-flight
TOFMS ..... time-of-flight mass spectrometer
TOPAS ..... travelling-wave optical parametric amplifier
TPES ..... threshold photoelectron spectroscopy
TR-FTES ..... time-resolved Fourier transform emission spectroscopy
TTL ..... transistor-transistor logic
UHF ..... unrestricted Hartree-Fock
UV ..... ultraviolet
VIS ..... visible
VMI ..... velocity map imaging
VUV ..... vacuum ultraviolet
WLC ..... white light continuum
WLG ..... white-light generation
XFEL ..... X-ray free-electron laser
XMS-CASPT2 ..... extended multistate complete active-space second-order perturbation theory
XUV ..... extreme ultraviolet radiation

Summary

ULTRAFAST STUDIES ON TIME-RESOLVED STRUCTURAL DYNAMICS OF PHOTODISSOCIATING MOLECULES

INTRODUCTION

Methyl iodide (CH_3I) has become a reference system for molecular photodissociation studies in the ultraviolet (UV) region. This molecule presents direct photodissociation as well as predissociation mechanisms, leading to the cleavage of the C−I bond, relatively simple but attractive due to the presence of conical intersections and non-adiabatic crossing as well as approachable by theoretical calculations thanks to its pseudo-diatomic structure. In particular, it has been of interest to several experimenters how the photoinduced dynamics of this simple system can be modified along the reaction coordinate through changes in the molecular structure; either by increasing the size of the hydrocarbon chain, by creating branches, introducing unsaturations, or some substituting halogen atoms or ionizing the molecule to get the cation in different electronic states.

AIMS

The present Doctoral Thesis aims to evaluate the influence of molecular structural changes on the direct photodissociation and predissociation dynamics of a family of alkyl iodides and dihalomethanes. For this purpose, the following studies have been carried out:

- Time-resolved direct photodissociation of the dihalomethanes chloroiodomethane (CH_2ICl) and bromoiodomethane (CH_2BrI) in the first absorption band at 268 nm to evaluate the halogen-atom effect substitution in the molecular structure.
- Time-resolved predissociation dynamics of a series of both linear and branched alkyl iodides, in the second absorption band around 201 nm, to study the correlation between the chemical structure and the predissociation dynamics.
- Time-resolved dissociation dynamics of vinyl iodide (C_2H_3I), at 199.2 and 200 nm, to evaluate the influence of the chemical structure and the presence of unsaturations in the alkyl radical on the time-resolved dynamics.
- Time-resolved photoinduced dynamics of the methyl iodide cation (CH_3I^+) in the presence of a moderate intense infrared laser field.

METHODOLOGY

To carry out the present experiments, the use of femtosecond laser pulses in the UV region was combined with pump-probe schemes, detecting the photofragments as a function of time in the femtosecond time scale by resonance-enhanced multiphoton ionization (REMPI) and velocity map imaging (VMI).

Some of the experiments were performed combining subfemtosecond pulses spectrally filtered in the extreme ultraviolet (XUV) region produced *via* high harmonic generation (HHG) with infrared (IR) laser pulses with moderate intensity. The experiments were performed by means of VMI with ion and photoelectron detection.

RESULTS, DISCUSSION AND CONCLUSIONS

Photodissociation dynamics of dihalomethanes: The photodissociation dynamics of dihalomethanes are characterized by the cleavage of the C–I bond mediated through repulsive states accessed by a parallel transition. The dynamics are mediated by absorption to the 5*A*' state for CH_2BrI, while there are two competing pathways through the 4*A*' or 5*A*' states for CH_2ICl. The reaction times increase with the size of the substituting halogen atom. A significant part of the available energy is converted into internal energy of the molecular fragments, mainly into rotational excitation, evidencing the anchor effect of the halogen atom, unlike CH_3I, where the available energy is primarily channeled into translational motion.

The performance of these experiments allowed us to determine the influence of the halogen-atom substitution, being the dynamics very similar to that of CH_3I and other alkyl iodide derivatives. The reaction times of this type of compounds can be rationalized from classical one-dimensional models considering the size of the radical and the available energy distribution. The quantum yields of the photoproducts, also justified by classical models, highlighted the one-dimensional character of the photodissociation of this type of compounds as opposed to the branched alkyl iodides, which have a particular multidimensional nature.

Predissociation dynamics of linear and branched alkyl iodides: The predissociation dynamics observed for these compounds in the *B*-band is similar to that of CH_3I in the second absorption band, as excitation to the Rydberg states 6*A*'' and 7*A*' occurs followed by a predissociation mechanism through the repulsive states 7*A*'', 8*A*' and 8*A*'' leading to the cleavage of the C−I bond and resulting in $I^*(^2P_{1/2})$. No $I(^2P_{3/2})$ fragments were observed through the 4*A*'' and 5*A*' states. However, the structural complexity of linear alkyl iodides, excited in the origin of the *B*-band, seems to enhance the coupling between the bound and repulsive states by shortening reaction times. Theoretical calculations indicate very similar

relative energies of the states' crossing point at the Franck-Condon region; thus, they point out the participation of additional vibrational modes in the fission process. The observed loss of anisotropy is justified by the rotation of the molecule and the predissociation lifetime. The vibronic transitions observed in the branched alkyl iodides, as well as in ethyl iodide, reveal changes in the couplings that lead to the variation of the predissociation times, as in methyl iodide.

Photodissociation dynamics of vinyl iodide: Photoexcitation of C_2H_3I at the excitation wavelengths of 199.2 and 200 nm leads to the C–I bond cleavage. Although the reaction times, the available energy disposal into different degrees of freedom, and the quantum yields are very similar at the two excitation wavelengths, the excitation at 200 nm, mediated by a parallel transition, leads to prompt dissociation through repulsive states. In contrast, the excitation at 199.2 nm is governed by a predissociative mechanism with a high multidimensional character since photodissociation is started with an initial π^* character and ends with a σ^* character.

These experiments allowed us to evaluate the influence of the chemical structure and the presence of unsaturations in the alkyl radical being the dynamics substantially different from that of CH_3I and other alkyl iodide derivatives in a similar excitation wavelength region.

Extreme ultraviolet photoinduced dynamics of the methyl iodide cation in the presence of a moderate intense infrared laser field: By excitation of XUV radiation at 88.9 eV, CH_3I can be prepared in the ground states of the cation (CH_3I^+), $\widetilde{X}\,^2E_{1/2}$ and $\widetilde{X}\,^2E_{3/2}$, with low internal energy content, as well as in the first electronically excited $\widetilde{A}\,^2A_1$ state, with high vibrational energy content. While no dynamics or fragmentation is expected from the lower states, in the bound excited state $\widetilde{A}\,^2A_1$, a vibrational wavepacket, initially trapped in a shallow well, can escape, dissociating directly into methyl (CH_3) and $I^+(^3P_2)$ fragments, or by internal conversion, dissociates through the ground $\widetilde{X}\,^2E_{3/2}$ and $\widetilde{X}\,^2E_{1/2}$ states giving rise to CH_3^++I($^2P_{3/2}$). A moderate intense IR laser field can induce modifications on the dynamics, fundamentally through the $\widetilde{A}^2A_1$ state, through a pump mechanism to higher electronic states giving rise to the formation of I^+, or by a dump mechanism to the $\widetilde{X}\,^2E_{3/2}$ and $\widetilde{X}\,^2E_{1/2}$ states.

These experiments show the usefulness of spectrally selected XUV femtosecond pulses for the selective study of molecular cation dynamics, avoiding secondary processes such as Coulomb explosion or dissociative photoionization, observed through multiphoton absorption employing IR pulses. With moderate intensity IR pulses, subsequent to the XUV excitation, tailored dynamics can be induced, and oscillating wavepacket dynamics can be probed.

Resumen

DINÁMICA ESTRUCTURAL ULTRARRÁPIDA DE FOTODISOCIACION MOLECULAR RESUELTA EN TIEMPO

INTRODUCCIÓN

El ioduro de metilo (CH_3I) se ha convertido en el sistema de referencia para estudios de fotodisociación molecular en la región ultravioleta (UV). Esta molécula presenta tanto dinámicas de fotodisociación directa como de predisociación, que conducen a la escisión del enlace C–I, relativamente simples pero interesante, así como abordable por cálculos teóricos gracias a su estructura de molécula pseudo-diatómica. En concreto, ha sido de interés de diversos experimentadores investigar cómo la dinámica de este sistema simple puede ser modificada a lo largo de la coordenada de reacción, mediante la realización de cambios en su estructura; bien, aumentando el tamaño de la cadena hidrocarbonada, creando ramificaciones, introduciendo insaturaciones o algún átomo sustituyente e incluso ionizando la molécula para acceder al catión en diferentes estados electrónicos.

OBJETIVOS

La presente Tesis Doctoral tiene como objetivo la evaluación de la influencia de los cambios estructurales moleculares sobre la dinámica de fotodisociación y predisociación del ioduro de metilo. Para este propósito, se ha estudiado:

- La fotodisociación directa resuelta en tiempo de los dihalometanos cloroiodometano (CH_2ICl) y bromoiodometano (CH_2BrI), en la primera banda de absorción a 268 nm para evaluar el efecto de la sustitución por átomo de halógeno en la estructura molecular.
- La predisociación resuelta en tiempo de una serie de ioduros de alquilo, tanto lineales como ramificados, en la segunda banda de absorción en torno a 201 nm, para estudiar la **c**orrelación entre la estructura molecular y la dinámica de predisociación.
- La disociación resuelta en tiempo del ioduro de vinilo (C_2H_3I), a 199.2 y 200 nm, para evaluar la influencia de la estructura molecular y la presencia de insaturaciones en el radical alquílico en la fotodisociación resuelta en tiempo.

- La dinámica fotoinducida en el catión de ioduro de metilo (CH_3I^+) por pulsos de luz en el ultravioleta extremo (XUV) en presencia de un campo laser infrarrojo (IR) de intensidad moderada.

METODOLOGÍA

Para la realización de estos experimentos, se ha combinado la utilización de pulsos laser de femtosegundos en la región UV, empleando esquemas de bombeo y sonda y detectando los fotofragmentos en la escala temporal de los femtosegundos por ionización multifotónica mejorada por resonancia (REMPI, del inglés *resonance-enchanced multiphoton ionization*) mediante la técnica de cartografía de velocidades con imágenes de iones.

En parte de los experimentos, se ha combinado el uso de pulsos de luz de subfemtosegundos filtrados espectralmente en la región XUV, procedentes de la generación de altos armónicos (HHG, del inglés *high-harmonic generation*), con pulsos láser IR de intensidad moderada. Los experimentos bombeo-sonda se realizaron empleando la técnica de cartografía de velocidades con detección de iones y fotoelectrones.

RESULTADOS, DISCUSIÓN Y CONCLUSIONES

Dinámica de fotodisociación de dihalometanos derivados del ioduro de metilo: La dinámica de fotodisociación de los dihalometanos cloroiodometano (CH_2ICl) y bromoiodometano (CH_2BrI), está caracterizada por la ruptura del enlace C–I mediada a través de estados electrónicos repulsivos accedidos mediante transiciones paralelas. La dinámica está mediada por la absorción al estado 5*A*' para el bromoiodometano (CH_2BrI), mientras que existen dos vías en competición a través de los estados 4*A*' o 5*A*' para el cloroiodometano (CH_2ICl). Los tiempos de reacción son tanto mayores cuanto mayor es el tamaño del átomo de halógeno sustituyente. Una parte significativa de la energía disponible se convierte en energía interna de los fragmentos moleculares, fundamentalmente grados de libertad rotacionales, evidenciándose el efecto “ancla” del átomo sustituyente, a diferencia del ioduro de (CH_3I), donde la energía disponible se canaliza, mayoritariamente, en grados de libertad traslacionales.

La realización de estos experimentos ha permitido determinar la influencia de la sustitución por átomos de halógeno, siendo la dinámica bastante similar a la del CH_3I y otros derivados alquílicos. Los tiempos de reacción de este tipo de moléculas pueden racionalizarse a partir de modelos monodimensionales clásicos teniendo en cuenta el tamaño del radical y el reparto de la energía disponible. Los rendimientos cuánticos de formación de los fotoproductos, también racionalizados por modelos clásicos, destacan el carácter monodimensional de la fotodisociación de este tipo de moléculas,

en contraposición con los ioduros de alquilo ramificados, que acusan un cierto carácter multidimensional.

Dinámica de predisociación de ioduros de alquilo lineales y ramificados derivados del ioduro de metilo: La dinámica de predisociación observada para estas moléculas es similar a la del CH_3I en la segunda banda de absorción, pues se produce la excitación a los estados de Rydberg 6*A*'' y 7*A*' seguida por un proceso predisociativo a través de los estados repulsivos 7*A*'', 8*A*' y 8*A*'', que conduce a la ruptura del enlace C–I, dando lugar a I*($^2P_{1/2}$). No se observaron fragmentos I($^2P_{3/2}$) formados a través de los estados 4*A*'' y 5*A*'. Sin embargo, la complejidad estructural de los ioduros de alquilo lineales, excitados en el origen de la banda *B*, parece incentivar el acoplamiento entre los estados ligado y repulsivo acortando los tiempos de reacción. Los cálculos teóricos señalan posiciones relativas del cruce entre estados en la región de Franck-Condon muy similares, por lo que se apunta a la participación de modos vibracionales adicionales en el proceso de fisión. La pérdida de anisotropía está justificada por la rotación de la molécula y los tiempos de predisociación. Las transiciones vibrónicas observadas en los ioduros de alquilo ramificados, así como en el ioduro de etilo (C_2H_5I), revelan cambios en los acoplamientos electrónicos que conducen a la variación de los tiempos de predisociación, al igual que en el ioduro de metilo.

Dinámica de fotodisociación del ioduro de vinilo: La dinámica de fotodisociación del ioduro de vinilo (C_2H_3I) a las longitudes de onda de excitación de 199.2 y 200 nm conduce a la ruptura del enlace C–I. Aunque los tiempos de reacción, el reparto de la energía disponible en diferentes grados de libertad y los rendimientos cuánticos son muy similares, la excitación a 200 nm, mediada por una transición paralela, conduce a una disociación rápida a través de estados repulsivos, mientras que la excitación a 199.2 nm está gobernado por un mecanismo predisociativo de alto carácter multidimensional, ya que la fotodisociación se inicia con un carácter π* y finaliza con un carácter σ*.

Estos experimentos han permitido evaluar la influencia de la estructura molecular y la presencia de insaturaciones en el radical alquílico, siendo la dinámica sustancialmente diferente a la del CH_3I y otros derivados alquílicos a longitudes de onda de excitación similares.

Dinámica fotoinducida en el catión de ioduro de metilo por pulsos de luz en el ultravioleta extremo en presencia de un campo laser infrarrojo de intensidad moderada: Por excitación con radiación XUV de femtosegundos en torno a 88.9 eV, el CH_3I puede ser preparado en los estados del catión $\widetilde{X}\,^2E_{1/2}$ y $\widetilde{X}\,^2E_{3/2}$ con un bajo contenido de energía interna, así como en el estado electrónico excitado $\widetilde{A}\,^2A_1$, con un alto contenido de energía vibracional. Mientras no se espera ninguna dinámica ni fragmentación en los estado electrónicos fundamentales del catión $\widetilde{X}\,^2E_{3/2}$ y $\widetilde{X}\,^2E_{1/2}$, en el estado excitado ligeramente enlazado $\widetilde{A}\,^2A_1$ el paquete de ondas vibracional preparado permanece atrapado en el pozo de

potencial, si bien presenta una cierta probabilidad de escapar, disociando de forma directa en los fragmentos CH_3+I^+($^3P_2$), o disociando a través del estado fundamental $\widetilde{X}\,^2E$ poblado por conversión interna con alta energía vibracional, dando lugar a CH_3^++I($^2P_{3/2}$). Un campo de intensidad moderada en el IR puede inducir modificaciones en la dinámica observada fundamentalmente a través del estado $\widetilde{A}\,^2A_1$ mediante un mecanismo de bombeo a estados electrónicos superiores, dando lugar a la formación de I^+, o de "dump" al estado $\widetilde{X}\,^2E$.

Estos experimentos ponen de manifiesto la utilidad de pulsos de luz en el XUV seleccionados espectralmente para el estudio selectivo de la dinámica de cationes moleculares, evitando procesos secundarios como la explosión coulombiana o la fotoionización disociativa, previamente observados mediante absorción multifotónica con pulsos de IR. Con pulsos de IR de intensidad moderada, subsecuentes a la excitación por el pulso ultravioleta extremo, se pueden inducir dinámicas a medida y observar la dinámica de paquetes de onda.

Chapter 1 – Introduction

1.1. LIGHT-MATTER INTERACTION

Spectroscopy studies the interaction of electromagnetic radiation with matter, which can occur through absorption, emission or dispersion/scattering processes. These processes involve the participation of energy transitions, either rotational, vibrational or electronic, which directly depend on the energy of the electromagnetic radiation. Therefore, the different spectroscopic techniques that have been developed in the last decades allows us to explore in detail the electronic structure of atoms and molecules, their vibration (stretch, bending, torsion and strength of chemical bonds) and rotation (length of bonds) by employing different light sources across the electromagnetic spectrum.

Light-matter interaction is usually addressed through a semi-classical approach, in which the system is described using quantum mechanics and the electromagnetic radiation is described by the classic wave theory, employing Maxwell's equations. This approach is usually sufficient, as its predictions match those of a full quantum mechanics approach, since on numerous occasions, the intensity of light can be conceived as a continuous photon or quanta flux, and because the wavelength of the radiation is much larger than the size of the studied atoms and molecules.

Every single charged particle system, such as atoms and molecules, is characterized by a series of quantized energy levels obtained by solving the time-independent Schrödinger equation. However, if electromagnetic radiation interacts with the charged particle system, it causes a time-dependent perturbation that can induce transitions between the different quantum states, with a transition probability determined using the time-dependent Schrödinger equation.

In a first approximation, the role of the magnetic field can be neglected since the electric field is considerably more intense. Besides, as already mentioned, the wavelength of the radiation is much longer than the diameter of molecules or atoms. This difference means that the spatial variation of the electric field is minimal, so it can also be neglected to deduce the operator that represents the time-dependent interaction. This leads to the so-called dipole approximation, and the transitions it describes are called electric dipole transitions. The first-order time-dependent perturbation theory can be used to calculate the probability of an electric dipole transition. The necessary conditions to obtain a maximum transition probability imply, on the one hand, that resonance exists between radiation and the quantum

states of the system and, on the other hand, that the selection rules are met. These rules prevent the operator's integral dipole moment or transition dipole moment (TDM) from being canceled.

This Doctoral Thesis deals in detail with molecular photodissociation, a particular case of light-matter interaction arising from absorption of laser radiation by molecular systems under the electric dipole approximation framework.

1.2. MOLECULAR PHOTODISSOCIATION

Molecular photodissociation consists of an irreversible cleavage of one or multiple chemical bonds due to the absorption of one or multiple photons by a molecular system, provided that the absorbed energy overcomes the bonding energy of the weakest bond. The required energy to produce the cleavage of the bond is known as the dissociation energy. The dissociation energy is denoted as D_0 when relative to the lowest vibrational energy level or D_e when it is relative to the equilibrium potential well depth.

To visualize photodissociation processes, potential energy surfaces are employed. A potential energy surface describes the potential energy of a system, mainly of a set of atoms, as a function of certain parameters, usually their position. For an N nuclei system, there are 3N-6 degrees of freedom (3N-5 for linear molecules), and therefore, the potential energy surface is a space of 3N-6 (or 3N-5) dimensions. A photodissociation process is usually referred along the reaction coordinate through which the bond is cleaved. So then, a one-dimensional potential energy curve represents the dissociation of the molecule for which the potential energy depends only on the internuclear distance between fragments.

In figure 1.1, a set of potential energy curves for a molecule AB is represented. In its ground state AB, the molecule, upon absorption of one or multiple photons in the ultraviolet (UV) or visible (VIS) range, is driven to a repulsive excited state AB* so that the molecule progressively increases its internuclear distance until the photodissociation finally occurs, leading to two neutral fragments A and B, according to:

$$AB + nh\nu \xrightarrow{1} AB^* \xrightarrow{2} A(\alpha) + B(\beta) \tag{1.1}$$

where *AB* represents the initial parent molecule in the ground state, $nh\nu$ is the energy of the absorbed n number of photons of frequency ν, *AB** represents the excited state before photodissociation and α and β and are the quantum states of fragments *A* and *B*, respectively. The first step (1) indicates the absorption of the n photons by the parent molecule *AB* and the second step (2) represents the fragmentation of the excited state *AB** giving rise to fragments *A* and *B* in their corresponding quantum states α and β. Each possible combination of quantum states of fragments *A* and *B* is called dissociation channel.

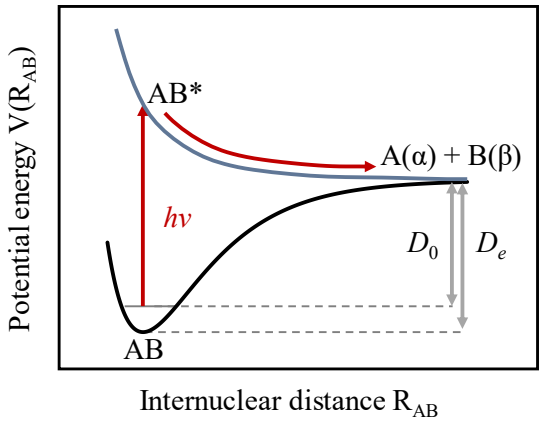

Figure 1.1. *Photodissociation of a molecule AB, along the reaction coordinate R_{AB}. The molecule AB, in its ground state, upon excitation of UV/VIS radiation is driven to a repulsive excited state AB*; the excited molecule AB* progressively increases its internuclear distance R_{AB} until the photodissociation finally occurs, leading to two neutral fragments A and B in the corresponding quantum states α and β. The dissociation energy of the A-B bond is denoted as D_0 or D_e (see text).*

Part of the excitation energy is employed to break the bond between fragments, and the rest of it is energy excess, which can be channeled into translational energy and internal energy of the photoproducts, including electronic, vibrational and rotational energy. The energy balance requires that:

$$E_{photon} = D_0 + E_{excess} = D_0 + E_{trans} + E_{\text{int}} \tag{1.2}$$

where E_{photon} is the energy of the absorbed photon(s), D_0 is the dissociation energy, E_{excess} is the excess energy and E_{trans} and E_{int} are the translational and internal energy of the photoproducts, respectively.

Photodissociation studies aim to find the explanation for how photons cause the bond to break, the lifetime of the excited state, how the energy excess is distributed between the different degrees of freedom, and the distribution of the internal quantum states of the various fragments. These studies also focus on the dependence of the photodissociation on the initial state of the parent molecule and the influence of temperature on the evolution of the process.

For a full description of a photodissociation process, a series of observables is needed, such as the dissociation energies of each dissociation limit, the symmetries of the ground and excited electronic states, the absorption cross-section of each transition, the timescales of the dissociation related to the quantum states of the excited states, the ratios or yields of each dissociation channel, the translational and angular distribution of the photoproducts, the corresponding vectorial correlations and the characterization of crossings between electronic states.

1.2.1. Transition probability and Franck-Condon principle

For a photodissociation to take place, photons must be resonantly absorbed between the involved electronic states. The probability of the photon being absorbed and the transition taking place is governed by the selection rules, which determine whether a transition is allowed or not. This probability determines the intensity of the emission lines from an excited state, and it depends on the nature of the initial and final state wave functions, how strongly photons interact with them, and the intensity of the incident light. This probability is commonly called transition strength, and it is usually described in terms of the oscillator strength *f*. The transition probability R^2 from the initial to the final excited states is mainly related to the TDM and the degree of overlap of the nuclear wave functions in the initial and final states according to:

$$R = \left\langle X_i \middle| D \middle| X_j \right\rangle \tag{1.3}$$

where $\widehat{D}$ is the dipole moment operator and $|Xi,j$ are the wave functions of the initial X_i and final X_j states.

Equation (1.3) reflects that the strength of a transition is relative to how strongly the dipole moment of a resonance between energy states can couple to the electric field of the light wave. In the context of the Born-Oppenheimer approximation,[1] equation (1.3) can be factorized into electronic, vibrational and rotational contributions:

$$R^2 = \left\langle X_i \middle| D \middle| X_j \right\rangle^2 = \left|R_e\right|^2 q_{v'v''} S_{J'J''} \tag{1.4}$$

where the first term $|R_e|^2$ reflects the electronic dipole transition probability between the electronic states; the second term $q_{v'v''}$ is associated with the vibrational levels of the lower state *v*'' and the excited state *v*', and is commonly known as the Franck-Condon factors, and the third term $S_{J'J''}$ stems for the rotational levels involved in the transition, *J*'' and *J'*, known as the rotational line-strength factors or Hönl-London factors.[2]

According to the Franck-Condon principle,[3] the most likely vibronic transitions occur without significant changes in the position of the nuclei due to their mass. Then, the resulting transition can be considered instantaneous compared to the timescale of the movement of the nuclei. In this way, the transition can be represented by a vertical line in the potential energy diagram as schematically represented in figure 1.2.[3, 4]

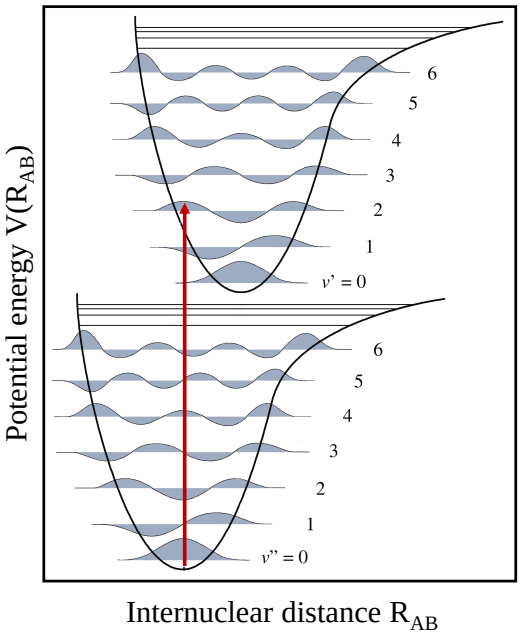

Figure 1.2. *Potential energy curves for the ground and excited states of a molecule AB. The vibrational levels are represented as wave functions, and a vertical arrow represents the electronic transition following the Franck-Condon principle. Since electronic transitions are very fast compared with nuclear motions, vibrational transitions are favored when they correspond to a minimal change in the nuclear coordinates. The potential wells are shown favoring transitions between v"=0 and v'=2.*

1.2.2. Types of photodissociation processes

Photodissociation is usually classified as direct or indirect depending on the presence or absence of potential barrier or other types of impediments before the excision of the excited molecule into the different fragments.

1.2.2.1. Direct photodissociation

In a direct photodissociation, the molecule dissociates into neutral fragments in their corresponding quantum states through a repulsive potential energy curve, related to an antibonding molecular orbital, without the participation of barriers or crossings with other surfaces. The consequence is that the time for the process to be completed is very short, and the lifetime of the excited complex is therefore very short, usually within a vibrational period (10^{-15}-10^{-13} s). Direct photodissociation often takes place with UV long pulses of low intensity and narrow bandwidth so that the absorption of the photon creates a single quantum state in the upper electronic manifold being the energy of the excited state the energy transferred by the photon plus the internal energy of the parent molecule. According to the reflection principle,[5] the energy dependence of the absorption spectrum and the final distribution of the product states is directly dependent on the distribution of the initial coordinates of the parent molecule in the ground electronic state. The corresponding absorption spectrum has no structure; it is

an absorption continuum. Thus, when the excitation occurs to a single excited state and from the ground vibrational state of the ground electronic state, the shape of the spectrum is approximately Gaussian.

Figure 1.3 represents the case of a direct photodissociation of a molecule AB from a repulsive excited state AB* along the reaction coordinate R_{AB}. The molecule evolves on the repulsive potential energy curve to give rise to fragments A and B.

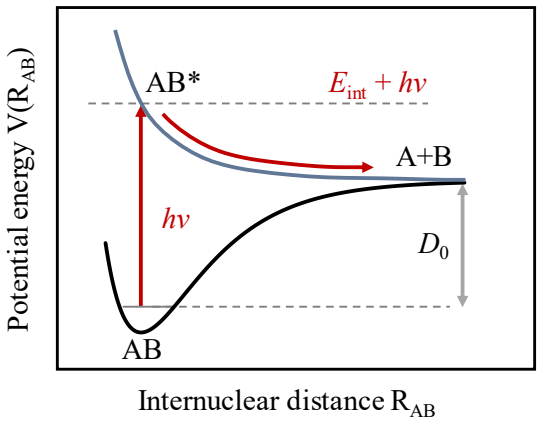

Figure 1.3. *Representation of a direct photodissociation for a molecule AB after one-photon absorption with energy hv, dissociating via one excited state into fragments A and B, along the reaction coordinate R_{AB}. The vertical arrow in light grey represents the dissociation energy D_0. Figure adapted from reference* [5].

Direct photodissociation can also take place through other mechanisms. For example, the absorption of several photons of intense lasers in the infrared (IR) region can produce the excitation of an ensemble of quantum states above the dissociation threshold producing the cleavage of the bond *via* the ground state. This case is represented in figure 1.4.

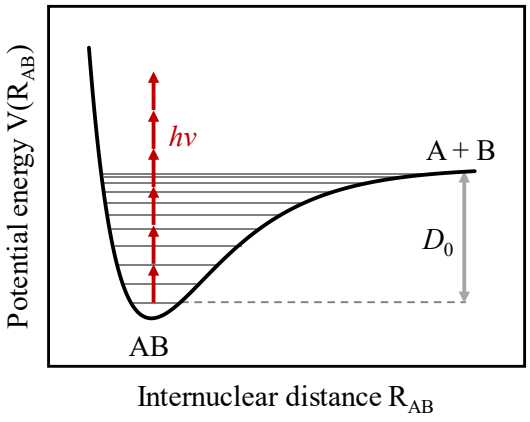

Figure 1.4. *Representation of a direct photodissociation for a molecule AB after multiphoton absorption of photons with energy hv, typically in the IR, dissociating via the ground-state into fragments A and B, along the reaction coordinate R_{AB}. The absorption of n photons produces a broad ensemble of quantum states above the dissociation threshold. Figure adapted from reference* [5].

1.2.2.2. Indirect photodissociation

In the case of indirect photodissociation, the bond cleavage is not instantaneous. Once the molecule is promoted to an excited electronic state, it faces impediments such as the existence of potential barriers or other types of dynamic constraints that must overcome to dissociate. The presence of these impediments considerably increases the average lifetime of the excited state, being longer than several periods of molecular vibration, and thus, the timescale of this process is of the order of 10^{-12} s or longer. The theoretical treatment of indirect photodissociation requires a fully quantum-mechanical description.[5] The corresponding absorption spectrum may have a discrete structure since the excitation is to a bound state. Indirect dissociation also has multiple variants. The three types of indirect photodissociation are represented in figure 1.5.

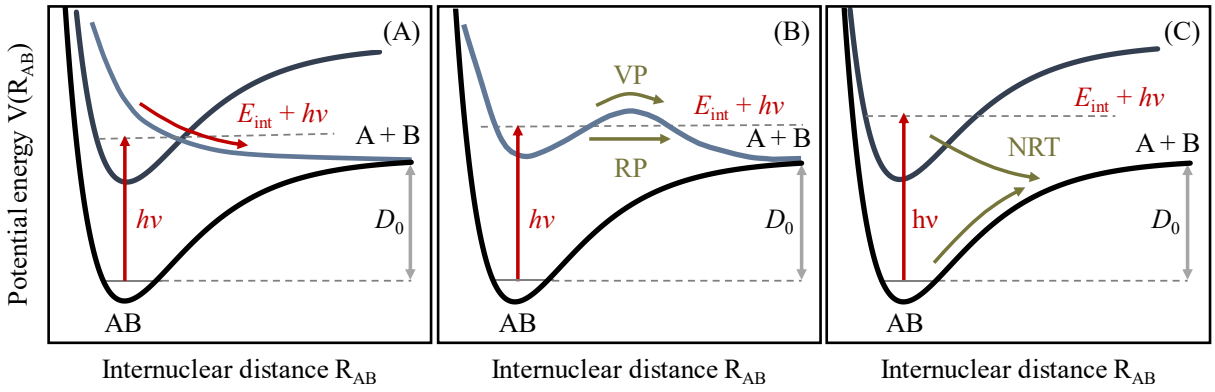

Figure 1.5. *Representation of indirect photodissociation processes for a molecule AB. (A) Electronic predissociation; once the molecule is excited into a bound state, photodissociation takes place through a transition or coupling to a dissociative state. (B) Vibrational or rotational predissociation due to absorption into a quasi-bound state where an exit barrier exists. (C) Unimolecular dissociation, in which the molecule dissociates from the ground electronic state by a non-radiative transition (NRT) such as internal conversion from an excited bound state. Figure adapted from reference [5].*

Figure 1.5 (A) represents one of the most relevant cases of indirect photodissociation called Herzberg type I electronic predissociation. The molecule is firstly excited into an excited bound electronic state. Nevertheless, this state is coupled at the same time with another excited repulsive electronic state, through which the molecule can dissociate; thus, dissociation occurs through a different state from the initially excited one. Predissociation timescales depend on the coupling between the different states involved, which defines the probability of transition from the bound state to the repulsive state.

Figure 1.5 (B) represents the case of an indirect photodissociation *via* excitation to a quasi-bound state. This type of indirect photodissociation is called Herzberg type II vibrational predissociation. The immediate bond cleavage does not occur due to the existence of a barrier in the exit region that blocks the dissociation channel. However, photodissociation can eventually occur through an intramolecular

redistribution of vibrational energy between the different degrees of nuclear freedom (vibrational predissociation) or by tunnel effect (rotational predissociation). The timescale ranges from a few to thousands of vibrational oscillation periods depending on the speed with which the barrier is crossed or the efficiency of the internal energy redistribution between the different degrees of freedom of the excited state. This longer duration entails that the fragments' final states distribution is not dependent on the distribution of the initial coordinates of the parent molecule in the ground electronic state, as occurs in a direct photodissociation.

In the third case, represented in figure 1.5 (C), the parent molecule is excited to a bound state from which, by internal conversion, it can return to the ground state *via* a non-radiative transition with a high internal energy content above the dissociation threshold, and therefore, dissociation takes place.

The different photodissociation types can occur simultaneously depending on the characteristics of the various excited electronic states of the molecule and the excitation energy. Figure 1.6 shows an example of a molecule AB, in which three possible excitation pathways, a, b, and c, from the ground electronic state, X(Σ), to the excited states A(Π) (bound), B(Σ) (repulsive), C(Σ) (bound) and D(Π) (repulsive) are opened giving rise to three different dissociation channels: fragment A, in the ground state, in correlation with fragment B in three possible quantum states i, j and k.

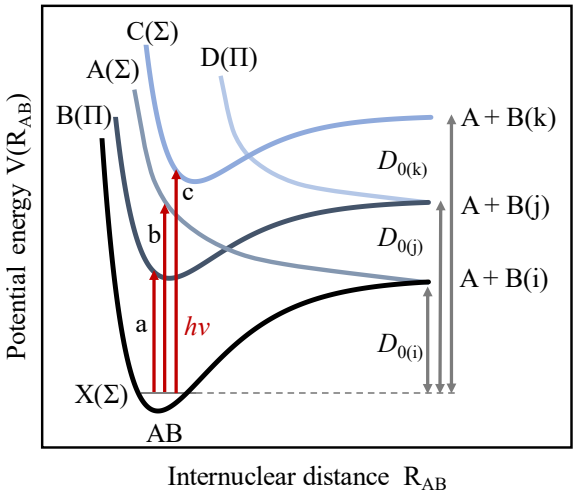

Figure 1.6. *Potential energy curves for a molecule AB where different possible photodissociation pathways are represented; (a) Direct excitation to the bound state A(Π), which correlates with the second dissociation limit A+B(j); however, from A(Π), it is also possible to access the first dissociation limit A+B(i) through the crossing of A(Π) with B(Σ). (b) Direct excitation to the dissociative state B(Σ), which correlates with the first dissociation limit A+B(i). (c) Direct excitation to a second bound state C(Σ) that correlates with the third dissociation limit A+B (k), and similarly to the previous situation, C(Σ) is crossed by another dissociative state D(Π) that correlates with the second dissociation limit A+B(j).*

In case (a), the initial absorption promotes the molecule to the bound state A(Π), which correlates to the second dissociation limit, i.e., A+B(j). However, a transition from the A(Π) state to the repulsive B(Σ) state is also possible, and the products A+B(i) of the first dissociation limit can be obtained. In case (b), the initial absorption promotes the molecule to the B(Σ) state, which is dissociative and correlates with the first dissociation limit, i.e., A+B(i). In case (c), the initial absorption promotes the molecule to state C(Σ), which correlates with the third dissociation limit, *i.e.*, A+B(k). Also, predissociation through a fourth dissociative state D(Π) can lead to the formation of products A+B(j) corresponding to the second dissociation limit.

1.2.3. Conical intersections

Molecular photodissociation can occur along multiple photodissociation channels, not those directly correlated with the initially excited state. For this reason, there must be a crossing point between potential energy surfaces that allows the total or partial transfer of population from the initially excited state to another that correlates with the final dissociation channel. These junctions are called conical intersections.

A conical intersection is defined as the set of molecular geometries where two potential energy surfaces have exact degeneracy in the multidimensional nuclear coordinate space. The dimensions of the space of the conical intersection are (3N-6(5))-2. A system can evolve by modifying these 3N-8(7) coordinates without breaking the degeneration. The two coordinates that break degeneration expand the so-called branching space.[6, 7] Representing the energy of the two states involved in the intersection on the coordinates of the branching space results in a shape of a double funnel or double cone as depicted in figure 1.7,[8, 9] which gives the conical intersection its name.

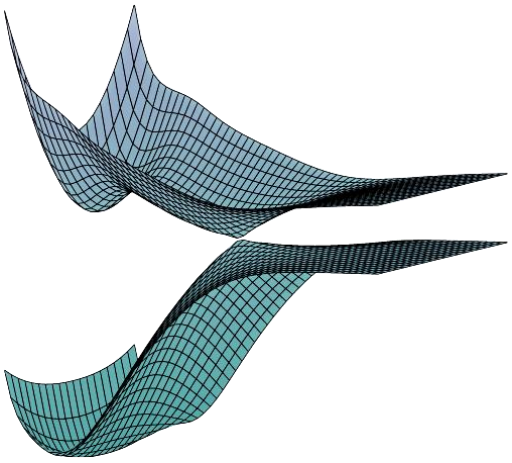

Figure 1.7. *Representation of a conical intersection between two potential energy surfaces. Its presence enables the possibility of non-adiabatic processes to occur. Figure adapted from reference [10].*

The conditions for conical intersections were first introduced by von Neumann and Wigner in 1929,[6] two years after the Born-Oppenheimer approximation first description.[1] Broadly speaking, for this intersection to occur, two conditions must be met: that the energy of the two involved states, calculated without considering the interaction between them, is the same and that the interaction between them is null.[6] In this context, the Born-Oppenheimer approximation is no longer valid, allowing non-adiabatic processes to take place.[7] Non-radiative decay from one potential energy surface to another can occur at any point on the hypersurface of the conical intersection. However, the low-energy regions of the intersection are the most important, as they correspond to the points most likely to undergo internal conversion or crossover between states.

Conical intersections are highly present in polyatomic systems and are essential for the rationalization of many photochemical phenomena because they are responsible for the possible formation of several products through different dissociation channels. The conditions met for conical intersections cause very strong electronic interstate couplings as well as local vibrational mode-mode couplings; thus, as first pointed out by Teller in 1937,[8] conical intersections dominate non-adiabatic nuclear dynamics at the shortest (femtosecond) timescales.[7, 8]

1.2.4. Quantum yield and branching ratio

The quantum yield Φ is defined as the proportion of a given photoproduct in a given quantum state in relation to the amount of that photoproduct in all possible quantum states in which it can be formed in the photodissociation process considering the excitation energy:

$$\Phi = \frac{[A]}{[A] + [A^*]} \tag{1.5}$$

$$\Phi^* = \frac{[A^*]}{[A] + [A^*]} \tag{1.6}$$

where, Φ and Φ* are the quantum yields for the formation of the photoproduct A in its ground state A or excited state A*. The quotient between quantum yields Φ and Φ* is called branching ratio.

Naturally, the quantum yield is defined in the case when there are different photodissociation pathways opened upon excitation at a given excitation wavelength, for example, due to the absorption of different states or the presence of state crossings, such as conical intersections.

1.2.5. Photoionization and dissociative photoionization

In addition to photodissociation, depending on the excitation energy other photoinduced processes can occur, such as photoionization and dissociative photoionization. Figure 1.8 represents the three different types of photoinduced processes for a molecule AB along the reaction coordinate R_{AB}.

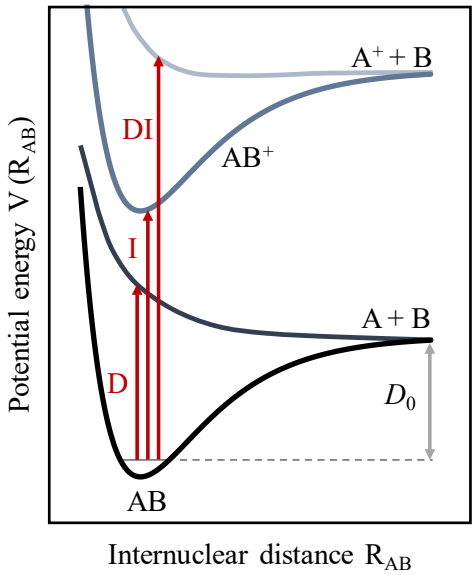

Figure 1.8. *Representation of a set of potential energy curves for a molecule AB and its cation AB^+. Several possible photoinitiated processes are displayed: photodissociation (D), photoionization (I) and dissociative photoionization (DI).*

In a photoionization process, represented by the equation (1.7), the energy of the absorbed photon(s) is equal to or greater than the ionization potential (IP) of the molecule, thus producing the removal of the most loosely bound electron from its valence shell. In this way, the molecule turns in its cationic form either in its ground state or in excited states and with a certain content of rovibrational excitation. The photoelectron emission is a direct and non-resonant process[11] that takes place on the attosecond timescale (1 attosecond=10^{-18} s).[12]

$$AB + nh\nu \rightarrow AB^+ + e^- \tag{1.7}$$

where *AB* represents the initial parent molecule in the ground state, $nh\nu$ is the energy of the absorbed *n* number of photons of frequency *v*, AB^+ is the ionized parent molecule and e^- is the ejected electron.

Generally, the number of absorbed photons is the minimum required for ionization to occur. However, processes involving more photons than the minimum necessary can also take place, leading to the so-called above-threshold ionization (ATI). ATI readily appears employing light pulses short enough to eliminate the influence of collisions, *i.e.*, at intensities above 1 TW/cm^2.[13] The kinetic energy of the electron is then given by:

$$E_{kin} = (k+s)\cdot h\nu - IP \tag{1.8}$$

where E_{kin} is the kinetic energy of the electron, k is the minimum number of the absorbed photons of energy $h\nu$ required for photoionization, s is the number of extra absorbed photons and IP is the ionization potential of the molecule.[14]

Photoionization can be direct when the molecular cation is formed directly in the ionic state with quasi-instantaneous electron ejection or indirect, when the excitation promotes the neutral molecule to a highly excited Rydberg state above the IP, with subsequent relaxation to the ionic state and electron ejection, in a process commonly known as autoionization.[15]

Photoionization is usually studied through photoemission/photoelectron spectroscopy (PES). The energy, abundance and angular distributions of the ejected photoelectrons are a fingerprint of the molecular orbitals from which they are originated, and thus, they provide relevant information of the molecular electronic structure. The photoelectron spectrum is constituted by bands, each corresponding to the removal of an electron from a particular molecular orbital. The structure of the band is related to the different vibrational and rotational levels within each of the electronic states of the ion. Thus, provided that the rotational structure is not predominant, it gives information about the active vibrational modes and, therefore, it allows to determine the structure and the symmetry of the electronic states of the cation.[16] If ATI occurs, the spectrum presents, aside from the main peak, successive peaks separated by the photon energy.[17]

Dissociative photoionization represented by the equation (1.9), can be conceived as a combination of photodissociation and photoionization. In this case, due to the photon absorption, the parent molecule can be promoted to an excited repulsive ionic state, producing the loss of an electron and the fragmentation of the molecule into a neutral and an ionic fragment. Dissociative photoionization can be classified as well as direct or indirect.

$$AB + nh\nu \rightarrow A^{+} + B + e^{-} \tag{1.9}$$

where AB represents the initial parent molecule in the ground state, $nh\nu$ is the energy of the absorbed n number of photons of frequency ν, A^{+} is the ionized photofragment, B is the neutral fragment and e^{-} is the ejected electron.

1.3. KINEMATICS AND ANGULAR DISTRIBUTION OF PHOTOPRODUCTS

1.3.1. Formation of Newton spheres

If the molecule absorbs photons with an energy equal or greater than the dissociation energy, the bond cleavage is produced, leading to two fragments that are ejected in opposite directions in space with the same linear momentum. Depending on whether photodissociation, photoionization or dissociative photoionization takes place, the distribution of the total translational energy is different.

In a photodissociation process, the total translational energy is divided between the two fragments to ensure momentum and energy conservation.

In a photoionization process, as the mass of the electron is much less than the mass of the ionized parent molecule, the electron receives practically all the translational energy. Therefore, the ion appears with a negligible amount of translational energy.

In dissociative photoionization, it involves a fragmentation into three bodies and, from a kinematical point of view, is a mixture of photodissociation and photoionization. The electron takes almost all the excess energy in the ionization step, usually in a potential energy surface region in which there is a strong potential interaction between the fragments. So, when the bond is broken, this energy is transformed into translational energy, and therefore, fragments can be observed with a non-negligible amount of translational energy.

If the dissociation of a single molecule is considered as an event, and the spatial origin is set in the center of mass (CM) of the molecule, for a given dissociation channel, each event generates fragments with the same velocity but different directions, *i.e.*, each event generates fragments A with the same velocity but in different directions and the same happens for fragments B. The sum of all photodissociation events results in a spherical distribution in the velocity space commonly called Newton sphere. Each fragment with a different speed generates a different Newton sphere.

Figure 1.9 shows, as an example, two events for which the mass of fragment A is considered to be lower than the mass of fragment B and, therefore, the velocity of fragment A is higher than that of fragment B. The size of the sphere provides information on the internal and translational energy balance of the process. Equally interesting is the surface pattern of the Newton sphere as it provides information about the angular distribution of the photoproducts representing the probability of finding the fragments preferentially ejected in certain regions of the space.

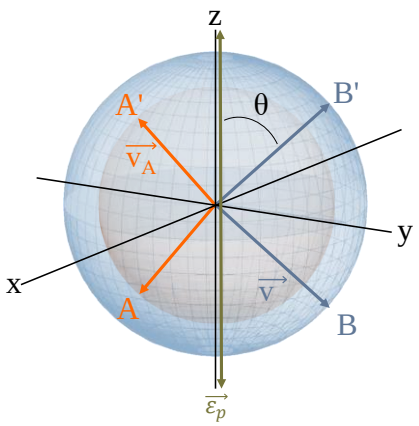

***Figure 1.9**. Newton spheres corresponding to two events of the photodissociation of a molecule AB. The mass of fragment A is greater than the mass of fragment B and therefore, the speed of fragment B is greater than that of fragment A, leading fragments A to smaller Newton spheres.*

1.3.2. Kinematics of photodissociation and photoionization

If a molecule AB breaks into two fragments A and B, the energy balance of the photodissociation is given by:

$$E_{\text{int}}(AB) + E_{trans}(AB) + nh\nu = E_{\text{int}}(A) + E_{\text{int}}(B) + E_{trans}(A) + E_{trans}(B) + D_0 \qquad (1.10)$$

where E_{int} and E_{trans} are the internal energy and the translational energy of the molecule *AB* of the fragments *A* and *B*, respectively, *nhv* is the energy of the absorbed *n* number of photons of frequency *v* and D_0 is the dissociation energy.

If working under supersonic expansion conditions, the internal energy E_{int}(AB) of the molecule can be considered as negligible as supersonic expansion leads to a strong cooling of the internal states of the parent molecule. If, in addition, the origin of coordinates is placed in the CM of the molecule, the translational energy E_{trans}(AB) of the molecule AB can be neglected as well. In this way, the equation (1.10) can be simplified, defining the available energy E_{av} as:

$$E_{av} = nh\nu - D_0 = E_{\text{int}}(A) + E_{\text{int}}(B) + E_{trans}(A) + E_{trans}(B) \qquad (1.11)$$

where E_{av} is the available energy, *nhv* is the energy of the absorbed *n* number of photons of frequency *v*, D_0 is the dissociation energy, E_{int} and E_{trans} are the internal energy and the translational energy of the fragments *A* and *B*.

In the same way, it is possible to define the kinetic energy release (KER) as:

$$KER = E_{trans}(A) + E_{trans}(B) = \frac{1}{2} m_A \left|\overrightarrow{v_A}\right|^2 + \frac{1}{2} m_B \left|\overrightarrow{v_B}\right|^2 \tag{1.12}$$

where *KER* is the kinetic energy release, E_{trans} is the translational energy of the fragments *A* and *B*, m_A and m_B are the masses of the fragments *A* and *B* and $|\overrightarrow{v_A}|$ and $|\overrightarrow{v_B}|$ are the modules of the velocity vector of each fragment. The direction of these velocity vectors is measured relative to the direction of the light polarization vector, $\overrightarrow{\varepsilon_p}$, typically defined along the Z axis. The angle formed by each velocity vector and the light polarization vector is denoted as θ (see figure 1.9).

The linear momentum conservation in the CM implies that:

$$m_A \overrightarrow{v_A} + m_B \overrightarrow{v_B} = 0 \tag{1.13}$$

So, combining equations (1.12) and (1.13), the translational energy of each fragment A and B can be estimated as:

$$E_{trans}(A) = \frac{m_B}{m_A + m_B} KER \tag{1.14}$$

$$E_{trans}(B) = \frac{m_A}{m_A + m_B} KER \tag{1.15}$$

where E_{trans} is the translational energy of the fragments *A* and *B*, $m_A/m_{A+}m_B$ and $m_B/m_{A+}m_B$ are the so-called mass partitioning factors.

The KER is directly related to the available energy E_{av} by:

$$KER = E_{av} - E_{\text{int}}(A) - E_{\text{int}}(B) = nh\nu - D_0 - E_{\text{int}}(A) - E_{\text{int}}(B) \tag{1.16}$$

where both the excitation energy $nh\nu$ and the internal energy E_{int} of each fragment are known. The equation (1.16) can be used to determine the dissociation energy D_0 in the case this value is unknown.

In the case of photoionization, the energy balance is given by:

$$E_{\text{int}}(AB) + E_{trans}(AB) + nh\nu = E_{\text{int}}(AB^+) + E_{trans}(AB^+) + E_{trans}(e^-) + IP \tag{1.17}$$

where E_{int} is the internal energy of the molecule *AB*, the cation AB^+ and fragments *A* and *B*, $nh\nu$ is the energy of the absorbed *n* number of photons of frequency ν, E_{trans} is the translational energy of the molecule *AB*, the cation AB^+ and the ejected electron e^-, and *IP* is the ionization potential.

Likewise, the energy balance can be simplified if the internal E_{int}(AB) and the translational energy E_{trans}(AB) energy of the parent molecule AB are considered negligible. Due to the conservation of linear momentum, most of the excess energy is transformed into translational energy of the electron, leaving the ion with a very low ejection velocity; thus, the translational energy of the ionized parent molecule $E_{trans}(AB^+)$ can also be neglected. Regarding the internal energy of the ionized parent molecule $E_{int}(AB^+)$, it does not necessarily have to be zero. Thus, the total available energy E_{av} is given by:[11]

$$E_{av} = nh\nu - IP = E_{trans}(e^-) + E_{int}(AB^+) \tag{1.18}$$

where E_{av} is the available energy, $nh\nu$ is the energy of the absorbed *n* number of photons of frequency ν, *IP* is the ionization potential, E_{trans} is the translational energy of the ejected electron e^-, and E_{int} is the internal energy of the molecule AB.

The total translational energy E_{trans} and the translational energy of photoelectrons $E_{trans}(e^-)$ originated from the ionization of the parent molecule AB can be estimated as:

$$E_{trans}(e^-) = E_{av} - E_{int}(AB^+) \tag{1.19}$$

$$E_{trans}(e^-) = \frac{m_{AB^+}}{m_{AB}} E_{trans} \rightarrow E_{trans}(e^-) = E_{trans} \tag{1.20}$$

where E_{trans} is the translational energy of the ejected electron e^-, E_{av} is the available energy, E_{int} is the internal energy of the cation AB^+, m_{AB^+} is the mass of the ionized parent molecule, and m_{AB} is the mass of the parent molecule before being ionized. As the mass of the parent molecule m_{AB} is practically the same as the ionized parent molecule m_{AB^+}, then the translational energy E_{trans} is equal to the electron translational energy $E_{trans}(e^-)$.

In general, the energy of the photoelectrons is described in terms of the binding energy (BI) which accounts for the difference in energy between the ionized and neutral atoms and it is independent of the excitation wavelength. The BI can be calculated as:

$$BI = nh\nu - E_{trans}(e^-) \tag{1.21}$$

where *BI* is the binding energy, *nhv* is the energy of the *n* photons of *v* frequency and $E_{trans}(e^-)$ is the translational energy of the photoelectrons.

1.3.3. Angular distribution of photoproducts

In addition to the translational energy distribution of the fragments, its angular distribution provides valuable information regarding the photodissociation mechanism. This distribution of particles on a Newton's spheres is generally anisotropic and is given, in part, by the direction of the transition dipole moment vector $\vec{\mu}$ with respect to the coordinates of the molecular system. The electronic transition between two states, produced by the absorption of a photon of linearly polarized light, preferably takes place when the light polarization vector $\vec{\varepsilon_p}$ is aligned with transition dipole moment vector $\vec{\mu}$. This, in turn, confers an initial alignment to the excited molecules in the laboratory framework.

The nature of the transition depends on the symmetry of the initial and final states. Thus, for a diatomic molecule, two extreme situations can be considered: parallel and perpendicular transitions. In parallel transitions, the transition dipole moment $\vec{\mu}$ is parallel to the internuclear axis of the molecule. This occurs in transitions between equal symmetry states ($\Sigma\leftrightarrow\Sigma$ or $\Pi\leftrightarrow\Pi$ transitions). In contrast, in perpendicular transitions, the transition dipole moment $\vec{\mu}$ is perpendicular to the internuclear axis of the molecule. This occurs in transitions between different symmetry states ($\Sigma\leftrightarrow\Pi$ transitions).

If after absorption of linearly polarized light, the dissociation is fast enough, the preferential alignment of the excited molecules is transmitted to the output velocities of the fragments, $\vec{v_t}$, since this velocity is aligned in the direction of the internuclear axis of the diatomic molecule, thus establishing a relationship between the velocity vector of the fragments $\vec{v_t}$ and the light polarization vector $\vec{\varepsilon_p}$. In this case, anisotropic angular distributions are observed. This situation occurs in fast and direct photodissociation processes with timescales much faster than the rotational period of the molecule.

In the case of predissociation, the rotation of the molecule in the excited bound state plays a leading role with regard to the angular distribution of the fragments. Indeed, when the predissociation lifetime is of the same order as the rotational period of the molecule, the spatial alignment is lost over time, leading to more isotropic angular distributions.

In all cases, the angular distribution of fragments from photodissociation after excitation with a single photon of linearly polarized light and in the absence of polarization effects in the fragments, such as alignment of the orbital angular momentum (atomic fragment) or rotational angular momentum (molecular fragment), can be described by the flowing equation:[18-20]

$$I(\theta) = \frac{\sigma}{4\pi}[1 + \beta P_2(\cos\theta)] \tag{1.22}$$

where $I(\theta)$ is the angular distribution of the photoproducts as a function of the angle θ between the light polarization vector $\vec{\varepsilon_p}$ and the velocity of the fragments $\vec{v_t}$, σ is the effective absorption cross-section, 4π is a normalization factor for a full solid angle, β is the anisotropy parameter, which characterizes the shape of the angular distribution and $P_2(\cos\theta)$ is the second Legendre polynomial, defined by:

$$P_2(\cos\theta) = \frac{1}{2}(3\cos^2\theta - 1) \tag{1.23}$$

In this work, polyatomic systems are studied assuming they behave as diatomic molecules along the dissociating coordinate. Under this approximation, for a fast dissociation of a diatomic molecule, the equation (1.22) takes the following values for the limit cases for pure parallel or pure perpendicular transitions.

Pure parallel transition β=2 $I(\theta) \propto \cos^2\theta$ (1.24)

Pure perpendicular transition β=-1 $I(\theta) \propto \sin^2\theta$ (1.25)

Figure 1.10 shows a representation of the equation (1.22) for a given Newton sphere for the limit anisotropy values of β=2 (parallel transition), β=-1 (perpendicular transition) and for an isotropic distribution with β=0.

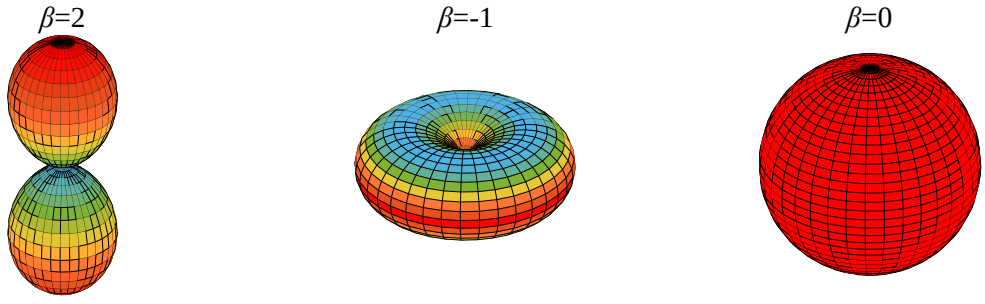

$I(\theta) = \frac{3}{4\pi}\cos^2(\theta)$ $I(\theta) = \frac{3}{8\pi}\sin^2(\theta)$ $I(\theta) = \frac{1}{4\pi}$

Figure 1.10. *Representation of equation (1.22) for a given Newton sphere for the limit values of the anisotropy parameter β=2, β=-1 and β=0. When β=2, fragment's distribution takes the form of* $I(\theta) \propto \cos^2(\theta)$ *(pure parallel transition), when β=-1, fragment distribution takes the form of* $I(\theta) \propto \sin^2(\theta)$ *(pure perpendicular transition) and when β=0 an isotropic distribution is found. The areas with warmer colors (red) represent the orientations with the highest probability of fragmentation, while the areas with colder colors (blue) represent the orientations with the least probability of fragmentation. Figure adapted from reference* [21].

The anisotropy parameter β can take values between the limit values corresponding to pure parallel (β=2) and perpendicular (β=-1) transitions. Thus, the angular distribution can be expressed as a linear combination of these two extreme cases by:

$$I(\theta)=A\cdot\cos^2\theta+B\cdot\sin^2\theta \tag{1.26}$$

where A and B are the participation coefficients of each type of transition and equal to:

$$A=\frac{(1+\beta)}{4\pi} \tag{1.27}$$

$$B=\frac{(1-\beta)}{4\pi} \tag{1.28}$$

So, it is possible to determine the percentage of the parallel or perpendicular character of the initial transition through the angular distribution. The anisotropy parameter β provides information about the electronic transition and the symmetries of the excited states in the case of multi-channel processes.

In the case of orbital angular momentum alignment effects (atomic fragments) or rotational alignment effects (molecular fragments), and mainly when the fragments are detected by (2+1) resonance-enhanced multiphoton ionization (REMPI), in a one-photon excitation process with linearly polarized light, the equation (1.22) is no longer valid and additional terms must be included:[18-20]

$$I(\theta)=\frac{\sigma}{4\pi}\sum_{n=0}^{N}\beta_{2n}P_{2n}(\cos\theta) \tag{1.29}$$

where $I(\theta)$ is the angular distribution of the photoproducts as a function of the angle θ between the light polarization vector $\vec{\varepsilon_p}$ and the velocity of the fragments $\vec{v_i}$, σ is the effective absorption cross-section, 4π is a normalization factor for a full solid angle, β_{2n}^{N} are the anisotropy parameters and $P_n(\cos\theta)$ the n-order Legendre polynomials.

This expansion is also suitable for cases of multiphoton absorption. Multiphoton processes of more than two photons can be approximately studied using only two anisotropy parameters β_2 and β_4. In this case, the anisotropy parameters β_2 and β_4 also have limit values, as reflected in table 1.1, dependent on the different number of absorbed photons.[22]

Table 1.1. *Limit values of anisotropy parameters β_2 and β_4 for parallel and perpendicular transitions dependent on the different number of absorbed photons.*[22]

	Parallel transition		Perpendicular transition	
Number of photons	β_2	β_4	β_2	β_4
1	2	0	– 1	0
2	2.86	1.14	– 1.43	0.43
3	3.33	2.18	– 1.67	0.82
4	3.64	3.02	– 1.83	1.13

1.3.3.1. Anisotropy upon molecular rotation

When the dissociation lifetime is longer than the rotational period of the molecule, the spatial alignment achieved by the absorption of linearly polarized light is lost over time due to the rotation of the parent molecule during the lifetime in the excited state. The greater the rotation of the molecule, the faster the initial alignment is lost, and therefore this alignment is transmitted to the photoproducts to a lesser extent. As a consequence, the products exit in all directions of space, leading to isotropic angular distributions.

When the lifetime τ of the parent molecule in the excited state is similar to the rotational period of the molecule τ_{rot}, the final anisotropy parameter $\beta(\omega, \tau)$ for a one-photon perpendicular transition can be described, following classical models by:[23, 24]

$$\beta(\omega,\tau) = \beta(0)\frac{1+(\omega\tau)^2}{1+4(\omega\tau)^2} \tag{1.30}$$

where $\beta(\omega, \tau)$ is the final anisotropy parameter, $\beta(0)$ is the initial anisotropy parameter which equals -1 for pure perpendicular transitions, τ is the lifetime of the molecule in the excited state and ω is the modulus of the angular velocity of the excited molecule so that the rotational energy is given by:

$$E_{rot} = \frac{I_a\omega_a^2 + I_b\omega_b^2 + I_c\omega_c^2}{2} \tag{1.31}$$

being I_a, I_b and I_c the three moments of inertia of the molecule, whose values can be determined from rotational spectroscopy measurements or theoretical methods.

Note that although the angular distribution tends to become more isotropic, the anisotropy parameter β never reaches a value of zero. The limit values of the anisotropy parameter β for predissociations are 0.5 for parallel transitions and -0.25 for perpendicular transitions.

Besides, the angular distribution of photoproducts can be written as:

$$I(\theta) = \int_0^\infty B(\omega; T_{rot}) \frac{\sigma}{4\pi} [1 + \beta(\omega, \tau) P_2(\cos\theta)] d\omega \tag{1.32}$$

where $B(\omega, T_{rot})$ is the Boltzmann distribution for the rotational temperature T_{rot} of the parent molecule. $B(\omega, T_{rot})$ can, in turn, be expressed as:

$$B(\omega; T_{rot}) = \exp\left(-\frac{E_{rot}}{k_B T_{rot}} \right) = \exp\left(-\frac{I_a \omega_a^2 + I_b \omega_b^2 + I_c \omega_c^2}{2 k_B T_{rot}} \right) \tag{1.33}$$

where k_B is the Boltzmann constant.

Equation (1.33) cannot be easily classically solved when all three moments of inertia have a role. In that case, it is more convenient to consider the Boltzmann distribution over the quantum rotational levels.

1.4. EXPERIMENTAL METHODS APPLIED TO PHOTODISSOCIATION

One of the fundamental steps in the complete characterization of a photodissociation process is identifying the fragments and determining their internal (vibrational, rotational) and translational energy content and their angular distribution. A more extensive characterization may include the orientation or alignment of any vector quantities of the products. For the complete characterization of photodissociation processes, imaging techniques are used.

1.4.1. Product imaging. Velocity map ion and photoelectron imaging

In the first photodissociation experiments, employing the so-called photofragment translational spectroscopy (PTS),[25, 26] a quadrupolar mass spectrometer (QMS) was used to detect the fragments arising from the photodissociation of a molecule, along the flight direction perpendicular to the mutually orthogonal molecular and laser beams. The velocity of the products was determined from the traveled distance and flight time. Additionally, the signal intensity was measured as a function of the angle between the laser polarization vector and the flight direction to obtain the angular distribution of photoproducts.

Nevertheless, one of the main drawbacks of PTS was the impossibility of determining the velocity distribution of state-selected products. This problem was addressed when in the late 1970s, Doppler spectroscopy was applied to molecular dynamics.[27, 28] By resolving the frequency shift of the light, *i.e.*,

the Doppler profile, it was possible to determine the angle between the direction of the scattered particle and the velocity distribution of state-selected species. Likewise, it was also possible to explore the vector correlations between, for example, the direction of a diatomic product's rotational vector and the relative recoil velocity vector.[29, 30]

A further development was made by Hall *et al.*[31] and Loo *et al.*,[32] who demonstrated that a Wiley-McLaren time-of-flight mass spectrometer (TOFMS)[33] could be used to create a one-dimensional projection of the three-dimensional velocity distribution of an ionized photodissociation product. The first forays into two-dimensional fragment detection were carried out by Solomon *et al.*[34] who showed that it was possible to visualize the direction of photodissociation using a hemispherical bulb coated on the interior with tellurium. Later on, Yates and co-workers in 1974 implemented a microchannel plate (MCP) amplifier backed by a phosphor screen as a detection system for the collection of electron stimulated ion desorption ion angular distributions (ESDIAD).[35]

In 1986, during a Faraday Discussion, Houston and Chandler had the idea of combining TOFMS and detection of charged products using MCPs and a fluorescent screen to "see" the products. Their ideas led to the first experimental results in 1987.[36] In their ion imaging photodissociation experiments of methyl iodide (CH_3I) at 266 nm, methyl radicals (CH_3) in their ground vibrational level ($v=0$) were ionized using a multiphoton process at 330 nm. Following ionization, the methyl (CH_3) fragments were accelerated towards the MCP by an electric field, until colliding against a detector composed of an MCP coupled with a phosphor screen, thus forming a bi-dimensional image of the ion sphere. In the first experiments, the image could clearly be seen by eye, and the screen was pictured with polaroid film. A later improvement used a CCD camera to record and average the results from each laser shot. Advantages of this technique soon became apparent. First, the image was the two-dimensional projection of the full, three-dimensional velocity distribution, correlating both speed and angular information about the ionized fragment. Second, the multiphoton ionization technique could typically be used to ionize a single vibrational/rotational state of the product. Assuming that the energy of the photon and the internal energy of the parent molecule were known, conservation of energy and linear momentum could be used to calculate the translational energy of the co-fragments. Nevertheless, the resolution of the technique was primarily limited by the significant volume of interaction between the molecules and the focused laser beam so that the spheres formed at different points flew into the detector producing a blurred and irregular image, as depicted in figure 1.11.

Figure 1.11. *Evolution of ion imaging techniques. Vibrationless methyl $CH_3(v=0)$ fragments images produced by projecting onto two dimensions the three-dimensional spatial distribution of products from photodissociation of CH_3I with 266 nm laser light. The plane of the projection is parallel to the polarization axis of the pump laser beam. Image obtained by Houston and Chandler in 1987.*[36]

In 1997, Eppink and Parker improved the ion imaging technique by developing the velocity map imaging (VMI) technique.[37] With this technique, it is possible to achieve a significant increase in resolution by using an Einzel lens system or "asymmetric immersion lens";[37] that is a gridless electrostatic lens system that focuses the trajectories of the charged spheres towards the detector by applying an inhomogeneous electric field. Through this upgraded version, the translational energy resolution with respect to conventional ion images was improved by a factor of 20, as reflected in figure 1.12, reaching a typical resolution of 2 to 10 %. Since then, VMI has become a valuable tool for the study of the molecular dynamics of photoinitiated chemical reactions.[38, 39]

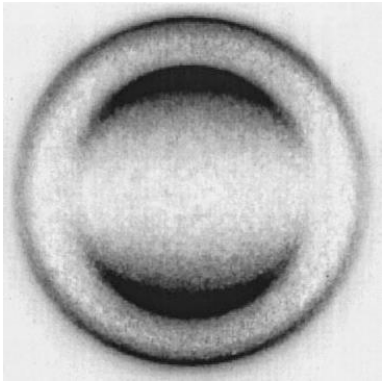

Figure 1.12. *Evolution of ion imaging techniques. Vibrationless methyl $CH_3(v=0)$ fragments images produced by projecting onto two dimensions the three-dimensional spatial distribution of products from photodissociation of CH_3I with 266 nm laser light. The plane of the projection is parallel to the polarization axis of the pump laser beam. Image obtained by Eppink and Parker in 1998.*[40]

The basis of the VMI technique is shown schematically in figure 1.13.

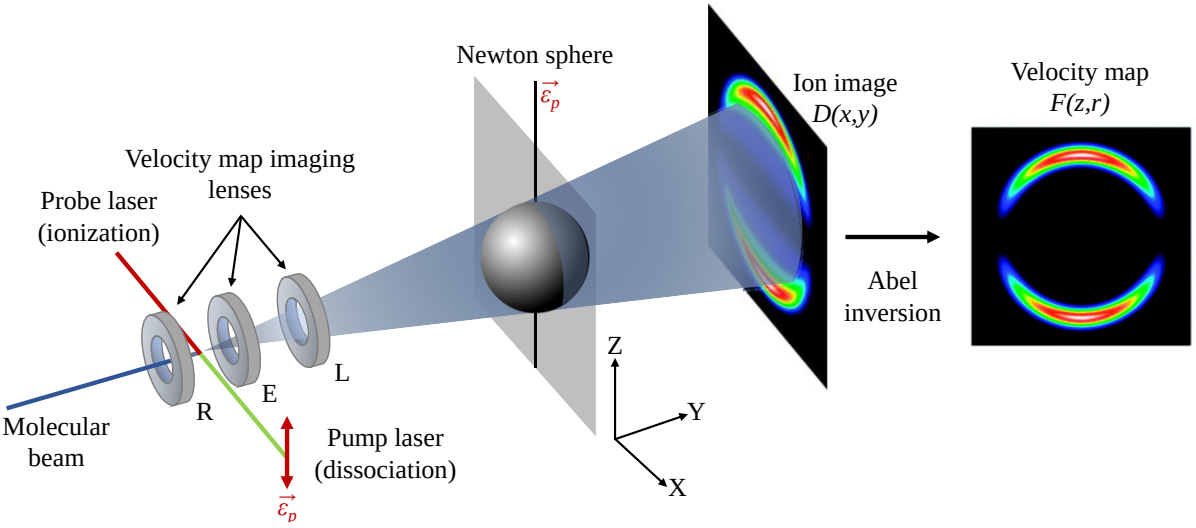

Figure 1.13. *Working principle of a VMI spectrometer. First, the pump laser interacts with the molecular beam between the repeller (R) and extractor (E) lenses producing the dissociation of the molecules. Afterward, the probe laser ionizes the photofragments generated after photodissociation. The electrostatic field created by the lenses accelerates the charged particles towards the detector. On their way, the ionized Newton spheres expand because of their translational energy. This spherical distribution is projected onto the bi-dimensional sensitive position detector constituted by an MCP coupled to a phosphor screen. The initial velocity distribution can be obtained via Abel-inversion. The red double arrow represents the direction of the linear polarization of the laser beam. Figure adapted from reference* [41].

A collimated molecular beam propagates along the Y axis direction and interacts with the photodissociation laser pulses, whose polarization must be parallel to the plane of the detector, the XY plane. In this way, the photodissociation of the molecules takes place. From the CM of the parent molecule, a pair of fragments are ejected in opposite directions so that the total translational energy is divided between them ensuring the energy and momentum conservation laws. For each fragment, a spherical velocity distribution in space with a specific anisotropy is originated. *i.e.*, a Newton sphere.

Afterward, the neutral fragments should be detected. Two of the most sensitive laser-based detection techniques are laser-induced fluorescence (LIF) and multiphoton ionization (MPI). MPI consists of irradiating an atomic or molecular sample with an energy suitable to reach the ionization threshold through the simultaneous absorption of several photons, in the UV or vacuum ultraviolet (VUV). If the energy of the first set of *m* photons resonantly excites a bound-bound transition to a high lying electronic state of the product and subsequently, additional *n* photons cause a bound free transition into the ionization continuum, the efficiency of the process increases several orders of magnitude leading to the so-called resonance-enhanced multiphoton ionization or (m+n) REMPI, schematically represented in figure 1.14.

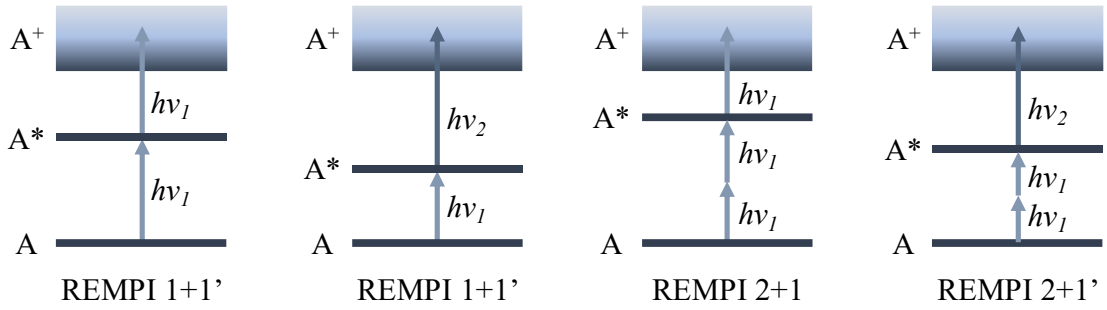

Figure 1.14. *Representation of different (m+n') REMPI schemes. The first number indicates the number of necessary photons to reach the intermediate excited state A*, and the second number indicates the number of photons needed to reach the ionization threshold A^+ from the intermediate state A*. The apostrophe next to the number indicates those photons with different wavelengths.*

The REMPI technique is widely used in photofragment detection due to its high selectivity to detect a particular fragment in a particular state, for example, a molecular fragment in a defined vibrational state or an atom in a specific electronic state.[42] The most significant advantages of this technique is that it does not significantly change the nascent velocity distributions of the neutral species as the electron takes all of the excess energy in the ionization, [43] and the increased efficiency in ion detection.[33]

The charged particles are formed in an electrostatic lens system, which essentially consists of three plates, as shown in figure 1.13, in a configuration that follows the original Wiley-McLaren design,[33] but without grids. The lenses are called referred to, from left to right, as repeller (R), extractor (E) and lens (L). Positive or negative voltages, for ion or photoelectron detection, respectively, are applied to the repeller and extractor plates so that an electric field is generated in the Z axis, allowing the extraction of the ionized particles towards the detector. The voltage ratio between the repeller and extractor plates must be appropriately chosen so that the ions with the same velocity vector are focused on the same position of the detector independently of their region of formation.[37] The third lens is grounded, producing the acceleration of the ionized Newton's spheres or photoelectrons towards a field-free zone called the time-of-flight (TOF) region. In this region, the particles fly with constant speed since they do not suffer any external forces, and they are temporarily separated due to the velocity differences acquired in the electric field zone. Thus, particles with different masses are discriminated by the different times they take to reach the detector. This effect is used to make a selective detection based on ion mass so that the detector is activated or "gated" only in the time interval corresponding to the arrival of the ion of interest.

Considering a photofragment, with a certain KER, with a speed v_y perpendicular to the free flight axis, the ions are arranged in a circular configuration of radius R. This radius depends on the TOF according to:

$$R \approx M v_y t \approx ML\sqrt{\frac{KER}{qV}} \tag{1.34}$$

where M is the magnification factor which takes values between 0.9 and 1.4, a constant that depends on the geometric characteristics of the electrostatic lens, L is the length of the flight zone, q is the charge of the particle, V is the electrostatic potential, v_y the speed of the particles in the direction perpendicular to the TOF axis and t the TOF of the particles.

The time of arrival of the ion to the detector is then given by:

$$t \approx M\frac{L}{v_z} \approx ML\sqrt{\frac{m}{2qV}} \tag{1.35}$$

where m is the mass of the particle and v_z is the speed of the particles on the TOF axis z. In this way, the system behaves like a TOFMS.

The spheres collide against the detector generating a bi-dimensional image, which is necessary to manipulate mathematically to retrieve the original three-dimensional distribution of the fragments.

1.4.2. Reconstruction of bi-dimensional images

The spatial distribution of particles reaching the detector is the projection of a three-dimensional object onto a plane. To extract relevant information about the photodissociation process, a method that allows the reconstruction of the three-dimensional distribution of particle speeds from this measured projection must be applied. Two types of methods are mainly used for this purpose: inversion methods and forward convolution methods.[44]

1.4.2.1. Inversion methods

Inversion methods assume that if the original three-dimensional distribution has cylindrical symmetry, then its two-dimensional projection on a plane containing this axis includes enough information to reconstruct the original three-dimensional distribution. This condition is ensured provided that the polarization direction of the dissociation and ionization lasers is parallel to the detector plane.

According to figure 1.13, if the detector is contained in the XZ plane, and since the polarization of the lasers in that propagation geometry can only be perpendicular to the X axis, it is mandatory to polarize the radiation along the Z axis to ensure cylindrical symmetry to apply the inversion methods.

Under these conditions, the velocity distributions on the cuts of Newton spheres by planes containing the Z axis are equivalent, and the inversion methods are focused on rebuilding these two-dimensional velocity distributions.

Considering the *z* axis as the cylindric symmetry axis, as shown in figure 1.15; $I(x, y, z)$ represents the three-dimensional distribution of the image and $P(x, z)$ is the bi-dimensional projection of it on the detector plane (*xz* plane).

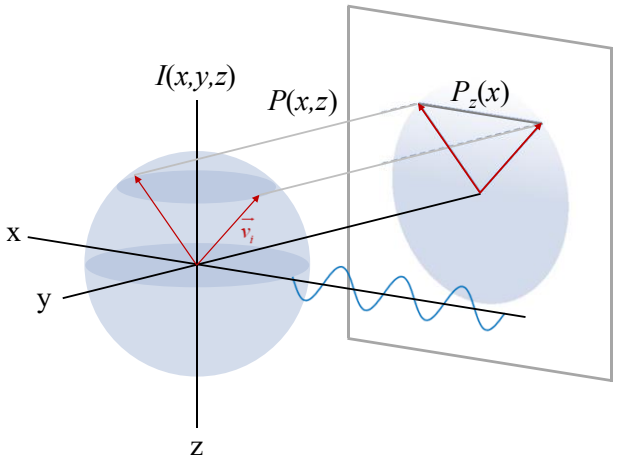

Figure 1.15. *Representation of the three-dimensional velocity distribution of fragments with cylindrical symmetry around the z axis and its projection on a bi-dimensional plane. In a VMI experiment, the detector is at the end of the y axis, and the laser propagates along the x axis with linear polarization parallel to the z axis. Figure adapted from reference* [45].

The bi-dimensional distribution of measured ions, $P(x, z)$, can be written based on the original three-dimensional distribution, $I(x, y, z)$ as:

$$P(x,z) = \int_{-\infty}^{\infty} I(x,y,z)dy \tag{1.36}$$

The intensity profile in *x* that has each value of *z* in the bi-dimensional projection P(*x*, *z*), *i.e.*, $P_z(x)$, is the projection of a two-dimensional function $I_z(x, y)$. This makes it possible to analyze each image to be done line by line (for each *z* value). Thus, if only one row of the image along the *x* axis for a given value of *z* is considered, being $z=z_0$, a function $f(x)$ that depends only on *x* can be defined and when substituted in equation (1.36) leads to:

$$f(x) = P(x,z_0) = \int_{-\infty}^{\infty} s(x,y)dy = 2\int_{0}^{\infty} s(x,y)dy \tag{1.37}$$

where $s(x, y)=I(x, y, z_0)$ and corresponds to a slice of the three-dimensional distribution perpendicular to the cylindrical symmetry axis.

From this point on, there are several mathematical procedures to recover $s(x, y)$ from $f(x)$, which is the set of measured functions, to reconstruct the original velocity distribution, such as the Abel transform, Fourier-Hankel transform,[46] the backward projection or onion peeling[44] or iterative methods.[47] Among the most recent methods of image inversion, it is worth mentioning the basis set expansion (BASEX) method,[48] in which the Abel transform method is applied, and its evolution, the basis set expansion in polar coordinates (pBASEX) method,[49] in which the BASEX method is applied in a polar coordinate system. Since both the BASEX and pBASEX methods are the two methods applied in the treatment of the images measured in the present work, they are described in some detail, and the Abel transform.

Abel transform is frequently used for the analysis of spherically or cylindrically symmetric functions. The Abel transform of an $s(r)$ function is given by:

$$f(x) = 2\int_x^\infty \frac{s(r)r}{\sqrt{r^2 - x^2}}\,dr \tag{1.38}$$

The inverse transform, by which $s(r)$ is retrieved from the measured function $f(x)$, is obtained by applying a Fourier transform according to:

$$s(r) = \frac{1}{\pi}\int_r^\infty \frac{df\,/\,dx}{\sqrt{x^2 - r^2}}\,dx \tag{1.39}$$

The equation (1.39) can be applied directly to extract $s(r)$ from the measured function $f(x)$. In this way, it is possible to reconstruct the original three-dimensional distribution since by applying the equation (1.37), for each slice of the projected image, $f(x, z_0)$, it is possible to obtain the function $s(r, z_0)$. However, solving the equation (1.39) is not easy due to the singularity of the function in $r^2=x^2$ and the fact that the derivative in the integral magnifies the noise of the measured image.

1.4.2.1.1 Fourier-Hankel transform

Fourier-Hankel transform, proposed by Smith *et al.*[46] works on Fourier transform of the equation (1.37):

$$F\{f(x)\} = \int_{-\infty}^{\infty}\int_{-\infty}^{\infty} s\left(\sqrt{x^2 + y^2}\right)e^{-2\pi i x q}\,dx\,dy \tag{1.40}$$

where $s(r)$ is obtained through:

$$s(r) = H[F\{f(x)\}] = 2\pi\int_0^\infty qJ_0(2\pi rq)\left[\int_{-\infty}^{\infty} f(x)e^{-2\pi xq}dx\right]dq \tag{1.41}$$

where J_0 is the zero-order Bessel function.

In other words, it is a matter of applying the Fourier transform to a one-dimensional function and then applying the inverse Hankel transform, which turns out to be the same as applying the inverse Abel transform to that function.

This method eliminates much of the noise introduced into the Abel transform; however, it is not completely removed since the Bessel function J_0 oscillates rapidly in the vicinity of the origin so that the noise is considerable along a central line of the reconstructed image.

1.4.2.1.2 Backward projection or onion peeling method

In the backward projection or onion peeling method,[44] a transform of the coordinates of the velocity distribution space (r, θ) is transmitted to the image plane (x, z). In general, this function is very complex, although when the electrostatic energy acquired by the ions in the acceleration region is much higher than its initial translational energy, it can be simplified. Hence, an analytical expression can be applied to project the points of the image measured backward to recover its origins in the distribution of speeds that want to be reconstructed.

1.4.2.1.3 Iterative methods

The method developed by Vrakking is an iterative method[47] in which, through the angular and velocity distributions obtained from the bi-dimensional image, a test three-dimensional distribution of speeds is generated, from which a test bi-dimensional image is reconstructed. The speed distributions taken from the measured bi-dimensional distributions and the test three-dimensional are compared, then corrections are applied to the test three-dimensional distributions, and the two bi-dimensional distributions are compared. These steps are repeated until the measured and calculated bi-dimensional distributions are equal. Since this method uses radial information, the noise is projected towards the center of the image, which usually does not contain relevant information. However, due to its iterative character, it is computationally time-consuming thus, direct reconstruction methods are generally preferred.

1.4.2.1.4 Basis set expansion (BASEX)

In the basis set expansion (BASEX) method, developed by Reisler *et al.*,[48] the data of the projection is expanded in a basis set of functions that are analytical projections of functions similar to

Gaussian functions but without singularities. The coefficients of this expansion directly provide the information required to reconstruct the three-dimensional distribution of speeds.

The three-dimensional distribution of speeds, which is cylindrically symmetric, can be described as a function that depends on two coordinates, $I=I(r, z)$, where the z axis is the axis of symmetry. The projection of this function in the xz plane of the detector, $P(x, z)$, is given by the Abel integral according to:

$$P(x,z) = 2\int_{|x|}^{\infty} \frac{rI(r,z)}{\sqrt{r^2 - x^2}}\, dr \tag{1.42}$$

In practical terms, the projection $P(x, z)$ is measured as a set of data whose elements are defined in a bi-dimensional space, $(x_i\, z_j)=(i, j)$, determined by the number of pixels in the charge-coupled device (CCD) camera, being the total size in pixels of $N_x \cdot N_z$, which is normally around 10^5-10^6. Thus, experimentally, a digitized projection function, P, is obtained whose P_{ij} elements are given by:

$$P_{ij} = s\int h(x - x_i, z - z_i)\, dx dz \int_{|x|}^{\infty} \frac{rI(r,z)}{\sqrt{r^2 - x^2}}\, dr \tag{1.43}$$

where $h(x, z)$ defines an instrumental function.

The idea of the BASEX method is to expand the $I(r, z)$ function into basis functions $f_k(r, z)$, in this way, according to:

$$I(r,z) = \sum_{k=0}^{K-1} C_k\, f_k(r,z) \tag{1.44}$$

It is then possible to describe the three-dimensional speed distribution function, $I(r, z)$ and its projection P, as expansions of basis set of functions using the same coefficients by:

$$P_{ij} = \sum_{k=0}^{K-1} C_k G_{kij} \tag{1.45}$$

or, expressed in matrix form by:

$$P = CG \tag{1.46}$$

where C is the vector of coefficients, $C=(C_0,\ldots,C_{K-1})$ and G the base projection matrix, $G=(G_0,...,G_{K-1})^T$.

It should be noted that, in general, the number of basis functions can be less or greater than the number of pixels, making the problem either insufficiently determined or containing too many ligatures. In that case, there is no G^{-1}, which is what should be calculated, in principle, to obtain the vector of coefficients *C*. A solution to this problem is found in the Tikhonov regularization procedure, [50] according to which coefficients *C* can be written as:

$$C = PG^T(GC^T + q^2 I)^{-1} \tag{1.47}$$

where *q* is a regularization parameter, and *I* is the identity matrix. The separability of the problem in *x* and *z* allows writing the functions as equations (1.48) and (1.49):

$$I(r,z) = \sum_{k=0}^{K_x-1}\sum_{m=0}^{K_z-1} C_{km}\rho_k(r)\zeta_m(z) \tag{1.48}$$

$$P_{ij} = \sum_{k=0}^{K-1} C_{km} X_{ki} Z_{mj} \tag{1.49}$$

i.e., using two-dimensional basis functions, and finally getting the vector of *C* coefficients as *C=APB*, where:

$$A(XX^T + q_1^2 I)^{-1} X \tag{1.50}$$

$$B = Z^T(ZZ^T + q_2^2 I)^{-1} \tag{1.51}$$

and these matrices are written as:

$$X_{ki} = 2\int h_x(x - x_i)dx \int_{|x|}^{\infty} \frac{r\rho_k(r)}{\sqrt{r^2 - x^2}} dr \tag{1.52}$$

$$Z_{mj} = \int h_z(z - z_j)\zeta_m(z)dz \tag{1.53}$$

Because arrays *A* and *B* are independent of projection *P*, there is only the need to calculate them once and store them. In this way, the calculation of the vector of coefficients *C* can be performed through simple multiplication of matrices.

After performing the inversion, the next step is to obtain the velocity distributions, $P(v)$, for which the signal (inverted) must be integrated over the angle for each radius by applying:

$$P(v) = \frac{1}{(P(v))_{\max}} \int_0^{\pi} I(v,\theta) v \sin\theta d\theta \tag{1.54}$$

being $1/(P(v)_{max}$ a normalization constant, v=r, and θ can be obtained from z=r·cosθ. From this equation, BASEX can apply two methods to calculate the velocity distribution.

The first method, and the one that BASEX applies by default, is based on transforming equation (1.54) into a discretized form:

$$P(v) = \frac{1}{(P(v))_{\max}} \sum_{n=0}^{v} I\left(v, \frac{\pi n}{2v}\right) v \sin\left(\frac{\pi n}{2v}\right) \tag{1.55}$$

where $v(1,...,v_{max})$ and $I(v, \pi n/2v)$ are calculated using a weighted average of four neighboring pixels in the reconstructed image.

The alternative for calculating the velocity distribution is by the analytical integration of the basis functions using the equation (1.54). Thus, the velocity distribution is given by an exact function according to:

$$P(v) = 2\frac{1}{(P(v))_{\max}} \sum_{k=0}^{K_x-1} \sum_{m=0}^{K_z-1} v^2 C_{km} b_{km} R_{m^2+k^2}(v) \tag{1.56}$$

where C_{km} are the expansion coefficients, $R_{m^2+k^2}(v)$ is a function of the type $R_n(v)=(e/n)^n v^{2n} e^{-v^2}$ and b_{km} are coefficients that are numerically evaluated according to:

$$b_{km} = \frac{(k^2+m^2)^{k^2+m^2}}{(k^2)^{k^2}(m^2)^{m^2}} \cdot \frac{\Gamma(k^2+1)\Gamma(m^2+1/2)}{\Gamma(k^2+m^2+3/2)} \tag{1.57}$$

where $\Gamma(x)$ is the Euler's gamma function.

The BASEX method is an improvement over the inversion methods mentioned above. However, the noise problem persists, which is concentrated on the transversal axis of the image.

1.4.2.1.5 Basis set expansion in polar coordinates (pBASEX)

Finally, the pBASEX method[49] is based on the BASEX method but on a polar coordinate system, *i.e.*, a basis of polar functions is chosen on which the measured image is decomposed. The number of basis functions must be adequate to reproduce the image characteristics. Applying polar coordinates in

the definition of basis functions causes noise to accumulate in the central region of the image, which may be preferable in specific applications.

Each method has its advantages and drawbacks. For example, the Fourier-Hankel transform is the fastest reconstruction method, suitable for high-quality images and low dynamic ranges since this reconstruction method magnifies experimental noise. It can produce artifacts for images with intense sharp features. BASEX is fast and provides radial distributions with no computational costs, whereas pBASEX despite being fast, forces spherical harmonics, which can be misleading.[51]

Figure 1.16 displays an image corresponding to CH_3I photodissociation in the origin of the second absorption band (*B*-band) upon excitation at 201.19 nm and resonant detection of $CH_3(v=0)$ fragments at 333.5 nm, using femtosecond laser pulses and recorded at an asymptotic time delay between the pump and probe pulses, reconstructed by BASEX, pBASEX and Fourier-Hankel transform inversion methods.

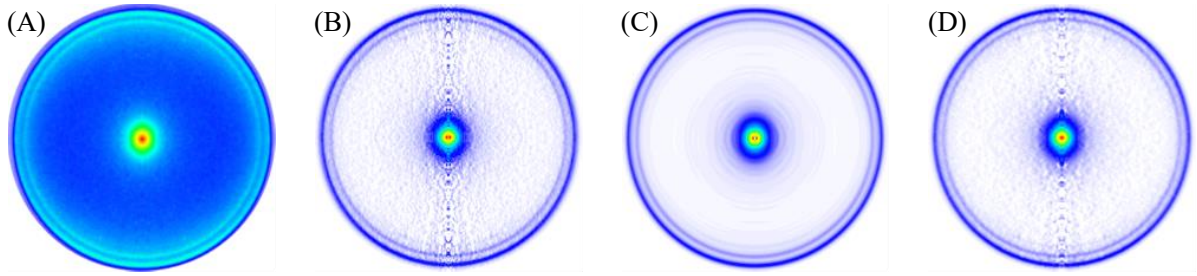

Figure 1.16. *Image of resonant detection of $CH_3(v=0)$ fragments at 333.5 nm originated from CH_3I photodissociation in the origin of the B-band upon excitation at 201.19 nm, using pump and probe femtosecond laser pulses at an asymptotic time delay of 10 ps. (A) Measured and symmetrized image top-bottom and left-right. (B) Image reconstructed by BASEX. (C) Image reconstructed by pBASEX. (D) Image reconstructed by Fourier-Hankel transform.*

1.4.2.2. Forward convolution methods

When cylindrical symmetry is not achievable, for example, in the case of rotational inelastic scattering and reactive bimolecular collisions experiments, the slices of Newton's spheres cease to be equivalent, so inversion methods are no longer valid. Instead, forward convolution methods must be applied. With convolution methods, the measured two-dimensional image is simulated until it converges in an iterative process. Subsequently, once the appropriate simulated bi-dimensional image is found, the three-dimensional distribution is obtained from it.

1.4.2.3. Alternative methods

Vallance and co-workers[52] developed an alternative method within the semiclassical framework of Dixon's bipolar moment formalism[29] for extracting velocity and angular momentum distributions

from velocity map ion images. By taking advantage of the fact that the intensity distribution in a velocity map image can be expressed as a Fourier series in the angular coordinate of the image; the analysis of the Fourier moments of the image measured in different geometries can provide information on speed distributions, angular differential cross-sections, and angular momentum alignment and orientation. To use the Fourier moment analysis, it is necessary to collect a set of images on two different REMPI transitions and use a series of experimental geometries, defined by the polarizations and relative propagation directions of the pump and probe lasers.[53] This method does not require that three-dimensional distribution has cylindrical symmetry, and thus, it is possible to investigate angular momentum alignment and orientation of molecules which is not feasible *via* inversion methods. This method is also insensitive to noise in the image data, contrary to the aforementioned inversion methods.

1.4.3. Slice imaging

There is a variant of the conventional VMI called slice imaging. The main difference is that using a delayed pulsed extraction of the ions following photodissociation, it is possible to spread the velocity ion cloud out of which the central slice of the ion packet is selected. A narrow detector time gate (< 40 ns) is employed, and. This central slice has the full velocity and angular distributions, so they can be measured directly from the images without performing inversion methods. As opposed to inversion methods, slice imaging is suitable for studying systems with product angular momentum alignment. Nevertheless, one of the drawbacks is that by selecting a slice out of the ion cloud, there is a subsequent loss of signal, which is not always desirable.

The first version of this technique, called pulsed slicing, was developed by Kotsiopoulos and collaborators.[54] Soon after, Suits and co-workers[55] and Liu and co-workers,[56] independently developed a new variant called direct current (DC) slicing. The difference between these two types of slicing lies in how the elongation of the ion sphere is achieved and the resolution of the measured images.

Nevertheless, slice imaging faces some inconveniences: On one hand, the expansion of the ion cloud must be such that when it is crushed against the detector, its radius does not exceed the dimensions of the detector. On the other hand, the low repeller voltages can affect the ion detection efficiency, which depends on the impact velocity. With slow velocities, ions might have perturbed trajectories on their flight towards the detector, a highly feasible problem, especially in pulsed slicing. In addition, if a slice of the ion sphere is selected, this can lead to difficulties in the analysis, particularly in detecting polarized photofragments.

These challenges were faced by Brouard and co-workers[57] with the development of the Post Extraction Inversion Slice Imaging (PEISI), based on modifying a conventional DC slicing setup by adding two additional electrodes. In this method, ion spheres obtained under high extraction voltages

are stretched along the TOF by applying a pulsed voltage in the post-extraction region, avoiding transverse stretching. Particularly, they couple the technique to an event-triggered, position-sensitive sensor, which allows achieving an increased resolution compared to previous DC slicing approaches. Images do not need to possess an axis of cylindrical symmetry in the detector plane, allowing studies of angular momentum polarization and bimolecular scattering.

1.5. REAL-TIME PHOTODISSOCIATION DYNAMICS: FEMTOCHEMISTRY

The study of chemical kinetics, based on the mechanisms involved in a chemical process and its velocity, took-off at the end of the 19th century when Arrhenius empirically demonstrated the dependence of the speed of a chemical reaction on temperature and in turn on the rate constant of the reaction. Nevertheless, chemical kinetics addresses molecular reactivity from a macroscopic perspective by averaging all viable elementary mechanisms in a chemical reaction. But what if elementary chemical reactions want to be studied on a microscopic level? Molecular dynamics aims to answer this question by deciphering how reactive molecules approach, collide, and exchange energy to produce the cleavage and formation of bonds from reagents to products.[58] In this field, the theoretical approaches were first developed before experimental ones, with the studies of Eyring and Polanyi.[59-61] The first calculation of classic pathways for hydrogen (H) exchange reaction by Hirschfelder *et al.*[62] demonstrated that the timescale needed to follow the molecular dynamics of the cleavage and formation of chemical bonds was the femtosecond timescale. Later, it was demonstrated that these timescales could vary from the picoseconds to the femtoseconds as a reaction function.

The specific timescales of a molecular dissociation or a simple chemical reaction are determined by the distances in the microscopic world and its natural energies. If the movement of atoms wants to be tracked with a resolution of 0.1 Å, a "camera" capable of a time resolution of about 10^{-14} s, that is, 10 fs, needs to be employed. With a temporal resolution on the femtosecond timescale, it is possible to "freeze" atomic structures during chemical reactions as they move from reagents to products. In the 1930s, when these theoretical models were developed, it was unthinkable to design an experimental setup that could approach this temporal resolution. It took more than fifty years for experimental techniques to evolve sufficiently to reach the time resolution desirable for observing chemical reaction mechanisms.

Since the discovery of the laser in 1960 by Maiman,[63] laser sources have replaced conventional light sources in spectrometers, demonstrating their superiority in large part of experiments. Lasers allow energy to be deposited in the system with high control over several crucial properties, including wavelength, intensity, polarization and, uniquely, temporal duration. Furthermore, lasers have other useful properties such as low divergence, narrow linewidth and tunability. These characteristics permit, for instance, the use of long optical paths, the minimization of the scattering of light in optics, the

possibility of focusing light on small volumes, and limiting the resolution only to the linewidths of particles that absorb or emit radiation. Also, if the sample is in the form of a molecular beam, this leads to a strong cooling of the internal degrees of freedom of the constituent molecules, concentrating the entire population in a few vibrotational and rotational states. This, in combination with the mentioned properties, leads to significant spectrum simplification.

Although spectroscopic techniques based on laser light sources with relatively good temporal resolution have been used for many years, they could not descend from the temporal scale of microseconds, mainly due to the limitations of the used pulsed sources. Fortunately, during the last decades, various techniques have allowed a progressive shortening of pulses until, through the mode-locking technique,[58] these durations approached the range of tens to hundreds of femtoseconds. With this resolution, it is possible to measure the cleavage of a chemical bond in real-time.

1.5.1. Femtosecond pump-probe spectroscopy

An unprecedented milestone employing femtosecond laser sources was the pioneering experiments conducted by Zewail and co-workers[60-64] in the late 1980s. A series of molecular photodissociation experiments were carried out in which, for the first time, the time of cleavage of a chemical bond (*i.e.*, in real-time) was measured but also the detection and characterization of activated complexes from a chemical reaction were carried out, by what it was named femtosecond transition-state spectroscopy (FTS). This technique led to the birth of a new discipline within the field of Chemistry; Femtochemistry. The importance of these experiments was recognized only ten years later with the Nobel Prize in Chemistry awarded to A. Zewail, "*for his studies on the transition states of chemical reactions through the spectroscopy of femtoseconds*".[65]

Femtochemistry focuses on the real-time study of the atomic movements involved in chemical reactions, such as those related to the cleavage and formation of chemical bonds and geometric changes in molecules. So, it concerns the real-time dependence of the molecular system as it evolves from the Franck-Condon region, through the transition state, into the possible fragmentation channels and how this motion can be studied in the laboratory.

Direct probing of the temporal evolution of a dissociating system in time-resolved experiments is achieved by the pump-probe technique illustrated in figure 1.17. A femtosecond laser pulse with wavelength λ_1, namely the pump laser, excites the parent molecule AB into a repulsive state, thereby creating a wave packet that starts to evolve on the potential energy surface V_1. The center of the temporal profile of the pump laser is considered the origin of times so that the initial internuclear distance R_0 of the molecule is defined as the distance between the fragments A and B at time zero, which is similar to the internuclear equilibrium distance R_e. From the repulsive potential energy surface V_1, the wave packet

evolves as a function of time, resulting in the increase of the internuclear distance until it reaches a certain value R_∞ for which fragments A and B no longer interact. At different delay times, the system is irradiated by a second femtosecond laser pulse with wavelength λ_2, called the probe laser, to interrogate the progress of the reaction at a particular time τ. Depending on whether the reaction is monitored by transient species or by final photoproducts, this results in two different FTS experiments: in resonance or out of resonance.

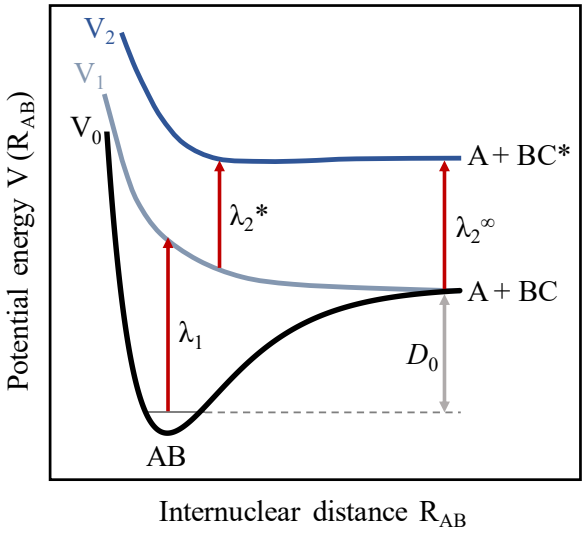

Figure 1.17. *Representation of a femtosecond pump-probe experiment. The pump laser (λ_1) excites the molecule AB from the ground state (V_0) to a repulsive excited state (V_1). At a certain delay time τ, the probe laser (λ_2) interrogates the state of the photodissociation either by probing the transition region (if the probe laser wavelength is tuned to λ_2^*) or the free fragments (if tuned to λ_2^∞). Figure adapted from reference [66].*

1.5.1.1. Femtosecond transition spectroscopy in resonance

In FTS in resonance measurements, the wavelength of the probe laser is tuned to one of the free fragments so that the absorption of the probe laser by the molecular system is negligible until the fragments reach a certain internuclear distance at which they do not interact with each other (R_∞, λ_2=λ_2 (t_f)). At this precise moment, an optical detection window (or optical coupling region) is opened on the potential energy surface V_1, defined by the laser bandwidth, such that those molecular configurations at time τ, which allow for a vertical transition to the potential energy surface V_2 are the only ones that absorb the probe photon. This optical coupling region depends on the energy difference between the potentials V_1 and V_2 and the frequency and spectral width of the probe laser. The spectral width of femtosecond lasers causes molecules to be detected in a range of values R_∞ so that at a time τ, fragments at a distance R in which they still interact to some extent with their co-fragments, can undergo a vertical transition to V_2 and be detected. Besides, each molecule has a different initial internuclear distance R and takes an additional amount of time to reach the optical coupling region.

In this case, the behavior of the detected signal from the products, with respect to time, is known as the transient and provides a direct measurement of the time it takes for the bond to break. A step function to fit this transient would be expected, but for this, it should be fulfilled that the laser pulses were delta functions in time and energy, and with the wave packet moving through the potential energy surface V_1 would have to do it without dispersion, being the width of the absorption line negligible. In general, neither of these two conditions are fulfilled, which means that the shape of the transient is not a step function.

The pump and probe laser pulses' temporal width has an important effect on the shape of the transients. Being $I_{pump}(t)$ and $I_{probe}(t)$ the temporal intensity profiles of the pump and probe pulses, the FTS transient, $A(t)$, is the convolution of the step function (ideal) with the cross-correlation function of lasers, $C(t)$, according to:[67]

$$A(t) = \int_{-\infty}^{t} C(x - \tau_{1/2})dx \tag{1.58}$$

$$C(t) = \int_{\infty}^{\infty} I_{pump}(t - y)I_{probe}(y)dy \tag{1.59}$$

Considering a molecular response function, $M(t)$, the final transient is given by:

$$A(t) = \int_{-\infty}^{\infty} dx I_{probe}(t - x) \int_{-\infty}^{\infty} dy I_{pump}(y)M(x - y) \tag{1.60}$$

In general, the shape of the transient is also affected by the wave packet dispersion as it propagates on the potential energy surface.

1.5.1.2. Femtosecond transition spectroscopy out of resonance

In FTS out of resonance measurements, the wavelength of the probe laser is tuned to the transition state complexes, out of resonance of the photoproducts A or B ($\lambda_2 \neq \lambda_2^*(t^{\neq})$). In this sense, different regions of potential energy surface V_1 along the reaction coordinate are explored, and so the nature of the transition state complex AB*.

As the species capable of absorbing the probe laser photons enter the R* region, the detected signal increases until the transient molecules leave the optical coupling region of the potential energy surface V_1 due to the changes in internuclear distance R over time, and from there the signal decays. For each value of $\lambda_2^*(t^{\neq})$, there is a transient corresponding to a transient species for a given internuclear

distance R*. By scanning the successive internuclear distances R* with different probe laser wavelengths $\lambda_2^*(t^{\neq})$, it is possible to obtain information on the shape of the potential energy surface along the reaction coordinate.

An example of an FTS experiment in and out of resonance can be seen in figure 1.18, corresponding to the photodissociation of cyanogen iodide (ICN).[68] The different transients are presented for different wavelengths of the probe laser: Transient (1) corresponds to a region of the potential energy surface at the early stages of the photodissociation, while transient (3) corresponds to a region near R_∞. As $\lambda_2^*(t^{\neq})$ approaches $\lambda_2(t_f)$, due to the spectral width of the probe femtosecond laser pulse, the optical window for the detection of the free fragments begins to open as well, and for transients (2) and (3), the signal does not decay to zero at long delay times, appearing a component of the transient characteristic of the free fragments.

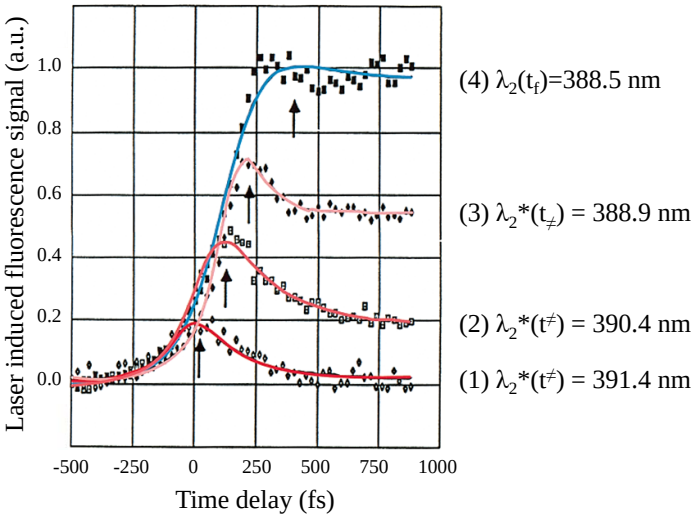

Figure 1.18. *FTS experiments corresponding to the photodissociation of ICN. In the resonance experiments, the probe laser is tuned to the LIF detection of the free cyanide fragments (blue transient for $\lambda_2(t_f)$=388.5 nm). Red transients measured out of resonance for $\lambda_2^*(t^{\neq})$, =388.9 nm, 390.4 nm and 391.4 nm are shown. Figure adapted from reference [68].*

1.6. LASER LIGHT INTENSITY

Due to the extreme temporal brevity of ultrashort pulses, the achieved peak intensities can be several orders of magnitude higher than longer temporal sources or continuous wave (CW) laser sources. This feature is a significant advantage when producing multiphoton transitions since the probability of a non-linear absorption phenomenon of order N scales with the N power of the laser intensity. However, this apparent advantage can become a problem, and caution must be exercised in several respects. On the one hand, if the intensities reach the region above 10^{12} W/cm^2, the interaction between the molecular system and the radiation can no longer be described with Perturbation theory since the electric field of the laser can be of comparable in magnitude to intramolecular forces. New phenomena can appear in

these circumstances, such as the Stark Shift effect,[69] high-harmonic generation (HHG),[70] ATI[14] or Coulomb explosion.[71] Therefore, in cases where the molecular system is to be studied with the minimum disturbances by radiation, it is essential to limit the laser intensities.

As stated above, short pulses can easily induce multiphoton absorption processes allowing the opening of many photodissociation channels upon excitation. By opening more photodissociation channels that correlate with a given photoproduct, determining its origin can be ambiguous, leading to an enormous difficulty in detangling the corresponding formation mechanism. Therefore, it is essential to work on the appropriate intensity regime and have techniques that enable identifying the original channels of each observed fragment without ambiguity. For example, techniques based on resonant processes in the probing step (such as REMPI) or the detection of fragments with velocity resolution in one of its versions (electron spectrometers, TOFMS for ion detection or images of ions or photoelectrons, especially in VMI configuration).

1.7. CONTROL OF CHEMICAL REACTIONS UNDER ELECTRIC FIELDS

In parallel to the exploration of the dynamics of molecular processes, ultrashort laser pulses have made it possible to control the outcome of chemical reactions in a process known as coherent control. Dynamic control of chemical reactions or photochemical processes has only been possible with the development of laser technology.[72-76] Although the first control experiments were performed with nanosecond pulses, femtosecond laser pulses and devices that allow their shaping have multiplied the possibilities of exerting control over chemical reactions.

In the first control experiments with laser light sources, the aim was to dissociate the molecule through the dissociation of a given bond using resonant radiation tuned at the fundamental frequency of the local molecular vibration. Nevertheless, the so-called Mode Selective Chemistry was only viable for certain cases,[73, 77-81] since, in general, the localized excitation energy in a molecular bond is redistributed very rapidly between the different molecular vibrational modes and therefore the expected selectivity is lost.

From these first tests up to the present day, meaningful theoretical and experimental progress has have been made, showing that by varying the temporal and spectral characteristics of coherent laser radiation, it is possible to exercise control over the result of the radiation-matter interaction through quantum interference effects.[82] This field is called quantum control or coherent control since the spectral and temporal characteristics of the applied electric fields are adjusted so that an initial quantum mechanical wave function is transformed into the desired final wave function thanks to the coherence of the laser sources. This coherent quantum mechanical manipulation of a molecular system makes it

possible to select the trajectory from the many possible ones on the potential energy surface, which leads to the desired product.

The main control strategies developed in the last decades include the control in the frequency domain,[83, 84] in the temporal domain (or pump-dump strategy),[85] adiabatic control[86] or wave packet interferometry.[87, 88] More recently, other control methodologies have been developed that make use of the spectral characteristics of femtosecond laser pulses such control with chirped ultrashort laser pulses, optimal adaptive control and control based on dynamic Stark effect.[89, 90]

Recently, besides the time or frequency domain, the laser intensity has acquired a relevant role in controlling photochemical processes. The different ways of strong-field control require understanding how molecules interact with laser fields in the nonperturbative, strong-field regime. In the case presented in this Doctoral Thesis, the control of the reaction is exerted using moderate-intensity probe pulses, which do not act as tracing tools but moving the population instead.

1.8. HIGH-ORDER HARMONIC GENERATION

All these atomic and molecular processes introduced above arise from the motion of electrons. Electron motion is governed by even shorter timescales, ranging from a few femtoseconds down to tens of attoseconds (10^{-18} s). Due to these extremely short timescales, femtosecond laser sources turn out to be insufficient for the study of electron dynamics. Fortunately, in 2001, attosecond pulse trains (APTs) obtained through high-order harmonic generation (HHG) were experimentally measured, making HHG, first discovered experimentally during the 1980s,[91-93] a useful light source for the new field of Attoscience.[94-96]

HHG is based on focusing high-energy femtosecond laser pulses in noble gases, generating phase-locked odd harmonics of the fundamental frequency. In this way, attosecond laser pulses of great variety and tunability can be achieved, despite the low energy.

Besides HHG, other sources have emerged in recent years for the generation of attosecond pulses: ultrabright X-ray free-electron lasers (XFELs) are very powerful sources that can produce ultrashort pulses at wavelengths down to the angstrom level, with energies up to tens of millijoules, providing access to unexplored non-linear processes.[96] The main drawback of XFEL facilities is their large scale, which severely limits their availability. Additionally, attosecond light pulses can also be achieved in plasmas induced by ultrashort relativistic-intensity lasers on a solid surface, a process is known as solid surface high-order harmonic generation (SSHHG), and have unusual properties not found in HHG generated in a gas medium, such as spectral redshift, and an intensity difference between even- and odd-order harmonics.[97, 98]

In the present case, HHG was chosen as a source of short wavelengths in the XUV domain not accessible by conventional sources, which are appropriate for experiments where access to highly excited species as well as cationic species is required.

1.8.1. High-order harmonic generation as a source of attosecond pulse trains

HHG by application of high-intensity electromagnetic fields under the non-perturbative regime (10^{12}-10^{16} W/cm^2) focused into a gas jet or cell with typical pressure ranging from a few tens of millibars to a few bars, is the most widespread and applied technique for the generation of attosecond pulses since it was first discovered experimentally in the 1980s.[91-93]Although less intense extreme ultraviolet (XUV) radiation is generated, it is achieved with more accessible experimental setups than XFELs.

To understand how HHG occurs in a gas medium, it must be understood how an atom responds to the ultra-intense electric field of a few femtoseconds laser pulse and then extend this response to a set of atoms in a gas cell. This single-atom response is described by the so-called three-step model,[99-101] a semiclassical approach schematically represented in figure 1.19. To describe the behavior of the electron in the driving electric field, there is also a quantum approach in the frame of the strong-field approximation (SFA), commonly known as Lewenstein's model.[102] Nevertheless, the first approach is sufficient to understand the HHG in the context of the present Doctoral Thesis.

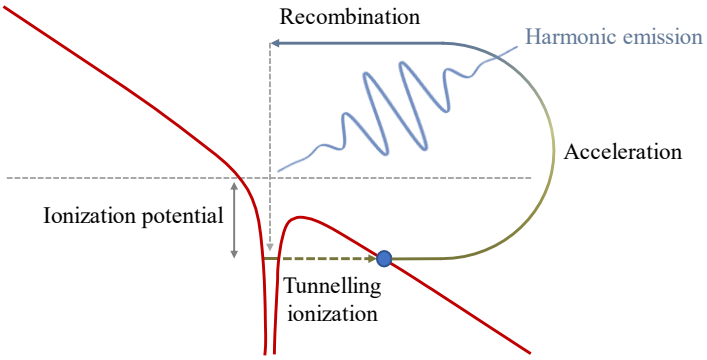

Figure 1.19. *Representation of the three-step model for the single-atom response. During HHG, the electric field distorts the atom's atomic binding potential, allowing electrons to tunnel through the binding potential. The oscillating field adds ponderomotive energy to the freed electrons. When the high-energy electrons recombine with the atom, a single high-energy photon (an attosecond burst of radiation) is emitted. Figure adapted from reference [103].*

The three steps are the following:

Ionization step: considering a single atom, first the tunnel ionization of its bound electrons occurs since the high-intensity electric field of the laser distorts the Coulomb binding potential, thus releasing them, twice during an optical cycle, into the continuum with no translational energy.[104]

Acceleration step: after ionization, electrons are then accelerated with high translational energy in the first half cycle of the laser field and reversed in the second half cycle,[105] due to a ponderomotive force, returning to the vicinity of the atom with high translational energy. This force provides a ponderomotive potential, given by the equation (1.61), to these oscillating electrons, and it is the source of most of the energy for HHG.

$$U_p = \frac{E_0^{\ 2}}{4\omega_0^{\ 2}} = 9.338 \cdot 10^{-8} \cdot I\left[TW/cm^2\right]\left(\lambda_{IR}\left[nm\right]\right)^2 \tag{1.61}$$

being U_p the ponderomotive potential and E_0, I and λ the amplitude, intensity and wavelength of the driving frequency of the laser.

Recombination step: once freed by strong-field ionization, electrons can re-enter the atomic binding field, recombining with the parent ion as the electric field changes sign for the second half of the laser optical cycle, producing a strong non-linear interaction that leads to the generation of a single high-energy photon; an attosecond burst of radiation. The whole process occurs every half cycle of the driving laser pulse.

Considering all the atoms in the gas cell, each produces an attosecond burst, which is added coherently to the rest, creating an attosecond light pulse. To achieve an efficient HHG, phase-matching should be achieved.

In an oscillating laser field, the result is an APT propagating along with the driving laser. The efficiency of this type of process is very low (10^{-5}-10^{-7}) and depends on the gas medium.[106-109] Coherent and linearly polarized few hundred attosecond pulses in duration are produced, with a total energy of a few femtojoules to nanojoules. HHG in gases generates spatially[110, 111] and temporally[111] coherent radiation with multiple odd harmonics[111-113] of the fundamental frequency. Only odd harmonics are present because attosecond bursts that occur on opposite half-cycles of the driving field destructively interfere at all the even harmonic frequencies.[102]

A representation of a typical harmonic spectrum is displayed in figure 1.20.[114] The HHG spectrum is divided into three regions: the first one contains strongly modulated harmonics whose intensity decreases with the harmonic order, the second region is commonly known as the *plateau*, where the intensity is approximately constant with the harmonic order, and the third area covers the weakly modulated cut-off regime, constituting the shortest harmonics wavelengths.[114] The spectrum typically covers the UV, XUV and soft-X-ray regimes.

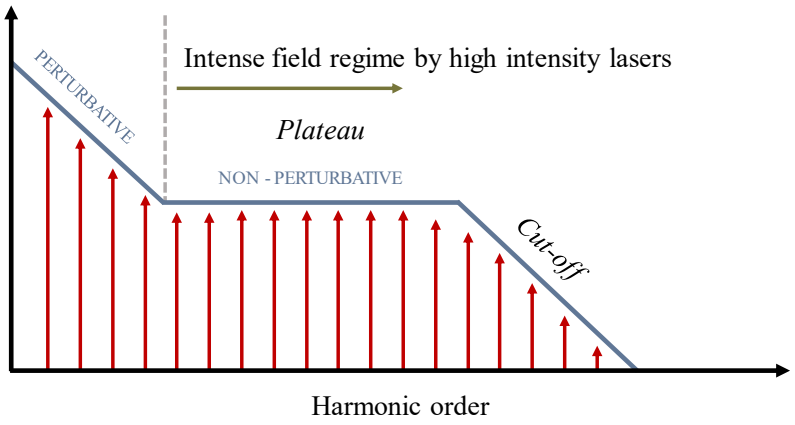

Figure 1.20. *Representation of a typical HHG spectrum generated by the interaction of an intense laser pulse with atoms, molecules or ions. In the spectrum, three regions can be distinguished: the first one consists of strongly modulated harmonics whose intensity decreases with the harmonic order, the plateau, where the intensity is approximately constant with the harmonic order, and the third area covers the weakly modulated cut-off regime, constituting the shortest harmonic wavelengths. Figure adapted from reference* [115].

The spectral position of the maximum photon energy is known as the cut-off, and it is determined by the laser pulse intensity, frequency and the IP of the atom. The cut-off energy is given by:[99, 116]

$$E_{cut-off} = IP + 3.17 \cdot U_p \tag{1.62}$$

where $E_{cut\text{-}off}$ is the energy of the cut-off, IP is the ionization potential of the target atom and U_p the ponderomotive energy.

Therefore, to generate very short wavelengths, it is necessary to use a gas consisting of atoms with a high IP, like argon (Ar), neon (Ne) or xenon (Xe), and a driving laser with a long wavelength and high intensity (10^{14}-10^{16} W/cm^2). These two requirements are met in the focused beams of many commercial ultrafast laser systems such as titanium (Ti):sapphire chirped pulse amplification (CPA) laser systems. However, if the laser intensity at focus is too high, barrier suppression ionization occurs instead, causing the ionized electrons to not recombine with their parent ions, thus reducing the efficiency of HHG.

The APT duration depends on the number of cycles in the driving laser. Several methods can reduce this train to a single isolated attosecond pulse (IAP), for example, by spectrally filtering the HHG energy spectrum or by polarization gating.[117]

1.8.2. High-order harmonic spectral filtering preserving the temporal resolution

Ultrafast laser pulses in the XUV obtained from HHG or XFELs have become a new tool for ultrafast time-resolved studies of molecules, liquids and solids. Several applications require the use of single harmonics or a group of few harmonics, which must be selected from the broad spectral bandwidth inherently generated. So, spectral filtering is necessary to produce bandwidth-limited pulses suitable for simultaneous time and energy resolution experiments.

For the spectral filtering of high-order harmonics, an XUV monochromator is required to select the photon energy. The most classic methods include designs based on multilayer mirrors[118] or classical diffraction gratings.[119, 120] These two methods provide very high spectral resolution at the expense of temporal resolution. A time delay compensating scheme using two diffraction gratings can be employed to preserve the temporal resolution, showing a very effective time compensation in a broad spectral region, ranging from VUV to soft X-rays, with much higher efficiency than the classical diffraction mountings.[121-123] An example of this type of setup is presented in section 2.2.1.

1.9. ORGANIZATION OF THE PRESENT WORK

The present Doctoral Thesis is organized as follows:

First, the experimental setups used to carry out the experiments during this Doctoral Thesis are detailed: the experimental setup located at the Center for Ultrafast Lasers (CLUR) of the Faculty of Chemical Sciences of Complutense University (Madrid, Spain) consisting of a femtosecond laser system and a molecular beam machine working under VMI configuration and the experimental setup located in the Kilohertz laboratory of the Max Born Institute (Berlin, Germany) based on a time-delay compensating monochromator (TDCM) setup provided with a VMI system.

Then, the most relevant results obtained during the completion of this Doctoral Thesis are described. The results are divided into five different chapters. In each of these chapters, a brief introduction is made where the system of study is approached, and a brief overview of previous studies is presented. Afterward, the specific methodology is described, divided, in turn, into experimental methodology (including aspects such as the optical assemblies and the molecular beam expansion conditions) and the theoretical methodology. Then the experimental and theoretical results are presented and discussed, followed by some brief conclusions.

Finally, the most relevant general conclusions extracted from the conducted studies are presented, based on the final goal of this Thesis, which is the evaluation of structural effects on the ultrafast photodissociation dynamics of dissociating molecules.

Chapter 2 – Experimental setups

The experiments presented in this Doctoral Thesis were mainly carried out employing the experimental setup located at the Center for Ultrafast Lasers (CLUR) of the Faculty of Chemical Sciences of Complutense University (Madrid, Spain). However, the results presented in chapter 7 were conducted with a secondary setup located in the Kilohertz laboratory of the Max Born Institute (Berlin, Germany).

In this chapter, a detailed description of the first experimental setup is given, while for the second setup only the most relevant details concerning the performance of the experiments are mentioned.

2.1. CENTER FOR ULTRAFAST LASERS EXPERIMENTAL SETUP

This experimental setup located at the Center for Ultrafast Lasers (CLUR) of the Faculty of Chemical Sciences of Complutense University (Madrid, Spain) consists of a femtosecond laser system and a molecular beam machine working under VMI configuration. The first part of this section is devoted to the description of the laser system (section 2.1.1-2.1.3) and the second part to that of the molecular beam machine (section 2.1.4). At the end of this section, the synchronization and data acquisition system (section 2.1.4.5) and the steps for performing a pump-probe experiment using this experimental setup (section 2.1.6) are also described.

2.1.1. Femtosecond laser system

The various parts of the laser system are represented schematically in figure 2.1 and are described in detail in the next subsections. The femtosecond laser system (Spectra-Physics) consists of an oscillator (Spectra-Physics Tsunami 3941-30-M1S) and a regenerative amplifier (Spectra-Physics Spitfire Pro). It is also equipped with two-third (THG) and fourth-harmonic generation (FHG) modules of the driving frequency, which differ in energy efficiency and in the temporal duration of the output pulses, an optical parametric amplifier (Spectra-Physics OPA 800CF) and a traveling-wave optical parametric amplifier (Light Conversion TOPAS Prime). The TOPAS is wavelength-extended with two modules equipped with non-linear optics for the generation of harmonics by sum-frequency generation (SFG) and second-harmonic generation (SHG).

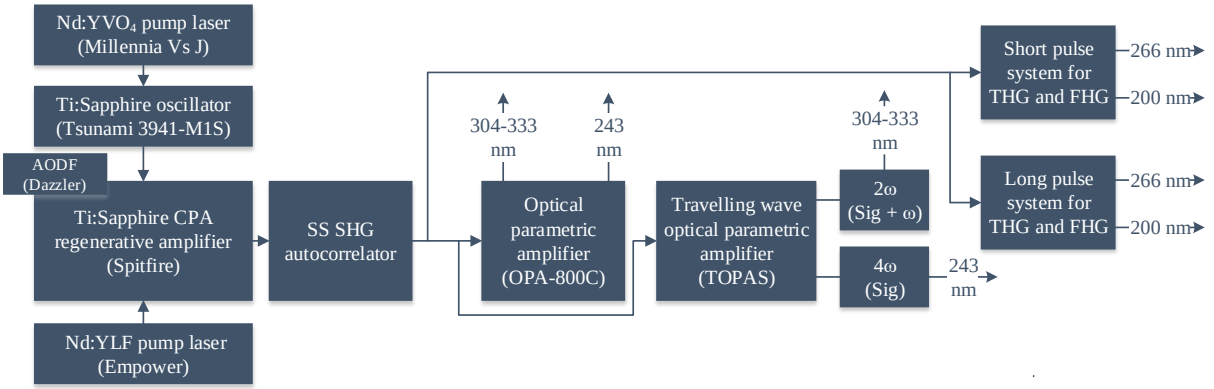

Figure 2.1. *Diagram of the experimental setup located at the Center for Ultrafast Lasers (CLUR). From left to right: femtosecond laser system including Millenia (CW pumping laser of the oscillator), Tsunami (oscillator), Empower (pumping laser for the regenerative amplifier), Dazzler (acousto-optic modulator), Spitfire (regenerative amplifier). Right after the laser system, the autocorrelator for the characterization of the pulse duration can be found. Some devices for radiation generation by non-linear conversion processes such as the OPA, the TOPAS with the two different modules for wavelength extension (see text) can be distinguished. In the right part of the scheme, the two THG and FHG systems can be seen. The details of each of the devices are collected in full throughout this section.*

2.1.1.1. Femtosecond titanium: sapphire laser oscillator

The oscillator is a Ti:sapphire femtosecond system (Spectra-Physics Tsunami 3941-30-M1S) pumped by up to 5 W of 532 nm CW radiation from a solid-state neodymium-doped yttrium orthovanadate (Nd:YVO_4) laser (Spectra-Physics Millennia Vs J). This solid-state laser is in turn pumped by diodes. The output of the diode laser pumps neodymium (III) ions (Nd^{3+}), which are found doping a crystal matrix of yttrium orthovanadate (YVO_4) and which constitute the active medium of the laser. This process provides laser radiation at 1064 nm, which is subsequently frequency-doubled in a non-linear lithium triborate (LBO) crystal to generate laser radiation at 532 nm, which is used to pump the oscillator.

The oscillator (Spectra-Physics Tsunami 3941-30-M1S) is schematically represented in figure 2.2. It is a solid-state laser in which the active medium is a sapphire (Al_2O_3) crystal doped with titanium (III) ions (Ti^{3+}) in an amount of about 0.1 %, responsible for laser emission. The Ti:sapphire laser belongs to the type of lasers known as vibronic lasers with band broadening.[124] In lasers whose active medium is doped with transition metal ions (Ti^{3+}), there is a strong coupling between the electronic states of the ions and the vibrational modes of the solid matrix (phonons). This interaction gives rise to a homogeneous broadening of the gain in the active medium, thus allowing wide tuning ranges and the generation of ultrashort pulses.[125]

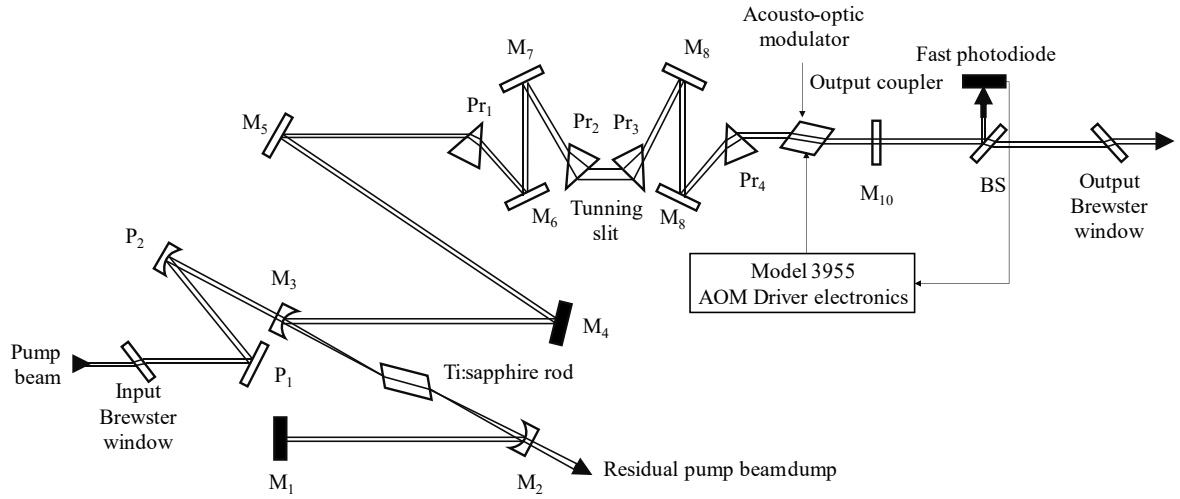

Figure 2.2. *Diagram of the Ti:sapphire Tsunami femtosecond laser oscillator. P_1 is the pump beam steering mirror, which directs the input pump beam onto the center of pump beam focus mirror P_2. It can be adjusted vertically and horizontally. The pump beam focus mirror P_2 directs the pump beam through the cavity focus mirror M_3 and focuses the pump beam into the Ti:sapphire rod. It can be adjusted vertically and horizontally as well, and it sits on a dovetail slide so that its distance from the Ti:sapphire rod can be adjusted. A setscrew on the edge of the slide holds it in place. The mirror is translated with respect to the rod to create a uniform focused spot size in the rod and compensate for the difference in beam divergence among different pump lasers. M_2 and M_3 are the cavity focus mirrors, which center and focus the cavity beam waist in the Ti:sapphire rod. They can be adjusted vertically and horizontally, and their distances from the rod are adjustable. M_3 has a dovetail slide that is held in place with a setscrew. M_4 and M_5 are the cavity fold mirrors, which fold the beam and allow for a compact laser. M_4 directs the cavity beam to M_5, and M_5 directs it to Pr_1 (fs configuration). The acousto-optic modulator is driven by the Model 3955 electronics module to ensure proper pulsing at start-up and has pitch and Bragg-angle controls. The M_{10} output coupler is one of two cavity end mirrors. Whereas the high reflector reflects all light back into the cavity, the output coupler allows a small percentage to pass through as the output beam. It can be adjusted vertically and horizontally to align the laser cavity and optimize the output power and mode quality. These controls are accessible when the laser headcover is in place. The rod translation control vertically translates the Ti:sapphire rod in a plane parallel to its face. It can be used to maximize output power during alignment. The dovetail slide is held in place with two screws. Figure and description adapted from the user's manual.*

The Ti:sapphire laser[126] has been the most widespread system for the generation of ultrashort femtosecond pulses thanks to the exceptional properties of the active medium:

- Sapphire crystals have high thermal conductivity, avoiding thermal effects even for high intensities or powers.
- Due to the absorption characteristics (absorption band centered around 500 nm that arises from the permitted *d-d* vibrational transitions of the Ti^{3+} in an octahedral environment provided by oxygen (O) atoms in the host crystalline structure), the active medium is ideal to be optically pumped by argon (Ar) ion lasers (514.5 nm), frequency-doubled neodymium-doped yttrium

aluminum garnet; (Nd:$Y_3Al_5O_{12}$ or Nd:YAG), neodymium-doped yttrium lithium fluoride (Nd: LiYF4 or Nd:YLF), Nd:YVO_4 (527-532 nm), and solid-state lasers pumped by diodes.

- The high bandwidth of the Ti^{3+} ion gain in the sapphire matrix allows for the generation of femtosecond pulses and a wide tuning range. The specific tuning range of each equipment depends on the sets of used optics.

The mode-locking technique achieves the production of femtosecond laser pulses in the oscillator.[127] In a continuous laser, the different longitudinal modes of the cavity oscillate independently with no phase relationship. Thus, the output of a continuous laser consists of random phase modes. In a mode-locked laser, however, the different modes have a fixed phase relationship between them so that they interfere constructively at one point in the cavity and destructive in the rest, thus generating a single laser pulse. The laser output consists of a pulse train with a repetition rate given by:

$$\tau = \frac{2L}{c} \tag{2.1}$$

being τ the time taken by light, with speed c, to travel back and forth within the L-length cavity. For the femtosecond laser pulses oscillator used in the present case, this time equals 13.2 ns, with a pulse repetition rate of 75.94 MHz. This time t is related to the frequency of spacing between the laser modes according to the equation (2.2):

$$\Delta \nu = \frac{1}{t} \tag{2.2}$$

For N locked modes, the locking bandwidth is N$\Delta\nu$. The number of locked modes determines the pulse duration so that the broader the laser bandwidth, the lower the pulse duration. Due to the large bandwidth of Ti:sapphire crystals, extraordinarily short pulse durations in the femtosecond range can be achieved.

The mode-locking is achieved by a regenerative method, schematically represented in figure 2.2. An acousto-optical modulator (AOM) located in the laser cavity is used in active mode-locking methods, consisting of an excellent optical quality material, such as quartz, with two perfectly polished surfaces parallel to the light propagation direction. Fixed to one of these surfaces, a piezoelectric transducer is placed, to which a radio frequency (RF) is applied, obtained directly from the laser cavity, to generate an acoustic wave in the modulator. This induces the generation of a time-dependent refractive index along an axis perpendicular to the light propagation direction. When light interacts with this acoustic grating, a portion is diffracted and shifted in frequency by an identical amount to the acoustic frequency. Therefore, the modulator diffracts the light outside the cavity only when the acoustic grating is present,

operating as a time-dependent loss and thus communicating the phase between the longitudinal modes of the cavity.

In addition to the intrinsic characteristics of the Ti:sapphire rod and the cavity, the temporal and spectral width of the oscillator pulses are primarily determined by:

- The spectral phase accumulated by the laser as it passes through various materials. This phenomenon is related to the fact that a large spectral width characterizes ultrashort pulses. In general, the linear refractive index of any material, such as Ti:sapphire crystals, depends on the frequency. This difference in refractive index results in a different group velocity between the different frequencies, producing a temporal separation. In a first approximation, only the first two terms of Taylor's series are considered, known as group velocity dispersion (GVD) and third-order dispersion (TOD). Positive GVD and TOD are defined when lower frequencies travel faster than higher frequencies; the pulse is then said to have a positive chirp, and the front of the pulse contains the lower frequencies of the spectrum. Conversely, negative GVD and TOD correspond to pulses with a negative chirp, where the front of the pulse contains the higher frequencies. GVD leads to a symmetric temporal widening, while TOD is responsible for the possible asymmetry of the pulse (pre- and post-pulses).
- The self-phase modulation (SPM)[127] is related to the non-linear refractive index of the Ti:sapphire crystal, which is more evident at high intensities. As the pulse propagates through the crystal, the front of the pulse experiences an increasing refractive index, resulting in a delay in the individual oscillations of the electric field. This results in a redshift of the pulse front and a blueshift at the end of the pulse. Therefore, SPM produces a widening of the pulse spectrum, also introducing an additional positive chirp.

To achieve as short pulses as possible, commonly referred to as Fourier-transform-limited (FTL) pulses, it is necessary to compensate for the pulse widening due to positive GVD, TOD, and SPM. This is achieved using a set of prisms, which provides a negative linear GVD for large bandwidths. The amount of GVD introduced to the pulse can be tuned by performing micrometric adjustments on the positions of the prisms, which results in an increase or decrease of the wavelength-dependent optical path. There is also a micrometric control of a moving slit located between these prisms and allows to select the central wavelength of the output pulse. The TOD is compensated using a chirped mirror, a mirror designed to reflect different wavelengths in different planes. This causes some wavelengths to travel for longer optical paths than others.

The oscillator output <30 fs pulses are tunable between 780 nm and 820 nm with an FWHM adjustable between 15 and 60 nm. The repetition rate is 75.94 MHz, and the average output power is

greater than 400 mW at 800 nm with a pulse energy of 5 nJ. Figure 2.3 shows the oscillator output spectrum centered at 804 nm, with an FWHM of ~39 nm, which corresponds to an FTL duration of 23 fs.

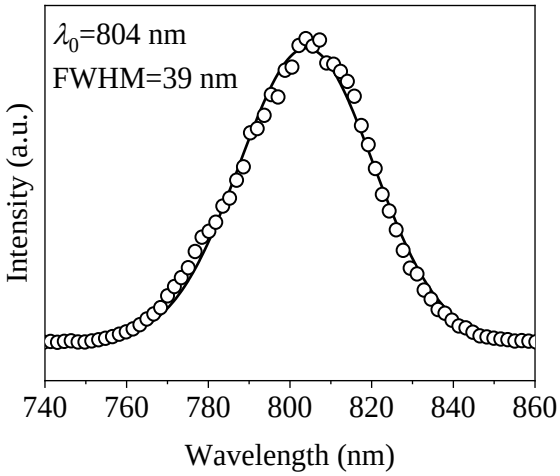

Figure 2.3. *Tsunami oscillator output spectrum. The experimental data (circles) is fitted to a Gaussian function (solid curve). The spectrum is centered at 804 nm and has an FWHM of 39 nm, equivalent to 23 fs for FTL pulses.*

The laser pulses coming from the oscillator are not FTL since they present an important quadratic phase and an FWHM ≈150 fs. These factory settings do not adversely affect the amplified laser pulses (section 2.1.1.2) since most of the spectral phase can be compensated with the Dazzler device, presented in section 2.1.1.3.

2.1.1.2. Regenerative amplifier

The output of the oscillator is amplified in a CPA Ti:sapphire regenerative amplifier.[127] The amplifier consists of two modules: the regenerative amplifier itself (Spectra-Physics Spitfire Pro) and its pumping laser (Spectra-Physics Empower).

The pump laser is a pulsed solid-state laser with gain switching (Q-switch) whose active medium is a diode-pumped Nd:YLF crystal. The fundamental radiation centered at 1053 nm is sent to the acousto-optic Q-Switch, obtaining laser pulses at 1 kHz of repetition frequency and duration on the nanosecond scale. The laser radiation is frequency-doubled, passing through a lithium triborate (LiB_3O_5 or LBO) crystal generating 527 nm. This non-linear crystal is maintained within a range of temperatures between 157-171 ºC to ensure the best conversion efficiency of the fundamental wavelength. The output laser pulses centered at 527 nm, with a power of ≈18 W, 1 kHz of repetition rate and ≈100 ns of pulse duration are used to pump the regenerative amplifier.

The main difficulty involved in amplifying femtosecond laser pulses is the risk of damage of the optical elements, especially the Ti:sapphire crystal, which acts as a gain medium in the amplifier, since femtosecond pulses have high power, as they concentrate all the energy in a very short time. Nevertheless, this risk can be minimized by using the CPA technique.[128] In CPA, a short duration, low-intensity pulse is first temporarily stretched (or chirped), thus reducing its peak power. Then, it is amplified by passing multiple times through the active medium, significantly increasing its energy. After amplification, the pulses are again recompressed, reaching high peak powers. With this technique, the energy of the femtosecond laser pulses from the oscillator can be amplified up to six orders of magnitude, keeping the duration at the output pulses in the range of the tens of femtoseconds. An outline of the CPA technique can be found in figure 2.4.

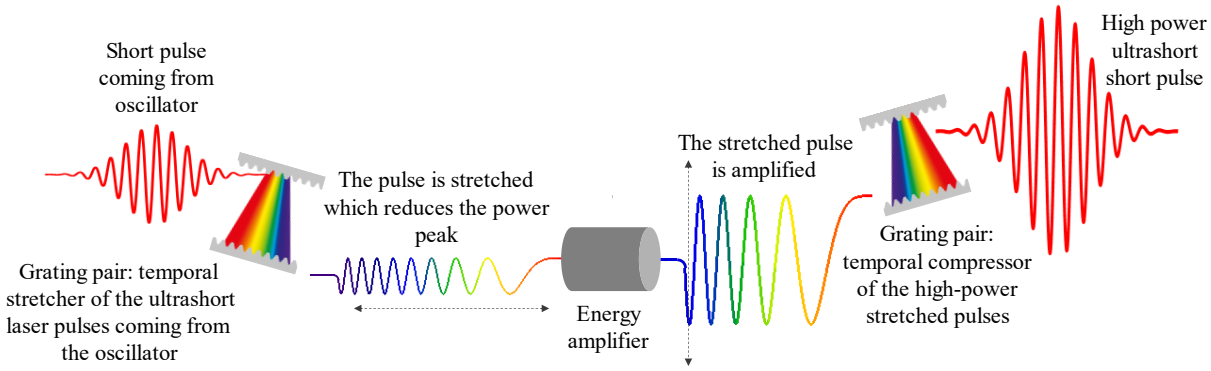

Figure 2.4. *Outline of the CPA technique. A short, low-intensity pulse is first stretched temporarily before amplification. The pulse is recompressed at the output of the amplifier, keeping the initial duration virtually intact but with much higher intensity.*

To achieve high-power ultrashort laser pulses through the CPA technique, the Spitfire amplifier consists of three parts: the stretcher, the regenerative amplifier, and the compressor. The optical schemes used in each step are described below.

Temporal stretching of ultrashort low-power pulses from the Tsunami oscillator: CPA technology is based on the fact that when a diffraction grating diffracts a femtosecond laser pulse, each pulse frequency does so at a different angle (angular dispersion). The temporal stretching of a pulse is achieved by a stretcher, which combines a series of diffraction gratings and mirrors in a configuration such that the higher frequency components of light are sent through the stretcher by a longer path than the lower frequency components, thus elongating the pulse. This significantly reduces its peak intensity or power, decreasing the probability of damage of the optical components. The pulse then has positive GVD or chirp. In the Spitfire amplifier, the low energy, short duration pulse from the Tsunami oscillator is extended up to 10,000 times to approximately 500 ps. Figure 2.5 schematically shows the system of temporal stretching of Spitfire Pro's pulses.

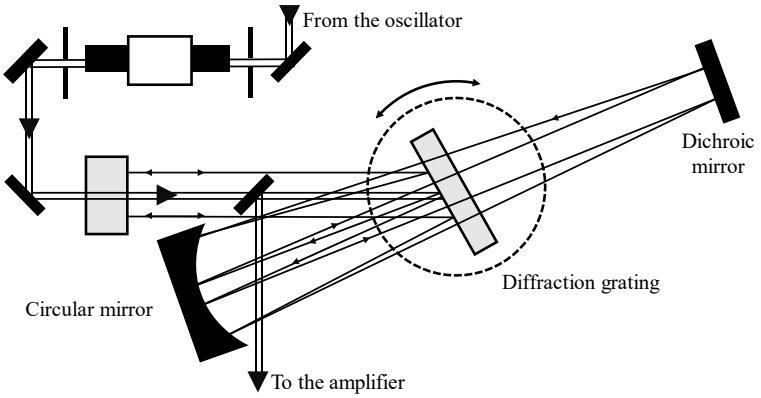

Figure 2.5. *Optical setup used to produce the temporal stretching of laser pulses in the Spitfire regenerative amplifier. Figure adapted from the user's manual.*

Amplification of stretched pulses: The regenerative amplification technique allows the pulse to pass several times through the active medium (Ti:sapphire crystal), significantly increasing the pulse energy. Figure 2.6 shows an outline of the amplification process.

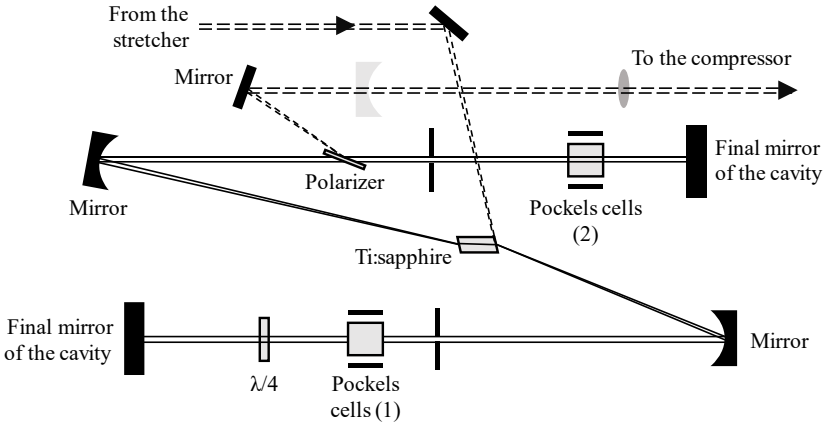

Figure 2.6. *Regenerative amplification scheme pulses in the Spitfire regenerative amplifier. Figure adapted from user's manual.*

The stretched pulse enters the Z-shaped resonant cavity when reflected by one of the faces of the Ti:sapphire crystal. Inside the cavity, two Pockels cells control the input and output pulses within the cavity through their vertical polarization. The first Pockels cell is responsible for selecting approximately one of each 76,000 pulses from the oscillator for further amplification, and the second Pockels cell extracts the pulse from the cavity once it has been sufficiently amplified. The activation of the Pockels cells is synchronized with the RF signal generated by the active mode-locking electronics of the oscillator. The activation phase, *i.e.*, the activation time of the Pockels cells with respect to the pulse train, must be adjustable over a wide range, from 0 to 200 ns. Since the pulse is extracted from the cavity when the second Pockels cell is activated, this can only occur when the pulse has passed through the cavity as many times as necessary (around 20), *i.e.*, after approximately 200 ns after activating the first Pockels cell.

Amplified pulse Compression: The pulse is then compressed after amplification employing an optical compressor, a device analogous to the stretcher in which the grating is positioned so that the shorter frequencies travel more path than the long ones, introducing negative GVD. Therefore, the pulse exits the system with a much shorter temporal duration and temporarily overlapping frequencies, that is, without dispersion. The degree of compression can be controlled by the longitudinal movement of a pair of mirrors located on two-step motors. In this way, one can optimize or obtain pulses of the desired duration. Figure 2.7 shows the design of the compression zone of the laser pulses in the regenerative amplifier.

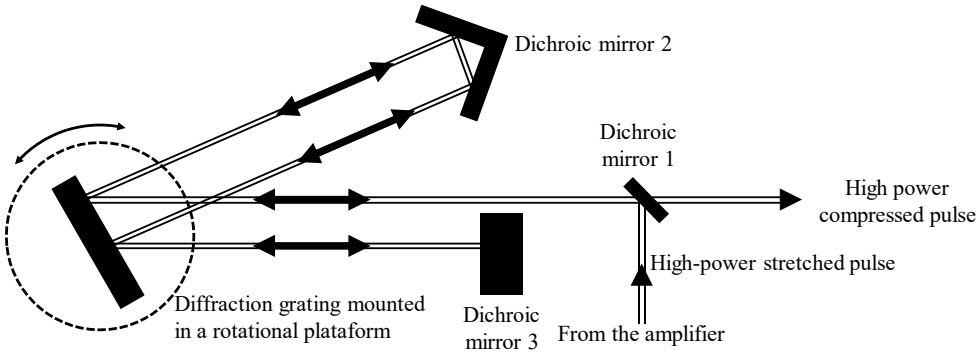

Figure 2.7. *Optical setup used to produce temporary compression of laser pulses in the Spitfire regenerative amplifier. Figure adapted from the user's manual.*

Figure 2.8 and figure 2.9 show the amplifier and the arrangement of the different elements (stretcher, amplifier and compressor) described above.

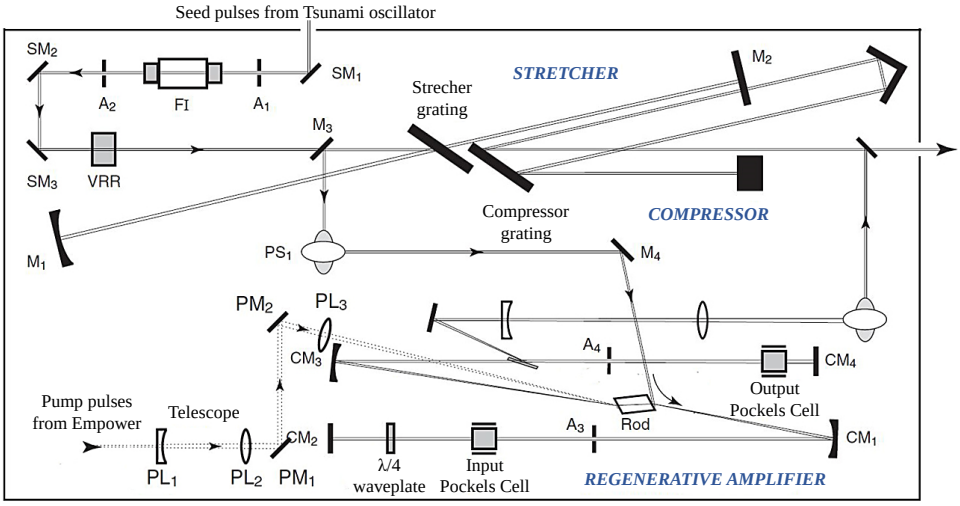

Figure 2.8. *Representation of the Spitfire regenerative amplifier where the stretcher, regenerative amplifier, and compressor, can be distinguished. The 527 nm pumping beam path from the Empower is also displayed. M - mirrors, A – apertures, FI - Faraday Isolator, VRR - vertical retro-reflector, PS – periscope, CM - cavity mirror, L – lenses, λ/4 waveplate - Quarter-wave plate. Figure adapted from the user's manual.*

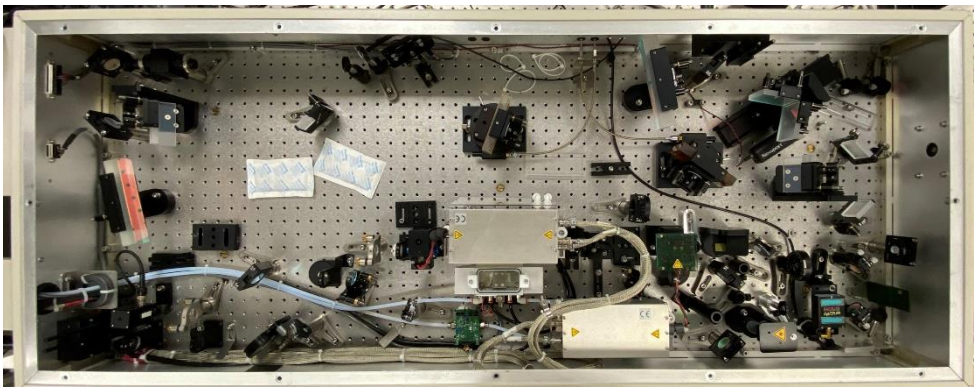

Figure 2.9. *Picture of the Spitfire regenerative amplifier where the stretcher (top left), regenerative amplifier (bottom left), compressor (top right), and the Dazzler device (bottom right) can be distinguished.*

Typical output pulses of the Spitfire regenerative amplifier are centered around 804 nm, with 50 fs temporal duration, an FWHM of around 46 nm, with 1 kHz repetition rate, and 3.2-3.4 mJ energy per pulse. The output pulses are horizontally polarized. Figure 2.10 shows the typical spectrum of a Spitfire Pro. Note that the spectral width obtained at the output of the amplifier is smaller than that of the oscillator. This is mainly since the amplifier does not amplify the entire spectrum of the pulses coming from the oscillator but amplifies the energy of each spectral component proportional to its initial intensity.

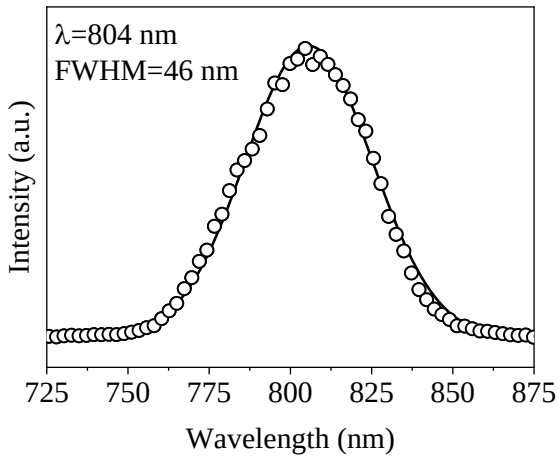

Figure 2.10. *Spitfire amplifier output spectrum. The experimental data (circles) is fitted to a Gaussian function. The spectrum is centered at 804 nm and has an FWHM of 46 nm, equivalent to 43 fs for FTL pulses.*

2.1.1.3. Phase control

The laser is also equipped with a pulse shaper (Fastlite Dazzler HR-800), allowing to control of the amplitude and spectral phase of femtosecond laser pulses. Without this device, the pulses generated

in the amplifier may not be FTL and/or present undesirable pre- and post-pulses. Figure 2.11 shows the working principle of the Dazzler.

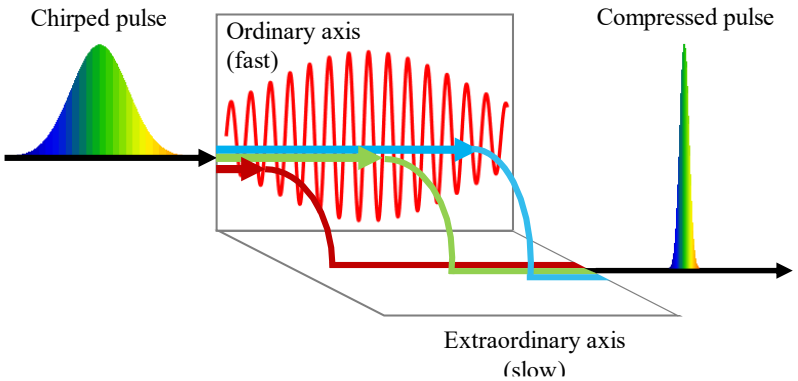

Figure 2.11. *Working principle of the Dazzler. Figure adapted from reference* [129].

The Dazzler is an AOM, also known as a Bragg cell, which consists of a piezoelectric transducer attached to a tellurium dioxide (TeO_2) crystal, which has high birefringence. An RF synthesizer generates an oscillating electrical signal that drives the transducer to vibrate, producing acoustic waves in the material. The acousto-optic wave travels through the crystal's ordinary axis at a speed *v*, well below the speed of light, making it appear motionless to the laser beam. Therefore, the laser beam spatially sees a diffraction grating that reproduces the temporal form of the RF signal. This diffraction grating is called acoustic grating.

In the acousto-optic programmable dispersive filter (AOPDF) device, the incident femtosecond pulse is initially polarized along the birefringent crystal's ordinary (fast) axis. The different spectral components can be diffracted on the extraordinary (slow) axis when two conditions are met:

Phase-matching: $$\vec{k}(\omega_{out}) = \vec{k}(\omega_{ac}) + \vec{k}(\omega_{in}) \quad (2.3)$$

Energy conservation: $$\omega_{out} = \omega_{ac} + \omega_{in} \quad (2.4)$$

where *in* refers to the incident femtosecond pulse coming from the oscillator, *out* to the output diffracted pulse, and *ac* to the acoustic wave.

The Dazzler's operating details can be found in reference [130]. In summary, this device allows controlling the spectral phase of the laser pulses through the control of the applied acoustic wave. In our laboratory, the Dazzler is in the regenerative amplifier to compensate for high orders (> 2) in the spectral phase of the pulses coming from the oscillator. In figure 2.8, the location of the Dazzler device can be distinguished.

2.1.2. Non-linear processes and generation of new wavelengths

Ti:sapphire laser system provides intense laser radiation in the femtosecond timescale, tunable in the wavelength 650-1080 nm range. However, numerous applications require other wavelengths not covered by the output of the Ti:sapphire laser. The generation of new wavelengths can be achieved through non-linear processes.

Based on Maxwell's equations, the interaction of matter with the electric field of radiation can be described in terms of polarization. For a linear interaction, the polarization is given by:

$$P(r,t) = \varepsilon_0 \chi(r) E(r,t) \tag{2.5}$$

where r is the spatial position, and t is the time, $P(r, t)$ is the polarization, $E(r, t)$ is the electric field, ε_0 is the vacuum permittivity and χ is the electrical susceptibility.

If the strength of the electric field of the light wave is in the range of atomic electric fields (E_{at}= $e/a_0^2 = 10^8$ V/m), non-linear effects can occur in the medium,[131] so polarization must be expanded in a Taylor series incorporating additional terms:

$$P(r,t) = \varepsilon_0 \chi^{(1)} E(r,t) + \varepsilon_0 \chi^{(2)} E^2(r,t) + \varepsilon_0 \chi^{(3)} E^3(r,t) + ... \tag{2.6}$$

where the coefficients $\chi^{(n)}$ are the n^{th} order susceptibilities of the medium. The term $\chi^{(1)}$ is related to the refractive index of the material; $\chi^{(2)}$ is responsible for two-photon processes such as SHG ($\chi^{(2)}(\omega, \omega; 2\omega)$); $\chi^{(3)}$ produces three-photon effects like THG ($\chi^{(3)}(\omega, \omega, \omega; 3\omega)$ or the non-linear refractive index ($\chi^{(3)}(\omega, -\omega, \omega; \omega)$).

The non-linear polarization is described then as:

$$P_{n,l}(r,t) = \varepsilon_0 \chi^{(2)} E^2(r,t) + \varepsilon_0 \chi^{(3)} E^3(r,t) + ... \tag{2.7}$$

and the equation for the electric field of the radiation remains:

$$\nabla^2 E - \mu_0 \varepsilon_0 \frac{\partial^2 E}{\partial t^2} = \mu_0 \frac{\partial^2 P}{\partial t^2} \tag{2.8}$$

In the case of the interaction of three waves with frequencies ω_1, ω_2 and ω_3, according to the scheme in figure 2.12, the second-order non-linear polarization, $P^{(2)}$, has three components which are given by:

$$P^{(2)}(\omega_1) = \varepsilon_0 \chi^{(2)}(\omega_3, \omega_2; \omega_1) E(\omega_3) E(\omega_2) \tag{2.9}$$

$$P^{(2)}(\omega_2) = \varepsilon_0 \chi^{(2)}(\omega_3, \omega_1; \omega_2) E(\omega_3) E(\omega_1) \tag{2.10}$$

$$P^{(2)}(\omega_3) = \varepsilon_0 \chi^{(2)}(\omega_1, \omega_2; \omega_3) E(\omega_1) E(\omega_2) \tag{2.11}$$

Using the slowly varying envelope approximation (sometimes also called slowly varying amplitude approximation), neglecting loss, and assuming steady-state solutions, the equation (2.8) is transformed into the following three coupled wave equations:

$$\frac{\partial E_1}{\partial z} = ikE_3 E_2 e^{i\Delta kz} \tag{2.12}$$

$$\frac{\partial E_2}{\partial z} = ikE_3 E_1 e^{i\Delta kz} \tag{2.13}$$

$$\frac{\partial E_3}{\partial z} = ikE_1 E_2 e^{-i\Delta kz} \tag{2.14}$$

where k is defined as:

$$k = \frac{\omega \chi^{(2)}}{nc} \tag{2.15}$$

Then, $E_i(\omega)$ is now written as:

$$E_i(\omega) = E_i e^{ik_i z} \tag{2.16}$$

where i=1, 2 or 3 and

$$\Delta k = k_3 - k_1 - k_2 \tag{2.17}$$

The three coupled wave equations describe the fundamental physics involved in SHG, SFG, difference frequency generation (DFG) and optical parametric amplification (OPA). The general solutions to these equations indicate that high efficiency in converting one wave into another requires a high-intensity pumping wave, high second-order susceptibility $\chi^{(2)}$, and good phase-matching.

If two beams of frequencies ω_1 and ω_2 are overlapped onto a suitable non-linear material with a total intensity exceeding the non-linear regime, beams corresponding to the SFG $\omega_{sum}=\omega_1+\omega_2$, or DFG $\omega_{diff}=\omega_1-\omega_2$, or both, with I_{sum} and I_{diff} intensities are generated.

Figure 2.12 shows the non-linear processes by which new frequencies are generated in the non-linear medium. Case (A) corresponds to SFG because of the interaction of the frequencies ω_1 and ω_2, and case (B) is optical parametric amplification.

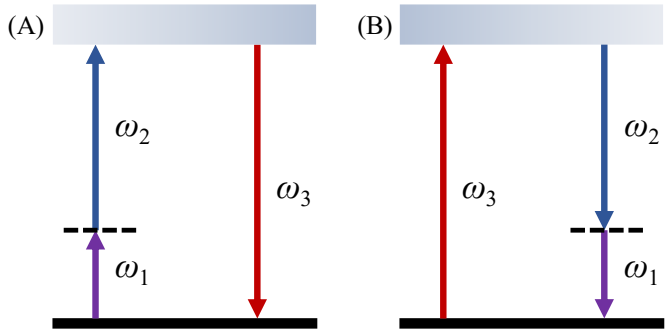

Figure 2.12. *Schematic representation of (A) an SFG process and (B) optical parametric amplification in a non-linear medium.*

2.1.2.1. Third and fourth-harmonic generation

Two different systems are used for THG and FHG of the fundamental wavelength of the Ti:sapphire CPA laser system.

One of the systems is based on two commercial modules (Spectra-Physics TP-1A and TP-1A-FHG-II), where the harmonic generation is produced employing non-linear beta barium borate (BBO) crystals and transmissive optics. In contrast, the other system is based on an optical setup where the harmonic generation is based on the use of non-linear BBO crystals and reflective optics to avoid astigmatism in the beam as well as significant pulse lengthening due to GVD, both of which would affect the conversion efficiencies in each BBO crystals. The latter system is provided with thinner BBO crystals than the former to achieve a compromise between short pulse durations and reasonable conversion efficiencies.[132]

2.1.2.1.1 Third and fourth-harmonic generation by transmissive optics

Figure 2.13 shows the optical setup of the commercial modules (Spectra-Physics TP-1A and TP-1A-FHG-II) for the THG and FHG of the fundamental wavelength of the Ti:sapphire CPA laser system.

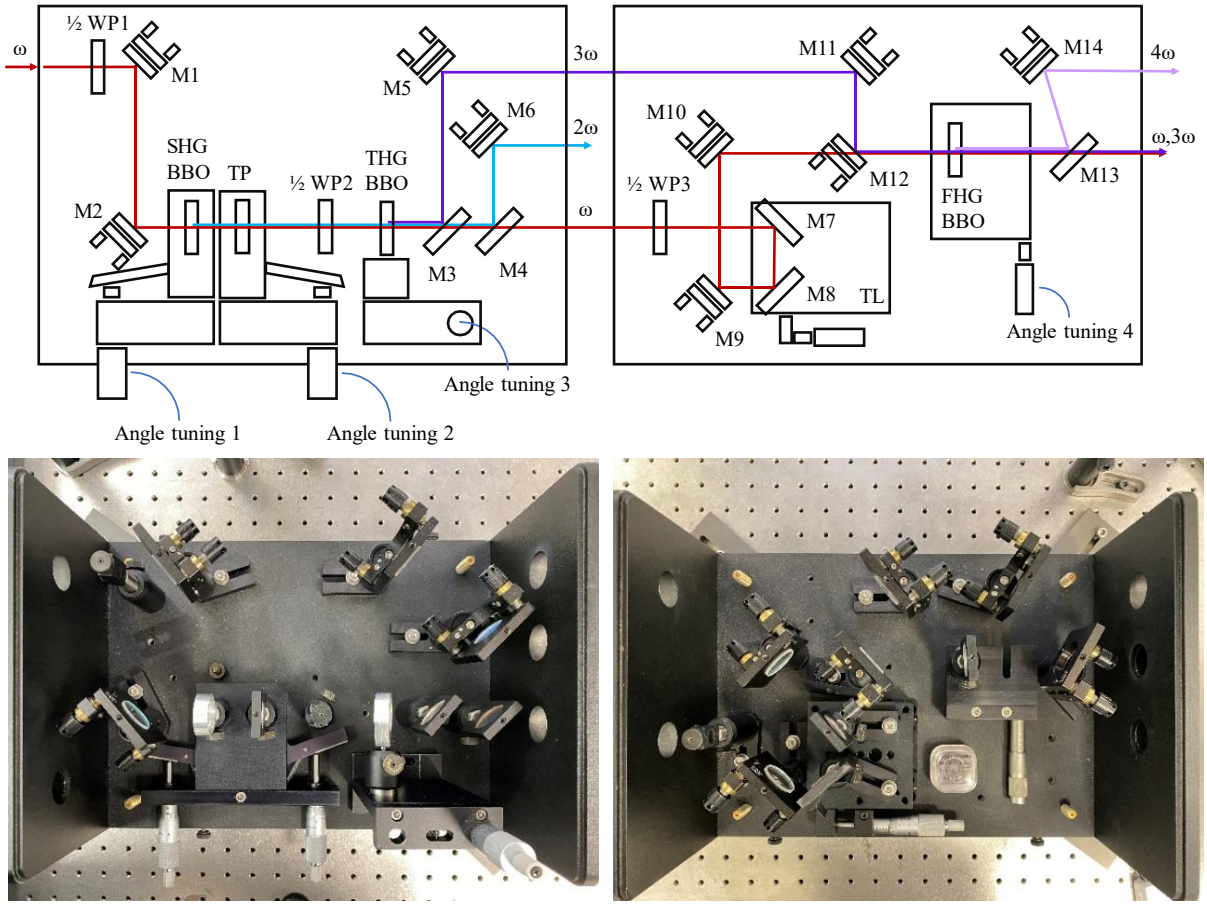

Figure 2.13. *(Top) Layout of the commercial Spectra-Physics modules for THG (left) and FHG (right). 1/2 WP, half-wave plate; M, mirror; SHG BBO, SHG crystal; TP, time plate; THG BBO, THG crystal for SFG; FHG BBO, FHG crystal for SFG. Figure adapted from the user's manual. (Bottom) Picture of the device's inside.*

The first module (left in figure 2.13) is pumped by an energy fraction from the regenerative amplifier (about 1.2 mJ). First, the beam polarization is rotated from horizontal to vertical, employing a half-wave plate. After that, SHG of the fundamental takes place in a non-linear BBO crystal producing radiation around 400 nm. The THG takes place by SFG between the fundamental and the second harmonic in another BBO crystal. Temporal compensation between the second harmonic and the fundamental pulses is achieved by a tunable time plate instead of the typical translational stage.[133] It consists of a special birefringent crystal mounted on a rotational stage. As represented in figure 2.14, it has a principal axis of refractive index n_0 parallel to its surface and a principal axis of refractive index n_{eff} forming an angle θ to its surface normal. The time plate is mounted such that it is rotatable about its principal axis n_0 allowing a time delay between the two laser pulses as they travel through the time plate, which is a function of the incident angle θ between its surface normal and the propagation direction of the laser pulses. Therefore, time delay can be continuously adjusted by rotating the time plate to change the incident angle θ.

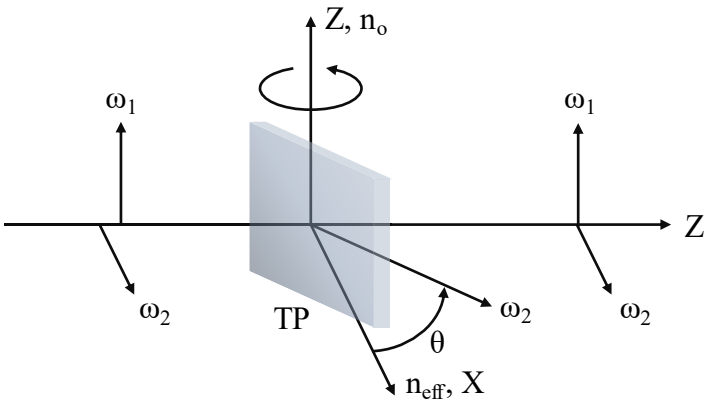

Figure 2.14. *Time delay compensation of two linearly polarized beams ω_1 and ω_2 utilizing a time plate. The time plate is an α-BBO crystal mounted in a rotation stage for tuning the time delay between the fundamental and SHG beams. The fundamental (ω_1) and the SHG beam (ω_2) are polarized vertically and horizontally, respectively. The time plate is configured so that the fundamental and the SHG beams are the ordinary (o) and extraordinary (e) waves, respectively, and the time delay can be tuned by rotating the time plate around it n_o axis (z-axis). The time plate provides a very smooth time delay control. Figure adapted from the user's manual.*

At the end of this first module, dichroic mirrors are placed to separate the different output wavelengths obtained from the non-linear processes.

Figure 2.15 shows a typical spectrum of the third harmonic centered at 268 nm.

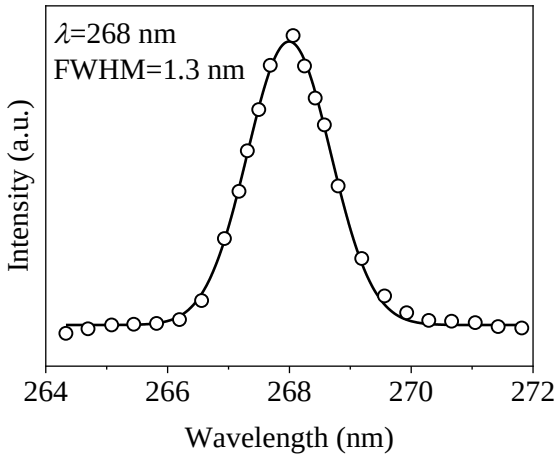

Figure 2.15. *Output spectrum of the third harmonic produced in the first module (left in figure 2.13). The spectrum is centered at 268 nm and has an FWHM of 1.3 nm. Circles represent experimental data fitted to a Gaussian function represented in solid line.*

In the second module (right in figure 2.13), the FHG takes place by SFG between the fundamental and the third harmonic. The temporal compensation between the pulses is achieved by a linear translational stage.

Figure 2.16 shows a typical spectrum of the fourth harmonic centered around 201.2 nm.

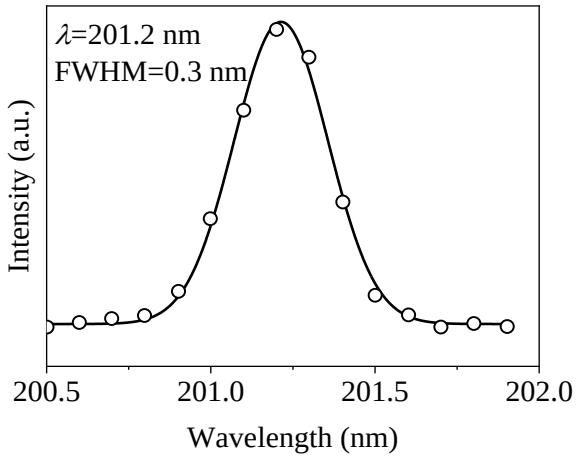

Figure 2.16. *Output spectrum of the fourth harmonic produced in the second module (right in figure 2.13). The spectrum is centered at 201.2 nm and has an FWHM of 0.3 nm. Circles represent experimental data fitted to a Gaussian function represented in solid line.*

All BBO crystals (U-Oplaz technologies) used in both modules are type I phase-matching and with a thickness of about 0.5 mm.

2.1.2.1.2 Third and fourth-harmonic generation by reflective optics

There is an alternative system for THG and FHG of the fundamental of the Ti:sapphire CPA laser system. Figure A. 1 of the appendix displays the optical scheme of this setup, based on the design described in reference [132]. It was built by Garikoitz Balerdi and Dr. Sonia Marggi-Poullain.

The setup is seeded by a fraction of the regenerative amplifier's energy (about 1.2 mJ). The beam spot from the amplifier is around 6 mm, so the first step is its size reduction by a 2:1 reflective telescope, consisting of a 1 m focal length concave (CC) mirror and a 0.5 m focal length convex (CX) mirror separated by the sum of their focal lengths ($d=f_1+f_2$=0.5 m). Mirrors are used instead of lenses to avoid the pulse stretching due to GVD. This stretching would, in turn, affect the conversion efficiencies in the BBO crystals. Afterward, the beam is split into two arms employing a 90/10 beamsplitter at an incident angle of 45º. The reflected beam is, in turn, sent to a 65/35 beamsplitter at an incident angle of 45º. Then the transmitted beam (65 %) is first directed to a second reflective telescope to a further size reduction by a factor of two. The polarization of this beam is rotated from horizontal to vertical through a half-wave plate and then sent to a BBO crystal for THG. The reflected beam (35 %) is sent to a linear translational stage and then to a BBO crystal for SHG. The resulting beam is filtered by a dichroic mirror, reflecting the SHG and transmitting the fundamental wavelength, which is then dumped by a beam block. The fundamental wavelength and the SHG beams are recombined in a BBO for THG. The output beam is sent to a highly reflective third harmonic and high transmission fundamental mirror. The fundamental is dumped, and the third harmonic is sent to the SFG BBO for FHG (60 mm thickness),

where it is recombined with a 10 % energy fraction of the first beamsplitter. Before arriving at the FHG BBO, the beam goes through a linear translation stage and a 2:1 telescope. Before the FHG BBO, a flip mirror is located to reflect the THG beam in case of need for experiments. If the mirror is flipped down, the FHG generation is feasible. Each non-linear mixing process is achieved with type I phase-matching. The BBO crystals (United Crystals) for SHG and THG are about 0.5 mm in thickness.

Due to the conservation of momentum and assuming a Gaussian beam profile, the beam diameter should decrease after each non-linear mixing process by a factor of $\sqrt{2}$. The interacting pulses must have the same beam size for the resulting pulse's diameter to be reduced by this factor. To maximize the conversion efficiency of the SFG process, the fundamental beam diameter must be reduced to be the same as the SHG beam. The same is done with the fundamental beam used for the FHG.

Another important consideration is the polarization of the beams entering each BBO. The fundamental beam from the amplifier is horizontally polarized, whereas the second harmonic is vertically polarized. So, for the THG generation *via* type I phase-matching in the corresponding BBO, the polarization of the fundamental should be rotated from horizontal to vertical, employing a half-wave plate. The third harmonic has horizontal polarization, and it is later recombined with the initially horizontally polarized fundamental for FHG with a final vertical polarization. Under the working configuration, to reconstruct the images using Abel transform, the fourth harmonic polarization must be rotated from vertical to horizontal, which is achieved by employing a periscope.

2.1.2.2. Optical parametric amplifier

For the generation of femtosecond laser radiation with a wavelength not accessible by frequency conversion by harmonic generation of the fundamental of a Ti:sapphire laser, optical parametric amplifiers (OPAs) are often used.

An OPA is a laser light source that emits light of variable wavelengths achieved by an optical parametric amplification process; the reverse process of SFG. In a parametric process within a non-linear material, represented in figure 2.17, the pump wave with frequency ω_p is split into two different waves with lower frequencies. The output wave with a higher frequency is called signal, whereas the one with a lower frequency is called idler. The phase-matching conditions in the non-linear crystal determine these frequencies.

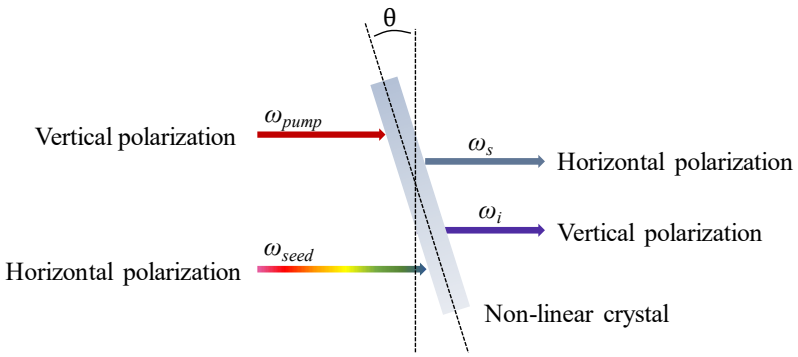

Figure 2.17. *Representation of an optical parametric amplification process in a non-linear crystal.* ω_{pump}*, pump beam;* ω_{seed}*, seed beam,* ω_s*, signal beam;* ω_i*, idler beam.*

The parametric gain at the phase-matched condition is given by:

$$G \propto d\sqrt{(\omega_s \omega_i I_p)} \tag{2.18}$$

where G is the parametric gain, ω is the signal beam, ω_i is the idler beam and I_p is the pump intensity.

Higher gain can be achieved employing shorter pump wavelengths, higher pump intensities, and when signal and idler match in frequency. This is favored using the high energy, second harmonic femtosecond pulses from a Ti:sapphire amplifier as the pump wavelength. Another critical factor in the amplification of ultrashort pulses is the effective interaction length between the pump and signal (or idler) pulses.

Parametric converted signal and idler waves could build up from either quantum noise or a seeded beam. OPAs present a pre-stage to generate the seed wave, either through parametric fluorescence (superfluorescence, *i.e.*, optical parametric generation (OPG) initiated from quantum noise), or through white-light generation (WLG). A superfluorescence seed can be generated using the same OPA crystal at the same phase-matched angle. However, since it is generated by tightly focusing a small amount of split-off pump beam into the crystal, the resultant superfluorescence becomes color separated, and its stability is extremely sensitive to small variations when tuning the output wavelength. On the contrary, the WLG seed is generated separately and is set for the whole tuning range, making the OPA output becomes easier to align and with a stable output over a wider tuning range than the other method.

When employing femtosecond and picoseconds pulses, white light can be originated by focusing a few microjoules of energy into materials, such as quartz, sapphire, or a liquid cell. Employing a solid-state material is preferable since WLG through liquids is challenging and not very convenient because the liquids must be changed from time to time, and some of them are toxic.

Figure 2.18 shows the optical scheme of the OPA available in the laboratory (Spectra-Physics OPA 800CF).

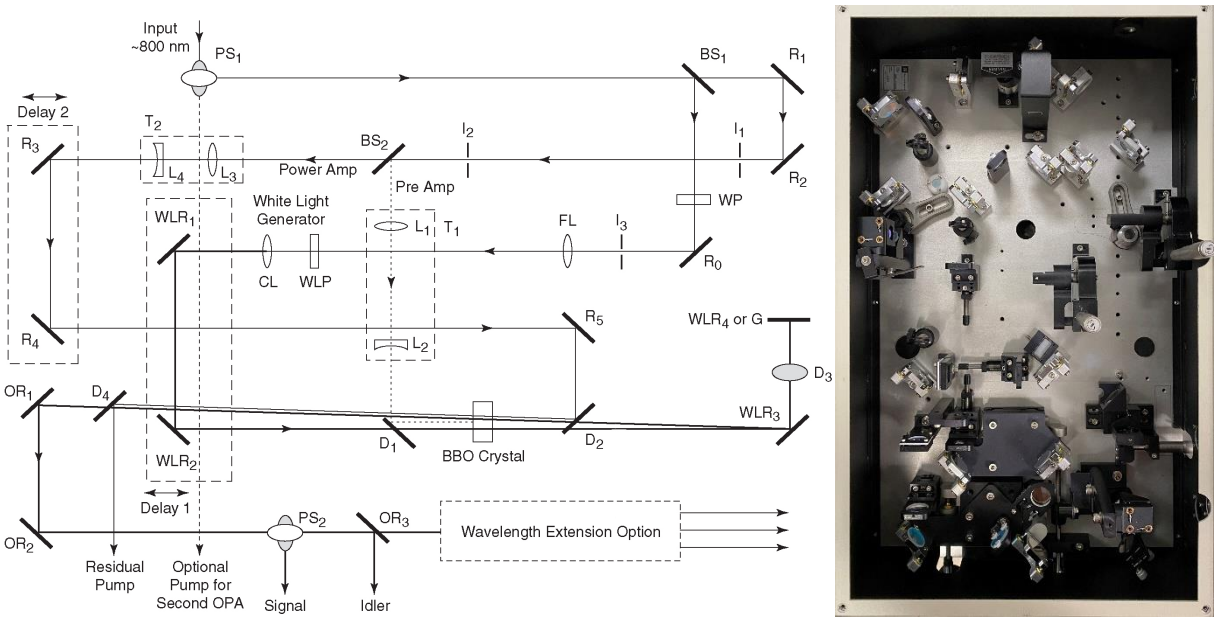

Figure 2.18. *(Left) Optical scheme of the parametric optical amplification (OPA) system. Beamsplitter ($BS_{1,2}$), collimating lens (CL), dichroic mirrors (D_{1-4}), focusing lens (FL), grating (G), irises (I_{1-3}), lenses (L_{1-4}), output reflectors (OR_{1-2}), periscope (PS_{1-2}), reflectors for 800 nm (R_{0-5}), telescopes (T_{1-2}), white-light plate (WLP), white-light reflectors (WLR_{1-4}). Figure adapted from the user's manual. (Right) Picture of the device's inside.*

An energy fraction from the regenerative amplifier (about 1 mJ) is used to pump the OPA. After a periscope (PS_1), which flips the polarization from horizontal to vertical, the pump beam is split into two beams by a beamsplitter (BS_1). The reflected less intense beam (< 4 %) is reflected by a mirror (R_0), goes through an iris (I_3), and it is focused (FL) into a white light plate (WLP) to produce a white light continuum (WLC) that provides the seed pulse for the OPA. It is re-collimated and relayed to the OPA crystal through a variable delay stage (Delay 1). The transmitted more intense beam (96 %), which is used to pump the OPA, is reflected by two mirrors (R_1 and R_2) and split again into two pump beams by a second beamsplitter (BS_2). Each is down collimated to pump the OPA crystal. About 15 % of this beam is used to pump the pre-amplification stage and the rest to pump the amplification stage.

In the pre-amplification stage, the beam is sent to a dichroic mirror (D_1) through a pair of lenses (L_1 and L_2) that acts like a telescope. The dichroic mirror has a high reflectance in the 750-840 nm region and is highly transmissive at longer wavelengths, allowing the recombination of the pre-amplifier with the white light beam in the type II BBO crystal. The signal beam must be orthogonally polarized to the pump and idler. The pump polarization is vertical, and the white light polarization is horizontal while the signal and idler polarizations are vertical and horizontal, respectively. The white light must overlap

the pump beam both spatially and temporally, which is achieved by optimizing the delay between these two pulses using a micrometric screw connected to a platform on which the WLR_1 and WLR_2 mirrors are placed (Delay 1). The signal and idler beams generated in the BBO crystal in the pre-amplification stage then pass through another dichroic (D_2). The pre-amplified idler beam is diffracted back towards the parametric crystal by two mirrors (WLR_3 and WLR_4), where it is used as a seed beam for the OPA amplification process.

The pump beam of the amplification process, that is, the beam transmitted through the second beamsplitter (BS_2), is driven to the non-linear crystal through some mirrors ($R_{1\text{-}5}$) and a dichroic mirror (D_2). In the BBO, it is overlapped collinearly with the idler beam that was reflected by the WLR_3 and WLR_4 mirrors, for the final amplification stage, with vertical and horizontal, respectively. The signal and idler beams have horizontal and vertical polarization, respectively. The temporal overlap between the pump and the pre-amplified white light pulses in the BBO is achieved by a second linear translation stage (Delay 2). The wavelengths of the signal and idler beams generated in the amplification stage are determined by the phase-matching angle of the BBO crystal. Therefore, OPA tuning is achieved by varying these angles and adjusting the positions of the linear translational stages (Delay 1 and Delay 2) for energy optimization. The fundamental residual beam can be separated from the signal and idler beams employing a dichroic mirror (D_4), and the signal and idler beams are separated in turn, utilizing a periscope. In the present case, signal, idler, and fundamental are used for the generation of harmonics.

Figure 2.19 shows a typical tuning curve and energies obtained from signal and idler when the OPA is pumped with a 0.8 mJ/pulse of 800 nm. By changing the phase angle of the BBO crystal, it is possible to tune the OPA in the range 1.1-3.0 μm with energies up to 130 μJ/pulse.

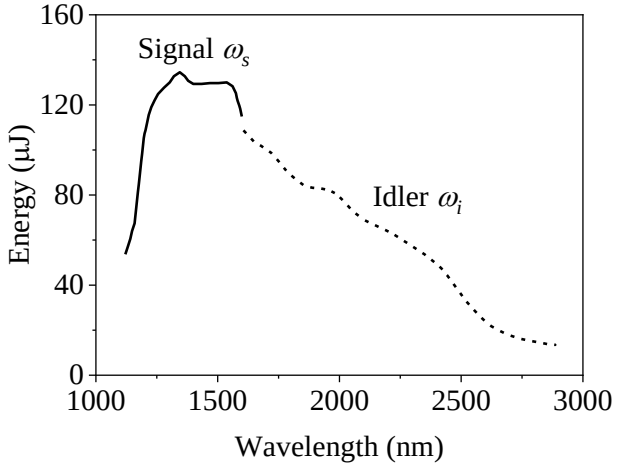

Figure 2.19. *OPA tuning curves of the signal and idler beams. Figure adapted from the user's manual.*

The OPA-800CF is provided with a wavelength extension for harmonic generation. This feature allowed the obtention of the three different wavelengths required for the experiments: 243.1, 304.5-306 and 333.5 nm.

- Laser radiation centered at 243.1 nm is achieved through SHG of the resulting SFG between the signal tuned at 1445-1710 nm and the fundamental radiation residual beam.
- Laser radiation in the range of 300-400 nm is achieved by FHG of the signal, whose tuning curve is displayed in figure 2.20.

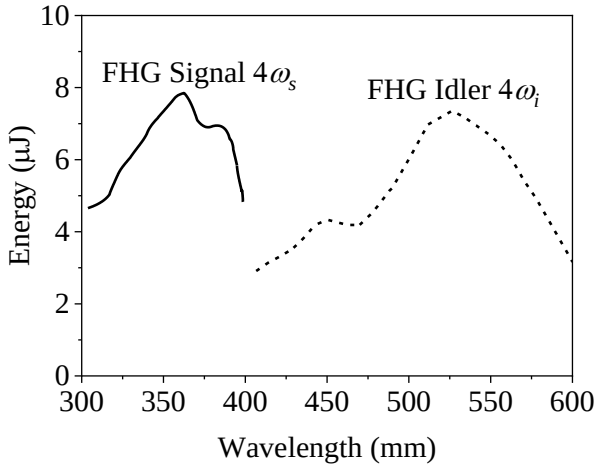

Figure 2.20. *Tuning curves of the FHG of the signal beam and the idler beam. Figure adapted from the user's manual.*

Figure 2.21 displays the OPA output spectra for 304.5 nm (FWHM=1.8 nm), and 333.5 nm (FWHM=2.5 nm), with typical energies per pulse in the range of 3-5 μJ.

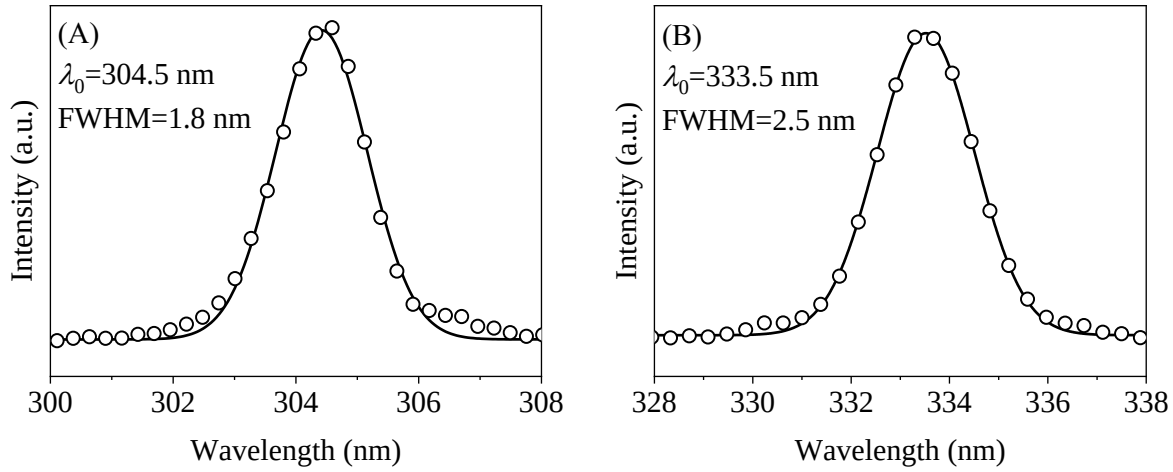

Figure 2.21. *Output spectra of the fourth harmonic of the signal. (A) The laser pulse is centered at ≈304.5 nm and has an FWHM of ≈1.8 nm. (B) The laser pulse is centered at ≈333.5 nm and has an FWHM of ≈2.5 nm. The experimental data (circles) is fitted to a Gaussian function represented by a solid curve.*

2.1.2.3. Travelling-wave optical parametric amplifier

The TOPAS (Light Conversion TOPAS Prime) is a two-stage parametric amplifier of WLC. The layout of the TOPAS is presented in figure 2.22.

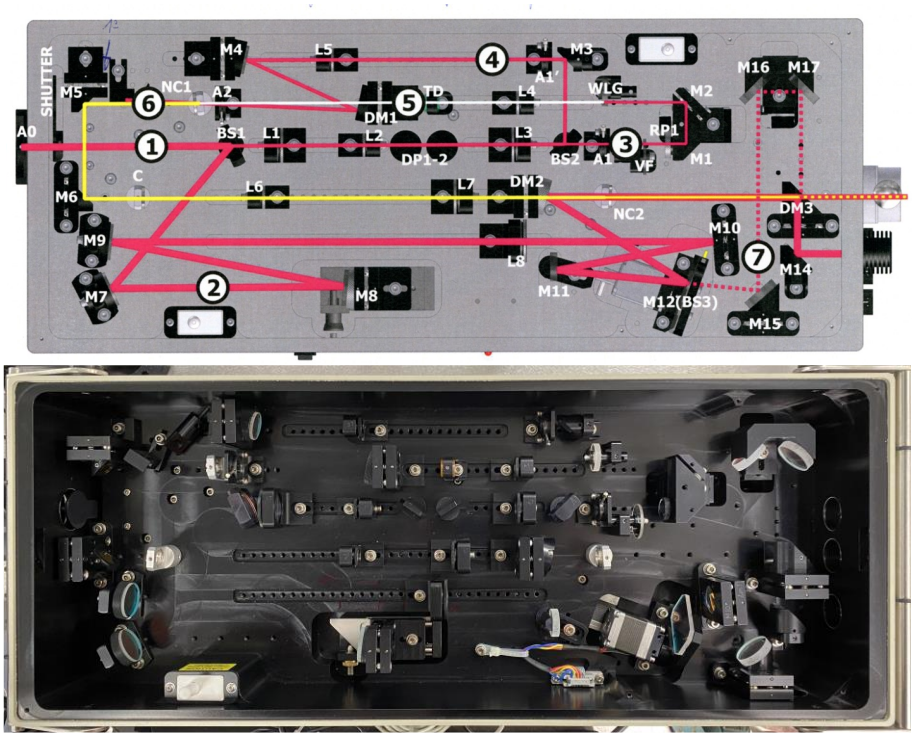

Figure 2.22. *(Top) Layout of TOPAS Prime. Pump beam delivery and splitting optics (PO), white-light continuum generator, a pre-amplifier or first amplification stage (PA1), a signal beam expander-collimator (SE), a power amplifier or second amplification stage (PA2) and an optional fresh pump stage for sum-frequency (FP). 1-input pump beam, 2-PA2 pump beam, 3-WLG pump beam, 4-PA1 pump beam, 5-White light beam, 6-Signal beam, 7-Optional fresh pump stage for SFG. Figure from the user's manual. (Bottom) Picture of the TOPAS Prime.*

Fundamental pump pulses with energies around 1-3 µJ are used to produce WLC in a sapphire plate. The WLC beam and another fraction (30-50 µJ) of the pump beam are focused on the pre-amplifier crystal. The pulses are temporally overlapped inside the non-linear crystal, where parametric amplification takes place. A non-collinear geometry is used for easy separation of the amplified signal beam. A beam block dumps the residual pump and idler beams after the crystal. The signal beam is expanded and collimated by a lens telescope and driven into the second amplification stage. The power-amplifier is pumped by the bulk of the input pump beam. A lens-mirror telescope reduces the pump beam size to achieve the necessary pump intensity. The beam is kept collimated after the telescope. The pump and signal beams are overlapped collinearly in the second non-linear crystal. As a result, the TOPAS outputs collinear well-collimated signal and idler beams.

The wavelength tuning at the pre-amplifier stage is achieved by changing the delay of the white-light pulse with respect to the first pump pulse and adjusting the crystal angle for optimal phase-matching. The wavelength tuning in the power-amplifier is achieved by adjusting the pre-amplifier wavelength and then optimizing the second crystal angle and signal delay with respect to the second pump beam. Once TOPAS is appropriately adjusted and calibrated, the output wavelength can be easily changed using the WINTOPAS software. The device employs computer-controlled translation and rotation stages that allow for fast and precise optimization of positions of specific optics when tuning the output wavelength of the device. The performance of the TOPAS highly depends on the operating wavelength.

In figure 2.23, the output energy and power of TOPAS as a function of the signal and idler wavelengths are represented.

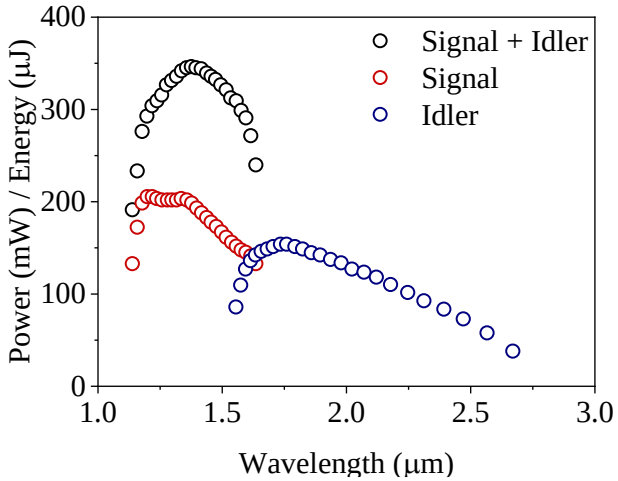

Figure 2.23. *Output energy and power of TOPAS versus signal and idler wavelengths. Figure adapted from the user's manual.*

Commercial optional frequency mixers can extend the tuning range into the VIS, UV and/or IR ranges. Instead of using these commercial subunits, other wavelengths were obtained through non-linear processes using an assembly of BBOs detailed below. The TOPAS output polarization must be considered: the signal has vertical polarization, whereas the idler has horizontal polarization.

2.1.2.3.1 Fourth-harmonic generation of signal

The TOPAS is provided with a module constituted by two SHG type I BBOs to obtain the FHG of the signal. According to figure 2.23, tunable radiation between 285 and 400 nm can be obtained with this setup. The optical setup can be seen in figure 2.24.

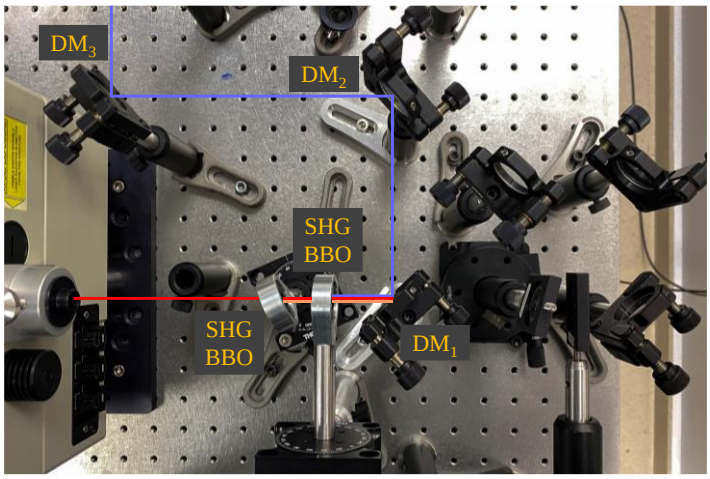

Figure 2.24. *TOPAS subunit for the FHG of the signal by two consecutive SHG type I BBOs.*

In a first type I BBO, the horizontally polarized second harmonic of the vertically polarized signal radiation is obtained. The phase matching is achieved thanks to the BBO rotation around an axis perpendicular to the optical table. Afterward, the vertically polarized fourth harmonic of the signal is obtained in a second type I BBO, whose rotation is made around an axis parallel to the optical table. The polarization of the resulting beam should be rotated from vertical to horizontal using a half-wave plate before reaching the reaction chamber to allow the image reconstruction using inversion methods.

2.1.2.3.2 Second-harmonic generation of the sum frequency generation between the signal and the fundamental

The TOPAS is provided with a second module constituted of SFG and SHG type I BBO crystals to obtain the SHG of resulting SFG between the signal and the fundamental beams. According to figure 2.23, tunable radiation between 235 and 269 nm can be obtained with this setup. The optical setup can be seen in figure 2.25.

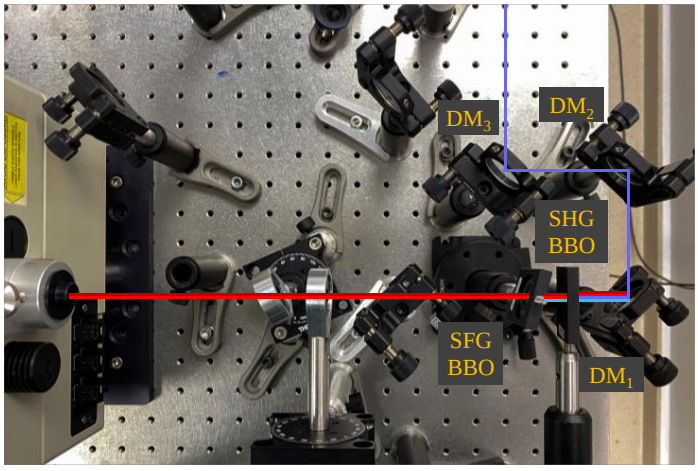

Figure 2.25. *TOPAS subunit for the generation of radiation by SFG between the signal and the fundamental radiation in a type I BBO and SHG of the resulting beam in a type I BBO.*

In a first type I BBO, the SFG occurs between the vertically polarized signal beam and the residual fundamental used to pump the TOPAS. The phase matching is achieved thanks to the BBO rotation around an axis perpendicular to the optical table. Afterward, the horizontally polarized SHG of the vertically polarized SFG output beam is obtained in a second type I BBO, whose rotation is made around an axis parallel to the optical table. Similarly, the polarization of the resulting beam should be rotated from vertical to horizontal using a half-wave plate before reaching the reaction chamber.

2.1.3. Characterization of femtosecond laser pulses

The characterization of the output laser pulses is fundamentally based on four types of measurements: the power, the spatial profile, the spectrum, and the pulse duration.

2.1.3.1. Power measurements

For the measurement of laser power, three power meters are available in the laboratory: the main power meter (Spectra-Physics 407A) is available for measuring the power of any laser beam ranging from 250 nm to 11 μm. This meter can measure power from a few mW to 20 W with an error of ±1 %. This spectral response of this device is very flat, *i.e.*, the efficiency is almost independent of the measured wavelength.

Two additional power meters are employed for the power measurements, especially from the OPA, TOPAS and harmonic generation modules. In the early stages of this Doctoral Thesis, a power meter (Gentec SOLO 2) was employed, allowing measurements from 0.1 nW to 10 kW with an error of 0.5 %±5 μV (best scale). This power meter was later replaced with a newer one (Gentec Maestro), allowing measurements from 1 μW-30 kW with an error of 0.25 %±5 μV (best scale).

2.1.3.2. Profile measurements

The beam profile is measured employing a beam profiling camera (Ophir Spiricon LT665 camera) with a beamsplitter attachment (Ophir LBS-300s attenuator). This beamsplitter allows the 0.01 % of the beam to be measured by the camera. This profile meter can operate with wavelengths from 190 nm to 1100 nm and measure laser beams with diameters up to 15 mm and powers ranging from 10 mW to 400 W. To prevent the possible saturation of the sensor, a set of adjustable neutral density filters are available. The camera works with the BeamGage software. Figure 2.26 displays the Spitfire regenerative amplifier laser beam measured after the recompression stage with the Ophir Spiricon LT665 beam profiling camera.

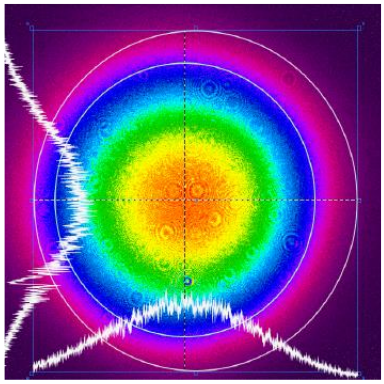

Figure 2.26. *Spitfire regenerative amplifier laser beam measured after the recompression stage with the Ophir Spiricon LT665 beam profiling camera.*

2.1.3.3. Spectrum measurements

For spectral measurements, there are two spectrometers. The output spectra of the oscillator and amplifier are recorded by a CVI spectrometer (CVI Laser Optics SM240). It is provided with a Sony ILX detector, with 2048 pixels and a pixel size of 14 μm x 200 μm and allows measurements in the 230 nm to 1.1 μm wavelength range with a resolution of 1 nm. The rest of the spectra are recorded by a Spectral Products spectrometer (Spectral Products SM440), provided with a better detector (Toshiba TCD 1304) with 3648 pixels and a pixel size of 8 μm x 200 μm. It allows measurements in the range from 200 nm to 1.05 μm with a resolution of 1 nm.

2.1.3.4. Pulse duration measurements

2.1.3.4.1 Infrared pulses

The temporal duration of the IR pulses from the amplifier is daily measured by a single-shot (SS) SHG autocorrelator (Positive Light).

In a SS autocorrelator, by recombining two replicas of the IR pulses with a non-collinear geometry in a non-linear potassium dihydrogen phosphate (KDP) crystal at a certain angle, a second harmonic signal is generated at each point of the overlap.[134] This signal is proportional to the product of the local intensity of each beam, corresponding to a specific time interval in the angle bisector formed by the recombined beams. Thus, the set of second harmonic intensities emitted along all parallel lines in the bisector angle composes a spatial intensity distribution of the second harmonic emission that can be measured with a CCD camera as displayed in figure 2.27.

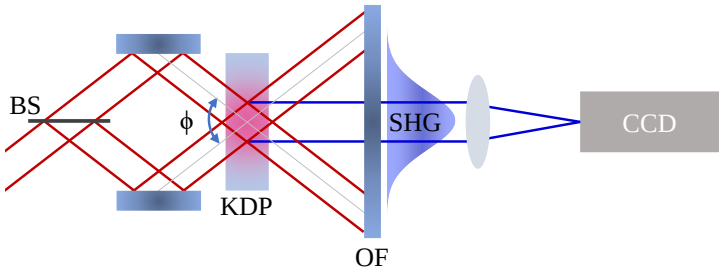

Figure 2.27. *Geometry of the beam recombination in a SS autocorrelator. Two pulses (in red) cross at an internal angle ϕ inside a non-linear crystal (KDP), and the resulting sum-frequency signal (in blue) is imaged onto a CCD detector, providing the second-order autocorrelation function.*

This spatial distribution is related to the pulse duration according to:

$$tp = \left(\frac{k}{c}\right) \cdot \Delta x \cdot \sin\phi \tag{2.19}$$

where t_p is the pulse duration, k is a numerical factor related to the pulse shape (k=1.44 for Gaussian pulses), c is the speed of light, and ϕ is the angle bisector formed by the recombined beams.

Finally, the system performs a sweep over the CCD camera lines and provides a signal observable on an oscilloscope as a function of a fictional timescale. A calibration procedure allows this fictional time to be linearly related to the real duration of the pulse. Figure 2.28 shows a typical autocorrelation trace on this fictional time base. The corresponding pulse duration is 45 fs, being the calibration factor equal to 0.30±0.02 fs/μs.

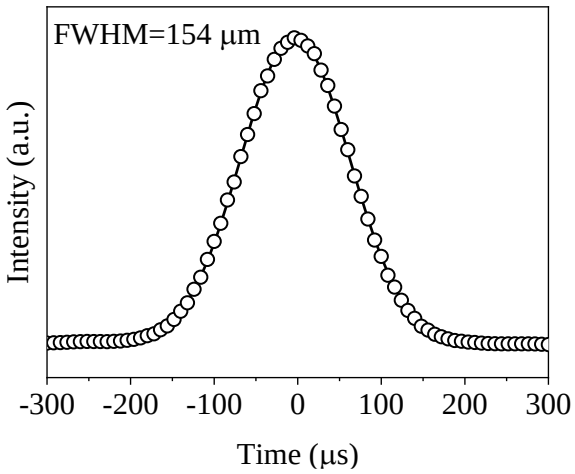

Figure 2.28. *Typical autocorrelation trace of Spitfire output pulses for pulses of 45 fs.*

The layout of the autocorrelator is displayed in figure 2.29.

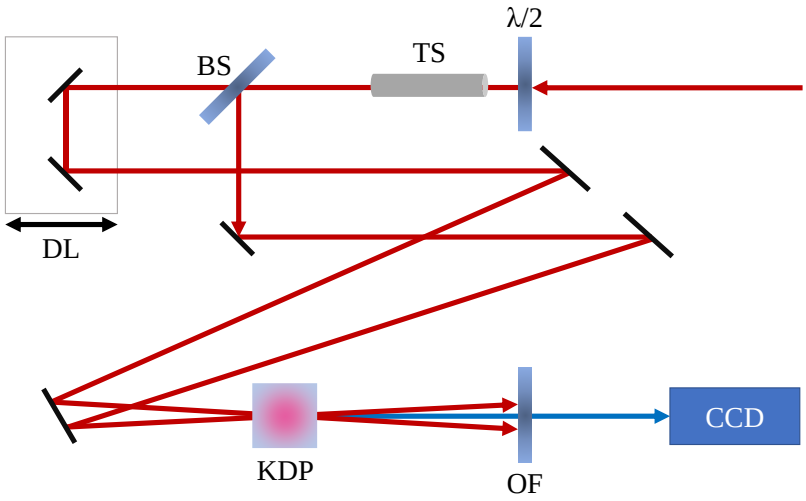

Figure 2.29. *Optical diagram of the SS SHG autocorrelator used in the characterization of the Spitfire regenerative amplifier output pulses. Half-wave plate (λ/2), telescope (TS), beamsplitter (BS), optical translational stage (DL), SHG crystal (KDP), optical filter (OF) to block residual non-frequency-doubled laser radiation and CCD camera.*

However, if a complete characterization of the pulses wants to be achieved, *i.e.*, not only pulse parameters such as the pulse energy or pulse duration but also the full time-dependent electric field or the optical spectrum including the frequency-dependent spectral phase, more sophisticated techniques such as frequency-resolved optical gating (FROG)[135, 136] or Chirpscan (Fastlite Dazscope) are required.[45, 89, 130]

2.1.3.4.2 Ultraviolet pulses

The characterization of the temporal width of UV laser pulses cannot be performed with conventional autocorrelation devices such as FROG Scan. Work is currently underway on the construction of a two-photon absorption UV autocorrelator.[132]

To determine the pulse duration of the UV pulses, cross-correlation measurements between the pump and the probe pulses using xenon (Xe) are performed. For this purpose, pump-probe experiments are carried out in which Xe is detected using a REMPI scheme (1+n') (one photon of 201 nm or 268 nm plus n' photons of the probe laser) as a function of the time delay between the pulses. Ionization of Xe is a non-resonant process when 201.2/268 nm and probe pulses are used. This ensures that the transient corresponds only to the cross-correlation of the laser pulses. The signal has the following analytical formula:

$$S(t) = \int_{-\infty}^{\infty} \left| E_{pump}(\tau) E_{probe}^{2}(t-\tau) \right|^{2} d\tau \qquad (2.20)$$

for a (1+2') process, where E_{pump} and E_{probe} are the electric fields of the pump and probe lasers and t is the time delay between them.

Assuming a Gaussian profile for the two laser pulses, the transient of Xe can be modeled with a Gaussian function of width τ_c according to:

$$S(t) = A \cdot \exp\left(-4 \ln 2 \left(\frac{t - t_0}{\tau_c} \right)^2 \right) \tag{2.21}$$

where A is the Gaussian amplitude, t is the time variable, t_0 represents the temporal overlap between the pump and probe pulses, and τ_c is the width of the Gaussian corresponding to the cross-correlation.

The cross-correlation width for a (1+2') process is given by:

$$\tau_c = \sqrt{\Delta t_{pump}^2 + \frac{\Delta t_{probe}^2}{2}} \tag{2.22}$$

where Δt_{pump} and Δt_{probe} are the pulse durations of pump and probe lasers, respectively.

Figure 2.30 depicts the transient corresponding to the ionization of Xe employing a photon of 268 nm (Spectra-Physics THG generation module) and two photons of 304 nm (OPA). The cross-correlation has an FWHM value of approximately 150 fs. If the probe pulses from the OPA have an approximate duration of 60 fs, the pulse duration of the 268 nm pulses should be around 150 fs.

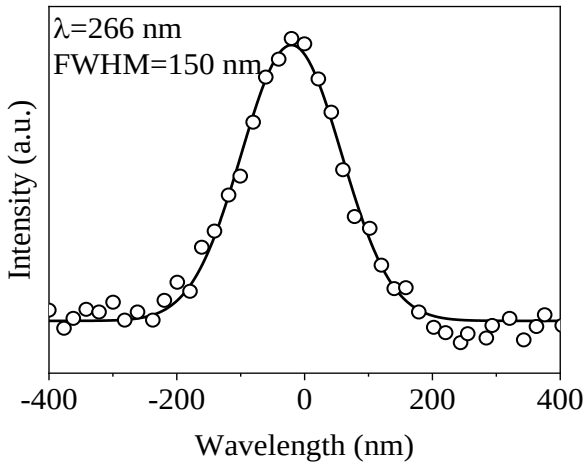

Figure 2.30. *Transient corresponding to the ionization of Xe upon absorption of one photon of 268 nm and two photons of 304 nm, representing the cross-correlation of the laser pulses. The Gaussian function used to fit the experimental data has an FWHM of 150 fs, implying that the duration of the 268 nm laser pulses is 150 fs assuming a temporal duration of 60 fs for the probe laser pulses.*

Figure 2.31 depicts the transient corresponding to the ionization of Xe employing a photon of 201.2 nm (Spectra-Physics FHG generation module) and two photons of 304 nm (OPA). The cross-correlation has an FWHM value of approximately 400 fs. If the probe pulses from the OPA have an approximate duration of 60 fs, the duration of the 201.2 nm pulses should be around 400 fs.

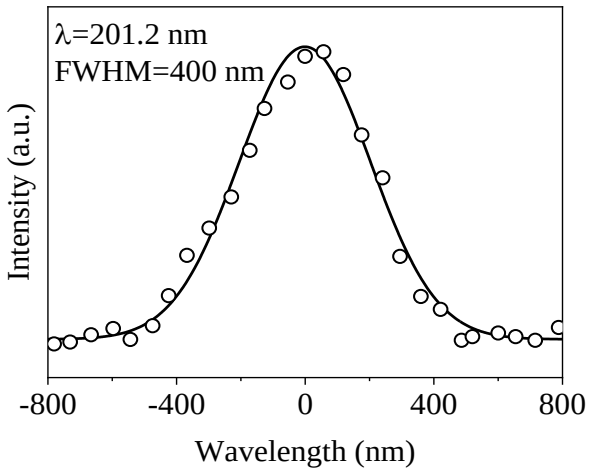

Figure 2.31. *Transient corresponding to the ionization of Xe upon absorption of one photon of 201.2 nm and two photons of 304 nm, representing the cross-correlation of laser pulses. An FWHM of 400 fs is obtained from the fit, implying that the duration of the laser pulses of 201.2 nm is 400 fs assuming a temporal width of 60 fs for probe laser pulses.*

Both pump pulse duration values are noticeably longer than the duration of the fundamental radiation pulses; the acquisition of GVD explains the increased pulse duration due to the propagation of the laser pulses through the non-linear crystals used for the generation of the harmonics in the Spectra-Physics modules.

For cross-correlation measurements, ethylene (C_2H_4) can also be employed since despite having photodissociation dynamics upon excitation with the pump pulses, they are faster than the pulse duration, so they do not interfere with the measurements.

2.1.4. Velocity map imaging setup

In this Doctoral Thesis, the experiments were carried out on a VMI machine designed and fine-tuned by Dr. Judith Durá for ion imaging[45] and lately modified by Dr. Gregory Gitzinger for photoelectron imaging.[130]

2.1.4.1. General description

Figure 2.32 represents the molecular beam machine with velocity map ion and photoelectron imaging used in the photodissociation experiments.

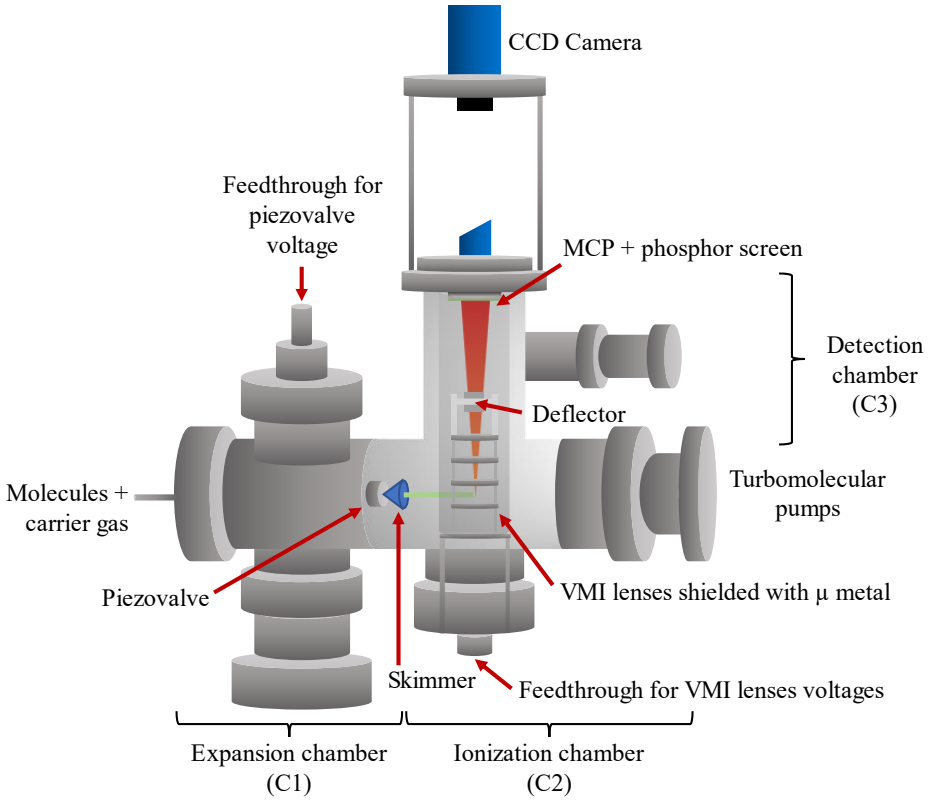

Figure 2.32. *Representation of the velocity map ion and photoelectron imaging machine. From left to right: sample injection system into the expansion chamber (C1). Gas pulses are generated employing a pulsed piezo valve and then, they are collimated passing through a skimmer. In the ionization chamber (C2), the molecular beam is located between the repeller (R) and extractor (E) electrostatic lenses. Ions or photoelectrons formed upon excitation and ionization with the pump and probe lasers are extracted and accelerated towards the detection chamber (C3), where they are detected through an MCP detector coupled to a phosphor screen. A deflector located between the VMI lens system and the detector is employed to deviate the trajectories of the undesirable ions before reaching the detector. A MuMetal shields the VMI lens system for photoelectron experiments. A CCD camera records the phosphorescence emitted by the phosphor screen in the form of a two-dimensional image.*

The system consists of three high vacuum chambers with differential pumping between the molecular beam expansion chamber (C1), the ionization chamber (C2) and the detection chamber (C3). Three different turbomolecular pumps, each connected to a separate rotary pump, are used to pump these three chambers. The cameras are fixed to a mobile stand, allowing them to be moved as a whole or independently.

Molecular beam or expansion chamber (C1). This cylindrically shaped chamber is built-in stainless steel and has a 50 L capacity. Vacuum is made through a turbomolecular pump (Pfeiffer TPU 1201), with a nominal pumping speed of 1250 L/s. The previous vacuum is made by a rotary pump (Pfeiffer DUO 65), with a nominal pumping speed of 70 m^3/h. The unloaded pressure is in the order of $6 \cdot 10^{-7}$ mbar. Under gas expansion conditions, the pressure is between $1 \cdot 10^{-4}$ mbar and $6 \cdot 10^{-5}$ mbar, depending on the opening conditions of the piezo valve and the desired pressure conditions in the nozzle.

This chamber communicates with the next one (C2, ionization chamber) through an aerodynamic-type trunk collimator or skimmer with an approximately hyperbolic profile and a very thin wall (around 100 µm) to avoid interference with the pulses. The inner diameter of the skimmer hole is 1 mm.

Ionization chamber (C2). This cylindrically shaped chamber is built-in stainless steel and has a 40 L capacity. Vacuum is made through a turbomolecular pump (Varian Turbo V 300HT) with a nominal pumping speed of 250 L/s. The previous vacuum is performed by a rotary pump (Pfeiffer-DUO 5M) with a nominal pumping speed of 5 m^3/h. The unloader pressure is in the order of $3 \cdot 10^{-7}$ mbar, while the working pressures are around $1 \cdot 10^{-5}$ mbar and $5 \cdot 10^{-6}$ mbar. This chamber houses the VMI system, which is presented in section 2.1.4.3.

The ionization chamber is provided with a "cold finger" for improving the signal-to-noise ratio of the experiments by reducing the background gas in the chamber.[137] It is a gravity-fed circulating liquid nitrogen Dewar whose design allows the liquid nitrogen to be directed to internal parts of the chamber. This device works as a trap that adheres to its surface interfering species that do not belong to the molecular beam.

Detection camera (C3). This cylindrically shaped chamber is built-in stainless steel and has a 35 L capacity. The vacuum is made by a turbomolecular pump (Pfeiffer-TMU 262 and later Pfeiffer-Hi Pace 300) with nominal pumping speeds of 210 L/s and 260 L/s, respectively. The previous vacuum is made by a rotary pump (Pfeiffer DUO 10M) with a nominal pumping speed of 10 m^3/h. The pressure is not measured in this chamber since the Penning vacuum meters generate a magnetic field that can affect the trajectory of the charged species, especially photoelectrons. A gate valve separates the detection and ionization chambers to isolate the vacuum from different chambers in case of need. This chamber has an orientation perpendicular to the optical table, as seen in figure 2.32. At the end of the C3 camera, the ion detection system is located, and it consists of an MCP coupled to the phosphor screen. The detection system is further described in section 2.1.4.3.

All flanges have International Organization for Standardization (ISO) ConFlat (CF) flange standard dimensions for copper joints.

The pressure measurement in each of the cameras is performed with Penning-type vacuum meters (Pfeiffer Vacuum PKR 251) and displayed in the drivers of the respective turbomolecular pumps. Penning-type meters can measure pressures in the range of 10^{-3}-10^{-9} mbar.

2.1.4.2. Piezoelectric valve and supersonic expansion of the molecular beam

In the expansion chamber, a supersonic expansion of the sample takes place employing a pulsed piezoelectric valve, whose different pieces were built in the mechanical workshop of the Complutense University of Madrid, based on the original design of Prof. Dieter Gerlich.[138] The valve is manually assembled. Figure 2.33 shows a drawing of the piezo valve, where all the components are distinguished.

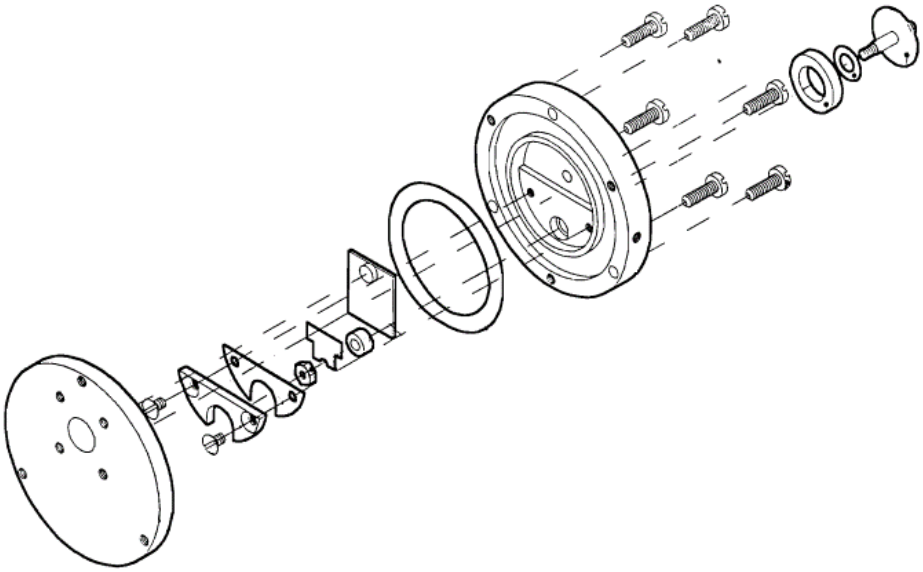

Figure 2.33. *Parts and assembly of the piezoelectric valve according to the original design of Prof. Dieter Gerlich. Figure from reference [138].*

The valve presents a series bimorph sheet (Ceramtec UK PZT503[139]) with a circular Viton piece glued to its surface. The bending movement of the sheet under the application of an electric field makes the Viton plugs a 0.5 mm diameter hole at the laser repetition rate (1 kHz) as represented in figure 2.34.

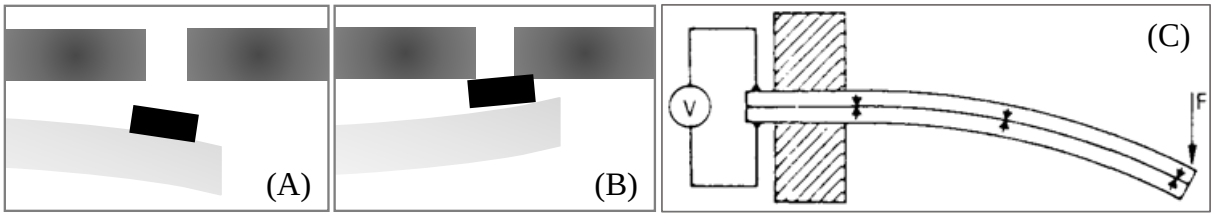

Figure 2.34. *Working principle of the piezoelectric valve: (A) A positive voltage is applied to the valve; the Viton part does not obstruct the outlet, and the gas passes through the valve orifice. (B) A negative voltage is applied to the piezoelectric material; the material then is deformed, thus plugging the valve orifice. (C) Series bimorph piezoelectric connections to voltage. Arrows indicate the polarization of the material.*

The power supply for the piezo valve (JR 193) was built by Javier Rodríguez Azadeño on request, following the scheme provided by Dr. Maurice Janssen.[140] Typical voltages range between 200-300 V, whereas valve openings are between 35 and 55 μs.

By collimating the expanded gas pulses through a truncated cone collimator (skimmer), located between the expansion and ionization chambers, a molecular beam is generated. This molecular beam travels along the ionization chamber in a molecular collision-free fashion. In the ionization chamber, the molecular beam intersects perpendicularly with the co-propagating pump and probe laser pulses.

All experiments were performed with a molecular beam formed by the target molecule and a carrier gas. Typical carrier gases can be helium (He) or argon (Ar), depending on the desired expansion conditions. Expansion pressures are varied from 1.5 to 2.5 atm. Standard containers for samples are glass bubblers or metal bubblers. This material change in the bubbler is due to the material of the junctions: the insertion of the gas into the piezoelectric valve is introduced using a stainless-steel tube of 6 mm diameter *via* a feed-through located in the expansion chamber with Swagelok type metal-metal junctions. Nevertheless, glass-metal junctions must be made with Cajon-type junctions, which do not support more than 2 atm overpressure. Thus, for the application of expansion pressures greater than 2 atm, a metal bubbler with Swagelok type junctions should be used, which withstand overpressures above 5 atm.

2.1.4.3. Velocity map imaging detection chamber

The VMI system with ion and photoelectron imaging consists, on the one hand of a set of four electrostatic lenses for the extraction and acceleration of the ions or photoelectrons formed in the ionization chamber and, on the other hand, of a detection system composed of a dual MCP, coupled to a phosphor screen and a CCD camera. Two different VMI systems are available in the laboratory:

- **Small lens system:** This electrostatic lens system consists of four stainless steel 80 mm diameter discs (extractor, repeller, lens (1) and lens (2)), manufactured in the mechanical workshop of the Complutense University of Madrid based on the design of Dr. Maurice Janssen.[141] The lenses are electrically insulated from each other by Teflon separators. The distance between the repeller and the extractor lenses is 15 mm; in turn, the latter is 25 mm away from the lens (1), and the lens (1) is separated from the lens (2) 15 mm. Both the lens (1) and the lens (2) are grounded. The extractor lens has a 20 mm centered circular hole, while the rest of the lenses has a 30 mm diameter hole.
- **Big lens system:** This electrostatic lens system is very similar to the previous one. However, the diameter of the lenses is 14 cm. These lenses were built to reduce the possible distortion of the electric field in the central region by the presence of the supporting rods and to implement the DC slicing technique. This system is preferentially used as it provides a better resolution to the experiment. This system is only usable for ion imaging since, due to its size, it does not allow the placement of a MuMetal in the chamber that houses it.

Figure 2.35 displays pictures of both systems. A detailed drawing of them, including measures, can be seen in figure a. 2 and figure a. 3 of the appendix.

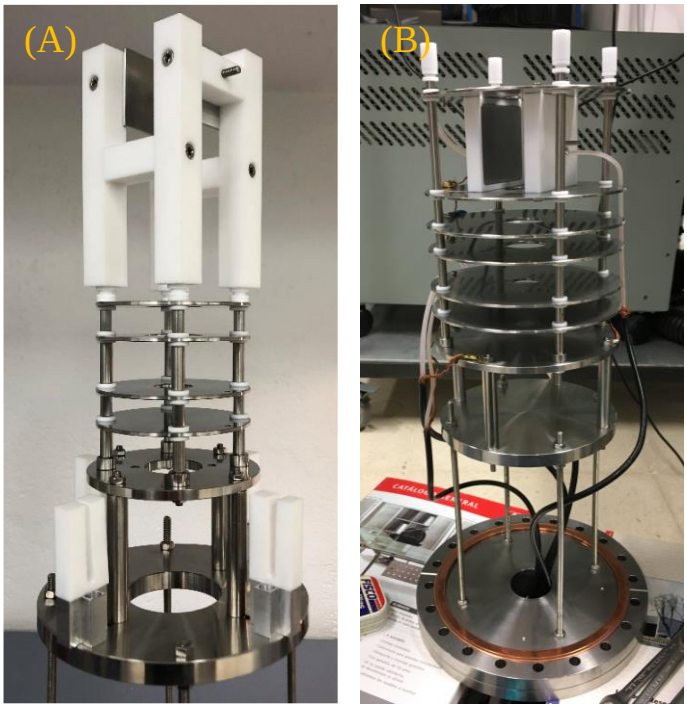

Figure 2.35. *(A) Small lenses VMI system provided of Teflon holders for MuMetal shield and deflector plates. (B) Big lenses VMI system provided of deflector plates.*

The high voltage (HV) required for the electrostatic lenses is supplied by an HV module (JR 128) through a feed-through (MCD Precision 9232021) located at the bottom of the ionization chamber.

Figure 2.36 shows a scheme of the lenses together with a representation of VMI condition; the ions or photoelectrons produced between the repeller and extractor lenses that have the same speed are focused by the electric field created with the lens system, after the free-flight zone, at the same point of the detector independently of the position of formation.

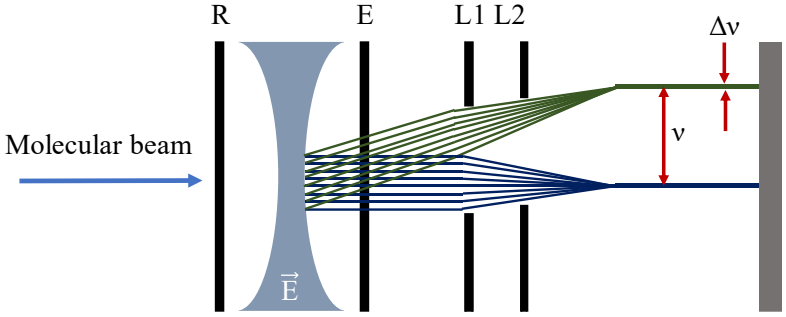

Figure 2.36. *Layout of the VMI condition. A single-axis system (molecular beam and parallel ions) is represented for clarity. The figure shows the electrostatic lens system, the detector's plane, and the trajectories of the charged particles from the extraction area to the detector plane. v is the speed difference between the two trajectories and Δv the velocity distribution.*

Photoelectrons, being charged particles with minimal mass and therefore capable of reaching very high speeds, are subject to the alteration of their trajectories due to the presence of magnetic fields, no matter how weak they are (Earth's magnetic field and those magnetic fields produced by the electronic devices in the laboratory). For this reason, it is essential to shield the VMI system with a MuMetal cylinder. MuMetal is a metallic alloy composed of nickel (75 %) and iron (15 %). It owes its name to the very high magnetic permeability property μ_r. Its relative permeability μ_r/μ_0, where μ_0 is the magnetic permeability of vacuum, is in the order of 80,000-100,000 (as a point of comparison, steel has a value below 1,000) and, therefore, this is mainly used in applications where efficient protection against continuous or low-frequency magnetic fields is required. The cylinders available in the laboratory have a thickness of 1.5 mm and a few holes, which are big enough to let the lasers and the molecular beam go through them, but small enough to prevent the propagation of the external magnetic field into the ionization chamber.

2.1.4.4. Detection system

After being accelerated, the charged particles end hitting the detector consisting of an MCP coupled to a phosphor screen and located in the detection chamber. *i.e.*, right at the end of the flight tube. The sensitive-position detector consists of two circular 40 mm MCPs (TOPAG Lasertechnik GmbH) with angled channels rotated 180° each other, producing a chevron (v-like) shape.[142] In chevron configuration, the electrons that exit the first MCP start a cascade in the next plate. The angle between the channels reduces particle feedback and significantly increases the gain at a given voltage compared to a straight-channel MCP. The maximum voltage that can be applied to each of the MCPs is 1000 V. The MCP is coupled to a P47 type phosphor screen (ProxiVision), which emits light radiation at 400 nm after excitation by electrons. Figure 2.37 shows a picture of the detection system where the MCP coupled to the phosphor screen detection system can be seen. This detector is based on a design by Prof. Theofanis Kitsopoulos.[54]

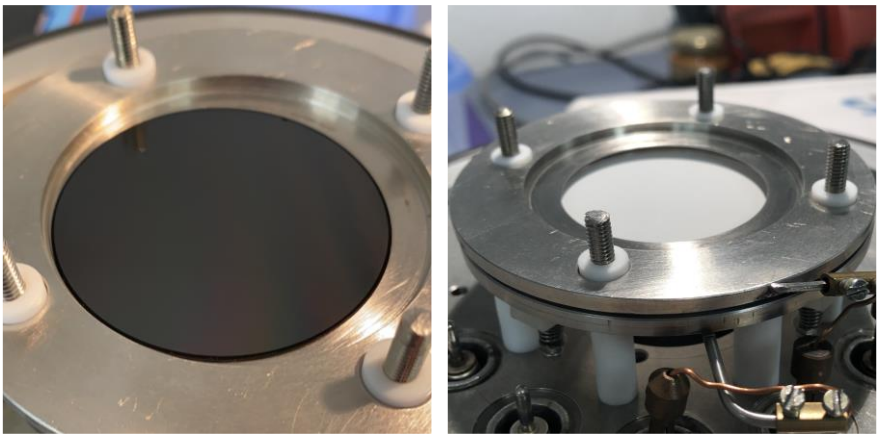

Figure 2.37. *On the left side, view of the MCP, and on the right side, view of the mounted detector where the phosphor screen, coupled to the MCP, can be appreciated.*

For the MCP to detect only the ions of a certain mass with a specific TOF, the MCP must operate in pulsed mode. In this way, only the ions that reach the detector at a specific time are detected, keeping the gain practically null for those ions that reach the detector at other times.

At the time of arrival of the particle of interest to the detector, the voltage of the dual MCP front face is changed to 0 V so that the gain is high, and the particles can be detected. The detector gain should remain constant during the full arrival time of the ion packet. At other times, the typical MCP voltage is applied so that the gain is reduced to a very low value, and so there is no possibility that other ions can be detected. The temporal gating is produced in the form of a transistor-transistor logic (TTL) pulse with a certain width. The voltage switching is achieved by a fast HV transistor switch (BEHLKE HTS 31-12-BKE in JR 131). Typical voltages are 1200-1500 V for the back face and 700 V for the front face of the dual MCP. The voltages applied to the MCP back, MCP front and phosphor screen are set on a driver (JR 128) made by Javier Rodríguez Azadeño on request.

Despite using a gated detection system, ions with high velocities can deteriorate the detector by the simple impact. For that reason, an improvement was implemented in the system based on locating a pair of deflector plates before the detector.[143-145] The deflector plates were designed and installed by Garikoitz Balerdi. These deflector plates deviate the trajectories of undesired ions perpendicular to the spectrometer axis before reaching the detector, as shown in figure 2.38. The voltage for the deflector is applied in the form of a TTL pulse from an HV power supply (Bertan Associates Inc. 205A-05R). The voltage switching is achieved by a fast HV transistor switch (BEHLKE HTS 151-03-GSM in JR 178).

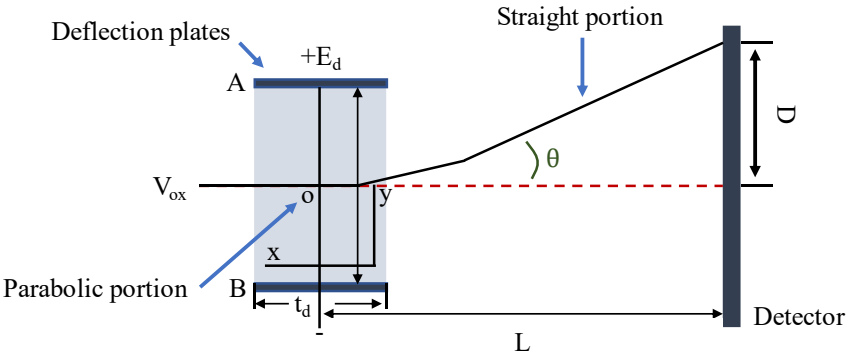

***Figure 2.38**. Arrangement of the deflection plates. A and B represent the two parallel deflector plates between which a difference potential is applied to produce a uniform electrostatic field in the y-direction proportional to the mass of the ion and the deflecting voltage.*

Each ion hits the MCP producing a cascade of electrons that reaches the coupled phosphor screen, typically powered by 3.5 kV, generating a phosphorescence that is detected by a CCD camera as a bi-dimensional image. The CCD camera (LaVision Imager QE) has a 50 mm lens to focus the image and a depth of 12 bits, 16 MHz, 1376 x 1040 pixels resolution, a spectral range of 300-1000 nm. Peltier cells cool it down to -15 ºC to reduce the thermal noise.

2.1.4.5. Velocity map imaging resolution

It is essential to determine the resolution of the VMI system, considering the different factors that can affect it. The factors limiting the resolution have various origins:

Linewidth of femtosecond laser pulses: Femtosecond laser pulses are characterized by a spectral bandwidth. When used as excitation sources for processes related to energy continuums such as ionizations, this spectral bandwidth induces a distribution of available energies and widens the observed translational energy distribution, lowering the resolution. However, when the excitation is to bound states, *i.e.*, the absorption line is narrow (in the order of a few tens of cm^{-1}), femtosecond lasers act as a spectral filter, and so the bandwidth is not a limiting factor.

The initial energy of the molecules in the molecular beam: Despite the characteristics of molecular beams, molecules indeed have a velocity distribution, which can be estimated through the parent ion signal. Part of this distribution can be selected as it is demonstrated in the following. The orifice of the pulsed valve is located approximately 20 cms far from the interaction area of the laser with the molecular beam. The speed of the molecules that travel this distance can be expressed as:

$$v = \frac{d}{t} \tag{2.23}$$

where v is the velocity of the molecules, d is the distance between the orifice of the piezoelectric valve and the interaction area and t the time taken by the molecules to travel the distance d.

The speed distribution selected by the laser pulse is given by:

$$\partial v = d\frac{\partial t}{t^2} + d\frac{\partial d}{t} \tag{2.24}$$

where ∂d represents the diameter of the laser in the interaction area, *i.e.*, ≈50 μm, and ∂t the duration of the opening of the piezoelectric valve (≈30 μs). With these values, $d\partial t/t^2 \approx 50\ m\cdot s^{-1} >> \partial d/t \approx 2\ m\cdot s^{-1}$. Therefore, the laser pulse selects a part of the translational energy distribution as a function of the valve opening duration according to:

$$\partial v \approx d\frac{\partial t}{t^2} \tag{2.25}$$

It can be seen in figure 2.39 how the speed of the molecules in the molecular beam evolves as a function of the delay time between the gas pulse and the laser pulse.

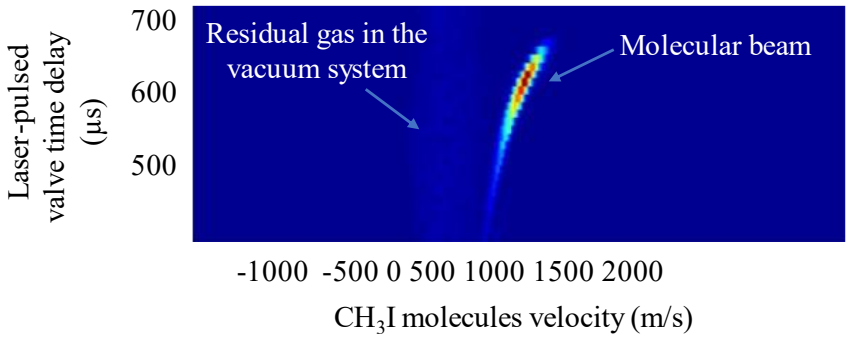

Figure 2.39. *Map of the speeds of the molecules in the molecular beam as a function of the delay time between the valve pulse and the laser pulse. At longer times, the fastest molecules appear and in shorter times, do the slowest molecules. The opening duration of the valve is around 30 μs.*

A measurement of the molecular beam quality can be made employing the value of the speed ratio parameter *S*, defined as:[146]

$$S = 1.665 \frac{v}{\Delta v} \tag{2.26}$$

where v is the velocity of the molecules and Δv is the velocity distribution observed in the particle image. The higher the *S* value, the better the quality of the molecular beam.

The velocity distribution of the molecules in the molecular beam does not affect the different fragments equally: indeed, it is transmitted to the fragments as a function of a mass factor; the greater the mass of the fragment, the greater its influence.

Size of an event (arrival of an ion or an electron) in the detector: An ion or an electron that arrives at the detector produces a spot of approximately 3 pixels, thus causing a loss of resolution, which is more critical when dealing with small radius photodissociation rings. A way to solve this problem is by employing the event counting technique.[147] Chang *et al.*[148] realized that further increase in resolution could be gained by implementing the real-time ion-counting method to recover low-level photon signals from noisy backgrounds by using a threshold level to reduce the noise. In this technique, only the local maximum of the group of pixels illuminated by a single ion is counted as a signal, thus improving the spatial resolution by locating a single position of ion impact rather than accumulating the entire area of illuminated pixels. However, the method has the disadvantage of lowering the signal-to-noise ratio, the reason why it has not been used in the present work.

Image distortion: The electrostatic lens system generates a non-uniform field in the area of ion and photoelectron formation. Under these conditions, charged particles of equal charge and mass and with the same initial speed are focused on the same point of the detector. However, elements in the

electric field, such as plate holders, can alter the field. As a result, the images can be slightly deformed, especially for large radius ones.

Vibrational and rotational excitation of the fragments: Molecular fragments have a vibrational and rotational energy distribution. This one is much wider if specific vibrational-rotational states are not selected in the probing step. Nevertheless, by employing specific REMPI schemes, it is possible to select a quantum state of the fragment, thus reducing the observed widening. In any case, the broadening is always affected by the rotational distribution of the fragments.

Space charge: The pulsed valve conditions turn out to be critical, especially when fragments with low translational energy are detected. Phenomena such as space charge, which is the repulsion between ions due to a too-high ion density, is always the most significant problem and can lead to image distortion along the highest density dimension. Space charge can also be produced if many ions focus in the same place, leading to rings broadening and lowering the image resolution.[43]

2.1.4.6. Velocity map imaging spectrometer calibration

The calibration of the VMI spectrometer consists of finding the relationship between the impact position of the fragments into the detector (in pixels) and their speed or translational energy content. To perform the calibration, a molecular photodissociation experiment of a reference system is usually performed. The photodissociation dynamics of CH_3I have been widely studied both in its first absorption band at around 266 nm, namely the *A*-band[149-154] (see section 3.1), and its second absorption band centered at 201.19 nm, namely the *B*-band[155-160] (see section 4.1), so it becomes an excellent reference system. The calibration is done by a photodissociation experiment either in the first or second absorption band at the convenience of the wavelengths to be used for the desired experiments.

2.1.4.6.1 Calibration procedure by means of a methyl iodide experiment upon excitation in the first absorption band.

As described in more detail in section 3.1, photodissociation of CH_3I upon excitation in the first absorption band (*A*-band) at 268 nm leads to the cleavage of the C−I bond producing CH_3 fragments in correlation with iodine (I) fragments both in its ground ($I(^2P_{3/2})$) or spin-orbit ($I(^2P_{1/2})$) states:

$$CH_3I + h\nu \rightarrow CH_3(\tilde{X}\,^2A_2^{''}) + I(^2P_{3/2}) \quad (2.27)$$

$$CH_3I + h\nu \rightarrow CH_3(\tilde{X}\,^2A_2^{''}) + I^*(^2P_{1/2}) \quad (2.28)$$

The energy difference between the two channels corresponds to the I spin-orbit coupling energy of 0.943 eV.[161] Therefore, each channel has different available energies for the photofragments and, therefore, different output fragment speeds.

Before proper calibration, VMI conditions should be achieved. To find these conditions, the shape of the ionized parent molecule, in this case, the methyl iodide cation (CH_3I^+), is monitored and optimized by varying the voltage ratio of the repeller and extractor lenses. A distinction shall be made according to the configuration of the system: For an on-axis configuration (the detection of particles is parallel to the molecular beam propagation direction), a circular and as small as possible image should be achieved due to the absence of speed in the direction perpendicular to the molecular beam propagation whereas for an off-axis configuration (the detection of particles is perpendicular to the propagation direction of the molecular beam), the parent ion image should ideally be a straight narrow vertical line due to the distribution of the component of the initial velocity of the molecules in the direction of propagation of the molecular beam.

The VMI system presents an off-axis configuration and therefore the latter option must be taken into consideration for finding the ionized parent molecule shape by fine-tuning the repeller and extractor voltages. Figure 2.40 displays the typical CH_3I^+ shape and the X and Y profiles in pixels, under VMI conditions working with off-axis configuration. VMI conditions are achieved when the ratio between the extractor and the repeller voltages is 0.79, being the voltage of the extractor 5200 V. However, these voltages should be routinely optimized for each experimental session. Once the conditions are found, these are valid for any other ion, provided that the voltages applied to the extractor and repeller lenses are not modified.

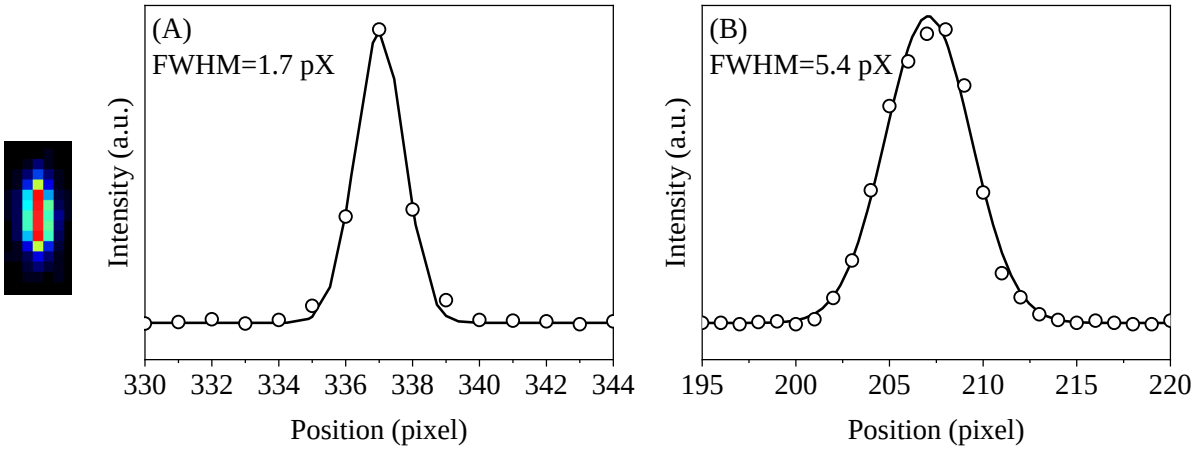

Figure 2.40. *Image of the parent methyl iodide cation (CH_3I^+). The shape of the image is elongated along the Y axis and narrow in the X axis for the reasons explained in the text. VMI conditions are met for the voltages $V_{repeller}$=5200 V and $V_{extractor}$=3964 V. The profiles of the image are displayed in pixel units. The FWHM of each of the profiles is indicated.*

The next step is the calibration, and for this, an image of the fragment through which the photodissociation is probed should is recorded in asymptotic conditions (R_∞). *i.e.*, at a pump-probe delay ranging the dozens of picoseconds.

With the wavelengths accessible with the femtosecond laser system, the probing of the CH_3I photodissociation can be carried out through resonant detection of CH_3 fragments or I fragments.

The detection of $CH_3(v=0)$ can be achieved by tuning the probe laser centered at 333.5 nm. At this wavelength, the fragments are detected employing a (2+1) REMPI scheme through the $2p^2A_2'' \rightarrow 3p^2A_2''$ transition. Figure 2.41 (A) shows the measured image of $CH_3(\nu=0)$ fragments upon dissociation of CH_3I at 268 nm and probed at 333.5 nm. Figure 2.41 (B) shows the corresponding inverted image using the pBASEX software. In figure 2.41 (B), three strongly anisotropic rings are distinguished, corresponding to parallel transitions since the signal is maximum along the laser polarization direction. The outermost and innermost rings correspond to the formation of $CH_3(v=0)$ fragments from the photodissociation channels indicated in equations (2.27) and (2.28). However, there is a third central ring that was not expected. The presence of this ring is due to the spectral width of the femtosecond lasers. The spectrum in figure 2.42 reveals the proximity of the 1_1^1 Q-band branch of the CH_3 fragment, centered at 333.9 nm, close to the 0_0^0 Q-band branch, centered at 333.5 nm. When the probe laser is tuned at 333.5 nm, it is possible to resonantly ionize not only $CH_3(\nu=0)$ fragments but also those CH_3 fragments that appear as reaction products with one quantum of excitation in the symmetric stretch ν_1 vibrational mode, $CH_3(\nu_1, \nu_2, \nu_3, \nu_4=1, 0, 0, 0)$, henceforth denoted as $CH_3(\nu_1=1)$.[149, 150] So, the intermediate ring corresponds to the $CH_3(\nu_1=1)+I(^2P_{3/2})$ dissociation channel.

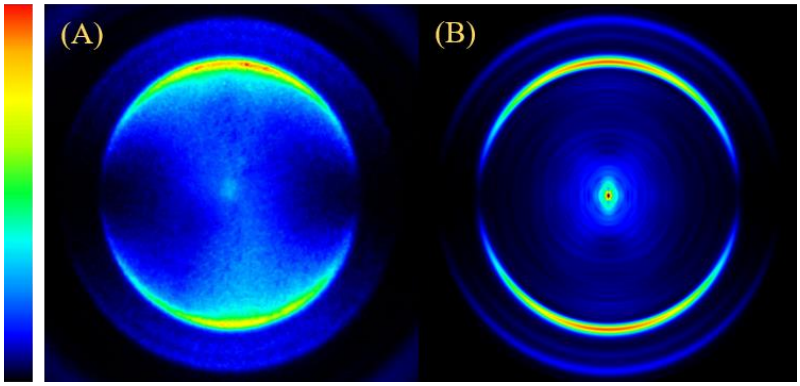

Figure 2.41. *(A) Measured image of $CH_3(v=0)$ fragments upon dissociation of CH_3I with femtosecond laser pulses centered at 268 nm. $CH_3(v=0)$ fragments are probed with a second femtosecond probe laser centered at 333.5 nm through a (2+1) REMPI scheme via the $3p_z$ Rydberg state. (B) Inverted image using the pBASEX software. The images are shown in false color. The relative intensity of each color is indicated on the left side on a scale of 0-1. Light polarization direction is parallel to the vertical axis of the image.*

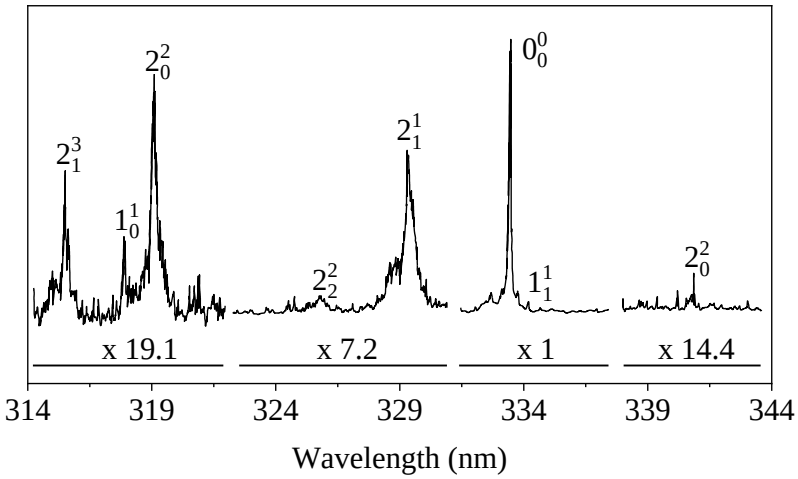

Figure 2.42. *Two-photon resonant, three-photon ionization spectrum of the CH_3 fragments through the $2p^2A_2''\rightarrow 3p^2A_2''$ transition. Figure adapted from reference [162].*

Being the excitation energy $h\nu$=4.63 eV for a photon of 268 nm and the dissociation energy D_0=2.41±0.03 eV,[163, 164] the available energy for each photodissociation channel ($CH_3(v=0)+I(^2P_{3/2})$ and $CH_3(v=0)+I^*(^2P_{1/2})$) is given by:

$$E_{av} = h\nu - D_0 = 4.63\text{ eV} - 2.41\text{ eV} = 2.22\text{ eV} \tag{2.29}$$

$$E_{av^*} = h\nu - D_0 - E_{SO}(\text{I}^*) = 4.63\text{ eV} - 2.41\text{ eV} - 0.943\text{ eV} = 1.273\text{ eV} \tag{2.30}$$

where E_{av} and E_{av^*} are the available energies for each dissociation channel, ($CH_3(v=0)+I(^2P_{3/2})$ and $CH_3(v=0)+I^*(^2P_{1/2})$) respectively, $h\nu$ is the excitation energy, D_0 is the C–I dissociation energy and E_{SO}(I*) is the I atom spin-orbit coupling energy.[40]

The translational energy of the $CH_3(v=0)$ fragments at the CM is calculated according to:

$$E_T^{CH_3(v=0)} = \frac{m_I}{m_{CH_3I}} E_T \tag{2.31}$$

where E_T is the total translational energy; that is, the excess energy after discounting the internal energies of the fragments.

Assuming that the molecule starts from the absolute zero temperature (T=0 K), *i.e.*, without vibrational or rotational excitation, the translational energy matches the available energy $E_T=E_{av}$. So then, the translational energy of $CH_3(v=0)$ for the $CH_3(v=0)+I(^2P_{3/2})$ channel is 1.98 eV, while for the $CH_3(v=0)+I^*(^2P_{1/2})$ channel is 1.14 eV.

If the angular integration of the inverted image is carried out, the distribution of $CH_3(v=0)$ fragments is obtained based on the distance to the center of the image in pixel units. This is represented in figure 2.43.

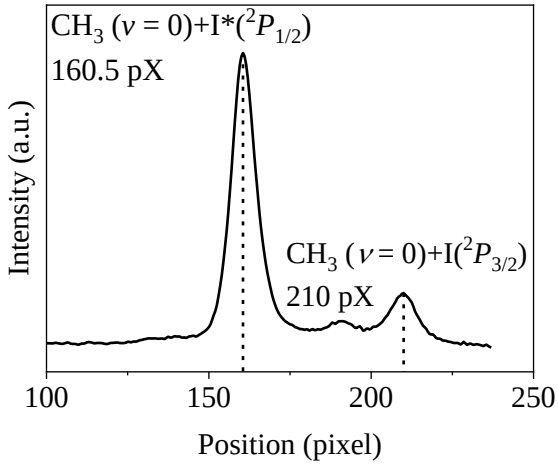

Figure 2.43. *Distribution in pixels (px) of CH_3 fragments obtained by angular integration of the inverted image in figure 2.41 (B). The three peaks that appear in the distribution correspond to the three photodissociation channels indicated in the text. The position in pixels of the two peaks used for calibration is indicated.*

Accordingly, the distribution shows three peaks corresponding to the three described rings. Calibration is performed using the position of the peaks corresponding to the $CH_3(v=0)$ fragments. For this, these positions should be compared to translational energy values found in the literature for CH_3I photodissociation dynamics in the *A*-band at 268 nm (Table 2.1).[149, 150, 153, 154]

Table 2.1. *Correspondence of the peak positions in pixels (pX) of the CH_3 fragment distribution with the corresponding translational energy reported in the literature.*[150]

Dissociation channel	CH_3 position (pX)	CH_3 translational (eV)
$CH_3(v=0)+I(^2P_{3/2})$	160.5	1.14
$CH_3(v=0)+I^*(^2P_{1/2})$	210	1.98

There is a quadratic dependence of the translational energy with the distance (in pixels) to the center of the image in VMI conditions:

$$E_T^{CH_3} = k \cdot px^2 \leftrightarrow \sqrt{E_T^{CH_3}} = k \cdot px \tag{2.32}$$

where *k* is the calibration constant, which is universal, *i.e.,* independent of mass, and *px* is the variable that describes the number of pixels from any point of the image to the center.

Representing the square root of the translational energy of the fragments versus their position (in pixels) from the center of the image; the calibration constant can be obtained as the value of the slope (as $\sqrt{k}$.) of the line resulting from a least-square fit. In figure 2.44, the square root of the CH_3 fragment translational energy is represented *versus* the position from the center of the image, in pixels. The resulting calibration constant is $k=4.46\cdot10^{-5}\pm3\cdot10^{-7}$ eV/px^2.

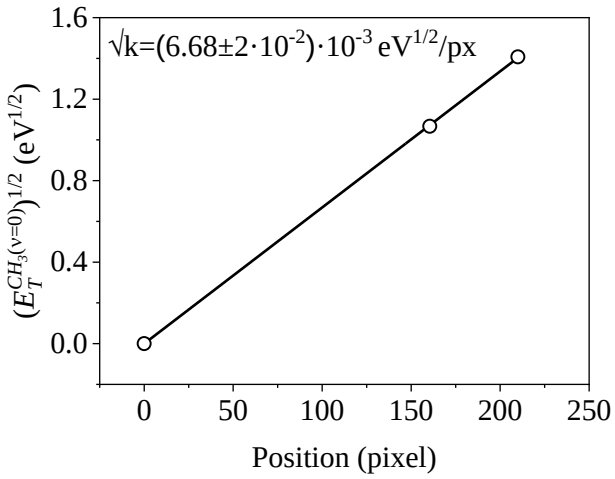

Figure 2.44. *Square root of the translational energy of CH_3(v=0) fragments versus the distance to the center in pixels, for the determination of the calibration constant k.*

The calibration constant does not depend on the fragment mass; therefore, it can be used for any other fragment with equal charge as long as the VMI voltages are not modified. The calibration procedure should be done regularly, especially when significant changes are made to the system.

Once the calibration constant is obtained, it must be considered that when representing the fragments' distribution according to their translational energy at the CM, the Jacobian of the pixel-translational energy transform must be applied. There is a linear dependence of the position (in pixels) with the velocity of the fragments in VMI conditions. Therefore, the velocity variable is used to establish the pixel-Jacobian transform (or velocities)-translational energy. For any distribution, it should be met that:

$$P(v)dv = P(E_T)dE_T \tag{2.33}$$

where P refers to the corresponding functions that define the distribution on the y axis in each case.

If from equation (2.33), $P(E_T)$ is cleared, and the derivate of the translational energy with respect velocity is considered as mv, then:

$$P(E_T) = P(v)\frac{dv}{dE_T} = \frac{P(v)}{mv} \tag{2.34}$$

Therefore, to change the representation in velocity (or pixels) to the representation in translational energy, the *y* values from the original distribution must be divided by a linear function of the velocity (that is, pixels) for each point.

Figure 2.45 displays the CH_3(v=0) fragment translational energy distribution after the calibration procedure is carried out.

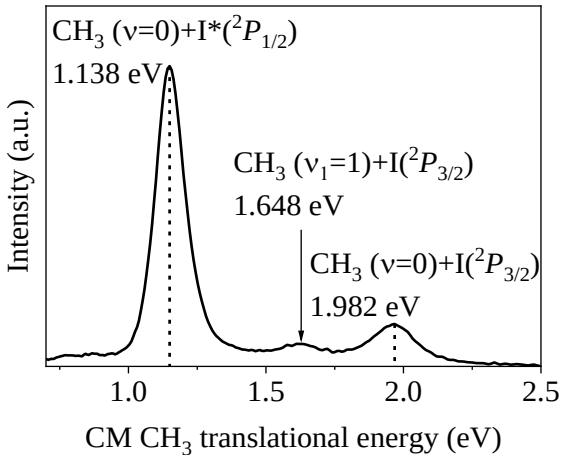

Figure 2.45 *Translational energy distribution of CH_3(v=0) fragments in the CM after calibration. See text for details.*

As mentioned above, this procedure could also be performed by probing the I atom fragment. In the wavelength region close to 300 nm, accessible by OPA and TOPAS devices, there is a series of two-photon REMPI transitions of both electronic states of I, which are listed in table 2.2.

Table 2.2. *(2+1) REMPI spectrum lines for $I(^2P_{3/2})$ and $I^*(^2P_{1/2})$.*[40]

Iodine state	Excitation wavelength (nm)	Intermediate state	Two-photon line force
$I(^2P_{3/2})$	303.68	6p $^4P_{1/2}$	4.37
$I^*(^2P_{1/2})$	304.02	6p $^4D_{1/2}$	0.90
$I(^2P_{3/2})$	304.55	6p $^4D_{7/2}$	5.18
$I(^2P_{3/2})$	304.67	6p $^4D_{1/2}$	1.00
$I^*(^2P_{1/2})$	305.57	6p $^4P_{3/2}$	2.00
$I^*(^2P_{1/2})$	306.73	6p $^4D_{3/2}$	1.63

Accordingly, the probe laser can be tuned at 304.5 for the (2+1) REMPI joint detection of $I(^2P_{3/2})$ and $I^*(^2P_{1/2})$ photoproducts (feasible due to the spectral width of the femtosecond laser pulses) or at 306

nm for exclusive detection of I*($^2P_{1/2}$) photoproducts. In the current configuration of the laser system, no REMPI schemes are accessible for the selective detection of I($^2P_{3/2}$). By tuning the probe laser at the 304.5 nm (FWHM 2.5 nm), I($^2P_{3/2}$) fragments are detected through transitions to the 6p$^4P_{1/2}$, 6p$^4D_{7/2}$ and 6p$^4D_{1/2}$ intermediate states and I*($^2P_{1/2}$) fragments through transitions to the 6p$^4D_{1/2}$ and 6p$^4P_{3/2}$ intermediate states, whereas by tuning the probe laser at 306 nm (FWHM 2.5 nm), I*($^2P_{1/2}$) fragments are detected through transitions to the 6p$^4P_{3/2}$ and 6p$^4D_{3/2}$ states.

2.1.4.6.2 Calibration procedure by means of a methyl iodide experiment upon excitation in the second absorption band.

If the calibration is performed through a photodissociation experiment in the origin of the second absorption band (*B*-band) of CH_3I at 201.19 nm, the procedure is the same. In this case, the only channel open upon dissociation gives rise to CH_3 fragments in correlation I*($^2P_{1/2}$) fragments:

$$CH_3I + h\nu \rightarrow CH_3(\tilde{X}\,^2A_2'') + I^*(^2P_{1/2}) \qquad (2.35)$$

The expected translational energies for CH_3 and I*($^2P_{1/2}$) fragments are indicated in table 2.3.

Table 2.3. *Energy of dissociation channels of CH_3I in the B-band at an excitation wavelength of 201.19 nm, corresponding to the origin of the B-band.*[155]

Dissociation channel	Total translational energy (eV)	I*($^2P_{1/2}$) translational energy (eV)	CH_3 translational energy (eV)
$CH_3(\nu=0)$+I*($^2P_{1/2}$)	2.810	0.397	2.512
$CH_3(\nu_1=1)$+I*($^2P_{1/2}$)	2.437	0.358	2.179

2.1.5. Synchronization of the experiment

A representative diagram of the synchronization of the different devices used in a typical experiment is represented in figure 2.46.

The master trigger (T_0) of the experiment is provided by the control electronics of the Pockels cells of the regenerative amplifier (Positive Light SDG II), at the laser frequency repetition rate (1 kHz) repetition rate, through TTL pulses synchronized with the output laser. With respect to the trigger, it is necessary to control the piezoelectric valve, the MCP gating and the deflector plates. Synchronization of the different devices is achieved by a digital delay generator (DDG) (Stanford Research Systems DDG 535). The DDG generates four TTL pulses delayed with respect to T_0 that are henceforth denoted as A, B, C and D.

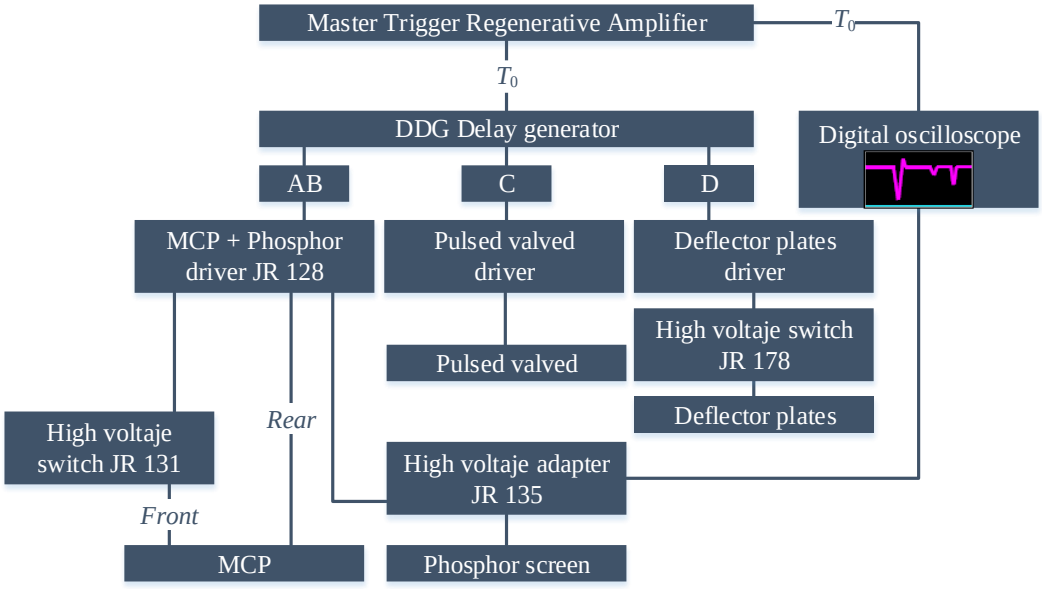

Figure 2.46. *Diagram of the synchronization of the devices in the VMI experiment with femtosecond laser pulses.*

The A and B pulses are used in combination (A⊓B) to control both the temporal position (A) and the width (B) of the MCP gate. The values for these delays are in the order of A=T+(1-20 μs) and B=A+(100-200 ns); *i.e.*, the gating pulses for the MCP are applied between 1 and 20 μs (typical fragments' TOFs values) after T_0, with a duration of between 100 and 200 ns. This AB pulse is sent from the DDG to the MCP driver (JR 128), which activates the gate by sending an HV pulse (700 V) to the MCP front through the HV switch (JR 131). The MCP driver also applies a continuous voltage to be MCP back (1200-1500 V) and to the phosphor screen (3500 V) through an HV adapter module (JR 135), which in turn allows the signal to be measured in a digital oscilloscope (LeCroy Waverunner 64Xi 600MHz). The oscilloscope displays the signals corresponding to the ions that reach the phosphor screen.

Considering the gas pulse, approximately as a TTL pulse whose width is similar to that of the electrical pulse applied to the piezoelectric element, the laser pulses can interact with the gas pulse right in the initial zone ("hot" zone of the molecular beam, *i.e.*, low relaxation of molecular internal degrees of freedom) or at the end of the gas pulse plateau ("cold" zone of the molecular beam, *i.e.*, efficient relaxation). The C pulse establishes the delay between the laser pulses and the gas pulses produced by the piezoelectric valve so that, the laser pulse intercepts the pulsed molecular beam in the desired area. The exiting delay between applying the voltage to the piezoelectric valve and the arrival of the gas pulse in the interaction zone (≈200 μs) makes synchronization with the same laser shot impossible. Therefore, the gas pulse is synchronized with the next laser shot. Typical values of the C channel are C=T+730 ms for a typical 45 μs valve openings.

The D channel controls the operation of the deflector plates. The value for this delay is in the order of D=T+(1-10 μs) so that the deflector acts between 1 and 10 μs after T_0. This pulse is sent from the DDG to the deflector HV power supply (Bertan Associates Inc. 205A-05R), which triggers the deflector by sending an HV pulse to the parallel plates. The voltage switching is achieved by a fast high voltage transistor switch (JR 178 provided with a BEHLKE HTS 151-03-GSM[165]).

Synchronization of the delays is done concerning the trigger rise (positive slope). The trigger has a temporal width of approximately 5 μs. Synchronization can also be done with respect to the descent (negative slope) of the trigger, but the time width should be considered in the timing of the A, B, C and D channels.

2.1.6. Pump-probe experiment performance

In this section, the different steps to carry out a pump-probe experiment using the experimental setup located at the Center for Ultrafast Lasers (CLUR) are described.

The first step is to turn it on and let the laser system stabilize. Then, a check of the general alignment of the laser is performed before entering the different devices. Once the alignment is checked, the optimization of the devices used for the experiments is carried out for its proper operation. It should be noted that the output wavelength of all devices is dependent on the wavelength at which the oscillator and amplifier are centered. Once the different devices are optimized, the optical paths of the lasers to the reaction chamber are aligned; for this purpose, diaphragms are set in the optical table so that the critical alignments are reproducible. A complete characterization of the output laser pulses, including power and pulse duration, is carried out. The output pulse duration can be optimized with the amplifier compressor.

The time delay between the pump and probe lasers is achieved utilizing a linear translation stage, located in the optical path of the probe laser, whose movement, with micrometric resolution, is controlled by a computer-controlled stepper motor. There are two linear translation stages available in the laboratory: one for the OPA (Newport UTS15OPP) and one for the TOPAS (Parker Automation 402006LNMPD1L3C4M1) laser lines. Specific details for both stages can be found in table 2.4.

Table 2.4. *Technical specifications of the linear translation stages employed for the OPA and TOPAS delay lines.*

Manufacturer	Model	Range		Step size	
		(mm)	(ns)	(μm)	(fs)
Newport	UTS15OPP	150	1	0.3	1
Parker Automation	402006LNMPD1L3C4M1	200	1.3	0.1	0.3

The pump and probe laser pulses are directed to the final dichroic mirror, where the beams are recombined. After this mirror, both collinear beams are focused by a 25 cm focal length lens into the ionization chamber of the molecular beam machine through a quartz window (UQG Optics). Telescopes can be employed to change the size of each beam at the focus and to focus each of the laser beams is the same focal plane behind the 25 cm focal length lens inside the ionization chamber; that is, at the midpoint between the extractor and repeller plates of the VMI system, where the molecular beam arrives.

A molecular photodissociation experiment with femtosecond laser pulses requires that the different devices (molecular beam, laser and detection system) are synchronized and have adequate temporal delays between them. In section 2.1.4.5, the synchronization of the devices is fully explained. The different devices can be turned on in this approximate order.

1. DDG (Stanford Research Systems DDG 535). As it is the module through which the different devices are synchronized, it must be the first one to be turned on.
2. Piezoelectric valve driver (JR 193). This device is responsible for pulsing the piezoelectric valve. The voltage and aperture of the piezoelectric valve are adjusted so that the pressure in the expansion chamber ranges between $1\text{-}5\cdot10^{-5}$ mbar. Typical voltages range between 200-300 V, whereas valve openings are between 35 and 55 µs.
3. Detector driver (JR 128, includes the MCP detector and phosphor screen). The typical voltages for the detection systems are 1200-1500 V (MCP back) and 3500 V (phosphor screen). MCP front is later switched on.
4. VMI lenses voltages driver (JR 196). The voltages are adjusted to 5200 V (repeller plate) and approximately 3950 V (extractor plate).

HVs should not be turned on if the pressure inside the chamber exceeds 10^{-4} mbar since the chances of having electrical arcs that deteriorate the system are high.

Once all the devices are turned on, the image of the parent molecule should be seen at least with one of the lasers. The position of the focusing lens at the entrance of the ionization chamber and the distance between the lenses that conform the telescope are adjusted to optimize the ionization signal displayed in the trace of a digital oscilloscope (LeCroy Waverunner 64Xi 600MHz). At this point, the voltages of the electrostatic lenses to find VMI conditions can be finely optimized, as described in section 2.1.4.6, considering the off-axis configuration.

To ensure the spatial overlap of the laser beams, the interaction zone is reproduced outside of the reaction chamber. A wedge is placed between the 25 cms focusing lens and the quartz window, as illustrated in figure 2.47**.** Then, the beams are reflected by the first face of the wedge and directed towards a 5 mm thickness cell with rhodamine 610 diluted in methanol located at the focus distance of

the lens. The spatial overlap of the lasers is made by observing, with inverted binoculars, the fluorescence induced by them in the dye and adjusting the position of the beams with the micrometric screws of the dichroic mirror. Once the beams are overlapped, the wedge is removed, allowing the laser beams to enter the chamber.

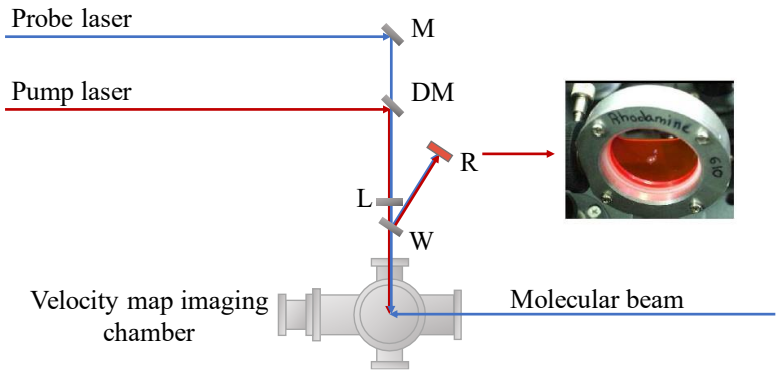

Figure 2.47. *Diagram of the device used to ensure the spatial overlap of the pump and probe laser beams in the interaction area. The use of a removable wedge window (W), located after the final focusing lens (L), allows the focal geometry to be reproduced at a point outside the ionization chamber, where a cell with rhodamine 610 solution in methanol (R) is located. The observation of the fluorescence produced in the rhodamine by the lasers allows the fine adjustment of the spatial overlap through the control of the final mirror (M) and the dichroic recombination mirror (DM).*

Once the best experimental conditions have been established, the detector can be gated to measure the corresponding image of the ion of interest. To do this, the voltage must be applied to the front MCP (at around 700 V) and, if feasible, to the deflector plates (around 700 V). The TOF of the ion can be easily known through the trace of the oscilloscope when the detector is not gated. It should be noted that there is a slight time difference between the TOF determined out of the oscilloscope trace and the time subsequently indicated on the DDG to gate the detector. The determination of the time difference Δt can be estimated from the following equation:

$$\Delta t = \frac{t_{AB^+}\sqrt{m_{B^+}/m_{AB^+}} - t_{B^+}}{\sqrt{m_{B^+}/m_{AB^+}} - 1} \tag{2.36}$$

where t_{AB+} is the TOF of the ionized parent molecule AB^+, t_{B+} is the TOF of a given ionized photofragment B^+, m_{AB+} is the mass of the ionized parent molecule AB^+ and m_{B+} is the mass of the ionized photofragment B^+. Conversely, if Δt is known, the equation (2.36) serves to estimate the TOF of different fragmentations of most complex molecular systems.

Finer spatial overlap between the two lasers can be achieved by maximizing the pump-probe signal of the detected ion at asymptotic condition (R_∞; *i.e.*, at a long time delay between the pump and

probe laser pulses). The aim is to obtain the highest possible signal with both lasers (pump-probe signal) and the minimum contribution of each separate laser to this signal. In this way, multiphoton absorption from each laser is minimized. The intensity of the pump laser pulse in the interaction region is controlled by the energy variation using variable attenuators in the form of a neutral density filter variable by transmission.

Once the signal is obtained with sufficient quality, the time-resolved study of the desired system can be carried out once the calibration procedure has been completed, as described in section 2.1.4.6. A distinction is made between results at asymptotic pump-probe time delays, *i.e.*, when the photodissociation process is considered finished (images, translational energy distributions and angular distributions) and time-resolved results (sequences of images and transients).

In any case, it is essential to find the temporal overlap or time zero between the pump and probe lasers, and this can be done experimentally in two approximate ways: the time zero can be determined by optimizing the MPI signal of the parent molecule, which is enhanced when the temporal and spatial overlap between the pump and probe laser takes places, or by performing correlation measurements as described in section 2.1.3.4.

For asymptotic measurements, the probe pulse is temporally delayed with respect to the pump laser longer than the estimated duration of photodissociation; that is, a time at which the reaction is complete. At this time, several images can be grabbed by varying the experimental conditions. Generally, three images are recorded; one corresponding to the total signal generated by the presence of both lasers, another image corresponding to the signal generated by the pump laser and another by the probe laser. The final image corresponds to the pump-probe signal, to which the signal from each separate laser has been removed. Each final image results from an average of N images with a given exposure time of the CCD camera so that the signal-to-noise ratio is optimal. Asymptotic images are typically 250 exposures of 250-1000 ms each. The CCD camera is controlled by the software provided by the manufacturer (LaVision DaVis 6.2). Once the images are obtained, they are inverted, following the BASEX or pBASEX routine described in section 1.4.2.1.

To determine the reaction time of a photodissociation process, it is necessary to obtain a set of images as a function of the time delay between the pump and probe laser pulses, ranging from negative temporal delays to asymptotic time delays. Such experiments are often called clocking experiments or delay scan experiments. This process is fully automatized and computer-controlled. A LabView program controls the stepper motor in charge of moving the linear translation stage while the synchronization between the linear translation stage movement and the acquisition of the images is controlled by a MATLAB script.

After a delay-scan experiment, a set of folders is generated in the computer, each corresponding to a full sweep of the translational stage. Each folder, in turn, contains as many images as time points have been recorded. Using a MATLAB script, the equivalent images to a specific time point are added, which improves the signal-to-noise ratio. This set of images must be later inverted and angularly, and radially integrated to obtain the fragment translational energy and angular distribution at each time step. This is fully automated by a software developed for that purpose. The analysis of these experiments is later detailed in section 2.1.6.1.

2.1.6.1. Analysis of time-resolved data

The temporal behavior of the reaction can be analyzed employing bi-dimensional or three-dimensional procedures, depending on the amount of information from the dissociation process that wants to be extracted.

2.1.6.1.1 Two-dimensional analysis applied to the evolution of the translational energy of the fragments as a function of the time delay

In some cases, the study of the dependence of the velocity distribution with time can be sufficient to extract all the relevant information of the experiment so that the analysis of the data can be reduced to a two-dimensional matrix.

The determination of the reaction times is performed considering all the velocity distributions of the fragments as a function of the time delay between the pump and probe laser pulses. The signal can be divided into a series of individual contributions that have their temporal form and shape with respect to the velocity. The velocity distributions are usually modeled employing an asymmetric Gaussian function defined by:

$$R(v) = \exp\left(4\ln 2\left(\frac{v - v_0}{\sigma_r} \right)^2 \right) H(v - v_0) + \exp\left(4\ln 2\left(\frac{v - v_0}{\sigma_l} \right)^2 \right) H(v - v_0) \qquad (2.37)$$

where v_0 is the peak position, σ_r and σ_l are the right and left side Gaussian widths, and $H(v)$ is a step function (Heaviside). The difference in the contribution widths can be explained in terms of the rotational distributions of the molecules in the molecular beam and the fragments.

The temporal behavior of the velocity distributions may vary depending on the type of photodissociation mechanism.

In the case of a predissociation mechanism, the contributions have a form of a rising exponential convoluted with the cross-correlation of the laser pulses according to:

$$\Gamma_i(t) = \exp\left(-4\ln 2\left(\frac{t-t_0}{\tau_{ci}}\right)^2\right) \otimes \left[\left(1-\exp\left(-\frac{t-t_0}{\tau_i}\right)\right) \times H(t-t_0)\right] \tag{2.38}$$

where τ_{ci} is the cross-correlation corresponding to the multiphoton ionization process, and τ_i is the time of formation of the fragments.

For a direct photodissociation mechanism, the contributions are usually fitted to a Boltzmann sigmoidal curve according to:

$$S = A_2 + \frac{A_1 - A_2}{1+\exp\left(\frac{t-t_0}{t_c}\right)} \tag{2.39}$$

where A_1 and A_2 are the initial and final intensity values of the sigmoidal function, characterized by a central temporal position t_0 (*i.e.*, the delay time for which the intensity has reached half its asymptotic value) and a rise time constant t_c, which describes the steepness of the rise.

Another example would be the MPI signal that has a temporal form of the cross-correlation of the laser pulses when it is a purely non-resonant phenomenon (due only to the temporal overlap of the laser pulses). This is described by:

$$\Gamma_i(t) = \exp\left(-4\ln 2\left(\frac{t-t_0}{\tau_{ci}}\right)^2\right) \tag{2.40}$$

where τ_{ci} is the cross-correlation corresponding to the multiphoton process.

In the absence of chirp in the velocity distributions, each contribution appears as a product of the temporal and velocity distribution shape according to:

$$C_i(v,t) = \Gamma_i \times R_i(v) \tag{2.41}$$

and the fitting functional is given by:

$$F(v,t) = \sum_i C_i(v,t) \tag{2.42}$$

2.1.6.1.2 Three-dimensional analysis applied to the evolution of anisotropy as a function of delay time

To analyze the evolution of anisotropy of each of the contributions in the image with respect to the time delay between the pump and probe laser pulses, a bi-dimensional fitting procedure turns to be insufficient since an additional angular dimension is required for that purpose.

Dr. Vincent Loriot developed a multidimensional method[166] by which it is feasible to separate different overlapping contributions present in a set of images corresponding to different reaction channels of interest from other secondary signals. This fitting procedure is essential when contributions with different time behavior are overlapping. This method provides very good results even though the contributions have similar energy and temporal form but differ by their angular distributions.

The simplest strategy would consist of fitting the inverted images, but that would require too many computational resources due to the large number of experimental points. Instead, the translational energy distributions are evaluated by angular integration at intervals of 10º, considering the symmetry of the images. In this way, only nine different distributions are extracted for each image between 0 and 90º. The expected angular modulation can be simulated by local integration of the Legendre polynomial as:

$$A(\theta_0,t) \propto \int_{\theta_0-\frac{\Delta\theta}{2}}^{\theta_0+\frac{\Delta\theta}{2}} [1+\beta(t)P_2(\cos\theta)]d\theta \tag{2.43}$$

where P_2 is the Legendre second-order polynomial.

The data is stored in a three-dimensional matrix where the dimensions are the translational energy distribution, the anisotropy, and the pump-probe time delay.

The temporal dependence of the anisotropy can be adequately modeled by:[130]

$$\beta(t) = \beta_0 + I_{pr}(t) \otimes \Delta\beta \times \left(\left(1 - \exp\left(-\frac{t-t_0}{\tau_\beta} \right) \right) H(t-t_0) \right) \tag{2.44}$$

where β_0 is the initial value of the anisotropy parameter, τ_β the relaxation time of the anisotropy parameter, $\Delta\beta$ the amplitude of the anisotropy parameter variation and $I_{pr}(t)$ is the cross-correlation of the laser pulses.

The numerical fitting, both for the bi-dimensional and the three-dimensional methods, is carried out employing the Levenberg-Marquardt unidimensional method.

2.2. MAX BORN INSTITUTE KILOHERTZ LABORATORY SETUP

In the research stays at the Max-Born Institute, two types of experiments were conducted. For that, the laser system is divided into two branches to suit each of the experiments.

The first set of experiments was carried out using monochromatized high-order harmonics by a TDCM setup.[167] In this setup, XUV radiation generated by the HHG source is spectrally filtered with a special XUV monochromator that is designed to preserve the temporal duration of the XUV pulses, essentially creating a source that delivers ultrashort bandwidth-limited pulses with tunable central wavelength. This way is possible to define the excitation photon energy, and this yields simpler results to interpret than those obtained using the full bandwidth of the high-order harmonics. In the second set of experiments, the entire bandwidth of the high harmonics, *i.e.*, the full APT, was used to carry out the reconstruction of attosecond interference by beating of two-photon transitions (RABBITT, RABBIT[168] or RABITT[169]) technique, in which a two-color pump-probe scheme employing XUV attosecond pulses and femtosecond near-infrared (NIR) probe pulses were used.

In RABBITT, assuming that the spectral bandwidth of the attosecond pulses in the train contains several harmonics, ionization of the target in the combined fields leads to a series of main bands (corresponding to the photoelectron energies upon absorption of one of the harmonic photons) and sidebands (corresponding to the additional absorption or emission of a NIR photon) in the photoelectron energy spectrum as schematically represented in figure 2.48. Since two pathways lead to each sideband, an interference pattern appears in the spectrum as a function of the time the attosecond pulse is applied over the optical half cycle of the NIR field.

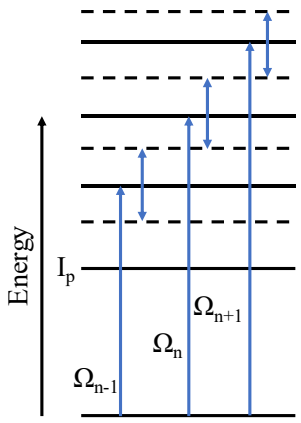

Figure 2.48. *Illustration of energy levels with main bands (solid lines) and sidebands (dashed lines) in the continuum of the spectrum, as well as transitions involved in the RABBITT principle. Figure adapted from reference [170].*

The temporal resolution is related to the modulation of the probability of the sideband peaks, which depends on the phase difference between consecutive harmonics and an intrinsic phase related to the target. In combination with the amplitudes of the harmonics, the phase information can be used to reconstruct the temporal profile of the attosecond pulses, and the electron wave packets initiated by these pulses.

The experimental results of this second set of experiments are not presented in the present Doctoral Thesis.

2.2.1. Femtosecond laser system and time-delay compensating monochromator setup

Only the most relevant details of this experimental system are described. A complete description of this setup can be found in the Doctoral Thesis of Dr. Martin Eckstein.[171]

The CPA laser system (Amplitude Systems) provides ultrashort pulses in the IR, with a tunable central wavelength at around 795 nm. It delivers pulses with a repetition rate of 1 kHz or 10 kHz with a pulse energy of 20 mJ or 2 mJ, respectively. The pulse duration can be varied between 20 fs and 35 fs. The output laser energy is split into two arms by a beamsplitter. About 70 % of the energy is transmitted, and it is used as the IR probe arm, whereas 30 % of the energy is reflected and is the source for HHG. The power of this beam should be adequately chosen to optimize the phase matching of the HHG process.

In the HHG vacuum chamber, the latter beam is focused by a 62.5 cm focusing mirror into a gas cell, filled with the HHG source (typically Ar or krypton (Kr)) to a pressure of 45 mbar, producing XUV pulses which are filtered from residual IR by a 100 nm thin aluminum (Al) filter. A spectrometer records the full XUV spectrum. The cell is mounted onto the tip of a straight tube, which serves as the gas feed-through into the vacuum chamber. The cell is sealed with a thin Al foil (50 μm) from the vacuum chamber. With the first laser shot, a small hole is burned in the foil, resulting in a perfect alignment of the laser beam to the hole. The manipulator holding the gas cell is represented in figure 2.49.

The full bandwidth of harmonics is driven to the TDCM schematically represented in figure 2.50. This system is very similar to the one described in reference [172]. The monochromator consists of two consecutive sections symmetric in reflection. In the first chamber (diffraction stage), the XUV beam, coming from, ideally, a point source, is collimated by a toroidal mirror, and it is reflected from a diffraction grating mounted in a conical diffraction configuration, improving the efficiency of the diffraction process. By diffracting the XUV, different XUV wavelengths are selected by rotating the grating around an axis in the reflection plane. The diffracted beam is focused by the second toroidal mirror employing a 200 μm wide slit. The imaging of the beams by the second mirror into the focal

plane is equivalent to propagation into the far-field and leads to maximal geometrical separation of different wavelengths in space resulting in an optimal wavelength/energy resolution.

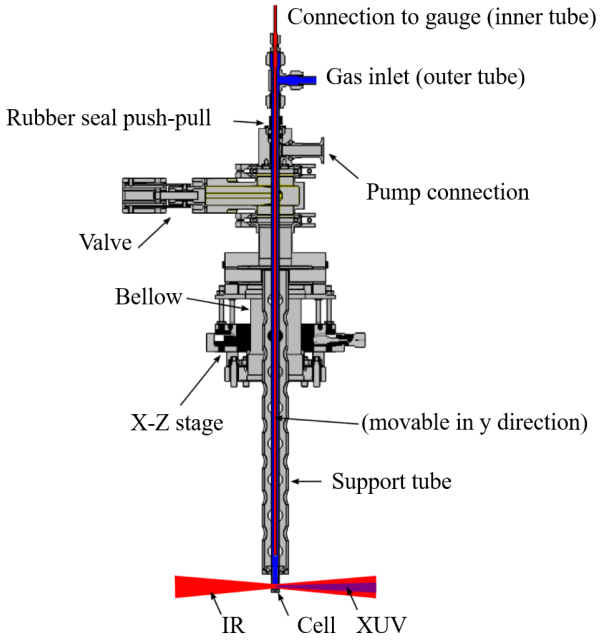

Figure 2.49. *HHG cell with the manipulator. The blue tube is the gas feed-through into the vacuum. The red tube is connected to a pressure gauge, measuring the pressure directly in the gas cell. The complete assembly of red and blue tubes can be moved out of the chamber in a volume that can be evacuated separately. This allows for a change of the aluminum foil that is sealing the gas cell. Figure from reference* [171].

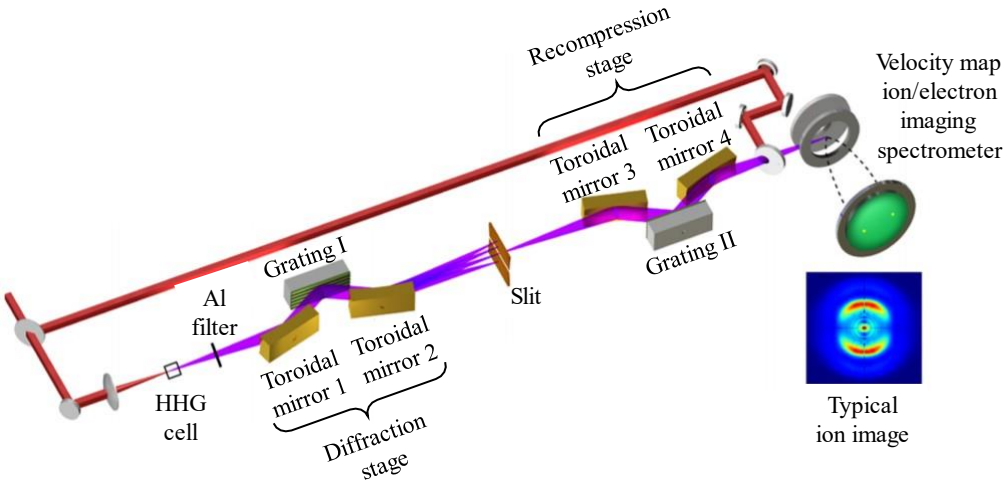

Figure 2.50. *Optical layout of the time-delay-compensating XUV monochromator setup, consisting of four toroidal mirrors (T1-T4), two diffraction gratings (G1, G2) operated in the off-plane mount and the monochromator slit. The XUV beam is spectrally dispersed by the first stage (T1+G1+T2) and is filtered by the slit. At this point, the beam is temporally stretched. The second stage (T3+G2+T4) recompresses the XUV pulses and guides the beam towards the end station. Figure adapted from reference* [171].

Phase-front tilt occurs when the arrival time of an ultrashort pulse varies across the beam profile due to a tilt between the pulse front and a direction perpendicular to the beam. This phenomenon is related to angular dispersion, *i.e.*, with a dependence of the wavefront orientation on the optical frequency. It can also result from simultaneous spatial and temporal chirp. A second grating compensates the phase-front tilt induced by the first grating in the recompression stage. A choice of three gratings with different groove densities (150, 300, and 600 lines/mm) allows optimization of the reflectance over the full range of wavelengths.

The monochromator transmission varies from 3 % to 16 % for harmonics between H13 (20.3 eV) and H31 (48.4 eV), which results in photon fluxes of 10^6 to 10^7 photons per pulse per harmonic.

After selecting the specific harmonic, it is recombined with the IR probe beam employing a holey mirror with a 3 mm hole. Both beams are focused on the interaction region of the VMI spectrometer.

2.2.2. Characterization of laser pulses

2.2.2.1. Spectral and temporal characterization

The characterization of the electric field of ultrashort laser pulses provides the maximum possible information of them, and it can be fully characterized by either knowing the spectral amplitude and the spectral phase (frequency domain) or the temporal amplitude and the temporal phase (temporal domain) of the pulses. In this setup, spectral phase interferometry for direct electric-field reconstruction (SPIDER) technique,[173, 174] was employed to recover the spectral phase and the spectral amplitude of ultrashort laser pulses. Despite working in the frequency domain, a Fourier transform can directly relate the temporal field. Thus, SPIDER turns out to be a complete diagnostic technique.

The phase of light can be recovered by interference. If two pulses in time separated by τ enter a spectrometer, the spectral intensity pattern shows interference fringes. If these identical pulses have a slightly different center frequency, the pattern may distort due to the spectral phases of each pulse.

If the complex field of the pulse is given by:

$$\sqrt{I(\omega)}\exp(i\phi(\omega)) \tag{2.45}$$

The frequency-shifted (or sheared) pulse is then given by:

$$\sqrt{I(\omega+\Omega)}\exp(i\phi(\omega+\Omega)) \tag{2.46}$$

When these pulses are mixed in a spectrometer, the resulting interferogram is given by:

$$S(\omega) = I(\omega) + I(\omega+\Omega) + \sqrt{I(\omega)I(\omega+\Omega)}\cos\left[\phi(\omega) - \phi(\omega+\Omega) + \omega t\right] \tag{2.47}$$

where $I(\omega)=|E(\omega)|^2$ is the spectral intensity of the individual pulses, $\varphi(\omega)$ is the spectral phase, ω is the amount of spectral shear, also called spectral shift, and τ is the temporal delay. This equation is the basis of the spectral shearing interferometry (SSI)[175, 176] and from it, by knowing Ω and τ, it is possible to characterize the spectral phase of the ultrashort laser pulses.[175, 176]

SPIDER implements SSI using non-linear optics. Since the shear needs to be a reasonable percentage of the pulse's spectral bandwidth, for ultrashort bandwidths of tens of THz, non-linear optical techniques are the optimum ones. In figure 2.51, the basic SPIDER setup[173] is represented, where the spectral shear is achieved by SFG.

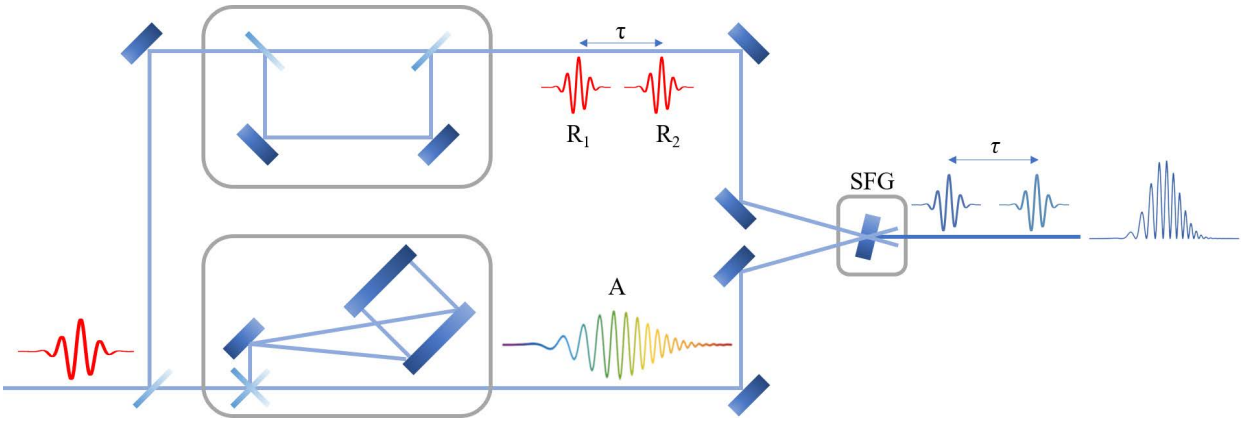

Figure 2.51. *Representation of the classic SPIDER setup. Two pulse replicas (R_1 and R_2), delayed by τ, are prepared together with an ancillary stretched pulse (A) and subsequently mixed in an SFG process to generate a pair of spectrally sheared copies of the measured pulse. Spectral fringes are recorded with a spectrometer. The phase is extracted from this interferogram.*

In the SPIDER device, an ultrafast pulse is split into two arms employing a beamsplitter. One of the arms is sent to a grating pair, stretching the pulse by adding a large negative chirp. The other arm goes to a mismatched Michelson interferometer, which generates a pulse pair. The pulse pair and the chirped pulse are mixed in a non-linear crystal, generating a pair of blue pulses. Since each pulse in the fundamental pulse pair overlapped with a different quasi-monochromatic temporal slice of the chirped pulse, the SFG blue pulses have a different but small central frequency, the requisite of spectral shear.[177] This way, the phase difference is turned into a gradient. This gradient of the unknown pulse phase can be integrated to reconstruct the original spectral phase. Together with a measurement of the spectrum (which can also be obtained from the SPIDER interferogram), the electric field either in the frequency or time domain can be calculated *via* a Fourier transform.[178]

2.2.2.2. Temporal resolution

The most straightforward way to determine the XUV-IR (one IR photon) cross-correlation is to look at the sidebands in the photoelectron spectrum of a noble gas.[179, 180] The XUV pulses ionize the gas in the presence of the moderately strong IR field. When the two pulses overlap in time and space on the gas jet, sidebands appear in the photoelectron spectrum, as shown in figure 2.52. These sidebands are spectrally shifted by the IR photon energy. This process is determined by the absorption of one harmonic photon plus either the absorption or emission of one IR photon.

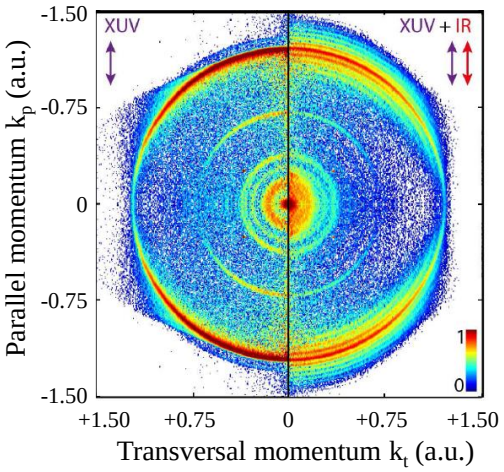

Figure 2.52. *Photoelectron VMI images recorded for ionization of Ar atoms by harmonic 23 (35.9 eV) without the IR field (left side) and in the presence of the IR pulse at zero-time delay (right side). The image without the IR shows two distinct outer rings and three rings close to the center (at low translational energies). The outermost ring corresponds to photoionization producing the $Ar^+(3s^2 3p^5\ ^2P)$ ionic final state. This state has a spin-orbit splitting of about 180 meV. The second ring corresponds to the $Ar^+(3s^1 3p^6\ ^2S)$ ionic state. The structures with low translational energies can be assigned to the formation of several electronically excited states of Ar^+. In the right half, the image is strongly modified by an IR pulse with an energy of 130 μJ. The main rings corresponding to single-photon ionization by the XUV pulse are weaker, and many additional concentric rings (sidebands) appear with an energy spacing of the IR photon energy. Figure from reference [123].*

The amplitude of the sidebands as a function of the time delay between the XUV and IR pulses provides the correlation signal.[181] In the present case, Ar (IP=15.57 eV) was employed to determine the cross-correlation between the 11th harmonic and the IR leading a value of 36±5 fs.

Besides, the temporal profile of the nth sideband can be calculated as a convolution of the XUV pulse profile with the IR pulse intensity profile raised to the power of n. If both XUV and IR pulses have Gaussian shapes with FWHM of Δt_{XUV} and Δt_{IR}, respectively, the temporal profile of the first and second sidebands are given by Gaussian distributions with widths.

$$\Delta t_1^2 = \Delta t_{XUV}^2 + \Delta t_{IR}^2 \tag{2.48}$$

$$\Delta t_2^2 = \Delta t_{XUV}^2 + \frac{\Delta t_{IR}^2}{2} \tag{2.49}$$

These expressions allow us to calculate both the XUV and IR pulse durations, knowing the Δt values for consecutive sidebands.

2.2.2.3. Laser intensity

The sideband intensity and their number depend on the electric field of the IR pulse at the moment of ionization by the XUV pulse.[179, 180] Therefore, sideband measurements can be used to determine the IR laser pulse intensity at the focus.

Plotted on a logarithmic scale, the fall-off of the sideband intensity shows a characteristic linear behavior.[182] The slope of the fall-off changes approximately at the positions indicated by the arrows in figure 2.52. These energies are related to the maximum translational energy, which an electron created by the XUV pulse can classically acquire through interaction with the IR pulse. For positive and negative sidebands, the kinetic energy (in atomic units) can be estimated as:[180, 182]

$$E_{kin} \pm = E_0 \pm \sqrt{8 E_0 U_p} + 2U_p \tag{2.50}$$

where E_0 is the initial energy of the photoelectron given by the difference between the XUV photon energy and the ionization potential, and U_p is the ponderomotive potential.

Thus, the value of the cut-off energy can be used to calculate the average intensity of the IR field at the focus in a more precise way than estimations based on the laser beam parameters, such as pulse duration and size of the focal spot.

2.2.3. Velocity map imaging setup

2.2.3.1. General description

In a conventional VMI spectrometer, the repeller electrode is a flat plate, and the skimmed atomic or molecular gas typically enters the interaction area through a small hole drilled in the repeller electrode or from one side in between the repeller and extractor. During a supersonic expansion into the vacuum, efficient rotational and vibrational cooling can be achieved, which leads to some simplification of the process. Nevertheless, in this type of conventional configuration, large amounts of gas need to be introduced into the vacuum system to obtain appreciable gas densities in the interaction region. This

problem can be mitigated, to some extent, if pulsed sample sources are used as long as the repetition rate is not too high.

In the case of HHG sources, which are very weak, low-density gas sources are a problem, especially in the case of using isolated attosecond pulses. In an isolated attosecond pulse experiment with a typical duration of 100 as, there are no more than 10^6 photons per pulse. This number of photons, combined with the typical density in an atomic/molecular beam of 10^{13} atoms/molecules per cubic centimeter, and considering a typical absorption cross-section of 10^{-17} cm^2 and a typical atomic/molecular beamwidth of 10^{-1} cm, leads to a probability of photon absorption of approximately 10^{-5}, which is low for many experiments. To solve these problems, the VMI spectrometer used in these experiments slightly differs concerning the flat electrodes version describe in section 2.1.4.3. The gas inlet is incorporated into a curved repeller,[183] from which the gas escapes near the XUV light focus. The central part of the repeller electrode, along a diameter of 1 mm, is flat to be parallel to the detection plane. From there, the repeller electrode assumes a conical shape with a 154° cone angle to accommodate the focus of the XUV light in front of the exit hole. The gas density maintained in the interaction region is only limited by the maximum pressure that the experimental chamber can maintain.

In the typical flat electrode version,[37] the resolution is independent of the shape of the electrodes, provided that the fields encountered by the particles on their path from the extraction region to the bi-dimensional detector are unchanged. In contrast, in this curved repeller setup, the energy resolution depends on the width of the flat part of the repeller and the distance from this flat part to the laser focus, since these two parameters determine both the fields experienced by the detected particles and the size of the interaction volume. At a certain distance from the repeller to the interaction region, the resolution significantly drops, so a compromise between the energy resolution and the signal yield should be achieved.

A full description of the VMI spectrometer available at the Max-Born Institute can be found in references [183] and [123].

2.2.3.2. Reconstruction of bi-dimensional images

The VMI images measured with this system show a bi-dimensional cut through the three-dimensional momentum distribution of the generated charged fragments. The momentum cuts are reconstructed from the raw data by using the BASEX[48] routine to perform the Abel-transformation. The three-dimensional momentum distribution is reconstructed from the bi-dimensional cut by exploiting the cylindrical symmetry of the generated fragments around the laser polarization axis. The presented images are always oriented such that the linear polarization of the electric field of the optical pulses is vertical.

2.2.3.3. Velocity map imaging spectrometer calibration

2.2.3.3.1 Velocity map imaging calibration for ions

To calibrate the ion translational energy axis, the vibrational progression of the $\tilde{C}\ ^2\Sigma_u^+$ state of the cation of molecular nitrogen (N_2^+) was employed. The $\tilde{C}$ state of N_2^+ is a bound state whose lowest vibrational level has a binding energy of 23.583 eV (slightly below the first dissociation limit (L1) of 24.293 eV). For vibrational levels $v \geq 3$, the total energy is above the first dissociation limit and the $\tilde{C}$ state can predissociate by vibrational coupling with the $\tilde{D}(^2\Pi_g)$ state. The $\tilde{D}(^2\Pi_g)$ state correlates to the first dissociation limit corresponding to $N^+(^3P)+N(^4S^o)$ products.[184, 185] The binding energies of the vibrational states are listed in table 2.5.

Table 2.5. *Vibrational energy levels for the* $\tilde{C}$ *state of* N_2.[184]

Vibrational quantum number v	Binding energy (eV)
0	23.583
1	23.831
2	24.083
3	24.331
4	24.576
5	24.817
6	25.054
7	25.286

The excitation energy in the ionic state is split between the translational energy of the fragments upon dissociation and the electronic excitation of the fragments. Due to momentum conservation, the translational energy is equally split between the two fragments. The KER can be estimated by the following equation:

$$KER = BI - EL \tag{2.51}$$

where *BI* is the binding energy of the ionic state and *EL* is the dissociation limit.

The electronic excitation stored in the individual fragments results in different dissociation limits *EL*, and the full KER can then be directly deduced by measuring the velocity of a single N^+ fragment. Figure 2.53 shows the bi-dimensional image through the three-dimensional momentum distribution for N^+ after inversion with pBASEX, in which some clear rings can be distinguished at small velocities.

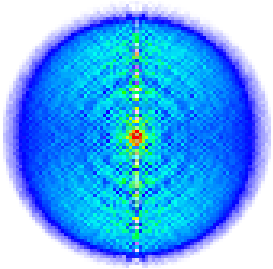

Figure 2.53. *pBASEX inverted bi-dimensional-slices through the three-dimensional momentum distribution for N^+ fragment.*

The image is angularly integrated considering the Jacobian of the three-dimensional surface, leading to the distribution in the momentum space displayed in figure 2.54 (A), where the vibrational states of the $\widetilde{C}$ state can be appreciated. The x axis is then converted to the energy space (R^2) as represented in figure 2.54 (B). The energy values of the observed rings must be estimated from the known vibrational energy levels (binding energies) of the N_2^+ $\widetilde{C}$ state[184] and the dissociation limit L1 of 24.293 eV.[186] Table 2.6 shows the estimated KER. The values are transformed into the fragment translational energy to perform the calibration, so a mass factor (m_N/m_{N2}) is applied.

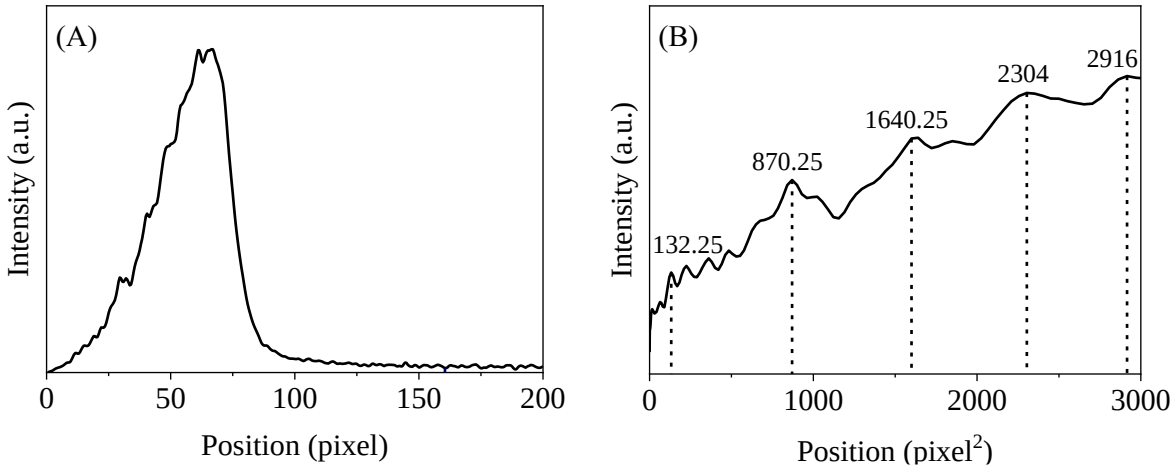

Figure 2.54. *(A) Radial distribution in the momentum space for vibrational progression in the $\widetilde{C}$ state of N_2^+ (B) Radial distribution in the energy space for vibrational progression in the $\widetilde{C}$ state of N_2^+.*

Table 2.6. *Estimated energy levels of the vibrational states of the N_2^+ $\widetilde{C}$ state from bibliographic data of binding energies[184] and dissociation limit.[186]*

Vibrational quantum number ν	Binding energy (eV)	Dissociation limit (eV)	Kinetic energy release (eV)	CM N translational energy (eV)
3	24.331	24.293	0.04	0.02
4	24.576	24.293	0.28	0.14
5	24.817	24.293	0.52	0.26
6	25.054	24.293	0.76	0.38
7	25.286	24.293	0.99	0.50

The energy of the rings should match the values in table 2.6. Table 2.7 shows the correspondence between the N^+ KER values and the pixels assigned in the distribution of figure 2.54 (B).

Table 2.7. *Estimated energy levels of the vibrational states of the N_2^+ $\widetilde{C}$ state from bibliographic data of binding energies and dissociation limit. Correspondence between the energy values and the pixels assigned in the distribution of figure 2.54 (B).*

Vibrational quantum number ν	Nitrogen position (px)	CM nitrogen translational energy (eV)
3	11.5	0.02
4	29.5	0.14
5	40.5	0.26
6	48	0.38
7	54	0.50

Knowing the dependency of energy on the radius from the center of the image ($E=k\cdot px^2$); by representing the energy versus the position of the rings from the center of the image (in pixels), the calibration factor can be obtained as the coefficient of an allometric function to the 2nd power employed as a fitting function of the data, as plotted in figure 2.55.

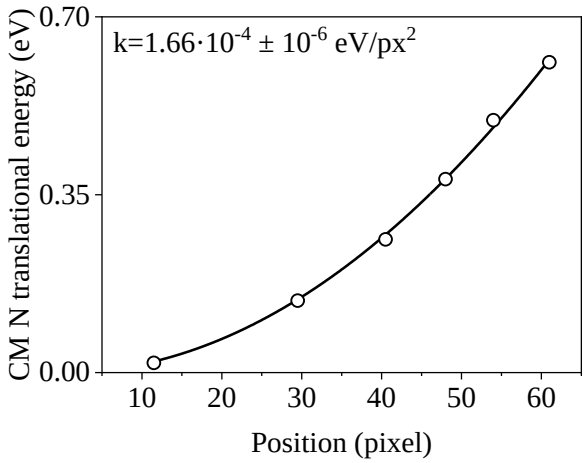

Figure 2.55. *CM nitrogen translational energy (in eV) represented versus the position of the rings from the center of the image (in pixels). The least-squares method fits the data to an allometric function to the 2nd power, being the calibration factor equal to the coefficient of the function. The resultant calibration factor k is $1.66\cdot10^{-3}\pm10^{-6}$ eV/px^2.*

2.2.3.3.2 Velocity map imaging calibration for photoelectrons

The electron translational energy axis was calibrated by using the positions of the $\widetilde{X}\,^2E_{1/2}$, $\widetilde{X}\,^2E_{3/2}$ lines of methyl iodide cation (CH_3I^+) with the different photon energies and the binding energies calculated by considering the ionization potential of the $\widetilde{X}\,^2E_{3/2}$ state of 9.54 eV.[187]

Chapter 3 – Halogen-atom effect on the ultrafast photodissociation dynamics of the dihalomethanes chloroiodomethane and bromoiodomethane

3.1. INTRODUCTION

During the last decades, interest in halomethanes (CH_3X, X=halogen atom) has substantially increased due to their relevant role in atmospheric chemistry. In particular, halogen atoms and radicals containing halogens happen to be effective catalysts involved in the ozone depletion from the stratosphere.[188, 189] The atmospheric decay of halomethanes depends largely on their photodissociation rates and product channels in the UV region. Thus, it is essential to determine their UV photodynamics for assessing their environmental impact.

Numerous experimental and theoretical researchers have focused on the photodissociation dynamics of halomethanes. In particular, CH_3I has served for many years as a prototype for the study of photodissociation reaction dynamics of polyatomic molecules in the gas phase as it has a relatively low number of atoms and a seemingly simple photodissociation mechanism. It is essential to know in detail the photodissociation dynamics of these molecules to understand the more complex dynamics of dihalogenated systems.

The first studies of the CH_3I date back to 1964, with the discovery of the first chemical iodine (I) laser by Kasper and Pimentel. Laser emission was observed at 1.3 μm corresponding to the stimulated emission of $^2P_{1/2}\rightarrow{}^2P_{3/2}$ atomic I transition after flash photolysis of gaseous CH_3I and trifluoromethyl iodide (CF_3I). The population inversion necessary for the laser emission was achieved through a photodissociation reaction.[190] Since then, both experimental and theoretical studies on CH_3I photodissociation have followed one another over time, leaving to date extensive knowledge about, for example, the mechanisms of redistribution of internal energy for the formation of products, the crossings between the involved potential energy surfaces or the nature of the electronic transitions. Many studies have been reported on the near UV photodissociation of CH_3I *via* the first absorption band, referred to as the *A*-band,[161, 191, 192 149, 150, 152, 153, 193, 194] since it constitutes an excellent model of prompt C−I cleavage mediated by a conical intersection.

The *A*-band, a broad featureless absorption continuum between 220-350 nm with a maximum around 260 nm, is attributed to an n(I)→σ*(C–I) transition where a non-bonding *npπ* electron of the I atom is promoted to the lowest available energy antibonding σ* molecular orbital.[191, 195] The final electronic configuration gives rise to two electronic states at the limit of the weak spin-orbit coupling: ^1E and ^3E. Nevertheless, due to the strong spin-orbit coupling, the electronic configuration leads to five states: *E*, *E*, A_1, A_2, and *E* for Ω=2, 1, 0^+, 0^- and 1, respectively;[196, 197] or designated in Mulliken notation[198] as $^3Q_2$, $^3Q_1$, $^3Q_{0+}$, $^3Q_{0-}$ and $^1Q_1$.[199]

Figure 3.1 displays the states arising under weak spin-orbit interaction, strong spin-orbit interaction and their correlation with their dissociation limits. Only the $^3Q_0$ state correlates with $CH_3(\tilde{X}\,^2A_2'')$+I*($^2P_{1/2}$) formation, while all other states correlate with $CH_3(\tilde{X}\,^2A_2'')$+I($^2P_{3/2}$) formation. Between the $E(^1Q_1)$ and $A_1(^3Q_{0+})$ states, there is a conical intersection that allows the formation of $CH_3(\tilde{X}\,^2A_2'')$+I($^2P_{3/2}$) from the $^3Q_0$ state *via* a non-adiabatic pathway.

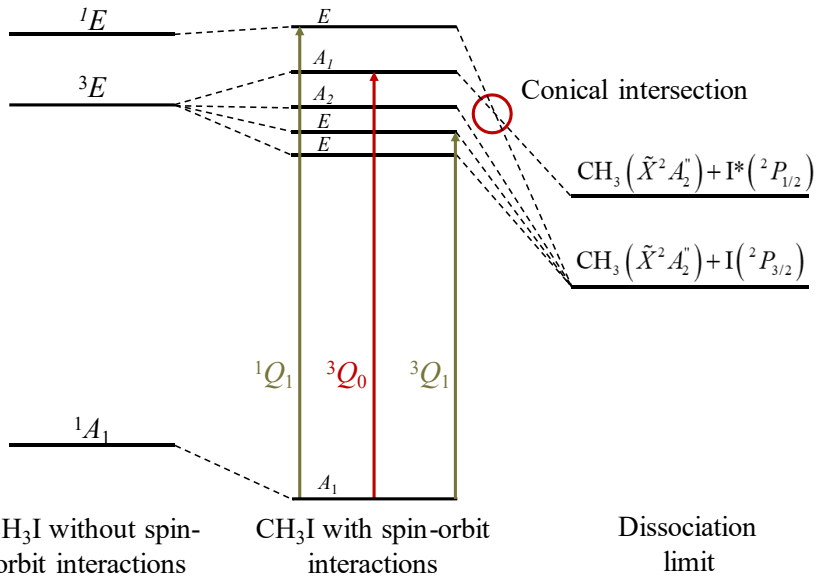

Figure 3.1 *Correlation diagram of CH_3I n⟶σ* transitions in the A-band. The states with C_{3v} symmetry are indicated with and without spin-orbit coupling, along with the dissociation limits. The transitions are labeled according to Mulliken's notations. The arrows indicate the allowed transitions by electric dipole: red arrow corresponds to a parallel transition, whereas green arrows correspond to perpendicular transitions. Figure adapted from reference [200].*

Figure 3.2 represents the magnetic circular dichroism (MCD) spectrum of CH_3I,[191] where the contribution to the total absorption of each of the states is represented. With these MCD experiments, it was possible to resolve the three excited states contributing to the absorption continuum, the peak energies and the oscillator strengths of the components. Of the five states, only three of them are accessible by electric dipole transitions: the strongest contribution is mediated by a parallel transition to the $^3Q_{0+}$ state (from now on referred as $^3Q_0$ for simplicity), while two perpendicular transitions to $^1Q_1$

and $^3Q_1$ states contribute with less than 2 % to the total absorption.[193] As well, a*b initio* calculations have helped to in-depth detail the excited states belonging to the *A*-band.[193]

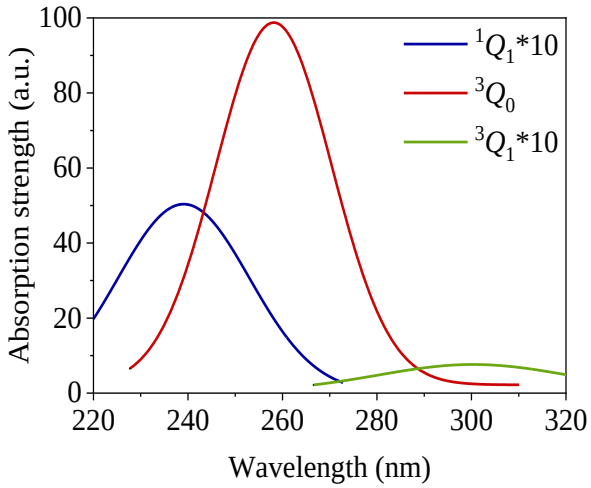

Figure 3.2 *Absorption spectrum of CH_3I and spectral decomposition corresponding to the three states ($^3Q_0$, $^1Q_1$ and $^3Q_1$) contributing to the total absorption. Curves corresponding to the $^1Q_1$ and the $^3Q_1$ states are magnified by a factor of 10, as their contribution to total absorption is less than 2 %.*[40]

Figure 3.3 shows a diagram of the *A*-band potential energy surfaces along the reaction coordinate C–I for the low energy states of CH_3I.[193]

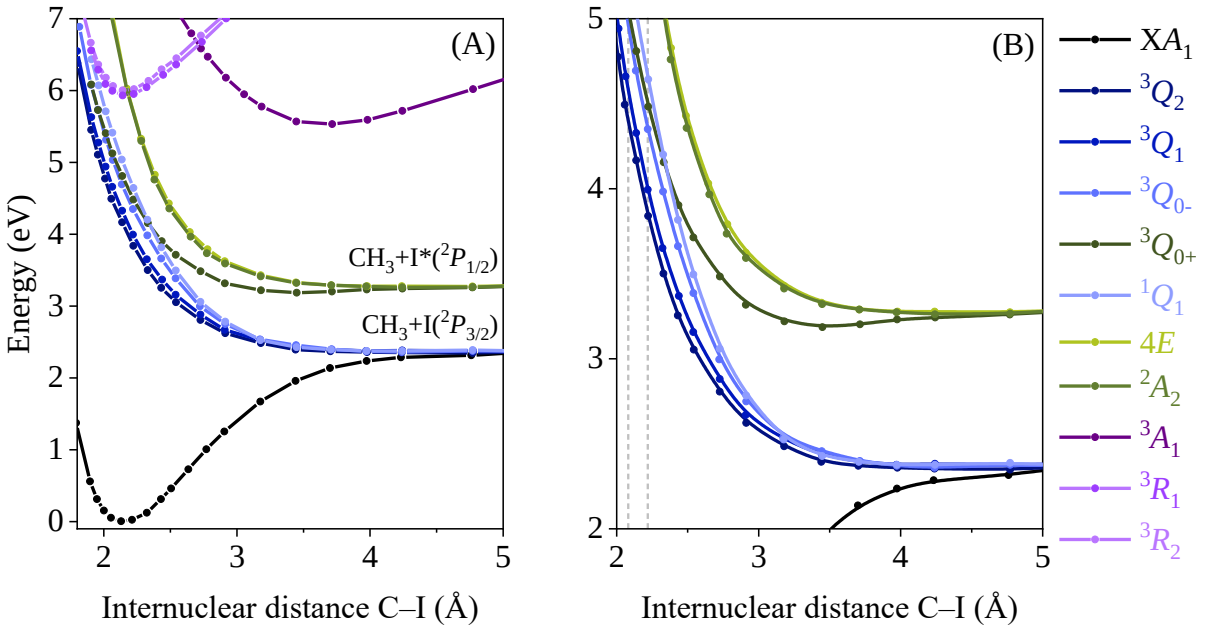

Figure 3.3 *(A) Potential energy surfaces calculated along the reaction coordinate C–I for the low energy states of CH_3I. (B) Expansion of the optically active states of the A-band. Dashed vertical lines indicate the Franck-Condon region. Figure adapted from reference* [193].

As reflected by the literature-reported quantum yield Φ^*=0.79,[40] the dissociation of CH_3I in the *A*-band mainly occurs through the repulsive $^3Q_0$ state leading to a significant formation of $CH_3(\tilde{X}$

$^2A_2''$)+I*($^2P_{1/2}$), while a small amount of $CH_3(\tilde{X}\,^2A_2'')$+I($^2P_{3/2}$) is produced by a transfer of population from the $^3Q_0$ to the $^1Q_1$ state *via* a conical intersection located close to the Franck-Condon region.

The photodissociation of CH_3I *via* the $^3Q_0$ state correlating with I*($^2P_{1/2}$) fragments is characterized by an anisotropy parameter $\beta\approx2$, typical of a pure parallel transition, while the observed value of the anisotropy parameter β for the formation of I($^2P_{3/2}$) fragments is also close to 2. Since the transition to the $^1Q_1$ state is perpendicular, this is also an indication that the observed I($^2P_{3/2}$) fragments must come from an initial absorption to the $^3Q_0$ state, followed by a transition to the $^1Q_1$ state *via* the conical intersection instead of a direct absorption to the $^1Q_1$ state. However, the observed anisotropy in these fragments has a minimal perpendicular contribution due to a direct absorption to this state.

Photodissociation dynamics of CH_3I in the *A*-band can be conceived as a one-dimensional problem, given the lightness of the hydrogen (H) atoms attached to the carbon (C) atom and the fact that dissociation is direct and fast along the dissociating C–I bond. However, some of the other degrees of freedom play an essential role in the dynamics. The C_{3v} geometry (corresponding to a linear geometry in a triatomic molecule) avoids the interactions between the $^3Q_0$ and $^1Q_1$ states due to geometric constraints. Therefore, non-adiabatic crossing between the $^3Q_0$ and $^1Q_1$ states is only possible when vibrational states that distort the C_{3v} geometry are involved. Theoretical studies have indicated that there is a slight torsion (<5 %) of the H_3C–I bond during dissociation, slightly breaking the C_{3v} symmetry, which makes feasible the curve crossing.[201, 202]

Most of the available energy, around 90 %, is converted into translational energy of the fragments, demonstrating the impulsive character of CH_3I photodissociation in the *A*-band.[162, 163, 203-209] However, there is a small amount channeled into vibrational excitation of the symmetric bending mode or umbrella mode (ν_2) of the methyl (CH_3) fragment, produced from the geometry change between CH_3I (pyramidal geometry) and the CH_3 photoproduct (flat geometry), during the fast photodissociation. As well, there is some excitation in the symmetric stretch mode (ν_1) mostly observed in the channel that correlates with I($^2P_{3/2}$) formation.[36, 163] It has also been observed that CH_3 radicals formed in correlation with I($^2P_{3/2}$) appear vibrationally hotter, even reversing the population, being the most populated state ν_2=1 (umbrella mode with a quantum of excitation).[210] *Ab initio* calculations of the Franck-Condon region show that this region is close to the minimum energy step in the $^3Q_0$ state, resulting in a minimum vibration in that state.[211] However, in the vicinity of the conical intersection, this minimum energy step is displaced for the $^1Q_1$ state with respect to the umbrella mode bending angle, thus making the transferred population from the state $^3Q_0$ to the $^1Q_1$ state undergoes a sudden change in geometry resulting in the vibrational excitation in the ν_2 mode in the $^1Q_1$ state and, in general, resulting in the channel that correlates with the formation of I($^2P_{3/2}$) vibrationally hotter.

Extensive experimental work has focused on this fundamental process, both in asymptotic conditions using nanosecond pulsed lasers[36, 40, 152, 192, 212] and time-resolved experiments using femtosecond pulsed lasers.[149-151, 153, 213] Eppink and Parker applied their VMI technique to study this photodissociation process across the entire *A*-band.[37, 40] The dissociation dynamics in the red and blue edges of this *A*-band have also been reported highlighting the dominant role of the $^3Q_1$ state and a reverse $^1Q_1 \rightarrow {}^3Q_0$ non-adiabatic dynamics.[152, 212]

Other time-resolved experiments upon excitation of the *A*-band using different spectroscopic techniques for probing the fragments and even following the temporal evolution of the transition state region have been carried out in the last few years.[214-218]

Attar *et al.*[214] measured the transition state region in the *A*-band photodissociation of CH_3I at 266 nm using femtosecond XUV transient absorption (TA) spectroscopy by real-time evolution of core-to-valence transitions near the I N-edge in the 45-60 eV range. Core-to-valence electronic states decay during the C–I bond cleavage simultaneously to the I($^2P_{3/2}$) and I*($^2P_{1/2}$) fragment resonant appearance. The transition state resonances were found to reach a maximum at ~40 fs and decay to complete C–I dissociation in ~90 fs. Later, Drescher *et al.*[215] performed similar experiments in which they observed a continuous shift in the energy of the emerging atomic absorption lines. They attributed this to a relaxation of the valence shell vacancy that occurs during the first few femtoseconds of the C–I bond dissociation.

Baumann *et al.*[216] performed single-shot UV/VUV pump-probe experiments to study the valence state photodissociation of CH_3I after excitation at 268 nm and probing by one- or two-photon ionization at 161 nm with a sub-10 fs time resolution. The probe-pump experiments allowed as well to study the dissociation from the 6p ($^2E_{3/2}$) Rydberg state. They attributed time constants of 98.2±1.9 fs and 28.5±2.8 fs for the biexponential decay of the parent ion from the $^3Q_0$ and $^1Q_1$ states, respectively. The time constant for the $^3Q_0$ state was directly related to the C–I bond cleavage along the reaction coordinate up to the asymptotic region of the potential energy surface, whereas the time constant for the $^1Q_1$ state was attributed to the duration of the $^1Q_1 \rightarrow \tilde{X}\,{}^1E_{3/2}$ ionization window considering the restrictions imposed by the VUV probing wavelength. Mechanisms were proposed to observed time constants for the I^+ and CH_3^+ fragment ions.

Warne *et al.*[218] studied the time-resolved photodissociation of CH_3I at 269 nm and 255 nm by UV (395 nm) MPI-PES. They observed different dynamics at the two excitation wavelengths with significant differences in the measured reaction times and dynamic structure, attributed to a significant contribution of the $^1Q_1$ state at 255 nm due to a more complex structure in the potential energy surface and increased appearance time.

The first theoretical modeling of CH_3I was carried out more than sixty years ago,[219] but undoubtedly, the significant advance in dynamics calculations of CH_3I was achieved with the appearance of *ab initio* potential energy surfaces.[220-222] Numerous theoretical works have dealt with this problem,[150, 153, 193, 201, 202, 211, 222-227] using various approaches, including a full-dimensional quantum approach.[226] Despite the intense efforts, some discrepancies with experimental findings persist on aspects such as the description of the absorption spectrum, the relevance of the absorption strength to the three dipole-allowed $^3Q_1$, $^1Q_1$, and $^3Q_0$ states, or the CH_3 vibrationally selected quantum yields.

In our group, several time-resolved measurements of CH_3I at 266 nm in the *A*-band employing femtosecond VMI were carried out during the last decade.[149, 150, 153, 154] The sub 100 fs reaction times measured were rationalized through wave packet calculations on the available *ab initio* potential energy surfaces using three-dimensional and four-dimensional reduced dimensionality models, namely, the C–I dissociation coordinate, the I-CH_3 bending mode, the CH_3 umbrella mode, and the C-H symmetric stretch mode.[150, 153] The models reproduced very well the experimental reaction times for the $CH_3(v_1, v_2)$+I*($^2P_{1/2}$) dissociation channels with v_1=0 and v_2=0, 1, 2 and also for the channel $CH_3(v_1$=0, v_2=0)+I($^2P_{3/2}$), but failed to predict the experimental reaction times for the $CH_3(v_1, v_2)$+I($^2P_{3/2}$) channels with (v_1, v_2)=(0, 1), (0, 2), and (1, 0), *i.e.*, when the CH_3 fragment produced along with spin-orbit ground-state I($^2P_{3/2}$) atoms is vibrationally excited. Different explanations were given for the disagreement, but the differences were not assessed.

Later, time-resolved measurements were extended to CH_3I excitation at 243 nm, supported by two theoretical approaches to shed light on the observations: first, a reduced dimensionality four-dimensional nonadiabatic wave packet calculation and second, a full dimension nine-dimensional trajectory surface-hopping calculation on the same potential energy surfaces, including the quantization of vibrational states of the CH_3 product. Also, high-level *ab initio* electronic structure calculations were carried out to describe the CH_3 3p_z Rydberg state involved in the (2+1) REMPI probing process as a function of the C–I distance.[154] The role of the conical intersection or a significant absorption to the $^1Q_1$ state were discarded to explain the observed vibrationally state-resolved clocking times at the two excitation wavelengths (268 and 243 nm). *Ab initio* calculations of the adiabatic ground and excited states potential energy curves of the CH_3 radical as a function of the distance to the heavy I atom could not account for the specific opening of the optical window for different vibrational states of CH_3. However, the nonadiabatic coupling between valence states and the 3p_z Rydberg state of the CH_3 fragment was revealed to give rise to efficient electronic predissociation with an increasing rate with vibrational excitation. It was pointed out that the presence of the heavy I atom might affect the couplings and predissociation rate of the different vibrational states of CH_3 differently, having unpredictable effects on the measured clocking times.

The photochemistry of alkyl iodides in the *A*-band has aroused great theoretical and experimental interest in recent years.[200, 203, 213, 228-233] One of the fundamental reasons is that the photodissociation of these molecules in the near UV is highly implicated in destroying the ozone layer. On the other hand, these systems offer a unique opportunity to understand the effect of the size and structure of the radical on the photodissociation dynamics.

The modification of the characteristics of a molecular photodissociation process by introducing key changes in the molecular structure represents an alternative way of controlling reaction dynamics. The photodissociation process of a polyatomic molecule can be visualized by looking at a single dimension related to the reaction coordinate. However, the interplay between the one-dimensional reaction coordinate and the rest of the degrees of freedom of the molecule can influence the dynamics very significantly. In this way, Corrales *et al.*[213] performed time-resolved VMI studies for a series of linear and branched alkyl iodides with increasing structural complexity to investigate the role of the energy flux between the bond cleavage dimension and the vibrational modes associated with the radical chain in a given family of molecules, in the energy distribution, quantum yields and C−I bond reaction times.[213] Specifically, they studied the non-adiabatic photodissociation dynamics of the family of alkyl iodides, RI, where R=CH_3, C_2H_5, *n*-C_3H_7, *i*-C_3H_7, *n*-C_4H_9 and *t*-C_4H_9 (methyl, ethyl, *n*-propyl, *i*-propyl, *n*-butyl and *t*-butyl, respectively) in which the alkyl radical was modified in two ways: by increasing the length of the linear chain (CH_3I, ethyl iodide (C_2H_5I), *n*-propyl iodide (*n*-C_3H_7I) and *n*-butyl iodide (*n*-C_4H_9I)), and by introducing branched chains (isopropyl iodide (*i*-C_3H_7) and tertbutyl iodide (*t*-C_4H_9)). An increasing number of low and high-frequency vibrational modes were introduced to modify the direct non-adiabatic multichannel dissociation along the C−I reaction coordinate. The main role of the energy flux into the internal degrees of freedom of the molecule, vibration, and rotation was demonstrated in real-time dynamics. Full-dimension time-resolved semi-classical dynamics calculations were carried out to support the experimental evidence and provided insight into the structure-dynamics relationship to understand structural control on time-resolved reactivity.

For the corresponding experiments presented in this chapter, this idea was extended to evaluate the substituent atom effect (X=H, Cl, Br) on the real-time dynamics of the C−I bond cleavage by comparing the ultrafast photodissociation dynamics of the dihalomethanes, chloroiodomethane (CH_2ICl) and bromoiodomethane (CH_2BrI), to the well-known CH_3I.[234]

Dihalomethanes (CH_2IX, X=Br, Cl) absorption spectra in the first absorption band, displayed in figure 3.4, present a broadband with a maximum centered at approximately 270 nm, assigned to the promotion of a non-bonding electron of the I atom to an anti-bonding orbital of the C−I bond (n(I)→σ*(C–I) transition). Comparing to the corresponding methyl halides, methyl bromide (CH_3Br) and methyl chloride (CH_3Cl), the bands centered at 270 nm, are more intense and red-shifted. These

features might be attributed to the fact that the central C atom has a more positive charge than the corresponding methyl halide so that the transitions that promote an electron to an antibonding orbital have a larger charge-transfer character. This transfer reduces the positive charge associated with the upper state, lowering its energy and producing a redshift.[235] The intensification of the broad bands compared to the corresponding bands of the monohalides indicates that there is a moderate coupling between the two chromophores.

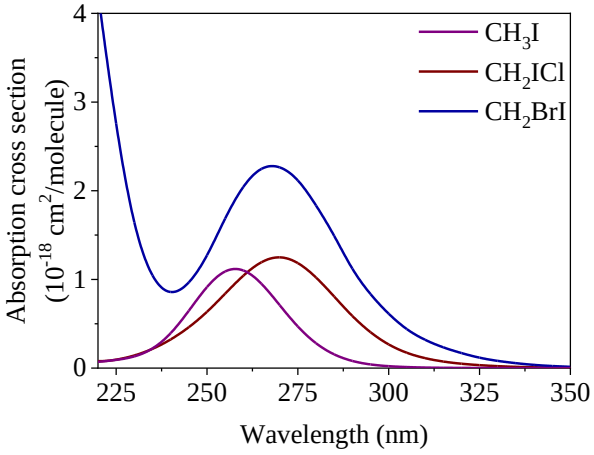

Figure 3.4. *UV absorption spectra of CH_3I (purple), CH_2ICl (dark red) and CH_2BrI (dark blue) at 298 K in the gas phase from 215 to 380 nm.*[236, 237]

In contrast to methyl halides (CH_3X, X=F, Cl, Br, I), dihalomethanes, and in particular CH_2XY (X=I, Y=Cl, Br), are C_s symmetry molecules with a more complex electronic structure, which along with the spin-orbit interactions due to the presence of heavy halogen atoms, reveal them as fascinating systems for dynamical studies.[238] The $^3Q_0$ state in C_{3v} symmetry transforms into the 4*A*' state in C_s symmetry, while the doubly degenerated $^3Q_1$ and $^1Q_1$ states split into the 3*A*' and 2*A*" states and the 4*A*" and 5*A*' states, respectively.[239] In C_s symmetry, *A*' electronic states are characterized by a transition dipole moment contained in the X-C-Y plane, while for *A*" states, it is perpendicular to that plane. The conical intersection in this symmetry is transformed into an avoided crossing.

Photodissociation dynamics of dihalomethanes such as CH_2ICl and CH_2BrI have been scarcely investigated. The few studies mainly focus on the energy partitioning between internal – rovibrational excitation – and translational modes studied employing nanosecond pulsed lasers.[240]

First experiments regarding dihalomethanes photodissociation date back to the 1980s'. Lee and Bersohn[235] were the first to study the photodissociation of a molecule with two chromophores, specifically CH_2BrI. Employing photofragment spectroscopy, they measured the photofragment mass spectrum and the angular distribution of I and bromine (Br) photofragments and discussed the latter

based on classical models. The results were compared to the corresponding methyl halides CH_3I and methyl bromide (CH_3Br).

Following studies include the work by Butler *et al.*[236] in which the photodissociation of CH_2BrI upon excitation at 193.3, 210, and 248.5 nm was examined employing PTS to measure the product translational energy distributions and polarization dependences for the primary processes. Their findings revealed that the excitation at 248 nm leads predominantly to C−I dissociation with a minor contribution of C−Br bond dissociation, whereas the scenario reverses at 193.3 nm, where the C−Br fission rules the dissociation. At 193.3 nm, concerted dissociation of iodine monobromide (IBr) photoproducts also takes place. Excitation at 210 nm within the *B*-band results in selective breaking of the C−Br bond and no fission of the C−I bond. Minor dissociation channels leading to concerted elimination of electronically excited IBr and a three-body fragmentation to give CH_2+Br+I at this excitation wavelength were also observed.

Vibrational mode-specific experimental work was conducted by Man *et al.*[241] along the *A*- and *B*-band by Raman spectroscopy to determine whether selective excitation of either the C−Br or C−I chromophores led to relatively simple pseudo-diatomic dissociation dynamics like that observed for CH_3I, or to more complex short-time photodissociation dynamics proper of higher alkyl iodides upon excitation of the C−I chromophore in the *A*-band. Results revealed some degree of multidimensional character and a noticeable coupling between the C−I and C−Br chromophores.

More recent time-resolved studies include the work of Attar *et al.*[242] based on the element-specific single-photon photodissociation dynamics of CH_2BrI at 266 nm, leading to a predominant C−I and minor C−Br bond cleavage. Both pathways were probed simultaneously through individual core-to-valence transitions. The core-to-valence absorption spectroscopy of CH_2Br radicals using femtosecond high-harmonic XUV TA spectroscopy was investigated, providing novel results on the 3*d* (Br) $M_{4/5}$ pre-edge absorption spectrum of the CH_2Br radical photoproduct corresponding to the C−I dissociation channel. The measured times for C−I dissociation leading to I($^2P_{3/2}$) and I*($^2P_{1/2}$) atomic products were 48±12 fs and 44±4 fs, respectively, while the measured C−Br dissociation reaction time leading to atomic Br was 114±17 fs. Femtosecond time-resolved core-level spectroscopy utilizing multiple reporter atoms simultaneously was demonstrated to be a unique tool for probing time-resolved dynamics.

Burt *et al.*[243] also investigated the UV photodissociation of CH_2BrI at 271.6 nm through time-resolved Coulomb explosion imaging employing NIR femtosecond laser pulses, in combination with the state-of-the-art pixel imaging mass spectrometry (PImMS) sensor,[244] allowing for coincidence imaging and hence correlations to be extracted for different fragmentation channels.[245, 246] Experimental results revealed a single photon dissociation leading to the C–I cleavage producing high internal energy

CH_2Br fragments in correlation with I($^2P_{3/2}$) or I($^2P_{1/2}$) atoms; whereas absorption of a second UV photon breaks the C-Br bond of CH_2Br. Around 65.6±1.6 % of the available energy was found to be channeled into internal energy of CH_2Br fragments, in good agreement with 67.9±1.5 % reported at 248 nm in previous studies by Butler *et al.*[236] Coulomb explosion imaging is demonstrated as a powerful technique for probing time-resolved dynamics over REMPI.

Some theoretical research has been carried out on CH_2BrI. For example, Liu *et al.*[247] computed vertical excitation energies and oscillator strengths for excited states in the *A* and *A*' bands using unrestricted Hartree-Fock (UHF), complete active space self-consistent field (CASSCF) and configuration interaction singles (CIS) methods, nevertheless the spin-orbit interaction was not taken into account. Results highlighted the significant bond selectivity in the bands, particularly in terms of differences in bond charge densities.

Liu *et al.*[248] carried out a more in-depth theoretical study employing multistate complete active-space second-order perturbation theory (MS-CASPT2) combined with the spin-orbit interaction CASSCF method. The reported potential energy curves as a function of both the C−Br and C−I distances pointed out the relevant role of the spin-orbit interaction in halomethanes, especially for those containing an I atom. Their theoretical calculations confirmed the dominant C−I cleavage in the *A*-band through direct dissociation across repulsive potential energy surfaces and predicted minor dissociation in the *A*'-band induced by relaxation to lower excited states *via* internal conversion or intersystem crossing. Some aspects, such as the isomerization of these compounds, were also addressed in the study.

Combined studies of theory and experiment are those carried out by Chicharro *et al.*,[239] who recently studied the photodissociation dynamics of CH_2BrI at 266 and 210 nm using slice imaging and VMI in combination with pump-probe nanosecond laser pulses, probing both the I and Br fragments. Experimental results were supported with high-level *ab initio* calculations of potential energy curves and absorption spectra. The results revealed that in the *A*-band at 266 nm, direct dissociation through the 5*A*' excited state leads to the formation of I($^2P_{3/2}$) fragments, whereas I*($^2P_{1/2}$) fragments are produced *via* the 5*A*'→4*A*'/4*A*" nonadiabatic crossing. In contrast, Br and Br* fragments' formation was attributed to indirect dissociation *via* a curve crossing between the 5*A*' with upper excited states such as the 9*A*'. At 210 nm (*A*'-band), the dissociation exclusively produces Br and Br* fragments, which are likely originated by a dissociation mechanism through the 9*A*' excited state.

Concerning CH_2ICl, the first studies are by Schmitt *et al.*[249] They studied the photodissociation of CH_2ICl by flash photolysis at 266.2 nm, demonstrating that after irradiation with low-intensity near-UV light, the cleavage of the C–I bond is dominant.

Senapati *et al.*[250] investigated the CH_2ICl dissociation dynamics at several excitation wavelengths including 222, 236, 266, 280, and 304 nm by probing the I*($^2P_{1/2}$) fragments arising from the C–I dissociation. The quantum yield of I*($^2P_{1/2}$) was measured employing REMPI, revealing a similar trend to CH_3I except for 236 nm; wavelength at which, it is pointed out that the crossing region between the two excited states is located near the exit valley away from the Franck-Condon excitation region. This work was completed with a second publication,[251] where they showed comparable results probing the Cl*($^2P_{1/2}$) fragment production. To explain the formation of these photoproducts, an interchromophore energy transfer mechanism between the C−I and C−Cl chromophores was proposed.[251]

Zhang *et al.*[252] also investigated the photodissociation dynamics of CH_2ICl in the *A*-band employing ion VMI in combination with REMPI detection. Translational energies and angular distributions of the corresponding photofragments were obtained from ion images of I($^2P_{3/2}$) and I*($^2P_{1/2}$) fragments upon excitation at 266 and 277 nm. The formation of I fragments was attributed to a fast dissociation process *via* a repulsive potential energy surface mediated by a conical intersection between $^3Q_0$ and $^1Q_1$ states, whose absorption strength is higher at shorter wavelengths. Some C−Cl fragmentation was similarly observed, but it was attributed to a CH_2Cl secondary UV photodissociation after CH_2ICl dissociation.

Allum *et al.*[246] carried out time-resolved Coulomb explosion imaging of CH_3I and CH_2ICl at 272 nm, employing 815 nm IR probe pulses. Results revealed that for CH_3I, the photodissociation in the first absorption band leads to the cleavage of the C–I bond producing CH_3 co-fragments in correlation with both spin-orbit states of the I atom, as well-reported in the literature. In the case of CH_2ICl, primary and secondary dissociations were studied by covariance analysis employing a PImMs sensor.[244, 245] This study allowed a nice comparison of the photochemical behavior of dihalomethanes in combination with previously mention work by Burt *et al.*[243] The halogen atom substitution effect was revealed in the available energy partitioning into different degrees of freedom: in halomethanes, the amount of energy partitioning into internal modes is more significant than in the CH_3I case, being the amount larger in CH_2Br in comparison with CH_2Cl, in accordance with simple impulsive models.

This chapter presents the most relevant results of the time-resolved photodissociation dynamics of CH_3I, CH_2ICl and CH_2BrI in the first absorption band (*A*-band) at an excitation wavelength of 268 nm. The study was carried out employing femtosecond VMI in combination with (2+1) REMPI to detect the produced I atoms, in both spin-orbit states, to elucidate the halogen-atom effect on the real-time dynamics of the C−I bond cleavage in the series of molecules. Total translational energy distribution and I angular distributions, and the I atom transients are reported and discussed. The experimental results are interpreted with the help of high-level *ab initio* calculations of potential energy curves and absorption spectra and full-dimension on-the-fly trajectory calculations, including surface-hopping, to unravel the

halogen-atom presence effect on the time-resolved photodynamics in terms of the different contributions of excited states as well as the role of the avoided crossing between the 4*A*' and 5*A*' excited states. The computed and experimental reaction times are rationalized based on the energy released into the internal degrees of freedom of the fragments during the dissociation.

3.2. METHODOLOGY

3.2.1. Experimental methodology

3.2.1.1. Laser configuration and optical assemblies

This section presents the specific methodological details of the experiments corresponding to the study of the time-resolved photodissociation dynamics of the dihalomethanes CH_2BrI and CH_2ICl in the *A*-band at around 268 nm, using velocity map ion imaging in combination with resonant ionization of the free fragments I($^2P_{3/2}$) and I*($^2P_{1/2}$) through (2+1) REMPI. Figure 3.5 summarizes the experimental setup employed for these experiments. The details are described below.

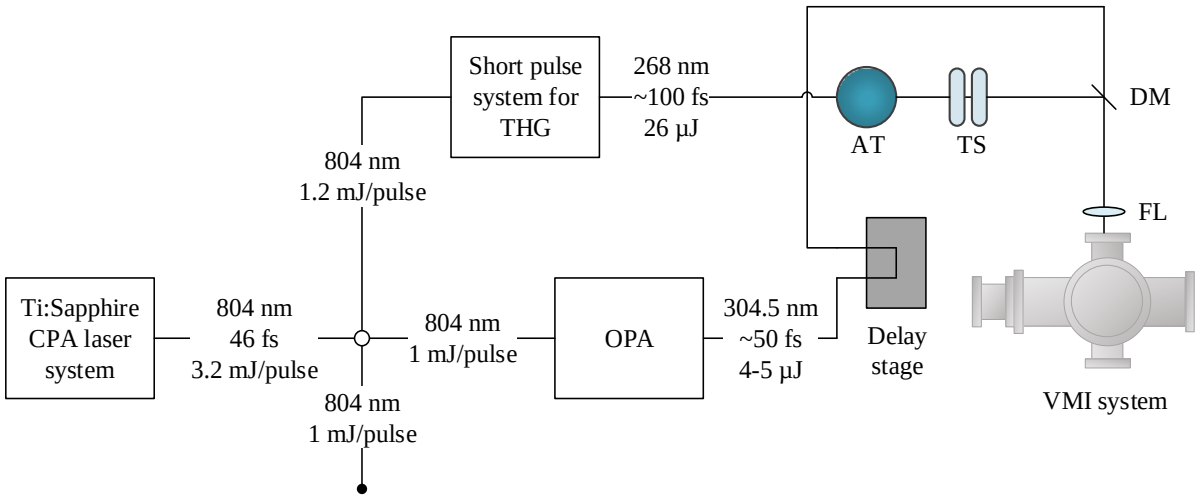

Figure 3.5. *Experimental setup for the time-resolved photodissociation studies of CH_2BrI and CH_2ICl in the first absorption band at 268 nm employing femtosecond laser pulses and velocity map ion imaging. The laser system, the OPA, and the short pulse system for THG are represented on the left side. Along the layout, several optical elements such as a dichroic mirror (DM), a telescope (TS), a power attenuator (AT), the probe delay translational stage, the final focusing lens (FL) and the wedge (W) are distinguished. The VMI machine is located in the lower right area of the figure. The detection system is arranged perpendicular to the plane of the paper and the gas inlet (off-axis configuration).*

The *A*-band excitation was carried out using a pump laser centered at 268 nm, whereas the probing of the reaction was accomplished through the (2+1) REMPI of I($^2P_{3/2}$) and I*($^2P_{1/2}$) photoproducts produced in correlation with molecular fragments. Two different (2+1) REMPI schemes were employed:

one at 304.5 for the joint detection of I($^2P_{3/2}$) and I*($^2P_{1/2}$) photoproducts and the other, centered at 306 nm for the exclusive detection of I*($^2P_{1/2}$) photoproducts (see table 2.2).

For this purpose, the output from the Spitfire regenerative amplifier (804 nm, 3.2 mJ/pulse, 46 fs pulse duration, 1 kHz repetition rate) was divided into different arms utilizing beamsplitters. Around 1.2 mJ/pulse was driven to the THG setup based on transmissive optics to produce 268 nm laser pulses with an output energy of 26 μJ/pulse and an FWHM of ~2.5 nm. A 1 mJ/pulse arm was used to pump the OPA. The signal around 1218-1224 nm was frequency quadruplicated to generate the probe laser centered at 304.5 or 306 nm with typically 4-5 mJ per pulse with an FWHM of ~1.9 nm. Afterward, the probe beam was driven to the Parker linear translation stage. Both lasers were recombined in the final dichroic mirror, and later they were focused inside the ionization chamber employing a 25 cm focusing lens. Both laser beams had the proper polarization to ensure the cylindrical symmetry for reconstructing the measured ion images.

Special care was taken with the intensity of the pump laser as the *A*-band of CH_3I and its dihalogenated derivatives is accessed through a single-photon transition. The intensities of the laser pulses in the interaction area were controlled by variable attenuators in the form of neutral density filters by transmission. The energies chosen for the pump and probe pulses were <1 μJ/pulse and 3 μJ/pulse, respectively, equivalent to intensities in the focus of around 10^{11} W/cm^2, in both cases.

3.2.1.2. Molecular beam conditions and detection system

For the realization of the experiments, CH_3I (Sigma Aldrich, 99 %), CH_2ICl (Sigma Aldrich, 97 %) and CH_2BrI (Sigma Aldrich, 97 %) were used. The sample was contained in a glass bubbler at room temperature, except for CH_3I, which was cooled down to 0 ºC with an ice bath (vapor pressure P_v=185 mbar[253]), due to its high vapor pressure at room temperature (P_v=533 mbar at 25 ºC).[253] The molecular beams were generated by expanding the vapors with helium (He) (Air Liquid 99.999 % Laboratory Quality) as carrier gas at 1.5 atm backing pressure, thus formed by a mixture of 5 % target molecule and 95 % He, through a piezoelectric valve with a 0.5 mm diameter orifice producing gas pulses of about 35-40 μs at 1 kHz frequency synchronized with the laser repetition rate. The unloaded pressure, *i.e.*, with the valve closed, is in the order of $6\cdot10^{-7}$ mbar at the expansion chamber (C1) and $3\cdot10^{-7}$ mbar in the ionization chamber (C2), whereas under typical experimental conditions during gas expansion, the pressure in the expansion chamber increases, between $1\cdot10^{-5}$ and $5\cdot10^{-5}$ mbar, depending on the opening of the piezo valve and the pressure conditions at the nozzle. Valve apertures were set at 35-40 μs, and voltages applied to the piezoelectric material were ~ 300 V. Typical working pressures in the ionization chamber were around $5\cdot10^{-6}$ mbar. The delay between the gas pulses and the laser pulses was such that its interaction occurred at the beginning of the gas pulse, thus producing more ions signal however at

the expense of a higher temperature of the parent molecules. This way formation of clusters in the molecular beam was significantly reduced.

For these experiments, the VMI system with small lenses was employed, and the VMI conditions were achieved with a voltage ratio between the repeller and extractor lenses of 0.76, being the repeller voltage around 5200 V. The calibration of the apparatus was performed using the known KER of the CH_3+I*($^2P_{1/2}$) and CH_3+I($^2P_{3/2}$) channels from the 268 nm photodissociation of CH_3I (see section 2.1.4.6.1).[149]

The photodissociation process was monitored by detecting the iodine ions (I^+) in a TOFMS configuration. According to the TOF mass spectra for CH_2ICl and CH_2BrI presented in figure 3.6, the arrival of I^+ to the detector occurred at 8.9 μs later than the arrival of the laser pulse at the interaction area, therefore the gating of the MCP was set at 8.9 μs with a duration of 200 ns. The deflector plates were used; nevertheless, it was challenging to deflect the parent molecules from the iodine photoproducts due to the similar mass, especially for CH_3I.

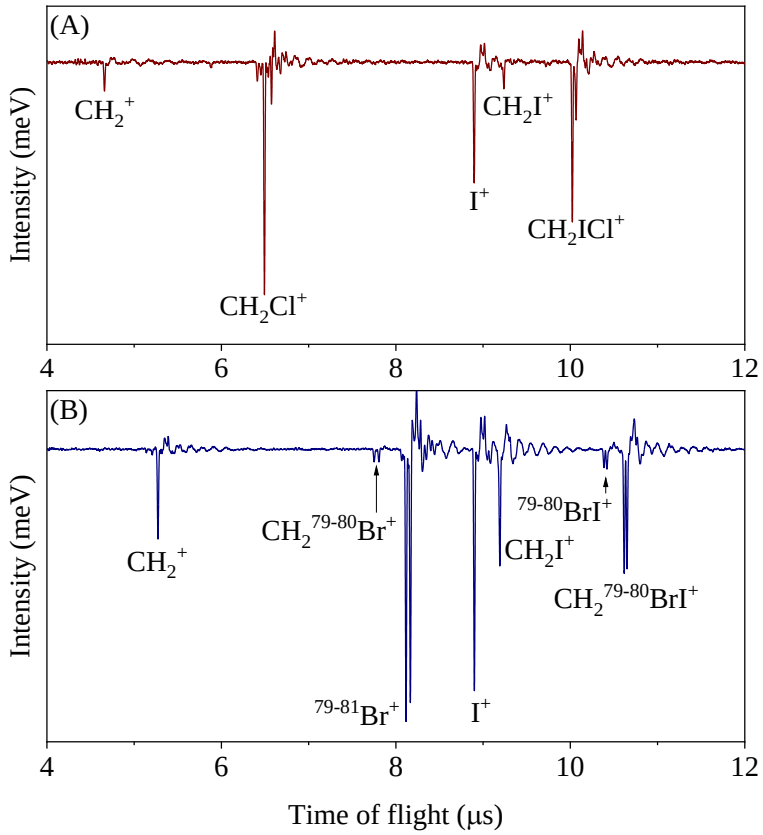

Figure 3.6. *Pump-probe TOF mass spectra with TOF time base (as measured in the digital oscilloscope) of (A) CH_2ICl and (B) CH_2BrI. Pump centered at 268 nm, probe pulse centered at 304.5 nm and time delay settled at 1 ps (asymptotic conditions). The different peaks are assigned to the different parent and fragment ions. Notice the presence of species for the most abundant isotopes of Br: ^{79}Br and ^{81}Br in the form of doublets.*

3.2.1.3. Temporal characterization of the femtosecond laser pulses

The temporal characterization of the laser pulses consisted of *in situ* measurements of the (1+2') REMPI transient for xenon (Xe) (1 photon from ≈268 nm and 2 photons of from the probe laser). The ionization of the Xe is a non-resonant process when using 268 nm and 304.5 nm pulses, ensuring that the observed transients correspond only to the cross-correlation of laser pulses. The cross-correlation function provided a value of 150 fs. This measurement also provided the time zero between the laser pulses.

The time zero was also determined by measuring the transients of the low energy contribution appearing in the center of all I images corresponding to MPI processes. The transient for this contribution was fitted to a Gaussian function but considering a fixed 40 fs temporal shift with respect to the temporal overlap between the pump and probe lasers.

3.2.2. Theoretical methodology

Multireference calculations were performed by Dr. Jesús González-Vázquez to simulate the absorption spectra and the dissociation dynamics of CH_3I, CH_2ICl and CH_2BrI using a semiclassical methodology.

The absorption spectra for the three molecules were calculated using a harmonic Wigner distribution of trajectories to describe the zero-point energy of the system. The geometry and frequencies of all molecules required for the calculation of the harmonic modes were obtained using the second-order Møller-Plesset perturbation theory (MP2) method with the Sapporo Relativistic basis set contracted to triple zeta,[254] whereas the electronic excitation energy was calculated using the state average (SA) CASSCF (SA-CASSCF) method corrected by perturbation theory (PT) in its spin-orbit multi-configurational quasi-degenerated perturbation theory (SO-MCQDPT)[255] form with level shifts of 0.02 and 0.01 hartrees.[256] Since SO-MCQDPT could not be used to calculate relaxed densities,[257] the dipoles, that require a large number of configurations to be included in the wave function[193] were obtained with a CIS method considering twenty singlet and twenty triplet states. Combining a CIS method with the calculation of several electronic states allowed us to recover part of the dynamical correlation required for a good description of the dipole moments. The selected active space contained six electrons in four orbitals (bonding C–I, antibonding C−I and two lone pairs on the I) for CH_3I and twelve electrons in eight orbitals (bonding and antibonding for C−I and C−Cl or C−Br, and two lone pairs on each halogen atom) for CH_2ICl and CH_2BrI. For CH_3I, six states were included in the state average while for CH_2ICl and CH_2BrI eighteen states were employed where all multiplicities were averaged. These calculations were performed with the General atomic and molecular electronic structure system (GAMESS) suite with relativistic integrals until third-order Douglas-Kroll-Hess[258-260] with

quadruple precision, taking into account explicitly the spin-orbit coupling as a two-electron operator.[261-264]

The one-dimensional potential energy curves were performed with MOLCAS[265, 266] with the relativistic contracted atomic natural orbitals (ANO-RCC) basis set.[267] Relativistic effects were taken into account using a regular Douglas-Kroll Hamiltonian[268-270] and the atomic mean-field integral (AMFI) approximation[271] to consider relativistic effects. The active space included in the calculation was the same as for the spectrum, but the state average was done independently for singlet and triplet states. The optimizations and gradients calculations were performed at CASSCF,[272] whereas the final energy for the one-dimensional curves was calculated at MS-CASPT2[273] with a level shift of 0.2.[274]

On-the-fly adiabatic full-dimension classical trajectory calculations were performed using a modified version of the surface hopping including arbitrary couplings (SHARC) method,[275, 276] which includes the surface hopping algorithm, linked with the MOLPRO code[277] for the CASPT2 gradients[278, 279] and the spin-orbit coupling using the multireference configuration interaction (MRCI) method.[280-282] In this approach, the gradient of spin-orbit states was calculated as linear combinations of the spin-free gradients, neglecting the spin-orbit coupling gradient. Moreover, in the present case, the contribution of the non-adiabatic coupling to the gradient was also neglected. By using these approximations, analytical gradients at single state CASPT2 were calculated for all singlet and triplet states at every time step and the spin-orbit gradient was constructed using contributions from perturbated modified spin-orbit couplings and the multistate coupling from an extra MS-CASPT2 calculation.

The calculated absorption spectra at SO-MCQDPT were employed to select the initial conditions and transformed to the CASPT2 formalism to be run. In this way, a perturbation treatment beyond the CASSCF approach was employed.

This was the first time that this type of calculation was performed including at the same time dynamical correlation and spin-orbit coupling. Moreover, the case of the I atom is a prototype case where spin-orbit coupling completely reshapes the spin-free curves, so that the inclusion of spin-orbit coupling in the SHARC formalism was crucial.

The endpoint for the trajectories was selected by using the translational energy of the different fragments. This energy had to be constant at the dissociation limit so that the molecule was considered dissociated when the translational energy was 90 % of the final one.

3.3. RESULTS

3.3.1. Experimental results

The asymptotic inverted I images from the photodissociation of CH_3I, CH_2ICl and CH_2BrI at 268 nm detected *via* (2+1) REMPI at 304.5 nm and 306 nm at 1 ps pump-probe time delay are presented in figure 3.7.

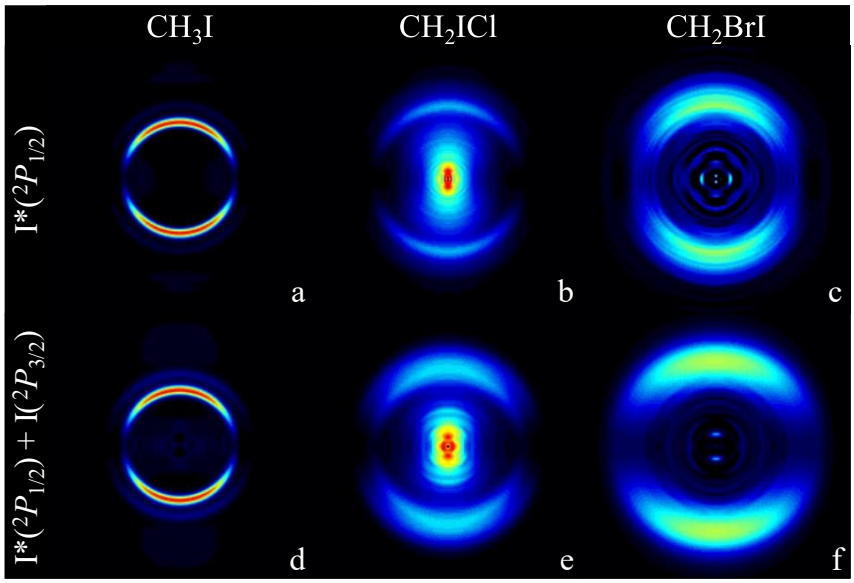

Figure 3.7. *Abel inverted I ion images from the photodissociation of CH_3I (a, d), CH_2ICl (b, e) and CH_2BrI (c, f) after excitation at 268 nm and detected via (2+1) REMPI at 306 nm (first row) and 304.5 nm (second row) measured at a delay of 1 ps between the pump and probe laser pulses (asymptotic images). In the images, the radius is proportional to the total translational energy of the fragments. Laser light polarization is along the vertical axis of the images. On the right-hand side, the detected species in each case are indicated.*

For CH_3I, at 306 nm detection (Figure 3.7 (a)) and as previously reported,[213] a single anisotropic ring is observed and assigned to the dissociation channel $CH_3+I^*(^2P_{1/2})$. At 304.5 nm detection (Figure 3.7 (d)), a second outermost anisotropic ring is observed and attributed to the dissociation channel $CH_3+I(^2P_{3/2})$.

Similar but less defined images are displayed for CH_2ICl. Also, a single ring is recovered at 306 nm detection (Figure 3.7 (b)) and assigned to $CH_2Cl+I^*(^2P_{1/2})$ formation, whereas, at 304.5 nm detection (Figure 3.7 (e)) two overlapped contributions are recovered. The second outermost ring is assigned to $CH_2Cl+I(^2P_{3/2})$ formation.

For CH_2BrI, a single wide blurry structure is observed at both detection wavelengths, although it becomes significantly broader at 304.5 nm (Figure 3.7 (f)). At 306 nm (Figure 3.7 (c)), the structure is

assigned to $CH_2Br+I^*(^2P_{1/2})$ formation, while at 304.5 (Figure 3.7 (f)) is assigned to the two overlapped dissociation channels: $CH_2Br+I^*(^2P_{1/2})$ and $CH_2B+I(^2P_{3/2})$.

For all cases, the weak signal in the center corresponds to dissociative MPI.

By angular integration of the inverted images, the I translational energy distributions in the CM reference system were obtained and subsequently converted into the corresponding CM total translational energy distributions depicted in figure 3.8, by applying the corresponding mass factor m_{CH2XI}/m_{CH2X}, where X=H, Br, Cl to the X axis,

Vertical bars indicate the total available energy for each dissociation channel; $CH_2X+I(^2P_{3/2})$ and $CH_2X+I^*(^2P_{1/2})$ (from now on, I and I*) estimated employing the following equation:

$$E_{av} = h\nu - D_0 - E_{SO}(I^*) + E_i^{molec} \tag{3.1}$$

where E_{av} is the available energy, $h\nu$ is the excitation photon energy, D_0 the dissociation energy, 2.41, 2.25 and 2.389 eV, for CH_3I,[161] CH_2ICl[283] and CH_2BrI,[236] respectively, $E_{SO}(I^*)$ the I spin-orbit coupling energy, 0.943 eV for I*,[161] and E_{int}^{molec} is the internal energy of the parent molecule which is considered negligible in the present work. Available energies for each molecule and dissociation channel are listed in table 3.1.

Table 3.1. *Estimated available energy corresponding to the dissociation of CH_3I, CH_2ICl and CH_2Brl at 268 nm in both dissociation channels $CH_2X+I^*(^2P_{1/2})$ and $CH_2X+I(^2P_{3/2})$.*

	Dissociation channel	Available energy E_{av} (eV)
CH_3I	I*	0.135
	I	0.235
CH_2ICl	I*	0.401
	I	0.666
CH_2BrI	I*	0.551
	I	0.952

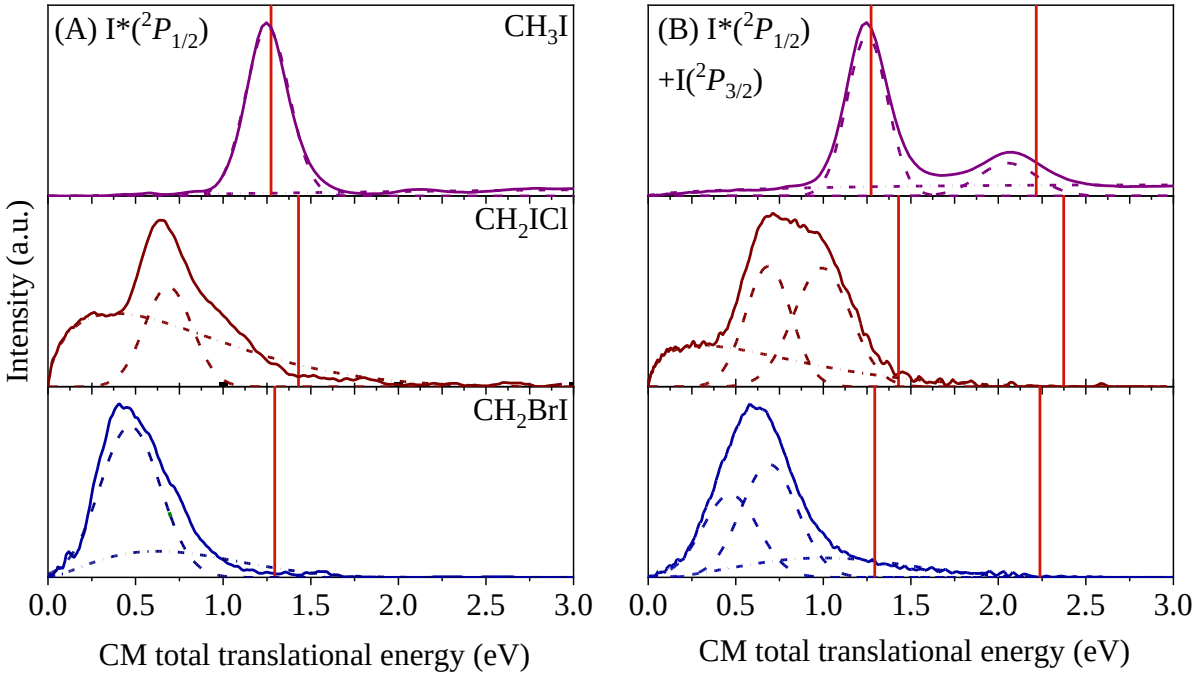

Figure 3.8. *(Left panel) CM total translational energy distributions of CH_3I (top), CH_2ICl (middle) and CH_2BrI (bottom) obtained by angular integration of the corresponding Abel inverted images measured for $I^*(^2P_{1/2})$ by (2+1) REMPI at 306 nm shown in figure 3.7 (a, b, c). (Right panel) CM total translational energy distributions of CH_3I (top), CH_2ICl (middle) and CH_2BrI (bottom) obtained by angular integration of the corresponding Abel inverted images measured for $I(^2P_{3/2})$ and $I^*(^2P_{1/2})$ by (2+1) REMPI at 304.5 nm shown in figure 3.7 (d, e, f). The Boltzmann-type fitted contribution is represented by a dot-dashed line, while the Gaussian functions used to fit the contributions from the $I^*(^2P_{1/2})$ and $I(^2P_{3/2})$ dissociation channels are represented by dashed lines. The total bimodal function sum of the two contributions is not shown for clarity. Vertical bars in red represent the estimated available energy for the $CH_2X+I^*(^2P_{1/2})$ (lower energy) and $CH_2X+I(^2P_{3/2})$ (higher energy) dissociation channels.*

At 306 nm detection (Figure 3.8 left panel), the translational energy distributions show a main peak corresponding to the $CH_2X+I^*(^2P_{1/2})$ dissociation channel. For CH_3I, this peak is narrow, but with the increasing mass of the substituent halogen atom (X=Cl, Br) this contribution becomes broader. This contribution was fitted to a Gaussian function given by:

$$y = A\exp\left(-2\left(\frac{x-x_c}{w}\right)^2\right) \tag{3.2}$$

where A is the gaussian amplitude centered at x_c and w is the corresponding width.

Besides this contribution, in the case of CH_2ICl, another less intense broad contribution can be observed at low translational energy, and it is attributed to dissociative MPI. This contribution appears at higher energies for CH_3I and CH_2BrI. This type of contribution was fitted using the following equation:

$$I(E_T) = AE_T^i(1-E_T)^j \tag{3.3}$$

where E_T represents the translational energy, i and j are fitting parameters, and A is a weighting parameter. This equation was first described by Muckerman[284] and lately used by Suits *et al.*,[285] and it is useful to easily reproduce Boltzmann-type distributions.

For 304.5 nm detection (Figure 3.8 right panel), for CH_3I, the two channels are well recovered in the translational energy distributions, while for an increasing mass of the substituent atom, it is harder to differentiate each of them as they overlap in energy. Two Gaussian functions were employed to fit the contributions assigned to the two dissociation channels, while the broad contribution assigned to dissociative MPI was similarly fitted employing equation (3.3). The fitting procedure implied a deconvolution of the overlapping channels for both dihalomethanes. The position of the Gaussian function corresponding to the I* channel was indeed determined and fixed by the results obtained at 306 nm. This deconvolution was nevertheless particularly difficult for CH_2BrI.

The experimental translational E_{trans} and internal E_{int} energies for each molecule and dissociation channel are listed in table 3.2.

Table 3.2. *Experimental translational energy E_T, and internal energy E_{int} for both dissociation channels (I and I*) corresponding to the dissociation of CH_3I, CH_2ICl and CH_2Brl upon excitation at 268 nm.*

	Dissociation channel	Translational energy E_T (eV)	Internal energy E_{int} (eV)
CH_3I	I*	0.123	0.012
	I	0.207	0.028
CH_2ICl	I*	0.193	0.209
	I	0.279	0.387
CH_2BrI	I*	0.200	0.351
	I	0.294	0.658

According to values found in table 3.2, in contrast to CH_3I, a significant shift is observed between the available energy E_{av} and the maximum translational energy E_{trans} for CH_2ICl and CH_2BrI. This difference reflects an increased internal energy – ro-vibrational – of the co-fragment since I and I* are atomic species. Besides, for these dihalomethanes, the considerable broadening of the structures in figure 3.8 can be attributed to a higher distribution of ro-vibrationally excited states of the molecular co-fragment produced in the dissociation. The estimated available energy E_{av} released into internal energy E_{int} of the co-fragment, f_{int}, can be estimated as:

$$f_{int} = \frac{E_{int}}{E_{av}} = \frac{E_{av} - E_{trans}}{E_{av}} \tag{3.4}$$

where E_{int} is the internal energy, E_{av} is the available energy and E_{trans} is the maximum translational energy.

The experimental energy partitioning f_{int} values are shown in table 3.3 for both dissociation channels and all studied molecules. Its value increases accordingly to the increasing mass of the substituent atom, comparing both dihalomethanes with CH_3I. Besides, higher values are obtained for the I channel compared to the I* channel. Butler *et al.* found energy partitioning f_{int} values for CH_2BrI of 0.69 for I and 0.68 for I* at 248.5 nm while Zhang *et al.*[252] found energy partitioning f_{int} values for CH_2ICl of 0.61 for I and 0.55 for I* at 266 nm and of 0.60 for I and 0.58 for I* at 277 nm.[252, 286] Thus, the present results are indeed in good agreement with previous studies of both dihalomethanes.

Table 3.3. *Fraction of the available energy that appears as internal energy (ro-vibrational) of the co-fragments, f_{int}, corresponding to the dissociation of CH_3I, CH_2ICl and CH_2Brl upon excitation at 268 nm.*

	Dissociation channel	Experimental energy partitioning f_{int}
CH_3I	I	0.12
	I*	0.09
CH_2ICl	I	0.58
	I*	0.52
CH_2BrI	I	0.69
	I*	0.64

The determination of the quantum yield Φ* is usually obtained through photoelectron imaging measurements. Ion imaging is not the best technique to do so since, despite probing by (2+1) REMPI, given the probe laser pulse bandwidth, the transitions of both fragments (I and I*) occur through different intermediate electronic states and several transitions, with different line forces, contribute at the same time. As no photoelectron imaging experiments were carried out, no accurate quantum yields Φ* were obtained for both dihalomethanes. A good approximation from the measured ion images was obtained from the following procedure: First, the areas of the Gaussian functions used for the fitting of the I and I* contributions of the translational energy distributions were obtained for CH_3I and both dihalomethanes (In the following, these are denoted as A_I and A_{I^*}, respectively). For each compound, the following area ratio was estimated:

$$\frac{[A_{I^*}]}{[A_{I^*}]+[A_I]} \tag{3.5}$$

At least one quantum yield Φ* of one of the compounds must be known at the studied excitation wavelength, as is the case for the quantum yield Φ* of CH_3I. The quantum yield of this compound is

well-reported in literature;[40] however, since photoelectron measurements were carried in the past by Dr. Maria E. Corrales and Dr. Gregory Gitzinger using the same experimental setup as the used in the present experiments.

Figure 3.9 displays the corresponding results: asymptotic Abel inverted photoelectron image measured in femtosecond pump-probe VMI experiments for CH_3I at 268 nm (pump) and 304.5 nm (probe) (left panel), and the corresponding CM electron translational energy distribution (right panel), where the green and blue curves correspond to the fitting contributions from I($^2P_{3/2}$) and I*($^2P_{1/2}$), respectively, and the red curve is the sum of both contributions.[89, 213]

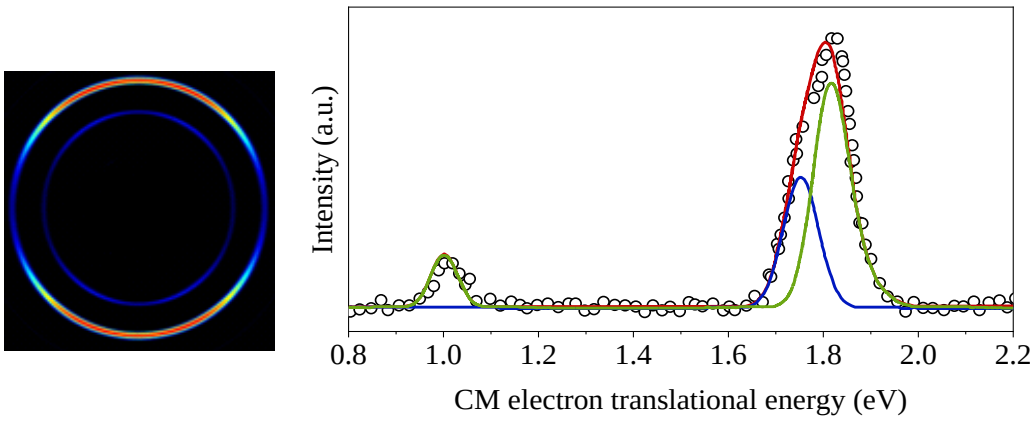

Figure 3.9. *(Left) Abel inverted photoelectron image measured in femtosecond pump-probe VMI experiments for CH_3I at 268 nm (pump) and 304.5 nm (probe). The probe laser pulse is at an asymptotic positive delay time (1 ps) with respect to the pump laser pulse. (Right) Corresponding CM electron translational energy distribution for CH_3I dissociation upon excitation at 268 nm. The blue and green curves correspond to the fitting contributions from I($^2P_{3/2}$) and I*($^2P_{1/2}$), respectively, and the red curve is the sum of both contributions.*[89, 213]

From these experiments, a quantum yield Φ*=0.75 was obtained and it was employed for this procedure. Knowing this quantum yield Φ* and the corresponding I and I* area ratio obtained from ion imaging, the quantum yield Φ* for the dihalomethanes can be extrapolated. These are shown in table 3.4. It should be noted that for CH_2BrI, the values are characterized by larger uncertainty due to the uncertainty of the deconvolution. The estimated quantum yield Φ* decreases remarkably for CH_2ICl and CH_2BrI compared with CH_3I, reflecting a more favorable formation of I in its ground spin-orbit state for the dihalomethanes.

Table 3.4. *Quantum yield for I*($^2P_{1/2}$) production, Φ* corresponding to the dissociation of CH_3I, CH_2ICl and CH_2BrI upon excitation at 268 nm.*

	Quantum yield Φ*
CH_3I	0.75
CH_2ICl	0.43
CH_2BrI	0.41

The angular distributions of I fragments were obtained by the radial integration of the inverted images along the radius corresponding to each of the rings. For CH_3I, the contribution from the I and I* channels at 304.5 nm can be well separated, and thus the angular distributions can be determined precisely for each channel. On the contrary, for CH_2ICl and CH_2BrI, as the two contributions are overlapped, the angular distribution was only obtained for the whole (I+I*) contribution.

The corresponding anisotropy parameters were obtained by fitting the angular distributions to:

$$I(\theta) \propto 1 + \sum_{k=1}^{n} \beta_{2k} P_{2k}(\cos\theta) \tag{3.6}$$

where θ represents the angle between the photolysis laser polarization and the fragment recoil velocity, $P_{2k}(\cos\theta)$ is the $2k^{th}$ order Legendre polynomials and β_{2k} are the anisotropy parameters.

The number of anisotropy parameters needed to characterize the angular distribution depends on the number of photons involved in the absorption process and the total angular momenta of the species detected. For a one-photon dissociation process and a (2+1) REMPI detection scheme through a single intermediate *J*-level, *n* is constrained by the maximum allowed integers of 2+1 or J+1, whichever is smallest.[287] For excited state spin-orbit I* fragment, J=1/2 and only one anisotropy parameter β_2 is necessary to characterize the angular distribution. For ground-state I fragment, J=3/2 and up to β_6 can be necessary. In the present experiments, all angular distributions (not shown) were fitted correctly using a single β_2 anisotropy parameter (being β_4 and β_6 close to zero).

The obtained values for the β_2 anisotropy parameter for the three molecules, summarized in table 3.5, present positive values for both I* and (I+I*) channels reflecting the main contribution of a transition characterized by a TDM parallel to the C−I bond. In particular, the β_2 values measured for CH_3I are in agreement with the ones previously reported[161] and consistent with the dominant transition to the $^3Q_0$ state, leading to a major formation of I* and a minor formation of I through a conical intersection with the $^1Q_1$ state. The smaller anisotropy parameter value measured for I is indeed attributed to the contribution of a weak perpendicular transition to the $^1Q_1$ leading to the formation of I adiabatically. For CH_2ICl, a similar trend is observed for I* and (I+I*) although minor values are measured as it happens

in CH_2BrI. The experimental anisotropy values for CH_2ICl are in perfect agreement but those found by Zhang *et al.*[252]

Table 3.5. *I and I+I* fragments' anisotropy parameters β_2 corresponding to the dissociation of CH_3I, CH_2ICl and CH_2Brl upon excitation at 268 nm.*

	Dissociation channel	Anisotropy parameter β_2
CH_3I	I	1.67
	I*	1.90
CH_2ICl	I+I*	1.48
	I*	1.73
CH_2BrI	I+I*	1.31
	I*	1.29

To determine the reaction time of each of the two different dissociation channels, clocking experiments were performed. A global bi-dimensional fitting procedure was employed to analyze the delay scans and obtain the corresponding I fragment transient. For 306 nm detection, a fitting procedure was employed to separate the I* dissociation channel from the background contribution using a Gaussian function and a Boltzmann-type function. On the contrary, at 304.5 nm detection, a second Gaussian function was included to unravel the transients attributed to each channel, I and I*. However, this procedure could not be performed for CH_2ICl due to the strong dissociative MPI contribution.

The resulting transients for the three molecules are depicted in figure 3.10. The transients were fitted to a Boltzmann sigmoidal curve given by:

$$S = A_2 + \frac{A_1 - A_2}{1 + \exp\left(\frac{t - t_0}{t_c}\right)} \tag{3.7}$$

where A_1 and A_2 are the initial and final intensity values of the sigmoidal function, characterized by a central temporal position t_0 (*i.e.*, the delay time for which the intensity has reached half of its asymptotic value) and a rise time constant t_c, which describes the steepness of the rise.

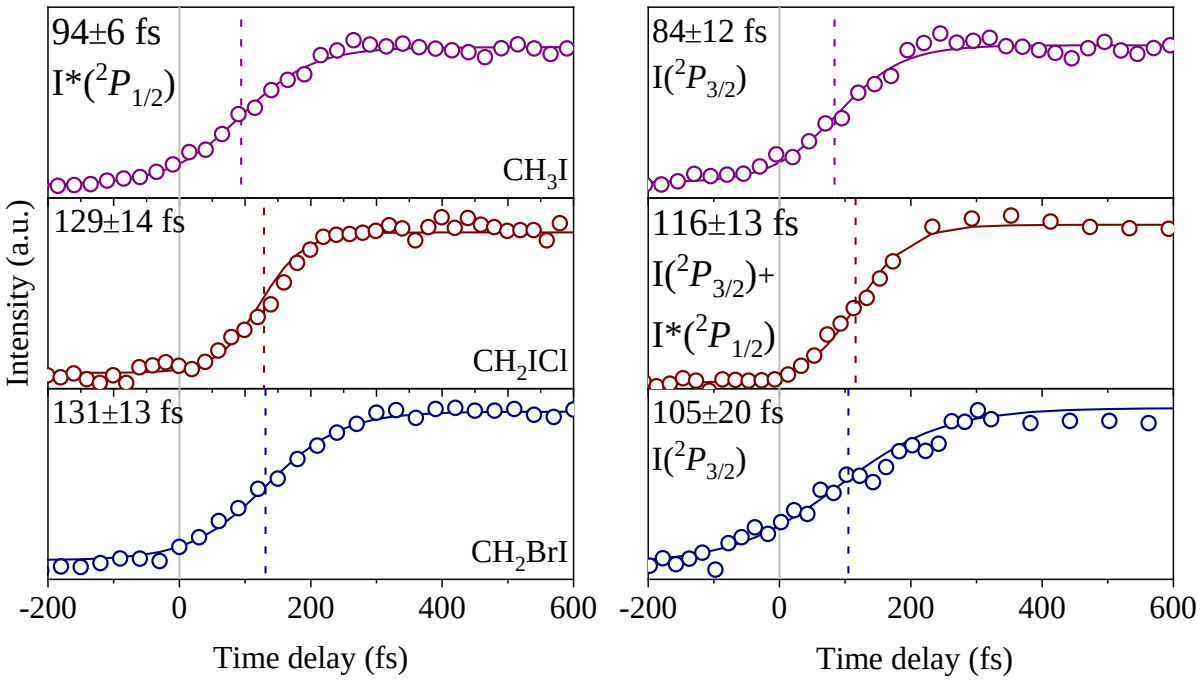

Figure 3.10. *(Left panel) Transients measured for CH_3I (top), CH_2ICl (middle) and CH_2BrI (bottom) for the $I^*(^2P_{1/2})$ channel fitted using a Boltzmann sigmoidal function (solid line). (Right panel) Transients measured for CH_3I (top), CH_2ICl (middle) and CH_2BrI (bottom) for the $I(^2P_{3/2})$ channel fitted using a Boltzmann sigmoidal function (solid line). The reaction (clocking) times are referred to the time zero found in situ by measuring the (1+1') ionization signal in Xe. Time zero is indicated in each panel using a vertical line in grey. The reaction time is defined as the time between time zero and the time corresponding to the middle of the rise of the transient (indicated by vertical dashed lines in grey in each panel). The reaction times obtained as a mean value of several measurements along with the standard deviations are indicated in each panel.*

The experimental reaction times τ_{exp} correspond to the time difference between time zero, determined as indicated in section 3.2.1.3, and the time corresponding to the half-height of the fitted sigmoidal function. The experimental reaction times τ_{exp} are summarized in table 3.6. The values reflect that for an increasing mass of the substituent atom, the measured reaction time steadily increases. The I channel is characterized by a shorter reaction time than that corresponding to the I* channel.

Table 3.6. *Experimental reaction times for the C–I bond cleavage, τ_{exp}, corresponding to the dissociation of CH_3I, CH_2ICl and CH_2Brl upon excitation at 268 nm.*

	Dissociation channel	Reaction time τ_{exp} (fs)
CH_3I	I	84±13
	I*	94±6
CH_2ICl	I+I*	116±13
	I*	129±14
CH_2BrI	I	105±20
	I*	131±13

3.3.2. Theoretical results

The first six electronic states resulting from the *ab initio* calculations for CH_3I, CH_2ICl and CH_2BrI, are listed in Table 3.7, in terms of the vertical energy at the Franck-Condon geometry, the electronic notation in C_s symmetry and the correspondence with Mulliken's notation in C_{3v} symmetry. The two first excited states – 1*A*" and 2*A*' in C_s – correspond to $^3Q_2$ in C_{3v}, as previously reported by Lepetit and co-workers for methyl bromide (CH_3Br).[288] The total TDM, as well as those computed with respect to each axis, are also summarized in table 3.7. It should be noted that the X-C–I plane (with X=Cl or Br) is located in the X-Y plane and the Y axis along the C−I bond. As expected, considering the properties of the C_s symmetry group, the 2*A*" and 4*A*" excited states are characterized by a TDM perpendicular to the X-C–I plane. In contrast, the 3*A*', 4*A*', 5*A*' excited states are attributed to TDMs in the plane but located at a certain angle with respect to the C−I bond, as observed in table 3.7, in contrast to CH_3I, where electronic states are characterized by TDMs completely parallel or perpendicular to the C−I bond.[239]

Table 3.7. *Ab initio vertical energy at the Franck-Condon geometry of CH_3I, CH_2ICl and CH_2BrI, symmetry in the C_s and C_{3v} symmetry groups as well as the TDM – total and for each axis – of the computed electronic state. X axis is located in the I–C–X plane, perpendicular to the C−I bond, Y axis in the I–C–X plane, along the C−I bond and the Z axis perpendicular to the I–C–X plane, where X=H, Cl or Br. The table has been truncated up to the 5A' ($^1Q_1$) state.*

CH_3I

State number	Franck-Condon energy (eV)	Symmetry (C_s)	Correlated symmetry (C_{3v})	Transition dipole moment			
				Total	X	Y	Z
1	0		-	0.66193	0.00013	0.66193	0.00000
2	4.20		$^3Q_2$	0.00067	0.00066	0.00009	0.00001
3	4.20		$^3Q_2$	0.00060	0.00001	0.00000	0.00060
4	4.36		$^3Q_1$	0.02046	0.00000	0.00000	0.02046
5	4.36		$^3Q_1$	0.02046	0.02046	0.00005	0.00000
6	4.71		$^3Q_{0-}$	0.00000	0.00000	0.00000	0.00000
7	4.79		$^3Q_{0+}$	0.12158	0.00028	0.12158	0.00000
8	5.07		$^1Q_1$	0.05258	0.05258	0.00004	0.00000
9	5.07		$^1Q_1$	0.05255	0.00000	0.00000	0.05255
10	6.53		$^2A_2$	0.00000	0.00000	0.00000	0.00000
11	6.55		4*E*	0.01528	0.01528	0.00002	0.00001
12	6.55			0.01529	0.00001	0.00000	0.01529

CH_2ICl

State number	Franck-Condon energy (eV)	Symmetry (C_s)	Correlated symmetry (C_{3v})	Transition dipole moment			
				Total	X	Y	Z
1	0	1*A*'	-	0.51543	0.434820	0.276770	0.000000
2	3.92	1*A*"	$^3Q_2$	0.00042	0.000000	0.000000	0.000421
3	3.92	2*A*'	$^3Q_2$	0.00679	0.000250	0.006780	0.000000
4	4.06	2*A*"	$^3Q_1$	0.01131	0.000000	0.000000	0.011310
5	4.07	3*A*'	$^3Q_1$	0.06245	0.042500	0.045760	0.000000
6	4.38	3*A*"	$^3Q_{0-}$	0.00120	0.000000	0.000000	0.001193
7	4.49	4*A*'	$^3Q_{0+}$	0.15119	0.062330	0.137750	0.000000
8	4.70	4*A*"	$^1Q_1$	0.02766	0.000000	0.000000	0.027661
9	4.76	5*A*'	$^1Q_1$	0.19746	0.122770	0.154660	0.000000
10	5.47	5*A*"	$^2A_2$	0.00136	0.000000	0.000000	0.001360
11	5.50	6*A*"	4*E*	0.01352	0.000000	0.000000	0.013521
12	5.51	6*A*'	–	0.06060	0.043330	0.042370	0.000000
13	6.09	7*A*'	–	0.04810	0.019330	0.044050	0.000000
14	6.09	7*A*"	–	0.00335	0.000000	0.000000	0.003352
15	6.09	8*A*'	–	0.05187	0.020330	0.047720	0.000000

CH_2BrI

State number	Franck-Condon energy (eV)	Symmetry (C_s)	Correlated symmetry (C_{3v})	Transition dipole moment			
				Total	X	Y	Z
1	0	1*A*'	-	0.48635	0.439920	0.207390	0.000000
2	3.83	1*A*"	$^3Q_2$	0.00241	0.000000	0.000000	0.002411
3	3.83	2*A*'	$^3Q_2$	0.00330	0.003140	0.001030	0.000000
4	3.96	2*A*"	$^3Q_1$	0.01134	0.000000	0.000000	0.011340
5	4.00	3*A*'	$^3Q_1$	0.11854	0.068830	0.096510	0.000000
6	4.28	3*A*"	$^3Q_{0-}$	0.00054	0.000000	0.000000	0.000540
7	4.39	4*A*'	$^3Q_{0+}$	0.13841	0.052570	0.128040	0.000000
8	4.60	4*A*"	$^1Q_1$	0.03196	0.000000	0.000000	0.031960
9	4.62	5*A*'	$^1Q_1$	0.34889	0.188250	0.293740	0.000000
10	5.01	5*A*"	2A2	0.00498	0.000000	0.000000	0.004976
11	5.05	6*A*'	4E	0.1049	0.061870	0.084710	0.000000
12	5.1	6*A*"	–	0.00884	0.000000	0.000000	0.008831
13	5.17	7*A*'	–	0.08522	0.013610	0.084130	0.000000
14	5.25	7*A*"	–	0.00077	0.000000	0.000000	0.000770
15	5.27	8*A*'	–	0.02185	0.004100	0.021460	0.000000

The absorption spectra computed for the three molecules in the first absorption band are represented in figure 3.11. They are compared with the experimental absorption spectra showing a good agreement.[289, 290] The allocation into the spectral components associated with the different excited states is also represented in figure 3.11, although this decomposition is tentative for the dihalomethanes. Out-of-plane movements are allowed in the computation of the spectra; the C_s symmetry is therefore broken and the *A*' or *A*" electronic symmetries may be quite speculative. Nevertheless, the CIS method used to compute the spectra allows us to obtain reasonable spectra as a function of the orientation of the TDMs (see figure 3.12 and references [234, 240]). An idea of the overestimated contributions of certain excited electronic states may be deduced by comparing both absorption spectra and considering the TDMs summarized in table 3.7. The absorption to *A*" symmetries and the 4*A*" excited state is indeed overestimated.

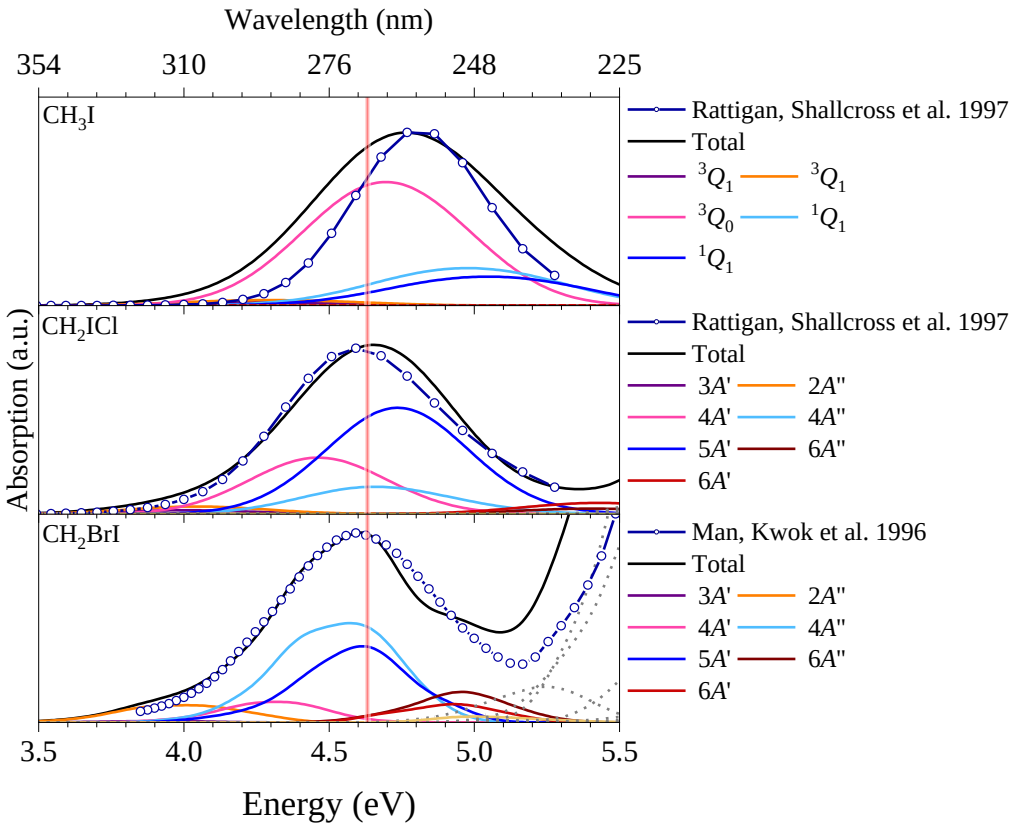

Figure 3.11. *Semiclassical computed absorption spectra for CH_3I (top), CH_2ICl (center) and CH_2BrI (bottom) and their decomposition into the spectral components associated with the different electronic states. Open circles with solid line represent the experimental absorption spectra taken from references [289, 290]. The vertical band indicates the excitation wavelength, 268 nm.*

In agreement with previous investigations,[193, 226] for CH_3I, the absorption at 268 nm is mainly governed by a parallel transition to the $^3Q_0$ state with a minor contribution of a perpendicular transition to the $^1Q_1$ state. The absorption to the $^3Q_1$ state contributes mainly to the red edge of the first absorption band, while the absorption to the $^1Q_1$ state governs in the blue edge, consistently with the literature.[152,

[194] For an increasing mass of the substituent atom in the dihalomethanes, the contribution of the 4*A*' excited state – the $^3Q_0$ state in C_{3v} symmetry – decreases in favor of the transitions to the [4*A*", 5*A*'] states – the $^1Q_1$ states in C_{3v} symmetry. In particular for CH_2BrI, excitation to the 4*A*' state is rather negligible in benefit of the [4*A*", 5*A*'] states, in agreement to previously reported absorption spectra for methyl bromide (CH_3Br).[288] The primary absorption of the $^3Q_0$ state in CH_3I is, in fact, due to the coupling with different singlet electronic states by the agency of the strong spin-orbit interaction characterizing the I atom. In CH_2IX molecules (X=Cl, Br), this coupling seems less effective, leading to a lower excitation of the 4*A*' state, especially for an increasing mass of the second halogen atom (from Cl to Br).

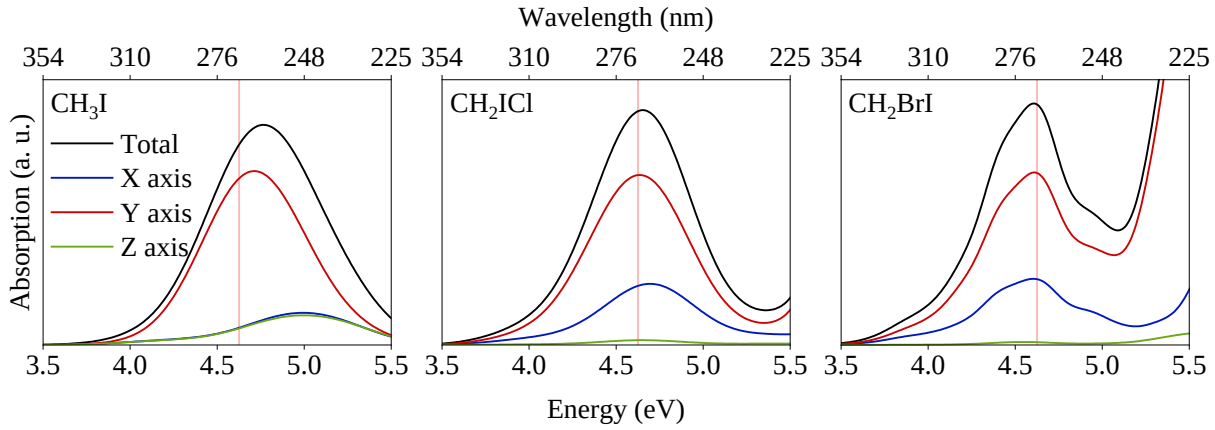

Figure 3.12. *Computed absorption spectra for CH_3I (left), CH_2ICl (center) and CH_2BrI (right) as a function of the TDM axis. X axis represents a perpendicular orientation with respect to the C−I bond (in the I−C−Cl plane for CH_2ICl and in the I−C−Br plane for CH_2BrI), Y axis represents a parallel orientation to the C−I bond and Z axis represents a perpendicular orientation with respect to the C−I bond and perpendicular to the I−C−Cl plane for CH_2ICl and in the I−C−Br plane for CH_2BrI. The vertical arrows indicate the excitation wavelength, 268 nm.*

Figure 3.13 depicts the adiabatic potential energy curves computed at the CASPT2 level for the three molecules as a function of the C−I distance. In this adiabatic representation, for CH_3I, the $^3Q_0$ state correlates to the I channel while the $^1Q_1$ state correlates to the I* channel in agreement with previous work.[193] The conical intersection between the $^3Q_0$ and $^1Q_1$ states for CH_3I is also well recovered. This implies that, in the diabatic representation, the $^3Q_0$ state correlates to the I* channel while the $^1Q_1$ state correlates to the I channel. For both dihalomethanes, the [2*A*", 3*A*'], the 4*A*", and the 4*A*' states correlate to the I channel, while the 5*A*' and 6*A*' states are correlated to the I* limit, similarly to CH_3I. An avoided crossing is observed between the 4*A*' and 5*A*' states close to the Franck-Condon region, as observed in the inset of figure 3.13 and as in previous studies.[234, 239] In the non-adiabatic representation, for dihalomethanes, photodissociation in the 4*A*' state leads directly to the I* channel while the I formation *via* an avoided crossing between the 4*A*' and 5*A*' states compete with the direct dissociation through the 5*A*' or 4*A*" states. The similarity of the curves is noteworthy irrespective of the halogen-atom substitution.

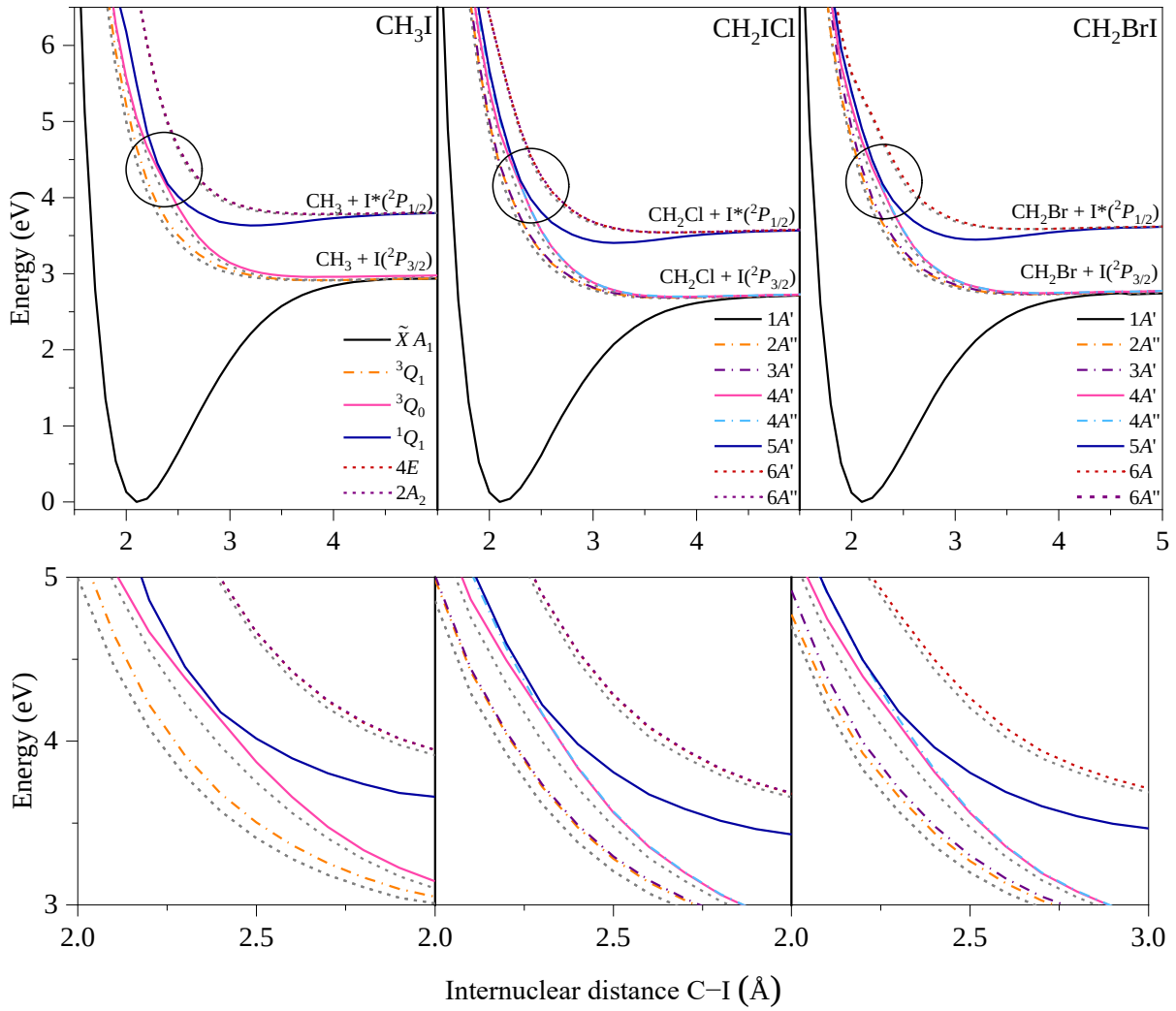

Figure 3.13. *Computed MS-CASPT2 potential energy curves for CH_3I (left), CH_2ICl (center) and CH_2BrI (right) as a function of the C−I distance, considering the relaxed planar geometry of the CH_2X moiety. Expanded views of the avoided crossing areas are shown in the insets.*

On-the-fly adiabatic full-dimension classical trajectory calculations including surface hopping were run at the *ab initio* CASSCF level of theory corrected using perturbation theory in its multistate version (MS-CASPT2). Figure 3.14 shows snapshots corresponding to selected trajectories for CH_3I, CH_2lCI and CH_2BrI yielding I* products. In contrast to CH_3I, the early steps of the bond cleavage process for both dihalomethanes are dominated by a significant rotational motion of the CH_2Cl/CH_2Br radical, mainly due to an "anchor" effect of the halogen atom (Cl or Br), while the corresponding vibrational motions play a minor role in the dynamics. The energy transfer into rotation of CH_2Cl/CH_2Br is very efficient, reducing the amount of energy released as translational energy of the I fragment. The *A*-band photodissociation dynamics appear to be consistent with an impulsive semi-rigid radical model qualitative description with the CH_2Br radical changing to a more planar structure.

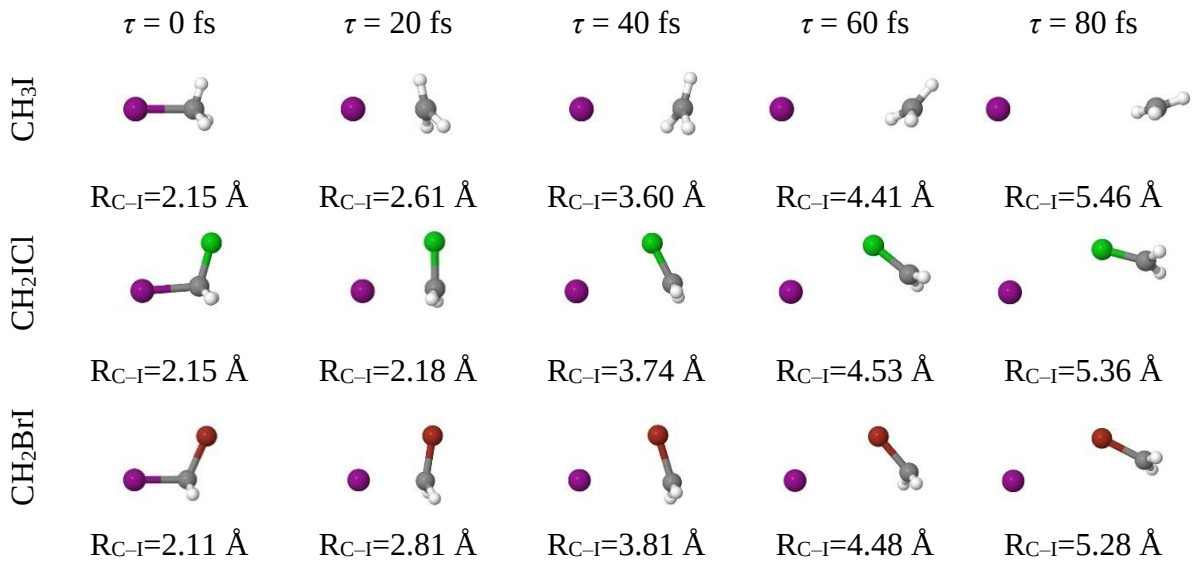

***Figure 3.14**. Snapshots corresponding to selected on-the-fly trajectories for the dissociation of CH_3I (top), CH_2ICl (center) and CH_2BrI (bottom). See the text for more details. In each frame, the time τ and R_{C-I}, i.e., the C−I distance, are indicated. At time zero, R_{C-I}=0 corresponds to the equilibrium distance of the molecule.*

The results of these on-the-fly trajectories are summarized in table 3.8 in terms of the energy fraction f_{int}, the quantum yield Φ* and the reaction times τ_{theo} for each molecule and dissociation channel.

***Table 3.8.** Computed fractions of the available energy that appears as internal energy (ro-vibrational) of the co-fragments, f_{int}, quantum yields for production of I *($^2P_{1/2}$), Φ*, and reaction times, τ_{theo}, corresponding to the dissociation of CH_3I, CH_2ICl and CH_2Brl upon excitation at 268 nm.*

	Dissociation channel	Energy partitioning f_{int}	Quantum yield Φ*	Reaction time τ_{theo} (fs)
CH_3I	I	0.31		66.1
	I*	0.27	0.77	73.3
CH_2ICl	I	0.85		91.8
	I*	0.80	0.23	100.0
CH_2BrI	I	0.82		104.2
	I*	0.81	0.28	109.2

Compared to the experimental values, the theoretical energy partitioning values f_{int} follow the same trend as a function of the dissociation channel and the increasing molecular mass, although the theoretical values are significantly higher. The differences are probably due to the zero-point energies of the parent molecule and of the fragments, which cannot be considered in the classical trajectory calculations, while they are indeed present in the experimental values. Besides, since the TDM, which is crucial to obtain an accurate absorption spectrum, was calculated using a full electron basis set. The trajectories were calculated using pseudo-potentials to speed up the computation. The matching between these two steps in the calculations is not trivial. Therefore, the excitation energy selected employing the

spectrum and the one used later during the trajectories may present some small differences. These differences may lead to higher theoretical energy partitioning f_{int} values in the case of the trajectory calculations. In any case, the theoretical and experimental values are qualitatively consistent.

The theoretical quantum yield Φ* obtained for CH_3I is in remarkably good agreement with the experimental value. In contrast, for the dihalomethanes, the values are significantly lower than the experimental ones reported in table 3.3, reflecting an overestimated production of I in its ground spin-orbit state. The mismatch existing in the calculations of absorption spectra and trajectories may lead to some differences in energy, which could provoke somewhat different curve crossing probabilities and, thus, slightly different quantum yield Φ* values.

The calculated reaction times increase for an increasing mass of the substituent atom similarly to the experimental values, although the theoretical values are slightly lower than the experimental ones. Also, for all molecules, the computed bond cleavage time for photodissociation into the I channel is longer than those corresponding to the I* channel. At the MS-CASPT2 level of theory employed in the trajectories, the computed dissociation energies for the molecules are lower than the experimental values by about 0.1 eV. Therefore, the wave packet is faster accelerated, leading to a higher terminal velocity for the I atom and thus to the lower reaction times obtained from the trajectories.

3.4. DISCUSSION

The dissociation dynamics for the present dihalomethanes can be discussed based on the reported theoretical and experimental results.

For CH_2BrI, according to the computed absorption spectrum and potential energy curves, the dissociation dynamics are governed by the major absorption to the 5*A*' state, which leads to dissociation into I in its spin-orbit state channel. In contrast, a transfer through the observed avoided crossing 5*A*'→4*A*'/4*A*" would lead to the I channel. The presence of the avoided crossing, and the competition between adiabatic and non-adiabatic dynamics would be responsible for the lower measured quantum yield Φ* compared to CH_3I.

Considering the computed absorption spectrum for CH_2lCI, two dissociation pathways can compete: through the 5*A*' excited state, similarly to CH_2BrI, or through the 4*A*' excited state, similarly to CH_3I. These two dissociation pathways, both involving a non-adiabatic crossing, lead to the formation of I and I* with an almost similar probability, as reflected by the measured quantum yield Φ*.

The non-adiabatic crossings may involve some vibrational selectivity, such as in CH_3I. The coupling between the $^3Q_0$ and $^1Q_1$ states, forbidden by symmetry, is indeed allowed by the vibrational

excitation in the bend (ν_6) and other *e*-symmetry vibrations leading to a reduction of symmetry from C_{3v} to C_s. The intersection becomes then a conical intersection, and the two states can effectively couple *via* the radial derivative terms of the Hamiltonian. This can happen similarly for CH_2ICl and CH_2BrI, particularly for the $4A'' \rightarrow 4A'/5A'$ transfer of population, which is forbidden by symmetry and requires a breakdown of symmetry induced by vibrational excitation of the molecule or a torsion of the C–I bond. The coupling between these states *via* the radial derivative terms of the Hamiltonian seems nevertheless to be significantly stronger than the $^3Q_0 \rightarrow {}^1Q_1$ equivalent coupling in CH_3I, particularly for CH_2BrI, considering the similar shape of the potential energy curves for these molecules.

The trend of quantum yields Φ* can be interpreted using a model combining a soft-radical impulsive model with a one-dimension Landau-Zener description of the curve crossing[291, 292] In this framework, a theoretical quantum yield Φ* can be estimated as:[200]

$$\Phi^* = \exp\left(-\frac{2\pi V_{12}}{\hbar |\Delta F| v}\right) \tag{3.8}$$

where V_{12} is the term that counts the coupling between surfaces, ΔF is the difference in gradients in the curves at the crossing point, and v is the speed of the molecule passing through the conical intersection.

Considering the localized nature of the involved n and σ* orbitals, it could be assumed that the terms V_{12} and ΔF should be very similar for the studied molecules and so, can be grouped by a single parameter ζ giving rise to:

$$\Phi^* = \exp\left(-\frac{\zeta}{v}\right) \tag{3.9}$$

where $\zeta = 2\pi V_{12}/\hbar|\Delta F|$.

The speed at the crossing point v, can be calculated either from the translational energy E_{trans} or from the available energy E_{av} in terms of the soft-radical-impulsive model at the excitation wavelength employing the following equation:

$$E_{trans} = \frac{1}{2}\mu_{R-I} v^2 = \left(\frac{\mu_a}{\mu_f}\right) E_{av} \tag{3.10}$$

where μ_a is the reduced mass of the C–I system and μ_f is the reduced mass of the R–I system.

At the point of crossing between states, the translational energy must fall to a certain value of the interval defined by the initial excitation energy value and the asymptotic energy given by the impulsive photodissociation model (characteristic of each molecule). However, for the studied molecules, the position of the translational energy at the point of crossing within each interval in question is determined by the same proportional constant, which can be introduced in the parameter ξ:

$$\Phi^* = \exp\left(-\frac{\mu_f \cdot \zeta}{\sqrt{2 \cdot \mu_a \cdot E_{av}}} \right) \tag{3.11}$$

Since the $^3Q_0$ state correlates with the formation of I*, the amount of energy available is given by:

$$E_{av} = h\nu - D_0 - E_{SO}\left(\mathrm{I}^*\right) \tag{3.12}$$

where hν is the excitation energy, D_0 is the dissociation energy at 0 K and E_{SO}(I*) is the spin-orbit energy of the I atom.

The extra translational energy available for the I atoms in the ground spin-orbit state is acquired after the non-adiabatic crossing, so it does not contribute to the speed of the wave packet at the crossing point.

The only required information is the mass of the radical, the mass of the I atom, the available energy E_{av} and the empirical value of the ζ parameter. The ζ parameter is determined using CH_3I as the calibration molecule whose quantum yield Φ*=0.75 is well known. Accordingly:

$$\zeta = \frac{-\ln \Phi^* \cdot \sqrt{2 \cdot \mu_a \cdot E_{av}}}{\mu_f} = \frac{-\ln(0.75) \cdot \sqrt{2 \cdot 10.972 \cdot 1.277}}{13.442} = 0.113 \tag{3.13}$$

As reflected in figure 3.15, the trend of quantum yields Φ* for alkyl iodides was successfully interpreted by Uma *et al.*[230, 293, 294] and Corrales *et al.*[89] using this model; however, they failed to predict the behavior of its branched counterparts. In branched molecules, the dissociation coordinate is expected not to be purely the C−I stretch mode but a combination of bending modes around the C bound in position to the I atom and the C−I stretch mode (important especially at short dissociation times). This highlighted the importance of the multidimensional nature of the potential energy surface involved in the dynamics.[89]

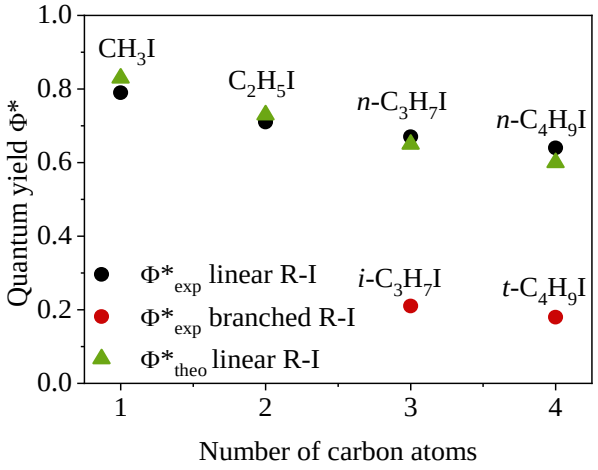

Figure 3.15. *Experimental quantum yields Φ^*_{exp} for linear (black circles) and branched alkyl iodides (red circles) and the corresponding predicted by the model Φ^*_{theo} detailed in the text (green triangles) as a function of the number of C atoms in the alkyl chain.*[89, 213]

To rationalize the quantum yields of dihalomethanes, the same model was employed in the present work. This model predicts that the dihalomethanes should have lower velocities at the crossing point compared to the corresponding unsubstituted analogs, moving slower on the excited state surface and so, having a greater probability that a fraction of the wave packet is transferred to the $^1Q_1$ state from the initially excited $^3Q_0$ state, thus leading to lower quantum yields Φ*.

In the case of dihalomethanes, employing equation (3.11), the obtained quantum yield values Φ* are listed in table 3.9. A nice agreement is found between the experimental Φ* and those predicted by the model. This agreement is visualized in figure 3.16, where the comparison between estimated from the Landau-Zener model and the experimental values for quantum yield Φ* versus the reduced mass of the radical and I μ_f is represented.

Table 3.9. *Estimated quantum yields Φ* corresponding to the dissociation of CH_3I, CH_2ICl and CH_2BrI upon excitation at 268 nm, from the Landau-Zener model (see the text for more details).*

	Parameter ζ	Reduced mass μ_f	Reduced mass μ_a	Available energy E_{av} (I*)	Theoretical quantum yield Φ*	Experimental quantum yield Φ*
CH_3I	0.113	13.442	10.972	1.277	0.750	0.750
CH_2ICl	0.113	35.600	10.972	1.430	0.487	0.430
CH_2BrI	0.113	53.978	10.972	1.294	0.317	0.410

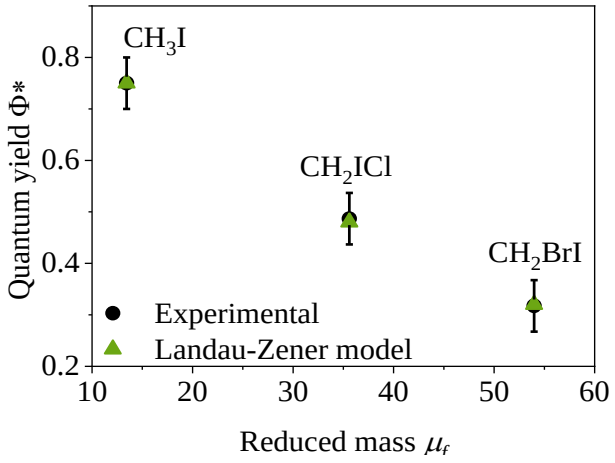

Figure 3.16. *Comparison between the estimated quantum yield Φ* from the Landau-Zener model and the experimental values versus the reduced mass of the radical and I, μ_f for CH_3I, CH_2ICl and CH_2BrI upon excitation at 268 nm.*

The presence of a second halogen atom, its electronegativity and the degree of substitution affect the ion yield. The mass of the molecule and the electronegative imply lower velocities at the crossing point and a higher coupling between these states *via* the radial derivative terms of the Hamiltonian, in particular for CH_2BrI, that leads as a whole to a more favorable I atom formation.

Previous studies on the photodissociation of fluorinated alkyl iodides, as CF_3I, highlighted, however, the non-fulfillment of this one-dimensional model. The quantum yields Φ* for the fluorinated alkyl iodides were found to be much higher than their corresponding alkyl iodide analogs over the entire *A*-band. An effective coupling between vibrational modes – CF_3 in-plane rocking and C−I stretching – allows the molecule to cross over from $^3Q_0$ to $^1Q_1$, yielding more I atom.[232]

The lower anisotropy parameter β_2 values for both dihalomethanes compared to CH_3I can be due to the higher contribution of perpendicular transitions. These last ones represent almost a fraction of 0.3 in both molecules, as highlighted in the absorption spectra computed as a function of the orientation of the TDM along the X, Y and Z axis (see figure 3.12). Considering the weights, $a_{\parallel}$ and $a_{\perp}$ for parallel and perpendicular transitions at 268 nm, respectively, the expected anisotropy parameter β_2 can be estimated as:

$$\beta_{obs} = a_{\parallel}\beta_{\parallel}^{lim} + a_{\perp}\beta_{\perp}^{lim} \tag{3.14}$$

where $\beta_{\parallel}^{lim}$ and $\beta_{\perp}^{lim}$ are the limiting values, -1 and 2, for pure perpendicular and parallel transitions, respectively.

Considering the computed absorption spectra, the expected anisotropy parameter β_{obs} for CH_3I is about 1.5, relatively close to the measured value for the I channel, while for CH_2ICI and CH_2BrI, the obtained values are around 1.15, relatively lower than the measured ones (see table 3.3). Several aspects can indeed contribute to the angular distribution of the I/I* fragments for these molecules. Firstly, as reflected in table 3.7, the recoil axis lies neither parallel nor perpendicular to the C−I bond for all *A*' excited states. The TDM for the 5*A*' state is estimated to be around 38º and 33º with respect to the C−I bond for CH_2lCI and CH_2BrI, respectively. The resulting anisotropy parameter β_2 would thus depend on the different excited states populated and involved in each dissociation channel as well as on the orientation of their respective TDM. Secondly, a dissociation process involving an avoided crossing may induce a reduction of the measured anisotropy parameters due, for instance, to a particular selection of ro-vibrationally excited population as discussed previously. This may lead to a distorted geometry for CH_2lCI and CH_2BrI and thus to a more isotropic angular distribution. Finally, the "anchor" effect observed in the snapshots (see figure 3.14) provokes some changes in the geometry, leading to a change of the orientation of the recoil axis during dissociation and, therefore, modifying the probed angular distribution of the fragment.

A simple one-dimensional model developed by Liu and Zewail[295] was employed to rationalize the measured reaction times by correlating them to the energy release. Following this model, the reaction time τ can be expressed by:

$$\tau = \mu^{1/2} \int_{R_i}^{R_f} \frac{dR}{\sqrt{2[E_{av} - V(R)]}} \tag{3.15}$$

where R_i and R_f are the initial and final separations between the I atom and its co-fragment, E_{av} is the total available energy after excitation, μ is the reduced mass of the molecule, and $V(R)$ is the potential energy of the molecule as a function of the C−I coordinate.

Assuming that $V(R)$ is very similar for all studied molecules, then if an exponential form is assumed for the potential energy curves,[295] it can be deduced that:

$$\tau \propto \sqrt{\frac{\mu}{2E'}} \tag{3.16}$$

where the new energy variable E' is defined as the difference between the available energy, E_{av}, and the internal energy E_{int} of the co-fragment according to:

$$E' = E_{av} - E_{int} = E_{av} \cdot (1 - f_{int}) \tag{3.17}$$

E' accounts indeed for the energy release in the internal degrees of freedom of the fragments during the dissociation process.[213]

The experimental and theoretical reaction times are represented in figure 3.17 and figure 3.18 as a function of $(\mu/2E')^{1/2}$, respectively. Since the computed dissociation energies are lower than the experimental ones for both dihalomethanes, the corresponding reaction times are shorter. Thus, the computed reaction times were scaled by considering the difference between the experimental and theoretical values of the dissociation energy for CH_3I.

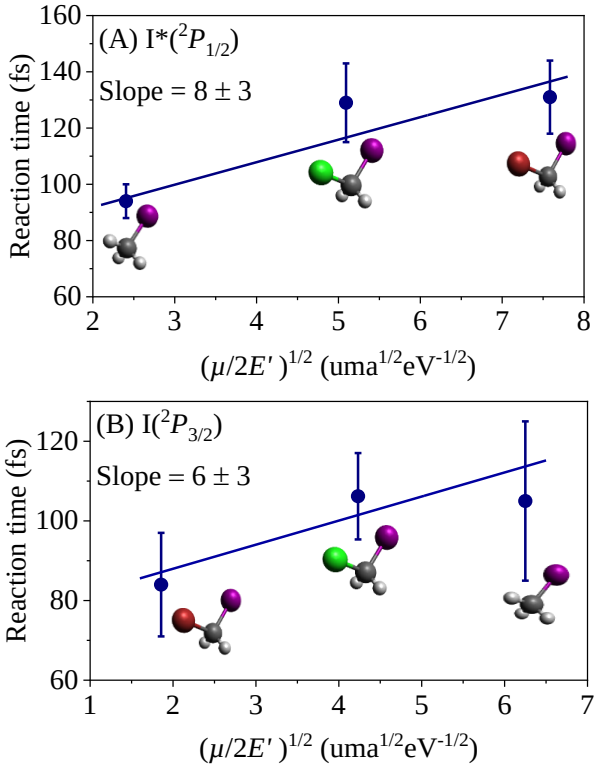

Figure 3.17. *Representation of the experimental reaction times versus $(\mu/2E')^{1/2}$, where μ is the reduced mass of the molecule around the C−I bond, and E' is a modified energy variable which considers the available energy after subtraction of the amount of energy channeled into internal modes of the radical R for each molecule. (A) Molecules dissociating into I*($^2P_{1/2}$). (B) Molecules dissociating into I($^2P_{3/2}$). Straight lines represent the result of a linear fit of the data, and the resulting slope is indicated in each case. For CH_2ICl with 304.5 nm detection, the reaction times for the I and I* channels could not be measured separately. In this case, the reaction time for the I channel was obtained by weighting the separate reaction times of the I and I* channels with the corresponding quantum yields for each channel deduced experimentally. This resulted in a reaction time for the I channel of 106±11 fs.*

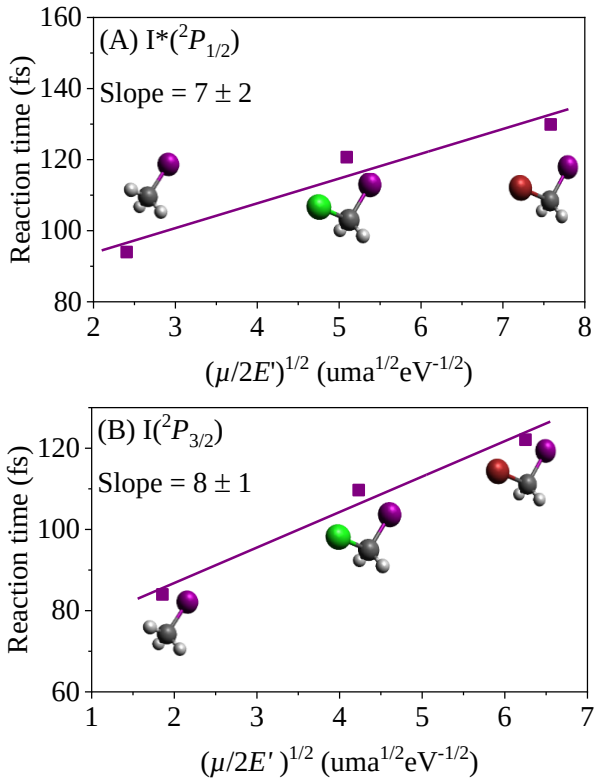

Figure 3.18. *Representation of the computed reaction times versus $(\mu/2E')^{1/2}$, where μ is the reduced mass of the molecule around the C−I bond, and E' is a modified energy variable which considers the available energy after subtraction of the amount of energy channeled into internal modes of the radical R for each molecule. (A) Molecules dissociating into I*($^2P_{1/2}$). (B) Molecules dissociating into I($^2P_{3/2}$) Straight lines represent the result of a linear fit of the theoretical results, and the resulting slope is indicated in each case.*

As can be seen, a similar trend is observed for both the experimental and theoretical reaction times considering the experimental error bars, maintaining a practically linear dependence between the reaction times and $(\mu/2E')^{1/2}$. The C−I reaction times are indeed fully accounted for by the radical size and the energy release into the radical fragment. This correlation between reaction times and energy disposal was also found in the series of alkyl iodide molecules,[213] which was also associated with a similar shape for the excited state potential energy curves in all these molecules. As observed in figure 3.17 and figure 3.18, very similar small slopes characterize the I and I* channels experimentally and theoretically, with values of 6±3 *vs.* 8±1 for experiment and theory for the I channel, and values of 8±3 *vs.* 7±2 for experiment and theory for the I* channel. These small values contrast with those corresponding to the linear alkyl iodides, which were found to be significantly larger: 36±1 and 29±1 for the I and I* channels,[213] respectively. In particular, comparing the reaction times for the long linear alkyl iodides *n*-C_3H_5I and *n*-C_4H_9I with those of CH_2ICl and CH_2BrI obtained in this work, the former are found to be significantly longer than the latter for both the I and I* channels of the reaction. The molecules share somewhat similar values of $(\mu/2E')^{1/2}$, reflecting the influence of the size of the radical and the energy release into the radical on the C−I bond cleavage times.

The energy partitioning between translational and internal modes in a photodissociation process across a repulsive potential energy surface can be estimated by introducing either of two radical limits of the impulsive mode. These models are the rigid radical and the soft radical approximations.[203, 229]

- In the rigid radical approximation,[203] it is assumed that the dissociation is impulsive and ignores the flow of energy into the vibrational degrees of freedom of the fragments. According to the rigid model, most of the available energy should be partitioned into translational energy.
- In the soft radical approximation,[229] it is assumed that the C atom in the C−I bond is weakly coupled to other atoms of the radical so that the available energy is fundamentally converted into translational energy of the C and I atoms. As a consequence of the momentum and energy conservation principle, this energy is converted into rotational and vibrational excitation energy of the co-fragment. Thus, the energy partition can be estimated by:

$$\frac{E_{\text{int}}^{R}}{E_{av}} = 1 - \frac{\mu_a}{\mu_f} \tag{3.18}$$

where E_{int}^{R} is the internal energy content of the radical, μ_f is the reduced mass of the radical and I fragments and μ_a is the reduced mass of C and I.

Energy partitioning values estimated for CH_3I, CH_2ICl and CH_2BrI, using equation (3.18) are found in table 3.10. The estimated values are compared to the experimental ones, with a fair agreement.

Table 3.10. *Energy partitioning values estimated for CH_3I, CH_2ICl and CH_2BrI according to the soft-radical model. Comparison with experimental values.*[213]

	Radical mass (amu)	Experimental energy partitioning f_{int}	Soft-radical model energy partitioning f_{int}
CH_3I	15.03	0.20	0.184
CH_2ICl	49.48	0.58	0.692
CH_2BrI	93.93	0.69	0.797

The photodissociation dynamics of several alkyl iodides in the UV range[213, 296-298] undergo mainly through C−I bond direct dissociation and produce I atoms, similar to what is found here for the dihalomethanes. Corrales *et al.*[213] demonstrated a tendency for the internal energy of the radical fragment to increase with the increasing structural linear chain and the vibrational degrees of freedom, successfully explained by using the soft radical. Table 3.11 shows the experimental partitioning energy values and those predicted from the soft-radical impulsive model for the series of linear alkyl iodide previously measured at the same excitation wavelength.[213]

Table 3.11. *Energy partitioning values are estimated for some linear alkyl iodides according to the soft-radical model. Comparison with experimental values.*[213]

	Radical mass (amu)	Experimental energy partitioning f_{int}	Soft-radical model energy partitioning f_{int}
CH_3I	15.03	0.20	0.184
C_2H_5I	29.06	0.53	0.536
C_3H_7I	43.09	0.67	0.659
C_4H_9I	57.11	0.68	0.721

The comparison of experimental and theoretical energy partitioning f_{int} values for dihalomethanes and linear alkyl iodides is reflected in figure 3.19. This comparison clearly shows that this limit model tends to underestimate the measured translational energy and thus overestimates the internal energy of the molecular photofragment.[239, 286] The expected values (~0.69 for CH_2ICl and ~0.80 for CH_2BrI) are indeed slightly above the measured ones.

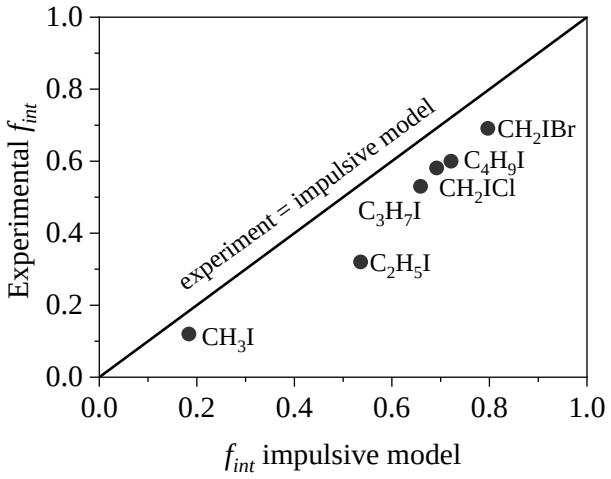

Figure 3.19. *Comparison of measured and theoretical energy partitioning f_{int} values for CH_3I, C_2H_5I, n-C_3H_7I,* n-C_4H_9I[213] *and CH_2ICl and CH_2BrI photodissociation upon excitation at 268 nm in the first absorption A-band.*

What makes a difference between dihalomethanes and alkyl iodides is the type of energy transfer into the internal modes - rotational and vibrational - of the radicals. As shown by on-the-fly full dimension trajectories, in the case of the linear alkyl iodides, although part of the energy transfer is going into rotational motion of the radical, a significant amount is directed into vibrations. In contrast, for the dihalomethanes, most of the energy transfer goes into the rotational motion of the rigid radical due to the "anchor" effect exerted by the heavy halogen atom (Cl or Br). This preference of energy flow into rotation rather than to vibrational modes is the reason for the shorter C−I cleavage times found for the dihalomethanes in comparison with the long linear chain alkyl iodides, explaining the significantly smaller slopes in the former as compared to the alkyl iodides. This work demonstrates the close

connection between the real-time dynamics (bond cleavage times) and the energy flow into specific rotational and vibrational modes of the polyatomic co-fragment.

3.5. CONCLUSIONS

A comparative study of the real-time photodissociation dynamics of CH_3I derived dihalomethanes, CH_2lCI and CH_2BrI, was carried out at an excitation wavelength of 268 nm, around the maximum of the first absorption band (*A*-band), to evaluate the halogen-atom substituent effect.

Experiments were performed employing the femtosecond velocity map ion imaging technique. High-level *ab initio* electronic structure calculations and full-dimension on-the-fly trajectories, including surface hopping, were carried out to explain the experimental findings. In this way, total translational energy distributions, angular distributions of I fragments and reaction times for the C−I bond cleavage were presented and discussed along with the computed absorption spectra, potential energy curves and on-the-fly trajectories.

The *A*-band excitation of both dihalomethanes at 268 nm results in the direct photodissociation leading to the cleavage of the C−I bond mediated by repulsive electronic states producing molecular fragments in correlation with both I and I*. Anisotropy parameters and theoretical calculations reveal that the dynamics are mainly governed by the absorption to the 5*A*' state for CH_2BrI, while two dissociation pathways, through the 4*A*' or the 5*A*' states, compete for CH_2ICI.

A significant part of the energy available is converted into the internal energy of the molecular fragments. The fission process of these molecules can be explained by the soft-radical model, as opposed to the monohalogenated analogs that are better adapted to the rigid-radical model.

An “anchor” effect from the substituent halogen-atom leads to a significant rotational motion of the molecule characterizing the photodissociation in both dihalomethanes, motion with is transferred to a remarkable rotational energy of the co-fragment. This energy flux into the internal degrees of freedom of the molecules is one of the key factors governing the real-time reaction dynamics.

The increasing C−I bond cleavage times are the result of the increasing co-fragment size and the energy release into the co-fragment, following a one-dimensional photodissociation model similarly to linear and branched alkyl iodide molecules.[213]

The role of the avoided crossing between the 5*A*', 4*A*' and 4*A*" states and the calculated absorption spectra resolved in electronic states are discussed in relation with the quantum yield Φ* and reaction times obtained both experimentally and theoretically, which are indeed in relatively good agreement.

Chapter 4 – Femtosecond predissociation dynamics of ethyl iodide in the *B*-band

4.1. INTRODUCTION

Methyl iodide (CH_3I) photodissociation dynamics in the *A*-band have become a benchmark for studying polyatomic molecules, as it is a relatively small polyatomic system presenting interesting fast non-adiabatic dynamics through purely repulsive potential energy surfaces and mediated by a conical intersection. This molecule has been the most studied one, giving rise to a vast literature. Yet, its photodissociation mechanism is still not completely understood. Most experimental and theoretical research has focused on its photodissociation at 266 nm corresponding to the maximum of the first absorption band, the *A*-band. In particular, a very extensive study of direct photodissociation through this band has been carried out in our research group,[149-151, 153] including the red[152] and blue edges[154, 194] of this absorption continuum, which has allowed us to characterize the final products and the time-resolved dynamics of the different dissociation channels.

Electronic predissociation from a discrete ro-vibrational level of a bound excited electronic state coupled to a repulsive electronic state is ubiquitous in molecular photochemistry. Electronic predissociation involving a transfer of population from an optically excited vibrational state of a bound Rydberg state to a valence repulsive state has been described in detail for CH_3I following excitation at around 200 nm, the second absorption band.[155-159, 299-302]

The second absorption band, namely the *B*-band, of CH_3I corresponds to the 190 to 205 nm absorption range and results from excitation of a lone pair $e(5p_{x,y})$ electron located on the iodine (I) atom to the available lowest energy a_1 (6*s*) Rydberg molecular bonding orbital. This excitation produces the $^{3,1}E$ states ($^{3,1}\Pi$ in $C_{\infty v}$ symmetry), where the triplet state is strongly separated due to spin-orbit interaction. This interaction is superior, in this case, to the exchange interaction leading to the formation of two pairs of "doublets": $E(^3\Pi_2)$, $E(^3\Pi_1)$ and $A_1(^3\Pi_0)$, $E(^1\Pi)$, instead of the typical combination of triplet-singlet states for a weak spin-orbit coupling. The absorption to these four states is artificially divided into the *B*- and *C*-bands. The transitions to the two-lower energy $^3R_2$ and $^3R_1$ states are known as *B*-band (190-205 nm), and the transitions to the two higher energy states $^3R_{0^+,0^-}$ and ^1R, are known as *C*-band (170-185 nm). Given the selection rules (no transitions to either triplets or states with Ω=2 are allowed from the ground state), the $^3R_1$ state dominates absorption from the ground state, although weak

features have been assigned to absorption to the $^3R_2$ state, which lies at slightly lower energies. All those transitions are of *E* character in C_{3v} symmetry and are therefore perpendicular. The CH_3I absorption in the *B*- and *C*-band is dominated by transitions to bound Rydberg states, followed by their prompt predissociation into $CH_3(^2A_2'')$+I*($^2P_{1/2}$) and $CH_3(^2A_2'')$+I($^2P_{3/2}$).

The first theoretical calculation concerning the predissociation dynamics of the lower states was carried out by Donaldson *et al.*[303] based on empirical potential energy surfaces for bonding states; a combination of theoretical[220] and experimental data for the dissociative surfaces and a series of hypothesis for the coupling between surfaces. This model revealed that at least two dissociative potentials of A_1 and A_2 symmetry play an important role in the predissociation of the *B*-band states.

The only *ab initio* calculations of the Rydberg states of CH_3I are the first calculations by Tadjeddine *et al.*[220] and the most recent by Alekseyev *et al.*[304] Figure 4.1 shows the computed potential energy curves calculated along the C−I stretch coordinate for the low-lying states of CH_3I calculated by Alekseyev *et al.*[304], where the states belonging to the *A*, *B* and *C*-bands can be distinguished.

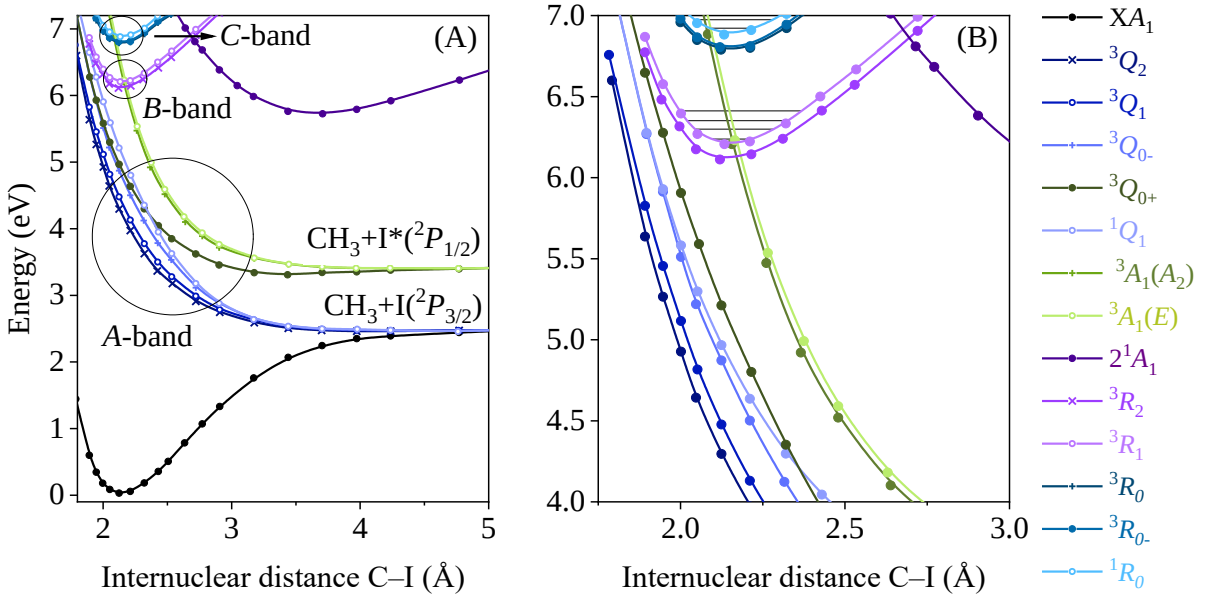

Figure 4.1. *(A) Computed potential energy curves calculated along the C−I stretch coordinate for the low-lying states of CH_3I, where the states corresponding to A, B and C-bands can be distinguished. A_1 states-filled circles, A_2 states-pluses, and E states-open circles and crosses (C_{3v} group notation). Crosses correspond to the Ω=2 states in the $C_{\infty v}$ group, open circles to Ω=1. The Λ-S notation (^3Q, ^3R, $^3A_1$) designates groups of the spin-orbit split states. (B) Calculated potential energy curves for the excited states of CH_3I relevant to the B- and C-band absorption and predissociation. The $C_{\infty v}$ group notation is used. The lowest four vibrational levels are shown for the $^3R_1$ and ^1R states. Figure adapted from reference [304].*

The strongest TDM is to the $^3R_1$ state of the *B*-band, whereas excitation to the $^3R_2$ state is very weak, although forbidden. In both cases, the transitions are perpendicular. Syage *et al.*[305] concluded that

the dissociative state mainly involved in the process of cleavage of C–I bond in CH_3I after absorption of a photon of around 200 nm was the $^3A_1$ (A_2) component of the repulsive $^3Q_0$ state belonging to the *A*-state. One of the most interesting aspects in the excitation to the *B*-band lies in the fact that the coupling details between the levels of the Rydberg state $^3R_1$ and the dissociative states of the *A*-band have a significant effect on the predissociation process and, therefore, provide significative differences in the observed dynamics as a function of the vibronic level at which the CH_3I molecule is initially excited.

Figure 4.2 displays the absorption spectrum of CH_3I in the 200 nm region. It exhibits a clear vibrational structure[299, 306-308] consisting of narrow absorption lines, contrary to the broad spectral character of the *A*-band, purely composed of dissociative valence levels. However, the resonances show considerable spectral broadening, indicating finite lifetimes, which are related to predissociation. This spectrum was first obtained by Felps *et al.*[306] and the assignment was made by Gedanken *et al.*[309] and Dobber *et al.*[308] The main number X in the X_Z^Y assignment indicates the vibrational mode of the molecule, and the Z subscript and Y superscript indicate the number of vibrational quanta in the X mode that the molecule has in the ground and the Rydberg state, respectively. For example, 0_0^0 refers to the transition from the ground electronic state without vibrational excitation to the Rydberg state in the vibrational ground state; 2_0^1 represents the excitation of the molecule from the ground state with v=0 to the Rydberg state with a vibrational quantum in the umbrella mode v_2; and so on. This nomenclature is uniquely for vibronic (vibrational-electronic) transitions; however, in what follows, it is used to describe the vibronic levels or the vibrational transitions under study.

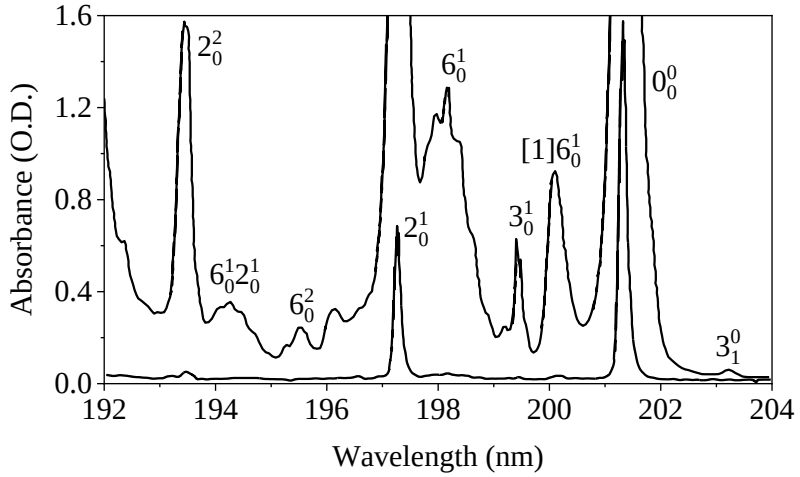

Figure 4.2. *Absorption spectrum of CH_3I in the 200 nm absorption region with assignments to vibronic transitions. Figure adapted from reference [299].*

The spectrum has two very intense absorption bands corresponding to the 0_0^0 (at 201.2 nm) and 2_0^1 (at 196.7 nm) transitions from the ground state to the $^3R_1$ Rydberg state, at its ground vibration level (0_0^0) and the level with a vibrational quantum in the umbrella mode v_2=1 (2_0^1). The corresponding signals

to other vibration levels of CH_3I in the *B*-band are very weak; therefore, the spectrum has been multiplied by a factor of ≈25, so that the weakest absorption bands are visible. All bands correspond to the $^3R_1$ state absorption, except for [1] 6_0^1 which corresponds to the $^3R_2$ state.[304] In the case of this transition, the presence of other absorption bands in their spectral environment causes the mixing of the quantum states, and the probability of absorption at this level is increased (Fermi resonance).[310]

Before the appearance of femtosecond lasers, to estimate the lifetime of excited states, the frequency domain was used to access temporal information by fitting the absorption lines to Lorentzian functions whose width is inversely proportional to the lifetime.[305, 311] Nevertheless, with this method, no dependence of lifetime on the excited level was achieved. Since the last decade of the 20th century, the use of femtosecond lasers has become widespread along with the pump and probe technique for determining precise reaction lifetimes. Baronavski and Owrutsky[299, 312] used this technique to directly measure in the time domain the temporal characteristics of the predissociation of CH_3I in the *B*-band by measuring the temporal evolution of the methyl iodide parent ion (CH_3I^+) after exciting the molecule with a first pump laser pulse centered around 200 nm at different vibrational states of the *B*-band, followed by the ionization of the parent molecule employing a probe laser pulse (experiment equivalent to the performance of a (1+1') REMPI time-resolved experiment). The transients as a function of the delay time between the pump and probe lasers provided the lifetimes corresponding to the excitation at different vibrational modes. Their results revealed longer lifetimes than those obtained with indirect methods and concluded extreme differences depending on the initial vibronic transition. These differences were presumably assigned to the geometry of involved states, *i.e.,* the $^3R_1$ state and the *A*-band dissociative states play a predominant role in the observed differences. However, they could not explain the changes in measured times since no potential energy surfaces were available by that time to relate the behavior between surfaces. They considered the importance of the stretching vibrational modes or the symmetry breakup to interpret the transition probability differences from the excited bound state to the dissociative states.

The theoretical results of Alekseyev *et al.*[304] implied a significant advance in the understanding of the dynamics of CH_3I through the *B*-band. They qualitatively understood the responsible mechanisms for the different responses of the molecular system depending on the vibrational levels of the Rydberg state in the *B*-band. Without providing quantitative data concerning the lifetimes, *ab initio* calculations indicated that the mechanism that causes the dissociation is a non-adiabatic crossing that allows the transfer of population to the *A*-band states, in particular, the $^3A_1$ state, for excitation wavelengths above 182 nm, and that this crossing is located near the CH_3I equilibrium distance at the ground *B*-band vibrational level. Therefore, the shape of the wave functions of 0 and 2 levels facilitates crossing to the *A*-band states; in contrast, the transition probability for level 3 is very weak, resulting in a slower

predissociation than the other vibrational levels. In this way, the calculations confirm the possibility of important changes in the lifetime depending on the initially excited vibronic level.

Gitzinger *et al.* measured the predissociation lifetimes of CH_3I in the origin of the *B*-band and on several vibronic levels employing femtosecond VMI through separate resonant detection of I and CH_3 fragment images, parent decay, and photoelectron images obtained through both resonant and non-resonant MPI. The lifetime was found to be 1.52±0.10 ps in the origin of the *B*-band while the specific vibrational state lifetimes, were found to be 0.85±0.04 ps and 4.34±0.13 ps for the 2_0^1 and 3_0^1 vibronic levels, corresponding to the excitation of the umbrella mode (ν_2) and the C−I stretching mode (ν_3), respectively.[155, 158] These measurements confirmed the great sensitivity of the lifetimes to the initially excited vibrational level, this being proof of the sensitivity of the interaction strength with the *A*-band potential energy surfaces to the detailed structure of each wave function.[155, 158]

Thiré *et al.* studied the predissociation of CH_3I in the origin of the *B*-band employing ion and photoelectron VMI,[156, 157] using, therefore, the same method of detection as Gitzinger *et al.* The results found in both cases are similar in many respects, with some differences in the transients of the CH_3 fragments and their subsequent interpretation. The authors claim that the lifetime obtained with resonant detection of the CH_3 fragments depends on the orientation of the CH_3 fragment concerning the polarization axis of the probe laser pulse. Such an effect was, nevertheless, not observed in Gitzinger *et al.* experiments.

The determination of quantum yields Φ* along the *B*-band has been quite controversial. Following excitation of CH_3I at ~201 nm, an electronic predissociation through the coupling between the initially populated $^3R_1$ and the repulsive $^3A_1$ state leads to the mayor dissociation into CH_3+I*. The calculations of Alekseyev *et al.*[304] predict a quantum yield equal to unity; however, experimentally, a small amount of I in its ground spin-orbit state in correlation with remarkably ro-vibrationally excited CH_3 is detected and attributed to a second curve crossing between $^3R_1$ and the repulsive state $^1Q_1$.[158, 159, 313] Nevertheless, even within the experimental results, there have been large discrepancies in the determination of its precise value.[158, 159, 194, 314, 315] Experiments by Hess *et al.*[314] exciting at 193 nm obtained a quantum yield of 0.70±0.04, while other studies by van Veen *et al.*[316] and Continetti *et al.*[315] at the same excitation wavelength indicated a value almost equal to one. Subsequently, Hancock *et al.*[317] reproduced an identical experiment to that of Hess *et al.* and attributed the value of less than 1 to an experimental artifact. According to Gitzinger *et al.*, the quantum yield Φ* ranges between 0.99 in the 0_0^0 and 0.87 in the 3_0^1 vibronic band,[159] attributing the presence of I($^2P_{3/2}$) due to the competition of two routes of decoupling, through the $^3A_1$ state and throughout the $^1Q_1$ state, due to the weak coupling between the $^3R_1$ Rydberg state (*B*-band) and the $^3A_1$ state (*A*-band), even at excitation energies far below the given by

Alekseyev *et al.*[304] Nanosecond experiments performed by González *et al.*[212] also confirmed the minor presence of this photofragment in correlation with vibrationally excited CH_3 fragments (ν=1).

While direct dynamics are governed by very short reaction times, on the femtosecond scale, predissociations are slower with a lifetime that can be comparable to the rotation timescale of the parent molecule in the excited state. This can lead to important effects in the observation of angular distributions with respect to the time delay between lasers. In this sense, the evolution of the anisotropy as a function of the pump-probe delay was also investigated by Gitzinger *et al.*[155, 158] Their results revealed for $I^*(^2P_{1/2})$ fragments lack of alignment effects and temporal behavior of an increasing exponential type, particular of a predissociative mechanism with an initial value close to -1, consistent with the perpendicular nature of the initial transition. From this initial moment, the anisotropy parameter β was found to increase gradually over time until reaching an asymptotic value, which slightly depends on the initial vibronic level, to be around -0.5 to -0.6 in all cases. The time constant associated with the rise of the anisotropy τ_β was determined to be always less than the corresponding lifetime τ, but in the same order of magnitude, indicating that the temporal evolution of anisotropy was related to the predissociation lifetime and, therefore, to the rotation of the CH_3I molecules in the excited state. Concerning the anisotropy of the CH_3 fragments, their angular distributions required at least two anisotropy parameters highlighting the rotational angular momentum alignment of the fragments. A theoretical interpretation of the experimental results was carried out employing a fitting procedure using quasiclassical theory to elucidate vector correlations in the photodissociation of symmetric top molecules. The important role of CH_3 fragment angular momentum alignment along with bending motion and rotation of the parent molecule and CH_3 fragment was demonstrated.[302]

Recently, Forbes *et al.*[318] also investigated the predissociation dynamics of the 6s Rydberg state of CH_3I by means of by time-resolved Coulomb explosion imaging employing XUV free-electron laser (FEL) pulses for the site-specific probing by the inner-shell ionization at the I atomic site exploiting the I $4d_{5/2,\,3/2} \rightarrow \in f$ shape resonances (60-140 eV), employing a VMI setup spectrometer coupled with the PImMS camera. For the *B*-band excitation at 201.2 nm, similar results were found to what was previously measured in our group,[155, 158] revealing a predissociation mechanism based on an initial excitation to the 6s Rydberg state and dissociation through internal conversion into the lower-lying *A*-state potential energy surface in the picosecond time scale (1.53±0.02 ps). Likewise, a quantum yield close to one for the $I^*(^2P_{1/2})+CH_3$ dissociation channel was observed. The angular distributions of photofragments were extracted out of slice images, revealing a strong perpendicular at short pump-probe delays and a subsequent loss of anisotropy due to rotation of the parent molecule prior to dissociation. As well, the effect of charge transfer was observed through differing delay-dependencies of the various I charge states.

In contrast, the photodissociation dynamics of ethyl iodide (C_2H_5I) have been little researched following excitation in the *B*-band. The reported studies are fundamentally focused on the first absorption band employing techniques such as PTS[203, 319] or VMI in combination with detection techniques such as REMPI[296, 320] and universal detection.[321] Details of the C_2H_5I dissociation dynamics can also be found in general studies of the alkyl iodides photodissociation regarding aspects such as structural and wavelength-dependent energy partitioning or quantum yields.[203, 213, 293, 322]

For C_2H_5I, according to high-level *ab initio* calculations, each of the Rydberg states split into two components due to the breakdown of the C_{3v} symmetry. The $^3R_2$ and $^3R_1$ states transform therefore into the [5*A*", 6*A*'] and [6*A*", 7*A*"] states, respectively, although the [5*A*", 6*A*'] are similarly dark states. At higher energies, the $^3R_{0+,-}$ and the $^1R_1$ states turn likewise into the [9*A*', 9*A*'] and [10*A*", 10*A*'] states, constituting the *C*-band.[323]

The absorption spectrum of C_2H_5I, presented in figure 4.3, is governed by a first peak assigned to the 0_0^0 origin of the *B*-band, whose spectral position is close to the origin of the *B*-band in CH_3I and several transitions to vibronic levels.[323] According to the reported vibrational frequencies for C_2H_5I and the ethyl iodide cation ($C_2H_5I^+$) in their respective electronic ground states,[324, 325] the three first peaks can be assigned to vibrational excitation of the C−I bend (ν_{11}=220 cm^{-1} for the ethyl iodide cation ($C_2H_5I^+$)) and the CH_3 torsion (ν_{18}=238 cm^{-1}) modes, whereas the last peak at 199.98 nm can be associated to ν_{10}, i.e., to the C−I stretch mode combined with the C−I bend mode (412 cm^{-1}). The strong absorption to the vibrational levels in the *B*-band is very intense in comparison with CH_3I.[187, 299]

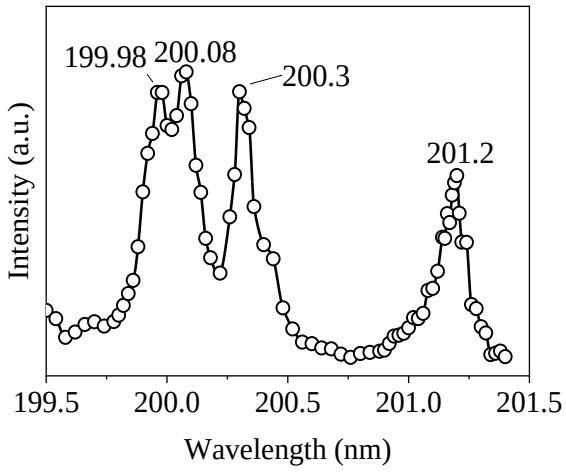

Figure 4.3. *I*($^2P_{1/2}$) fragment action spectrum from C_2H_5I photodissociation in the second absorption B-band between 199-201.5 nm (50251-49628 cm^{-1}). Figure adapted from reference [323].*

In the present study, femtosecond time-resolved velocity map ion imaging experiments of C_2H_5I on the second absorption band (*B*-band) at 201.19 and 200.08 nm, corresponding to the 0_0^0 and 18_0^1 vibronic transitions, *i.e.*, the origin of the *B*-band and the first most intense vibronic state assigned to

one quantum of excitation in the CH_3 torsion mode, were conducted and compared with CH_3I photodissociation experiments conducted at 201.19, 196.7 and 199.2 nm, corresponding to the 0_0^0, 2_0^1 and 3_0^1 vibronic transitions, respectively by Gitzinger *et al.*[155, 158]

The aim is to evaluate the effect of two relevant factors in the predissociation mechanism; on the one hand, the effect of the vibrational excitation of the parent molecule and, on the other hand, the structural effect, mainly in two observables: the predissociation lifetimes and the variation of the anisotropy with time. Therefore, the time-resolved images for the I and ethyl (C_2H_5) fragments are reported and analyzed to extract electronic predissociation lifetimes and the temporal evolution of the anisotropy. Experimental findings are complemented by *ab initio* calculations[323] of the potential energy curves as a function of the C−I distance to discuss the predissociation mechanism based on structural effects on the predissociation reaction. Besides, the evolution of the anisotropy as a function of the pump-probe time delay for I* and C_2H_5 fragments is discussed in terms of the parent molecule rotational temperature deduced from semiclassical models.

4.2. METHODOLOGY

4.2.1. Experimental methodology

4.2.1.1. Laser configuration and optical assemblies

This section presents the specific methodological details of the time-resolved predissociation dynamics experiments of C_2H_5I in the *B*-band, using velocity map ion imaging in combination with resonant ionization of the free fragments I($^2P_{3/2}$) and I*($^2P_{1/2}$) through (2+1) REMPI, and C_2H_5 radicals *via* (1+1) REMPI. Figure 4.4 summarizes the experimental setup employed for the predissociation experiments.

For the accomplishment of the time-resolved predissociation dynamics experiments for C_2H_5I in the second absorption band, a tunable pump laser centered around 201.2 nm or 200.08 nm was required to excite the origin of the *B*-band and the first most intense vibrationally excited state of the *B*-band, assigned to the 18_0^1 vibronic transition, respectively. The monitoring of the reaction was accomplished either through (2+1) REMPI of I*($^2P_{1/2}$) fragments using a probe laser centered at 304.5 nm (see section 2.1.4.6.1) or through (1+1) REMPI of C_2H_5 fragments using a probe laser centered at 244 nm. The first photon of 244 nm excites the C_2H_5 radical from the $\widetilde{X}\,^2A_1$ ground-state into the $\widetilde{X}\,^2A_1$ 3s Rydberg state, yielding a broad and featureless absorption band, which is represented in figure 4.5. Upon excitation to the Rydberg state, the C_2H_5 radical dissociates concomitantly into ethylene (C_2H_4) and hydrogen (H) with dissociation rates on the order of 10^7 s^{-1}.[296, 326, 327]

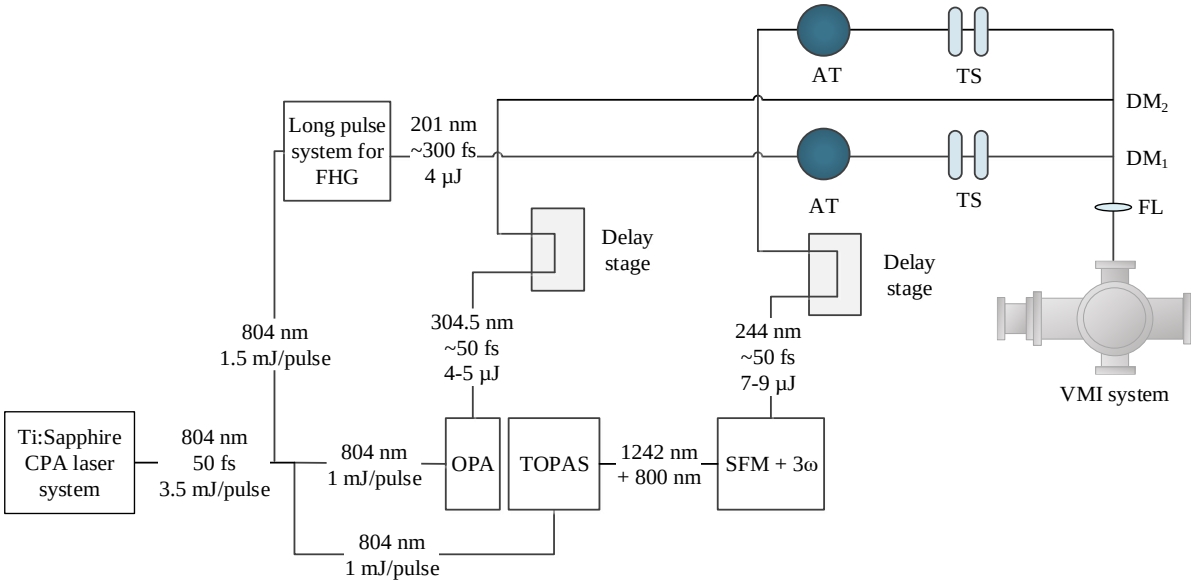

Figure 4.4. *Experimental setup for time-resolved predissociation dynamics of C_2H_5I in the second absorption band at around 201 nm employing femtosecond laser pulses and velocity map ion imaging. The laser system, the OPA, the TOPAS, and the long pulse system for FHG are represented on the left side. Several optical elements such as dichroic mirrors (DM), telescopes (TS), power attenuators (AT), the probe delay stages, the final focusing lens (FL) and the wedge (W) are distinguished. The VMI machine is located in the lower right area of the figure. The detection system is arranged perpendicular to the plane.*

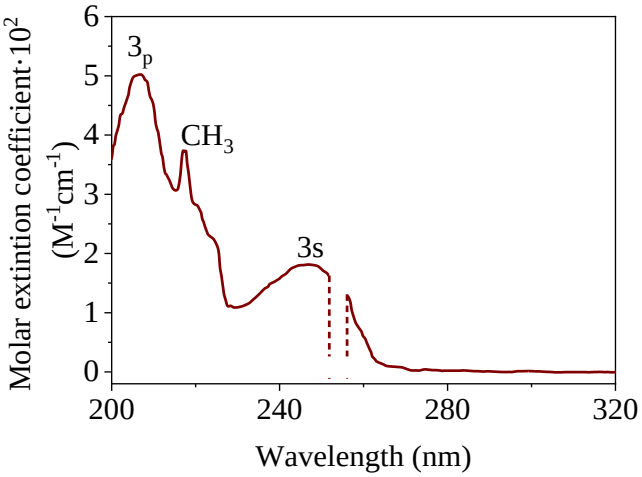

Figure 4.5. *Gas-phase absorption spectrum of the C_2H_5 radical. Radicals are generated by mercury (Hg) photosensitized reactions and observed by modulation spectroscopy. Dashed lines indicate Hg I stray light. Figure adapted from reference* [327].

In this way, three groups of experiments were carried out:

- Pump: 201.19 nm (0_0^0 of C_2H_5I) + Probe: 304.5 nm (I*)
- Pump: 201.19 nm (0_0^0 of C_2H_5I) + Probe: 244 nm (C_2H_5)
- Pump: 200.08 nm (18_0^1 of C_2H_5I) + Probe: 304.5 nm (I*)

For this purpose, the output of the Spitfire regenerative amplifier (804 nm laser pulses, 3.5 mJ/pulse, 50 fs pulse duration, 1 kHz repetition rate) was divided into three arms: one of the arms, with an energy around 1.5 mJ/pulse was driven to the long pulse system for FHG, producing tunable pump laser pulses around 201 nm with an output energy of 4 μJ/pulse. The output beam was telescoped. A 1 mJ/pulse arm was used to pump the OPA which, yielded pulses centered at 304.5 with energies typically around 3-4 mJ and with an FWHM bandwidth of around 1.7 nm. A third 1 mJ/pulse arm was employed to pump the TOPAS. The signal centered at 1250 nm was frequency mixed with 804 nm, and the SFG output was frequency-doubled to obtain radiation at 244 nm with an output energy of 7-9 μJ/pulse. The probe beams, either 304.5 nm or 244 nm, were sent to the corresponding linear translation stages for the corresponding pump-probe experiments with the pump beam centered at 201.19 or 200.08 nm. Specifically, the 244 nm beam was sent to the Newport linear translation stage, and the 304.5 nm beam was sent to the Parker linear translation stage. The pump and probe laser beams were recombined in the final dichroic mirror, and they were later focused inside the ionization chamber employing a 25 cm focusing lens. The linear polarization of the 244 nm beam was originally vertical, so it was 90º rotated utilizing an achromatic tunable half-wave plate to ensure the cylindrical symmetry for reconstructing the images.

The intensities chosen for the pump and probe pulses were estimated to be $1.5 \cdot 10^{10}$ and $2 \cdot 10^{11}$ W/cm^2, respectively, and were controlled by the energy variation using variable attenuators in the form of neutral density filters variable by transmission.

4.2.1.2. Molecular beam conditions and detection system

For the realization of the experiments, CH_3I (Sigma Aldrich, 99 %) and C_2H_5I (Sigma Aldrich, 99 %) were used employing glass bubblers at room temperature, except for CH_3I which was cooled down to 0 ºC with an ice bath due to its vapor pressure at room temperature. The molecular beams were generated by expanding the vapors with helium (He) (Air Liquid, 99.999 %) as carrier gas at 1.5-2 atm backing pressure, thus formed by a mixture of 5 % the target molecule and 95 % carrier gas, through the piezoelectric valve. Typical working pressures in the ionization chamber were around 10^{-6} mbar by employing valve apertures of 45 μs and voltages applied to the piezoelectric material of ~300 V. The delay between the gas pulse and the laser pulses was set such that its interaction occurred in the edge area of the gas pulse, generating fewer ions signal but originated from parent molecules with lower rotational temperature affecting, thus, the anisotropy variation with the pump-probe delay.

In the ion extraction system, a repeller and extractor ratio of 0.76 was maintained to ensure VMI conditions. In this case, the calibration of the apparatus was performed by using the known KER of the $CH_3(\nu=0)+I^*(^2P_{1/2})$ and $CH_3(\nu_1=1)+I^*(^2P_{1/2})$ channels from 201.19 nm photodissociation of CH_3I in the origin of the *B*-band (see section 2.1.4.6.2).[155]

The monitoring of the photodissociation process was carried out by detecting the fragment ions in the TOFMS configuration. According to the TOF mass spectrum of C_2H_5I display in figure 4.6, the arrival at the I^+ detector occurred 8.9 μs whereas the $C_2H_5^+$ fragment at 5.5 μs later than the arrival of the laser pulse at the interaction area, therefore the gating of the MCP was set at 8.9 μs and 5.5 μs respectively with a duration of 200 ns. The deflector plates were not used in the present case as they were not operative when doing experiments.

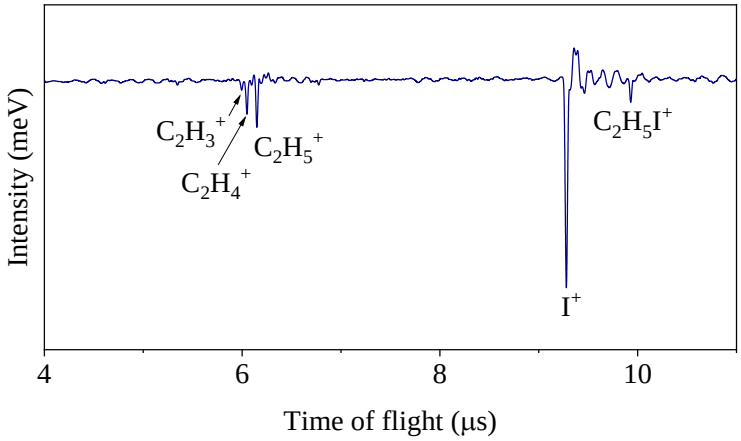

Figure 4.6. *Pump-probe TOF mass spectrum of C_2H_5I with TOF time base (as measured in the digital oscilloscope). Pump pulse centered at 201.19 nm, probe pulse centered at 304.5 nm and time delay settled at 10 ps (asymptotic conditions). The different peaks are assigned to the different parent and fragment ions as indicated.*

4.2.1.3. Temporal characterization of the femtosecond laser pulses

Time zero and cross-correlation measurement were determined by *in situ* measurements of the (1+2') REMPI transient for xenon (Xe) (1 photon of 200 nm and 2' photons of 304.5 nm). The cross-correlation function provided a value of 400 fs.

4.2.2. Theoretical methodology

Ab initio MRCI[280-282] electronic structure calculations of the ground and excited potential energy curves, including spin-orbit, were performed with MOLPRO (Version 2009.1)[277] using the ANO-TPZ basis set[267] with a supplementary monocentric basis located in the center of charge of the cationic molecule. The center of charge was estimated in the ground state of the cation using the Mulliken charges provided by a previous UHF calculation. This monocentric basis, employed to adequately describe the *s* diffuse orbital, was constructed from an even-tempered Gaussian basis with twenty-two exponents following the progression $\alpha_n=\alpha\beta^{n-1}$, where $\alpha=0.01$ and $\beta=1.46$.[328] To remove linear dependencies, the basis set was contracted to sixteen functions. A regular Douglas-Kroll Hamiltonian[268-270] and the AMFI approximation were employed[271] to take into account relativistic effects. The active

space contains six electrons in five orbitals (bonding and antibonding for the C−I bond, two lone pairs on the I atom and a diffuse *s* Rydberg orbital). A total number of thirteen states were included in the state average, including five 1*A*', two 1*A*'', four 3*A*' and two 3*A*''.

The geometry was optimized and the frequencies were calculated at the single-state CASTP2 level of theory[279, 329] for the ground electronic state using analytical gradients. The final one-dimensional potential energy curves, where the C_2H_5 moiety was frozen at the Franck-Condon geometry, were obtained at MRCI,[282]including the spin-orbit coupling in a perturbative modified frame,[330] *i.e.*, the spin-orbit coupling between the electronic states calculated for the different spin multiplicities is evaluated, and the resultant matrix is diagonalized, mixing the different multiplicities.

The calculations were performed by Dr. Jesús González-Vázquez.[323]

4.3. RESULTS

4.3.1. Experimental results

The predissociation dynamics of C_2H_5I were investigated at two excitation wavelengths which were selected from the I*($^2P_{1/2}$) action spectrum reported in figure 4.3, namely λ_{exc}=201.19 nm, attributed to the 0_0^0 5pπ→6s transition, *i.e.*, the origin of the *B*-band, and λ_{exc}=200.08 nm corresponding to the first most intense vibrationally excited state of the *B*-band, which is tentatively assigned to the 18_0^1 vibronic transition, corresponding to one quantum of excitation in the CH_3 torsion mode.[163, 323, 325, 331] While at 201.19 nm, the 0_0^0 is expected to be exclusively populated; at 200.08 nm, some excitation into close-by vibrationally excited levels might be feasible considering the spectral width of the femtosecond laser pulses and the broadening of the bands in the spectrum.

The experimental results, corresponding to the time-resolved detection of I*($^2P_{1/2}$) fragments (henceforth I*) at 304.5 nm, as well as those of C_2H_5 radicals at 244 nm are presented in the following, separately for each excitation wavelength.

4.3.1.1. The origin of the *B*-band

4.3.1.1.1 Iodine detection

The I fragment inverted images at selected pump-probe time delays are presented in figure 4.7. In these images, two contributions are observed: a broad structure at the center of the images, which is independent of the detection wavelength, assigned to dissociative MPI, and an anisotropic ring, assigned to the dissociation channel C_2H_5+I*, whose intensity increases as a function of the pump-probe time

delay until it reaches a plateau around a pump-probe delay of 5 ps. This contribution reflects a decreasing anisotropy as a function of time, since at short pump-probe delays, a perpendicular ring is distinguished, while for an asymptotic time delay of 10 ps, the ring becomes slightly more isotropic. The evolution of the anisotropy is not easily observed in the images at first sight; nevertheless, the analysis of the anisotropy, which is later presented, demonstrates it.

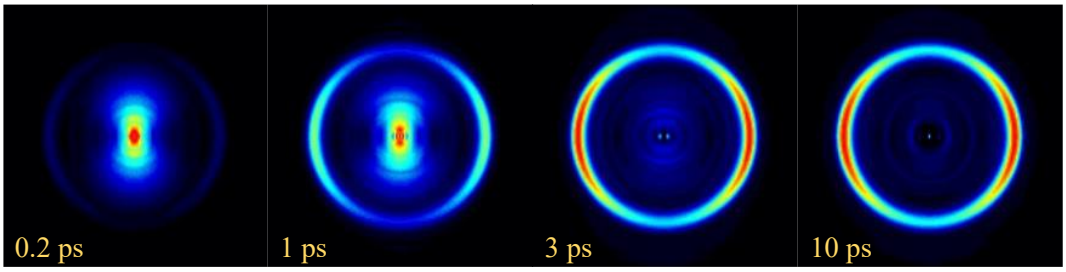

Figure 4.7. *Sequence of Abel-inverted (pBasex) I images as a function of the pump-probe time delay for a pump laser pulse centered at 201.19 nm (0_0^0 origin of the B-band) and (2+1) REMPI detection at 304.5 nm. The external ring is assigned to the I*($^2P_{1/2}$)+C_2H_5 channel while the inner contribution is assigned to MPI. The anisotropy evolution of the external ring is observed with the pump-probe increasing delay. Laser light polarization is along the vertical axis of the images.*

According to slice imaging experiments of C_2H_5I in the origin of the *B*-band employing nanosecond lasers,[323] two anisotropic rings were expected when probing at 304.5 nm, attributed to the formation of the ground and excited spin-orbit states of I. To discard the formation of I in the femtosecond experiments, the same measurements were carried out, tuning the probe laser at 306 nm, allowing us the selective detection of I*. These images revealed apparent similarities with the images shown in figure 4.7, which allowed us to attribute the observed ring to the exclusive formation of I*, so a quantum yield for the production of I* atoms close to unity can be estimated.

The corresponding CM I fragment translational energy distribution resulting from the angular integration of the inverted images at a pump-probe delay of 10 ps is depicted in figure 4.8. The main peak, assigned to the I*($^2P_{1/2}$)+C_2H_5 channel, was fitted to a Gaussian function while the weak broad contribution from dissociative MPI was fitted using the Boltzmann-type fitting function described in the previous chapter.[284] The vertical bar in figure 4.8 corresponds to the available energy or the maximum translational energy, $E_T^{max}(\mathrm{I})$, that can be acquired by the I* fragment according to the following equation:

$$E_{av}(\mathrm{I}^*) = \frac{m_{\mathrm{C_2H_5}}}{m_{\mathrm{C_2H_5I}}} E_{av} = \frac{m_{\mathrm{C_2H_5}}}{m_{\mathrm{C_2H_5I}}} [h\nu - D_0 - E_{\mathrm{SO}}(\mathrm{I}^*) + E_i(\mathrm{C_2H_5I})] \qquad (4.1)$$

where E_{av} represents the total available energy, E_{av}(I*) represents the available energy for the I* fragment, nhv the excitation photon energy, D_0 the C−I dissociation energy at 201.19 nm, 2.353 eV,[320]

E_{SO}(I*) the I spin-orbit splitting, 0.943 eV for the I*,[161] $E_i(C_2H_5I)$ is the internal energy of the parent molecule, which is considered negligible in the present experiment, and $m_{C_2H_5}$ and $m_{C_2H_5I}$ are the masses of the co-fragment C_2H_5 and the parent molecule C_2H_5I, respectively.

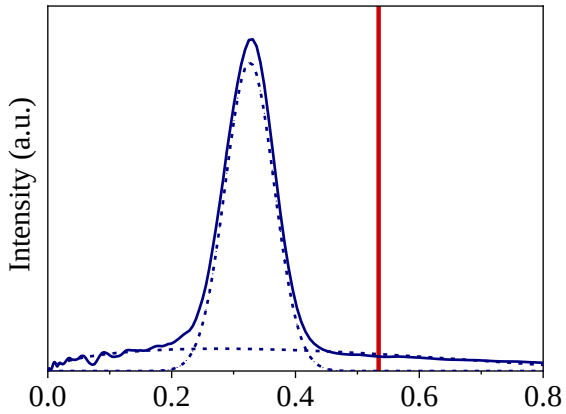

Figure 4.8. *CM translational energy distribution of the I atom for an asymptotic time delay between the pump (201.2 nm) and probe (304.5 nm) lasers of 10 ps. The Boltzmann-type and the Gaussian functions used to fit the two contributions are represented by blue dashed lines. The red vertical bar shows the maximum translational energy that can be acquired by the I fragment in the I*+C_2H_5 channel (see text).*

In contrast to CH_3I, a remarkable shift is observed between the I atom available energy and the maximum translational energy, reflecting a significant conversion of the available energy into internal energy of the C_2H_5 co-fragment, since I fragment is an atomic species. The fraction of the available energy released into internal motion f_{int} obtained for the C_2H_5+I* channel was estimated to be around 0.43±0.03, which is in good agreement with the value of 0.44 reported from the nanosecond experiments[323] and the value of 0.47 estimated using a purely impulsive model.[203] The considerable width of the peak reflects the ro-vibrational excitation of the C_2H_5 co-fragment.

Following nanosecond experiments, the channel correlating with ground-state I should have appeared as a second anisotropic ring at lower radii in the images and as a corresponding second peak around 0.25 eV in the translational energy distribution. Its presence might be feasible due to an avoided crossing located at a C–I internuclear distance of 2.0 Å, between the 6*A*" and 7*A*' bound states and the repulsive 4*A*" and 5*A*' states, belonging to the *A*-band.[323] The I channel is characterized by a remarkably higher energy partitioning f_{int} value. Considering the quantum yield Φ* for the production of I*, which was estimated to be close to 0.9 from the nanosecond experiments, the minor I channel seems to be embedded in the broad contribution from MPI in the present experiments carried out with femtosecond lasers.

The temporal evolution of the intensity of the I fragment in the images was monitored as a function of the pump-probe time delay to measure the C−I bond cleavage time. A global three-dimensional fitting procedure was employed to analyze the clocking experiments.[166] In this way, the anisotropic ring assigned to the C_2H_5+I* channel in figure 4.7 could be isolated based on its energy and anisotropy to obtain the transient presented in figure 4.9. The transient was fitted to a rising exponential function convoluted with the temporal response function described by:[158, 166]

$$S(t) = A\exp\left(-4ln2\left(\frac{t}{\tau_{cc}}\right)^2\right) \otimes \left[\left(1-e^{-\frac{t-t_0}{\tau}}\right)H(t-t_0)\right] \tag{4.2}$$

where τ is the predissociation lifetime of C_2H_5I into I*+C_2H_5, t_{cc} is the instrumental response function time, t_0 is the time of pump-probe temporal overlap, and A is an amplitude factor. $H(t)$ is the Heaviside step function, for which $H(t < 0)=0$ and $H(t > 0)=1$.

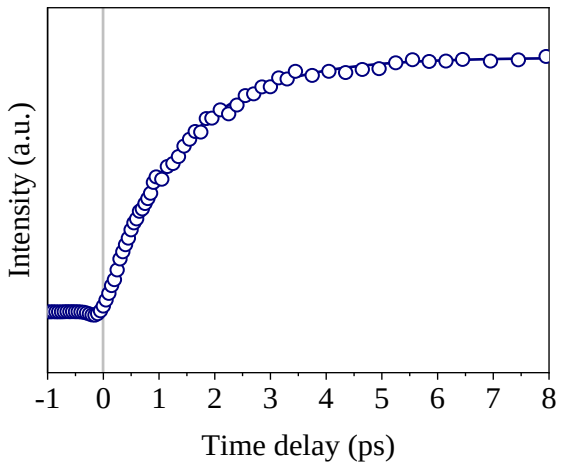

Figure 4.9. *Experimental transient (blue open circles) corresponding to the I* fragment appearance after B-band excitation of C_2H_5I at 201.2 nm. The probe laser was tuned at 304.5 nm, exploiting the (2+1) REMPI transition for the I* fragment. The time constant τ obtained for the lifetime of the excited state after several measurements is 1.34±0.05 ps. The blue solid line represents the fitting of the results to the equation (4.2).*

The reaction lifetime for the 0_0^0 band leading to I* fragments in correlation with C_2H_5 was found to be 1.34±0.05 ps, which is slightly smaller than the one found for I* in correlation with CH_3I fragments, *i.e.*, 1.52±0.05 ps,[155] reflecting a stronger coupling between the Rydberg and the repulsive states involved in the predissociation of C_2H_5I.

To get a more in-depth insight into the predissociation dynamics, the anisotropy characterizing the I* fragment as a function of pump-probe time delay was analyzed. The angular distributions,

obtained by radial integration of the images for each time delay by the multidimensional fitting procedure, were fitted to:

$$I(\theta) = \frac{\sigma}{4\pi} \sum_{i=0}^{2n+2} \beta_i P_i(\cos\theta) \tag{4.3}$$

which arises for a one-photon dissociation process and (m+n) REMPI detection. σ is the total absorption cross-section, θ is the angle between the polarization axis of the photolysis laser and the fragment recoil direction, β_i are anisotropy parameters reflecting the dissociation dynamics and the photofragment polarization, P_i are the Legendre polynomials of the i-th order and n is the number of photons of the resonant step of the REMPI process used for fragment detection. The i=0 term corresponds to the population of the studied species and given that the experimental setup has not been calibrated for total intensities, the whole distribution is normalized to β_0, and the quotient is treated as a normalization fitting parameter. The index i takes only even values since linearly polarized pump and probe laser pulses are employed. In addition, this index can be truncated at i=2 if no photofragment polarization effects are observed. I* cannot show polarization (alignment or orientation) since it presents an angular momentum J=1/2 and, therefore, a single β_2 parameter is only needed to fit the angular distributions.

The temporal evolution of the anisotropy parameter β_2 as a function of the pump-probe time delay is depicted in figure 4.10. As previously observed in the images, the anisotropy decreases with the pump-probe delay from β_2=-0.89±0.05 near time zero to a final value of $\beta_{2=}$-0.59±0.09 at asymptotic time delays.

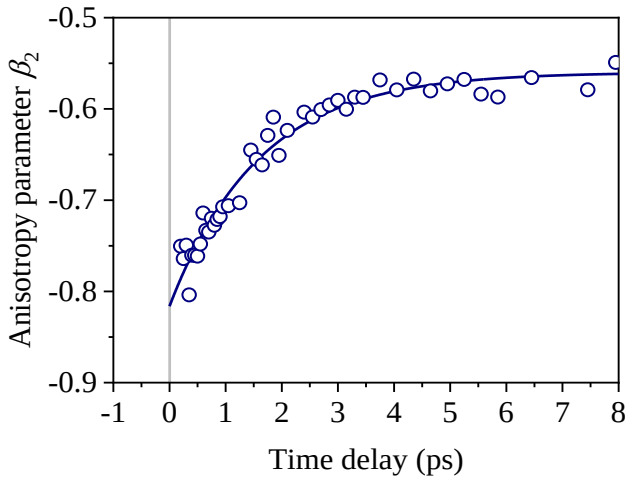

Figure 4.10. *Evolution of the anisotropy parameter, β_2 (blue open circles) resulting from fitting the angular distributions for I* obtained from the multidimensional fit to equation (4.4), as a function of the pump-probe time delay. The blue solid line represents the fitting of the results to an exponential function.*

A similar variation of the anisotropy as a function of the time delay was previously reported, for CH_3I predissociation in the origin of the *B*-band.[155] In that case, the variation of anisotropy as a function of the time delay was larger, from almost -1 in the early time region up to -0.50 at asymptotic time delays. Moreover, for C_2H_5I, it seems that the initial transition, highlighted by the anisotropy parameter β_2 measured at time zero, has a less perpendicular character than in the comparative case of CH_3I.

The variation of the anisotropy parameter over time depicted in figure 4.10 was fitted to an exponential function of the form given by:

$$\beta_2(t) = \beta_2^{init} + \Delta\beta_2 e^{-\frac{t-t_0}{\tau_{\beta_2}}} \tag{4.4}$$

where β_2^{init} represents the initial value of the anisotropy parameter (at time delay zero), $\Delta\beta_2$ is the total variation of the anisotropy parameter β_2 over time, and τ_{β_2} is the time constant of the exponential rise of the anisotropy parameter β_2 over time.

The obtained initial β_2^{init} and final β_2^{final} anisotropy parameters (at an asymptotic time delay of around 10 ps) are listed in table 4.1 along with the $\Delta\beta_2$ and τ_{β_2} values. An anisotropy relaxation time τ_{β_2} of 1.15±0.10 ps is obtained, slightly below the predissociation lifetime derived from the transient shown in figure 4.9.

Table 4.1. *Experimental values, derived from the I* time-resolved images, measured in the 0_0^0 origin of the B-band including the reaction lifetime, τ, the initial anisotropy parameter at early times, β_2^{init}, the anisotropy parameter at asymptotic time delays, β_2^{final}, and the anisotropy relaxation time, τ_{β_2}. The results are compared to the values for CH_3I in the origin of the B-band as reported in reference [155].*

	Reaction time τ (ps)	Initial anisotropy parameter β_2^{init}	Final anisotropy parameter β_2^{final}	Rise of anisotropy τ_{β_2} (ps)
C_2H_5I	1.34±0.05	-0.89±0.05	-0.59±0.09	1.15±0.10
CH_3I[155]	1.52±0.05	-0.97±0.03	-0.50±0.07	1.35±0.10

When the predissociation lifetime τ is similar to the rotational period of the molecule, as in the present case, the loss of anisotropy can be related to the rotation of the parent molecule, and therefore to its rotational temperature in the molecular beam, through classical models introduced in section 1.3.3.1. A value for the rotational temperature T_{rot} of approximately 75 K was obtained for the 0_0^0 transition of CH_3I [155, 158] considering an inertia moment of $I_b=1.118\cdot10^{-45}$ Kg·m^2 and a predissociation lifetime of τ=1.52 ps. In the present case, C_2H_5I is similarly considered as an approximate symmetric top rotor characterized by having three main non-null moments of inertia, two of them being equal

(I_b=I_c) and much larger than the third one (I_a). For a lifetime of τ=1.34 ps, a rotational temperature T_{rot} of approximately 100 K was found.

4.3.1.1.2 Ethyl detection

Similar time-resolved VMI measurements were carried for the C_2H_5 co-fragment probed by (1+1) REMPI at 244 nm.

Figure 4.11 shows four C_2H_5 images at selected pump-probe time delays. An anisotropic ring is observed in the outer region of the image, which was assigned to C_2H_5+I*. As expected, its intensity increases with the time delay, while its anisotropy decreases until reaching a plateau for a pump-probe delay of 5 ps, similarly to I* detection (see figure 4.7). In this case, the probe laser pulse induced a strong MPI signal in the center of the image, which saturates it in that area. Once the contribution of each laser separately was subtracted, a negative signal appeared in the center of the image, as observed in figure 4.11

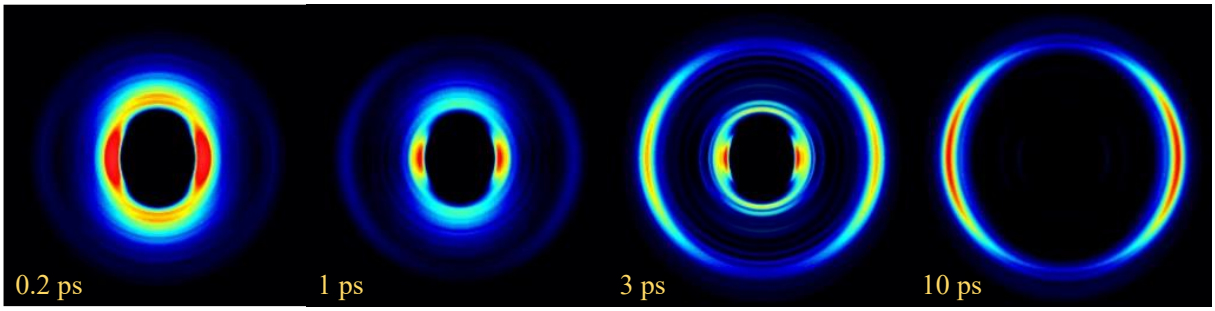

Figure 4.11. *Sequence of Abel-inverted (pBASEX) C_2H_5 images, in false color, as a function of pump-probe delay time for a pump laser center wavelength of 201.19 nm (origin of B-band) and a probe laser centered at 244 nm. The external ring is assigned to the I*($^2P_{1/2}$)+C_2H_5 channel while the inner contribution is assigned to MPI. The anisotropy evolution of the external ring is observed with the pump-probe increasing delay.*

The corresponding translational energy distribution obtained for an asymptotic time of 10 ps is depicted in figure 4.12. The available energy of C_2H_5 fragments indicated by a vertical bar in the translational energy distribution was estimated by:

$$E_{av}(C_2H_5) = \frac{m_I}{m_{C_2H_5I}} E_{av} = \frac{m_I}{m_{C_2H_5I}} [h\nu - D_0 - E_{SO}(I^*) + E_i(C_2H_5I)] \quad (4.5)$$

where E_{av} represents the total available energy, $E_{av}(C_2H_5)$ represents the available energy for the C_2H_5 fragment, $nh\nu$ the excitation photon energy, D_0 the C−I dissociation energy at 201.19 nm, 2.353 eV,[320] E_{SO}(I*) the I spin-orbit splitting, 0.943 eV for the I*,[161] $E_i(C_2H_5I)$ is the internal energy of the parent

molecule, which is considered negligible in the present experiment, and m_I and $m_{C_2H_5I}$ are the masses of the co-fragment I and the parent molecule C_2H_5I, respectively.

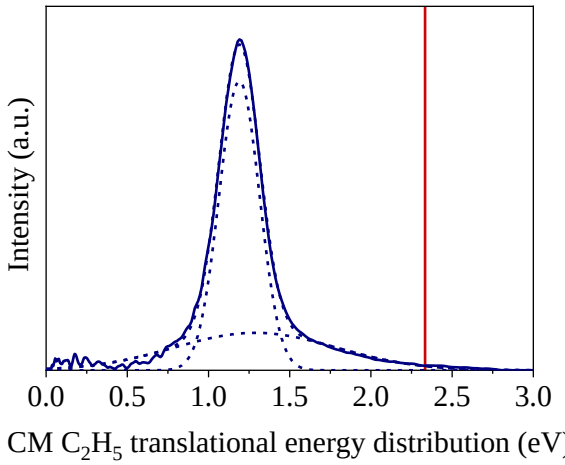

Figure 4.12. *CM translational energy distribution of the C_2H_5 fragment for an asymptotic delay time of 10 ps between the pump (201.2 nm) and probe (244 nm) lasers. The Boltzmann-type fitted contribution and the Gaussian function used to fit the contribution from the I*+C_2H_5 dissociation channel are represented by dotted lines, respectively. The red vertical line shows the available energy that could be acquired by the C_2H_5 radical in the I*+C_2H_5 channel (see text).*

The observed peak, assigned to the I*+C_2H_5 channel, is characterized by a similar energy partitioning f_{int} value of approximately 0.48. A possible second ring at a lower radius in the image, and accordingly a peak at a lower energy in the translational energy distribution, attributed to the I+C_2H_5 channel, is not observed, although it can likewise be embedded in the MPI contribution, taking into account the previously reported $\Phi^* \geq 0.9$.[323]

The contribution assigned to the I*+C_2H_5 channel in figure 4.12 was likewise isolated and analyzed as a function of the pump-probe time delay through the multidimensional fitting procedure to obtain the transient depicted in figure 4.13. By fitting the data to the equation (4.2), a reaction time of 1.30±0.10 ps was deduced, in very good agreement with the one determined from the I images (1.34±0.05 ps).

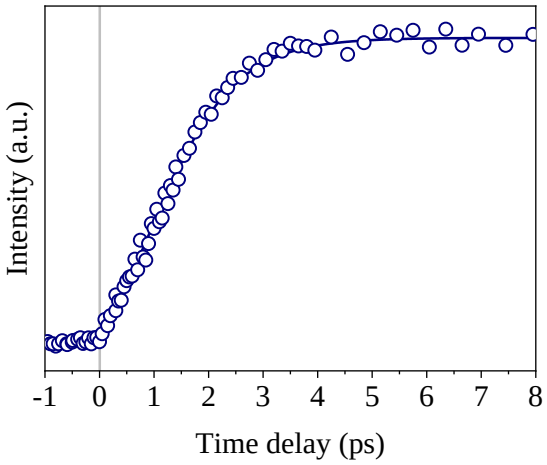

Figure 4.13. *Experimental transient (open circles) corresponding to the C_2H_5 fragment appearance after B-band excitation of C_2H_5I at 201.2 nm. The probe laser was centered at 244 nm, exploiting the (1+1) REMPI transition for C_2H_5. The time constant τ obtained for the lifetime of the excited state is 1.30±0.10 ps. The blue solid line represents the results fitted to the equation (4.2).*

The evolution of the anisotropy with the time delay was, as well, evaluated. Two anisotropy parameters, β_2 and β_4, were required to fit the angular distribution of the C_2H_5 fragments. The evolution of both anisotropy parameters over time is depicted in figure 4.14. Their temporal behavior was fitted to the equation (4.2). While the anisotropy parameter β_4 shows values around zero for all time delays, the anisotropy parameter β_2 evolves similarly to the one of I*, from around -0.9±0.1 at early times to -0.6±0.1 at long time delays. The uncertainties on the anisotropy parameters β_2 and β_4 are higher for this channel, especially for short pump-probe time delays, since the MPI signal in the center of the image contaminated the extracted angular distributions.

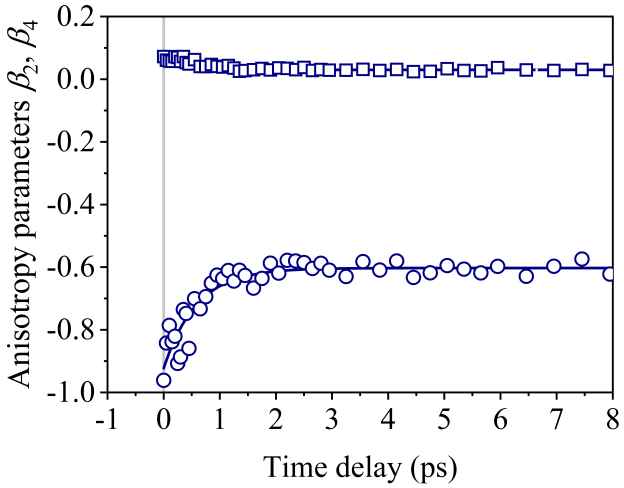

Figure 4.14. *Evolution of the anisotropy parameters, β_2 (open circles) and β_4 (open squares), resulting from fitting the angular distributions for C_2H_5 obtained from the multidimensional fit to equation (4.4), as a function of the pump-probe time delay. The blue solid line represents the fitting of the anisotropy parameters β_2 to an exponential function.*

The evolution of the anisotropy of the CH_3 fragment as a function of the time delay between the pump and probe pulses was investigated recently in CH_3I following excitation to the origin of the *B*-band.[302] The temporal evolution of the anisotropy parameters β_2, β_4 and β_6 characterizing the CH_3 angular distribution, which differed significantly from that extracted for the I* fragment, reflected the influence of CH_3 rotational angular momentum alignment and H_3C–I bending during the reaction. In the present case, the lack of anisotropy in β_4 and the resemblance in the anisotropy parameter β_2 evolution obtained for both the I* and the C_2H_5 fragments highlight the absence of significant vector correlations characterizing the dissociation, particularly at early times.

4.3.1.2. The vibronic band

4.3.1.2.1 Iodine detection

Similar time-resolved experiments were performed at an excitation wavelength of 200.08 nm, corresponding to the 18_0^1 vibronic band, employing (2+1) REMPI at 304.5 nm to detect the I fragments.

The inverted I images measured at an excitation wavelength of 200.08 nm at four selected pump-probe time delays are presented in figure 4.15. Besides the MPI signal at the center of the image, a nascent anisotropic ring is likewise assigned to the $I^*+C_2H_5$ channel. The formation of I in its ground spin-orbit state is neither observed at this excitation wavelength. The ring intensity increases with time delay, while its anisotropy slightly decreases until a plateau reached after 5 ps. It is remarkable that the intensity of the I signal is lower at this excitation wavelength despite the fact that, according to the action spectrum displayed in figure 4.3,[323] the absorption cross-section is slightly higher at the present excitation wavelength as compared to the origin of the *B*-band.

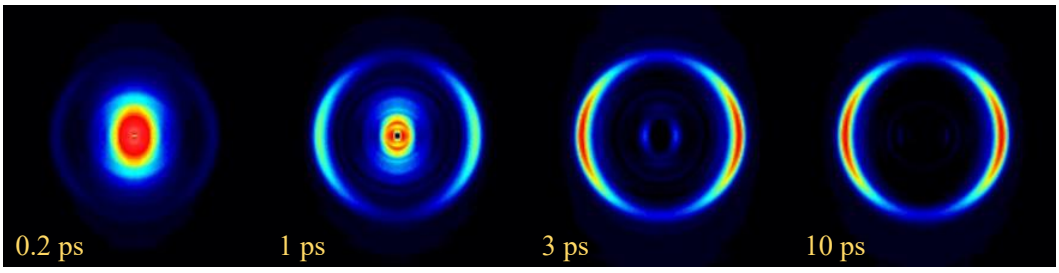

Figure 4.15. *Sequence of Abel-inverted (pBASEX) I images as a function of the pump-probe time delay for a pump laser pulse centered at 200.08 nm (18_0^1) and (2+1) REMPI detection at 304.5 nm. The external ring is assigned to the $I^*(^2P_{1/2})+C_2H_5$ channel while the inner contribution is assigned to MPI. The anisotropy evolution of the external ring is observed with the pump-probe increasing delay. Laser light polarization is along the vertical axis of the images.*

The CM I translational energy distribution for a pump-probe time delay of 10 ps is depicted in figure 4.16. The two contributions were similarly fitted, using a Boltzmann-type fitting function for the

broad contribution and a Gaussian function for the main contribution. The vertical bar indicates the available energy of the I* fragment.

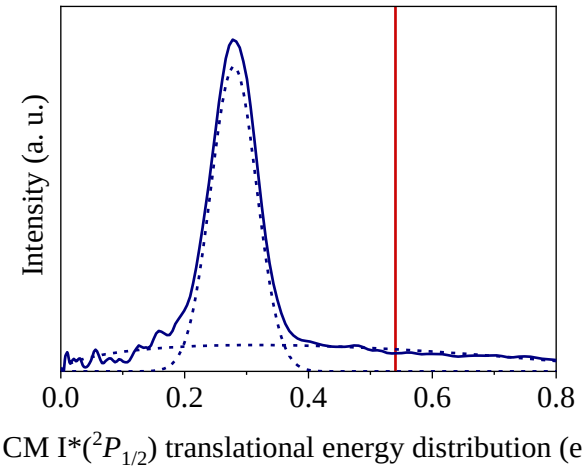

Figure 4.16. *CM translational energy distribution of the I atom for an asymptotic time delay between the pump (200.08 nm) and probe (304.5 nm) lasers (Δτ=10 ps). The Boltzmann-type fitted contribution and the Gaussian function used to fit the contribution from the I* dissociation channel are represented by dashed lines, respectively. The red vertical line shows the available energy that can be acquired by the I atom in the I*+C_2H_5 channel (see text).*

The maximum translational energy with respect to the available energy indicated by the vertical bar reflects the internal energy acquired by the C_2H_5 co-fragment. An energy partitioning f_{int} value of 0.46±0.02 was obtained, which is slightly higher than the obtained value for the 0_0^0 band (f_{int}=0.43±0.03), reflecting larger internal energy channeled into the C_2H_5 co-fragment after photodissociation at this higher excitation energy.

The corresponding transient is depicted in figure 4.17. A predissociation lifetime of 0.94±0.03 ps was obtained by fitting the resulting transient to the equation (4.2). This lifetime is significantly shorter than the one at the origin of the *B*-band. As previously reported for CH_3I, the vibrational activity of the excited C_2H_5I would be responsible for the probability enhancement of the transfer of population from the bound Rydberg 6*A*' and 7*A*" states into the repulsive states fastening the predissociation.

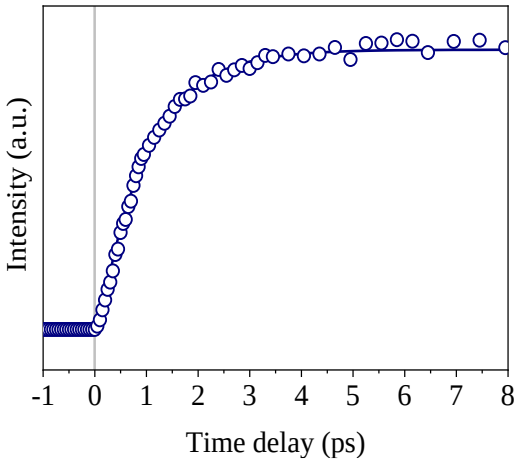

Figure 4.17. *Experimental transient (blue open circles) corresponding to the I* fragment appearance after B-band excitation of C2H5I at 200.08 nm. The probe laser was tuned at 304.5 nm, exploiting the (2+1) REMPI transition for the I* fragment. The time constant τ obtained for the lifetime of the excited state after several measurements is 0.94±0.03 ps. The blue solid line represents the fitting of the results to the equation (4.5).*

The anisotropy was similarly monitored as a function of the pump-probe time delay, and its evolution is shown in figure 4.18. The anisotropy parameter β_2 decreases with the pump-probe time delay from -0.87±0.08 at early times to -0.62±0.15, at asymptotic time delays. The decrease in anisotropy for this vibronic band with a lifetime of 0.94±0.03 ps is compatible with a rotational temperature T_{rot} of approximately 100 K. The anisotropy relaxation time obtained by fitting the results in figure 4.18 to the equation (4.4) is τ_β=1.15±0.10 ps, slightly higher than the corresponding predissociation lifetime.

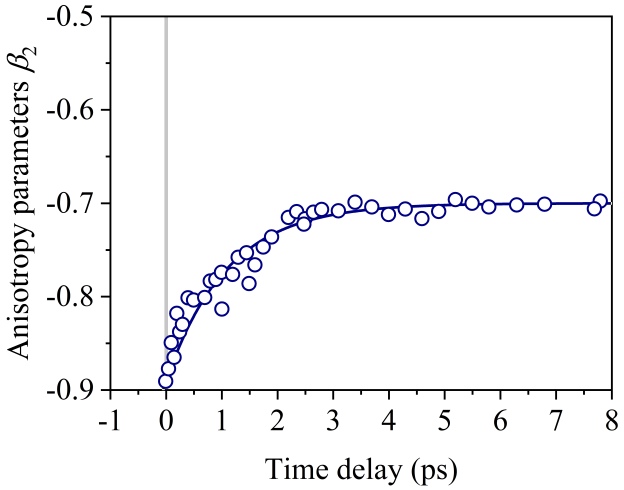

Figure 4.18. *Evolution of the anisotropy parameter, β_2 (blue open circles) resulting from fitting the angular distributions for I* obtained from the multidimensional fit to equation (4.4), as a function of the pump-probe time delay. The blue solid line represents the fitting of the results to an exponential function.*

The obtained initial β_2^{init} and final β_2^{final} anisotropy parameters are listed in table 4.2 along with the $\Delta\beta_2$ and τ_{β_2} values and compared with the corresponding CH_3I values in the 2_0^1 band.

Table 4.2. *Experimental values, derived from the I* time-resolved images, measured in the first most intense vibrationally excited band, the 18_0^1 band, including the lifetime, τ, the initial anisotropy parameter at early times, β_2^{init}, the anisotropy parameter at asymptotic time delays, β_2^{final}, and the anisotropy relaxation time, τ_{β_2}. The results are compared to the corresponding values reported for CH_3I in the 2_0^1 band.*[158]

	Reaction time τ (ps)	Initial anisotropy parameter β_2^{init}	Final anisotropy parameter β_2^{final}	Rise of anisotropy τ_{β_2} (ps)
C_2H_5I (18_0^1)	0.94±0.03	-0.87±0.08	-0.62±0.15	0.90±0.10
CH_3I (2_0^1)	0.86±0.04	-0.96±0.03	-0.61±0.05	0.75±0.10

4.3.2. Theoretical results

The electronic states of C_2H_5I resulting from *ab initio* calculations are listed in table 4.3 in terms of the vertical energy at the Franck-Condon geometry and the electronic notation in C_s symmetry. The correspondence in C_{3v} symmetry, including Mulliken's notation generally employed for methyl halides, is also indicated for their first electronic excited states. Also, the TDM as a function of the orientation axis is included. The XY plane is defined by the carbon and iodine atoms (C–C–I plane), where the Y axis lies along the C−I bond. In agreement with the properties of the C_s symmetry group, the TDM for *A*' electronic states is in the I−C−C plane, while *A*" electronic states are characterized by TDM perpendicularly oriented with respect to the I−C–C plane.

Table 4.3. *Vertical energy at the Franck-Condon geometry, symmetry in C_s, and the TDM for each axis. The X axis is located in the I-C–C plane, perpendicular to the C−I bond, the Y axis is located in the I–C–C plane, along the C−I bond, and the Z axis is perpendicular to the I–C–C plane. The correlated symmetry in C_{3v} (including the common Mulliken's notation for the A-band of CH_3I) is also indicated.*

State number	Franck-Condon energy (eV)	Correlated Symmetry (C_{3v})	Symmetry (C_s)	Transition dipole moment		
				X	Y	Z
1	0		1*A*'	0.0841	0.8029	0.0000
2	4.43	$^3Q_2$	2*A*'	0.0002	0.0017	0.0000
3	4.43	$^3Q_2$	1*A*"	0.0000	0.0000	0.0013
4	4.59	$^3Q_1$	3*A*'	0.0726	0.0022	0.0000
5	4.60	$^3Q_1$	2*A*"	0.0000	0.0000	0.0763
6	4.98	$^3Q_0$	3*A*"	0.0000	0.0000	0.0006
7	5.12	$^3Q_{0+}$	4*A*'	0.0068	0.1818	0.0000
8	5.34	$^1Q_1$	4*A*"	0.0000	0.0000	0.1730

State number	Franck-Condon energy (eV)	Correlated Symmetry (C_{3v})	Symmetry (C_s)	Transition dipole moment		
				X	Y	Z
9	5.35	$^1Q_1$	5*A*'	0.1684	0.0051	0.0000
10	6.07	$^3R_2$	6*A*’	0.0016	0.0009	0.0000
11	6.07	$^3R_2$	5*A*"	0.0000	0.0000	0.0002
12	6.12	$^3R_1$	7*A*'	0.4358	0.0553	0.0000
13	6.13	$^3R_1$	6*A*"	0.0000	0.0000	0.4663
14	6.41	$^2A_2$	7*A*"	0.0000	0.0000	0.0069
15	6.45	^4E	8*A*'	0.0887	0.0058	0.0000
16	6.46	^4E	8*A*"	0.0000	0.0000	0.0826
17	6.71	$^3R_0$	9*A*"	0.0000	0.0000	0.0008
18	6.71	$^3R_{0+}$	9*A*'	0.0341	0.0157	0.0000
19	6.77	$^1R_1$	1*A*'	0.5310	0.0693	0.0000
20	6.78	$^1R_1$	1*A*"	0.0000	0.0000	0.5356
21	8.92		11*A*'	0.0035	0.6077	0.0000
22	8.97		11*A*"	0.0000	0.0000	0.0002
23	8.97		12*A*'	0.0932	0.0282	0.0000
24	8.97		12*A*"	0.0000	0.0000	0.0953
25	9.53		13*A*'	0.1714	20.567	0.0000

Figure 4.19 shows the corresponding computed potential energy curves as a function of the C−I distance in their adiabatic representation. The electronic symmetry for relevant excited states is specified within the Franck-Condon geometry.

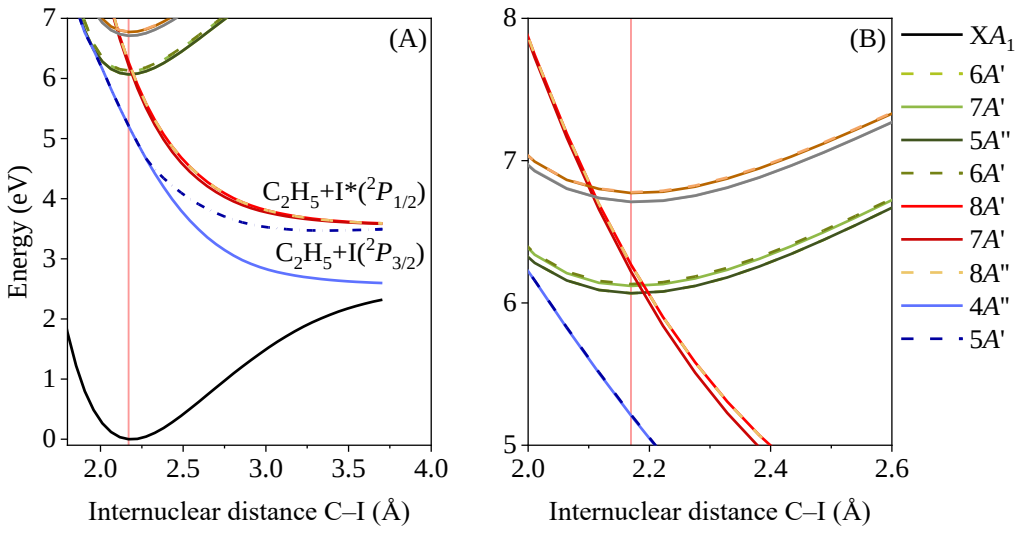

Figure 4.19. *(A) MRCI computed potential energy curves as a function of the C−I distance, considering a frozen geometry of the C_2H_5 moiety at the equilibrium geometry of the C_2H_5I molecule. (B) An expanded view of the electronic states of interest in the second absorption band. The dashed line represents the vertical excitation at the Franck-Condon geometry. The electronic symmetry of the relevant states is specified within the Franck-Condon geometry.*

The first nine electronic states, which are similar to CH_3I and other halomethanes,[225, 239] constitute the first absorption band (*A*-band). The 4*A*' state corresponding to the $^3Q_{0+}$ state in C_{3v} is characterized by the higher TDM absolute value of the *A*-band whereas the $^3Q_1$ and $^1Q_1$ states, which split into two components in C_s symmetry, the 2*A*'' and 3*A*' and the 4*A*'' and 5*A*' states, respectively, contribute mildly to the total TDM. The contribution from the 3*A*'' ($^3Q_{0+}$) as well as the [2*A*', 1*A*''] ($^3Q_2$) states, respectively, can be despised. The bound ground state correlates with the first dissociation limit, C_2H_5+I. Adiabatically, the [2*A*'', 3*A*'], 4*A*' and 4*A*'' states correlate with the I channel, while the 5*A*' state correlates with the C_2H_5+I* limit. An avoided crossing observed close to the Franck-Condon region involving the 4*A*', 4*A*'' and 5*A*' states governs the dynamics in this first absorption band. At higher energies, several Rydberg-character bound excited states lying between 6 and 7 eV are assigned to the $n(5p^I_{x,\,y})\rightarrow 6s_I$ transition. Similar to CH_3I, two pairs of Rydberg states are present around 6.1 and 6.7 eV, responsible for the *B*- and *C*- absorption bands, respectively.[225] The first pair of states corresponds to Rydberg states converging to the ground spin-orbit state of the ethyl iodide cation ($C_2H_5I^+$) while the second pair converge to the excited spin-orbit component. The Rydberg states can be observed with more clarity in figure 4.19 (B), which is an expanded view of the 5-8 eV excitation region.

Two avoided crossings located close to the Franck-Condon region are distinguished between each pair of Rydberg states and a few purely repulsive states, which correlate to the C_2H_5+I* limit. The avoided crossing around 6.1 eV is situated at a slightly longer C−I distance with respect to the Franck-Condon excitation region, while in the *C*-band, it is located at a slightly shorter distance. In table 4.3, the correlation between the electronic symmetry of these states in C_s and the corresponding symmetry in C_{3v} has also been indicated, although this assignment is exclusively valid within the Franck-Condon geometry. The [5*A*'', 6*A*'] and [6*A*'', 7*A*'] states correspond to the $^3R_2$ and $^3R_1$ Rydberg states,[225] respectively, which split into two states due to the breakdown of the C_{3v} symmetry. According to the computed TDMs, the two $^3R_2$ states are dark while the $^3R_1$ states, [6*A*'', 7*A*'] in C_s, are likely to be populated at an excitation energy around 6.12 eV (202 nm) through a perpendicular transition. Similarly, the [9*A*', 9*A*''] and [10*A*'', 10*A*'] states correspond to the upper $^3R_{0+,\,-}$ and $^1R_1$ Rydberg states, responsible for the *C*-band. The [9*A*', 9*A*''] states are also unlikely to be populated while the $^1R_1$ states, [10*A*'', 10*A*'] in C_s symmetry, are characterized by large TDMs along the X and Z axes. Finally, the three repulsive states which cross all the bound Rydberg states (7*A*'', 8*A*', 8*A*''), correlate with the $^2A_2$ and 4*E* states in C_{3v} symmetry. The A_2 symmetry transforms indeed to *A*'' in C_s while the *E* symmetry splits into two components, *A*' and *A*''. The TDMs are small, reflecting a low probability to populate them directly.

4.4. DISCUSSION

In line with previous work of the predissociation of C_2H_5I employing nanosecond VMI,[323] the experimental results presented here show a main channel resulting from the predissociation of C_2H_5I in

the *B*-band assigned to the formation of C_2H_5+I*($^2P_{1/2}$), characterized by an energy partitioning f_{int} values of ≈ 0.43 in the origin of the band and 0.46 in the vibronic level, revealing a significant fraction of the available energy channeled into ro-vibrational energy of the C_2H_5 fragment rather than into translational energy, and a predissociation lifetime τ in the picosecond timescale.

The measured lifetimes in the *B*-band are consistent with a predissociation mechanism from the initially populated 6*A*" and 7*A*' states *via* an avoided crossing with the 7*A*", 8*A*' and 8*A*" repulsive states, leading directly to dissociation into C_2H_5+I*. As observed, the lifetime decreases from 1.34±0.05 ps to 0.94±0.03 ps upon vibrational excitation with respect to the vibrationless state. The extreme sensitivity of the predissociation lifetimes to the vibrational excitation of the molecule in the *B*-band is related to the details of the non-adiabatic crossing between potential energy surface and the spatial distributions of the wave functions for each vibration level of the Rydberg state of the *B*-band. Accordingly, this lifetime decrease must reflect a more effective transfer of population *via* non-adiabatic couplings. Vibrational excitation in the CH_3 torsion mode appears to enhance the coupling between these bound and repulsive states favoring predissociation.

The results obtained in the present work for C_2H_5I and summarized in Table 4.2 are compared to the previously reported values for CH_3I in the 0_0^0 origin of the *B*-band and at the 2_0^1 band corresponding to vibrational excitation into v_2=1 (umbrella mode). The measured lifetime τ for the vibrationless Rydberg state appears to be shorter for C_2H_5I as compared to CH_3I. Since no other competing mechanism may be involved, this reflects that predissociation turns out to be more favorable for an increasing structural complexity. According to the reported potential energy curves for both molecules, the curve crossing is similarly located within the Franck-Condon region. Increasing the radical size from CH_3 to C_2H_5 implies a breakdown of symmetry from C_{3v} to C_s, which might allow a larger coupling between the initially populated bound states and the repulsive states, leading to dissociation.

In contrast, the lifetime measured following excitation at the vibronic band appears to be slightly longer for C_2H_5I in comparison to CH_3I, *i.e.*, 0.94±0.03 ps versus 0.86±0.04 ps. As previously reported for CH_3I, the vibrational activity of the excited parent molecule can strongly modify the predissociation lifetime depending on the excited vibrational mode. Excitation in the C−I stretching mode (ν_3) leads to a lifetime four times longer, while excitation into the umbrella mode (ν_2) permits to shorten twice the reaction time with respect to the vibrationless excited state. A qualitative explanation for this extreme sensitivity to the vibrational excitation was reported based on the spatial structure of the vibrational wave function related to the curve crossing position located within the Franck-Condon region.[158] For v_3=1, the wave function is indeed characterized by a node in the C−I dimension near the curve crossing position, which can imply a lower coupling and, therefore a slower predissociation. The results obtained here following excitation of C_2H_5I into the CH_3 torsion mode (ν_{18}) of the Rydberg state can be compared

to those for CH_3I excited into the umbrella mode ν_2. Both vibrational wave functions are likely to present a maximum amplitude within the Franck-Condon region and close to the C−I equilibrium distance since these modes are not associated with any C−I bond activity.

The initial anisotropy β_2^{init} values, summarized in table 4.1 for both excitation wavelengths, are consistent with the initial excitation of the 6*A*" and 7*A*' states. These two states are indeed characterized by TDMs mostly in the two axes perpendicular to the C−I bond. An expected initial anisotropy parameter, β_{init}, was estimated as:

$$\beta_{init} = a_{\perp}\beta_{\perp} + a_{\parallel}\beta_{\parallel} \tag{4.6}$$

where $\beta_{\perp}$ and $\beta_{\parallel}$ are the limit values for completely perpendicular and parallel transitions, -1 and 2, respectively.

The coefficients represent the corresponding weights extracted from the TDMs computed as a function of the axis (see table 4.3). In particular, $a_{\perp}$ represents the ratio between the TDM along the X and Z axes (defined as perpendicular with respect to the C−I bond) and the total TDM for excitation into the 6*A*" and 7*A*', while $aa_{\parallel}$ is the ratio between the TDM along the Y axis (defined as parallel to the C−I bond) and the total TDM. An estimated value of the initial anisotropy parameter β_{init} of -0.81 was found in good agreement with the initial measured value of -0.89±0.05 for the band origin.

Compared to CH_3I, the values are slightly less anisotropic: the breakdown of the C_{3v} symmetry slightly modifies the TDM, and a minor component parallel to the C−I bond, *i.e.*, a minor probability for a parallel transition, arises.[323]

A rather similar asymptotic anisotropy parameter β_2^{final} is measured for both molecules. This loss of anisotropy generally reflects a lifetime of the same order of magnitude as the rotational period of the molecule and is indeed attributed to the rotational motion of the excited parent molecule before dissociation. However, the measured asymptotic anisotropy parameter β_2^{final} differs remarkably from the one recently reported employing nanosecond VMI.[323] An anisotropy parameter β_2=-0.23 was similarly obtained for CH_3I at the 0_0^0 band employing nanosecond lasers in contrast to -0.5 in femtosecond experiments. This was attributed to the broad spectral bandwidth inherent to femtosecond pulses, which implies a minor excitation of the repulsive ^4E state belonging to the *A*-band, which is characterized by a perpendicular TDM and undergoes a direct dissociation into the I* channel. A small contribution of direct dissociation (estimated to be ≤ 0.002) is enough to lower the measured average asymptotic anisotropy β_2 value. In the present case, the difference is significantly higher, from an asymptotic value of β_2^{final}=-0.59±0.09 in the present experiments to β_2=-0.1 when employing nanosecond lasers. The broad

spectral bandwidth of femtosecond pulses can imply a higher contribution of direct dissociation in C_2H_5I. Comparing the measured I* action spectrum for both molecules,[158, 160] the relative intensity of the background with respect to the peak assigned to the 0_0^0 origin of the *B*-band is indeed higher in C_2H_5I.

The relaxation times τ_β, extracted from the evolution of the anisotropy with time delay, are, for both molecules, in the timescale than the lifetime, but slightly lower in value. Also, the predissociation of C_2H_5I at 200.08 nm, which is faster, has a more negative anisotropy parameter at asymptotic time delays, which indicates that the variation in anisotropy is highly related to the rotation of the molecule in the excited state before predissociation. This observation could help to rule out the presence of isoenergetic channels to the main one described. In the case of the excitation of CH_3I 3_0^1 band at 199.2 nm, which presented a slower predissociation, a more negative asymptotic value of β_2 was observed. To explain this feature, it was considered that this anomalous behavior of the anisotropy was due to the presence of an additional fast channel, leading to I*($^2P_{1/2}$) with the same content in kinetic energy but resulting from direct absorption to the dissociative states of the *A*-band, instead of through predissociation in the *B*-band. This fast minor dissociation pathway would be perpendicular, with no temporal changes, distorting the measures of angular dependence.

4.5. CONCLUSIONS

In this chapter, the most relevant results from femtosecond time-resolved velocity map ion imaging experiments carried out on the second absorption *B*-band of C_2H_5I at 201.19 and 200.08 nm probed in real-time by (2+1) REMPI of I fragments or by (1+1) REMPI of C_2H_5 fragments are presented. In both cases, the observed process is a typical electronic predissociation driven by, in principle, a single photodissociation pathway leading to the formation of C_2H_5 fragments with significant internal energy in correlation with I*($^2P_{1/2}$) similarly to what is found in CH_3I.[155, 158]

A lifetime of 1.34±0.05 ps was obtained upon the excitation of the origin of the *B*-band. Compared with the lifetime found for CH_3I (1.52±0.05 ps), a more favorable dissociation for an increasing alkyl chain structure due to the larger coupling between the Rydberg and repulsive states involved in the predissociation is found. A decrease in the lifetime (0.94±0.03 ps) of the vibrationally excited state of the Rydberg (18_0^1) indicates an enhanced probability of the transfer of population from the bound Rydberg states into the repulsive states leading to a faster dissociation upon vibrational excitation, similarly to CH_3I in the 3_0^1 band.[158]

The perpendicular character of the transition was determined through real-time detection of the anisotropy observed in the I and C_2H_5 atom images. The initial anisotropy value of β_2=-0.89±0.05 for the origin of the band and -0.87±0.08 for the vibronic transition, is in both cases, consistent with a

perpendicular transition compatible with the excitation to the [6*A*", 7*A*'] excited states with a minor component oriented parallel to the C−I bond.

The initial anisotropy is lost over time due to molecular rotation before dissociation and is compatible with a rotational temperature of the parent molecule of about 100 K. This temporal dependence of anisotropy in C_2H_5I is consistent with that previously reported for CH_3I predissociation in the *B*-band.[155-158]

Chapter 5 – Structural dynamics effects on the electronic predissociation of alkyl iodides

5.1. INTRODUCTION

Plenty of studies on the photodissociation dynamics of alkyl iodides and substituted alkyl iodides, especially in the *A*-band, have been carried out because, besides serving as model systems for studying polyatomic fragmentation,[200, 203, 230, 322, 332-338] these type of compounds offer a unique opportunity to evaluate several of the key factors that affect photodissociation dynamics such as radical size, substitution and structure (primary, secondary, and tertiary).

The absorption maximum in the first absorption band for linear alkyl iodides is around 260 nm, with a slight bathochromic shift for molecules with branching structure, indicating that the characteristics of the absorption process and subsequent photodissociation dynamics are very similar for all molecules. This was also observed by Gedanken *et al.* with the already mentioned MCD experiments.[191] As the case of methyl iodide (CH_3I), 70-80 % of the oscillator strength near the maximum absorption of the *A*-band is governed by the $^3Q_0$ state, or its equivalent, for all the studied molecules. The most studied dissociation mechanism for alkyl iodides begins with the absorption of a photon at around 268 nm. Afterward, the wave packet initially created in the $^3Q_0$ evolves until reaching the conical intersection with the $^1Q_1$ state, where part of it is transferred to this state. The wave packet that propagates on the $^3Q_0$ surface leads to the formation of the alkyl radical in correlation with I*($^2P_{1/2}$), in different ro-vibrational states of the radical, while the wave packet that propagates on the $^1Q_1$ surface leads to the formation of the alkyl radical in correlation with I($^2P_{3/2}$), also in different ro-vibrational states of the radical.

From a theoretical point of view, CH_3I is assumed to be a pseudo-triatomic molecule (X–C–I), being X a pseudo-atom of hydrogen (H) located at the CM of the three H atoms at a fixed distance C–X on the C_{3v} axis.[339] Photodissociation studies of some alkyl iodides carried out by Hale *et al.*[340] and Phillips *et al.*[341] employing resonant Raman spectroscopy, showed a long progression of stretch-deformation combination bands, additional to overtone progression of the C−I bond stretch mode ($\nu_3 \approx 530$ cm^{-1}), which is typically found in the Raman spectra of CH_3I. This suggests that the reaction coordinate loses its one-dimensional character to become a multidimensional combination of different stretch and deformation modes as the size of the hydrocarbon chain (R) increases. In this way, the

approximation that is assumed for CH_3I is no longer valid for alkyl iodides. This feature awoke the interest of numerous researchers in studying the influence of the radical on the ratio between the two existing reaction channels arising from the C–I bond cleavage, *i.e.* R+I($^2P_{3/2}$) and R+I*($^2P_{1/2}$) and on the angular and internal energy distributions of the alkyl radicals, by exciting the different alkyl iodides around the maximum of the first absorption band.[200, 203, 230, 231, 233, 342, 343]

Complete studies of a series of alkyl iodides include the pioneering work of Riley and Wilson.[203] They studied by PTS the photodissociation of CH_3I, ethyl iodide (C_2H_5I), *n*-propyl iodide (*n*-C_4H_7I) and isopropyl iodide (*i*-C_4H_7I) at 266.2 nm, to evaluate the process of unimolecular break-up of electronically excited molecules and to determine the energy partition between internal and translational energy of the resulting fragments. Results reveal a clear trend toward increased internal excitation with the size of the alkyl radical, which is an example of the effect of structure on the dynamics of molecular processes. The experimental findings were discussed based on dynamic models for energy partitioning in molecular photodissociation; a statistical model suitable for long-lived excited parent molecules and an impulsive model[344] best suited for a prompt-dissociation mechanism, as the case. The measured results fell in between the predictions of direct impulsive models based on "rigid" and "soft" radicals, and thus a possible picture for the photodissociation of the alkyl iodides is “a quasi-diatomic excitation of the C−I bond, followed by the recoil of the iodine (I) atom and a partially deformable alkyl radical”.

First studies regarding the determination of the quantum yield Φ* as a function of the structural complexity of alkyl iodides and their fluorinated and deuterated analogs following broad-band photolysis were performed by Donohue and Wiesenfeld.[322] Their results revealed a clear dependence of the structure of the alkyl group, those possessing secondary or tertiary α-carbon (C) atoms displaying the lowest yields.

Wavelength-dependent quantum yields Φ* were later reported for a series of linear as well as branched alkyl iodides by Uma *et al.*[293, 294, 345] While the dynamics of I* production in linear alkyl iodides was successfully explained using the well-known one-dimensional classical Landau-Zener model, [200] the same model could not be employed to explain the I*/I branching ratio in the branched iodides as a function of wavelength as well as the observed I* yields in CH_3I and deuterated methyl iodide (CD_3I), with almost the same potential energy surfaces.[346] This brought out the importance of the multidimensional nature of the potential energy surfaces involved in the dynamics.[232]

Contrary to what happens in the first absorption band, the study of this type of compounds is almost non-existent in the second absorption band and much less time-resolved studies. The most part is focused on CH_3I predissociation dynamics[155-158, 160, 299, 301, 313] whereas a few on C_2H_5I.[323, 347] It is expected that this type of compounds has a predissociation mechanism very similar to the one observed in CH_3I and C_2H_5I, based on the dissociation into a radical fragment In correlation with I* through a

more or less coupled dissociative state with a Rydberg bound state. The specific mechanism characteristics are expected to be dependent on the linear and/or branched structure.

In line with the time-resolved photodissociation studies done by Corrales *et. al*,[213] in this chapter, the predissociation dynamics of a series of linear (CH_3I, C_2H_5I, *n*-propyl iodide (*n*-C_3H_7I), *n*-butyl iodide (*n*-C_4H_9I)) and branched (isopropyl iodide (*i*-C_3H_7I) and *t*-C_4H_9I) alkyl iodides are studied employing femtosecond VMI following excitation on the second absorption band (*B*-band) to study the correlation between chemical structure and predissociation dynamics. This chapter can be understood as a continuation of the experiments presented in the previous chapter in which the chain size is systematically increased to evaluate the structural influence (increasing the size and/or branching of the alkyl chain) on the observed dynamics.

The time-resolved images for the I atoms are reported and analyzed to extract electronic predissociation lifetimes and the temporal evolution of the anisotropy due to the rotation of the parent molecule before dissociation. Experimental findings are complemented by *ab initio* calculations of the potential energy curves as a function of the C−I distance to discuss the predissociation mechanism based on structural effects on the predissociation reaction. Besides, the evolution of the anisotropy as a function of the pump-probe time delay for I* fragments is discussed in terms of the parent rotational temperature, related to the moments of inertia of compounds of increasing complexity.

5.2. METHODOLOGY

5.2.1. Experimental methodology

5.2.1.1. Laser configuration and optical assemblies

Methodological details of the experiments corresponding to the study of time-resolved predissociation dynamics of a series of linear and branched alkyl iodides in the *B*-band, using velocity map ion imaging in combination with resonant ionization of the free fragments I($^2P_{3/2}$), I*($^2P_{1/2}$) through (2+1) REMPI are in here described. Figure 5.1 displays the experimental setup employed for the experiments presented in this chapter.

For the accomplishment of time-resolved predissociation dynamics of linear and branched alkyl iodides in the second absorption band, a tunable pump laser centered around 201 nm was required. In table 5.1, the specific wavelengths selected to excite each molecule are indicated. In the case of linear alkyl iodides, the excitation wavelengths correspond to their origin of the *B*-band, and in the case of branched alkyl iodides, it corresponds to specific intense absorption maxima close to the origin of the

band since the laser could not be tuned to the corresponding 0_0^0 transitions, which are well shifted to the red.[348]

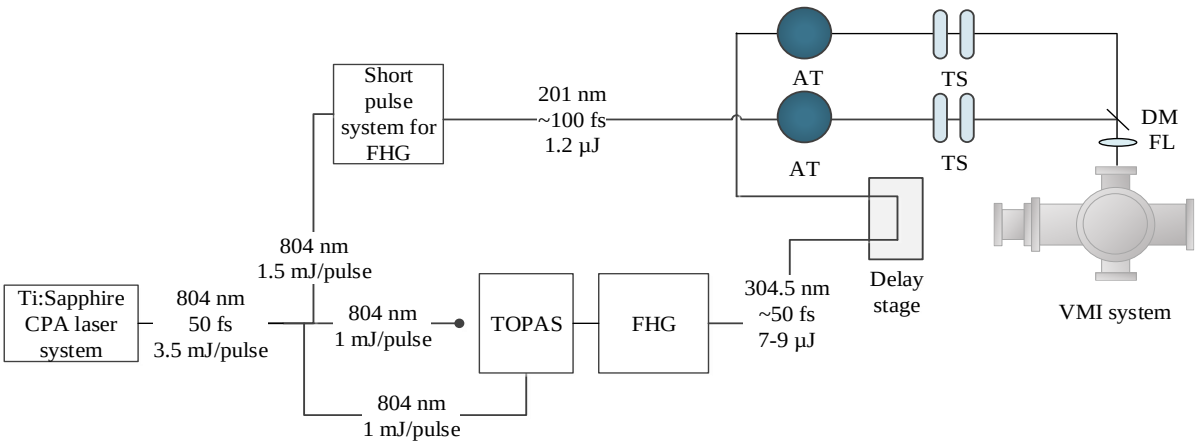

Figure 5.1. *Experimental setup for time-resolved predissociation dynamics of linear and branched alkyl iodides in the second absorption band at 201 nm employing femtosecond laser pulses and velocity map ion imaging. The laser system, the TOPAS, and the short pulse system for FHG are represented on the left side. Along the layout, several optical elements such as a dichroic mirror (DM), telescopes (TS), power attenuators (AT), the probe linear translational stage, the final focusing lens (FL) and the wedge (W) are distinguished. The VMI machine is located in the lower right area of the figure. The detection system is arranged perpendicular to the plane of the paper and the gas inlet (off-axis configuration).*

Table 5.1. *Excitation wavelengths employed for the study of a series of linear (CH_3I, C_2H_5I, n-C_3H_7I, n-C_4H_9I) and branched (i-C_3H_7I and t-C_4H_9I) alkyl iodides. For the linear molecules, the wavelength corresponds to the origin of the B-band, while for the branched alkyl iodides, it corresponds to specific vibronic transitions.*[349]

	Excitation wavelength (nm)	
	Origin of *B*-band	Vibronic excitation
CH_3I	201.19	--
C_2H_5I	201.19	--
n-C_3H_7I	201.12	--
n-C_4H_9I	201.18	--
i-C_3H_7I	--	201.06
t-C_4H_9I	--	201.18

The probing of the reaction was accomplished through (2+1) REMPI of I*($^2P_{1/2}$) fragments at 304.5 nm (see section 2.1.4.6.1), allowing the measurement of the reaction times corresponding to the breakage of the C−I bond where I*($^2P_{1/2}$) is produced in correlation with molecular fragments in different vibrational states.

For this purpose, the output laser pulses from the Spitfire regenerative amplifier (804 nm laser pulses, 3.5 mJ/pulse, 50 fs pulse duration, 1 kHz repetition rate) were employed. Around 1.5 mJ/pulse was driven to the FHG setup based on transmissive optics to produce tunable 201 nm laser pulses with output energy of 1.4 μJ/pulse and an FWHM of ~0.3 nm. The 304.5-306 nm probing radiation was obtained from the TOPAS, pumped by around 1 mJ/pulse. The TOPAS signal was centered at 1210 nm and then two-step frequency-doubled to produce this radiation with output energy of 7-9 μJ, which is then sent to the Newport linear translation stage. As in other experiments, both lasers were recombined in the final dichroic mirror, and later, they were focused inside the ionization chamber employing a 25 cm focusing lens. The output polarization of the radiation from TOPAS was vertical, so it was rotated from vertical to horizontal using an achromatic tunable half-wave plate.

The intensities chosen for the pump and probe pulses were around $1.5 \cdot 10^{10}$ and $2 \cdot 10^{11}$ W/cm^2, respectively.

5.2.1.2. Molecular beam conditions and detection system

For the realization of the present experiments, CH_3I (Sigma Aldrich, 99 %), C_2H_5I (Sigma Aldrich, 99 %), *n*-C_3H_7I (Sigma Aldrich, 99 %), *n*-C_4H_9I (Sigma Aldrich, 99 %) and branched alkyl iodides; *i*-C_3H_7I (Sigma Aldrich, 99 % copper stabilized) and tertbutyl iodide (*t*-C_4H_9I) (Sigma Aldrich, copper stabilized 95 %) were used employing glass bubblers at room temperature, except for CH_3I which was cooled down to 0 ºC with an ice bath due to its vapor pressure at room temperature. In the case of *t*-C_4H_9I, the experiments were done using an opaque steel bubbler since it is photosensitive. The molecular beams were generated by expanding the vapors with helium (He) (Air Liquid, 99.999 %) as carrier gas at 1.5-2 atm backing pressure, thus formed by a mixture of about 5 % alkyl iodide and 95 % carrier gas through the piezoelectric valve. Typical working pressures in the ionization chamber highly depended on the measured compound but ranged around 10^{-6}-10^{-5} mbar. The effective absorption cross-section of these compounds decreases with the increasing alkyl chain, so keeping the same conditions, the observed signal decreased accordingly. The experimental conditions were adjusted on the fly to obtain similar signal levels. Typical valve apertures were set ranging between 35-40 μs, and the applied voltage to the piezoelectric material was ~ 300 V.

Due to the same reason as in the C_2H_5I experiments, the delay between the gas pulse and the laser pulse was set such that its interaction occurs in the edge area of the gas pulse, generating fewer ions signal but originated from warmer parent molecules to avoid the presence of clusters in the molecular beam.

The monitoring of the photodissociation process was carried out by detecting the I^+ fragment in the TOFMS configuration. A $V_{extractor}/V_{repeller}$ ratio of 0.76 was maintained in the ion extraction system to ensure VMI conditions. In this case, the calibration of the apparatus was performed by using the known KER of the $CH_3(\nu=0)+I^*(^2P_{1/2})$ and $CH_3(\nu_1=1)+I^*(^2P_{1/2})$ channels from 201.19 nm photodissociation of CH_3I.[155]

According to the TOF mass spectra presented in figure 5.2, the arrival at the I^+ ion detector occurred 8.9 μs later than the arrival of the laser pulse at the interaction area, and therefore a temporary gate was used in the MCP centered at 8.9 μs with 200 ns of temporal width. The deflector plates were not used in the present case as they were not operative at the time of doing the experiments.

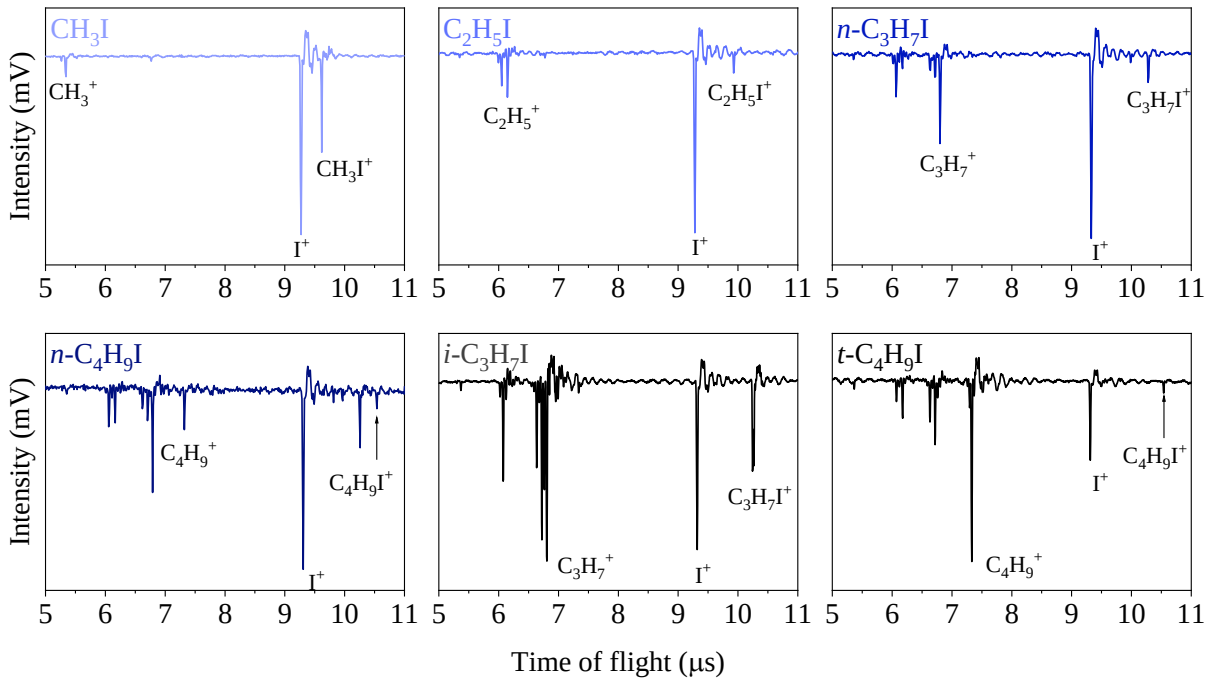

Figure 5.2. *Pump-probe TOF mass spectrum of linear (CH_3I, C_2H_5I,* n-*C_3H_7I, n-C_4H_9I) and branched alkyl iodides (i-C_3H_7I, t-C_4H_9I) studied in the present work with TOF time base (as measured in the digital oscilloscope). Pump pulse centered at ~201 nm, probe pulse centered at 304.5 nm, and time delay settled at 10 ps (asymptotic conditions). The different peaks are assigned to the different parent and fragment ions as indicated. Not all fragments are labeled for clarity.*

The determination of the time zero and the cross-correlation were performed by *in situ* measurements of the (1+2') REMPI transient for xenon (Xe). The cross-correlation function provided a value of 150 fs.

5.2.2. Absorption spectra

The absorption spectra shown in the present chapter were measured using the Fourier Transform Spectrometer (FTS),[350] one of the permanent endstations of the VUV beamline DESIRS[351] at the SOLEIL synchrotron radiation source. The FTS covers a large UV-VUV spectral range from 4 to 30 eV, with a line width of 0.08 cm^{-1} on a large spectral window, $\Delta E/E$=7 %.[352] The complete descriptions of the beamline and experimental setup can be found in references [352, 353]. The spectra were measured by Dr. Nelson de Oliveira, member of the DESIRS beamline directed by Dr. Laurent Nahon, as part of the experimental campaign entitled "High-resolution absorption spectra of alkyl iodide molecules" in collaboration with Dr. Luis Bañares group. These spectra have not yet been published.

5.2.3. Theoretical methodology

Ab initio MRCI electronic structure calculations of the ground and excited potential energy curves, including spin-orbit, were performed with MOLPRO (Version 2009.1) for the four linear alkyl iodides.[277] All the calculations were performed in the C_s symmetry point group.

Two sets of calculations were performed employing two different basis sets. A first set was carried out employing the aug-cc-pVDZ of Dunning for the C and H atoms, while for I, a 46 electrons Dirac-Fock effective core potential (ECP) accounting for spin-orbit couplings was used in addition to a basis set for the seven remaining electrons composed of [2*s*, 3*p*, 2*d*, 1*f*] with additional diffuse [*s*, *p*] functions for a total of [3*s*, 4*p*, 2*d*, 1*f*]. In the second set, the ANO-TZP basis set[267] was employed with a supplementary monocentric basis located in the center of charge of the cationic molecule. The center of charge was estimated in the ground state of the cation using the Mulliken charges provided by a previous UHF calculation. This monocentric basis, employed to describe the *s* diffuse orbital accurately, is constructed from an even-tempered Gaussian basis with twenty-two exponents following the progression $\alpha_n=\alpha\cdot\beta^{(n-1)}$, where α=0.01 and β=1.46.[328] To remove linear dependencies, the basis was contracted to sixteen functions. In the two calculations, the active space contains six electrons in five orbitals (bonding and antibonding for the C−I bond, two lone pairs on the I atom, and a diffuse *s* Rydberg orbital). A total number of thirteen states were included in the state average, including five $^1A'$, two $^1A''$, four $^3A'$ and two $^3A''$. A regular Douglas-Kroll Hamiltonian[268-270] and the AMFI approximation[271] were employed to take into account relativistic effects.

For all molecules, the geometry was optimized and the frequencies were calculated at the single-state CASTP2 level of theory[279, 329] for the ground electronic state using analytical gradients and, thus, the values for the three moments of inertia were obtained. The final one-dimensional potential energy curves, where the radical moiety was frozen at the Franck-Condon geometry, were obtained at MRCI,[282] including the spin-orbit coupling in a perturbative modified frame,[330] *i.e.*, the spin-orbit coupling

between the electronic states calculated for the different spin multiplicities is evaluated, and the resultant matrix is diagonalized, mixing the different multiplicities. Comparable potential energy curves were obtained in both calculations.

The calculations were performed by Dr. Jesús González-Vázquez and Dr. Alexandre Zanchet.

5.3. RESULTS

5.3.1. Experimental results

The gas-phase high-resolution absorption spectra for all the studied molecules are reported in figure 5.3. The excitation wavelengths for each molecule are also indicated. For linear molecules are assigned to the 0_0^0 transition of the *B*-band, according to the early work of Boschi *et al.*[354] In contrast, for the branched *i*-C_3H_7I, the selected wavelength is tentatively attributed to the vibronic band associated with the C−I stretching mode (or to the 0_0^0 transition of the *C*-state),[348] while for *t*-C_4H_9I, it is assigned to the 6_0^1 vibronic transition of the *B*-state, *i.e.*, the C−C stretching mode (806 cm^{-1} in the ground state).[355]

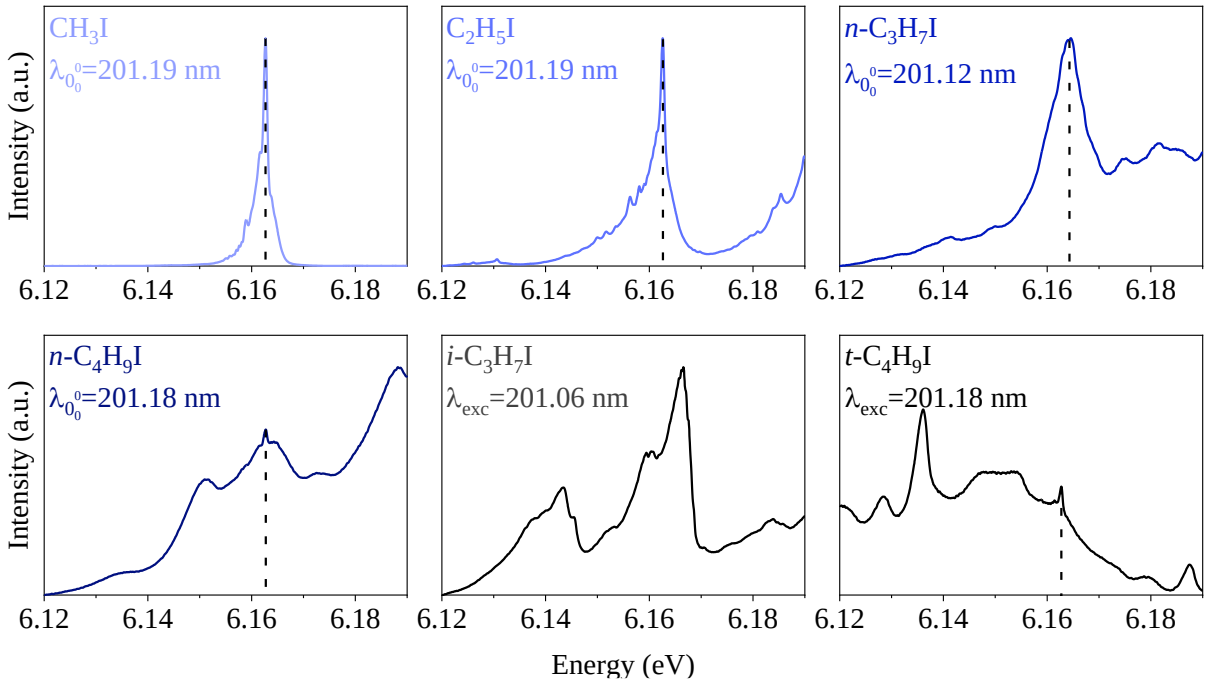

Figure 5.3 *Absorption spectra of the series of linear (CH_3I, C_2H_5I, n-C_3H_7I, n-C_4H_9I) and branched (i-C_3H_7I, t-C_4H_9I) alkyl iodides investigated in the present work measured using the FTS of VUV beamline DESIRS at the SOLEIL synchrotron radiation source.[349] The excitation wavelengths employed are indicated in each panel and highlighted by a vertical dashed line. For the linear molecules, this wavelength corresponds to the 0_0^0 origin of the B-band.[354] For the branched alkyl iodides, i-C_3H_7I, t-C_4H_9I, the wavelengths corresponds to specific vibronic transitions since the laser could not be tuned to the corresponding 0_0^0 transitions, which are well shifted to the red.*

Figure 5.4 shows a series of Abel inverted images of the I fragment from the photodissociation of all molecules excited at ~201 nm (pump) and detected *via* (2+1) REMPI at 304.5 nm at an asymptotic time delay of 10 ps, so that the radical fragment and the I atom are considered free (non-interacting) fragments.

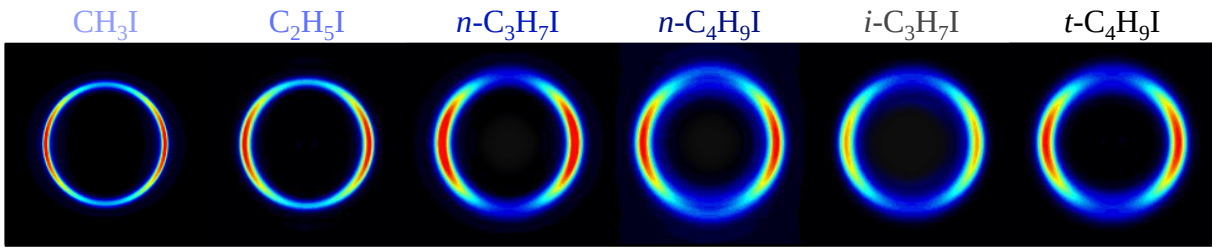

Figure 5.4. *Abel-inverted I images measured in femtosecond pump-probe velocity map imaging experiments for selected linear (CH_3I, C_2H_5I, n-C_3H_7I, n-C_4H_9I) and branched alkyl iodides (i-C_3H_7I, t-C_4H_9I) following excitation at ~201 nm (pump, see table 5.1). I* fragments are detected by (2+1) REMPI using a probe laser pulse centered at 304.5 nm. The time delay is fixed at 10 ps. In the images, the radius is proportional to the translational energy of the I fragment. The polarization of the pump and probe lasers is horizontal.*

Although the REMPI scheme at 304.5 nm allows the simultaneous detection of both I and I* fragment spin-orbit states, a single perpendicular ring, attributed to the R+I* dissociation channel, is observed in all images. This ring becomes broader as the size of the molecule increases. To discard the formation of I, the same images were measured by a (2+1) REMPI at 306 nm for the selective detection of I* yet turned out to be identical to the ones recorded at 304.5 nm. Therefore, the quantum yield Φ* does not seem to present significant changes as a function of the size of the molecule, its value being close to unity in all cases.[158, 161, 356, 357]

The corresponding total translational energy distributions obtained from the angular integration of the images are depicted in figure 5.5. The abscissa axis was converted from CM I translational energy to total translational energy by employing the mass factor m_{RI}/m_R, where RI is the mass of the molecule and R is the mass of the radical. The vertical bar displayed in each graph indicates the available energy E_{av} for each R+I* dissociation channel given by:

$$E_{av} = h\nu - D_0 - E_{SO}(\mathrm{I}^*) + E_{int}(\mathrm{RI}) \tag{5.1}$$

where $h\nu$ is the excitation photon energy, D_0 is the C–I dissociation energy, $E_{SO}(\mathrm{I}^*)$ is the I spin-orbit splitting, 0.943 eV for the I*,[161] and $E_{int}(\mathrm{RI})$ is the internal energy of the parent molecule RI, which is considered negligible in the present work. Dissociation energies for each molecule, as well as estimated available energies for the I* channel, are listed in table 5.2.

Table 5.2. *Experimental C–I dissociation energies, D_0 and corresponding available energies for the I* channel of the studied linear (CH_3I, C_2H_5I, n-C_3H_7I, n-C_4H_9I) and branched alkyl iodides (i-C_3H_7I, t-C_4H_9I)*

	Dissociation energy D_0 (eV)	Available energy E_{av} (eV)
CH_3I	2.41[192]	2.81
C_2H_5I	2.35[319]	2.87
n-C_3H_7I	2.36[229]	2.86
n-C_4H_9I	2.34[231]	2.88
i-C_3H_7I	2.30[229]	2.93
t-C_4H_9I	2.21[231]	3.01

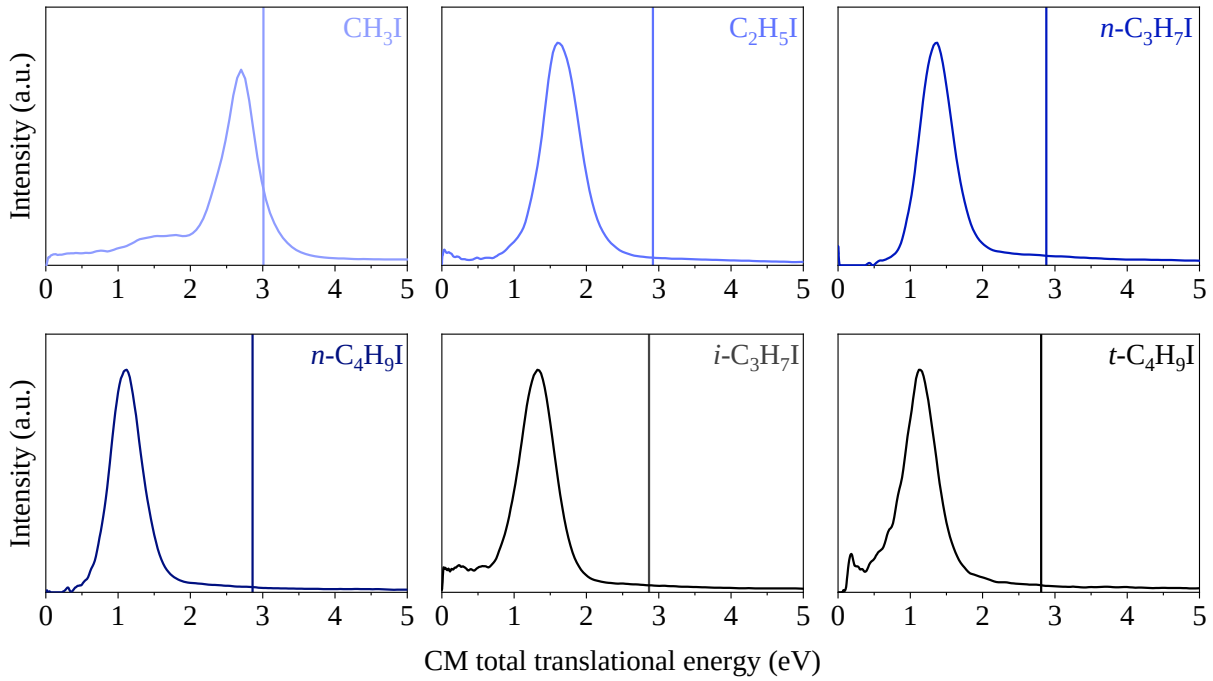

Figure 5.5. *CM total translational energy distributions obtained from the angular integration of the corresponding inverted images depicted in figure 5.4, for the studied linear (CH_3I, C_2H_5I, n-C_3H_7I, n-C_4H_9I) and branched alkyl iodides (i-C_3H_7I, t-C_4H_9I) studied in the present work. The solid vertical lines correspond to the available energy for the I* channel, listed in table 5.2.*

For all molecules, a single Gaussian-type broad peak is observed in agreement with the images. The peak is characterized by a similar considerable FWHM for all molecules. The CM I translational energy distributions present a peak that becomes broader with the size of the molecule, accounting for the mass factor.

In contrast to CH_3I, a significant shift between the available energy and the maximum translational energy is observed for all linear and branched alkyl iodides reflecting the internal energy acquired by the radical co-fragment, since I* is an atomic species. According to the energy partitioning f_{int} values listed in table 5.3, as the size of the linear radical R increases, and thus the vibrational degrees

of freedom, a larger fraction of the available energy is released into internal energy despite translational motion. The branched *i*-C_3H_7I presents a remarkably higher energy partitioning f_{int} value compared to the linear *n*-C_3H_7I, in contrast to *n*-C_4H_9I and *t*-C_4H_9I, characterized by a similar energy partitioning f_{int} values.

Table 5.3. *Experimental fraction of the available energy released into internal energy of the radical R, f_{int}, for the studied linear (CH_3I, C_2H_5I,* n-*C_3H_7I, n-C_4H_9I) and branched alkyl iodides (i-C_3H_7I, t-C_4H_9I). Uncertainties for the energy partitioning f_{int} values are around 10 %.*

	Energy partitioning f_{int}
CH_3I	0.01
C_2H_5I	0.44
n-C_3H_7I	0.47
n-C_4H_9I	0.60
i-C_3H_7I	0.56
t-C_4H_9I	0.61

The evolution of the intensity of the I fragment images as a function of the pump-probe time delay was monitored to obtain the predissociation lifetimes. The main contribution was isolated by using a multidimensional fitting procedure[166] and integrated as a function of time to obtain the transients shown in figure 5.6. The transient was fitted to a rising exponential convoluted with the temporal response function described by:[158, 166]

$$S(t) = A\exp\left(-4ln2\left(\frac{t}{\tau_{cc}}\right)^2\right)\otimes\left[\left(1-e^{-\frac{t-t_0}{\tau}}\right)H(t-t_0)\right] \qquad (5.2)$$

where τ is the predissociation lifetime of the studied molecule dissociating into I*+R, t_{cc} is the instrumental response function time, t_0 is the time of pump-probe temporal overlap, and A is an amplitude factor. $H(t)$ is the Heaviside step function, for which $H(t < 0)=0$ and $H(t > 0)=1$.

The lifetimes τ derived from this method are summarized in table 5.4. The obtained lifetime decreases considerably as the size of the linear molecule increases, leveling off for *n*-C_4H_9I. In contrast, the lifetimes are considerably longer for the two branched molecules, although diminishing significantly for *t*-C_4H_9I compared to *i*-C_3H_7I.

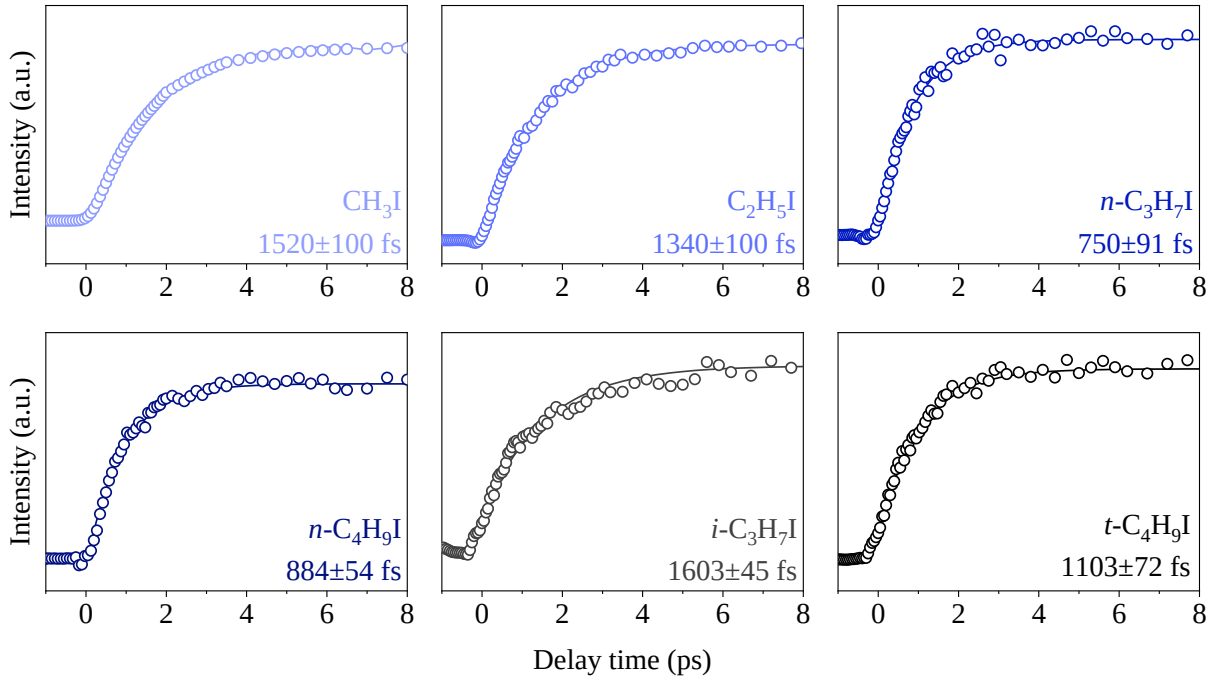

Figure 5.6 *Experimental transients corresponding to the I* atom appearance after B-band excitation at ~201 nm and detected through (2+1) REMPI scheme at 304.5 nm for the studied linear (CH_3I, C_2H_5I, n-C_3H_7I, n-C_4H_9I) and branched alkyl iodides (i-C_3H_7I, t-C_4H_9I). The lifetimes of the excited states are indicated in the corresponding panel and summarized in table 5.4*

Table 5.4. *Experimental predissociation lifetimes, τ, derived from the I* time-resolved images measured at ~201 nm for the studied linear (CH_3I, C_2H_5I, n-C_3H_7I, n-C_4H_9I) and branched alkyl iodides (i-C_3H_7I, t-C_4H_9I).*

	Reaction time τ (fs)
CH_3I	1520±100
C_2H_5I	1340±100
n-C_3H_7I	750±91
n-C_4H_9I	884±54
i-C_3H_7I	1603±45
t-C_4H_9I	1103±72

To analyze the evolution of the anisotropy during predissociation, angular distributions were obtained by radial integration of the inverted images at each time delay by the multidimensional fitting procedure. The angular distributions were fitted to:

$$I(\theta) = \frac{\sigma}{4\pi} \sum_{i=0}^{2n+2} \beta_i P_i(\cos\theta) \tag{5.3}$$

which arises for a one-photon dissociation process and (m+n) REMPI detection. σ is the total absorption cross-section, θ is the angle between the polarization axis of the photolysis laser and the fragment recoil

direction, β_i are anisotropy parameters reflecting the dissociation dynamics and the photofragment polarization, P_i are the Legendre polynomials of the i-th order and n is the number of photons of the resonant step of the REMPI process used for fragment detection. The i=0 term corresponds to the population of the studied species and given that the experimental setup has not been calibrated for total intensities, the whole distribution is normalized to β_0, and the quotient is treated as a normalization fitting parameter. The index i takes only even values since linearly polarized pump and probe laser pulses are employed. In addition, this index can be truncated at i=2 if no photofragment polarization effects are observed. I* cannot show polarization (alignment or orientation) since it presents an angular momentum J=1/2 and, therefore, a single β_2 parameter is only needed to fit the angular distributions.

Likewise, the temporal evolution of the anisotropy parameter over time, depicted in figure 5.7, was fitted to an exponential function of the form given by:

$$\beta_2(t) = \beta_2^{init} + \Delta\beta_2 e^{-\frac{t-t_0}{\tau_{\beta_2}}} \tag{5.4}$$

where β_2^{init} represents the initial value of the anisotropy parameter (at time delay zero), $\Delta\beta_2$ is the total variation of β_2 over time, and τ_{β_2} is the time constant of the exponential rise of the anisotropy over time.

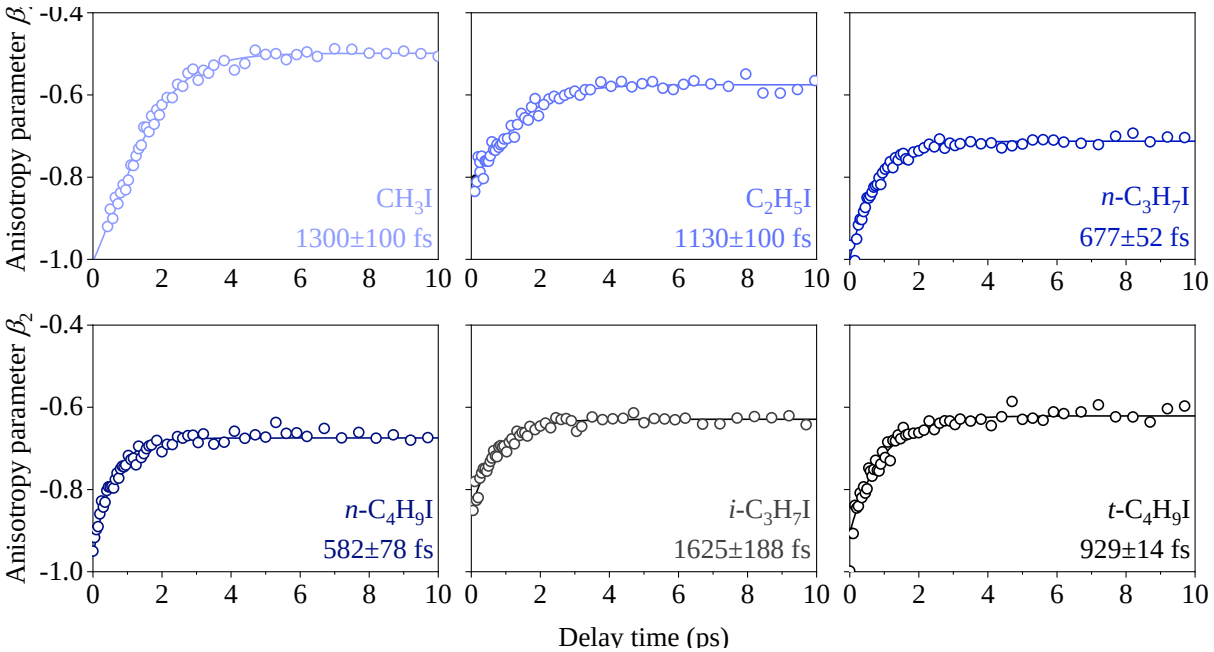

Figure 5.7 *Evolution of the anisotropy parameter, β_2 (open circles), resulting from fitting the measured angular distributions for I* with respect to the laser polarization direction to the equation (5.3), as a function of the pump-probe time delay for the studied linear (CH_3I, C_2H_5I, n-C_3H_7I, n-C_4H_9I) and branched alkyl iodides (i-C_3H_7I, t-C_4H_9I). Solid lines result from the fitting of the data to the equation (5.4).*

Table 5.5 compiles the anisotropy values β_2 obtained at the initial (β_2^{init}) and asymptotic time delay (β_2^{final}), the corresponding variation ($\Delta\beta_2$) and the rise time of the anisotropy (τ_{β_2}). For all studied alkyl iodides, the initial anisotropy parameter β_2 value shows negative values close to -1, reflecting the main contribution of a perpendicular transition, *i.e.*, a TDM perpendicular to the C−I bond, consistent with the initial population of the [6*A*", 7*A*'] Rydberg states. However, the anisotropy parameter β_2 decreases considerably with time delay, leading to final values ranging between ≈ -0.7 and -0.5 depending on the molecule. For the linear molecules, the loss of anisotropy seems to decrease as the size of the molecule increases, while the branched molecules are characterized by a slightly lower initial and final anisotropy parameter β_2 compared to their respective linear ones.

Table 5.5. *Experimental values derived from the I* time-resolved images measured at ~201 nm for the studied linear (CH_3I, C_2H_5I, n-C_3H_7I, n-C_4H_9I) and branched alkyl iodides (i-C_3H_7I, t-C_4H_9I), including the initial anisotropy parameter at early times β_2^{init}, the final anisotropy parameter at asymptotic time delays, β_2^{final}, the anisotropy variation, $\Delta\beta\tau_{\beta_2}$ and the anisotropy relaxation time, τ_{β_2}.*

	Initial anisotropy parameter β_2^{init}	Final anisotropy parameter β_2^{final}	Anisotropy variation $\Delta\beta_2$	Rise of anisotropy τ_{β_2} (fs)
CH_3I	-0.97±0.03	-0.50±0.01	-0.47±0.04	1300±100
C_2H_5I	-0.89±0.05	-0.59±0.09	-0.30±0.08	1130±100
n-C_3H_7I	-1.08±0.02	-0.74±0.01	-0.34±0.01	677±52
n-C_4H_9I	-1.02±0.09	-0.67±0.04	-0.35±0.09	582±78
i-C_3H_7I	-0.96±0.06	-0.63±0.03	-0.28±0.05	1625±188
t-C_4H_9I	-0.93±0.03	-0.63±0.02	-0.31±0.05	929±14

The remarkable loss of anisotropy was attributed to the rotation of the parent molecule during the excited state lifetime directly related to the initial rotation of the parent molecule, and here it is rationalized in terms of the classical models presented in section 1.3.3.1.[23]

The moments of inertia were computed for all the molecules and are summarized in Table 5.6. CH_3I is a prolate symmetric top and is characterized by having three main non-null moments of inertia, two of them being equal (I_b=I_c) and much larger than the third one (I_a). By approximation to a diatomic molecule, a single moment of inertia, oriented along the C–I bond was considered in previous works.[155, 157] The classical rotational energy distribution was then calculated, and the rotational temperature T_{rot} was directly deduced.

Table 5.6. *Calculated moments of inertia (I_a, I_b, I_c) for the studied linear (CH_3I, C_2H_5I, n-C_3H_7I, n-C_4H_9I) and branched alkyl iodides (i-C_3H_7I, t-C_4H_9I).*

	Inertia moments		
	I_a (amu · Å^2)	I_b (amu · Å^2)	I_c (amu · Å^2)
CH_3I	3.30	68.31	68.31
C_2H_5I	17.41	172.61	183.56
n-C_3H_7I	20.49	393.09	403.95
n-C_4H_9I	33.41	700.26	720.88
i-C_3H_7I	63.37	235.06	282.10
t-C_4H_9I	112.22	328.55	328.55

Due to the large mass of the I atom, it is relatively easy to populate rotational levels associated with small moments of inertia, even at low temperatures. Besides, as observed in table 5.6, the inertia moments increase considerably with the size of the molecule, particularly for the two branched molecules, where the three moments of inertia are of the same order of magnitude. This also contributes to an easier population of rotational levels. The approximation to a diatomic molecule is then no longer valid beyond the case of CH_3I, and the three moments of inertia have to be considered. Since the Boltzmann distribution for the rotational temperature cannot be easily calculated classically when all three inertia moments have a role, it is more convenient to consider the Boltzmann distribution over the quantum rotational levels. Therefore, all rotational levels up to J_{tot}=500 were computed for all molecules using the CALPGM program.[358] The Boltzmann distribution solving equation (1.33) is then straightforward, and the equation (1.32) can be easily solved for a considered temperature.

An iterative procedure was applied, consisting of simulating the final angular distribution considering the experimental initial and final anisotropy values and the predissociation lifetimes. The normalized angular distributions were simulated by solving the equation (1.32) for temperatures between 0 and 300 K in steps of 1 K until they converged to the experimental angular distribution. The rotational temperatures were derived and are summarized in table 5.7. The estimated error bars of the measured lifetimes were considered, and the subsequent non-negligible variation in the estimated rotational temperature T_{rot} is also indicated in table 5.7 with upper and lower error bars.

The estimated rotational temperature T_{rot} decreases significantly with the size of the molecule, in particular for the branched alkyl iodides. This is expected since larger inertia moments lead to more density of rotational states, which favors cooling by collisions in the molecular beam.

Table 5.7. *Rotational temperatures (T_{rot}) estimated with the semiclassical model (see text) considering the experimental predissociation lifetimes (τ) and their error bars for the studied linear (CH_3I, C_2H_5I, n-C_3H_7I, n-C_4H_9I) and branched alkyl iodides (i-C_3H_7I, t-C_4H_9I). The upper and lower error bars of the rotational temperature T_{rot} are obtained, considering the upper and lower values of the predissociation lifetimes τ.*

	Predissociation lifetime τ (fs)	Rotational temperature T_{rot} (K)
CH_3I	1520±100	54^{+4}_{-3}
C_2H_5I	1340±100	25^{+1}_{-0}
n-C_3H_7I	750±91	40^{+6}_{-4}
n-C_4H_9I	884±54	39^{+2}_{-7}
i-C_3H_7I	1603±45	20^{+1}_{-0}
t-C_4H_9I	1103±72	27^{+1}_{-2}

5.3.2. Theoretical results

Ab initio potential energy curves were computed as a function of the C−I internuclear distance for the four linear alkyl iodides, including all Rydberg states up to 8 eV, using the same level of theory and two different basis sets. All the potential energy curves are depicted in figure 5.8.

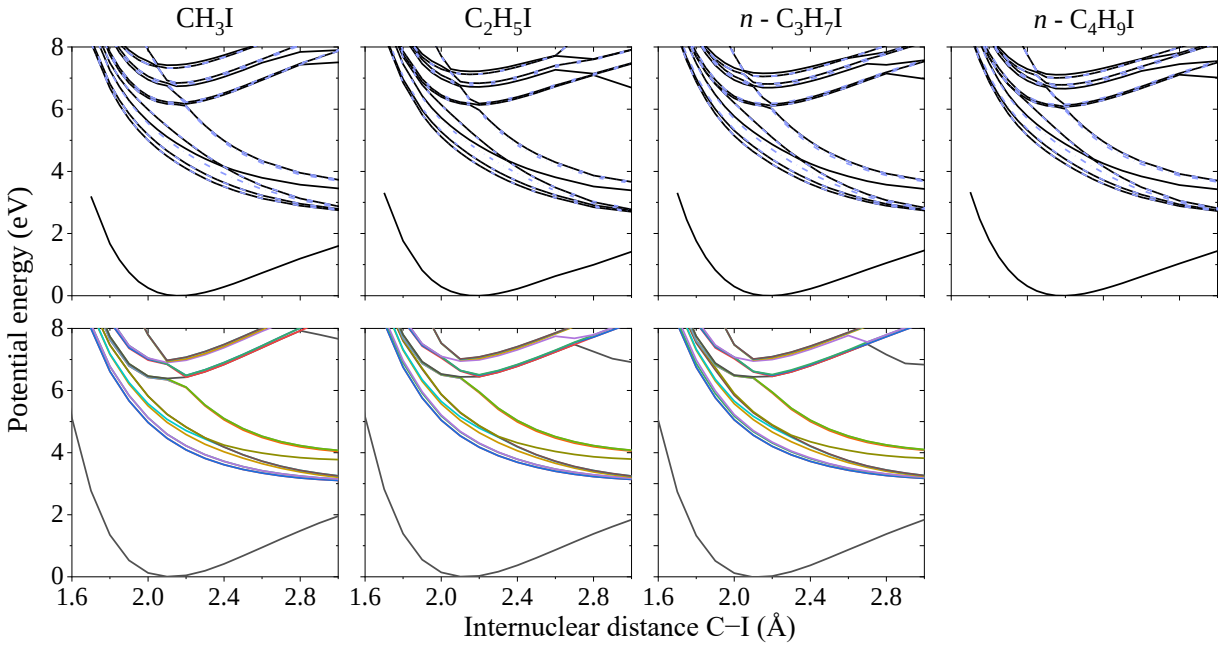

Figure 5.8. *MRCI adiabatic potential energy curves as a function of the C−I distance for the studied linear alkyl iodides (CH_3I, C_2H_5I, n-C_3H_7I, n-C_4H_9I). Two sets of calculations were performed employing two different basis sets. A first set (top panels) was carried out employing the aug-cC-pVDZ of Dunning for the C and H atoms, while for I, a 46 electrons Dirac-Fock ECP accounting for spin-orbit couplings were used in addition to a basis set for the 7 remaining electrons composed of [2s, 3p, 2d, 1f] with additional diffuse [s, p] functions for a total of [3s, 4p, 2d, 1f]. In the second set (bottom panels), the ANO-TZP basis set was employed with a supplementary monocentric basis located in the center of charge of the cationic molecule. The center of charge was estimated in the ground state of the*

cation using the Mulliken charges provided by a previous UHF calculation. Further details of each calculation can be found in the theoretical methodology. Common features detailed in the text are distinguished at both theory levels. In the top panels, solid lines refer to states of A' symmetry in the C_s point group, and the dashed lines are for A" states. In the bottom panels, the colors represent the states as in reference [323] for C_2H_5I.

Associated vertical excitation wavelengths to the *B*-band were estimated from the minimum of the potential energy curves and are reported in table 5.8. As observed, a pretty good agreement with the experimental excitation wavelengths was found.

Table 5.8. *Comparison of the experimental and theoretical excitation wavelengths for the studied linear (CH_3I, C_2H_5I, n-C_3H_7I, n-C_4H_9I) and branched alkyl iodides (i-C_3H_7I, t-C_4H_9I). Experimental values are taken from reference [349].*

	Experimental excitation wavelength (nm)	Theoretical vertical wavelength (nm)
CH_3I	201.19	199.2
C_2H_5I	201.19	200.4
n-C_3H_7I	201.12	201.2
n-C_4H_9I	201.18	202.2

The potential energy curves for the linear alkyl iodides show remarkable similarities; likewise, the experiments should reflect a similar reaction mechanism leading to the formation of R+I*. Several repulsive states associated with the first absorption *A*-band and the different Rydberg states characterizing the *B*- and *C*-bands are observed. In addition, the excited state corresponding to the ion-pair formation, presenting a minimum at longer C–I internuclear distances around 3.5 Å, appears to be stabilized for an increasing size of the molecule and the repulsive states 4*A*" and 5*A*', which correspond to the $^1Q_1$ in CH_3I, increasingly cross the Rydberg states comprising the *B*-band as the size of the radical increases.

Following excitation at ~201 nm, *i.e.*, the 0_0^0 transition for the series of linear molecules, the initially populated bound Rydberg states 6*A*" and 7*A*' (the doubly degenerate $^3R_1$ in CH_3I) can undergo predissociation through the observed crossing with the purely repulsive states 7*A*", 8*A*' and 8*A*" (the $^3A_1$(E) and $^3A_1$(A_2) states in CH_3I), leading to the significant formation of R+I*.

Figure 5.9 depicts expanded views of the adiabatic potential energy curves for the series of linear molecules shown in the top panels of figure 5.8. In these plots, the curves were made to cross to facilitate the view of the crossing region, but no diabatization was carried out. A version of these plots without crossing the curves can be found in figure 5.9. In both figures, the vertical line represents the center of the Franck-Condon region from the minimum of the ground state potential energy curve. As observed, the crossing is located to the right of the vertical bar for CH_3I, whereas the opposite situation occurs for

the larger linear alkyl iodides, *i.e.*, the crossing is to the left of the vertical bars. Besides, the crossing gets slightly closer to the ground state C–I equilibrium distance for an increasing size of the linear molecule.

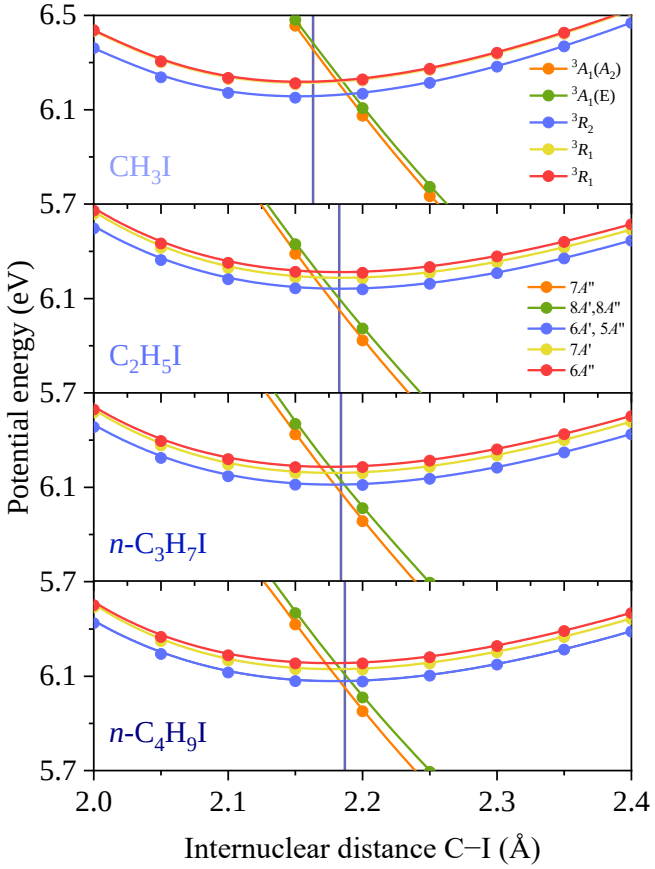

Figure 5.9 *Expanded view of the PECs for the linear alkyl iodides, CH_3I, C_2H_5I, n-C_3H_7I and n-C_4H_9I, showing the initially populated 6A" and 7A' Rydberg states ($^3R_1$ in CH_3I) as well as the curve-crossing region leading to electronic predissociation. Vertical bars indicate the C–I equilibrium distance in the ground state for each molecule. Adiabatic curves were made to cross for a better visualization of the subtle changes in the crossing region in going from one molecule to the next with increasing structural complexity. No diabatization was performed though. Interestingly, the doubly degenerate $^3R_1$ Rydberg states in CH_3I, split into two non-degenerate 6A" and 7A' states for the rest of linear alkyl iodides.*

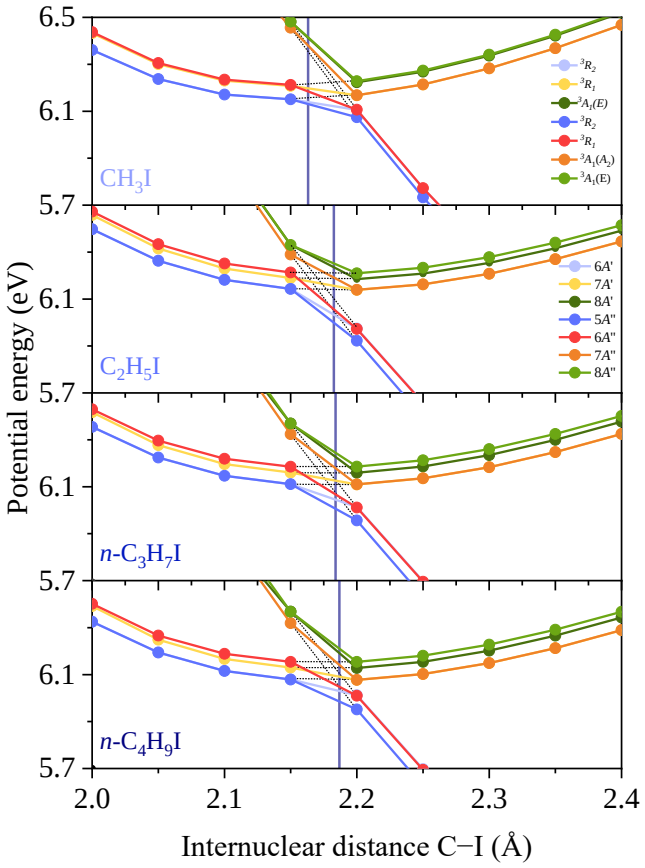

Figure 5.10. *Same as in Figure 5.9 but in expanded view to better appreciate the details of the crossing region in the second absorption B-band. Dashed black lines represent the extrapolation of the different curves to better appreciate the crossings between the Rydberg states and the purely repulsive states. The vertical blue line represents the vertical excitation at the Franck-Condon geometry from the ground state. The electronic symmetry of relevant states is specified within the Franck-Condon geometry. In the case of CH_3I, the crossing remains at longer bond distances than the excitation region; whereas in crescent-chain alkyl iodides, this crossing is located at shorter bond distances than the excitation region, although the crossing is mostly located over the Franck-Condon region.*

5.4. DISCUSSION

In this work, the time-resolved predissociation dynamics of several linear and branched alkyl iodides were examined in the origin of the *B*-band for the linear ones, whereas for some specific vibronic transition for the branched one, from velocity map ion imaging measurements. Results reveal that typical predissociation parameters such as lifetimes and the variation of anisotropy upon molecular rotation before dissociation depend on the structural characteristics of the alkyl iodides as happens with specific parameters in the *A*-band, such as the energy flux or the reaction quantum yields.

As reflected by *ab initio* potential energy surface calculations, excitation at ~201 nm, for the series of linear molecules, leads to the significant formation of R+I* following initial excitation to Rydberg

6*A*" and 7*A*' states and predissociation *via* the purely repulsive 7*A*", 8*A*' and 8*A*" states, which agrees with the experimental results.

The detection of I* fragments provided valuable information on the process of excitation and dissociation. The anisotropy parameter β presents a temporal behavior of an increasing exponential type, with an initial value ≈-1, consistent with the perpendicular nature of the transition to the *B*-band. The anisotropy parameter increases gradually over time until it reaches an asymptotic value (long times) that depends on the structural properties of the alkyl iodide as well as the predissociation lifetime. The time constant associated with anisotropy is always lower than that for the lifetime, except for the *n*-C_3H_7I. As in no case, the process has been probed from the co-fragment, except for CH_3I and C_2H_5I, no conclusions can be drawn about the possible alignment of the molecular fragment.

Both the images and the translational energy distributions show the evident variation of the anisotropy as the delay time increases, which allow us to firmly rule out the possibility of dissociation channels that correlate with ground spin-orbit I or other dissociation mechanisms that correlate with spin-orbit excited I. This conclusion can also be drawn based on the theoretical results, which show the absence of any competing mechanisms. The measured predissociation lifetimes ranging 0.75-1.5 ps must, therefore, reflect the dynamics around the crossing: either the position of the curve crossing with respect to the Franck-Condon region or the non-adiabatic coupling between the Rydberg and repulsive states. Although the closer proximity of the crossing to the Franck-Condon region with a long linear chain could be responsible for easier the predissociation and shorten the lifetimes, the difference is nevertheless minimal and, the computed coupling between the Rydberg and the repulsive states appears to be similar for all molecules. This indicates that it may not be the reason for the observed trend and, therefore, additional structural effects on the coupling between the states must occur.

The multidimensional nature of predissociation is presumably evident. For an increasing size of the radical, second or even more coordinates could enhance the coupling, leading to reduced lifetimes. This means that in the normal mode coordinates, a specific vibrational mode could induce dynamical effects. Moreover, the role of a vibrational mode on a coupling between excited states generally entails some further vibrational excitation of the molecular fragment produced. The increasing f_{int} parameter for the larger molecules could in this way reflect a more significant effect of a particular vibrational mode on the coupling leading to predissociation. Alekseyev *et al.*[304] already predicted an enhancement of the non-adiabatic coupling employing the ν_6 rocking vibration mode in CH_3I, while experiments performed exciting the 2_0^1 vibronic band demonstrated that the ν_2 umbrella mode yielded faster predissociation lifetimes.[158] Some umbrella or bending vibrational mode could similarly enhance the non-adiabatic coupling in the other linear alkyl iodides, leading to faster predissociation. Further time-resolved VMI experiments exciting selected vibronic transitions so that the amplitude of a particular

mode is increased would be particularly valuable in combination with *ab initio* calculations in selected dimensions.

Note that for the two branched alkyl iodides, *i*-C_3H_7I and *t*-C_4H_9I, the excitation wavelengths corresponding to the origin of the *B*-band (0_0^0 transition), 201.81 nm and 203.75 nm, respectively,[349] could not be selected due to the limited tunability of our femtosecond laser system around 201.0 nm. For the branched *i*-C_3H_7I, absorption with the selected wavelength (201.06 nm) is tentatively assigned to the vibronic band associated with the C−I stretching mode,[348] while for *t*-C_4H_9I, the excitation wavelength of 201.18 nm is assigned to absorption to the 6_0^1 vibronic transition of the *B*-state, corresponding to the C−C stretching mode.[355] The lifetimes measured for these two molecules at the selected vibronic states are longer (1603±45 fs and 1103±72 fs) than the corresponding lifetimes of their linear counterparts (750±91 fs and 884±54 fs) by factors of 2.14 and 1.25, respectively.[347] In general terms, vibronic excitation in CH_3I and C_2H_5I yields shorter lifetimes than those measured for the 0_0^0 transitions. For instance, the lifetimes of the 0_0^0 vibronic bands for CH_3I and C_2H_5I are, respectively, 1520±100 fs and 1341±100 fs, whereas those lifetimes for the 2_0^1 and 18_0^1 vibronic bands for the two molecules are, respectively, 0.86±0.04 ps and 0.94±0.03 ps. The fact that in the branched molecules, predissociation lifetimes are being measured after vibronic excitation, which are longer than those lifetimes of the linear counterparts, seems to indicate that the crossing region is affected by the complexity of the branched molecules in a way that is intermediate to that of the corresponding linear molecules. *Ab initio* calculations for branched alkyl iodides would be useful to understand the measured lifetimes. Therefore, besides some structural effect on the non-adiabatic coupling between the Rydberg and the repulsive states, the remarkably larger lifetimes measured could be directly related to the initially populated vibronic state.

A second dissociation channel R+I, corresponding to the formation of I in its ground spin-orbit state was reported for CH_3I and attributed to a second curve crossing between the initially populated $^3R_1$ Rydberg states and the $^1Q_1$ repulsive state from the *A*-band, located at shorter C−I distances. For an increasing size of the linear radical and symmetry reduction to C_s, the repulsive 4*A*" and 5*A*' are pushed inside the Rydberg states, as observed in figure 5.8. This would suggest a more favorable formation of I for an increasing structural complexity, in agreement with our previous investigation on the predissociation dynamics of C_2H_5I employing nanosecond lasers.[323] However, in the present experiment, despite all the efforts, the I channel was not detected following excitation of the selected molecules thus I channel remains a minor reaction pathway. Therefore, the coupling between those states and/or the overlap with the vibrational ground state wave function must be somewhat unfavorable, regardless of the increasing structural complexity and higher degrees of freedom of the molecule. However, it is possible that if the trend follows, the I channel can become a competing channel for more complex alkyl iodides.

5.5. CONCLUSIONS

The correlation between chemical structure and the predissociation dynamics following excitation on the second absorption band (*B*-band) at ~201 nm was evaluated for a series of linear and branched alkyl iodides with increasing structural complexity. Femtosecond time-resolved velocity map ion imaging experiments employing (2+1) REMPI for the detection of I fragments were performed along with high-level *ab initio* calculations of potential energy curves as a function of the C−I distance employing two different basis sets.

In agreement with the results, for all molecules, the initially populated bound Rydberg states 6*A*" and 7*A*' undergo major predissociation through a crossing with the purely repulsive states 7*A*", 8*A*' and 8*A*" leading to the major R+I* channel. The I channel, formed through a second crossing with the 4*A*" and 5*A*' repulsive states, is found to remain a minor channel and could not be observed in the present experiments.

The electronic predissociation lifetimes ranging between 0.8 and 1.5 ps were derived from the measured I* atom transients. The experimental values confirm a clear time dependency of the radical structure, as lifetimes are reduced with the increasing complexity of the linear alkyl chain. *Ab initio* calculations along C−I coordinate reveal small shifts in the position of the crossings in the potential energy curves and similar non-adiabatic couplings between the initially populated Rydberg states and the repulsive states, so most probable, for an increasing size of the radical, a second or even more coordinates would be responsible for the enhancement of the coupling.

The initial values of the anisotropy are consistent with an initial transition to the Rydberg states 6*A*" and 7*A*', and their variation goes hand in hand with the measured lifetimes. For longer lifetimes, the variation of anisotropy is more remarkable and with a time constant shorter than the lifetime. The anisotropy variation is attributed to the rotation of the parent molecule before dissociation in the excited Rydberg state. As the loss of anisotropy appears to be fully accounted for this cause, the parent molecular rotation during predissociation and thus, the rotational temperature of the parent molecule in the molecular beam could be derived by employing semiclassical models.

It would be relevant to be able to access the origin of the band of branched systems to accurately evaluate the changes induced by the branching of the structure, as similar works performed in the *A*-band.[203, 213, 229-231, 322]

Chapter 6 – Time-resolved photodissociation dynamics of vinyl iodide at 199.2 and 200 nm

6.1. INTRODUCTION

Ethylene (C_2H_4) is one of the most relevant chemical compounds in the chemical industry; ranked as the third most produced compound after sulfuric acid (H_2SO_4) and nitrogen (N_2). Moreover, it is the precursor of many other relevant compounds such as polyethylene ($(C_2H_4)_n$), ethylene glycol ($C_2H_6O_2$), ethylene dichloride ($C_2H_4Cl_2$) and styrene (C_8H_8), compounds, which are, in turn, essential in the production of plastics, textiles, synthetic rubbers and insulators. C_2H_4 is also a natural hormone synthesized by plants, and it is involved in practically all stages of plant development from seed germination, stem and root elongation, flowering to leaves and flower senescence, fruit development and ripening. For these reasons, it is essential knowing both the reactivity and the decomposition of this compound from the industrial and scientific point of view.[359-370]

The photochemistry of C_2H_4 has awakened the interest of chemists since the middle of the 20th century, specifically in the VUV region, both at experimental and theoretical levels, due to its attractive unimolecular dissociation mechanism and adequacy as a model for *ab initio* calculations of six atom systems. Thanks to a large number of experiments using light sources with different wavelengths, it has been possible to know that the decomposition of C_2H_4 upon absorption of high energy photon occurs through elimination mechanisms that can lead either to the formation of atomic or molecular hydrogen (H) in correlation with acetylene (C_2H_2).[359-364, 371] The different reaction channels are indicated below, where the first two are related to H atom elimination channels, and the last two are related to H_2 elimination channels.

$$C_2H_4 \rightarrow H_2C{=}CH{:}+H \quad (6.1)$$

$$C_2H_4 \rightarrow HC \equiv CH+2H \quad (6.2)$$

$$C_2H_4 \rightarrow HC \equiv CH+H_2 \quad (6.3)$$

$$C_2H_4 \rightarrow H_2C{=}C{:}+H_2 \quad (6.4)$$

The first different details concerning the mechanisms were established through branching ratios, the mean translational energy, and rovibrational content of the photoproducts in collision-free environments at 193 nm.[368-370, 372, 373] However, many questions remained unresolved regarding the structure of intermediate complexes and the potential energy curves involved in the different processes.[367] Some of these doubts were clarified with the advent of recent laser techniques, through which it was possible to detect transient short-lived species, such as vinylidene ($H_2C=C:$) radicals, that could not be detected until then and that were essential for outlining the mechanisms.[365, 366, 374]

To date, the mechanisms of elimination of H atoms are well-known and characterized.[368, 369, 375] Following excitation with a VUV photon, C_2H_4 can internally convert to the ground electronic state after which H atom elimination occurs *via* simple bond cleavage, leading to the formation of energized vinyl (C_2H_3) radicals. The excited C_2H_3 radicals can then either subsequently decay into C_2H_2 plus another H atom (provided the initial excitation energy is high enough) or react with other species that might be present. However, to date, the proposed mechanisms of elimination of molecular H_2[373] remain quite questionable[369, 370] despite the substantial contribution made by isotopic substitution experiments.[360, 361, 369, 373]

The cis-trans isomerization processes of C_2H_4, substituted C_2H_4, and polyenes ($(C_2H_4)_n$) are fundamental mechanisms in natural processes such as photo-reception processes in proteins. Upon $\pi \rightarrow \pi^*$ electronic excitation, the molecule twists about the C=C double bond axis followed by rapid internal conversion to the ground state. The equilibrium geometry of the lowest π^*_{CC}-π_{CC} excited state of C_2H_4 has a minimum at a perpendicular geometry of the two CH_2 moieties. In contrast, as the ground state has a planar geometry, photo-induced cis/trans-isomerization may occur during return to the ground electronic state.[375, 376] Other photochemical processes may be strongly affected by the vibrational modes that couple different low-lying states with the ground state. The roles of different substituted functional groups, including halogen atoms, are useful probes in understanding the photochemical dynamics of alkenes by altering the resonance and electrostatic effects from those of C_2H_4.[377]

As already pointed out, plenty of experimental and theoretical research has focused on the photodissociation dynamics of organic molecules containing C–X (X=Cl, Br, and I) bonds. Halogen-substituted ethylenes may have different behavior from its aliphatic analogs, related to the different structures of electronic states because of the presence of the double bond, a second chromophore of the molecule. Halogen substitution in ethylene introduces $^1(\pi(X), \sigma^*(C–X))$ and $^1(n(X), \sigma^*(C–X))$ repulsive surfaces in the proximity of the $^1(\pi, \pi^*)$, provoking a surface crossing between the latter state and the $^1(\pi$ or n, $\sigma^*)$ state, inducing a prompt C–X bond cleavage.[378, 379]

These compounds may undergo photodissociation pathways *via* simple C-H and C–X bond cleavage, molecular eliminations (HX, H_2), and three-body dissociation. Following UV excitation, the

photodissociation is governed by a mechanism in which the halogen is produced in correlation with C_2H_3 radical on excited states (atomic channel), competing with internal conversion to the ground state, from which it leads predominantly to hydrogen halide (HX) in correlation with C_2H_2 (molecular elimination). The molecular dissociation/atomic dissociation ratio may vary depending on the excitation wavelength and the substituting halogen atom,[377] changing dramatically from vinyl fluoride (C_2H_3F) to vinyl iodide (C_2H_3I). For vinyl fluoride (C_2H_3F), molecular dissociation is the unique pathway, whereas, for C_2H_3I, the atomic photodissociation channel is the major route.[380, 381] In the case of vinyl bromine (C_2H_3Br) and vinyl chloride (C_2H_3Cl), both channels are produced. C–X bond fission can produce both $^2P_{3/2}$ and $^2P_{1/2}$ spin-orbit states of the halogen atom X. HX elimination can proceed through either 4-centered or 3-centered transition states, producing acetylene or vinylidene ($C{=}CH_2$), respectively. Vinylidene has only a small barrier to isomerization and can turn into acetylene rapidly.[382] The products of the two HX elimination pathways are identical, although the disposal of energy among the fragments may not be. Equations (6.5)-(6.8) show the different photodissociation channels for C_2H_3I.[383]

$$C_2H_3I \rightarrow C_2H_3(^2A') + I\left(^2P_{3/2}\right) \tag{6.5}$$

$$C_2H_3I \rightarrow C_2H_3(^2A') + I^*\left(^2P_{1/2}\right) \tag{6.6}$$

$$C_2H_3I \rightarrow C_2H_2(\tilde{X}\,^1\Sigma_g^+) + HI\left(\tilde{X}\,^1\Sigma^+\right) \tag{6.7}$$

$$C_2H_3I \rightarrow C_2H_2(\tilde{X}\,^1A_1) + HI\left(\tilde{X}\,^1\Sigma^+\right) \tag{6.8}$$

Preliminary assignments of the abortion spectrum of vinyl halides in the UV region show a broad $\pi_{CC}\rightarrow\pi_{CC}^*$ transition along with sharp Rydberg series transitions. The absorption maximum of the $\pi_{CC}\rightarrow\pi_{CC}^*$ transition shifts towards the red as the halogen atom changes from fluorine (F) to iodine (I) (166.5 nm for C_2H_3F,[384] 184 nm for C_2H_3Cl,[385] 194 nm for C_2H_3Br[386, 387] and 217 nm for C_2H_3I[348, 388]) a result of the resonance interactions in the *p* molecular orbitals and the inductive effect of the electron-withdrawing halogen atom. The assignments of other valence transitions are not yet clear. The asymmetric spectral shape of the broad $\pi_{CC}\rightarrow\pi_{CC}^*$ absorption is attributed to small contributions from $n_x\rightarrow\sigma^*_{CX}$ or $n_x\rightarrow\pi^*_{CX}$ transitions.[389]

Vinyl halides, especially C_2H_3Cl,[378, 389-392] C_2H_3Br[393, 394] and less C_2H_3F[395-397] have been the subject of numerous experimental and theoretical studies due to their importance in fundamental processes in photochemistry. The first studies focused on the different reaction mechanisms of H migration and HX elimination through photosensitizer and IR multiphoton techniques.[398-403] As well, some studies focused on the mechanism of energy partitioning among various degrees of freedom in the products from the elimination channel.

Blank *et al.*[391] studied the photodissociation of C_2H_3Cl following $\pi \rightarrow \pi^*$ excitation at 193 nm using PTS. Five dissociation channels were identified. The first channel was attributed to chlorine (Cl) elimination, with large translational energy, and originated from an excited-state dissociation, whereas the rest of the channels results from the competition on the ground electronic state following internal conversion from the initial excited state and are related to atomic and molecular H elimination, hydrochloric acid (HCl) elimination, and translationally slow Cl atom elimination channels. Two secondary decomposition channels were also observed and attributed to the elimination of Cl atom from chlorovinyl radicals following the primary H atom elimination channel, and H atom elimination from C_2H_3 radicals following the primary atomic Cl elimination.

Suzuki and co-workers also measured the Cl atoms arising from the photodissociation of C_2H_3Cl at 193 nm by state-resolved two-dimensional ion imaging,[378] providing insight regarding their energy and angular distribution of Cl atoms in both spin-orbit states. The energy distributions for both electronic states revealed two components, a Gaussian-like first component with high anisotropy, highlighting a prompt dissociation mechanism *via* the (π, σ^*) repulsive excited state, and a second slow low-anisotropy component attributed to a dissociation pathway *via* the ground state, which evidenced an efficient non-adiabatic transition by the motion perpendicular to the C–Cl stretching coordinate.

Similarly, Suzuki and co-workers also measured the bromine (Br) atoms from the photodissociation of C_2H_3Br at 193 nm.[404] Both ground and excited spin-orbit Br atom distributions were found to be dominated by strong anisotropic high translational energy components pointing out to the dissociation of the C–Br bond *via* a surface crossing between the excited state and the repulsive state(s).

Sato *et al.*[395] studied the photodissociation mechanism of C_2H_3F at 157 nm employing mass-resolved photofragment TOF spectroscopy to study the HF elimination process, the main primary dissociation process and the corresponding dominant four-center mechanism from the measured translational energy distributions. Other observed dissociation processes include the C–H bond cleavage as well as the molecular elimination of H_2. Their results were discussed based on *ab initio* molecular orbital calculations, motivated by previous calculations by Kato and Morokuma.[405]

Photodissociation of C_2H_3F at 157 nm was also investigated by Yang and co-workers[397] using PTS. Five dissociation pathways were identified, out of which molecular HF elimination and the triple dissociation channel were found to be equally important, while other channels were all minor. The product kinetic energy distributions for all dissociation channels, as well as the branching ratio, were determined.

The only gas-phase studies of C_2H_3I were reported by Yamashita *et al.*,[380, 381] Cao *et al.*[383] and Osborn *et al.*[377]

Yamashita *et al.*[380, 381] studied the photodecomposition of C_2H_3I at room temperature by photolysis at 313 and 254 nm using a high-intensity light source and a static reactor. This study aimed to determine the primary photodissociation processes and study the energy dependence of the primary and secondary processes by varying the excitation wavelength by observing both molecular and free radical processes in the primary process. The ratio of the contribution of molecular to free radical processes was found to be about 1:6 in the studied wavelength range.

Cao *et al.*[383] studied the photofragmentation of C_2H_3I by PTS with a rotatable pulsed molecular beam crossed with a krypton fluoride (KrF) excimer laser beam (248 nm). At this excitation wavelength, the cleavage of the C−I bond takes place to generate C_2H_3 radicals in correlation with I fragments in their two possible spin-orbit states, *i.e.*, $C_2H_3I+I^*(^2P_{1/2})$ and $C_2H_3I+I(^2P_{3/2})$, with a ratio I*/I of 1.33. Results provided information regarding the total translational energy of the recoiling fragments and the internal energy of the C_2H_3 radicals. Energy partitioning of the fragments was found to be consistent with a direct impulsive model through a strongly dissociative potential energy surface along the C−I bond with a small contribution of slow I atoms attributed to ground state dissociation. Results lack photofragment angular distributions, which would have provided valuable information on the nature of the states involved in UV photolysis of C_2H_3I. The dissociation energy was determined to be 61.9±1.0 kcal/mol according to the maximum translational energy observed in the photofragments, 1.35 eV in the I* channel, and 2.31 eV in the I channel, respectively.

Most recent studies of C_2H_3I photodissociation were reported by Osborn *et al.*[377] at several wavelengths between 193 and 266 nm using three techniques: time-resolved Fourier transform emission spectroscopy (TR-FTES), multiple pass laser absorption spectroscopy and ion VMI in combination with (2+1) REMPI. Upon excitation of the different wavelengths, the only observed open dissociation channel is C−I bond cleavage to produce C_2H_3+I/I^* with quantum yields varying substantially with excitation energy. I ion VMI combined with (2+1) REMPI detection for I atoms and hydrogen iodide (HI) through the $X\ ^1\Sigma^+ \rightarrow g\ ^3\Sigma^-(0^+)$ transition[406] provided the corresponding translational energy and angular distributions. A considerable amount of the available energy was found to be partitioned into the internal degrees of freedom of the C_2H_3 radical. The anisotropy parameters of I and I* at all wavelengths were larger than 1 and consistent with a transition moment roughly parallel to the C−I bond. It was concluded that the dissociation takes place *via* at least two repulsive electronic states. Unlike photodissociation of other vinyl halides (C_2H_3X, X=F, Cl, Br), in which the HX product channel is significant,[391, 392, 394-397, 405, 407, 408] no HI elimination was observed, neglecting thus the contribution from internal conversion to the ground state. Their experimental findings were completed with ground-

state potential energy surface *ab initio* calculations providing a model that suggests that the highest occupied molecular orbital (HOMO) in vinyl halides has increasing X($np_{\perp}$) non-bonding character with increasing halogen mass, leading to a reduced torsional force around the C−C bond in the excited state. Because the ground state energy is highest when the CH_2 plane is perpendicular to the CHX plane, a reduced torsional force in the excited state correlates with a lower rate for internal conversion compared to the excited state C–X bond fission. This model explains the gradual change in vinyl halides' photodissociation mechanisms from the dominance of internal conversion in vinyl fluoride (C_2H_3F) to the dominance of excited state dissociation in C_2H_3I. This study also concludes trends in vinyl halides: calculations revealed that the energy of the atomic dissociation asymptote drops significantly for F→Cl→Br→I, dissociation pathway which is also favored by less favored elimination through the molecular pathway. This trend implies that internal conversion to the ground electronic state becomes increasingly more difficult as the halogen atom becomes heavier.

In the present chapter, time-resolved photodissociation dynamics of C_2H_3I in the region near 200 nm, specifically at 199.2 and 200 nm, using VMI and resonant ionization of the free fragments I($^2P_{3/2}$) and I*($^2P_{1/2}$) through (2+1) REMPI, are presented. These experiments allowed us to study the effect of an unsaturation on the photodissociation dynamics of linear alkyl iodides in the *A*-band, corresponding to the cleavage of the C−I bond through the dissociation channels where I($^2P_{3/2}$) and I*($^2P_{1/2}$) are formed in correlation with the C_2H_3 fragments.

Time-resolved images for the I fragments and the corresponding translational energy and angular distributions and C−I transients are reported and discussed. Experimental findings are complemented by *ab initio* calculations of the potential energy curves as a function of the C−I distance to discuss the dissociation mechanism.

In addition, a comprehensive analysis of the absorption spectrum of C_2H_3I in the region of interest is presented.

6.2. METHODOLOGY

6.2.1. Experimental methodology

6.2.1.1. Laser configuration and optical assemblies

This section presents the specific methodological details of the experiments corresponding to the study of time-resolved photodissociation dynamics of C_2H_3I at 199.2 nm and 200 nm, using velocity map ion imaging in combination with resonant ionization of the free fragments I($^2P_{3/2}$), I*($^2P_{1/2}$) through (2+1) REMPI. Figure 6.1 summarizes the optical assembly of the experiments performed in this section.

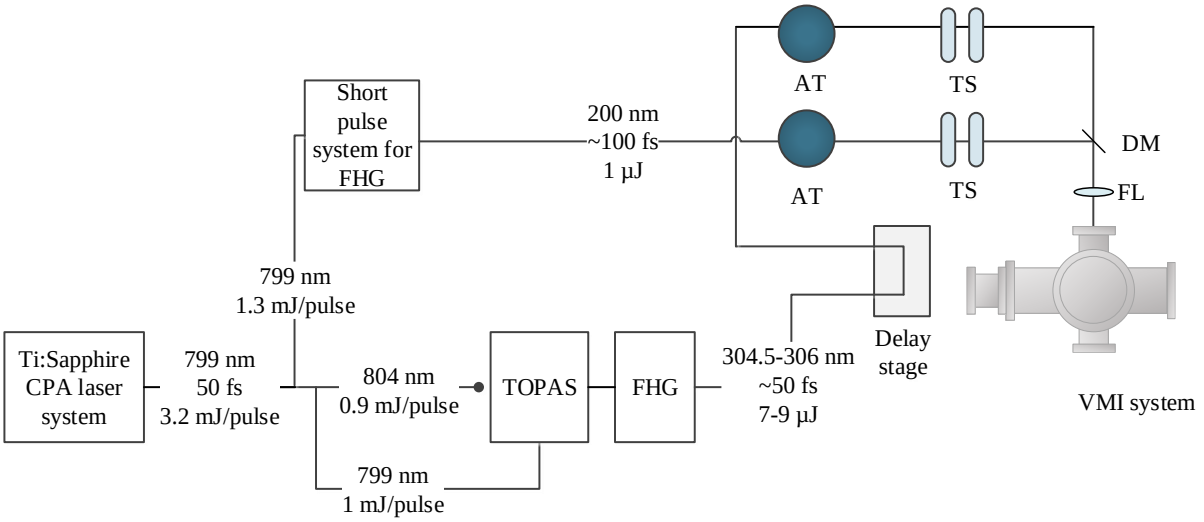

Figure 6.1. *Experimental setup for time-resolved predissociation dynamics of C_2H_3I at ~200 nm employing femtosecond laser pulses and velocity map ion imaging. The laser system, the TOPAS, and the short pulse system for FHG are represented on the left side. Along the layout, several optical elements such as a dichroic mirror (DM), telescopes (TS), power attenuators (AT), the probe linear translational stage, the final focusing lens (FL) and the wedge (W) are distinguished. The VMI machine is located in the lower right area of the figure. The detection system is arranged perpendicular to the plane of the paper and the gas inlet (off-axis configuration).*

For the accomplishment of the photodissociation studies of C_2H_3I around 200 nm, a pump laser tuned at 199.2 nm and 200 nm was required, corresponding to the first absorption maximum of the sharp trident-shaped transitions reflected in its absorption spectrum of figure 6.2 and the red edge of this broad peak, respectively, *i.e.* in resonance and out of resonance with the first peak in that region of the absorption spectrum, and a probe laser centered at 304.5 or 306 nm for the (2+1) REMPI detection of $I(^2P_{3/2})$ and $I^*(^2P_{1/2})$ photoproducts (see section 2.1.4.6.1).

Excitation at 199.2 nm corresponds to the maximum of the first band consisting of a peak with a considerable width with an absorption cross-section $\sigma=3\cdot10^{-16}$ Mb that rests on a background of absorption with an absorption cross-section $\sigma=1\cdot10^{-16}$ Mb, implying the possible absorption to different electronic states, whereas 200 nm corresponds to the red edge of this peak. Preliminary assignments based on this spectrum relate this first peak at 199.2 nm with a vibrational transition to the 6s Rydberg state coupled with a quantum of vibrational excitation of the mode ν_5, which corresponds to the C−I stretch mode, which is denoted, therefore, as $n_i \rightarrow n_s 5_0^1$. The excitation in this region leads to the cleavage of the C−I bond and the consequent formation of the C_2H_3 and I fragments, the latter in its ground and excited spin-orbit states.

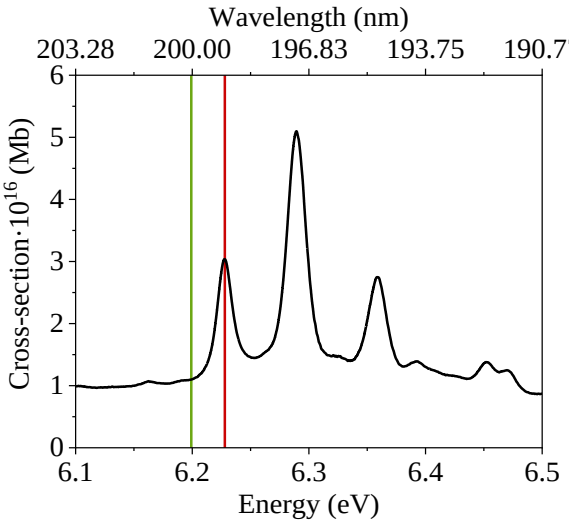

Figure 6.2. *Gas-phase absorption spectrum of C_2H_3I in the 194-204 nm region measured using the FTS of VUV beamline DESIRS at the SOLEIL synchrotron radiation source.[349] In the present work, the excitation of C_2H_3I is carried out at 199.2 nm (vertical red line) and 200 nm (vertical green line), which correspond to the maximum of the first band of the vibrational progression and the corresponding red edge.*

To carry out these experiments, the output laser pulses from the Spitfire regenerative amplifier (799 nm laser pulses, 3.2 mJ/pulse, 50 fs pulse duration, 1 kHz repetition rate) were employed. One of the arms, with an energy around 1.3 mJ/pulse was driven to the FHG setup based on transmissive optics. With the output of the amplifier centered at 799 nm, this unit produced tunable radiation around 199-200 nm with an output energy of 1 μJ. The 304.5-306 nm radiation for probing I*($^2P_{1/2}$) and I($^2P_{3/2}$) photoproducts *via* a (2+1) REMPI was obtained from the TOPAS pumped by around 1 mJ/pulse of the amplifier. The TOPAS signal was tuned at 1210 nm and then two-step frequency-doubled to produce this radiation with an output energy of 7-9 μJ. The output was sent to the Newport linear translation stage. As in other experiments, both lasers were recombined in the final dichroic mirror and later, they were focused inside the ionization chamber employing a 25 cm focusing lens. The polarization of the pump laser was horizontal, whereas that of the 304.5-306 nm probe laser coming from the TOPAS was vertical. So, to ensure the cylindrical symmetry of the experiment, the polarization of the probe laser was rotated 90° employing an achromatic tunable half-wave plate.

The intensities chosen for the pump and probe pulses were around $1.5 \cdot 10^{10}$ and $2 \cdot 10^{11}$ W/cm^2 respectively.

6.2.1.2. Molecular beam conditions and detection system

For the realization of the present experiments, C_2H_3I (Fluorochem Limited, 85 %) was used. The experiments were performed in an opaque steel bubbler since C_2H_3I is photosensitive at room temperature. The molecular beam was generated by expanding the vapors with helium (He) (Air Liquid,

99.999 %) as carrier gas at 1.5 atm overpressure, thus formed by a mixture of 5 % C_2H_3I and 95 % carrier gas, through a piezoelectric valve with a 0.5 mm diameter orifice that produces gas pulses of 40 µs at 1 kHz frequency. Voltages applied to the piezoelectric material of the expansion valve were ~ 300-400 V. The delay between the gas pulse and the laser pulse was such that the interaction occurred in the edge area of the gas pulse.

The monitoring of the photodissociation process was carried out by detecting the I^+ fragments in a TOFMS configuration. A voltage ratio of 0.76 between the repeller and the extractor was maintained in the ion extraction system to ensure VMI conditions. In this case, the calibration of the apparatus was performed by using the known translational energy (KE) release of the $CH_3(v=0)+I^*(^2P_{1/2})$ and $CH_3(v_1=1)+I^*(^2P_{1/2})$ channels from 201.19 nm photodissociation of methyl iodide (CH_3I).[155]

According to figure 6.3, the arrival at the I^+ ion detector occurred 8.9 µs later than the arrival of the laser pulse at the interaction area, therefore the gating of the MCP was set at 8.9 µs and 5.5 µs respectively with a duration of 200 ns. The deflector plates were not used in the present case since the deflection of the C_2H_3I parent molecule from the I fragment was not possible.

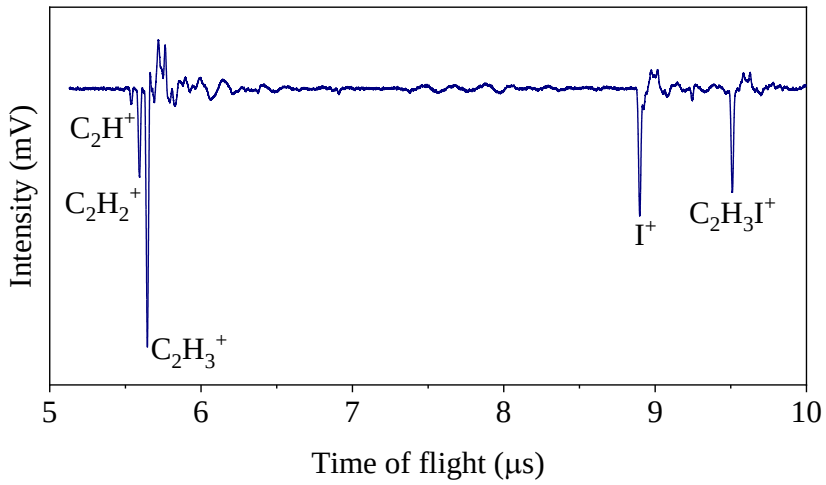

Figure 6.3. *Pump-probe TOF mass spectrum of C_2H_3I with TOF time base (as measured in the digital oscilloscope). Pump pulse centered at 200 nm, probe pulse centered at 304.5 nm and time delay settled at 10 ps (asymptotic conditions). The different peaks are assigned to the different parent and fragment ions as indicated.*

6.2.1.3. Temporal characterization of the femtosecond laser pulses

The determination of the time zero and the cross-correlation was performed by *in situ* measurements of the (1+2') REMPI transient for Xe. The cross-correlation function provided a value of 150 fs.

6.2.2. Absorption spectrum

The spectrum shown in the present chapter was measured using the FTS,[350] one of the permanent endstations of the VUV beamline DESIRS[351] at the SOLEIL synchrotron radiation source. The FTS covers a large UV-VUV spectral range from 4 to 30 eV, with a line width of 0.08 cm^{-1} on a large spectral window, $\Delta E/E$=7 %.[352] The complete descriptions of the beamline and experimental setup can be found in references [352, 353]. The spectrum was measured by Dr. Nelson de Oliveira, member of the DESIRS beamline directed by Dr. Laurent Nahon, as part of the experimental campaign entitled "High-resolution absorption spectra of alkyl iodide molecules" in collaboration with Dr. Luis Bañares group. These spectra have not yet been published.[349]

6.2.3. Theoretical methodology

To characterize the electronic structure of C_2H_3I, several electronic states were calculated using multireference methods based on SA CASSCF wave functions. Relativistic effects were taken into account using a second-order Douglas-Kroll Hamiltonian[268, 269] formalism combined with an ANO-RCC[267, 409] basis set contracted to a doble zeta polarized (ANO-RCC-DZVP). The two-electron integrals were evaluated using the density fitting approximation,[410] where the selected auxiliary basis set was constructed using the uncontracted ANO-RCC basis. The active space used in the CASSCF calculations was composed of eight electrons in seven orbitals. Specifically, the set of orbitals considered in this study contained two lone pairs in the I atom, the bonding and antibonding $\sigma_{C–I}$ and π_{C-C} and the corresponding Rydberg of symmetry *s*. Two sets of orbitals were obtained using the SA technique, the first one considering nineteen singlets and the second one averaging over eighteen triplets. Finally, the energy was corrected by PT in its extended multistate CASPT2 (XMS-CASPT2) formalism[411] with an imaginary shift of 0.3 a.u. These calculations were performed using the Brilliantly Advanced General Electronic-structure Library (BAGEL) code,[412] including analytical gradients[413-415] when required. Finally, spin-orbit coupling was taken into account using the AMFI approximation,[271] resulting in 73 electronic states. This calculation was performed extracting the CASSCF wave function (CI vector and orbitals) from the BAGEL code and importing it to the OpenMolcas code,[416] where the spin-orbit coupling was evaluated using a PM-CASSCF approximation. The calculated states were selected to describe the seven first spin-free dissociation levels: $I+C_2H_3$, $I^*+C_2H_3$, $I+C_2H_3$*(valence) $I^*+C_2H_3$*, $I+C_2H_3$*(Rydberg) and $I^*+C_2H_3$*(Rydberg) together with the ion-pair $I^-+C_2H_3^+$. To estimate the reliability of the method, all curves were compared with the equivalent ones calculated only with OpenMolcas.[416]

To understand the dissociation of C_2H_3I, relaxed potential energy curves, where the C_2H_3 moiety was optimized in its spin-free doublet ground cationic state were calculated. In this case, the gradients

obtained with BAGEL using the XMS-CASPT2 were passed to the ORCA program to optimize the molecule with constrained C−I distance.

Beyond the relaxed curves, to estimate the most probable path of the dissociation process a damped dynamics was also simulated using the SHARC method,[276] where the Hamiltonian and the spin-free gradients were described using the previous electronic structure protocol giving an estimation of the most probably way. In this methodology, the velocities were reset to zero at every time step, forcing the system to follow the deepest direction. This is similar to the minimum energy path (MEP) or intrinsic reaction coordinate (IRC) of the reaction.

Finally, the semiclassical spectrum was simulated using a Wigner distribution to represent the initial vibrational distribution of the ground state. A total of 1000 geometries were obtained considering the MP2 Hessian within the harmonic approximation. For each geometry, a single point calculation was performed, obtaining the vertical electronic energy at XMS-CASPT2 with dipoles and spin-orbit couplings at PM-CASSCF (vide supra).

All theoretical calculations were carried out by Dr. Jesús González Vázquez.

6.3. RESULTS

6.3.1. Experimental results

Figure 6.4 shows Abel inverted I images from the photodissociation of C_2H_3I at 200 nm (a, b) and 199.2 nm (c, d) detected *via* (2+1) REMPI at 304.5 nm (I+I*) and 306 nm (I*) at an asymptotic pump-probe delay of 10 ps. At both excitation wavelengths, for 306 nm detection, a broad anisotropic ring is observed and assigned to the dissociation channel C_2H_3+I*($^2P_{1/2}$) while at 304.5 nm detection, a second outermost overlapped anisotropic ring is observed and attributed to the C_2H_3+I($^2P_{3/2}$) channel. The widening of the rings is considerable, accounting for the high internal energy content of the C_2H_3 co-fragment. At 200 nm, the fragmentation channels show an apparent parallel anisotropy since the signal is recovered along the laser polarization direction vector, which is defined vertically to the images presented here. In contrast, for 199.2 nm, the anisotropy is perpendicular as the signal is located along the equatorial region. It should be noted that the contribution of I seems to have a slight parallel character, as the sum of both contributions I+I* seems more anisotropic than at 200 nm. The very weak signal in the center is attributed to dissociative MPI. The widening of the rings could also be due to a simultaneous excitation of several states with TDM oriented in the same direction and correlating with the same asymptote.

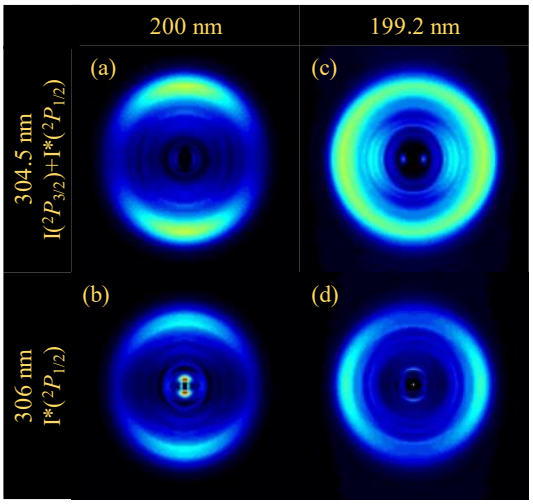

Figure 6.4. *Abel inverted I images for C_2H_3I measured in femtosecond pump-probe VMI experiments upon excitation at 200 nm (a, b) and 199.2 nm (c, d), corresponding to the first absorption maximum of the sharp trident-shaped transitions in the absorption spectrum, and the red edge of this broad peak, respectively (see figure 6.2). The time delay between the pump and probe pulses is 10 ps. In the images, the radius is proportional to the total translational energy of the fragments. The linear polarization of the lasers is along the vertical axis of the images.*

The corresponding CM I translational energy distributions resulting from the angular integration of the inverted images are depicted in figure 6.5. Vertical bars indicate the available energy for each dissociation channel, C_2H_3+I($^2P_{3/2}$) and C_2H_3+I*($^2P_{1/2}$), henceforth denoted as I and I*, estimated by:

$$E_{av}^{I} = \left(\frac{m_{\mathrm{I}}}{m_{\mathrm{C_2H_3I}}} \right) \cdot (h\nu - D_0 - E_{\mathrm{SO}}(\mathrm{I}^*) + E_i^{molec}) \tag{6.9}$$

where E_{av}(I) is the available energy of I fragments, m_{I} is the I mass, m_{C2H3I} is the mass of C_2H_3I, $h\nu$ is the excitation photon energy (6.20 eV for 200 nm and 6.22 eV for 199.2 nm), D_0 is the dissociation energy, 2.684,[383] E_{SO}(I*) the I spin-orbit splitting, 0.943 eV for the I*,[40] and E_i^{molec} is the internal energy of the parent molecule which is considered negligible. The estimated available energy values for I fragments at both excitation wavelengths are displayed in table 6.1.

Table 6.1. *Estimated total available energy for I fragments for both dissociation channels, I and I*, corresponding to the dissociation of C_2H_3I upon excitation at 200 and 199.2 nm.*

Excitation wavelength (nm)	Channel	Excitation energy $h\nu$ (eV)	Available energy E_{av} (eV)	Available energy E_{av}^{I} (eV)
200	I	6.199	3.515	0.618
	I*	6.199	2.572	0.452
199.2	I	6.224	3.540	0.622
	I*	6.224	2.597	0.456

At 306 nm detection (Figure 6.5 B, D), the translational energy distributions show a main peak assigned to the I* channel. A Gaussian function was employed to fit this main contribution while the Boltzmann-type broad-contribution observed at low energy attributed to dissociative MPI was fitted using the equation (6.10).[284, 285]

$$I(E_T) = AE_T^i(1-E_T)^j \tag{6.10}$$

At 304.5 nm detection (Figure 6.5 A, C), the translational energy distributions show a broad profile assigned to the overlapping I and I* channels. Two Gaussian functions were employed in this case to fit the contributions assigned to the two dissociation channels, while the broad contribution assigned to dissociative MPI was similarly fitted employing equation (6.10). The fitting procedure implied a deconvolution of the overlapping structures for both excitation wavelengths. The position of the Gaussian function corresponding to the I* channel was indeed determined and fixed by the results obtained at 306 nm.

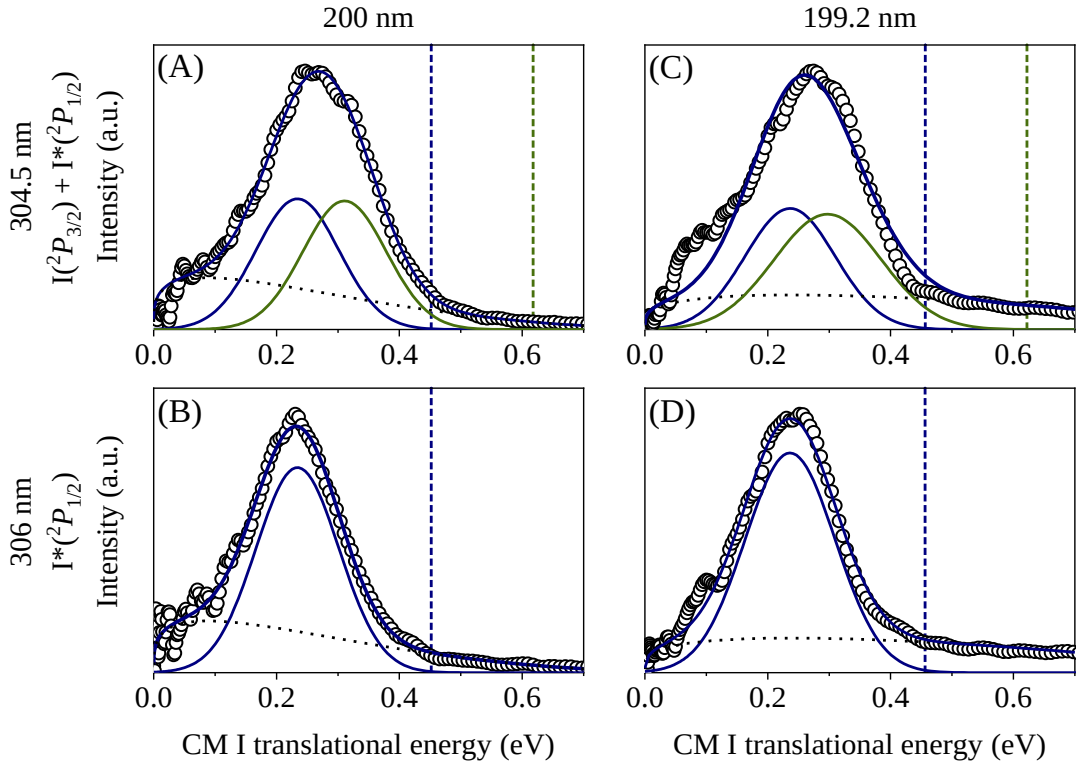

Figure 6.5. *CM I translational energy distributions of C_2H_3I obtained by angular integration of the corresponding Abel inverted images measured for I*($^2P_{1/2}$) at 306 nm (b, d) and for I($^2P_{3/2}$) and I*($^2P_{1/2}$) at 304.5 nm (a, c) by (2+1) REMPI. The Boltzmann-type fitted contributions are represented by a dotted line, while the Gaussian functions used to fit the contributions from the I($^2P_{3/2}$) and I*($^2P_{1/2}$) dissociation channels are represented by solid green and blue lines, respectively. The total bimodal function sum of the two contributions is not shown for clarity. Vertical dashed bars represent the available energy for the I* (lower energy) and I (higher energy) channels, respectively.*

A significant shift in the translational energy distributions between the observed distributions and the available energy is observed for both excitations, reflecting an increased internal energy – ro-vibrational – of the co-fragment since I is an atomic species. The considerable broadening of the rings in figure 6.4 can be attributed to a broad distribution of ro-vibrational states of the C_2H_3 fragments produced in the dissociation. The most probable fractions of the total available energy released into the internal energy of the co-fragment, f_{int}, are presented in table 6.2. The energy partitioning f_{int} values are similar for both cases, but somewhat higher values are obtained for the I channel compared to the I* channel. As can be seen, practically half of the available energy is converted into translational energy, while the other half is converted into internal energy of C_2H_3 fragments.

Table 6.2. *Fraction of the available energy that appears as internal energy (ro-vibrational) of the co-fragments f_{int} for both dissociation channels (I and I*) corresponding to the dissociation of C_2H_3I upon excitation at 200 and 199.2 nm.*

Excitation wavelength (nm)	Channel	Energy partitioning, f_{int}
200	I	0.55
	I*	0.49
199.2	I	0.56
	I*	0.46

Assuming a single-photon direct dissociation and that every molecule which absorbs a photon does dissociate to give I or I* atom, the quantum yield for the production of I*($^2P_{1/2}$), is deduced from the areas of the two Gaussian functions used to fit the translational energy distributions depicted in figure 6.5. To consider the different REMPI line strengths for I and I*, the already reported quantum yield Φ* for CH_3I at 268 nm[40] was used for calibration. The estimated quantum yield Φ*, shown in table 6.3, is around 0.5 for both channels; nevertheless, the formation of I* is slightly more favorable at the two excitation wavelengths. These values are in good agreement with those obtained by Zou *et al.*,[377] in spite of the fact that the obtained values here are estimates due to the complexity of the deconvolution by the high degree of energy overlap of both translational energy distributions corresponding to each of the dissociation channels.

Table 6.3. *Quantum yield for the production of I*($^2P_{1/2}$) corresponding to the dissociation of C_2H_3I upon excitation at 200 and 199.2 nm.*

Excitation wavelength (nm)	Quantum Yield, Φ*
200	0.56
199.2	0.51

Our experimental findings reveal a significant contribution of CH_2 symmetric stretch ν_3, with a fundamental frequency of 2905.1 cm^{-1} or 0.361 eV (0.063 eV in terms of equation (6.9)), after a fitting procedure based on series of Gaussian functions represented in figure 6.6. Nevertheless, other vibrational modes are compatible with the translational energy distribution structure, like the asymmetric stretch ν_2. For the fitting procedure, the Boltzmann type MPI contribution was first removed to reveal the pure contribution of the direct photodissociation processes for both measured translational energy distributions. Then, for the I* translational energy distribution (detection at 306 nm), a series of Gaussian functions with equal FWHM and variable position was used, so that the energetic difference between the maxima of the Gaussian functions corresponded to the energetic difference of each quantum of excitation. To fit both the I* and I translational energy distribution (detection at 304.5 nm), first, the Gaussian functions used to fit the distribution at 306 nm detection were recovered to separate the contribution for I*, by adjusting the intensity of the Gaussian functions employing the estimated quantum yields. By knowing their contribution, it was possible to fit the I contribution the same way as for I* in the I* translational energy distribution at 306 nm.

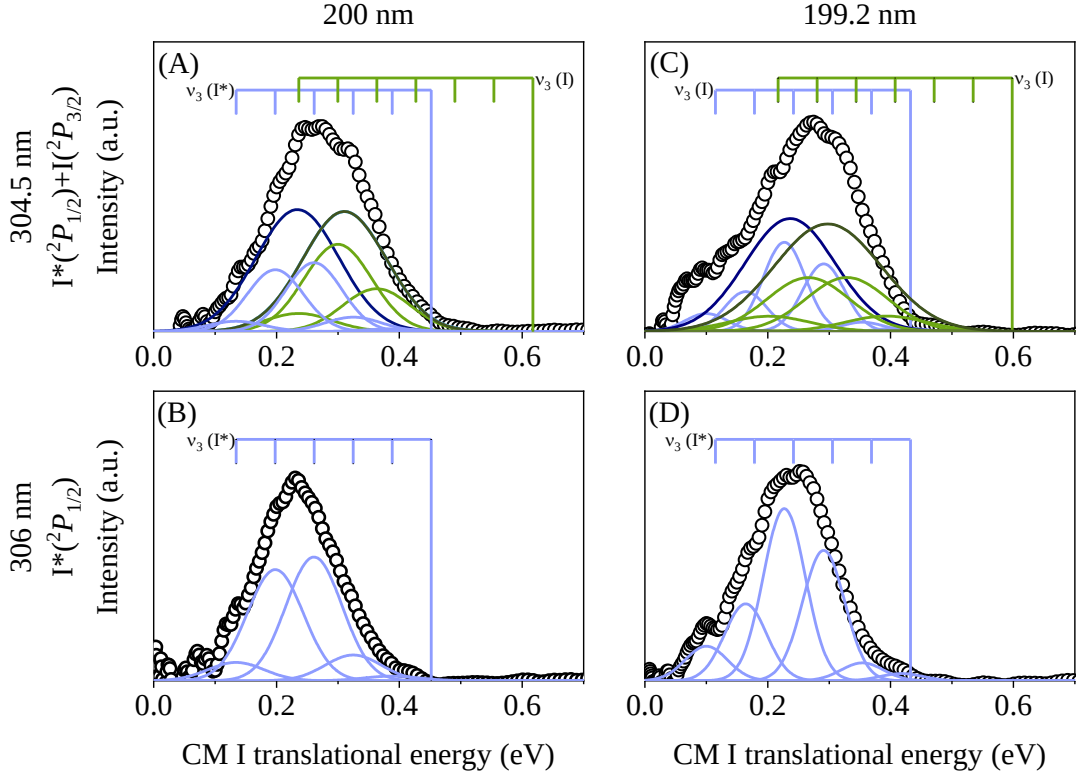

Figure 6.6. *CM I translational energy distributions of C_2H_3I obtained by angular integration of the corresponding Abel inverted images measured for $I^*(^2P_{1/2})$ at 306 nm (b, d) and for $I(^2P_{3/2})$ and $I^*(^2P_{1/2})$ at 304.5 nm (a, c) by (2+1) REMPI. Vertical dashed bars represent the available energy for the I* (lower energy) and I (higher energy) channels, respectively while combs represent different vibrational levels of the CH_2 symmetric stretch of the C_2H_3 co-fragments. Dark blue and dark green lines represent the I* and I fragment contributions exactly as in figure 6.5, while lighter Gaussian functions describing the vibrational contributions obtained from the fitting procedure described in the main text.*

In figure 6.7, the normalized distributions of vibrational populations of the C_2H_3 co-fragment in the CH_2 symmetric stretch ν_3 are represented for 200 and 199.2 nm. They were obtained from the areas of the Gaussian functions corresponding to each quantum of vibrational excitation of the C_2H_3 fragment displayed in figure 6.6. The vibrational populations estimated for the C_2H_3 fragments confirm a hotter vibrational distribution for those fragments correlating with I in comparison with I*. For 200 nm excitation, the most populated state corresponds to ν_3=3 for those fragments correlating with I*, and ν_3=5 for fragments correlating with I. For 199.2 nm excitation, the most populated state corresponds to ν_3=3 for those fragments correlating with I*, and ν_3=4-5 for fragments correlating with I.

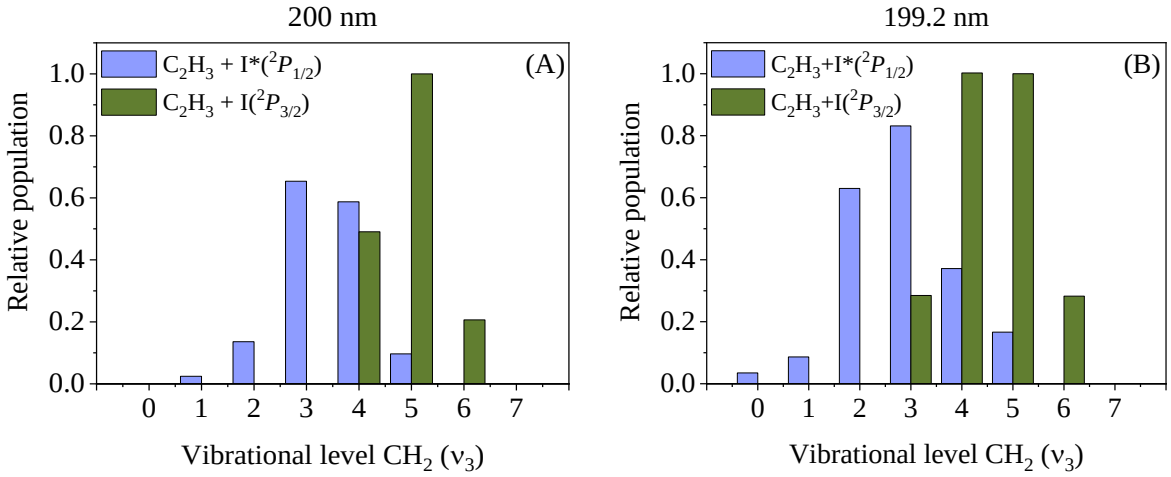

Figure 6.7. *Normalized distribution of vibrational populations of the C_2H_3 co-fragment for excitation at 200 nm (A) and at 199.2 nm (B) according to its dissociation channel, I and I*. Blue bars represent the C_2H_3+I* channel, while green bars represent the C_2H_3+I channel.*

The corresponding angular distributions obtained by radial integration of the inverted images are depicted in figure 6.8. For both cases, the contribution from the I and I* channels at 304.5 nm are overlapped, and thus the angular distribution is therefore obtained for the whole (I+I*) contribution. The anisotropy parameters are obtained by fitting the angular distributions to:

$$I(\theta) \propto 1 + \sum_{k=1}^{n} \beta_{2k} P_{2k}(\cos\theta) \tag{6.11}$$

where θ represents the angle between the photolysis laser polarization and the fragment recoil velocity, $P_{2k}(\cos\theta)$ is the $2k^{th}$ order Legendre polynomials and β_{2k} are the anisotropy parameters. The number of anisotropy parameters needed to characterize the angular distribution depends on the number of photons involved in the absorption process and the total angular momenta of the species detected. For a one-photon dissociation process and a (2+1) REMPI detection scheme through a single intermediate *J*-level, *n* is constrained by the maximum allowed integers of 2+1 or J+1, whichever is smallest.[287] For excited

state spin-orbit I* fragment, J=1/2 and only one anisotropy parameter β_2 is necessary to characterize the angular distribution. For ground-state I fragment, J=3/2 and up to β_6 can be necessary.

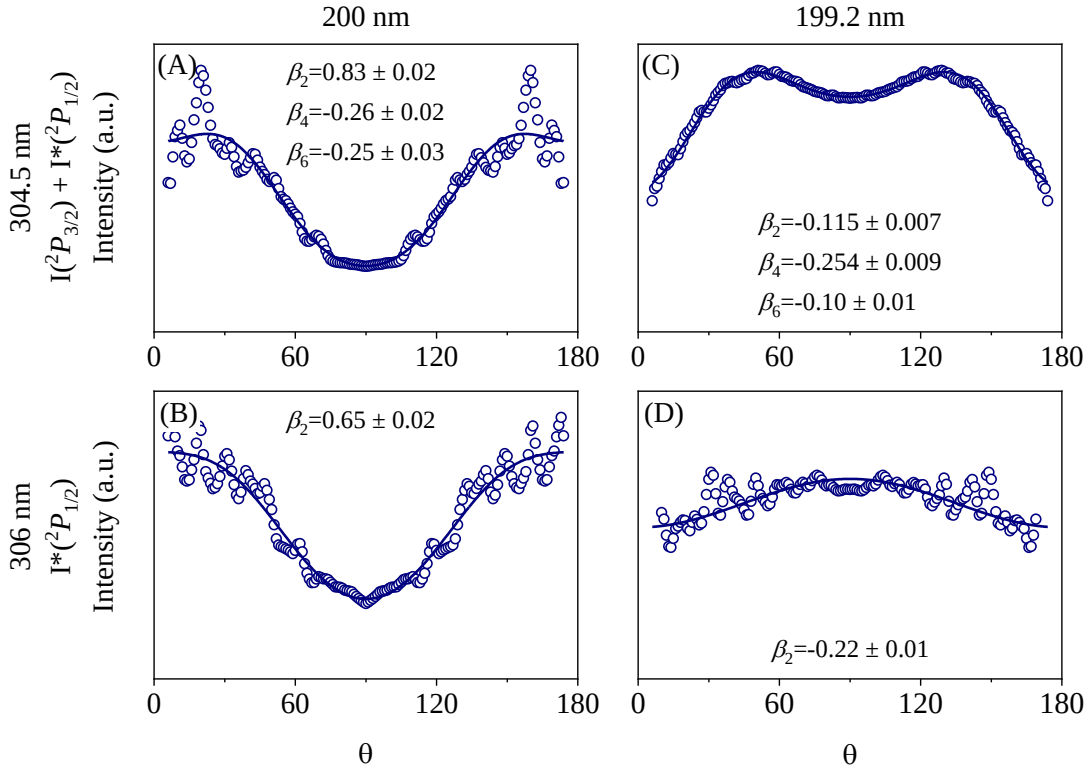

Figure 6.8. *Angular distributions of fragments I+I* and I* photofragments from C_2H_3I photodissociation at 200 and 199.2 nm, detected by REMPI (2+1) at 304.5 nm (A) for 200 nm and (C for 199.2 nm) and 306 nm (B for 200 nm and D for 199.2 nm). Intensity ranges from 0 to 1.1.*

The β_2 anisotropy parameters, summarized in table 6.4, present at 200 nm positive values for both I* and (I+I*) channels, reflecting the main contribution of a transition characterized by a TDM parallel to the C−I bond. For 199.2 nm, negative values of β_2 for both I* and (I+I*) channels are obtained, reflecting the main contribution of a transition characterized by a TDM perpendicular to the C−I bond.

Table 6.4. *Anisotropy parameters β_2 for both dissociation channels, I and I*+I, corresponding to the dissociation of C_2H_3I upon excitation at 200 and 199.2 nm. The indicated values have been obtained from an average of several repetitions of the experiment.*

Excitation wavelength (nm)	Channel	Anisotropy parameter, β_2
200	I+I*	0.83±0.02
	I*	0.65±0.02
199.2	I+I*	-0.115±0.007
	I*	-0.22±0.01

The evolution of the intensity of the I fragment images as a function of the pump-probe time delay was monitored to measure the C−I bond cleavage times. For the measurements using the detection at

306 nm, a fitting procedure was employed to separate the I* dissociation channel from the dissociative MPI contribution using a Gaussian function and one Boltzmann-type function. In the case of detection of I+I* at 304.5 nm, due to the high degree of overlap of the two dissociation channels, the reaction time of the I channels could not be isolated; instead, reaction times are provided for both channels I+I* altogether. The resulting transients, depicted in figure 6.9, measured for both excitation wavelengths for the I* channel and I+I* were fitted to a Boltzmann sigmoidal curve *S* given by:

$$S = A_2 + \frac{A_1 - A_2}{1 + \exp\left(\frac{t - t_0}{t_c}\right)} \tag{6.12}$$

where A_1 and A_2 are the initial and final intensity values of the function, characterized by a center temporal position t_0 (*i.e.*, the delay time for which the intensity has reached half its asymptotic value) and a rise time constant t_c, which describes the steepness of the rise.

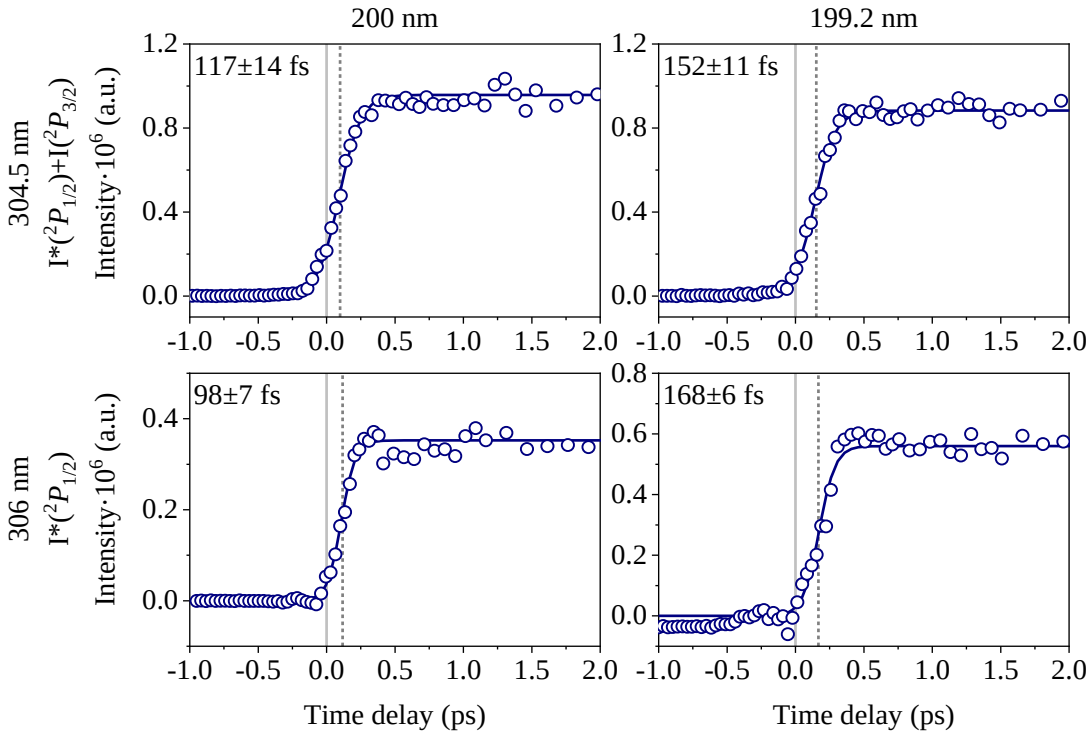

Figure 6.9. *C–I transients (open circles) for C_2H_3I for the I*($^2P_{1/2}$) (bottom panels) and I*($^2P_{1/2}$)+I($^2P_{3/2}$) (upper panels) channels at 200 nm (left) and 199.2 nm (right), fitted using a Boltzmann sigmoidal function (dark blue solid line). The reaction (clocking) times are referred to the time zero found in situ by measuring the MPI signal in the center of the images (vertical light grey line). The reaction time is defined as the time between time zero and the time corresponding to the middle of the rise of the transient (vertical dark grey dashed line). The reaction times are obtained as a mean value of several measurements and the standard deviations are indicated in each panel.*

The obtained C−I bond cleavage times, τ_{exp}, are summarized in table 6.5. The transient of the low-energy contribution appearing in the center of all I images (MPI contribution) fitted to a Gaussian function was employed as the time-zero reference.

Table 6.5. *C–I reaction times for both dissociation channels, I and I*, corresponding to the dissociation of C_2H_3I upon excitation at 200 and 199.2 nm.*

Excitation wavelength (nm)	Channel	Reaction time, τ_{exp} (fs)
200	I+I*	98±7
	I*	117±14
199.2	I+I*	152±11
	I*	168±6

Reaction times are in the hundreds of femtoseconds; nevertheless, at 200 nm, they are subtly shorter than at 199.2 nm. Additionally, the I channel seems to be characterized by a shorter reaction time than that corresponding to the I* channel, as expected.

6.3.2. Spectroscopic analysis

The spectroscopic analysis of the absorption spectrum performed by Dr. Paulo Limão-Vieira is presented in this section. The results are only shown in the 5.4-6.8 eV region, the excitation region that concerns the present experiments.

C_2H_3I is a C_s symmetry molecule in the electronic ground state. A close inspection of the ground state molecular orbitals from the work of Zou *et al.*[377] shows that the HOMO and the third highest (HOMO-2) have an I($5p_\perp$) and π_{CC} character. The lowest-lying ionization energies relevant to this work are 9.26, 10.01 and 11.50 eV[388] and are assigned to the removal of an electron from the $(n_{I(\perp)})(9a''^{-1})$, $(n_{I(l)})(25a'^{-1})$ and $(\pi_{CC})(8a''^{-1})$ orbitals, respectively, according to Kishimoto *et al.*[417] and in good agreement with the data of Mines and Thomson,[418] and Shuman *et al.*[419]

The absolute high-resolution VUV photoabsorption cross-section spectrum of C_2H_3I measured using the FTS of VUV beamline DESIRS at the SOLEIL synchrotron radiation source is shown in figure 6.10 in the photon energy range 5.0-10 eV. The experimental conditions under which the spectrum measurement was carried out allowed us to obtain a fine structure much better resolved than previous absorption spectra by Boschi and Salahub[348] and Sze *et al.*[388] The electronic excitation spectrum is mainly assigned to valence ($n_{I(\perp)}\rightarrow\pi_{CC*}$, $n_{I(l)}\rightarrow\sigma_{CI*}$ and $n_{I(l)}\rightarrow\pi_{CC*}$) and Rydberg ($n_I\rightarrow ns$) transitions.[348, 388] The normal mode description has been assigned according to the information in the vibrational spectrum of Torkington and Thompson[420] and involves mainly the C=C stretching (ν_4) and C–I stretching (ν_5) modes, with energies in the ground state of 0.198 eV (1593 cm^{-1}) and 0.066 eV (535 cm^{-}

^{1}), respectively. Sze *et al.*[388] reported the lowest-lying ionic state vibrational energy values of 0.156 eV (ν_4) and 0.037 eV (ν_5), which are relevant for identifying vibrational series present in the Rydberg series assigned below.

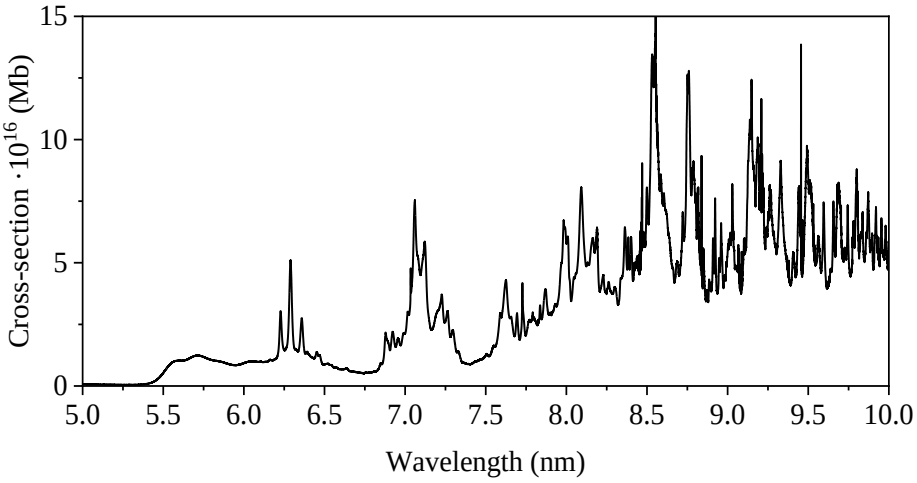

Figure 6.10. *High-resolution VUV photoabsorption spectrum of C_2H_3I in the 5.0-10 eV photon energy range measured using the FTS of VUV beamline DESIRS at the SOLEIL synchrotron radiation source.*[349]

6.3.2.1. Photon energy range of 5.4-6.2 eV

The 5.4-6.2 eV photon range of the measured absorption spectrum is depicted in figure 6.11. The spectrum is characterized by a broad feature peaking at 5.71(3) eV, which has been previously reported as the *B*-band[348, 388] and assigned to a valence $n_{I(\perp)}\rightarrow\pi_{CC}^*$ ($\tilde{X}^1A'\rightarrow{}^1A'$) transition[377] with a local cross-section of 12.3 Mb (see table 6.6).

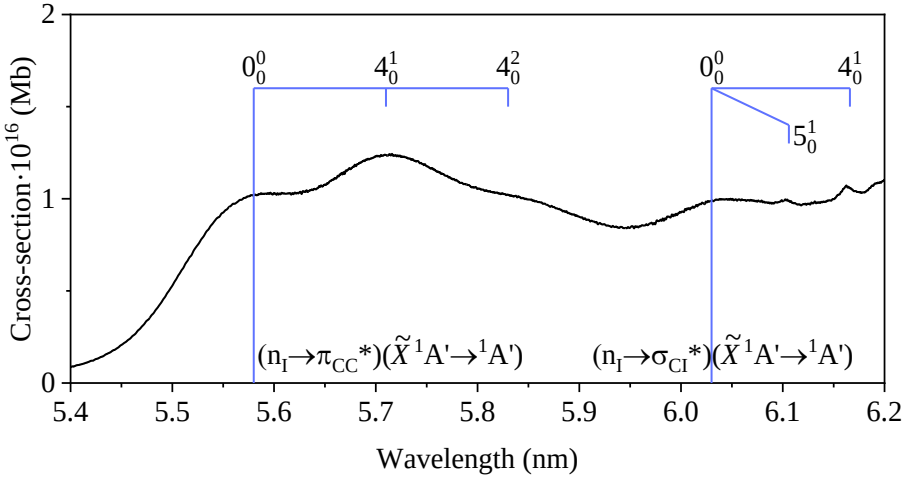

Figure 6.11. *VUV photoabsorption spectrum of C_2H_3I in the 5.4-6.2 eV photon energy range and the corresponding assignments of the main absorption features.*

Table 6.6. *Experimental vertical excitation energies (in eV) of C_2H_3I compared with previous data in the literature.*

Energy (eV)	Cross-section (Mb)	Assignment	Energy (eV)[348]	Energy (eV)[388]
5.71(3)	12.3	$n_{I(\perp)} \rightarrow \pi_{CC}^*$	5.579	5.700
6.03(8)	9.9	$n_{I(\parallel)} \rightarrow \sigma_{CI}^*$	6.050	6.060
6.230				6.232
6.291	50.7	$n_I \rightarrow ns$	~6.296	6.279
6.361				6.342
–	–	$n_{I(\parallel)} \rightarrow \pi_{CC}^*$	–	6.467

The last decimal of the energy is given in parenthesis for these less resolved features.

The 0_0^0 band origin is located at 5.58(5) eV, followed by a weak progression of broad features assigned to the C=C stretching mode (v_4). There is a second absorption feature at 6.03(8) eV, accommodating v_4 and one quantum of the C−I stretching mode (v_5) (see table 6.7). Boschi and Salahub[348] speculated about the assignment of the latter as either being part of the former band separated by 3600 cm^{-1} (0.446 eV) from its origin and assigned to a C-H stretching quantum or just simply due to another electronic transition. A close inspection of this feature at 6.03(8) eV shows a different slope from the feature at 5.58(5) eV, so it is believed that the former may belong to a different electronic transition. Boschi and Salahub[348] and Sze *et al.*[388] reported an electronic transition at 6.050 and 6.060 eV, respectively, arising from an $n_{I(\parallel)} \rightarrow \sigma_{CI}^*$ transition (Table 6.6).

Table 6.7. *Proposed vibrational assignments in the 5.4-6.2 eV absorption region of C_2H_3I compared with previous work of Boschi and Salahub.*[348]

Energy (eV)	Assignment	ΔE, v_4 (eV)	ΔE, v_5 (eV)	Energy (eV)[348]	Assignment*
5.58(5)(*b*)	0_0^0	–	–	5.598	0_0^0
5.71(3)(*b*)	4_0^1	0.128	–	5.727	1_0^1
5.83(6)(*b*,*s*)	4_0^2	0.123	–	5.862	1_0^2
6.03(8)(*b*)	0_0^0	–	–	6.048	–
6.106	5_0^1	–	0.068	–	–
6.166	4_0^1	0.128	–	–	–

*The last digit of the energy value is given in parenthesis for these less-resolved features. (b) Broad structure, (s) shoulder structure. *Note that in ref.* [348] *authors assign the excitation of three modes, C=C stretching to* ν_1*, C–I stretching to* ν_2*, and C–C–I bending to* ν_3*.*

6.3.2.2. Photon energy range of 6.0-6.8 eV

The absorption spectrum in the 6.0-6.8 eV energy range is depicted in figure 6.12, and the corresponding vibrational assignments are collected in table 6.8 and table 6.9.

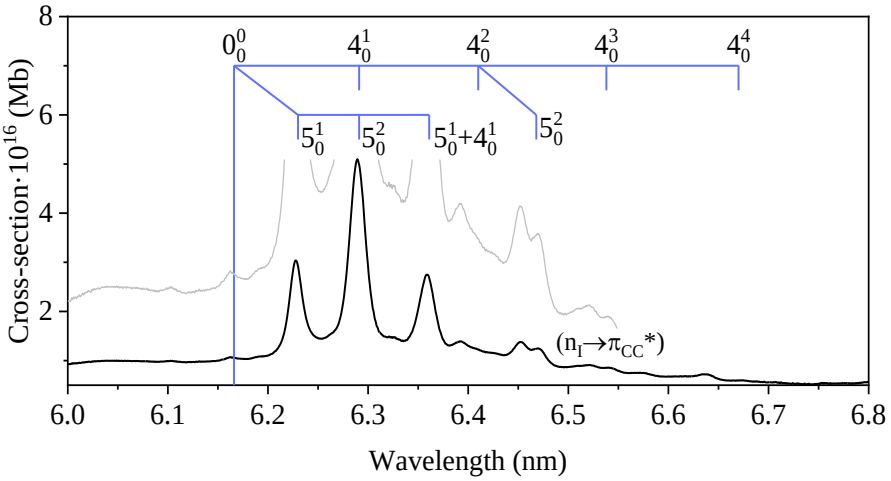

Figure 6.12. *VUV absorption spectrum of C_2H_3I in the 6.0-6.8 eV photon energy range and assignments of the main absorption features.*

The feature at 6.291 eV has been assigned to an *n*=6s member of a Rydberg series converging to the lowest ionization energy (see below table 6.10). Boschi and Salahub[348] and Sze *et al.*[388] reported an absorption band at ~6.296 and 6.279 eV, respectively, and assigned it to an ($n_I \rightarrow 6s$) transition. A close inspection of this feature and its role within the associated band resembles a more valence-like character rather than Rydberg, which can only be really probed by theoretical calculations. If this were the case, the 0_0^0 band can be tentatively assigned at 6.166 eV with a maximum at 6.291 eV and a local cross-section of 5.07 Mb. Within this energy range, there are also visible some vibrational assignments (Table 6.8) together with progressions involving the C=C stretching mode (ν_4) coupled with the C−I stretching mode, ν_5 (Table 6.9). A careful inspection of the absorption band reveals that the feature at 6.455 eV, assigned to the excitation of C−I stretching mode (ν_5) coupled with a progression of the C=C stretching mode (ν_4) (see table 6.9), has been assigned in the pseudo-optical experiment of Sze *et al.*[388] to an $n_{I(|)} \rightarrow \pi_{CC}^*$ transition at 6.467 eV.

Table 6.8. *Proposed vibrational assignments in the 6.0-6.8 eV absorption region of C_2H_3I compared to previous work of Boschi and Salahub.*[348]

Energy (eV)	Assignment	ΔE, ν_4 (eV)	ΔE, ν_5 (eV)	Energy (eV)[348]	Assignment*
6.166	0_0^0 (?)	–	–	6.221	0_0^0
6.230	5_0^1	–	0.064	6.281	2_0^1
6.291	4_0^1 / 5_0^2	0.125	0.061	6.338	2_0^2
6.361	$5_0^1+4_0^1$	–	–	–	–
6.41(2)(*s*)	4_0^2	0.121	–	–	–
6.468	4_0^2 / 5_0^2	–	0.056	–	–
6.538	4_0^3	0.126	–	–	–
6.67(5)(*w*, *b*)	4_0^4	0.137	–	–	–

*The last decimal of the energy value is given in parenthesis for these less-resolved features. (s) Shoulder structure, (w) weak feature, (b) broad structure. * Note that in ref. [348] authors assign the excitation of three modes, C=C stretching to ν_1, C–I stretching to ν_2, and C–C–I bending to ν_3.*

Table 6.9. *Proposed vibrational assignments for progressions in the 6.0-6.8 eV absorption band of C_2H_3I compared to previous work of Boschi and Salahub.*[348]

Energy (eV)	Assignment	ΔE, ν_4 (eV)	ΔE, ν_5 (eV)	Energy (eV)[348]	Assignment*
6.19(7)(*s*)	4^n	–	–	–	–
6.32(5)(*s*)	4^{n+1}	0.128	–	6.392	1_0^1
6.452	4^{n+2}	0.127	–	6.450	$1_0^1+2_0^1$
6.50(8)(*s*, *w*)	$4^{n+2}+5_0^1$	–	0.056	6.506	$1_0^1+2_0^2$
6.56(6)(*b*, *w*)	$4^{n+2}+5_0^2$	–	0.058	6.560	1_0^2
6.64(2)(*b*)	$4^{n+2}+5_0^1+4_0^1$	–	–	–	–
6.57(8)(*b*)	4^{n+3}	0.126	–	–	–
6.26(7)(*s*)	4^n	–	–	–	–
6.396	4^{n+1}	0.129	–	–	–
6.452	$4^{n+1}+5_0^1$	–	0.056	–	–
6.51(9)(*b*)	4^{n+2}	0.123	–	–	–
6.64(2)(*b*)	4^{n+3}	0.123	–	6.617	$1_0^2+2_0^1$
6.42(1)(*s*)	4^n	–	–	–	–
6.544	4^{n+1}	0.123	–	–	–
6.67(5)(*w*, *b*)	4^{n+2}	0.130	–	6.672	$1_0^2+2_0^2$

The last decimal of the energy value is given in parenthesis for these less-resolved features. The last digit of the energy value is given in parenthesis for these less-resolved features.(s) Shoulder structure, (b) broad structure, (w) weak feature.
**Note that in ref. [348] authors assign the excitation of three modes, C=C stretching to ν_1, C–I stretching to ν_2, and C–C–I bending to ν_3.*

6.3.2.3. Rydberg transitions

C_2H_3I electronic excitation in the photon energy range studied in this work displays Rydberg character, according to Boschi and Salahub[348] and Sze *et al.*[388] A summary of the experimental energies, assignments and quantum defects can be found in table 6.10. The peak positions have been tested using the Rydberg formula[388] given by:

$$E_n = E_I - \frac{R}{n-\delta} \tag{6.13}$$

where E_I is the ionization energy, n is the principal quantum number of the Rydberg orbital of energy E_n, R is the Rydberg constant (13.61 eV), and δ is the quantum defect resulting from the penetration of the Rydberg orbital into the core.

Yet, with quantum defect calculations as the only guide, assignments cannot be proposed for these bands with confidence, so values for higher n Rydberg states in table 6.10 are tentative assignments.

The lowest-lying Rydberg transition is assigned to $n_I \rightarrow 6s$, with the first member located at 6.230 eV and having an effective quantum number, $n^*=2.12$. However, $n=6$ is also proposed at 6.291 and 6.361 eV; these in good agreement with the assignments from Sze *et al.*[388] (see Table 6.10).

Table 6.10. *Energy value (eV) and effective quantum number (n*) of the Rydberg series converging to the ionic electronic ground state of C_2H_3I compared to previous work of Sze et al.*[388]

Vertical energy (eV)	n*	Assignment	Vertical energy (eV)[388]	n*
IE_1=9.26 eV[a] ($2a''^{-1}$)				
6.230	2.12		6.232	2.12
6.291	2.14	6s	6.279	2.14
6.361	2.17		6.342	2.16

6.3.3. Theoretical results

The electronic states resulting from the *ab initio* calculations for C_2H_3I are listed in table 6.11 in terms of the vertical excitation energy at the Franck-Condon geometry, up to 7 eV. The oscillator strength for each state and the main state character (singlet or triplet) are also indicated. It is not possible to indicate the symmetry of the states for two reasons: first, the calculations lack of symmetry and second, the spin-orbit coupling mixes different symmetries, and it would be necessary to work with double groups of symmetry to be able to assign them to each state.

Table 6.11. *Ab initio vertical excitation energies of the computed electronic states in the Franck-Condon region for C_2H_3I from 0 up to 7 eV. The oscillator strength for each state and the main state character (singlet or triplet) are also indicated.*

State number	Franck-Condon energy (eV)	Oscillator strength (10^2 a.u)	State character
1	0.00	0.00	Singlet
2	4.23	0.00	Triplet
3	4.24	0.00	Triplet
4	4.24	0.00	Triplet
5	4.42	0.00	Triplet
6	4.42	0.00	Triplet
7	4.49	0.04	Triplet
8	4.67	0.17	Singlet-Triplet
9	4.99	0.00	Triplet
10	5.06	0.05	Triplet
11	5.12	0.20	Singlet-Triplet
12	5.45	0.71	Singlet
13	6.10	15.77	Singlet
14	6.38	0.00	Singlet

State number	Franck-Condon energy (eV)	Oscillator strength (10^2 a.u)	State character
15	6.38	0.00	Triplet
16	6.40	0.01	Triplet
17	6.59	4.46	Triplet
18	6.62	0.00	Triplet
19	6.62	0.03	Triplet
20	6.67	0.04	Triplet
21	6.74	3.46	Triplet
22	6.80	0.00	Triplet
23	6.81	0.10	Triplet
24	6.87	0.00	Triplet
25	6.87	0.50	Triplet
26	6.88	0.24	Triplet
27	6.97	0.03	Singlet

The computed absorption spectrum in the region between 5-10 eV obtained at CAS (8,7) from 1000 trajectories and constrained to a spectral width of 0.2 eV is represented in figure 6.13, along with the different spectral components associated with the different excited states.

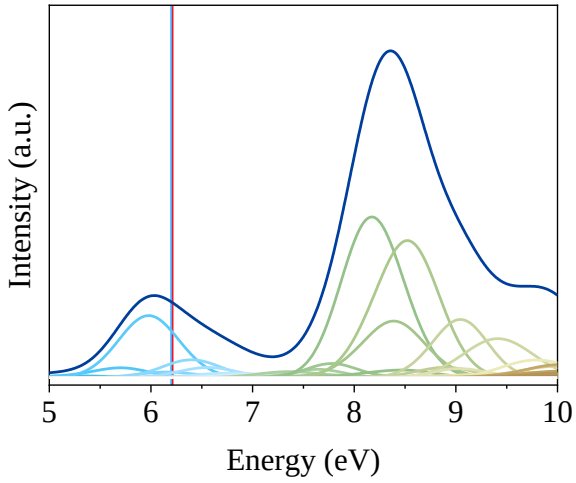

Figure 6.13. *Semiclassical computed absorption spectrum for C_2H_3I (dark blue) in the energy range between 5-10 eV and its decomposition into the spectral components associated with the different electronic states. In the top x axis, the corresponding excitation wavelength is indicated. The vertical bands in blue and red indicate the two different excitation wavelengths, 200 and 199.2 nm, employed in the present experiments. The contribution to the absorption of states 12 and 13, with oscillator strengths of $0.71 \cdot 10^{-2}$ and $15.77 \cdot 10^{-2}$a.u. respectively is highlighted.*

The theoretical spectrum is characterized by a continuous band in the range 5-7 eV, in good agreement with the experimental spectrum. It is not possible to glimpse the components of the trident characteristic of the experimental spectrum since they are embedded in the band corresponding to the

dissociative continuum. In addition, the calculated energies for the different electronic states may be shifted with respect to the experimental values, and thus the position of the excitation energy in the spectrum (vertical bands) is only tentative. Notice the contribution from states 12 and 13 (see table 6.11) in the energy range of 5-7 eV, which are those with oscillator strengths compatible with the absorption in this energy range in the Franck-Condon region (see below).

In figure 6.14, the computed absorption spectrum for C_2H_3I as a function of the total TDM and those computed with respect to each axis is represented. Note that the X axis is located in the I−C=C plane, perpendicular to the C−I bond, the Y axis is perpendicular to the I−C=C plane, and the Z axis is in the I−C=C plane, along the C−I bond. Accordingly, in the 199.2 and 200 nm region, the absorption is dominated by transitions parallel (Z) and perpendicular (X) to the C–I axis. It seems there is no significant contribution from a TDM oriented perpendicular to the I−C=C plane, which is usually the contribution that is overestimated.

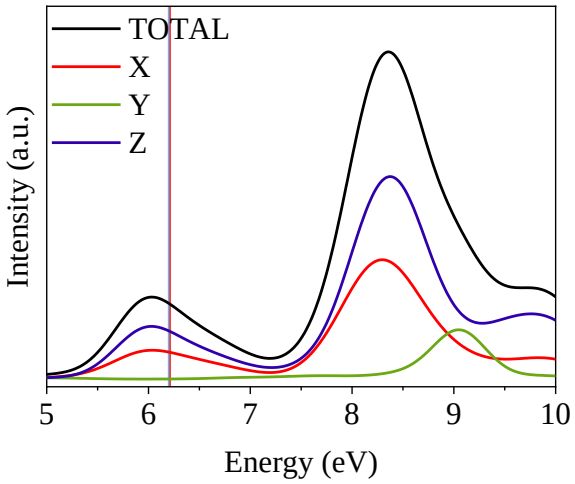

Figure 6.14. *Computed absorption spectra for C_2H_3I as a function of the total TDM axis (black line) and those computed for each axis. The X axis (red line) is located in the I-C=C plane, perpendicular to the C−I bond (red line), the Y axis (green line) is perpendicular to the I−C=C plane and the Z axis (blue line)is in the I-C=C plane, along the C−I bond. The contribution to the absorption of states 12 and 13, with oscillator strengths of $0.71\cdot10^{-2}$ and $15.77\cdot10^{-2}$ a.u. respectively is highlighted.*

Figure 6.15 depicts the adiabatic potential energy curves computed at the XMS-CASPT2 level for C_2H_3I as a function of the C−I internuclear distance up to 10 eV. According to the potential energy curves, two dissociation limits are available below 200 and 199.2 nm. The first dissociation limit, which corresponds to $C_2H_3(\widetilde{X})$ in correlation with $I(^2P_{3/2})$, appears at 3.17 eV, whereas the second dissociation limit, which corresponds to $C_2H_3(\widetilde{X})$ in correlation with $I^*(^2P_{1/2})$, appears at 4.05 eV, thus 0.88 eV above the first dissociation limit, which is about the spin-orbit coupling energy of $I(^2P_J)$. The following dissociation limits, which correspond to $C_2H_3(\widetilde{A})$ in correlation with $I(^2P_{3/2})$ and $I^*(^2P_{1/2})$ are, nevertheless, not accessible by the excitation wavelengths used in the present experiments. The values

of these dissociation limits are not indicated since the obtained potential energy curves are not entirely accurate since the geometry optimization was carried out only for the ground state, and this has a profound effect on the asymptotic energies of the excited state curves correlating with $C_2H_3(\widetilde{A})$.

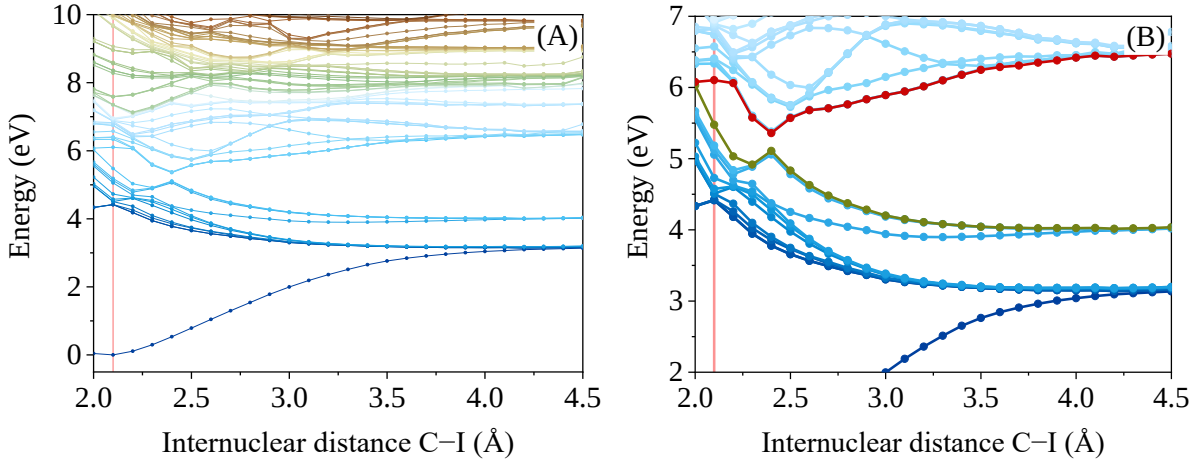

***Figure 6.15**. (A) Computed XMS-CASPT2 potential energy curves for C_2H_3I as a function of the C−I internuclear distance up to 10 eV. (B) Expanded view in the energy region of interest. States 12 and 13 are highlighted in green and red, respectively. The vertical bar indicates the Franck-Condon region.*

In figure 6.16, the same potential energy curves of figure 6.15 are represented but highlighting the regions of the potential energy curves with the most significant probability of absorption, taking into account the oscillator strength values listed in table 6.11.

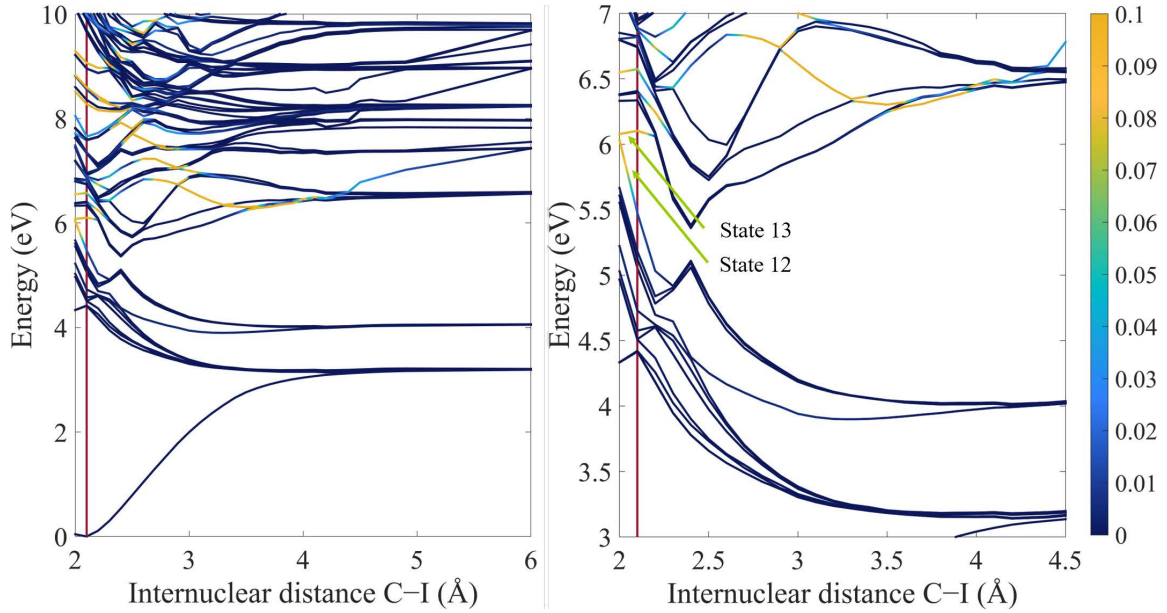

***Figure 6.16**. (A) Computed XMS-CASPT2 potential energy curves for C_2H_3I as a function of the C−I internuclear distance. (B) Expanded view in the energy region of interest. States 12 and 13 are also indicated. The vertical colormap indicates the oscillator strength: dark blue indicates the lowest absorption probability, while yellow represents the highest absorption probability. The vertical bar in dark red indicates the Franck-Condon region.*

According to figure 6.16 and the oscillator strength values listed in table 6.11, in the Franck Condon region, the brightest states are states 12 and 13 with corresponding oscillator strength values of $7.1 \cdot 10^{-3}$ and $1.6 \cdot 10^{-1}$ and vertical excitation energies of 5.45 and 6.10 eV, respectively.

For optimizing the energy and geometry of C_2H_3I during dissociation, a minimization algorithm was employed using damped dynamics (see theoretical method section). It is important to note that the time base that appears in the following figures representing the MEP is not related to the reaction times but rather to the optimization steps.

Figure 6.17 (A), (B), (C) and (D) show the variation of the internuclear distance C–I, the internuclear distance C=C, the dihedral angle H–C=C–H and the variation of the energy for damped dynamics starting from bound state 12. As can be seen, the reaction coordinate is governed by an elongation of the C−I bond and a simultaneous reduction of the internuclear C=C bond, leading to a prompt C−I bond dissociation, which is reflected in the smooth variation of the dihedral angle H–C=C–H and of the energy.

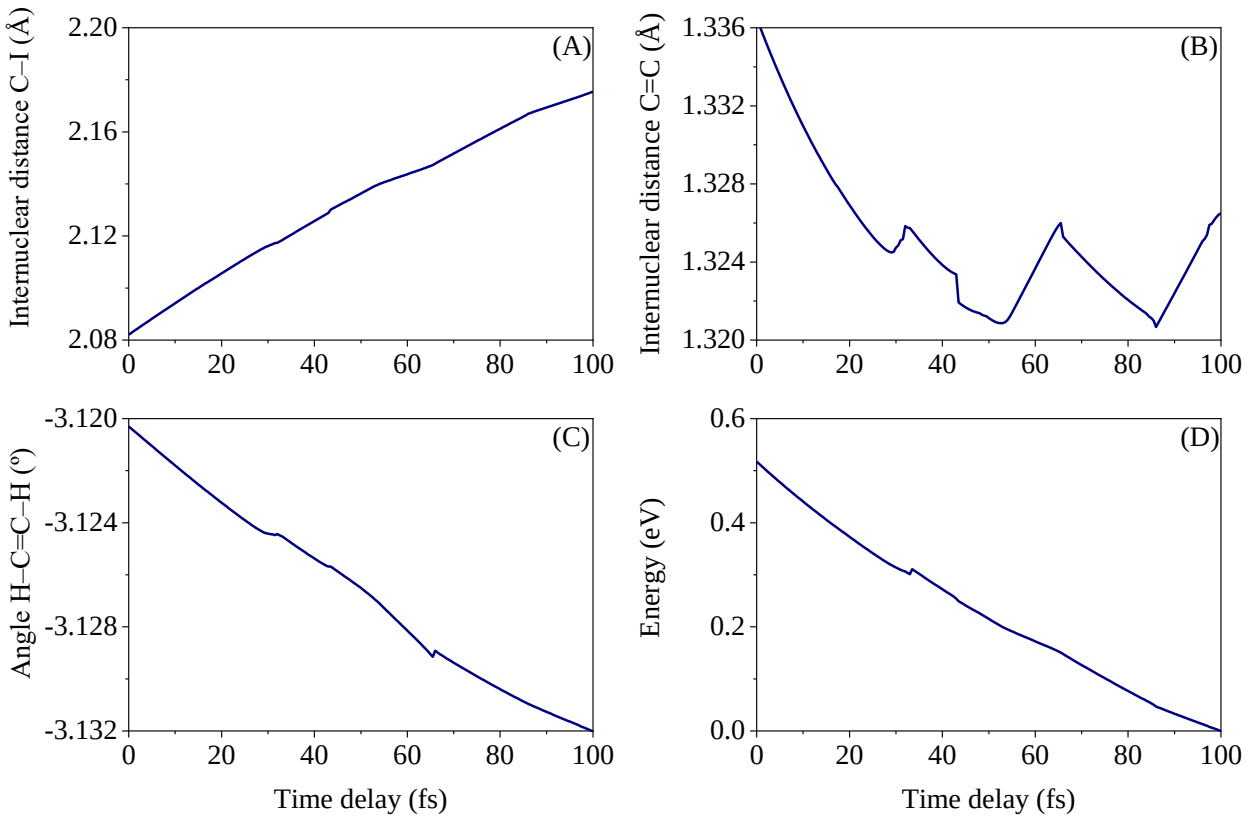

***Figure 6.17**. Average evolution of (A) the C–I internuclear distance, (B) the C=C internuclear distance, (C) the dihedral angle H-C=C-H and (D) the energy for the damped dynamics starting from state 12.*

Likewise, figure 6.18 (A), (B), (C) and (D) show the variation of the internuclear distance C–I, the internuclear distance C=C, the dihedral angle H–C=C–H and the variation of the energy for damped

dynamics starting from state 13. As can be seen, an elongation of the C=C bond along with the torsion of the CH_2 group and a simultaneous reduction of the C–I bond, take place up to roughly 70 fs of optimization. From this point, a transfer of population from the initially excited state 13 to the lower energy state 12 is produced *via* a non-adiabatic crossing, leading to a continuous elongation and consequent cleavage of the C−I bond and simultaneously to a C=C bond reduction. Notice the change in the slope of the variation of energy once the crossing has occurred. Due to the observed initial structural evolution of the molecule along the C=C bond distance, the potential energy curves along the C–I bond seems not to be of great usefulness given the dimensionality of the dynamics.

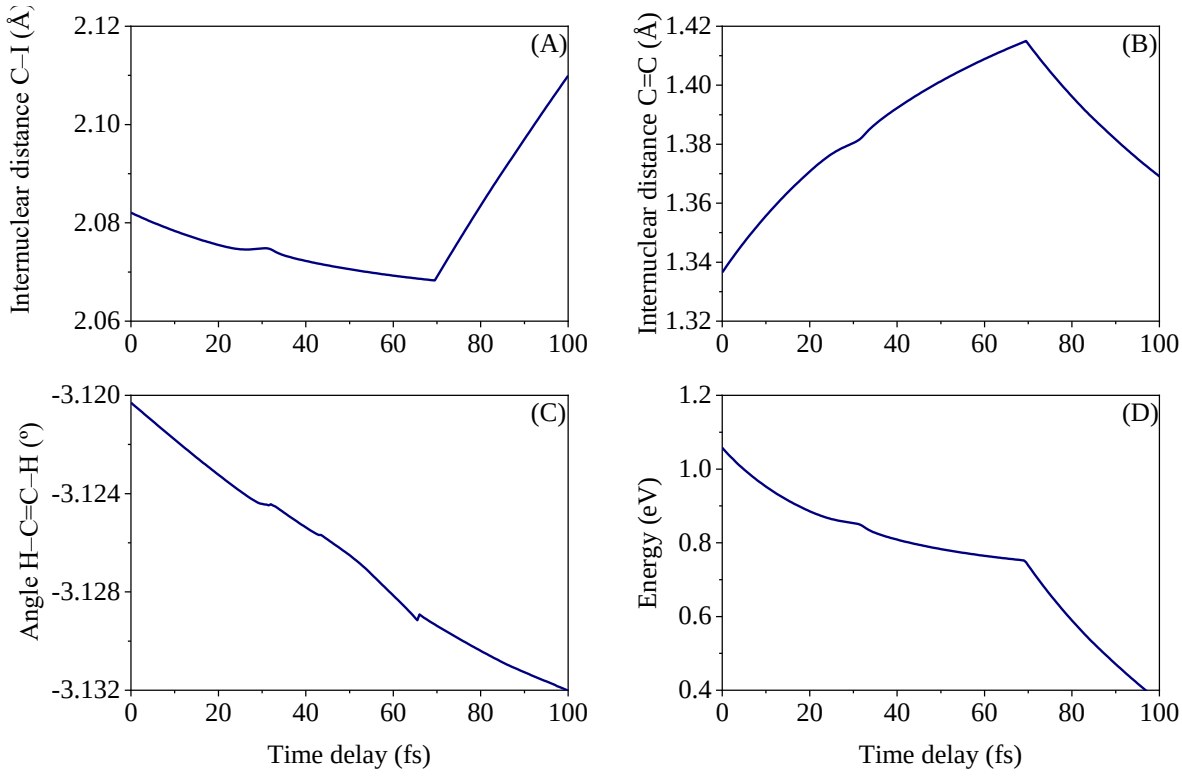

***Figure 6.18**. Average evolution of (A) the C–I internuclear distance, (B) the C=C internuclear distance, (C) the dihedral angle H-C=C-H and (D) the energy for the damped dynamics starting from state 13.*

In this type of representation, only the marked geometrical changes induced by the crossing of potential energy surfaces involving different reaction coordinates are observed. There can be non-adiabatic crossings in the same coordinate that are not seen in these representations. To identify conical intersections responsible for non-adiabatic pathways along the reaction coordinate, it is necessary to either optimize these features or carry out full dimension on-the-fly trajectories.

On-the-fly adiabatic full-dimension classical trajectory calculations including surface hopping were run from state 13 at the *ab initio* CASSCF level of theory corrected using perturbation theory in its multistate version (MS-CASPT2). Figure 6.19 shows snapshots corresponding to a selected trajectory for C_2H_3I starting from state 13, dissociating into C_2H_3+I.

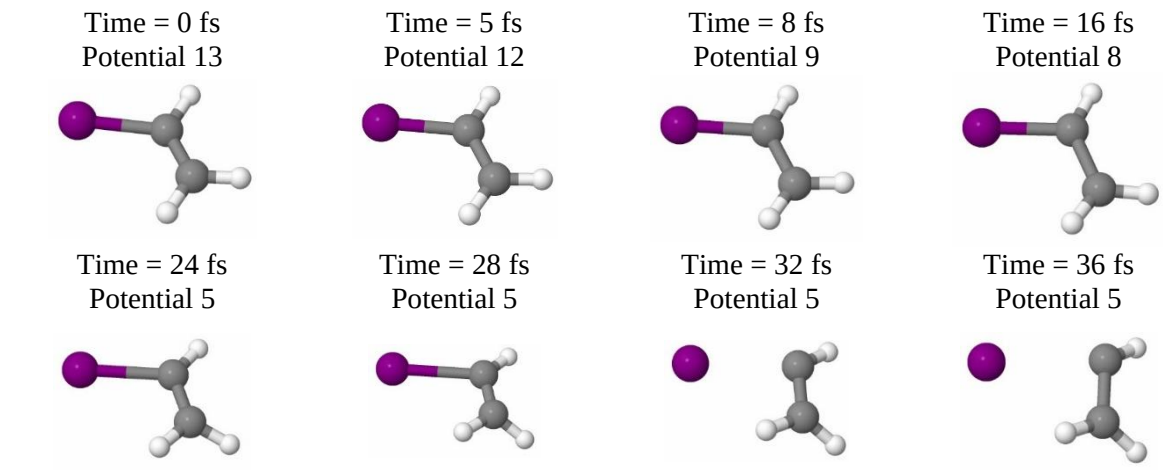

***Figure 6.19**. Snapshots corresponding to a selected full dimension on-the-fly trajectory starting from state 13 showing the C–I bond dissociation process for C_2H_3I. In each frame, the time and the potential in which the molecule is found at that precise moment are indicated. At time zero, the C–I distance corresponds to the equilibrium distance of the molecule.*

In figure 6.20, it is depicted, on the one hand, the potential energy variation in terms of the reaction time for the selected trajectory starting from state 13 (represented by a red dashed line) and, on the other hand, the involved electronic states in this trajectory, *i.e.*, states 5, 8, 9, 12 and 13 (represented by continuous lines).

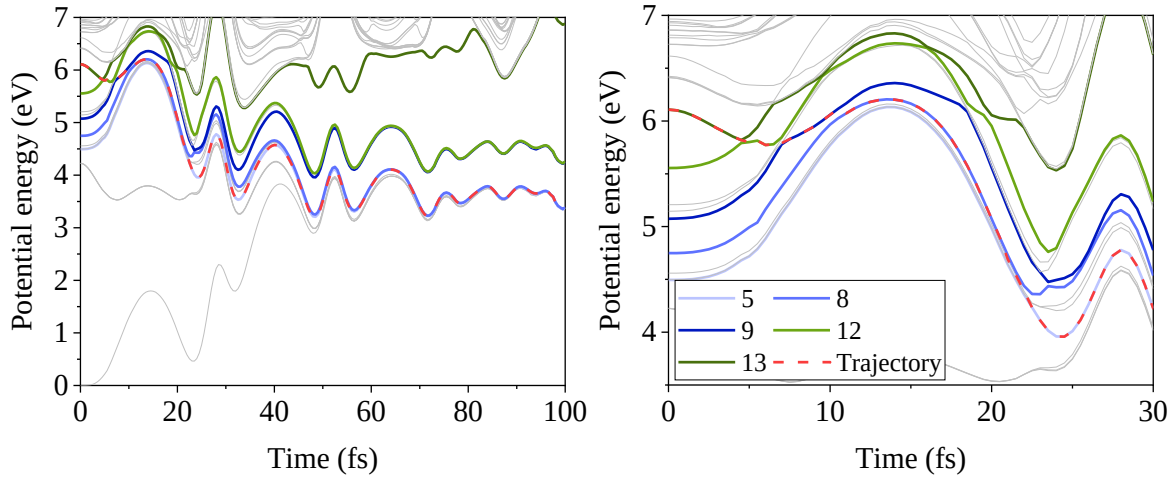

***Figure 6.20**. Potential energy variation in terms of the reaction time for a selected trajectory starting from state 13 (red dashed line). The involved electronic states in this trajectory, i.e., states 5, 8, 9, 12 and 13 (represented by continuous lines in light blue, mid blue, dark blue, light green and dark green, respectively) are depicted. The different surface hoppings can be appreciated.*

The trajectory initially starts in state 13; however, a population transfer from this state to state 12 is produced at around 5 fs. Afterward, almost immediately, at 7 fs, there is a next potential change to state 9 followed by another transfer to state 8, at 10 fs. From this state, the last potential change takes place to state 5, at 21 fs, which is the one that correlates with the dissociation limit leading to ground-

state I. This is the result of the selected trajectory, but many trajectories must be run to have statistics, including both channels yielding I and I* in correlation with $C_2H_3(\widetilde{X})$.

6.4. DISCUSSION

The dissociation dynamics of C_2H_3I at excitation wavelengths of 199.2 and 200 nm can be discussed based on the reported experimental results and theoretical calculations, and the assignments of the absorption spectrum.

Out of the spectroscopic analysis performed by Dr. Paulo Limão-Vieira, excitation at 200 nm is mediated by an $n_{I(l)} \rightarrow \sigma_{C-I^*}$ transition corresponding to the absorption from the continuum, which constitutes the background of the absorption spectrum. As seen in previous chapters, this type of excitation typically leads to prompt dissociation of the C−I bond without major structural changes, as reflected by the damped dynamics starting from state 12. Furthermore, this type of excitation is mediated by an initial parallel transition in good agreement with the angular distributions measured for the I photoproducts. In contrast, excitation in the first peak of the trident-shaped structure at 199.2 nm was firstly assigned to a vibrational transition to the 6s Rydberg state coupled with a quantum of vibrational excitation of the mode ν_5, which corresponds to the C−I stretch mode, denoted as $n_i \rightarrow n_s 5_0^1$. Nevertheless, newer assignments revealed this feature to have a more valence-like character rather than a Rydberg character. This, in combination with theoretical calculations, revealed this trident-shaped structure to be a vibrational progression from valence states due to a $\pi \rightarrow \pi^*$excitation. This type of excitation, which is to a bound state must induce severe structural changes to lead to a feasible dissociation of the C–I bond, as reflected in the damped dynamics starting from state 13. In this case, it is expected that the excitation as this wavelength is characterized by a dominant perpendicular transition, also in good agreement with the experimental findings.

The fact that there is both a parallel and a perpendicular contribution in the computed absorption spectrum shown in figure 6.14 reveals the participation of the background (characteristic of an $n_{I(l)} \rightarrow \sigma_{C-I}$ transition of parallel character corresponding to the excitation at 200 nm), and the trident-shaped structure (assigned to a vibrational progression of a $\pi \rightarrow \pi^*$ transition of perpendicular character associated with the excitation at 199.2 nm). However, this latter transition is not correctly rescued from the spectrum as the computed spectrum lacks vibrational resolution.

According to damped dynamics calculations, the excitation at 199.2 nm leads, in the first step of the dissociation, to the elongation or stretching of the C=C bond and out-of-plane vibrations, *i.e.*, the torsion of the CH_2 group, due to promotion of an electron to a π^* orbital. This variation of geometry approaches the molecule to the vicinity of a conical intersection through which a transfer of population to a lower state is produced. The molecule changes its character from π^*, to a mixed π^*/σ^* character

and finally to a σ* character leading to elongation and consequent cleavage of the C−I bond. In this sense, this photodissociation mechanism has an inherently multidimensional character. This type of mechanism is found similar in other halogenated species[421-424] such as the chloroethene anion[425] produced by dissociative electron attachment (DEA):

$$AB + e^- \rightarrow A + B^+ + e^- \tag{6.14}$$

Figure 6.21 displays a schematic representation of the π*/σ* mechanism of DEA in halogenated unsaturated compounds.

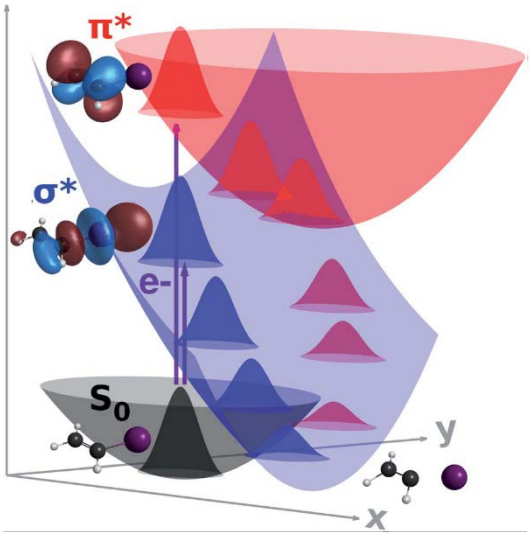

Figure 6.21. *Schematic potential energy surfaces for the neutral ground state (grey), and diabatic σ* (blue) and π* (red) anion states of C_2H_3I, along the dissociating (x) and coupling (y) coordinates. Electron attachment into the σ* state promptly induces cleavage into the I ion, whereas a π*/σ* coupling offers a route for dissociation when the π* state is initially formed. Figure from reference [426].*

In DEA processes, first, the electron is captured into the π* orbital of the C=C bond, resulting in a resonance state which is energetically lower-lying and possesses a longer lifetime than the metastable state obtained from the capture into the σ* orbital of the C–halogen bond. The electron is then transferred into the σ* orbital at a nuclear configuration where the lifetime of the corresponding repulsive state is long enough to lead to the dissociation of the molecule eventually. This transfer takes place *via* nuclear motion.[427-429] Similar mechanism occurs in many other unsaturated organic compounds, which have in common that a halogen atom is connected to one of the carbon (C) atoms involved in the double bond, such as chlorobenzene,[423, 430, 431] mono- to tetrachloroethene,[425, 431, 432] and chlorouracil.[421, 424]

On the other hand, excitation at 200 nm is governed by an elongation of the C−I bond and simultaneous reduction of the internuclear C=C bond distance typical of initial excitation of an $n_{I(l)} \rightarrow \sigma_{C-I}$ transition, leading as well to a fast cleavage of the C−I bond.

Excitation at both wavelengths leads ultimately to photodissociation of the molecule through both channels, C_2H_3+I and C_2H_3+I*, as shown by the estimated quantum yields Φ* of approximately 50 %. To explain the appearance of both channels, it is necessary to resort to complex non-adiabatic mechanisms between different potential energy curves. Figure 6.20 points out the existence of a conical intersection that may lead to I and I* release as long as the nuclear wave packet survives long enough for the system to cross non-adiabatically.

Concerning the available energy partitioning, approximately 50 % of it is channeled into internal energy of the corresponding C_2H_3 co-fragment, always being the energy partitioning f_{int} values somewhat lower for the channels that correlate with I, which implies that the co-fragments generated in the dissociation channels that give rise to I are more vibrationally excited. The widening of the rings and corresponding translational energy distributions must come from a high internal energy content from the molecular co-fragment, primarily vibrational excitation in ν_3. The geometric changes that occur during dissociation may be responsible for the significant excitation in this vibrational mode as occurs in CH_3I. The pyramidal geometry that the methyl (CH_3) fragment possesses in the CH_3I molecule changes to a planar geometry in the CH_3 fragment during the CH_3I photodissociation in the *A*-band, producing considerable vibrational excitation, concentrated mainly in the umbrella mode (ν_2). Along the same dissociative surface, this change in geometry takes place progressively, resulting in relatively cool vibrational distributions. In contrast, non-adiabatic transitions can force geometric changes producing a higher degree of vibrational excitation in the C_2H_3 radical in the channel that correlates with the formation of I. This effect is reflected in figure 6.7, which shows a relatively cool vibrational distribution for the I* channel (where the majority of the C_2H_3 population is in ν_3=3). In contrast, for I channel, the distribution is significantly hotter (the majority of the C_2H_3 population is in ν_3=5).

The initial character of the transitions is suggested by the anisotropy parameter β_2 obtained from the angular distributions of the measured I photofragments. The excitation at 199.2 nm is governed by an initial transition of perpendicular character, with corresponding anisotropy parameters of β_2=-0.22±0.01 (I*) and β_2=-0.115±0.007 (I+I*), whereas the excitation at 200 nm is governed by a parallel transition, with corresponding anisotropy parameters of β_2=0.65±0.02 (I*) and β_2=0.83±0.02 (I+I*). The obtained anisotropy parameters are not close to the typical limit values of pure parallel transitions (β_2=2) for 200 nm excitation or pure perpendicular transitions (β_2=-1) for 199.2 nm excitation due to a possible memory loss induced by various geometric changes of the molecule as well as the presence of several conical intersections prior to dissociation. The difference between the experimental values and the limit anisotropy values is more pronounced at 199.2 nm than at 200 nm. As previously noted, the geometric changes experienced by C_2H_3I before dissociating after excitation at 199.2 nm are more drastic due to a more complex mechanism. As happened with dihalomethanes, conical intersections can induce a

particular selection of ro-vibrationally excited population leading to distorted geometries and thus to more isotropic angular distributions.

The dissociation is somewhat faster at 200 nm compared to 199.2 nm, being the reaction times 98±7 fs (I+I*) and 117±14 fs (I*) for 200 nm and 152±11 fs (I+I*) and 168±6 fs (I*) for 199.2 nm. The excitation to the state 12 leads to the simple cleavage of the C–I bond through purely dissociative potentials with reaction times close to hundreds of femtoseconds, while the excitation to state 13 leads to a dissociation mediated by a predissociative mechanism, with inherent slower reaction times, although either a short-lived state or the coupling between surfaces seem to be highly optimal leading to a reduction of the reaction time from the usual timescales of predissociative mechanisms of picoseconds to femtoseconds.

6.5. CONCLUSIONS

In this chapter, time-resolved dynamics of C_2H_3I were examined at 199.2 and 200 nm to evaluate the influence of the chemical structure and the presence of unsaturations in the alkyl radical. For that purpose, the experiments were carried out employing velocity map ion imaging in combination with (2+1) REMPI of I and I* photoproducts. The experimental results comprise the total translational energy distributions, angular distributions of I fragments and reaction times for the C−I bond cleavage and are discussed along with the computed absorption spectra, potential energy curves, damped dynamics and trajectories obtained through high-level *ab initio* electronic structure calculations and full-dimension on-the-fly trajectories including surface hopping.

Despite performing the excitation with two wavelengths with a difference of only 0.8 nm, the panorama changes substantially. While the excitation at 200 nm, mediated by an initial parallel transition, drives C_2H_3I to a prompt photodissociation along the C−I reaction coordinate; for excitation at 199.2 nm, mediated by an initial perpendicular transition, the photodissociation has a high multidimensional character, since the initial excitation leads first to the elongation of the C=C bond followed by the elongation of the C–I bond leading ultimately to dissociation.

In both cases, the excitation results in the cleavage of the C−I bond producing I and I* fragments in correlation with the C_2H_3 with an available energy evenly distributed between the internal and translational degrees of freedom. The internal energy is dominated by the vibrational excitation of the molecular co-fragment. The presence of both photodissociation channels can be explained by non-adiabatic dissociation pathways mediated by the presence of several conical intersections. On the other hand, reaction times are characteristic of ultrafast phenomena on the femtosecond time scale; however, the photodissociation due to excitation at 200 nm is slightly faster as it is mediated by repulsive states; while the excitation at 199.2 nm is inherently somewhat slower due to the predissociative mechanism.

Chapter 7 – Femtosecond extreme ultraviolet induced photodynamics in the methyl iodide cation

7.1. INTRODUCTION

Over the past decades, methyl iodide (CH_3I) has been the most studied system by far through a wide variety of experimental techniques and theoretical approaches and resulting in a plethora of literature. CH_3I has served for many years as a prototypical system for a variety of photo-induced dynamics[149, 152, 163, 192, 201, 203, 214, 215, 217, 234, 321, 333, 340, 433-437] from its photodissociation in the first absorption band[40, 149-154, 162, 163, 192, 205, 206, 212, 357, 438, 439] to X-ray photoabsorption processes.[440, 441] The photodissociation methyl iodide cation (CH_3I^+), however, has been scarcely investigated.

The electronic structure of CH_3I^+ in the energy range between 9-16 eV is depicted in figure 7.1.

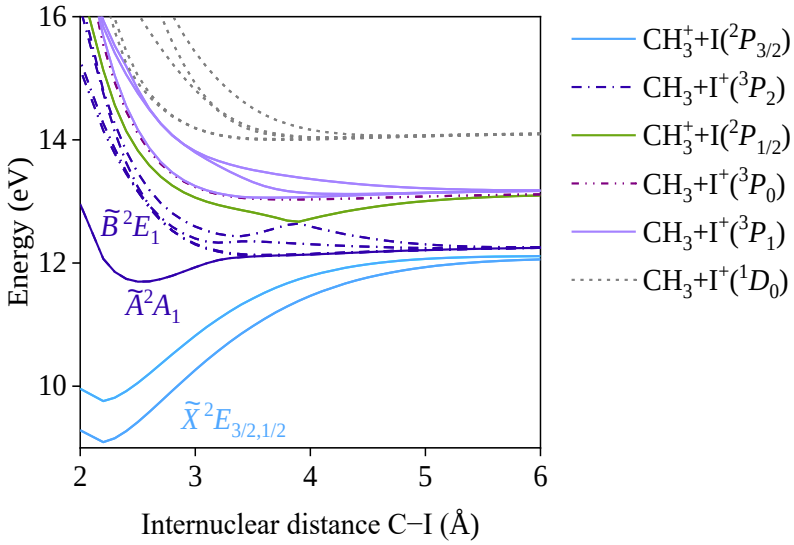

***Figure 7.1**. Computed MRCISD potential energy curves for CH_3I^+ relaxing the methyl (CH_3) moiety in the ground cationic state, using CASPT2. Figure adapted from reference [442].*

The ground electronic state $\widetilde{X}$ of CH_3I^+ is a bound state arising from the ionization of a non-bonding electron from the outermost $5p\pi_I e$ orbital of the neutral CH_3I and has almost the same geometry as the ground state of the neutral. It is Jahn-Teller distorted due to the instability of the non-linear molecular ion towards asymmetric vibrational motion, reducing the symmetry to C_s.[443] It presents two spin-orbit components $\widetilde{X}^2E_{3/2}$ and $\widetilde{X}^2E_{1/2}$, with ionization energies of 9.53 and 10.15 eV, respectively.[331,

[444, 445] On the other hand, the first excited state $\widetilde{A}\,^2A_1$, a loosely bound state with the band origin located at 11.9 eV,[228] arises from the ejection of a bonding electron from the σa_1 orbital. Its rovibrational structure reveals that the active modes in the $\widetilde{A}\,^2A_1$ state are the symmetric CH stretch (ν_1), umbrella (ν_2) and C−I stretch (ν_3), being the C−I stretch the dominant one superimposed on the symmetric CH stretch and umbrella normal modes.[228, 444, 446-448] The presence of a well-resolved vibrational structure in the corresponding bands of the photoelectron spectrum[444] and the photofragmentation spectra[228, 446, 449] reveals that this state has a relatively long lifetime of 10^{-10} s[228] yielding to statistical photodissociation, with a dissociation rate constant near threshold of 10^7 s^{-1}.[450] The dissociation gives rise to CH_3^+ fragments, with small translational energy, due to internal conversion into the vibrational continuum of the $\widetilde{X}$ state. In the region of 14 to 16 eV, the $\widetilde{B}\,^2E_1$ "state" is located, and it is composed of a manifold of states, instead of a single state, as it was recently discovered by recent calculations.[442]

Albeit not as abundant as the research on neutral CH_3I, some background literature is available on the photoionization of CH_3I, employing different spectroscopic techniques, such as photoionization mass spectrometry (PIMS)[451-453] or fixed wavelength (Helium I) photoelectron spectroscopy.[454-456]

Karlsson *et al.*[444] employed He(I) resonance radiation at 21.22 eV to induce the valence electron spectra of some methyl halides, including CH_3I. Besides resolving the vibrational progression in the $\widetilde{A}\,^2A_1$ state for the first time and attributing it predominantly to the ν_3 normal mode (C−I stretch), they provide the high-resolution photoelectron data of the ground states $\widetilde{X}\,^2E_{3/2}$, $\widetilde{X}\,^2E_{1/2}$.

Later on, synchrotron studies in the photon energy range 14-120 eV were performed by Holland *et al.*[445] focusing on the photoelectron angular distributions and branching ratios for the main bands.

Using synchrotron radiation, Locht *et al.*[457] measured the vacuum UV photoabsorption spectrum of CH_3I, between 5-20 eV. They observed numerous lines that were assigned to two groups of Rydberg series converging, respectively, to the two components of the spin-orbit split ground state of the corresponding molecular ion.

On the other hand, photoionization studies regarding the fragmentation of CH_3I^+ are relatively scarce and are mainly focused on the CH_3^+ fragment.[458, 459] The latter include the work of Tadjeddine *et al.*[458] who measured the angular distribution and translational energy distribution of the CH_3^+ fragment after a 600 nm photon absorption by the $\widetilde{X}\,^2E_{1/2}$ state of the cation; as well as the work of Kawasaki *et al.*[459] who measured the angular distribution of CH_3^+ fragments induced by REMPI. From their results, they propose a mechanism in which CH_3I^+ predissociates *via* the $\widetilde{A}\,^2E_{1/2}$ state.

More complete studies comprise a series of photoelectron photoion coincidence (PEPICO) experiments performed by Eland *et al.*,[460] Mintz *et al.*[450] and Powis,[461] in which the correlation between the initial population of ionic states and the final ionic products was extensively studied.[450, 460, 461]

Eland *et al.*[460] observed that CH_3^+ fragments are the only ones energetically feasible in the low energy part of the $\widetilde{A}\,^2A_1$ state, so to explain the appearance of these photofragments, an internal conversion to the ground state $\widetilde{X}\,^2E$ as dissociation pathway is pointed out. Whereas for high vibrational levels of the $\widetilde{A}\,^2A_1$ state, the formation of I^+ fragments is predominant over CH_3^+ formation. According to a vibrationally statistical dissociation, the measured KER of these fragments was rather small and close to a Maxwellian distribution.

In a separate PEPICO study, Mintz *et al.*[450] studied in depth-detail the formation of CH_3^+ from the dissociation of the $\widetilde{A}\,^2A_1$ state. The difference found between the experimental results and a pure unimolecular mechanism was attributed to the formation of I^+ *via* an alternative competitive mechanism, which was not experimentally demonstrated. They observed that near the threshold, the lifetimes of the CD_3^+ ions were approximately 10^{-7} s, and those for CH_3^+ only marginally shorter.

PEPICO studies by Powis[461] concern the fragmentation of the cation and the product's translational energy. In this work, it was proposed that the ions formed in the $\widetilde{A}\,^2A_1$ state by direct photoionization are transferred to the ground $\widetilde{X}\,^2E$ state and then dissociate yielding CH_3^+ with a statistical mechanism; however, when the cation is prepared with high vibrational content, either by autoionization or decay from the $\widetilde{B}$ state, different reaction mechanisms are opened, yielding to CH_3^+ in correlation with I* or I^+. These mechanisms appear to be as well statistical and in competition.

Photodissociation studies by Goss *et al.*[228, 446] using a tandem QMS and a flashlamp-pumped tunable dye laser revealed the high-resolution rovibrational structure of CH_3I^+, providing the frequencies of excited normal modes in the $\widetilde{X}\,^2E_{3/2}$, $\widetilde{X}\,^2E_{1/2}$ and $\widetilde{A}\,^2A_1$ states and as well the lower limits for the lifetimes of the states, estimating a lifetime for the $\widetilde{A}\,^2A_1$ state to be at least 10^{-11}-10^{-12} s. Ions formed in the $\widetilde{X}\,^2E_{1/2}$ state were found to be extremely long-lived. The experimental findings are well-along with the PEPICO studies by Eland *et al.*,[460] and Mintz *et al.*[450] and provide further insight concerning CH_3I^+ fragmentation. Slight corrections on the vibrational constants were obtained by performing the same experiments with rotationally cooled CH_3I and REMPI schemes.[447, 448]

Regarding photodissociation dynamics, there are some studies on different alkyl iodide cations[462-465] but, in particular, very little on CH_3I^+.

Locht *et al.*[331] employing threshold photoelectron spectroscopy (TPES) and PIMS studied CH_3I in the 8-20 eV photon energy range. The interpretation and assignments are supported by *ab initio* calculations. The TPES study shows many new discrete features in the Jahn-Teller split ground state of the cation and a continuous band starting at about 11.7 eV, which was attributed to autoionizing transitions.

Marggi-Poullain *et al.*[442] studied the photodissociation dynamics of CH_3I^+ using VMI in combination with nanosecond lasers. The prepared CH_3I^+ in the $\widetilde{X}\,^2E_{3/2}$ state *via* a (2+1) REMPI scheme through the 6p→5pπ Rydberg state was subsequently excited at several wavelengths between 242 and 260 nm. Results comprise the translational energy distributions for the CH_3^+ and I^+ ions in combination with high-level *ab initio* calculations. This study provides insight into the different dissociative potential energy surfaces and shows how a state-selective population can control the dissociation pathway.

The studies mentioned above have allowed the characterization of the different dissociation channels, the appearance energies for the CH_3^+ and I^+ photofragments (see table 7.1.) and the corresponding mechanisms upon excitation of CH_3I^+ across the $\widetilde{X}\,^2E_{3/2}$, $\widetilde{X}\,^2E_{1/2}$ and $\widetilde{A}\,^2A_1$ states.

Table 7.1. *Experimental appearance energies of CH_3^+ and I^+ photofragments, adapted from references [331, 460, 466].*

Dissociation channel	Energy (eV)		
	Eland *et al.*[460]	Tsuda *et al.*[467]	Locht *et al.*[331]
$CH_3^+ + I(^2P_{3/2})$	12.25	12.2	12.26
$CH_3 + I^+(^3P_2)$	12.87	12.9	12.82*
$CH_3^+ + I(^2P_{1/2})$	13.19	13.2	13.10
$CH_3 + I^+(^3P_0)$	13.69	13.6	13.62*
$CH_3 + I^+(^3P_1)$	13.77	13.6	

** At 298 K*

The dynamics of molecules under intense laser fields have been extensively studied in the past decades, both at experimental and theoretical levels, with a deep understanding only for small molecules, especially diatomic molecules. However, ionization and subsequent dissociation of polyatomic molecules with laser intensities with an intermediate range of 10^{13}-10^{15} W/cm^2, is still challenging.[468] The photoionization of CH_3I and the subsequent dissociation has been mainly investigated employing strong-field MPI. In these experiments, which are mostly single-pulse measurements,[469-474] intense IR femtosecond laser pulses were employed to ionize the molecule leading to dissociative photoionization as well as to Coulomb explosion of CH_3I^{n+} (n>1), producing charged CH_3^+ and I^+ fragments. In some of them, the dependence of the dynamics on the IR intensity was also investigated.[471, 475, 476] The different

reaction pathways through dissociative photoionization and Coulomb explosion leading to CH_3^+ and I^+ fragments were discussed based on the images and, in particular, dissociation in the $\widetilde{A}\,^2A_1$ excited state was suggested to occur through internal conversion into ground state CH_3I^+, while direct dissociation in the $\widetilde{B}\,^2E_1$ state was also observed. Other works have focused on the angular distributions and measurements of emission asymmetries employing, *e.g.*, well-aligned molecules or phase-controlled two-color laser fields, where the results were rationalized in terms of the symmetry of the ionizing orbitals involved.[469, 474, 475, 477, 478]

These studies have been recently complemented with pump-probe experiments. Loh and co-workers employed femtosecond XUV absorption spectroscopy to investigate strong-field induced dynamics of CH_3I^+ *via* multiphoton excitation, using 5.6 fs few-cycle IR pulses with a peak intensity of $1.9\cdot10^{14}$ W/cm^2, followed by femtosecond XUV probing of the iodine (I) 4*d* core-level transitions.[479, 480] Besides, multimode vibrational coherences observed in the populated cationic state, the results revealed that two dissociation mechanisms govern the dynamics. While a fast direct dissociation on the $\widetilde{A}\,^2A_1$ first excited state was found to occur in ≤100 femtoseconds, a spin-orbit state selective dissociation of CH_3I^+ through the $\widetilde{X}\,^2E_{1/2}$ state *via* a laser-induced curve-crossing from the initially populated $\widetilde{A}\,^2A_1$ was observed in the sub-picosecond regime (0.76±0.16 ps). The dissociation *via* the $\widetilde{X}\,^2E_{3/2}$ state was not observed unlike the case of some larger alkyl iodides cations, for which, its state-selective statistical-fashioned photodissociation *via* this state was observed.[481, 482] To explain this phenomenon, a state-selective laser-induced coupling between the $\widetilde{A}\,^2A_1$ and $\widetilde{X}\,^2E_{1/2}$ states by using few-cycle intense IR pulses, which act as a temporal gate, is claimed allowing for laser-induced crossing only within the pulse envelope. Such selective coupling seems to vanish when intense laser pulses of longer duration are employed, as revealed by previous strong-field experiments performed by Tang and co-workers using reflection TOF mass spectrometry (RTOF-MS) with ~100 fs pulses.[470]

Time-resolved coincident ion momentum imaging experiments were also recently reported by Malakar *et al.*[483] They used a pump-probe scheme employing two 25 fs 790 nm pulses with $1.5\text{-}4\cdot10^{14}$ W/cm^2 peak intensities to strong-field ionized CH_3I, mostly into the $\widetilde{A}\,^2A_1$ state and probed the spatial and temporal evolution of bound and dissociating nuclear wave packets by Coulomb explosion imaging. The use of the Cold Target Recoil Ion Momentum Spectroscopy (COLTRIMS) allowed the detection of photofragments in coincidence, achieving a nice simplification in identifying the different ionization and fragmentation pathways. The obtained time-independent results go along with the ones previously reported in single-pulse measurements.[472, 473, 484] Nevertheless, novel oscillatory features, characterized by a 130 fs periodicity and dephasing within 1 ps were observed and attributed to the vibrational wave packet in the C−I symmetric stretch mode, moving in the $\widetilde{A}\,^2A_1$ state.

In photoionization processes, a vibrational wave packet is typically launched on the cation electronic potential energy surfaces. In time-resolved experiments, the wave packet dynamics can be observed by projecting the constituent vibrational states to a common final state to be detected in the experiment. In a simple picture, in which only two vibrational states are involved in the wave packet, the beating frequency observed is equal to the frequency that corresponds to the energy separation between these two states. The development of HHG based XUV sources opened up possibilities for studies of vibrational dynamics in cations in the time domain. HHG sources provide enough energy to access molecular cations by one-photon transitions and sufficiently short pulses to observe even fast vibrational modes. In this sense, vibrational wave packets have been observed for several diatomic molecules, such as H_2,[485-487] N_2,[488] O_2,[488, 489] and CO.

Kelkensberg et al.[487] carried out XUV-IR pump-probe experiments, where the duration of both the XUV and IR pulses were shorter than the vibrational period of H_2^+ (15 fs), which allowed them to observe the dephasing and rephasing of the vibrational wave packet in the simplest molecular system upon ionization of the neutral molecule by the XUV pulse. The probing step is described using a bond-softening picture and the effect of the pulse duration on the propagation of the wave packet is stressed; i.e., when the IR field is present during the propagation of the wave packet (the pulse duration is as long as the period of the beating oscillation), the potential energy curve on which the wave packet propagates and along which dissociation eventually takes place is affected; whereas, when the IR pulse is sufficiently shorter than the oscillation period, the wave packet freely propagates until the IR pulse modifies the potential such that dissociation occurs.

Fischer *et al.*[486] performed a comparable experiment using a reaction microscope (COLTRIMS). They described the probing step as a coupling to a dissociative state but explained the phase-dependent momenta also with a bond-softening model, *i.e.*, depending on the phase of the wave packet, the proton sees a downward or upward moving potential, resulting in lower and higher momenta, respectively.

Cörlin *et al.*[490] carried out an XUV-IR pump-probe experiment for O_2, which actually is very similar to the present experiments carried out on CH_3I^+. They observed a vibrational 40 fs oscillating wave packet in the first excited state of the O_2^+ cation, which they probed by resonant absorption of a single IR photon to a weakly repulsive state. In this experiment, the wave packet is most pronounced in the low translational energy of O^+ cations. They observed the dephasing and revival of the wave packet and they stated that such an XUV-IR pump-probe scheme is suitable for investigating the wave packet dynamics within any electronic state in a diatomic molecule, as long as this state can be resonantly coupled to a repulsive state by the IR probe pulse.

However, as in strong-field MPI experiments, the use of the full bandwidth produced by HHG sources drives multiple reaction pathways and fragments, hence a challenging interpretation. By

employing an XUV TDCM,[123, 171] it is possible to define the photon energy at the expense of temporal resolution and allow us to study state-by-state and distinguish processes in cations from those in highly excited neutrals. The former are present with all harmonics above the corresponding ionization threshold, and the latter are resonant and thus only present with specific photon energies.

In the experiments presented in this chapter, we employed a monochromized XUV pump-IR probe scheme to revisit how a moderate-intensity IR pulse can control and modify, specifically, vibrational wave packet dynamics. Under this working scheme, it is possible to largely reduce the number of open dissociation channels and thus to get a deeper understanding of the dissociation dynamics in CH_3I^+. The VMI technique was employed to detect CH_3^+ and I^+ fragments and corresponding photoelectrons. According to the recorded static XUV photoelectron spectra using the 9th harmonic (13.95 eV), the ground $\widetilde{X}\,^2E_{1/2}$, $\widetilde{X}\,^2E_{3/2}$ and the $\widetilde{A}\,^2A_1$ states are populated, leading eventually to dissociation into CH_3^+ and I^+ fragments through different dissociation pathways, which can be modified by the IR pulse. The experimental results are complemented by improved high-level *ab initio* calculations of the potential energy curves, which were previously reported in reference [442] and with full-dimension trajectories.

7.2. METHODOLOGY

7.2.1. Experimental methodology

7.2.1.1. Laser configuration and optical assemblies

This section presents the specific methodological details of the experiments corresponding to the study of the time-resolved photodynamics of CH_3I^+ upon excitation with the 9th harmonic (13.95 eV) of the 800 nm fundamental, in combination with IR pulses in pump-probe experiments with variable time delay, using velocity map ion imaging for the detection of CH_3^+ and I^+ fragments and velocity map photoelectron imaging. Figure 7.2 summarizes the experimental setup employed for the experiments.

To accomplish the time-resolved photodynamics of the excited states of CH_3I^+, the 9th harmonic of the 800 nm fundamental driving pulse selected by an XUV TDCM and a probe laser pulse centered at 800 nm were used. For this purpose, the Amplitude regenerative amplifier's output pulses centered at 800 nm with an energy of 5 mJ/pulse (up to 20 mJ), around 25 fs pulse duration and a spectral width of 42 nm was divided by a 50:50 beamsplitter in two arms. One arm was focused by an f=62.5 cm focusing mirror into a gas cell situated in a vacuum chamber and filled with krypton (Kr) to a pressure of 45 mbar generating high-order harmonics. The residual IR pulses were separated from the XUV pulses by a 100 nm thin aluminum filter. The XUV pulses were wavelength-selected by a TDCM with a spectral resolution of 300 meV and an output pulse duration of 20-25 fs.[491] The other IR beam constituted the

"probe" beam. Both beams were recombined after the TDCM by two motorized mirrors. The second mirror has a small hole of 3 mm in the middle, such that the XUV beam can pass through it. The recombination mirror is mounted onto two motorized linear stages to align the hole position to the XUV beam. The steering of the IR arm was done by tilting the mirror. Afterward, both beams were focused in the center of a VMI spectrometer.[183] The proper polarization of the laser was ensured for the reconstruction of the images, which was performed with the BASEX routine.[48]

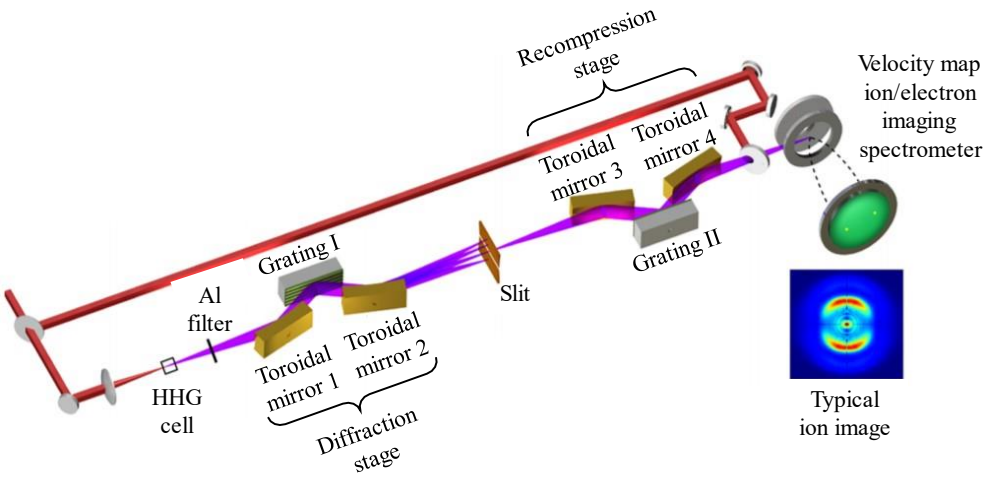

Figure 7.2. *Optical layout of the XUV TDCM setup, consisting of four toroidal mirrors (T1-T4), two diffraction gratings (G1, G2) operated in the off-plane mount and the monochromator slit (S1). The XUV beam is spectrally dispersed by the first stage (T1+G1+T2) and is filtered by the slit (S1). At this point, the beam is stretched in time. The second stage (T3+G2+T4) recompresses the XUV pulse and guides the beam towards the interaction region of an experimental end station. The VMI machine is located in the right area of the figure. The detection system is arranged parallel to the plane of the paper and the gas inlet (on-axis configuration). Figure adapted from reference* [171].

To find the spatial overlap of the lasers, the spatial map imaging (SMI) mode was used.[37, 492, 493] In SMI mode, a one-to-one mapping between the ionization coordinate and the impact coordinate takes place on the detector. In this way, the particle impact position is then most sensitive to where the charged particle is created, and therefore, the interaction region can be imaged. This is a useful mode for alignment purposes, providing a means of ensuring precise positioning of the XUV light focal spot, as well as good overlap between the laser beam and the molecular beam.[494, 495] The difference between VMI and SMI relies on the relative voltages of the extractor and the repeller lenses. In SMI, this relation equals one, whereas a relation between repeller and extractor between 0.78-0.8 leads to typical VMI conditions.[496]

The intensity of the IR pulse was estimated to be around $1.3 \cdot 10^{13}$ W/cm^2 (see section 2.2.2.3) and maintained at this moderate level to avoid strong multiphoton absorption and multiple ionization, yielding Coulomb explosion.

7.2.1.2. Molecular beam conditions and detection system

For the realization of the present experiments, CH_3I was used. Unlike previous experiments, where the molecule of interest was introduced into the interaction zone mixed with a carrier gas in the form of a pulsed molecular beam formed by supersonic expansion, pure CH_3I was introduced as an effusive beam. In an effusive beam, the ro-vibrational content of the parent molecules increases due to the soft expansion of the pure sample through the nozzle.[497-499] The effusive beam was introduced in the interaction region *via* a 150 μm hole in the VMI curved repeller electrode through a reservoir containing the sample at room temperature. The curved repeller configuration allowed us to have high target densities at the focus of the light pulses and in the center of the VMI to compensate for the low density of photons from the XUV radiation source.

The monitoring of the photodissociation process was carried out by detecting the CH_3^+ and I^+ ion fragments and photoelectrons in a TOFMS configuration. Both photoelectrons and ions could be detected by changing the polarity of both the repeller and the extractor. A MuMetal shielded the VMI spectrometer. Under VMI conditions, typical voltages were (±) 2 kV and (±) 1.9 kV for the repeller and extractor plates, respectively.

According to the TOF spectrum shown in figure 7.3, the arrival of I^+ and CH_3^+ to the detector occurred ~15 μs and ~9 μs later than the arrival of the laser pulse at the interaction area. Therefore, a gating scheme with a time resolution below 300 ns was applied to the detector to select specific fragment ions based on their TOF, in a 26 cm flight tube.

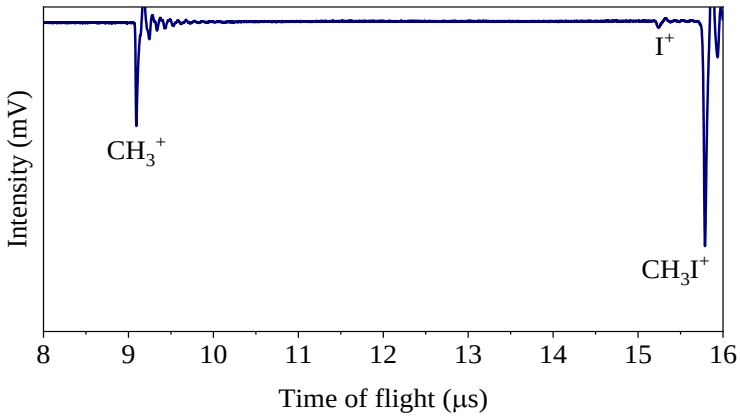

Figure 7.3. *TOF spectrum recorded in the presence of XUV (9th harmonic) and IR pulses.*

The calibration of the apparatus was performed by using the vibrational progression in N_2^+ $\tilde{C}$ state, as described in section 2.2.3.2.

7.2.1.3. Temporal characterization of the laser pulses

Before the experiment, lasers pulses were characterized by employing the SPIDER technique (see section 2.2.2.1).

The XUV-IR cross-correlation was optimized by maximizing the ATI in argon (Ar)[179, 500] (IR beam) and optimizing the HHG (XUV beam). The difference of second-order dispersion between the two beams was compensated by adding additional glass in the XUV arm. The cross-correlation was determined to be 36±5 fs.

7.2.2. Theoretical methodology

To characterize the electronic structure of CH_3I^+, several electronic states were calculated using multireference methods based on SA CASSCF wave functions. Relativistic effects were taken into account by using a second-order Douglas-Kroll Hamiltonian[268, 269] formalism in combination with an ANO-RCC[267, 409] basis set contracted to a triple zeta polarized (ANO-RCC-TZVP). The two-electron integrals were evaluated using the density fitting approximation,[410] where the selected auxiliary basis set was constructed using the uncontracted ANO-RCC basis. The active space used in the CASSCF calculations was composed of six electrons in four orbitals. Specifically, the set of orbitals considered in this study contained two lone pairs in the I atom, σ-bonding and σ-antibonding. Two sets of orbitals were obtained using the SA technique, the first one considering eleven doublets and the second one averaging over three quadruplets. Finally, the energy was corrected by perturbation theory in its extended multistate CASPT2 (XMS-CASPT2) formalism[411] with an imaginary shift of 0.3. These calculations were performed using the BAGEL code,[412] including analytical gradients[413-415] when required. Finally, spin-orbit coupling was taken into account using the AMFI approximation,[271] resulting in 36 electronic states. This calculation was performed extracting the CASSCF wave function (CI vector and orbitals) from the BAGEL code and importing it to the OpenMolcas code,[416] where the spin-orbit coupling was evaluated using a perturbation modified approximation (PM-CASSCF). The calculated states were selected to describe the dissociation limits of the first five channels correctly: CH_3^++I($^2P_{3/2}$); CH_3+I^+($^3P_2$); CH_3^++I($^2P_{1/2}$); CH_3+I^+($^3P_0$) and CH_3+I^+($^3P_1$), similarly to reference [442].

To estimate the reliability of the method (especially the selection of the auxiliary basis set), the electronic energies were evaluated as a function of the C−I distance. In this case, a relaxed curve was performed using the external optimizer of ORCA[501] in combination with the analytical gradients and spin-orbit coupling described above.

The CH_3 moiety was optimized in its spin-free doublet ground cationic state with XMS-CASPT2, *i.e.*, the gradients obtained with BAGEL were passed to the ORCA program to optimize the molecule with constrained C−I distance.

A set of geometries and velocities was obtained considering the Hessian of an MP2 optimization, using a Wigner distribution in Cartesian coordinates based on the harmonic approximation with an open-source code.[502] For each geometry, the Dyson norm was also evaluated using the OpenMolcas code[416] in its spin-orbit variant. As in the previous case, the wave function and energies were evaluated using the XMS-CASPT2 method, and the same PM-CASSCF formalism was employed to calculate the Dyson orbitals. Additionally, the calculation of the Dyson orbitals required obtaining a neutral initial state that was represented coupling three singlet and three triplet states, in the same way as for the cationic states. The cation dynamics were performed using the SHARC method,[276] where the Hamiltonian and the spin-free gradients were described using the previous electronic structure protocol and the surface hopping probability was evaluated based on the variation of the densities.[503]

Finally, the effect of the probe IR pulse was simulated selecting the geometries of the trajectories at given times and propagating the electronic time-dependent Schrödinger equation with the split-operator technique,[504-506] where the diagonal elements of the electronic Hamiltonian (obtained at the different geometries) are the XMS-CASPT2 energies, whereas the off-diagonal elements are the spin-orbit coupling values obtained at PM-CASSCF level. The laser pulse interaction was described within the dipole approximation in the length gauge with PM-CASSCF. Specifically, a sine square laser pulse with a frequency corresponding to 800 nm, amplitude of $5.3 \cdot 10^{-3}$ a.u., which is equivalent to an intensity of 0.98 TW/cm^2, and time duration of 15 fs at FWHM, was employed. This laser intensity with this pulse duration was used to simplify the obtained results and to make the approximation of fixed nuclei, through which the simulations are performed, more real.

All theoretical calculations were carried out by Dr. Jesús González Vázquez.

7.3. RESULTS

7.3.1. Experimental results

The static XUV photoelectron spectrum of CH_3I obtained with the 9th harmonic (13.95 eV) is displayed in figure 7.4. The electron translational energy axis was calibrated using the positions of the $\widetilde{X}\,^2E_{1/2}$, $\widetilde{X}\,^2E_{3/2}$ lines at this photon energy and then converted into binding energy. The binding energies for the different electronic states of CH_3I^+ are 9.53 and 10.15 eV[331, 444, 445] for the ground $\widetilde{X}\,^2E_{3/2}$ and $\widetilde{X}\,^2E_{1/2}$ states, and 11.9 eV[228] for the first excited state $\widetilde{A}\,^2A_1$.

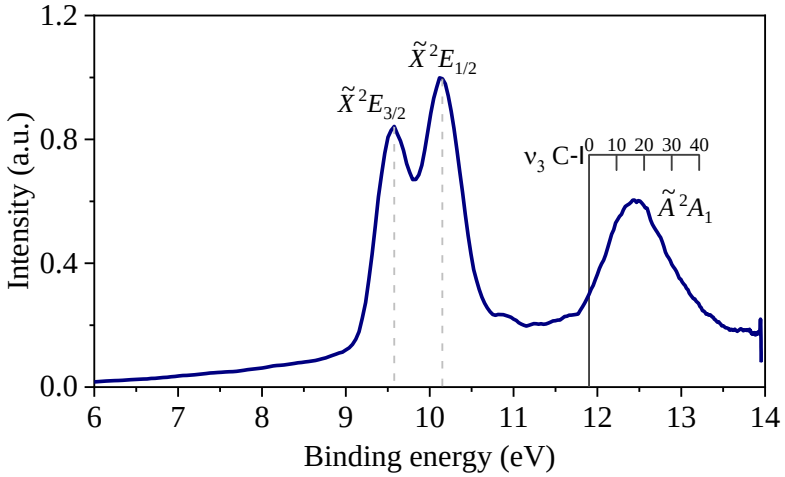

Figure 7.4. *Static photoelectron spectrum of CH_3I obtained with XUV radiation corresponding to the 9th harmonic (13.95 eV). The XUV pulses ionize CH_3I in the spin-orbit split ground state $\tilde{X}^2E_{1/2}$, $\tilde{X}^2E_{3/2}$ with binding energies of 9.53 eV and 10.15 eV, respectively, and in the $\tilde{A}^2A_1$ state with a binding energy of 11.9 eV. The binding energy axis was calibrated using the positions of the $\tilde{X}^2E_{1/2}$, $\tilde{X}^2E_{3/2}$ lines.*

With this photon energy (13.95 eV), CH_3I^+ can be prepared with low internal energy content in the spin-orbit split ground states ($\tilde{X}^2E_{1/2}$, $\tilde{X}^2E_{3/2}$), since ionization leading to the formation of these states requires almost no nuclear rearrangement, and in the first excited state ($\tilde{A}^2A_1$) with some ro-vibrational excitation. The internal energy content of the cation prepared in the $\tilde{A}^2A_1$ state was considered by calculating the binding energies corresponding to the vibrational states in the C−I stretch ν_3 mode (265 cm^{-1}). In the figure, the energy of the different quanta has been indicated using a "comb". As can be observed, the cation is prepared in this state with a significant vibrational excitation, since the distribution peaks at a vibrational quantum number of about 15, being the vibrational states with ν>10 above the lowest dissociation limit CH_3^++I($^2P_{3/2}$). So it is expected that the cation prepared in this state dissociates, in part, through internal conversion, producing CH_3^+ fragments and or adiabatically, generating I^+ fragments.[228] This distribution of vibrational states in the $\tilde{A}^2A_1$ state is indeed very similar to the Franck-Condon vibrational state distribution calculated by Malakar *et al*,[483] Though they observed a distribution peaking around 7-9; a difference they attribute to vibrational redistribution occurring during the pump pulse and losses *via* dissociation.

The TOF mass spectrum was recorded using the 9th harmonic with and without the presence of the IR pulses. The different spectra are displayed in figure 7.5. The spectra show three peaks which are assigned to the parent CH_3I^+, and the fragment ions I^+ and CH_3^+. Predominant CH_3I^+ and CH_3^+ signals prevail over a lower I^+ signal.

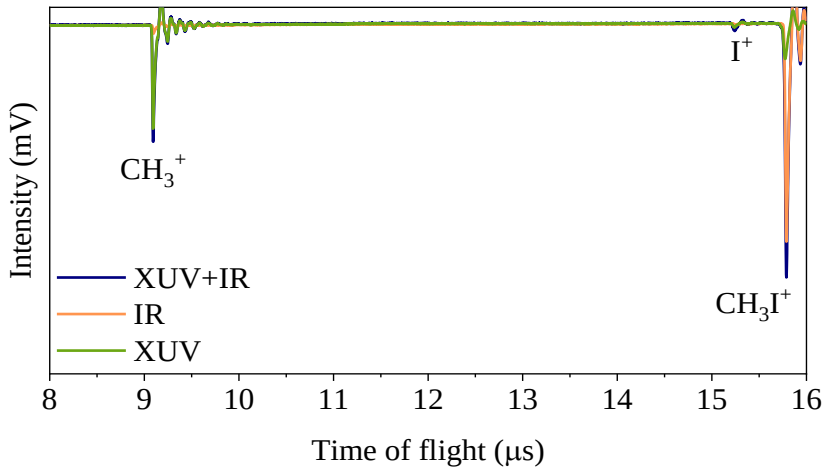

Figure 7.5. *TOF spectrum with XUV (9th harmonic)+IR (blue), TOF spectrum with IR only (orange) and TOF spectrum with XUV only (green).*

Considering the low intensity of the XUV pulse, a single-photon ionization of the parent molecule is expected and, thus, the presence of the I^+ fragments indicates that dissociative photoionization of CH_3I^+ from the $\widetilde{A}\,^2A_1$ state takes place. To explain, the presence of CH_3^+ fragments in the TOFMS, the dissociation in the ground state must take place due to internal conversion between the $\widetilde{A}\,^2A_1$ state and hot vibrational bands in the spin-orbit split ground state of the cation, which is completely feasible considering the hot vibrational state distribution observed in the photoelectron spectra and with an energy above the lowest dissociation limit CH_3^++I($^2P_{3/2}$). This internal conversion implies a statistical dissociation in the ground state, yielding CH_3^+ fragments, a mechanism which is consistent with the dissociation rate constant 10^{-7} s,[450] being the lifetime of the $\widetilde{A}\,^2A_1$ state of 10^{-10} s.[446] This unimolecular dissociation scenario is also consistent with the low KER for the CH_3^++I($^2P_{3/2}$) channel (see below).

VMI images were recorded for both the CH_3^+ and I^+ fragments from negative to positive pump (XUV)-probe (IR) delays. Figure 7.6 displays the corresponding total KER maps as a function of the pump-probe time delay for dissociation into CH_3^++I and CH_3+I^+, upon excitation with the 9th harmonic. Some common characteristics can be distinguished in the maps; just one time-dependent structure can be observed at positive pump-probe delay times with a clear oscillatory structure in the KER range up to 0.06-0.08 eV for CH_3^+ and up to 0.12-0.15 eV for I^+. The yield of the CH_3^+ fragments decreases when IR comes after XUV, while the yield of the I^+ fragments increases at the counterpart. The detection of both fragments and that there is an increased signal for the I fragments to the detriment of the evident decrease in the signal for the CH_3^+ fragments, give us a hint that there is an interplay between more than one excited state guided by the IR pulse. Another feature to highlight is the evolution of the average signal. At positive time delays between the XUV and the NIR pulses, the yield of CH_3^+ fragments decreases with time while that of I^+ is the other way round, the yield increases with time delay.

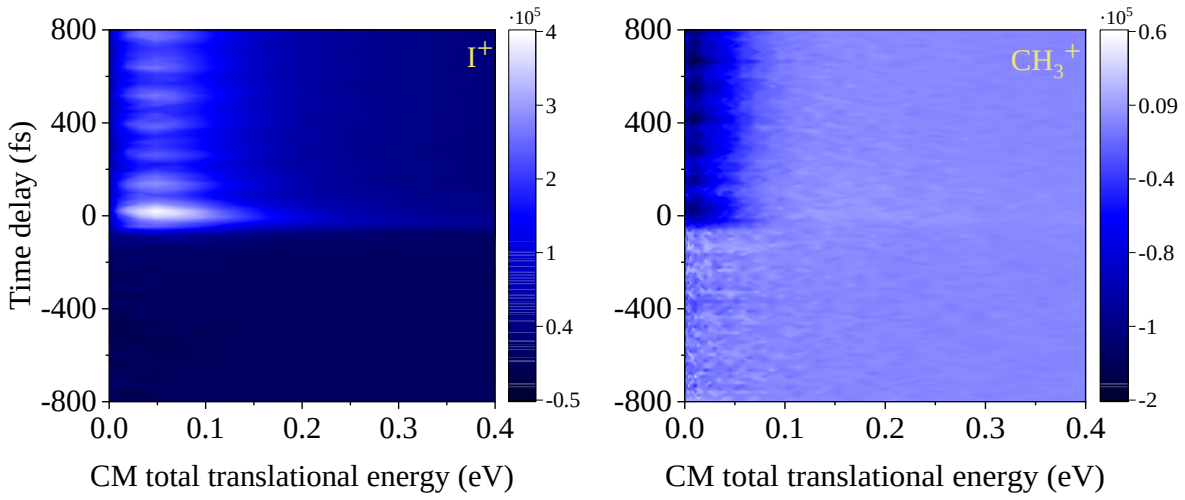

Figure 7.6. *Pump (XUV) - probe (IR) time delay dependent KER maps, for I^+ (left) and CH_3^+ (right) fragments. In these maps, the average IR-XUV signal, i.e., the signal at negative pump-probe delays has been subtracted to the full map.*

Due to the low KER of the fragments, it was not possible to extract the angular distributions of the photofragments and thus obtaining the corresponding anisotropy parameter, β.

The integration of the signal in the region of translational energy of interest *versus* time leads to the transients represented in figure 7.7. In the transient, the enhanced signal for the I^+ transient and the depleted signal for the CH_3^+ transient is observed. On the one hand, the analysis of the I^+ transient was carried out by fitting three contributions to the data, including an exponential decay characterized by a time constant τ_d, an exponential rise with a time constant τ_r, and a cosine function of period *T*, as depicted by the dashed fitting curves. The sum of the contributions gives rise to the overall fit, and it successfully recovers all the features observed in the experimental transient. On the other hand, in the case of the CH_3^+ transient, a Gaussian function at time zero delay characterized by an FWHM=σ_G, a negative exponential rise (τ_r) and cosine function (period *T*) were employed. In all cases, the different contribution functions were convoluted with a Gaussian function considering the cross-correlation between the XUV and IR pulses and representing the instrumental response. Table 7.2 shows the relevant time constants of the different contributions obtained from the fit of the I^+ and CH_3^+ transients.

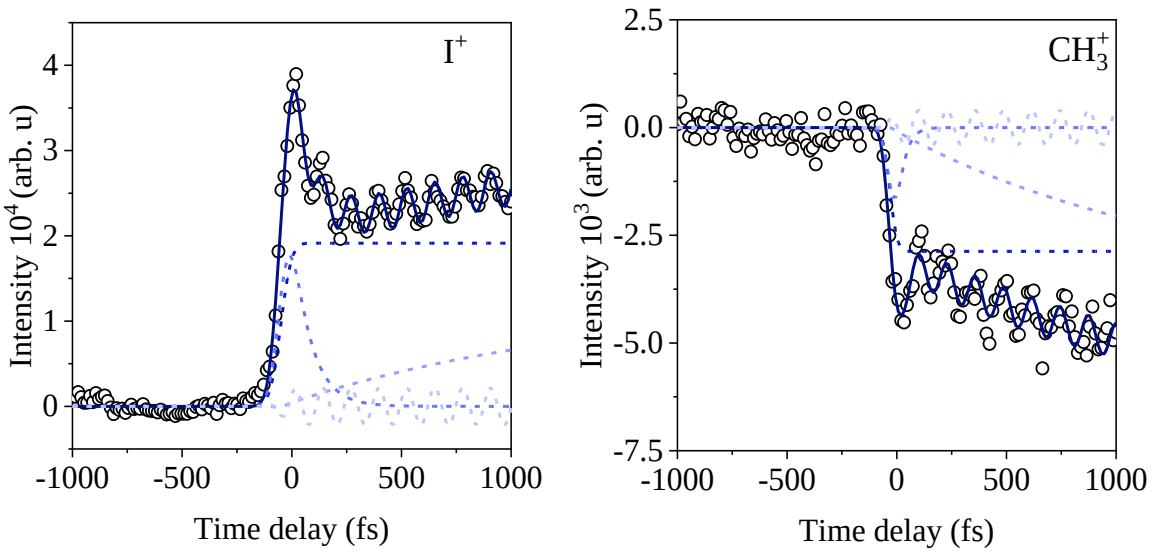

Figure 7.7. *Ion yield versus XUV-IR time delay for I^+ and CH_3^+ fragments. Black circles represent the experimental data. The blue solid line considers the overall fit whereas the blue dashed lines are the fitting contributions (see text for more details). The time constants obtained from the different fitting contributions are listed in table 7.2.*

Table 7.2. *Time constants (with error bars) obtained from the fit of the experimental transients for both fragment ions I^+ and CH_3^+ obtained in pump (XUV)-probe (IR) experiments. For the I^+ transient, an exponential decay time (τ_d), a rise time (τ_r) and the period of the cosine function (T) are listed. For the CH_3^+ transient, the width of a Gaussian at time zero (σ_G), a negative exponential rise time (τ_r) and the period of the cosine function (T) are shown.*

Parameters	I^+	CH_3^+
σ_G (fs)	-	32±2
τ_d (fs)	83±5	-
τ_r (fs)	1354±100	1347±100
T (fs)	127±10	129±10

7.3.2. Theoretical results

A semiclassical simulation of the static XUV photoelectron spectrum was performed using the norm of the Dyson orbitals for each geometry of a total of 200 geometries forming a Wigner distribution in the vibrational ground state of the neutral CH_3I ($\widetilde{X}\,A_1$). The resulting ionization probability, convoluted with a Gaussian function of 0.1 eV width, as a function of the ionization energy, is depicted in figure 7.8. Three bands are observed, located at similar positions as the vertical excitation energies (indicated by vertical bars in the figure) of the first three ion states $\widetilde{X}^2E_{1/2}$, $\widetilde{X}^2E_{3/2}$ and $\widetilde{A}^2A_1$ calculated at the Frank-Condon geometry, *i.e.*, 9.57 eV, 10.15 eV and 12.46 eV, respectively. Similarly to the experimental spectrum (see figure 7.4), the lower energy bands correspond to the spin-orbit split ground state ($\widetilde{X}^2E_{1/2}, \widetilde{X}^2E_{3/2}$) of the cation, while the band at larger vertical energy corresponds to the first

excited state of the cation ($\widetilde{A}\,^2A_1$). This third band spreads out over a larger energy range, although considerably narrower than the one observed experimentally, due to the lack of quantization in the vibrational modes in the present semiclassical simulation. The geometries from the Wigner distribution, distributed on the ionic states, typically constitute the initial conditions employed to carry out full-dimension trajectories.

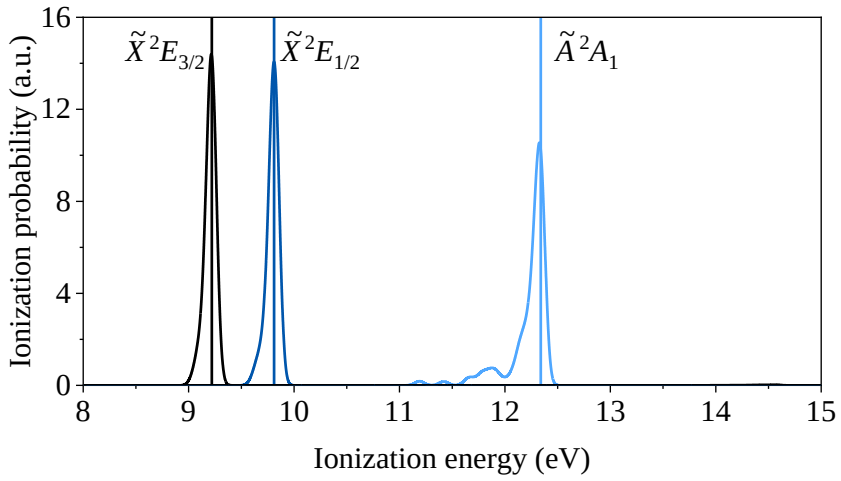

Figure 7.8. *Simulation of the static photoelectron spectrum by calculating the ionization probability described with Dyson norms convoluted with a 0.1 eV Gaussian profile as a function of the ionization energy. Vertical lines represent the ionization energies at Frank-Condon of the first three states of* CH_3I^+.

Figure 7.9 represents the potential energy (solid) and total energy (dashed) for each of the three ionic states for all initial conditions (geometries from the Wigner distribution). While figure 7.8 represents the ionization energy, defined as the difference between the energy of the ionic state and the initial energy of the $CH_3I\,\widetilde{X}\,A_1$ ground state, figure 7.9 represents the total energy, referenced to the minimum energy of the neutral molecule in its ground state. The potential energy distribution shows three asymmetric bands, which correspond to the three considered ionic states, while the total energy distributions are broad, reflecting the broad contribution of kinetic energies. Vertical bars in figure 7.9 correspond to the two first dissociation limits $I(^2P_{3/2})+CH_3^+$ and $I^+(^3P_2)+CH_3$ at 12.29 and 12.95 eV, respectively. As observed, the third ionic state of the cation ($\widetilde{A}\,^2A_1$) can dissociate predominately into CH_3^+ and a small fraction into I^+. In contrast, dissociation from the two first ionic states ($\widetilde{X}\,^2E_{1/2}, \widetilde{X}\,^2E_{3/2}$) is very unlikely, and only a small fraction can dissociate into the first dissociation limit.

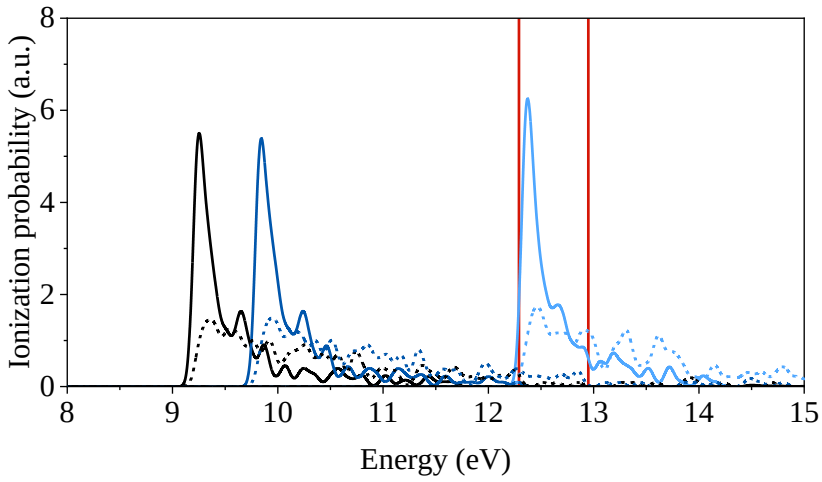

Figure 7.9. *Potential energy (solid) and total energy (dashed) distributions of the considered initial conditions where vertical lines depict the different dissociation thresholds, $I(^2P_{3/2})+CH_3^+$ and $I^+(^3P_2)+CH_3$.*

To unravel the observed dynamics of the CH_3I^+ in the excited $\tilde{A}\,^2A_1$ and ground $\tilde{X}^2E_{1/2}, \tilde{X}^2E_{3/2}$ states, potential energy curves of the first electronic states of CH_3I^+ in C_s symmetry along the C–I dissociative coordinate were calculated and are shown in figure 7.10. Since the potential energy curves were first computed and described in detail in reference [442], the most relevant aspects with particular emphasis on the energies are only recalled, which were improved here in comparison with the previous calculations.[442]

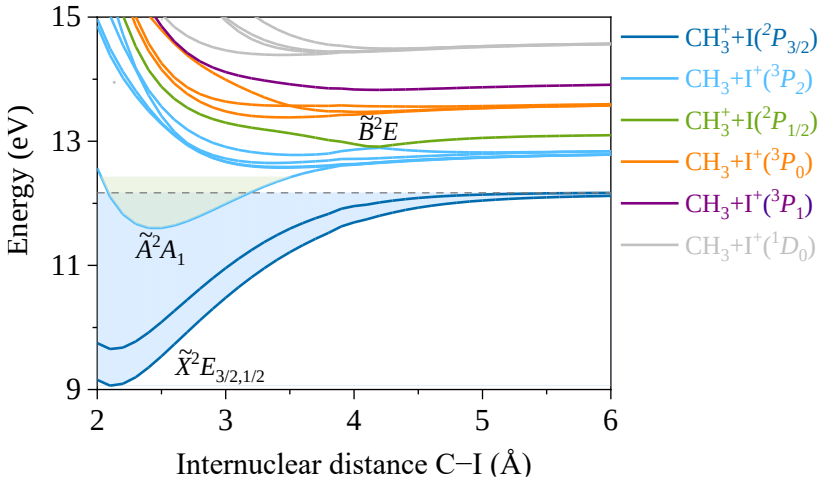

Figure 7.10. *Ab initio potential energy curves for CH_3I^+ at the XMS-CASPT2 level of theory including spin-orbit coupling at PM-CASSCF and relaxing the CH_3 moiety in the ground cationic state. The horizontal dashed line represents the overlap between highly vibrationally excited states of the $\tilde{X}^2E_{1/2}$, $\tilde{X}^2E_{3/2}$ ground states of the cation with vibrational states of the excited $\tilde{A}\,^2A_1$ state.*

The spin-orbit ground states of the cation, the $\tilde{X}^2E_{1/2}$ and $\tilde{X}^2E_{3/2}$ states, correlate with the lowest dissociation limit CH_3^++I($^2P_{3/2}$) at 12.29 eV, while the loosely bound first excited electronic state $\tilde{A}\,^2A_1$ correlates with the dissociation limit CH_3+I^+($^3P_2$) at 12.95 eV. Although the potential energy curves

correlating with the dissociation limits CH_3^++I($^2P_{3/2}$) and CH_3+I^+($^3P_2$) are well separated at every C−I distance in this one-dimensional picture, a degeneration point at a large C−I distance (4.15 Å) was optimized in a multidimensional search, although it could not be properly optimized. At higher energies, repulsive potential energy curves from the so-called $\widetilde{B}$ band are observed, correlating with the dissociation limits CH_3+I^+($^3P_2$) and CH_3^++I($^2P_{1/2}$), as well as higher curves which drive to neutral CH_3 fragments in correlation with different electronic states of the ionized I fragments. The computed dissociation limits are somewhat higher than those from the literature by theoretical calculations by Locht *et al.*[331] (*i.e.,* 11.99 and 15.59 eV) and experimentally by Wang *et al.*[471] (*i.e.,* 12.18 and 12.90). The present calculated dissociation limits are in considerable better agreement with the experimental values than those previously obtained by using the multireference configuration interaction method with singles and doubles (MRCISD) (*i.e.,* 12.54 and 12.72 eV).[442]

7.4. DISCUSSION

7.4.1. The role of the extreme ultraviolet pulse

According to the photoelectron spectra depicted in figure 7.4 (experimental) and figure 7.8 (theoretical), the 9th harmonic XUV pulse (13.95 eV) prepares a vibrational wave packet of the molecular cation in both electronic ground states $\widetilde{X}\,^2E_{1/2}$ and $\widetilde{X}\,^2E_{3/2}$, as well as in vibrationally excited levels of the $\widetilde{A}\,^2A_1$ state. Part of the vibrational wave packet prepared in the excited $\widetilde{A}\,^2A_1$ state can escape the shallow well *via* two alternative routes: a minor part can adiabatically dissociate into CH_3+I^+($^3P_2$), while a significant part can be driven to the hot vibrational levels of the spin-orbit split ground states of the cation $\widetilde{X}\,^2E_{1/2}$, $\widetilde{X}\,^2E_{3/2}$ by internal conversion,[460] where it may dissociate yielding CH_3^++I($^2P_{3/2}$) with low KER. On the other hand, no further nuclear dynamics and fragmentation are expected to be observed from the split ground states $\widetilde{X}\,^2E_{1/2}$ and $\widetilde{X}\,^2E_{3/2}$.

Figure 7.11 depicts the results of on-the-fly multidimensional trajectory calculations carried out on the $\widetilde{A}\,^2A_1$ state to confirm such dynamics upon one-photon XUV ionization. Most of the trajectories depict the oscillating wave packet which remained trapped in the potential well (blue lines), while a minor number of them show that the wave packet has enough energy to dissociate directly into CH_3+I^+($^3P_2$) (red lines). The major formation of CH_3^+ observed in the mass spectrum of figure 7.5 reflects, however, the dissociation in vibrationally hot $\widetilde{X}\,^2E_{1/2}$, $\widetilde{X}\,^2E_{3/2}$ ground state, following internal conversion from the $\widetilde{A}\,^2A_1$ state, formation that is not predicted by the trajectories in here represented.

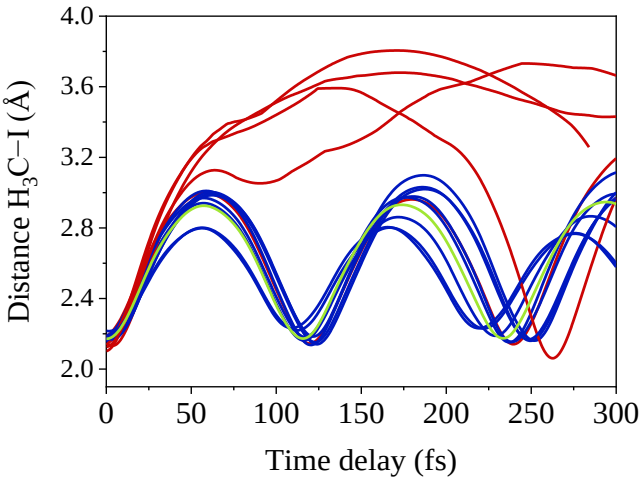

Figure 7.11. *Time evolution of the distance between the I atom and the center of mass of the CH_3 fragment in on-the-fly multidimensional trajectory calculations. The color of the curves indicates if the trajectory has enough energy to dissociate into CH_3^+ fragments (blue) or into I^+ fragments (red). The green line represents the evolution of the equilibrium geometry trajectory that cannot dissociate into I^+.*

7.4.2. The role of the infrared pulse

The IR pulse launched after the XUV pulse can induce further dynamics on either of the two cationic states initially prepared by the 9th harmonic, *i.e.*, the $\widetilde{X}\,^2E_{1/2}$, $\widetilde{X}\,^2E_{3/2}$ and $\widetilde{A}\,^2A_1$ states. Further dynamics from the $\widetilde{X}\,^2E_{1/2}$ and $\widetilde{X}\,^2E_{3/2}$ states are not likely to lead to any fragmentation pathway compatible with the experimental findings since at least the absorption of two photons would be required. In contrast, one-photon IR absorption can easily modify the dissociation dynamics on the $\widetilde{A}\,^2A_1$ state. As illustrated by red arrows in figure 7.12, the IR pulse can indeed induce two possible mechanisms:

1. A dump mechanism from the $\widetilde{A}\,^2A_1$ state down to any of the spin-orbit states of the ground state $\widetilde{X}\,^2E$ of the cation, which would not produce any fragmentation because the wave packet would be trapped in the deep well of this state. This dump mechanism has not been identified based on the current experimental results.
2. A pump mechanism, where part of the oscillating wave packet which is trapped in the $\widetilde{A}\,^2A_1$ state can absorb one (or more) IR photons, at a certain C–I distance beyond the Franck-Condon region while it is propagating outwards (*i.e.*, at certain time delays), and then access higher repulsive $\widetilde{B}$ states through which it can quickly dissociate, producing I^+ with low kinetic energy.[483]

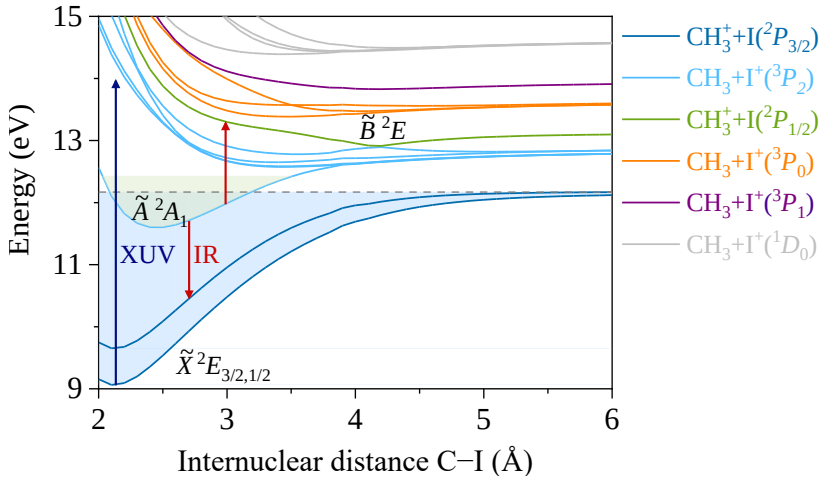

Figure 7.12. *Ab initio potential energy curves for CH_3I^+. The blue vertical arrow indicates one-photon absorption of the 9th harmonic (88.89 nm: 13.95 eV). The up and down red arrows describe the pump and dump processes associated with the interaction with the IR pulse. The horizontal dashed line shows the overlapping between highly vibrationally excited states of the $\tilde{X}\,^2E_{1/2}$, $\tilde{X}\,^2E_{3/2}$ ground states of the cation with vibrational states of the excited $\tilde{A}\,^2A_1$ state.*

Figure 7.13 shows a simulation of the population transfer to upper and lower potential energy curves induced by the interaction of the oscillating wave packet in the $\tilde{A}\,^2A_1$ state with the IR probe pulse, considering an intensity of 0.98 TW/cm^2 for the latter. A positive transfer probability (blue line) reflects a pump process, where upper electronic states from the *B*-band manifold are populated, while a negative transfer probability (red line) indicates a dump process, which drives some population into the bound states $\tilde{X}\,^2E_{1/2}$ and $\tilde{X}\,^2E_{3/2}$. Although considerably dependent on the intensity of the IR pulse, these transfers of population are highly probable at an intensity of $1.3{\cdot}10^{13}$ W/cm^2, like that employed in the present experiments.

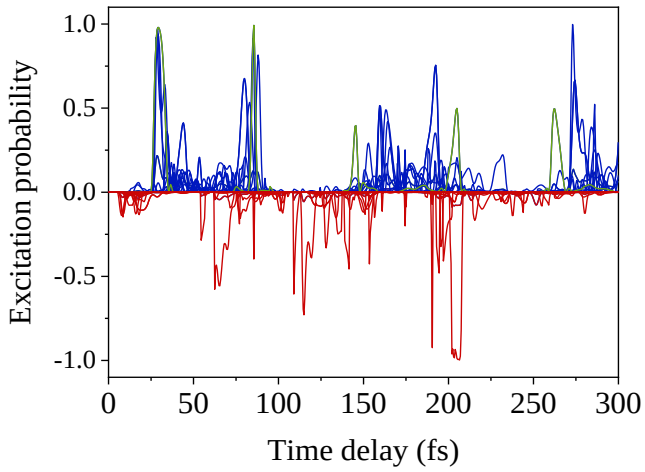

Figure 7.13. *Population transfer probability to the upper B-band states (blue line) and lower bound $\tilde{X}\,^2E_{1/2}$, $\tilde{X}\,^2E_{3/2}$ states (red line) due to the IR probe pulses with an intensity of 0.98 TW/cm^2. The green line indicates the case where only the equilibrium geometry is considered.*

7.4.3. Time-delay dependent features in the kinetic energy release maps and transients

One of the most striking features seen in both the KER maps (figure 7.6) and the transients (figure 7.7) measured for each fragment is an oscillatory structure at positive delay times between the XUV and IR pulses, which reflects the motion of the vibrational wave packet in the $\widetilde{A}\,^2A_1$ state. Upon one-photon ionization by the XUV pulse, a coherent superposition of vibrational states is prepared in this state thus, the oscillatory feature results from the interference between the populated vibrational states. The vibrational wave packet is prepared in the Franck-Condon region (associated with the CH_3I ground state), which is close to the inner turning point of the $\widetilde{A}\,^2A_1$ state potential energy curve. From the fitting of the transients, the time constant associated with the vibrational wave packet period (T) is 127±10 fs, whereas the power spectrum resulting from the fast Fourier transform (FFT) of the oscillation shows a prominent peak at 262 cm^{-1}, which is similar but somewhat lower to the vibrational frequency of the C−I stretching mode (ν_3) of 294 cm^{-1}. This result is in very good agreement with the oscillatory behavior observed by Malakar *et al.* in their multiphoton IR-IR pump-probe experiments.[483]

While initially in phase, the wave packet dephases as it moves along the C–I coordinate and rephases at recurring times determined by the difference in the vibrational frequency characterizing each level. The fading and revival of the wave packet could have been observed if longer delay scans had been performed.[507-510] Malakar *et al.*[483] observed in their KER maps, extended up to 1.5 ps pump-probe delay, the fading of the oscillatory structure, which, as predicted by their calculations, gives an account of the dephase of the initial well-localized wave packet as it moves along the C−I coordinate on the time scale of 1 ps due to the broad distribution of vibrational states. Although not experimentally observed, they predicted the revival of the wave packet within 6 ps.

The wave packet probed by the IR photon observed in the present work is then favored when the wave packet is in phase and leads to subsequent fast dissociation, giving rise to a local maximum of I^+, correlated to a local minimum of CH_3^+. The low translational energy of the fragment ions can be explained by the fact that the $\widetilde{A}$-$\widetilde{B}$ transition occurs at C−I distances beyond the Franck-Condon region while the vibrational wave packet propagates outwards the $\widetilde{A}\,^2A_1$ state potential energy curve.

Besides the oscillatory feature, the measured transients depicted in figure 7.7 and the corresponding time constants (see table 7.2) for the CH_3^+ and I^+ fragments are characterized by:

- A depletion of the CH_3^+ fragment yield in favor of the I^+ fragment.
- A fast ~80 fs decay of the enhanced I^+ formation.
- A slow ~1.3 ps exponential rise characterizing the enhanced formation of I^+ and the depletion of CH_3^+.

The strong coupling between the $\widetilde{A}\,^2A_1$ state and the ground split $\widetilde{X}^2E_{3/2,1/2}$ states favors the transfer of wave packet population from the excited state $\widetilde{A}\,^2A_1$ to highly excited vibrational states of the ground state $\widetilde{X}^2E$ by internal conversion. Then, the wave packet evolves to dissociative photoionization in the ground state yielding $CH_3^+ + I(^2P_{3/2})$ in a slow fashion (picosecond time scale). The slow ~1.3 ps exponential rise is assigned to this internal conversion process, which is induced solely upon one-photon ionization by the XUV pulse. Nevertheless, this slow process yielding CH_3^+ competes with the pump IR-induced mechanism as reflected by the progressive decrease of the CH_3^+ signal as the time delay between XUV and IR pulses increases. As the $\widetilde{A}\,^2A_1$ state population declines due to the IR-induced dynamics, this dissociation pathway becomes less favorable. Signal depletion in CH_3^+ is explained by the absorption of IR photons to the $\widetilde{B}\,^2E_1$ states correlating with I^+ formation. Thus, the exponential rise in the I^+ transient is related to the negative exponential rise in the depleted CH_3^+ transient, both having roughly the same time constant of 1.3 ps.

On the other hand, the ~80 fs decay observed for the I^+ fragment can indeed reflect some competing adiabatic dissociation on the $\widetilde{A}\,^2A_1$ state induced by the XUV pulse alone, reducing the population on the $\widetilde{A}\,^2A_1$ state, and therefore the population available for the IR pump process.

Figure 7.14 depicts an outline of the XUV-IR photoinduced dynamics on the potential energy curves of CH_3I^+ observed in the present experiments.

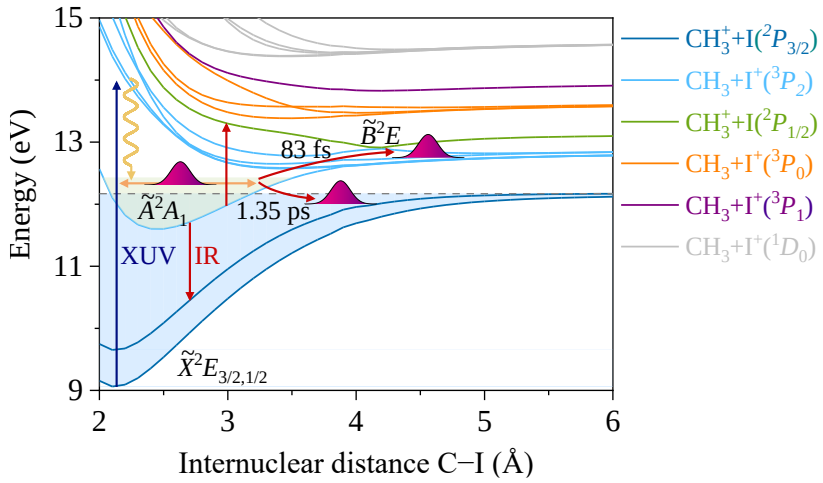

Figure 7.14. *Representation of the XUV-IR induced photodynamics of CH_3I^+ along the calculated potential energy curves deduced from the present experiments and the theoretical results. See the text for more details.*

7.5. CONCLUSIONS

The time-resolved photoionization of CH_3I and subsequent photodissociation have been explored through ion and photoelectron VMI upon one-photon excitation with XUV radiation spectrally selected

by a TDCM, under the influence of a moderate IR pulse. employed to control and modify the vibrational wave packet dynamics. The results and their consequent discussion were focused on the experiments conducted upon excitation with the 9th harmonic (13.95 eV), which populates both spin-orbit components of the ground state $\widetilde{X}^2E$ and the first electronically excited state $\widetilde{A}^2A_1$.

The temporal evolution of the CH_3^+ and I^+ fragments shows an oscillatory behavior reflecting the evolution of the vibrational wave packet in the $\widetilde{A}^2A_1$ state. A fast decay in the I^+ transient is attributed to fast dissociation occurring adiabatically in the $\widetilde{A}^2A_1$ state and a depleted slow exponential in the CH_3^+ transient is assigned to the non-adiabatic transfer of part of the vibrational wave packet to the vibrationally excited ground $\widetilde{X}^2E$ state where it further dissociates, producing CH_3^++I($^2P_{3/2}$). The IR pulses enhance the coupling between electronic states leading to a slow depletion of the CH_3^+ fragments in the ground $\widetilde{X}^2E$ state and an enhancement of I^+ by absorption of mid-intensity IR pulses yielding dissociative photoionization in the upper $\widetilde{B}^2E_1$ states manifold.

The experimental results are supported by high-level *ab initio* calculations of potential energy curves of the electronic states of CH_3I^+ as well as with full-dimensional on-the-fly trajectories on the first electronically excited state $\widetilde{A}^2A_1$ prepared by the XUV photon, considering the presence of a moderate IR pulse kept at a peak intensity of around $1.3\cdot10^{13}$ W/cm^2 to avoid strong multiphoton absorption and/or multiple ionization.

The trajectories predict the presence of an oscillating wave packet in the first excited state of the cation after the absorption of the XUV photons, as well as the possibility of these wave packets to escape from the potential well of this slightly bound state, leading to I^+ fragments by direct dissociation. The formation of CH_3^+ predominantly through a transfer of population from the $\widetilde{A}^2A_1$ to the hot vibrational levels of the $\widetilde{X}^2E_{3/2}$, $\widetilde{X}^2E_{1/2}$ states is not covered by these calculations.

The role of the IR pulse is primarily to promote the population of state $\widetilde{A}^2A_1$ to state $\widetilde{B}^2E_1$ by favoring the production of I^+ to the detriment of CH_3^+ formation as well as a probing tool of the vibrational wave packet oscillating in the state $\widetilde{A}^2A_1$ into the repulsive $\widetilde{B}^2E_1$ states.

Chapter 8 – General conclusions

In this Doctoral Thesis, structural effects on the real-time photodissociation dynamics of a family of molecules including dihalomethanes, linear and branched alkyl iodides and vinyl iodide, with a common reaction coordinate, *i.e.*, the cleavage of the C−I bond, have been examined. For this purpose, the use of femtosecond pulses in the UV range in pump-probe schemes have been used in combination with velocity map ion imaging.

The time-resolved photodissociation dynamics dependence on specific molecular structural modifications were followed by the detection of nascent iodine (I) atom fragments, I($^2P_{3/2}$) and I*($^2P_{1/2}$), using (2+1) REMPI, arising from the dissociation of the molecules along the C–I bond cleavage reaction coordinate after UV excitation. The structural effects were observed in the fragment translational and internal energy and angular distributions and in the C−I reaction times. The variation of the anisotropy in relation to the rotation of the molecule prior to dissociation was studied in predissociative processes. Semiclassical models regarding molecular rotation supported the experimental findings.

In all cases, the experimental results were interpreted through *ab initio* electronic structure calculations and eventually with classical full-dimensional on-the-fly trajectories calculations. The calculations were performed by Dr. Jesús González-Vázquez and Dr. Alexandre Zanchet. Dr. Paulo Limão-Vieira participated in performing spectroscopic assignments of the absorption spectrum of vinyl iodide (C_2H_3I).

The performed experiments show that pulsed lasers with femtosecond time resolution combined with pump-probe schemes and imaging techniques prove to be the proper tool for the study of photodissociation reactions in the time scale where the bond cleavage occurs since they allow us to initiate and trace the process at each temporal moment, creating a molecular movie. In addition, the use of velocity map imaging allows us to determine a series of observables, such as the speed, energy distribution and angular distribution of the photofragments, which fully characterize the processes under study. It is shown that theoretical calculations should always accompany the experiments to carry out a detailed and complete investigation of the process. The theoretical calculations are essential to reveal and explain the finest observed details.

However, the use of femtosecond laser pulses is limited to time-resolved processes involved in the cleavage and formation of chemical bonds, *i.e.*, nuclear dynamics. To study faster processes, such

as electron dynamics in molecular systems, it is needed to go down to even shorter temporal scales, that is, attoseconds (10^{-18} s). The production of attosecond light pulses can be achieved by generating XUV radiation through HHG. Spectrally filtered XUV radiation by using a TDCM has proved to be an extremely useful tool to unambiguously study the dynamics of cationic states in the femtosecond timescale, without interference from secondary processes such as the dynamics of highly excited states that can intervene when using the full XUV bandwidth arising from the HHG. Using this type of spectrally filtered XUV radiation, it has been possible to study the photo-induced dynamics of methyl iodide cation (CH_3I^+). Furthermore, by using moderate intense IR laser pulses, it has been possible to follow and induce the photodynamics of the cation prepared by the XUV pulse so that it has been possible to control the ability of the molecule to dissociate through specific dissociation channels. In addition, these pulses have been used to probe the oscillation of the prepared vibrational wave packet.

The most relevant conclusions of the molecular systems studied in the present Doctoral Thesis are presented in the following.

Photodissociation dynamics of dihalomethanes: The one-dimensional photodissociation dynamics of dihalomethanes (chloroiodomethane (CH_2ICl) and bromoiodomethane (CH_2BrI)) are very similar to that of methyl iodide (CH_3I) and other linear alkyl iodide derivatives in the first absorption band at around 268 nm, characterized by the cleavage of the C–I bond mediated through repulsive states accessed by an initial parallel transition. The halogen atom substitution effect is manifested in the increased reaction times with the size of the substituting atom and in the available energy mainly channeled into rotational excitation of the molecular co-fragment due to the “anchor” effect of the halogen atom.

Predissociation dynamics of linear and branched alkyl iodides: The predissociation dynamics observed for these compounds in the *B*-band are similar to that of CH_3I, leading to the cleavage of the C–I bond and mainly resulting in $I^*(^2P_{1/2})$ fragments in correlation with molecular radicals. Contrary to what was expected, no formation of $I(^2P_{3/2})$ fragments was detected. The increasing linear chain enhances the coupling between the bound and repulsive states by shortening reaction times, presumably due to the increasing multidimensional nature of the process. The shortening of the reaction times has a direct effect on the lower variation of the anisotropy due to the shorter lifetime of the molecule in the excited state, where it rotates prior to predissociate. The vibrational activity of the molecule before the photodissociation also has effects similar to those observed in methyl iodide.

Photodissociation dynamics of vinyl iodide: The photodissociation of vinyl iodide (C_2H_3I) at the excitation wavelengths of 199.2 and 200 nm leads to the cleavage of the C–I bond cleavage. Although the reaction times, the available energy disposal into different degrees of freedom, and the quantum yields Φ^* are very similar at both excitation wavelengths, the photodissociation mechanisms

are very different. Excitation at 200 nm, mediated by an initial parallel transition, leads to a typical prompt dissociation through repulsive states. In contrast, the excitation at 199.2 nm is governed by a complex predissociative mechanism with a high multidimensional character in which more than one coordinate in the fission process is involved. The presence of a double bond in the alkyl chain radically changes the observed dissociation dynamics in the analogous alkane.

Extreme ultraviolet photoinduced dynamics of the methyl iodide cation in the presence of a moderate intense infrared laser field: The observed dynamics for CH_3I^+ by the excitation of monochromized XUV radiation at 88.9 eV is the one well-reported in the literature; nevertheless, the presence of moderate intense IR laser field can induce tailored dynamics, fundamentally through the $\widetilde{A}^2 A_1$ state, in which the initial wave packet is prepared by the XUV pump, through a pump mechanism to higher electronic states giving rise to the formation of I^+, or by a dump mechanism to the $\widetilde{X}^2E_{3/2,}\widetilde{X}^2E_{1/2}$ states. Additionally, the IR pulses can be used to probe the oscillating wave packet dynamics.

Bibliography

[1] M. Born and R. Oppenheimer, *Annalen der Physik*, 1927, **389**, 457-484.

[2] H. H. Telle, A. G. Ureña and R. J. Donovan, *Laser Chemistry: Spectroscopy, Dynamics and Applications*, Wiley, 2007.

[3] J. Franck and E. Dymond, *Transactions of the Faraday Society*, 1926, **21**, 536-542.

[4] E. Condon, *Physical Review*, 1926, **28**, 1182.

[5] R. Schinke, in *Photodissociation Dynamics: Spectroscopy and Fragmentation of Small Polyatomic Molecules*, Cambridge University Press, 1995.

[6] J. von Neumann and E. P. Wigner, in *The Collected Works of Eugene Paul Wigner*, Springer, 1993.

[7] D. Yarkony, in *Advanced Series in Physical Chemistry*, vol. 15, eds. W. Domcke, D. Yarkony and H. Köppel, World Scientific, 2004.

[8] E. Teller, *The Journal of Physical Chemistry*, 1937, **41**, 109-116.

[9] H. E. Zimmerman, *Journal of the American Chemical Society*, 1966, **88**, 1566-1567.

[10] P. D. W. Domcke, Lehrstuhl für Theoretische Chemie, https://www.department.ch.tum.de/theo/startseite/.

[11] J. H. D. Eland, *Photoelectron Spectroscopy: An Introduction to Ultraviolet Photoelectron Spectroscopy in the Gas Phase*, Butterworth-Heinemann, 1984.

[12] P. Eckle, A. Pfeiffer, C. Cirelli, A. Staudte, R. Dörner, H. Muller, M. Büttiker and U. Keller, *Science*, 2008, **322**, 1525-1529.

[13] J. H. Eberly, J. Javanainen and K. Rzążewski, *Physics Reports*, 1991, **204**, 331-383.

[14] P. Agostini, F. Fabre, G. Mainfray, G. Petite and N. K. Rahman, *Physical Review Letters*, 1979, **42**, 1127.

[15] H. Wang, M. Chini, S. Chen, C.-H. Zhang, F. He, Y. Cheng, Y. Wu, U. Thumm and Z. Chang, *Physical Review Letters*, 2010, **105**, 143002.

[16] J. M. Hollas, *High Resolution Spectroscopy*, Butterworth-Heinemann, 2013.

[17] J. Parker and C. W. Clark, *Journal of the Optical Society of America B*, 1996, **13**, 371-379.

[18] R. N. Zare and D. R. Herschbach, *Proceedings of the IEEE*, 1963, **51**, 173-182.

[19] R. N. Zare, *Molecular Photochemistry*, 1972, **4**, 1-37.

[20] R. N. Zare, *Angular Momentum: Understanding Spatial Aspects in Chemistry and Physics*, John Wiley & Sons, 1988.

[21] J. G. Izquierdo, *Fotodisociación molecular con pulsos láser de nanosegundos y femtosegundos y cartografía de velocidades con imágenes de iones*, Ph. D. Thesis, Universidad Complutense de Madrid, 2007.

[22] W. G. Roeterdink and M. H. Janssen, *Physical Chemistry Chemical Physics*, 2002, **4**, 601-612.

[23] C. Jonah, *The Journal of Chemical Physics*, 1971, **55**, 1915-1922.

[24] S. C. Yang and R. Bersohn, *The Journal of Chemical Physics*, 1974, **61**, 4400-4407.

[25] R. W. Diesen, J. C. Wahr and S. E. Adler, *The Journal of Chemical Physics*, 1969, **50**, 3635-3636.

[26] G. E. Busch, J. F. Cornelius, R. T. Mahoney, R. I. Morse, D. W. Schlosser and K. R. Wilson, *Review of Scientific Instruments*, 1970, **41**, 1066-1073.

[27] W. D. Phillips, J. A. Serri, D. J. Ely, D. E. Pritchard, K. R. Way and J. L. Kinsey, *Physical Review Letters*, 1978, **41**, 937-940.

[28] R. Schmiedl, H. Dugan, W. Meier and K. H. Welge, *Zeitschrift für Physik A Atoms and Nuclei*, 1982, **304**, 137-142.

[29] R. N. Dixon, *The Journal of Chemical Physics*, 1986, **85**, 1866-1879.

[30] G. E. Hall, N. Sivakumar, P. L. Houston and I. I. Burak, *Phys Rev Lett*, 1986, **56**, 1671-1674.

[31] G. E. Hall, N. Sivakumar, R. Ogorzalek, G. Chawla, H.-P. Haerri, P. L. Houston, I. Burak and J. W. Hepburn, *Faraday Discussions of the Chemical Society*, 1986, **82**, 13-24.

[32] R. O. Loo, G. E. Hall, H. P. Haerri and P. L. Houston, *The Journal of Physical Chemistry*, 1988, **92**, 5-8.

[33] W. Wiley and I. H. McLaren, *Review of Scientific Instruments*, 1955, **26**, 1150-1157.

[34] C. Jonah, P. Chandra and R. Bersohn, *The Journal of Chemical Physics*, 1971, **55**, 1903-1907.

[35] J. Solomon, *The Journal of Chemical Physics*, 1967, **47**, 889-895.

[36] D. W. Chandler and P. L. Houston, *The Journal of Chemical Physics*, 1987, **87**, 1445-1447.

[37] A. T. Eppink and D. H. Parker, *Review of Scientific Instruments*, 1997, **68**, 3477-3484.

[38] D. W. Chandler and D. H. Parker, in *Advances in Photochemistry*, vol. 25, eds. D. C. Neckers, D. H. Volman and G. V. Bünau, John Wiley & Sons, 1999.

[39] A. G. Suits and R. E. Continetti, in *Imaging in Chemical Dynamics*, eds. A. G. Suits and R. E. Continetti, ACS Publications, 2001.

[40] A. T. J. B. Eppink and D. H. Parker, *The Journal of Chemical Physics*, 1998, **109**, 4758.

[41] B. Dick, *Physical Chemistry Chemical Physics*, 2014, **16**, 570-580.

[42] H. H. Telle, A. G. Ureña and R. J. Donovan, *Laser chemistry: spectroscopy, dynamics and applications*, John Wiley & Sons, 2007.

[43] D. H. Parker and A. T. J. B. Eppink, in *Imaging in Molecular Dynamics: Technology and Applications*, ed. B. J. Whitaker, Cambridge University Press, 2003.

[44] A. Eppink, S. Wu and B. Whitaker, *Imaging in Molecular Dynamics*, 2003.

[45] J. D. Díez, *Fotodisociación en tiempo real de moléculas y agregados con pulsos láser de femtosegundos y técnicas de imágenes de iones*, Ph. D. Thesis, Universidad Complutense de Madrid, 2009.

[46] L. M. Smith, D. R. Keefer and S. Sudharsanan, *Journal of Quantitative Spectroscopy and Radiative Transfer*, 1988, **39**, 367-373.

[47] M. J. Vrakking, *Review of Scientific Instruments*, 2001, **72**, 4084-4089.

[48] V. Dribinski, A. Ossadtchi, V. A. Mandelshtam and H. Reisler, *Review of Scientific Instruments*, 2002, **73**, 2634-2642.

[49] G. A. Garcia, L. Nahon and I. Powis, *Review of Scientific Instruments*, 2004, **75**, 4989-4996.

[50] A. N. Tikhonov, *Soviet Mathematics Doklady*, 1963, **4**, 1035-1038.

[51] O. Kornilov, personal communication.

[52] M. J. Bass, M. Brouard, A. P. Clark and C. Vallance, *The Journal of Chemical Physics*, 2002, **117**, 8723-8735.

[53] M. N. R. Ashfold, N. H. Nahler, A. J. Orr-Ewing, O. P. J. Vieuxmaire, R. L. Toomes, T. N. Kitsopoulos, I. A. Garcia, D. A. Chestakov, S.-M. Wu and D. H. Parker, *Physical Chemistry Chemical Physics*, 2006, **8**, 26-53.

[54] C. R. Gebhardt, T. P. Rakitzis, P. C. Samartzis, V. Ladopoulos and T. N. Kitsopoulos, *Review of Scientific Instruments*, 2001, **72**, 3848-3853.

[55] D. Townsend, M. P. Minitti and A. G. Suits, *Review of Scientific Instruments*, 2003, **74**, 2530-2539.

[56] J. J. Lin, J. Zhou, W. Shiu and K. Liu, *Review of Scientific Instruments*, 2003, **74**, 2495-2500.

[57] F. Allum, R. Mason, M. Burt, C. S. Slater, E. Squires, B. Winter and M. Brouard, *Molecular Physics*, 2020, e1842531.

[58] R. D. Levine and R. B. Bernstein, *Molecular Reaction Dynamics and Chemical Reactivity*, Oxford University Press, 1987.

[59] H. Eyring and M. Polanyi, *Zeitschrift Fur Physikalische Chemie-Abteilung B-Chemie Der Elementarprozesse Aufbau Der Materie*, 1931, **12**, 279-311.

[60] A. H. Zewail and R. B. Bernstein, *Chemical & Engineering News*, 1988, **66**, 24-43.

[61] M. Gruebele and A. H. Zewail, *Physics Today*, 1990, **43**, 24.

[62] A. H. Zewail, *Scientific American*, 1990, **263**, 76-83.

[63] A. H. Zewail, *Angewandte Chemie International Edition*, 2000, **39**, 2586-2631.

[64] M. J. Rosker, M. Dantus and A. H. Zewail, *Science*, 1988, **241**, 1200-1202.

[65] The Nobel Prize in Chemistry 1999, https://www.nobelprize.org/prizes/chemistry/1999/zewail/facts/.

[66] A. H. Zewail, *Science*, 1988, **242**, 1645-1653.

[67] M. J. Rosker, M. Dantus and A. H. Zewail, *The Journal of Chemical Physics*, 1988, **89**, 6113-6127.

[68] A. H. Zewail, *The Journal of Physical Chemistry A*, 2000, **104**, 5660-5694.

[69] B. J. Sussman, D. Townsend, M. Y. Ivanov and A. Stolow, *Science*, 2006, **314**, 278-281.

[70] A. Baltuška, T. Udem, M. Uiberacker, M. Hentschel, E. Goulielmakis, C. Gohle, R. Holzwarth, V. Yakovlev, A. Scrinzi and T. W. Hänsch, *Nature*, 2003, **421**, 611-615.

[71] M. E. Corrales, J. González-Vázquez, R. de Nalda and L. Bañares, *The Journal of Physical Chemistry Letters*, 2019, **10**, 138-143.

[72] J. J. Gerdy, M. Dantus, R. M. Bowman and A. H. Zewail, *Chemical Physics Letters*, 1990, **171**, 1-4.

[73] A. Zewail, *Physics Today*, 1980, **33**, 27-33.

[74] P. Brumer and M. Shapiro, *Annual Review of Physical Chemistry*, 1992, **43**, 257-282.

[75] R. J. Gordon and S. A. Rice, *Annual Review of Physical Chemistry*, 1997, **48**, 601-641.

[76] H. Rabitz, R. de Vivie-Riedle, M. Motzkus and K. Kompa, *Science*, 2000, **288**, 824.

[77] V. Letokhov, *Physics Today*, 1977, **30**, 23-32.

[78] N. Bloembergen and E. Yablonovitch, *Physics Today*, 1978, **31**, 23-31.

[79] N. Bloembergen and A. H. Zewail, *The Journal of Physical Chemistry*, 1984, **88**, 5459-5465.

[80] T. Elsaesser and W. Kaiser, *Annual Review of Physical Chemistry*, 1991, **42**, 83-107.

[81] A. H. Zewail, *The Journal of Physical Chemistry*, 1996, **100**, 12701-12724.

[82] A. P. Peirce, M. A. Dahleh and H. Rabitz, *Physical Review A*, 1988, **37**, 4950-4964.

[83] C. Chen, Y.-Y. Yin and D. S. Elliott, *Physical Review Letters*, 1990, **64**, 507-510.

[84] L. Zhu, V. Kleiman, X. Li, S. P. Lu, K. Trentelman and R. J. Gordon, *Science*, 1995, **270**, 77-80.

[85] D. J. Tannor and S. A. Rice, *The Journal of Chemical Physics*, 1985, **83**, 5013-5018.

[86] U. Gaubatz, P. Rudecki, M. Becker, S. Schiemann, M. Külz and K. Bergmann, *Chemical Physics Letters*, 1988, **149**, 463-468.

[87] M. Salour and C. Cohen-Tannoudji, *Physical Review Letters*, 1977, **38**, 757.

[88] R. Teets, J. Eckstein and T. Hänsch, *Physical Review Letters*, 1977, **38**, 760.

[89] M. E. Corrales Castellanos, *Efectos estructurales y control láser de dinámicas moleculares ultrarrápidas*, Ph. D. Thesis, Universidad Complutense de Madrid, 2015.

[90] B. J. Sussman, D. Townsend, M. Y. Ivanov and A. Stolow, *Science*, 2006, **314**, 278.

[91] J. Bokor, P. H. Bucksbaum and R. R. Freeman, *Optics Letters*, 1983, **8**, 217-219.

[92] A. McPherson, G. Gibson, H. Jara, U. Johann, T. S. Luk, I. A. McIntyre, K. Boyer and C. K. Rhodes, *Journal of the Optical Society of America B*, 1987, **4**, 595-601.

[93] M. Ferray, A. L'Huillier, X. F. Li, L. A. Lompre, G. Mainfray and C. Manus, *Journal of Physics B Atomic Molecular Physics*, 1988, **21**, L31.

[94] P. M. Paul, E. S. Toma, P. Breger, G. Mullot, F. Augé, P. Balcou, H. G. Muller and P. Agostini, *Science*, 2001, **292**, 1689-1692.

[95] P. H. Bucksbaum, *Optics and Photonics News*, 2015, **26**, 28-35.

[96] M. Nisoli, *Optics and Photonics News*, 2019, **30**, 32-39.

[97] A. Borot, A. Malvache, X. Chen, D. Douillet, G. Iaquianiello, T. Lefrou, P. Audebert, J.-P. Geindre, G. Mourou and F. Quéré, *Optics Letters*, 2011, **36**, 1461-1463.

[98] G. D. Tsakiris, K. Eidmann, J. Meyer-ter-Vehn and F. Krausz, *New Journal of Physics*, 2006, **8**, 19-19.

[99] J. L. Krause, K. J. Schafer and K. C. Kulander, *Physical Review Letters*, 1992, **68**, 3535.

[100] P. B. Corkum, *Physical Review Letters*, 1993, **71**, 1994.

[101] K. Schafer, B. Yang, L. DiMauro and K. Kulander, *Physical Review Letters*, 1993, **70**, 1599.

[102] M. Lewenstein, P. Balcou, M. Y. Ivanov, A. L'Huillier and P. B. Corkum, *Physical Review A*, 1994, **49**, 2117-2132.

[103] P. B. Corkum and F. Krausz, *Nature Physics*, 2007, **3**, 381-387.

[104] L. Keldysh, *Journal of Experimental and Theoretical Physics*, 1965, **20**, 1307-1314.

[105] D. Attwood, *Soft X-Rays and Extreme Ultraviolet Radiation: Principles and Applications*, Cambridge University Press, 1999.

[106] E. Constant, D. Garzella, P. Breger, E. Mével, C. Dorrer, C. Le Blanc, F. Salin and P. Agostini, *Physical Review Letters*, 1999, **82**, 1668.

[107] Y. Tamaki, J. Itatani, Y. Nagata, M. Obara and K. Midorikawa, *Physical Review Letters*, 1999, **82**, 1422.

[108] Y. Tamaki, J. Itatani, M. Obara and K. Midorikawa, *Physical Review A*, 2000, **62**, 063802.

[109] E. Takahashi, Y. Nabekawa, M. Nurhuda and K. Midorikawa, *The Journal of the Optical Society of America B*, 2003, **20**, 158-165.

[110] T. Ditmire, E. Gumbrell, R. Smith, J. Tisch, D. Meyerhofer and M. Hutchinson, *Physical Review Letters*, 1996, **77**, 4756.

[111] R. A. Bartels, A. Paul, H. Green, H. C. Kapteyn, M. M. Murnane, S. Backus, I. P. Christov, Y. Liu, D. Attwood and C. Jacobsen, *Science*, 2002, **297**, 376-378.

[112] A. McPherson, G. Gibson, H. Jara, U. Johann, T. S. Luk, I. McIntyre, K. Boyer and C. K. Rhodes, *Journal of the Optical Society of America B*, 1987, **4**, 595-601.

[113] M. Ferray, A. L'Huillier, X. Li, L. Lompre, G. Mainfray and C. Manus, *Journal of Physics B: Atomic, Molecular and Optical Physics*, 1988, **21**, L31.

[114] S. Yurish, *Advances in Optics*, IFSA Publishing, 2018.

[115] K. Dinh and L. Dao, *Phase-matched High Order Harmonic Generation and Application*, Nova Publishers Inc, 2013.

[116] A. L'Huillier, M. Lewenstein, P. Salieres, P. Balcou, M. Y. Ivanov, J. Larsson and C.-G. Wahlström, *Physical Review A*, 1993, **48**, R3433.

[117] C. D. Lin, A.-T. Le, C. Jin and H. Wei, *Attosecond and Strong-Field Physics: Principles and Applications*, Cambridge University Press, 2018.

[118] P. Siffalovic, M. Drescher, M. Spieweck, T. Wiesenthal, Y. C. Lim, R. Weidner, A. Elizarov and U. Heinzmann, *Review of Scientific Instruments*, 2001, **72**, 30-35.

[119] L. Nugent-Glandorf, M. Scheer, D. A. Samuels, V. Bierbaum and S. R. Leone, *Review of Scientific Instruments*, 2002, **73**, 1875-1886.

[120] M. Ito, Y. Kataoka, T. Okamoto, M. Yamashita and T. Sekikawa, *Optics Express*, 2010, **18**, 6071-6078.

[121] P. Villoresi, *Applied Optics*, 1999, **38**, 6040-6049.

[122] L. Poletto, *Applied Physics B*, 2004, **78**, 1013-1016.

[123] M. Eckstein, J. Hummert, M. Kubin, C.-H. Yang, F. Frassetto, L. Poletto, M. J. Vrakking and O. Kornilov, *arXiv:1604.02650*, 2016.

[124] P. Schwendimann, E. Sigmund and K. Zeile, *Physical Review A*, 1988, **37**, 3018.

[125] R. Paschotta, *Encyclopedia of Laser Physics and Technology* vol. 1, Wiley-VCH, 2008.

[126] P. F. Moulton, *Journal of the Optical Society of America B*, 1986, **3**, 125-133.

[127] R. Mellish, C. van der Poel, A. Valster, N. Barry, S. Hyde, R. Jones, P. French and J. Taylor, *Optics Letters*, 1995, **20**, 2312-2314.

[128] D. Strickland and G. Mourou, *Optics Communications*, 1985, **56**, 219-221.

[129] D. Kaplan and P. Tournois, *Journal de Physique IV*, 2002, **12**, 69-75.

[130] G. Gitzinger, *Dinámica de predisociacion y control de la fotoionización de yoduro de metilo con pulsos láser de femtosegundos*, Ph. D. Thesis, Universidad Complutense de Madrid, 2012.

[131] R. W. Boyd, *Nonlinear Optics*, Elsevier Science, 2003.

[132] P. C. Wright, *Generation, Characterization and Application of the 3rd and 4th Harmonics of a Titanium:sapphire Femtosecond Laser*, Master Thesis, University of Ottawa, 2012.

[133] C. Wan, *Tunable time plate*, Patent US5852620A, 1998

[134] I. A. Walmsley and C. Dorrer, *Advances in Optics and Photonics*, 2009, **1**, 308-437.

[135] D. J. Kane and R. Trebino, *IEEE Journal of Quantum Electronics*, 1993, **29**, 571-579.

[136] D. J. Kane and R. Trebino, *Optics Letters*, 1993, **18**, 823-825.

[137] A. J. Murray, *Measurement Science and Technology*, 2001, **13**, N12.

[138] P. D. Gerlich, Fast Pulsed Piezo Valve, https://www.tu-chemnitz.de/physik/ION/Technology/Piezo_Valve/index.html.

[139] CeramTec.

[140] D. Irimia, D. Dobrikov, R. Kortekaas, H. Voet, D. A. van den Ende, W. A. Groen and M. H. M. Janssen, *Review of Scientific Instruments*, 2009, **80**, 113303.

[141] M. L. Lipciuc, A. J. van den Brom, L. Dinu and M. H. Janssen, *Review of Scientific Instruments*, 2005, **76**, 123103.

[142] W. B. Colson, J. McPherson and F. T. King, *Review of Scientific Instruments*, 1973, **44**, 1694-1696.

[143] M. H. Kim, B. D. Leskiw and A. G. Suits, *The Journal of Physical Chemistry A*, 2005, **109**, 7839-7842.

[144] B. D. Leskiw, M. H. Kim, G. E. Hall and A. G. Suits, *Review of Scientific Instruments*, 2005, **76**, 104101.

[145] A. Suits, M. H. Kim and B. D. Leskiw, *Velocity imaging tandem mass spectrometer*, Patent US7534996, 2009

[146] D. Irimia, R. Kortekaas and M. H. Janssen, *Physical Chemistry Chemical Physics*, 2009, **11**, 3958-3966.

[147] L. Dinu, A. T. J. B. Eppink, F. Rosca-Pruna, H. L. Offerhaus, W. J. v. d. Zande and M. J. J. Vrakking, *Review of Scientific Instruments*, 2002, **73**, 4206-4213.

[148] B.-Y. Chang, R. C. Hoetzlein, J. A. Mueller, J. D. Geiser and P. L. Houston, *Review of Scientific Instruments*, 1998, **69**, 1665-1670.

[149] R. de Nalda, J. G. Izquierdo, J. Durá and L. Bañares, *The Journal of Chemical Physics*, 2007, **126**, 021101.

[150] R. de Nalda, J. Durá, A. García-Vela, J. G. Izquierdo, J. González-Vázquez and L. Bañares, *The Journal of Chemical Physics*, 2008, **128**, 244309.

[151] J. Durá, R. de Nalda, G. A. Amaral and L. Bañares, *The Journal of Chemical Physics*, 2009, **131**, 134311.

[152] L. Rubio-Lago, A. García-Vela, A. Arregui, G. A. Amaral and L. Bañares, *The Journal of Chemical Physics*, 2009, **131**, 174309.

[153] A. García-Vela, R. De Nalda, J. Durá, J. González-Vázquez and L. Bañares, *The Journal of Chemical Physics*, 2011, **135**, 154306.

[154] M. L. Murillo-Sánchez, J. González-Vázquez, M. E. Corrales, R. de Nalda, E. Martínez-Núñez, A. García-Vela and L. Bañares, *The Journal of Chemical Physics*, 2020, **152**, 014304.

[155] G. Gitzinger, M. E. Corrales, V. Loriot, G. A. Amaral, R. d. Nalda and L. Bañares, *The Journal of Chemical Physics*, 2010, **132**, 234313.

[156] N. Thiré, R. Cireasa, V. Blanchet and S. T Pratt, 2010, **12**, 15644-15652.

[157] N. Thiré, R. Cireasa, D. Staedter, V. Blanchet and S. Pratt, *Physical Chemistry Chemical Physics*, 2011, **13**, 18485-18496.

[158] G. Gitzinger, M. E. Corrales, V. Loriot, R. de Nalda and L. Bañares, *The Journal of Chemical Physics*, 2012, **136**, 074303.

[159] H. Xu and S. Pratt, *The Journal of Chemical Physics*, 2013, **139**, 214310.

[160] M. G. González, J. D. Rodríguez, L. Rubio-Lago and L. Bañares, *Physical Chemistry Chemical Physics*, 2014, **16**, 26330-26341.

[161] A. Eppink and D. H. Parker, *The Journal of Chemical Physics*, 1998, **109**, 4758.

[162] R. Ogorzalek Loo, H. P. Haerri, G. Hall and P. Houston, *The Journal of Chemical Physics*, 1989, **90**, 4222-4236.

[163] D. W. Chandler, J. W. Thoman, M. H. M. Janssen and D. H. Parker, *Chemical Physics Letters*, 1989, **156**, 151-158.

[164] A. Eppink and D. H. Parker, *The Journal of Chemical Physics* 1998, **109**, 4758.

[165] BEHLKE, Fast high voltage transistor switches HTS 81-06-GSM and HTS 151-03-GSM, https://www.behlke.com/pdf/151-03-gsm.pdf.

[166] V. Loriot, L. Bañares and R. de Nalda, *Applied Sciences*, 2018, **8**, 1227.

[167] M. Eckstein, C.-H. Yang, M. Kubin, F. Frassetto, L. Poletto, H.-H. Ritze, M. J. Vrakking and O. Kornilov, *The Journal of Physical Chemistry Letters*, 2015, **6**, 419-425.

[168] M. Isinger, D. Busto, S. Mikaelsson, S. Zhong, C. Guo, P. Salières, C. L. Arnold, A. L'Huillier and M. Gisselbrecht, *Philosophical Transactions of the Royal Society A: Mathematical, Physical and Engineering Sciences*, 2019, **377**, 20170475.

[169] K. Varjú, Y. Mairesse, P. Agostini, P. Breger, B. Carré, L. J. Frasinski, E. Gustafsson, P. Johnsson, J. Mauritsson, H. Merdji, P. Monchicourt, A. L'Huillier and P. Salières, *Physical Review Letters*, 2005, **95**, 243901.

[170] B. D. Guenther and D. Steel, *Encyclopedia of Modern Optics*, Elsevier Science, 2018.

[171] M. Eckstein, *Investigation of Ultrafast Electronic and Nuclear Dynamics in Molecular Nitrogen using an XUV Time Delay Compensating Monochromator*, Ph. D. Thesis, 2015.

[172] L. Poletto, P. Villoresi, F. Frassetto, F. Calegari, F. Ferrari, M. Lucchini, G. Sansone and M. Nisoli, *Review of Scientific Instruments*, 2009, **80**, 123109.

[173] C. Iaconis and I. A. Walmsley, *Optics Letters*, 1998, **23**, 792-794.

[174] SPIDER, https://www2.physics.ox.ac.uk/research/ultrafast-quantum-optics-and-optical-metrology/ultrafast-metrology/spider.

[175] V. A. Zubov and T. I. Kuznetsova, *Soviet Journal of Quantum Electronics*, 1991, **21**, 1285-1286.

[176] V. Wong and I. A. Walmsley, *Optics Letters*, 1994, **19**, 287-289.

[177] M. E. Anderson, A. Monmayrant, S. P. Gorza, P. Wasylczyk and I. A. Walmsley, *Laser Physics Letters*, 2008, **5**, 259-266.

[178] T. Witting, SPIDER, https://tobiaswitting.wordpress.com/research/ultrafast-metrology/spider/.

[179] N. M. Kroll and K. M. Watson, *Physical Review A*, 1973, **8**, 804-809.

[180] A. Maquet and R. TaÏeb, *Journal of Modern Optics*, 2007, **54**, 1847-1857.

[181] M. Grishin, *Advances in Solid State Lasers: Development and Applications*, IntechOpen, 2010.

[182] P. Radcliffe, M. Arbeiter, W. Li, S. Düsterer, H. Redlin, P. Hayden, P. Hough, V. Richardson, J. Costello and T. Fennel, *New Journal of Physics*, 2012, **14**, 043008.

[183] O. Ghafur, W. Siu, P. Johnsson, M. F. Kling, M. Drescher and M. Vrakking, *Review of Scientific Instruments*, 2009, **80**, 033110.

[184] P. Baltzer, M. Larsson, L. Karlsson, B. Wannberg and M. Carlsson Göthe, *Physical Review A*, 1992, **46**, 5545-5553.

[185] C. Walter, P. Cosby and H. Helm, *The Journal of Chemical Physics*, 2000, **112**, 4621-4633.

[186] J. Eland and E. Duerr, *Chemical Physics*, 1998, **229**, 13-19.

[187] S. Eden, P. Limao-Vieira, S. V. Hoffmann and N. Mason, *Chemical Physics*, 2007, **331**, 232-244.

[188] M. J. Molina and F. S. Rowland, *Nature*, 1974, **249**, 810-812.

[189] P. Zou, W. Sean McGivern and S. W. North, *Physical Chemistry Chemical Physics*, 2000, **2**, 3785-3790.

[190] J. V. Kasper and G. C. Pimentel, *Applied Physics Letters*, 1964, **5**, 231-233.

[191] A. Gedanken and M. D. Rowe, *Chemical Physics Letters*, 1975, **34**, 39-43.

[192] A. T. J. B. Eppink and D. H. Parker, *The Journal of Chemical Physics*, 1999, **110**, 832-844.

[193] A. B. Alekseyev, H. Liebermann, R. J. Buenker and S. N. Yurchenko, *The Journal of Chemical Physics*, 2007, **126**, 234102.

[194] M. González, J. Rodríguez, L. Rubio-Lago, A. García-Vela and L. Bañares, *Physical Chemistry Chemical Physics*, 2011, **13**, 16404-16415.

[195] R. S. Mulliken and E. Teller, *Physical Review*, 1942, **61**, 283-296.

[196] R. S. Mulliken, *The Journal of Chemical Physics*, 1940, **8**, 382-395.

[197] T. Hunter and K. Kristjansson, *Chemical Physics Letters*, 1978, **58**, 291-294.

[198] R. S. Mulliken, *The Journal of Chemical Physics*, 1955, **23**, 1997-2011.

[199] R. S. Mulliken, *Physical Review*, 1935, **47**, 413-415.

[200] F. G. Godwin, P. A. Gorry, P. M. Hughes, D. Raybone, T. M. Watkinson and J. C. Whitehead, *Chemical Physics Letters*, 1987, **135**, 163-169.

[201] Y. Amatatsu, K. Morokuma and S. Yabushita, *The Journal of Chemical Physics*, 1991, **94**, 4858-4876.

[202] Y. Amatatsu, S. Yabushita and K. Morokuma, *The Journal of Chemical Physics*, 1996, **104**, 9783-9794.

[203] S. J. Riley and K. R. Wilson, *Faraday Discussions of the Chemical Society*, 1972, **53**, 132-146.

[204] R. Sparks, K. Shobatake, L. Carlson and Y.-T. Lee, *The Journal of Chemical Physics*, 1981, **75**, 3838-3846.

[205] H. W. Hermann and S. R. Leone, *The Journal of Chemical Physics*, 1982, **76**, 4766-4774.

[206] M. Barry and P. Gorry, *Molecular Physics*, 1984, **52**, 461-473.

[207] G. Van Veen, T. Baller, A. De Vries and N. Van Veen, *Chemical Physics*, 1984, **87**, 405-417.

[208] R. O. Loo, G. Hall, H. Haerri and P. Houston, *The Journal of Physical Chemistry*, 1988, **92**, 5-8.

[209] G. Hall, T. J. Sears and J. M. Frye, *The Journal of Chemical Physics*, 1989, **90**, 6234-6242.

[210] G. Li, H. J. Hwang and H. C. Jung, *Review of scientific instruments*, 2005, **76**, 023105.

[211] A. D. Hammerich, U. Manthe, R. Kosloff, H. D. Meyer and L. S. Cederbaum, *The Journal of Chemical Physics*, 1994, **101**, 5623-5646.

[212] M. González, J. Rodríguez, L. Rubio-Lago, A. García-Vela and L. Bañares, *Physical Chemistry Chemical Physics*, 2011, **13**, 16404-16415.

[213] M. E. Corrales, V. Loriot, G. Balerdi, J. González-Vázquez, R. de Nalda, L. Bañares and A. H. Zewail, *Physical Chemistry Chemical Physics*, 2014, **16**, 8812-8818.

[214] A. R. Attar, A. Bhattacherjee and S. R. Leone, *The Journal of Physical Chemistry Letters*, 2015, **6**, 5072-5077.

[215] L. Drescher, M. Galbraith, G. Reitsma, J. Dura, N. Zhavoronkov, S. Patchkovskii, M. Vrakking and J. Mikosch, *The Journal of Chemical Physics*, 2016, **145**, 011101.

[216] A. Baumann, D. Rompotis, O. Schepp, M. Wieland and M. Drescher, *The Journal of Physical Chemistry A*, 2018, **122**, 4779-4784.

[217] F. Braußе, G. Goldsztejn, K. Amini, R. Boll, S. Bari, C. Bomme, M. Brouard, M. Burt, B. C. De Miranda and S. Düsterer, *Physical Review A*, 2018, **97**, 043429.

[218] E. M. Warne, B. Downes-Ward, J. Woodhouse, M. A. Parkes, D. Bellshaw, E. Springate, P. Majchrzak, Y. Zhang, G. Karras and A. S. Wyatt, *Physical Chemistry Chemical Physics*, 2019, **21**, 11142-11149.

[219] D. Porret and C. F. Goodeve, *Proceedings of the Royal Society of London. Series A. Mathematical and Physical Sciences*, 1938, **165**, 31-42.

[220] M. Tadjeddine, J. Flament and C. Teichteil, *Chemical Physics*, 1987, **118**, 45-55.

[221] S. Yabushita and K. Morokuma, *Chemical Physics Letters*, 1988, **153**, 517-521.

[222] D. Xie, H. Guo, Y. Amatatsu and R. Kosloff, *The Journal of Physical Chemistry A*, 2000, **104**, 1009-1019.

[223] H. Guo and G. C. Schatz, *The Journal of Chemical Physics*, 1990, **93**, 393-402.

[224] H. Guo, *The Journal of Chemical Physics*, 1992, **96**, 6629-6642.

[225] A. B. Alekseyev, H.-P. Liebermann and R. J. Buenker, *The Journal of Chemical Physics*, 2007, **126**, 234103.

[226] C. R. Evenhuis and U. Manthe, *The Journal of Physical Chemistry A*, 2011, **115**, 5992-6001.

[227] N. Wittenbrink and W. Eisfeld, *The Journal of Chemical Physics*, 2018, **148**, 094102.

[228] S. Goss, D. McGilvery, J. Morrison and D. Smith, *The Journal of Chemical Physics*, 1981, **75**, 1820-1828.

[229] F. Godwin, C. Paterson and P. Gorry, *Molecular Physics*, 1987, **61**, 827-848.

[230] S. Uma and P. K. Das, *The Journal of Chemical Physics*, 1996, **104**, 4470-4474.

[231] Y. S. Kim, W. K. Kang, D.-C. Kim and K.-H. Jung, *The Journal of Physical Chemistry A*, 1997, **101**, 7576-7581.

[232] K. Kavita and P. K. Das, *The Journal of Chemical Physics*, 2000, **112**, 8426-8431.

[233] V. A. Shubert, M. Rednic and S. T. Pratt, *The Journal of Chemical Physics*, 2009, **130**, 134306.

[234] M. L. Murillo-Sánchez, S. Marggi Poullain, J. González-Vázquez, M. E. Corrales, G. Balerdi and L. Bañares, *Chemical Physics Letters*, 2017, **683**, 22-28.

[235] S. J. Lee and R. Bersohn, *The Journal of Physical Chemistry*, 1982, **86**, 728-730.

[236] L. J. Butler, E. J. Hintsa, S. F. Shane and Y. T. Lee, *The Journal of Chemical Physics*, 1987, **86**, 2051-2074.

[237] H. Keller-Rudek, G. Moortgat, R. Sander and R. Sörensen, *Earth System Science Data*, 2013, **5**, 365-373.

[238] J. G. Underwood and I. Powis, *Physical Chemistry Chemical Physics*, 2000, **2**, 747-756.

[239] D. V. Chicharro, S. M. Poullain, J. González-Vázquez and L. Bañares, *The Journal of Chemical Physics*, 2017, **147**, 013945.

[240] S. M. Poullain, D. V. Chicharro, E. Navarro, L. Rubio-Lago, J. González-Vázquez and L. Bañares, *Physical Chemistry Chemical Physics*, 2018, **20**, 3490-3503.

[241] S.-Q. Man, W. M. Kwok and D. L. Phillips, *The Journal of Physical Chemistry*, 1995, **99**, 15705-15708.

[242] A. R. Attar, L. Piticco and S. R. Leone, *The Journal of Chemical Physics*, 2014, **141**, 164308.

[243] M. Burt, R. Boll, J. W. L. Lee, K. Amini, H. Köckert, C. Vallance, A. S. Gentleman, S. R. Mackenzie, S. Bari, C. Bomme, S. Düsterer, B. Erk, B. Manschwetus, E. Müller, D. Rompotis, E. Savelyev, N. Schirmel, S. Techert, R. Treusch, J. Küpper, S. Trippel, J. Wiese, H. Stapelfeldt, B. C. de Miranda, R. Guillemin, I. Ismail, L. Journel, T. Marchenko, J. Palaudoux, F. Penent, M.

N. Piancastelli, M. Simon, O. Travnikova, F. Brausse, G. Goldsztejn, A. Rouzée, M. Géléoc, R. Geneaux, T. Ruchon, J. Underwood, D. M. P. Holland, A. S. Mereshchenko, P. K. Olshin, P. Johnsson, S. Maclot, J. Lahl, A. Rudenko, F. Ziaee, M. Brouard and D. Rolles, *Physical Review A*, 2017, **96**, 043415.

[244] C. Vallance, M. Brouard, A. Nomerotski, R. Nickerson and R. Turchetta, Pixel Imaging Mass Spectrometry-PImMS 2, http://pimms.chem.ox.ac.uk/pimms2.php.

[245] C. S. Slater, S. Blake, M. Brouard, A. Lauer, C. Vallance, J. J. John, R. Turchetta, A. Nomerotski, L. Christensen, J. H. Nielsen, M. P. Johansson and H. Stapelfeldt, *Physical Review A*, 2014, **89**, 011401.

[246] F. Allum, M. Burt, K. Amini, R. Boll, H. Köckert, P. K. Olshin, S. Bari, C. Bomme, F. Braußе, B. C. d. Miranda, S. Düsterer, B. Erk, M. Géléoc, R. Geneaux, A. S. Gentleman, G. Goldsztejn, R. Guillemin, D. M. P. Holland, I. Ismail, P. Johnsson, L. Journel, J. Küpper, J. Lahl, J. W. L. Lee, S. Maclot, S. R. Mackenzie, B. Manschwetus, A. S. Mereshchenko, R. Mason, J. Palaudoux, M. N. Piancastelli, F. Penent, D. Rompotis, A. Rouzée, T. Ruchon, A. Rudenko, E. Savelyev, M. Simon, N. Schirmel, H. Stapelfeldt, S. Techert, O. Travnikova, S. Trippel, J. G. Underwood, C. Vallance, J. Wiese, F. Ziaee, M. Brouard, T. Marchenko and D. Rolles, *The Journal of Chemical Physics*, 2018, **149**, 204313.

[247] K. Liu, H. Zhao, C. Wang, A. Zhang, S. Ma and Z. Li, *The Journal of Chemical Physics*, 2005, **122**, 044310.

[248] Y. J. Liu, D. Ajitha, J. W. Krogh, A. N. Tarnovsky and R. Lindh, *ChemPhysChem*, 2006, **7**, 955-963.

[249] G. Schmitt and F. J. Comes, *Journal of Photochemistry and Photobiology A: Chemistry*, 1987, **41**, 13-30.

[250] D. Senapati, K. Kavita and P. K. Das, *The Journal of Physical Chemistry A*, 2002, **106**, 8479-8482.

[251] D. Senapati and P. K. Das, *Chemical Physics Letters*, 2004, **393**, 535-538.

[252] C.-H. Zhang, Y. Zhang, S. Zhang and B. Zhang, *Acta Physico-Chimica Sinica*, 2009, **25**, 1708-1712.

[253] D. R. Stull, *Industrial & Engineering Chemistry*, 1947, **39**, 517-540.

[254] T. Noro, M. Sekiya and T. Koga, *Theoretical Chemistry Accounts*, 2012, **131**, 1-8.

[255] H. Nakano, *Chemical Physics Letters*, 1993, **207**, 372-378.

[256] H. A. Witek, Y. K. Choe, J. P. Finley and K. Hirao, *Journal of Computational Chemistry*, 2002, **23**, 957-965.

[257] D. G. Fedorov and J. P. Finley, *Physical Review A*, 2001, **64**, 042502.

[258] B. A. Hess, *Physical Review A*, 1986, **33**, 3742.

[259] T. Nakajima and K. Hirao, *The Journal of Chemical Physics*, 2000, **113**, 7786-7789.

[260] T. Nakajima and K. Hirao, *The Journal of Chemical Physics*, 2003, **119**, 4105-4111.

[261] T. R. Furlani and H. F. King, *The Journal of Chemical Physics*, 1985, **82**, 5577-5583.

[262] H. F. King and T. R. Furlani, *Journal of Computational Chemistry*, 1988, **9**, 771-778.

[263] D. G. Fedorov and M. S. Gordon, *The Journal of Chemical Physics*, 2000, **112**, 5611-5623.

[264] D. G. Fedorov, S. Koseki, M. W. Schmidt and M. S. Gordon, *International Reviews in Physical Chemistry*, 2003, **22**, 551-592.

[265] G. Karlström, R. Lindh, P.-Å. Malmqvist, B. O. Roos, U. Ryde, V. Veryazov, P.-O. Widmark, M. Cossi, B. Schimmelpfennig and P. Neogrady, *Computational Materials Science*, 2003, **28**, 222-239.

[266] F. Aquilante, J. Autschbach, R. K. Carlson, L. F. Chibotaru, M. G. Delcey, L. De Vico, N. Ferré, L. M. Frutos, L. Gagliardi and M. Garavelli, *Journal of Computational Chemistry*, 2016, **37**, 506-541.

[267] B. O. Roos, R. Lindh, P.-Å. Malmqvist, V. Veryazov and P.-O. Widmark, *The Journal of Physical Chemistry A*, 2004, **108**, 2851-2858.

[268] M. Reiher and A. Wolf, *The Journal of Chemical Physics*, 2004, **121**, 2037-2047.

[269] M. Reiher and A. Wolf, *The Journal of Chemical Physics*, 2004, **121**, 10945-10956.

[270] D. Peng and M. Reiher, *Theoretical Chemistry Accounts*, 2012, **131**, 1-20.

[271] B. Schimmelpfennig, *Stockholm University*, 1996.

[272] B. O. Roos, P. R. Taylor and P. E. Si, *Chemical Physics*, 1980, **48**, 157-173.

[273] J. Finley, P.-Å. Malmqvist, B. O. Roos and L. Serrano-Andrés, *Chemical Physics Letters*, 1998, **288**, 299-306.

[274] B. O. Roos and K. Andersson, *Chemical Physics Letters*, 1995, **245**, 215-223.

[275] P. Marquetand, M. Richter, J. González-Vázquez, I. Sola and L. González, *Faraday Discussions*, 2011, **153**, 261-273.

[276] M. Richter, P. Marquetand, J. González-Vázquez, I. Sola and L. González, *Journal of Chemical Theory and Computation*, 2011, **7**, 1253-1258.

[277] H. Werner, P. Knowles, G. Knizia, F. Manby, M. Schütz, P. Celani, T. Korona, R. Lindh, A. Mitrushenkov and G. Rauhut, *Molpro. Version 2010.1, a package of ab initio programs*, 2010.

[278] P. Celani and H.-J. Werner, *The Journal of Chemical Physics*, 2000, **112**, 5546-5557.

[279] P. Celani and H.-J. Werner, *The Journal of Chemical Physics*, 2003, **119**, 5044-5057.

[280] P. J. Knowles and H.-J. Werner, *Chemical Physics Letters*, 1988, **145**, 514-522.

[281] H. J. Werner and P. J. Knowles, *The Journal of Chemical Physics*, 1988, **89**, 5803-5814.

[282] P. J. Knowles and H.-J. Werner, *Theoretica Chimica Acta*, 1992, **84**, 95-103.

[283] A. F. Lago, J. P. Kercher, A. Bödi, B. Sztáray, B. Miller, D. Wurzelmann and T. Baer, *The Journal of Physical Chemistry A*, 2005, **109**, 1802-1809.

[284] J. Muckerman, *The Journal of Physical Chemistry*, 1989, **93**, 179-184.

[285] V. Goncharov, N. Herath and A. G. Suits, *The Journal of Physical Chemistry A*, 2008, **112**, 9423-9428.

[286] W. G. Merrill, F. F. Crim and A. S. Case, *Physical Chemistry Chemical Physics*, 2016, **18**, 32999-33008.

[287] R. N. Dixon, *The Journal Of Chemical Physics*, 2005, **122**, 194302.

[288] C. Escure, T. Leininger and B. Lepetit, *The Journal of Chemical Physics*, 2009, **130**, 244305.

[289] S. Q. Man, W. M. Kwok, D. L. Phillips and A. E. Johnson, *The Journal of Chemical Physics*, 1996, **105**, 5842-5857.

[290] O. V. Rattigan, D. E. Shallcross and R. A. Cox, *Journal of the Chemical Society, Faraday Transactions*, 1997, **93**, 2839-2846.

[291] L. D. Landau, *Z. Sowjetunion*, 1932, **2**, 46-51.

[292] C. Zener, *Proceedings of the Royal Society of London. Series A, Containing Papers of a Mathematical and Physical Character*, 1932, **137**, 696-702.

[293] S. Uma and P. K. Das, *Canadian Journal of Chemistry*, 1994, **72**, 865-869.

[294] S. Uma and P. K. Das, *Chemical Physics Letters*, 1995, **241**, 335-338.

[295] Q. Liu and A. H. Zewail, *The Journal of Physical Chemistry*, 1993, **97**, 2209-2220.

[296] Y. Tang, W.-B. Lee, Z. Hu, B. Zhang and K.-C. Lin, *The Journal of Chemical Physics*, 2007, **126**, 064302.

[297] Y. Zhang, J. Wang, Q.-S. Zheng, Y.-Z. Liu, R.-R. Zhang, C.-J. Hu, B.-F. Tang and B. Zhang, *Acta Physico-Chimica Sinica*, 2009, **25**, 661-667.

[298] Y. Liu, Q. Zheng, Y. Zhang, R. Zhang, Y. Wang and B. Zhang, *ChemPhysChem*, 2009, **10**, 830-834.

[299] A. Baronavski and J. Owrutsky, *The Journal of Chemical Physics*, 1998, **108**, 3445-3452.

[300] M. E. Corrales, J. González Vázquez, G. Balerdi, I. R. Solá, R. de Nalda and L. Bañares, *Nature Chemistry*, 2014, **6**, 785-790.

[301] S. Marggi Poullain, M. G Gonzalez, P. Samartzis, T. Kitsopoulos, L. Rubio-Lago and L. Bañares, *Physical Chemistry Chemical Physics*, 2015, **17**, 29958-29968.

[302] M. E. Corrales, P. S. Shternin, L. Rubio-Lago, R. de Nalda, O. S. Vasyutinskii and L. Bañares, *The Journal of Physical Chemistry Letters*, 2016, **7**, 4458-4463.

[303] D. Donaldson, M. S. Child and V. Vaida, *The Journal of Chemical Physics*, 1988, **88**, 7410-7417.

[304] A. B. Alekseyev, H.-P. Liebermann and R. J. Buenker, *The Journal of Chemical Physics*, 2011, **134**, 044303.

[305] J. A. Syage, *Chemical Physics Letters*, 1993, **212**, 124-128.

[306] S. Felps, P. Hochmann, P. Brint and S. McGlynn, *Journal of Molecular Spectroscopy*, 1976, **59**, 355-379.

[307] D. Donaldson, V. Vaida and R. Naaman, *The Journal of Chemical Physics*, 1987, **87**, 2522-2530.

[308] M. Dobber, W. Buma and C. De Lange, *The Journal of Chemical Physics*, 1993, **99**, 836-853.

[309] A. Gedanken, M. Robin and Y. Yafet, *The Journal of Chemical Physics*, 1982, **76**, 4798-4808.

[310] P. Kondratyuk, *Spectrochimica Acta Part A: Molecular and Biomolecular Spectroscopy*, 2005, **61**, 589-593.

[311] J. Syage and J. Steadman, *The Journal of Physical Chemistry*, 1990, **94**, 7343-7346.

[312] J. C. Owrutsky and A. P. Baronavski, *Chemical Physics Letters*, 1994, **222**, 335-338.

[313] M. G. González, J. D. Rodríguez, L. Rubio-Lago and L. Bañares, *The Journal of Chemical Physics*, 2011, **135**, 021102.

[314] W. P. Hess, R. Naaman and S. R. Leone, *The Journal of Physical Chemistry*, 1987, **91**, 6085-6087.

[315] R. Continetti, B. Balko and Y. Lee, *The Journal of Chemical Physics*, 1988, **89**, 3383-3384.

[316] G. Van Veen, T. Baller and A. De Vries, *Chemical Physics*, 1985, **97**, 179-186.

[317] A. Gilchrist, G. Hancock, R. Peverall, G. Richmond, G. Ritchie and S. Taylor, *The Journal of Physical Chemistry A*, 2008, **112**, 4531-4536.

[318] R. Forbes, F. Allum, S. Bari, R. Boll, K. Borne, M. Brouard, P. H. Bucksbaum, N. Ekanayake, B. Erk and A. J. Howard, *Journal of Physics B: Atomic, Molecular and Optical Physics*, 2020, **53**, 224001.

[319] C. Paterson, F. Godwin and P. Gorry, *Molecular Physics*, 1987, **60**, 729-747.

[320] X.-P. Zhang, W.-B. Lee and K.-C. Lin, *The Journal of Physical Chemistry A*, 2009, **113**, 35-39.

[321] S. H. Gardiner, M. L. Lipciuc, T. N. Karsili, M. N. Ashfold and C. Vallance, *Physical Chemistry Chemical Physics*, 2015, **17**, 4096-4106.

[322] T. Donohue and J. R. Wiesenfeld, *The Journal of Chemical Physics*, 1975, **63**, 3130-3135.

[323] S. Marggi Poullain, P. Recio, D. V. Chicharro, L. Rubio-Lago, J. González-Vázquez and L. Bañares, *Physical Chemistry Chemical Physics*, 2019, **21**, 14250-14260.

[324] J. Durig, J. Thompson, V. Thyagesan and J. Witt, *Journal of Molecular Structure*, 1975, **24**, 41-58.

[325] N. Knoblauch, A. Strobel, I. Fischer and V. E. Bondybey, *The Journal of Chemical Physics*, 1995, **103**, 5417-5427.

[326] B. H. L. III, P. E. M. Siegbahn and B. Liu, *The Journal of Chemical Physics*, 1984, **81**, 710-716.

[327] H. R. Wendt and H. E. Hunziker, *The Journal of Chemical Physics*, 1984, **81**, 717-723.

[328] C. Marante, L. Argenti and F. Martín, *Physical Review A*, 2014, **90**, 012506.

[329] H.-J. Werner, *Molecular Physics*, 1996, **89**, 645-661.

[330] A. Berning, M. Schweizer, H.-J. Werner, P. J. Knowles and P. Palmieri, *Molecular Physics*, 2000, **98**, 1823-1833.

[331] R. Locht, D. Dehareng, K. Hottmann, H. Jochims, H. Baumgärtel and B. Leyh, *Journal of Physics B: Atomic, Molecular and Optical Physics*, 2010, **43**, 105101.

[332] M. Dzvonik, S. Yang and R. Bersohn, *The Journal of Chemical Physics*, 1974, **61**, 4408-4421.

[333] Q. Zhu, J. Cao, Y. Wen, J. Zhang, X. Zhong, Y. Huang, W. Fang and X. Wu, *Chemical Physics Letters*, 1988, **144**, 486-492.

[334] D. W. Chandler, M. H. Janssen, S. Stolte, R. N. Strickland, J. W. Thoman and D. H. Parker, *The Journal of Physical Chemistry*, 1990, **94**, 4839-4846.

[335] P. Felder, *Chemical Physics*, 1991, **155**, 435-445.

[336] P. Felder, *Chemical Physics Letters*, 1992, **197**, 425-432.

[337] W. K. Kang, K. W. Jung, D. C. Kim and K.-H. Jung, *Chemical Physics*, 1995, **196**, 363-370.

[338] F. Aguirre and S. T. Pratt, *The Journal of Chemical Physics*, 2003, **118**, 1175-1183.

[339] M. Shapiro and R. Bersohn, *The Journal of Chemical Physics*, 1980, **73**, 3810-3817.

[340] M. O. Hale, G. E. Galica, S. G. Glogover and J. L. Kinsey, *The Journal of Physical Chemistry*, 1986, **90**, 4997-5000.

[341] D. L. Phillips, B. A. Lawrence and J. J. Valentini, *The Journal of Physical Chemistry*, 1991, **95**, 9085-9091.

[342] P. Brewer, P. Das, G. S. Ondrey and R. Bersohn, *The Journal of Chemical Physics*, 1983, **79**, 720-723.

[343] H. Fan and S. Pratt, *The Journal of Chemical Physics*, 2005, **123**, 204301.

[344] G. E. Busch and K. R. Wilson, *The Journal of Chemical Physics*, 1972, **56**, 3626-3638.

[345] S. Uma and P. K. Das, *The Journal of chemical physics*, 1996, **104**, 4470-4474.

[346] K. Q. Lao, M. D. Person, P. Xayariboun and L. J. Butler, *The Journal of Chemical Physics*, 1990, **92**, 823-841.

[347] M. L. Murillo-Sánchez, S. Marggi Poullain, V. Loriot, M. E. Corrales and L. Bañares, *Physical Chemistry Chemical Physics*, 2019, **21**, 15695-15704.

[348] R. Boschi and D. Salahub, *Molecular Physics*, 1972, **24**, 735-752.

[349] N. de Oliveira, *Private communication*.

[350] N. de Oliveira, M. Roudjane, D. Joyeux, D. Phalippou, J.-C. Rodier and L. Nahon, *Nature Photonics*, 2011, **5**, 149-153.

[351] L. Nahon, N. de Oliveira, G. Garcia, J. Gil, D. Joyeux, B. Lagarde and F. Polack, *Journal of Physics: Conference Series*, 2013, **425**, 122004.

[352] N. de Oliveira, D. Joyeux, M. Roudjane, J.-F. Gil, B. Pilette, L. Archer, K. Ito and L. Nahon, *Journal Of Synchrotron Radiation*, 2016, **23**, 887-900.

[353] N. de Oliveira, D. Joyeux, D. Phalippou, J.-C. Rodier, F. Polack, M. Vervloet and L. Nahon, *Review of Scientific Instruments*, 2009, **80**, 043101.

[354] R. Boschi and D. Salahub, *Molecular Physics*, 1972, **24**, 289-299.

[355] P. Limão-Vieira, *Private communication*.

[356] C. E. Moore, *Atomic Energy Levels*, U.S. Government Printing Office, 1949.

[357] Y. J. Jung, Y. S. Kim, W. K. Kang and K. H. Jung, *The Journal of Chemical Physics*, 1997, **107**, 7187-7193.

[358] H. M. Pickett, *Journal of Molecular Spectroscopy*, 1991, **148**, 371-377.

[359] A. B. Callear and R. J. Cvetanović, *The Journal of Chemical Physics*, 1956, **24**, 873-878.

[360] P. Ausloos and R. G. Jr., *The Journal of Chemical Physics*, 1962, **36**, 5-9.

[361] H. Okabe and J. R. McNesby, *The Journal of Chemical Physics*, 1962, **36**, 601-604.

[362] R. Back and D. Griffiths, *The Journal of Chemical Physics*, 1967, **46**, 4839-4843.

[363] H. Hara and I. Tanaka, *Bulletin of the Chemical Society of Japan*, 1973, **46**, 3012-3015.

[364] H. Hiroshi and T. Ikuzo, *Bulletin of the Chemical Society of Japan*, 1974, **47**, 1543-1544.

[365] A. H. Laufer, *Journal of Photochemistry*, 1984, **27**, 267-271.

[366] A. Fahr and A. H. Laufer, *Journal of Photochemistry*, 1986, **34**, 261-266.

[367] G. J. Collin, in *Advances in Photochemistry*, eds. D. H. Volman, G. S. Hammond and K. Gollnick, John Wiley & Sons, 1988.

[368] S. Satyapal, G. W. Johnston, R. Bersohn and I. Oref, *The Journal of Chemical Physics*, 1990, **93**, 6398-6402.

[369] B. Balko, J. Zhang and Y. T. Lee, *The Journal of Chemical Physics*, 1992, **97**, 935-942.

[370] A. Stolow, B. A. Balko, E. F. Cromwell, J. Zhang and Y. T. Lee, *Journal of Photochemistry and Photobiology A: Chemistry*, 1992, **62**, 285-300.

[371] M. C. Sauer Jr and L. M. Dorfman, *The Journal of Chemical Physics*, 1961, **35**, 497-502.

[372] E. F. Cromwell, A. Stolow, M. J. Vrakking and Y. T. Lee, *The Journal of Chemical Physics*, 1992, **97**, 4029-4040.

[373] J. J. Lin, D. W. Hwang, Y. T. Lee and X. Yang, *The Journal of Chemical Physics*, 1998, **109**, 2979-2982.

[374] K. M. Ervin, S. Gronert, S. E. Barlow, M. K. Gilles, A. G. Harrison, V. M. Bierbaum, C. H. DePuy, W. C. Lineberger and G. B. Ellison, *Journal of the American Chemical Society*, 1990, **112**, 5750-5759.

[375] R. J. Buenker, V. Bonačić‐Koutecký and L. Pogliani, *The Journal of Chemical Physics*, 1980, **73**, 1836-1849.

[376] I. Ohmine, *The Journal of Chemical Physics*, 1985, **83**, 2348-2362.

[377] P. Zou, K. E. Strecker, J. Ramirez-Serrano, L. E. Jusinski, C. A. Taatjes and D. L. Osborn, *Physical Chemistry Chemical Physics*, 2008, **10**, 713-728.

[378] K. Tonokura, L. B. Daniels, T. Suzuki and K. Yamashita, *The Journal of Physical Chemistry A*, 1997, **101**, 7754-7764.

[379] M. S. Park, K. W. Lee and K.-H. Jung, *The Journal of Chemical Physics*, 2001, **114**, 10368-10374.

[380] S. Yamashita, S. Noguchi and T. Hayakawa, *Bulletin of the Chemical Society of Japan*, 1972, **45**, 659-664.

[381] S. Yamashita, *Chemistry Letters*, 1975, **4**, 967-970.

[382] K. M. Ervin, J. Ho and W. C. Lineberger, *The Journal of Chemical Physics*, 1989, **91**, 5974-5992.

[383] J. Cao, J. Zhang, X. Zhong, Y. Huang, W. Fang, X. Wu and Q. Zhu, *Chemical Physics*, 1989, **138**, 377-382.

[384] G. Bélanger and C. Sandorfy, *The Journal of Chemical Physics*, 1971, **55**, 2055-2060.

[385] S. Sood and K. Watanabe, *The Journal of Chemical Physics*, 1966, **45**, 2913-2915.

[386] J. Schander and B. Russell, *Journal of the American Chemical Society*, 1976, **98**, 6900-6904.

[387] V. L. Orkin, F. Louis, R. E. Huie and M. J. Kurylo, *The Journal of Physical Chemistry A*, 2002, **106**, 10195-10199.

[388] K. Sze, C. Brion, A. Katrib and B. El-Issa, *Chemical Physics*, 1989, **137**, 369-390.

[389] M. J. Berry, *The Journal of Chemical Physics*, 1974, **61**, 3114-3143.

[390] P. T. Reilly, Y. Xie and R. J. Gordon, *Chemical Physics Letters*, 1991, **178**, 511-516.

[391] D. A. Blank, W. Sun, A. G. Suits, Y. T. Lee, S. W. North and G. E. Hall, *The Journal of Chemical Physics*, 1998, **108**, 5414-5425.

[392] S.-R. Lin, S.-C. Lin, Y.-C. Lee, Y.-C. Chou, I.-C. Chen and Y.-P. Lee, *The Journal of Chemical Physics*, 2001, **114**, 160-168.

[393] K. Saito, T. Yokubo, T. Fuse, H. Tahara, O. Kondo, T. Higashihara and I. Murakami, *Bulletin of the Chemical Society of Japan*, 1979, **52**, 3507-3510.

[394] A. M. Wodtke, E. J. Hintsa, J. Somorjai and Y. T. Lee, *Israel Journal of Chemistry*, 1989, **29**, 383-391.

[395] K. Sato, S. Tsunashima, T. Takayanagi, G. Fijisawa and A. Yokoyama, *Chemical Physics Letters*, 1995, **242**, 401-406.

[396] S.-R. Lin, S.-C. Lin, Y.-C. Lee, Y.-C. Chou, I.-C. Chen and Y.-P. Lee, *The Journal of Chemical Physics*, 2001, **114**, 7396-7406.

[397] J. Tu, J. J. Lin, Y. T. Lee and X. Yang, *The Journal of Chemical Physics*, 2002, **116**, 6982-6989.

[398] S. Tsunashima, H. E. Gunning and O. P. Strausz, *Journal of the American Chemical Society*, 1976, **98**, 1690-1696.

[399] C. Quick Jr and C. Wittig, *Chemical Physics*, 1978, **32**, 75-80.

[400] A. S. Sudbo/, P. Schulz, Y. Shen and Y. Lee, *The Journal of Chemical Physics*, 1978, **69**, 2312-2322.

[401] C. Quick Jr and C. Wittig, *The Journal of Chemical Physics*, 1980, **72**, 1694-1700.

[402] H. Watanabe, H. Horiguchi and S. Tsuchiya, *Bulletin of the Chemical Society of Japan*, 1980, **53**, 1530-1536.

[403] C. Reiser, F. M. Lussier, C. C. Jensen and J. I. Steinfeld, *Journal of the American Chemical Society*, 1979, **101**, 350-357.

[404] H. Katayanagi, N. Yonekuira and T. Suzuki, *Chemical physics*, 1998, **231**, 345-353.

[405] S. Kato and K. Morokuma, *The Journal of Chemical Physics*, 1981, **74**, 6285-6297.

[406] S. A. Wright and J. D. McDonald, *The Journal of Chemical Physics*, 1994, **101**, 238-245.

[407] Y. Huang, Y. A. Yang, G. He, S. Hashimoto and R. J. Gordon, *The Journal of Chemical Physics*, 1995, **103**, 5476-5487.

[408] L. Letendre, D.-K. Liu, C. D. Pibel, J. B. Halpern and H.-L. Dai, *The Journal of Chemical Physics*, 2000, **112**, 9209-9212.

[409] P.-O. Widmark, P.-Å. Malmqvist and B. O. Roos, *Theoretica Chimica Acta*, 1990, **77**, 291-306.

[410] W. Győrffy, T. Shiozaki, G. Knizia and H.-J. Werner, *The Journal of Chemical Physics*, 2013, **138**, 104104.

[411] T. Shiozaki, W. Gyorffy, P. Celani and H. J. Werner, *The Journal of Chemical Physics*, 2011, **135**, 081106.

[412] T. Shiozaki, *WIREs Computational Molecular Science*, 2018, **8**, e1331.

[413] B. Vlaisavljevich and T. Shiozaki, *Journal of Chemical Theory and Computation*, 2016, **12**, 3781-3787.

[414] J. W. Park and T. Shiozaki, *Journal of Chemical Theory and Computation*, 2017, **13**, 3676-3683.

[415] J. W. Park and T. Shiozaki, *Journal of Chemical Theory and Computation*, 2017, **13**, 2561-2570.

[416] I. Fdez. Galván, M. Vacher, A. Alavi, C. Angeli, F. Aquilante, J. Autschbach, J. J. Bao, S. I. Bokarev, N. A. Bogdanov, R. K. Carlson, L. F. Chibotaru, J. Creutzberg, N. Dattani, M. G. Delcey, S. S. Dong, A. Dreuw, L. Freitag, L. M. Frutos, L. Gagliardi, F. Gendron, A. Giussani, L. González, G. Grell, M. Guo, C. E. Hoyer, M. Johansson, S. Keller, S. Knecht, G. Kovačević, E. Källman, G. Li Manni, M. Lundberg, Y. Ma, S. Mai, J. P. Malhado, P. Å. Malmqvist, P. Marquetand, S. A. Mewes, J. Norell, M. Olivucci, M. Oppel, Q. M. Phung, K. Pierloot, F. Plasser, M. Reiher, A. M. Sand, I. Schapiro, P. Sharma, C. J. Stein, L. K. Sørensen, D. G. Truhlar, M. Ugandi, L. Ungur, A. Valentini, S. Vancoillie, V. Veryazov, O. Weser, T. A. Wesołowski, P.-O.

Widmark, S. Wouters, A. Zech, J. P. Zobel and R. Lindh, *Journal of Chemical Theory and Computation*, 2019, **15**, 5925-5964.

[417] N. Kishimoto, K. Ohshimo and K. Ohno, *Journal of Electron Spectroscopy and Related Phenomena*, 1999, **104**, 145-154.

[418] G. Mines and H. Thompson, *Spectrochimica Acta Part A: Molecular Spectroscopy*, 1973, **29**, 1377-1383.

[419] N. S. Shuman, M. A. Ochieng, B. Sztáray and T. Baer, *The Journal of Physical Chemistry A*, 2008, **112**, 5647-5652.

[420] P. Torkington and H. W. Thompson, *Journal of the Chemical Society*, 1944, 303-305.

[421] H. Abdoul-Carime, M. A. Huels, F. Brüning, E. Illenberger and L. Sanche, *The Journal of Chemical Physics*, 2000, **113**, 2517-2521.

[422] F. Kossoski and M. T. d. N. Varella, *Physical Chemistry Chemical Physics*, 2015, **17**, 17271-17278.

[423] A. Modelli and M. Venuti, *The Journal of Physical Chemistry A*, 2001, **105**, 5836-5841.

[424] T. Sommerfeld, *ChemPhysChem*, 2001, **2**, 677-679.

[425] R. Kaufel, E. Illenberger and H. Baumgärtel, *Chemical Physics Letters*, 1984, **106**, 342-346.

[426] F. Kossoski and M. Barbatti, *Chemical Science*, 2020, **11**, 9827-9835.

[427] J. K. Olthoff, J. H. Moore and J. A. Tossell, *The Journal of Chemical Physics*, 1986, **85**, 249-254.

[428] R. Yoshimura and T. Tada, *Chemical Physics Letters*, 1994, **222**, 626-632.

[429] T. Skalický, C. Chollet, N. Pasquier and M. Allan, *Physical Chemistry Chemical Physics*, 2002, **4**, 3583-3590.

[430] J. A. Stockdale and G. S. Hurst, *The Journal of Chemical Physics*, 1964, **41**, 255-261.

[431] K. L. Stricklett, S. C. Chu and P. D. Burrow, *Chemical Physics Letters*, 1986, **131**, 279-284.

[432] P. D. Burrow, A. Modelli, N. S. Chiu and K. D. Jordan, *Chemical Physics Letters*, 1981, **82**, 270-276.

[433] D. Zhong, P. Y. Cheng and A. H. Zewail, *The Journal of Chemical Physics*, 1996, **105**, 7864-7867.

[434] A. T. J. B. Eppink and D. H. Parker, *The Journal of Chemical Physics*, 1998, **109**, 4758-4767.

[435] D. Zhong and A. H. Zewail, *The Journal of Physical Chemistry A*, 1998, **102**, 4031-4058.

[436] J. Durá, R. de Nalda, J. Álvarez, J. G. Izquierdo, G. A. Amaral and L. Bañares, *ChemPhysChem*, 2008, **9**, 1245-1249.

[437] M. Burt, R. Boll, J. W. L. Lee, K. Amini, H. Köckert, C. Vallance, A. S. Gentleman, S. R. Mackenzie, S. Bari, C. Bomme, S. Düsterer, B. Erk, B. Manschwetus, E. Müller, D. Rompotis, E. Savelyev, N. Schirmel, S. Techert, R. Treusch, J. Küpper, S. Trippel, J. Wiese, H. Stapelfeldt, B. C. de Miranda, R. Guillemin, I. Ismail, L. Journel, T. Marchenko, J. Palaudoux, F. Penent, M.

N. Piancastelli, M. Simon, O. Travnikova, F. Brausse, G. Goldsztejn, A. Rouzée, M. Géléoc, R. Geneaux, T. Ruchon, J. Underwood, D. M. P. Holland, A. S. Mereshchenko, P. K. Olshin, P. Johnsson, S. Maclot, J. Lahl, A. Rudenko, F. Ziaee, M. Brouard and D. Rolles, *Physical Review A*, 2017, **96**, 043415.

[438] J. F. Black and I. Powis, *Chemical Physics Letters*, 1988, **148**, 479-485.

[439] R. A. Hertz and J. A. Syage, *The Journal of Chemical Physics*, 1994, **100**, 9265-9268.

[440] K. Motomura, E. Kukk, H. Fukuzawa, S.-i. Wada, K. Nagaya, S. Ohmura, S. Mondal, T. Tachibana, Y. Ito, R. Koga, T. Sakai, K. Matsunami, A. Rudenko, C. Nicolas, X.-J. Liu, C. Miron, Y. Zhang, Y. Jiang, J. Chen, M. Anand, D. E. Kim, K. Tono, M. Yabashi, M. Yao and K. Ueda, *The Journal of Physical Chemistry Letters*, 2015, **6**, 2944-2949.

[441] A. Rudenko, L. Inhester, K. Hanasaki, X. Li, S. J. Robatjazi, B. Erk, R. Boll, K. Toyota, Y. Hao, O. Vendrell, C. Bomme, E. Savelyev, B. Rudek, L. Foucar, S. H. Southworth, C. S. Lehmann, B. Kraessig, T. Marchenko, M. Simon, K. Ueda, K. R. Ferguson, M. Bucher, T. Gorkhover, S. Carron, R. Alonso-Mori, J. E. Koglin, J. Correa, G. J. Williams, S. Boutet, L. Young, C. Bostedt, S. K. Son, R. Santra and D. Rolles, *Nature*, 2017, **546**, 129-132.

[442] S. Marggi Poullain, D. V. Chicharro, J. González-Vázquez, L. Rubio-Lago and L. Bañares, *Physical Chemistry Chemical Physics*, 2017, **19**, 7886-7896.

[443] M. Gruetter, J. Michaud and F. Merkt, *The Journal of Chemical Physics*, 2011, **134**, 054308.

[444] L. Karlsson, R. Jadrny, L. Mattsson, F. T. Chau and K. Siegbahn, *Physica Scripta*, 1977, **16**, 225.

[445] D. Holland, I. Powis, G. Öhrwall, L. Karlsson and W. von Niessen, *Chemical Physics*, 2006, **326**, 535-550.

[446] S. Goss, J. Morrison and D. Smith, *The Journal of Chemical Physics*, 1981, **75**, 757-762.

[447] W. A. Chupka, S. D. Colson, M. S. Seaver and A. M. Woodward, *Chemical Physics Letters*, 1983, **95**, 171-176.

[448] A. M. Woodward, S. D. Colson, W. A. Chupka and M. G. White, *The Journal of Physical Chemistry*, 1986, **90**, 274-278.

[449] D.-C. McGilvery and J. Morrison, *The Journal of Chemical Physics*, 1977, **67**, 368-369.

[450] D. M. Mintz and T. Baer, *The Journal of Chemical Physics*, 1976, **65**, 2407-2415.

[451] J. Morrison, H. Hurzeler, M. G. Inghram and H. Stanton, *The Journal of Chemical Physics*, 1960, **33**, 821-824.

[452] A. Nicholson, *The Journal of Chemical Physics*, 1965, **43**, 1171-1177.

[453] B. P. Tsai and T. Baer, *The Journal of Chemical Physics*, 1974, **61**, 2047-2049.

[454] A. Potts, H. Lempka, D. Streets and W. C. Price, *Philosophical Transactions of the Royal Society of London. Series A, Mathematical and Physical Sciences*, 1970, **268**, 59-76.

[455] J. Ragle, I. Stenhouse, D. Frost and C. McDowell, *The Journal of Chemical Physics*, 1970, **53**, 178-184.

[456] R. A. A. Boschi and D. R. Salahub, *Canadian Journal of Chemistry*, 1974, **52**, 1217-1228.

[457] R. Locht, B. Leyh, H. Jochims and H. Baumgärtel, *Chemical Physics*, 2009, **365**, 109-128.

[458] M. Tadjeddine, G. Bouchoux, L. Malegat, J. Durup, C. Pernot and J. Weiner, *Chemical Physics*, 1982, **69**, 229-246.

[459] M. Kawasaki, H. Sato, T. Kikuchi, S. Kobayashi and T. Arikawa, *The Journal of Chemical Physics*, 1987, **87**, 5739-5745.

[460] J. Eland, R. Frey, A. Kuestler, H. Schulte and B. Brehm, *International Journal of Mass Spectrometry and Ion Physics*, 1976, **22**, 155-170.

[461] I. Powis, *Chemical Physics*, 1983, **74**, 421-432.

[462] F. Aguirre and S. Pratt, *The Journal of Chemical Physics*, 2003, **118**, 6318-6326.

[463] F. Aguirre and S. Pratt, *The Journal of Chemical Physics*, 2003, **119**, 9476-9485.

[464] V. Blanchet, P. C. Samartzis and A. M. Wodtke, *The Journal of Chemical Physics*, 2009, **130**, 034304.

[465] F. Wang, M. L. Lipciuc, X. Yang and T. N. Kitsopoulos, *Physical Chemistry Chemical Physics*, 2009, **11**, 2234-2240.

[466] S. Tsuda, C. Melton and W. Hamill, *The Journal of Chemical Physics*, 1964, **41**, 689-695.

[467] S. Tsuda, C. E. Melton and W. H. Hamill, *The Journal of Chemical Physics*, 1964, **41**, 689-695.

[468] C. Kosmidis, P. Siozos, S. Kaziannis, L. Robson, K. W. D. Ledingham, P. McKenna and D. A. Jaroszynski, *The Journal of Physical Chemistry A*, 2005, **109**, 1279-1285.

[469] P. Graham, K. W. D. Ledingham, R. P. Singhai, S. M. Hankin, T. McCanny, X. Fang, C. Kosmidis, P. Tzallas, P. F. Taday and A. J. Langley, *Journal of Physics B: Atomic, Molecular and Optical Physics*, 2001, **34**, 4015-4026.

[470] H. Liu, Z. Yang, Z. Gao and Z. Tang, *The Journal of chemical physics*, 2007, **126**, 044316.

[471] Y. Wang, S. Zhang, Z. Wei and B. Zhang, *The Journal of Physical Chemistry A*, 2008, **112**, 3846-3851.

[472] M. E. Corrales, G. Gitzinger, J. González-Vázquez, V. Loriot, R. de Nalda and L. Bañares, *The Journal of Physical Chemistry A*, 2012, **116**, 2669-2677.

[473] S. K. Lee, F. Cudry, Y. F. Lin, S. Lingenfelter, A. H. Winney, L. Fan and W. Li, *Review of Scientific Instruments*, 2014, **85**, 123303.

[474] A. H. Winney, G. Basnayake, D. A. Debrah, Y. F. Lin, S. K. Lee, P. Hoerner, Q. Liao, H. B. Schlegel and W. Li, *The Journal of Physical Chemistry Letters*, 2018, **9**, 2539-2545.

[475] S. G. Walt, N. Bhargava Ram, A. von Conta, O. I. Tolstikhin, L. B. Madsen, F. Jensen and H. J. Wörner, *The Journal of Physical Chemistry A*, 2015, **119**, 11772-11782.

[476] M. E. Corrales, R. de Nalda and L. Bañares, *Nature Communications*, 2017, **8**, 1345.

[477] S. Luo, S. Zhou, W. Hu, X. Li, P. Ma, J. Yu, R. Zhu, C. Wang, F. Liu and B. Yan, *Physical Review A*, 2017, **96**, 063415.

[478] S. Luo, W. Hu, J. Yu, X. Li, L. He, C. Wang, F. Liu and D. Ding, *The Journal of Physical Chemistry A*, 2017, **121**, 6547-6553.

[479] Z. Wei, J. Li, S. T. See and Z.-H. Loh, *The Journal of Physical Chemistry Letters*, 2017, **8**, 6067-6072.

[480] Z. Wei, J. Li, L. Wang, S. T. See, M. H. Jhon, Y. Zhang, F. Shi, M. Yang and Z.-H. Loh, *Nature Communications*, 2017, **8**, 735.

[481] S. T. Park, S. K. Kim and M. S. Kim, *The Journal of Chemical Physics*, 2001, **115**, 2492-2498.

[482] S. T. Park, S. K. Kim and M. S. Kim, *The Journal of Chemical Physics*, 2001, **114**, 5568-5576.

[483] Y. Malakar, W. Pearson, M. Zohrabi, B. Kaderiya, F. Ziaee, S. Xue, A. Le, I. Ben-Itzhak, D. Rolles and A. Rudenko, *Physical Chemistry Chemical Physics*, 2019, **21**, 14090-14102.

[484] D. Zhang, S. Luo, H. Xu, M. Jin, F. Liu, B. Yan, Z. Wang, H. Liu, D. Jiang and A. Eppink, *The European Physical Journal D*, 2017, **71**, 1-13.

[485] C. Calvert, W. Bryan, W. Newell and I. Williams, *Physics Reports*, 2010, **491**, 1-28.

[486] A. Fischer, M. Gärttner, P. Cörlin, A. Sperl, M. Schönwald, T. Mizuno, G. Sansone, A. Senftleben, J. Ullrich, B. Feuerstein, T. Pfeifer and R. Moshammer, *Physical Review A*, 2016, **93**, 012507.

[487] F. Kelkensberg, C. Lefebvre, W. Siu, O. Ghafur, T. Nguyen-Dang, O. Atabek, A. Keller, V. Serov, P. Johnsson and M. Swoboda, *Physical Review Letters*, 2009, **103**, 123005.

[488] M. Magrakvelidze, O. Herrwerth, Y. Jiang, A. Rudenko, M. Kurka, L. Foucar, K. Kühnel, M. Kübel, N. G. Johnson and C. Schröter, *Physical Review A*, 2012, **86**, 013415.

[489] P. Coerlin, A. Fischer, M. Schoenwald, A. Sperl, T. Mizuno, T. Pfeifer, R. Moshammer and U. Thumm, *Bulletin of the American Physical Society*, 2015, **60**.

[490] P. Cörlin, A. Fischer, M. Schönwald, A. Sperl, T. Mizuno, U. Thumm, T. Pfeifer and R. Moshammer, *Physical Review A*, 2015, **91**, 043415.

[491] M. Eckstein, C.-H. Yang, F. Frassetto, L. Poletto, G. Sansone, M. J. J. Vrakking and O. Kornilov, *Physical Review Letters*, 2016, **116**, 163003.

[492] A. I. Chichinin, K. H. Gericke, S. Kauczok and C. Maul, *International Reviews in Physical Chemistry*, 2009, **28**, 607-680.

[493] M. Stei, J. von Vangerow, R. Otto, A. H. Kelkar, E. Carrascosa, T. Best and R. Wester, *The Journal of Chemical Physics*, 2013, **138**, 214201.

[494] P. Johnsson, A. Rouzée, W. Siu, Y. Huismans, F. Lépine, T. Marchenko, S. Düsterer, F. Tavella, N. Stojanovic, H. Redlin, A. Azima and M. J. J. Vrakking, *Optics Letters*, 2010, **35**, 4163-4165.

[495] L. Rading, J. Lahl, S. Maclot, F. Campi, H. Coudert-Alteirac, B. Oostenrijk, J. Peschel, H. Wikmark, P. Rudawski and M. Gisselbrecht, *Applied Sciences*, 2018, **8**, 998.

[496] W. C. Wiley and I. H. McLaren, *Review of Scientific Instruments*, 1955, **26**, 1150-1157.

[497] R. E. Smalley, L. Wharton and D. H. Levy, *Accounts of Chemical Research*, 1977, **10**, 139-145.

[498] E. Mejia-Ospino, I. Alvarez and C. Cisneros, *Revista Mexicana De Física*, 2004, **50**, 170-178.

[499] D. Williams, *Molecular Physics: Methods of Experimental Physics*, Elsevier Science, 2013.

[500] A. Maquet and R. TaÏeb, *Journal of Modern Optics*, 2007, **54**, 1847-1857.

[501] F. Neese, *WIREs Computational Molecular Science*, 2012, **2**, 73-78.

[502] J. González-Vázquez, *Generator of initial conditions*, 2019.

[503] J. Petersen and R. Mitrić, *Physical Chemistry Chemical Physics*, 2012, **14**, 8299-8306.

[504] M. D. Feit, J. A. Fleck and A. Steiger, *Journal of Computational Physics*, 1982, **47**, 412-433.

[505] M. D. Feit and J. A. F. Jr., *The Journal of Chemical Physics*, 1983, **78**, 301-308.

[506] M. D. Feit and J. A. F. Jr., *The Journal of Chemical Physics*, 1984, **80**, 2578-2584.

[507] A. Rudenko, K. Zrost, C. D. Schröter, V. L. B. d. Jesus, B. Feuerstein, R. Moshammer and J. Ullrich, *Journal of Physics B: Atomic, Molecular and Optical Physics*, 2004, **37**, L407-L413.

[508] T. Ergler, A. Rudenko, B. Feuerstein, K. Zrost, C. Schröter, R. Moshammer and J. Ullrich, *Physical Review Letters*, 2006, **97**, 193001.

[509] B. Jochim, R. Erdwien, Y. Malakar, T. Severt, B. Berry, P. Feizollah, J. Rajput, B. Kaderiya, W. L. Pearson, K. D. Carnes, A. Rudenko and I. Ben-Itzhak, *New Journal of Physics*, 2017, **19**, 103006.

[510] C. Maharjan, *Momentum imaging studies of electron and ion dynamics in a strong laser field*, Ph. D. Thesis, Kansas State University, 2007.

Publications related to the doctoral thesis

PAPERS

[1] *Femtosecond XUV-IR induced photodynamics in the methyl iodide cation*
M. L. Murillo-Sánchez, G. Reitsma, S. Marggi-Poullain, P. Fernández-Milán, J. González-Vázquez, R. de Nalda, F. Martín, M. J. J. Vrakking, O. Kornilov and L. Bañares, *New Journal of Physics*, (In preparation).

[2] *Time-resolved photodissociation dynamics of vinyl iodide at 199.2 and 200 nm*
M. L. Murillo-Sánchez, S. Marggi-Poullain, A. Zanchet, J. González-Vázquez and L. Bañares, *Physical Chemistry Chemical Physics*, (In preparation).

[3] *Structural dynamics effects on the electronic predissociation of alkyl iodides*
M. L. Murillo-Sánchez, A. Zanchet, S. Marggi-Poullain, J. González-Vázquez and L. Bañares. *Scientific Reports*, 2020, **10**, (1), 6700.

[4] *Femtochemistry under scrutiny: Clocking state-resolved channels in the photodissociation of CH_3I in the A-band*
M. L. Murillo-Sánchez, J. González-Vázquez, M. E. Corrales, R. de Nalda, E. Martínez-Núñez, A. García-Vela and L. Bañares, *The Journal of Chemical Physics*, 2020, **152**, (1), 014304.

[5] *Femtosecond predissociation dynamics of ethyl iodide in the B-band*
M. L. Murillo-Sánchez, S. Marggi-Poullain, V. Loriot, M. E. Corrales and L. Bañares, *Physical Chemistry Chemical Physics*, 2019, **21**, (28), 15695-15704.

[6] *Halogen-atom effect on the ultrafast photodissociation dynamics of the dihalomethanes CH_2ICl and CH_2BrI*
M. L. Murillo-Sánchez, S. Marggi-Poullain, J. J. Bajo, M. E. Corrales, J. González-Vázquez, I. R. Solá and L. Bañares, *Physical Chemistry Chemical Physics*, 2018, **20**, (32), 20766-20778 (Inside front cover).

[7] *Femtosecond photodissociation dynamics of chloroiodomethane in the first absorption band*
M. L. Murillo-Sánchez, S. Marggi-Poullain, J. González-Vázquez, M. E. Corrales, G. Balerdi and L. Bañares. Chemical Physics Letters, 2017, **683**, 22-28 (Ahmed Zewail Commemoration Issue).

PROCEEDINGS

[8] *Femtosecond XUV induced dynamics of the methyl iodide cation*
G. Reitsma, M. L. Murillo-Sánchez, R. de Nalda, M. E. Corrales, S. Marggi-Poullain, J. González-Vázquez, M. J. J. Vrakking, L. Bañares and O. Kornilov, *EPJ Web of Conferences*, 2019, **205**, 02020.

[9] *Femtochemistry at its finest: Structure, energy flow and dynamics in photodissociating molecules*
L. Bañares, M. L. Murillo-Sánchez, S. Marggi-Poullain, M. E. Corrales and J. González-Vázquez, *Abstracts of Papers of the American Chemical Society*, 2018, **256.**

[10] *Femtosecond dynamics in the iodomethane cation investigated by XUV-IR pump-probe ion imaging*
L. Bañares, G. Reitsma, M. L. Murillo-Sánchez, R. de Nalda, M. E. Corrales, S. M. Marggi-Poullain, J. Gonzalez-Vázquez, M. J. J. Vrakking and O. Kornilov, *Abstracts of Papers of the American Chemical Society*, 2018, **256**, 1.

Contributions to congresses related to the doctoral thesis

ORAL PRESENTATIONS

Structural dynamics effects on the UV electronic predissociation of alkyl iodides at 201 nm
M. L. Murillo-Sánchez; A. Zanchet, S. Marggi-Poullain; L. Bañares.
Ultrafast Science & Technology Spain 2019 (USTS 2019).
Madrid, Spain. 6-8 November 2019.

Monochromized HHG pump NIR probe experiments of Methyl Iodide
M.L. Murillo-Sánchez, G. Reitsma, R. de Nalda, M.E. Corrales, S. Marggi-Poullain, J. Gonzalez-Vázquez, L. Bañares, M.J.J. Vrakking, and O. Kornilov
Seminar at Max Born Institute for Nonlinear Optics and Short Pulse Spectroscopy.
Berlin, Germany. 30 October 2019.

Dinámica de disociación del yoduro de vinilo a 199.2 y 200 nm
M. L. Murillo-Sánchez, I. Mondéjar, J. González-Vázquez, L. Bañares
IV Simposio Anual en Química Avanzada de la Facultad de Ciencias Químicas de la Universidad Complutense de Madrid.
Madrid, Spain. 16 July 2017.

Structural dynamics effects on the UV electronic predissociation of alkyl iodides at 201 nm
M. L. Murillo-Sánchez; S. Marggi-Poullain; L. Bañares.
Iberian Meeting on Atomic and Molecular Physics (IBER 2019).
Évora, Portugal. 10-12 July 2019.

Dinámica de predisociación en tiempo real del yoduro de etilo en la banda B
M. L. Murillo-Sánchez, S. Marggi-Poullain, V. Loriot, M. E. Corrales, L. Bañares.
VI Simposio de Jóvenes Investigadores. Instituto Química Física Rocasolano-Consejo Superior de Investigaciones Científicas.
Madrid, Spain. 10 June 2019.

Femtosecond predissociation dynamics of ethyl iodide in the B band

M. L. Murillo-Sánchez; M. E. Corrales; L. Bañares.

XI Jornadas de Jóvenes Investigadores en Física Atómica y Molecular (J2IFAM 2019).

Cadiz, Spain. 26-29 March 2019.

Awarded with the best communication presented prize.

Femtosecond XUV-IR dynamics of the methyl iodide cation

L. Bañares, G. Reitsma, M.L. Murillo-Sánchez, R. de Nalda, M.E. Corrales, S. Marggi-Poullain, J. González-Vázquez, M.J.J. Vrakking, and O. Kornilov.

Chemical Applications of Ultrafast X-ray/XUV Spectroscopy & Scattering. 256th American Chemical Society.

Boston, Massachusetts. USA, 19-23 August 2018.

Femtochemistry at its finest: Structure, energy flow and dynamics in photodissociating molecules

L. Bañares, M. L. Murillo-Sánchez, S. Marggi-Poullain, M. E. Corrales and J. González-Vázquez.

Ultrafast Molecular Sciences by Femtosecond Photons & Electrons: Symposium in honor of Ahmed Zewail. 256th American Chemical Society.

Boston, Massachusetts. USA, 19-23 August 2018.

Femtosecond velocity map imaging study of the CH_3I photodissociation in the A-band at 243 nm and 268 nm

M. L. Murillo-Sánchez; M. E. Corrales; L. Bañares.

X Jornadas de Jóvenes Investigadores en Física Atómica y Molecular (J2IFAM 2018).

Barcelona, Spain. 4-6 April 2018.

Femtosecond predissociation dynamics of ethyl iodide from the origin of the B band

M. L. Murillo-Sánchez; M. E. Corrales; L. Bañares.

II Simposio Anual en Química Avanzada de la Facultad de Ciencias Químicas de la Universidad Complutense de Madrid. Madrid.

Spain. 18-21 September 2017.

A comparative study of the real-time photodissociation dynamics of chloroiodomethane and bromoiodomethane in the A band. A femtosecond velocity map imaging study

M. L. Murillo-Sánchez; S. Marggi-Poullain; J. González-Vázquez; M. E. Corrales; G. Balerdi; L. Bañares.

Iberian Meeting on Atomic and Molecular Physics (IBER 2018).

Barcelona, Spain. 12-14 September 2017.

Dinámica de fotodisociación resuelta en tiempo del cloroiodometano en la primera banda de absorción
M. L. Murillo-Sánchez; S. Marggi-Poullain; J. González-Vázquez; M. E. Corrales; G. Balerdi; L. Bañares.
IX Jornadas de Jóvenes Investigadores en Física Atómica y Molecular (J2IFAM 2017).
Sevilla, Spain. 22-24 March 2017.

POSTERS

Femtosecond XUV-IR dynamics of the methyl iodide cation
M. L. Murillo-Sánchez, G. Reitsma, R. de Nalda, M. E. Corrales, S. Marggi-Poullain, J. González-Vázquez, M. J. J. Vrakking, L. Bañares and O. Kornilov
Ultrafast Science & Technology Spain 2019 (USTS 2019)**.**
Madrid, Spain. 6-8 November 2019.

Time-resolved photodissociation dynamics of vinyl iodide in the UV at 199.2 and 200 nm
M. L. Murillo-Sánchez; I. Mondéjar; L. Bañares.
Ultrafast Science & Technology Spain 2019 (USTS 2019)**.**
Madrid, Spain. 6-8 November 2019.

Time-resolved photodissociation dynamics of vinyl iodide in the UV at 199.2 and 200 nm
M. L. Murillo-Sánchez; I. Mondéjar; L. Bañares.
Iberian Meeting on Atomic and Molecular Physics (IBER 2019)**.**
Évora, Portugal. 10-12 July 2019.

A comparative study of the real-time photodissociation dynamics of chloroiodomethane and bromoiodomethane in the A band. A femtosecond velocity map imaging study
M. L. Murillo-Sánchez; S. Marggi-Poullain; J.J. Bajo; J. González-Vázquez; M. E. Corrales; G. Balerdi; L. Bañares.
XI Jornadas de Jóvenes Investigadores en Física Atómica y Molecular (J2IFAM 2019).
Cádiz, Spain. 26-29 March 2019.

Femtosecond XUV-IR dynamics of the methyl iodide cation
G. Reitsma, M.L. Murillo-Sánchez, R. de Nalda, M.E. Corrales, S. Marggi-Poullain, J. González-Vázquez, M.J.J. Vrakking, L. Bañares, and O. Kornilov.
International Conference on Ultrafast Phenomena (UP 2018).
Hamburg, Germany.15-20 Jul 2018.

A comparative study of the real-time photodissociation dynamics of chloroiodomethane and bromoiodomethane in the A band. A femtosecond velocity map imaging study

M. L. Murillo-Sánchez; S. Marggi-Poullain; J.J. Bajo; J. González-Vázquez; M. E. Corrales; G. Balerdi; L. Bañares.

X Jornadas de Jóvenes Investigadores en Física Atómica y Molecular (J2IFAM 2018).

Barcelona, Spain. 4-6 April 2018.

A comparative study of the real-time photodissociation dynamics of chloroiodomethane and bromoiodomethane in the A band. A femtosecond velocity map imaging study

M. L. Murillo-Sánchez; S. Marggi-Poullain; J.J. Bajo; J. González-Vázquez; M. E. Corrales; G. Balerdi; L. Bañares. Ultrafast Science & Technology Spain 2017 (USTS 2017).

Salamanca, Spain. 22-24 October 2017.

PCCP Poster Prize.

Femtosecond predissociation dynamics of ethyl iodide from the origin of the B band

M. L. Murillo-Sánchez; M. E. Corrales; L. Bañares.

Iberian Meeting on Atomic and Molecular Physics (IBER 2018)**.**

Barcelona, Spain. 12-14 September 2018.

Femtosecond Photodissociation Dynamics of the halomethanes CH_2ClI and CH_2BrI in the first absorption band

M. L. Murillo-Sánchez; S. Marggi-Poullain; G. Balerdi; L. Bañares.

XXI edición de la Conferencia Europea sobre Dinámica de Sistemas Moleculares (MOLEC 2016).

Toledo, Spain. 11-16 September 2016.

Appendix

SETUP FOR THIRD AND FOURTH HARMONIC GENERATION OF THE FUNDAMENTAL WAVELENGTH OF THE LASER SYSTEM

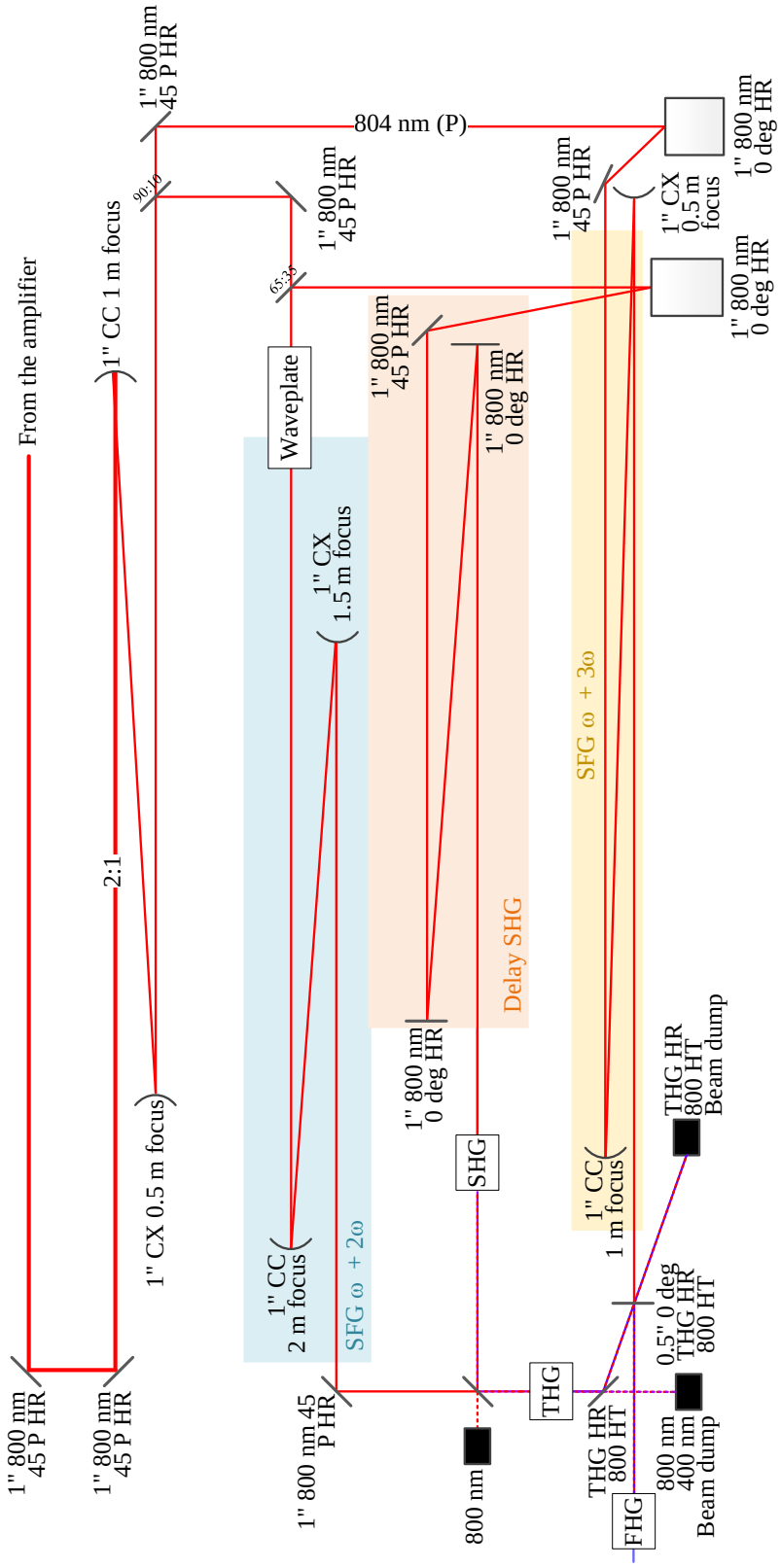

Figure A. 1. *Layout of the optical setup for THG and FHG of the fundamental wavelength of the Ti:sapphire CPA laser system.*

VELOCITY MAP IMAGING SMALL LENSES EXTRACTION SYSTEM

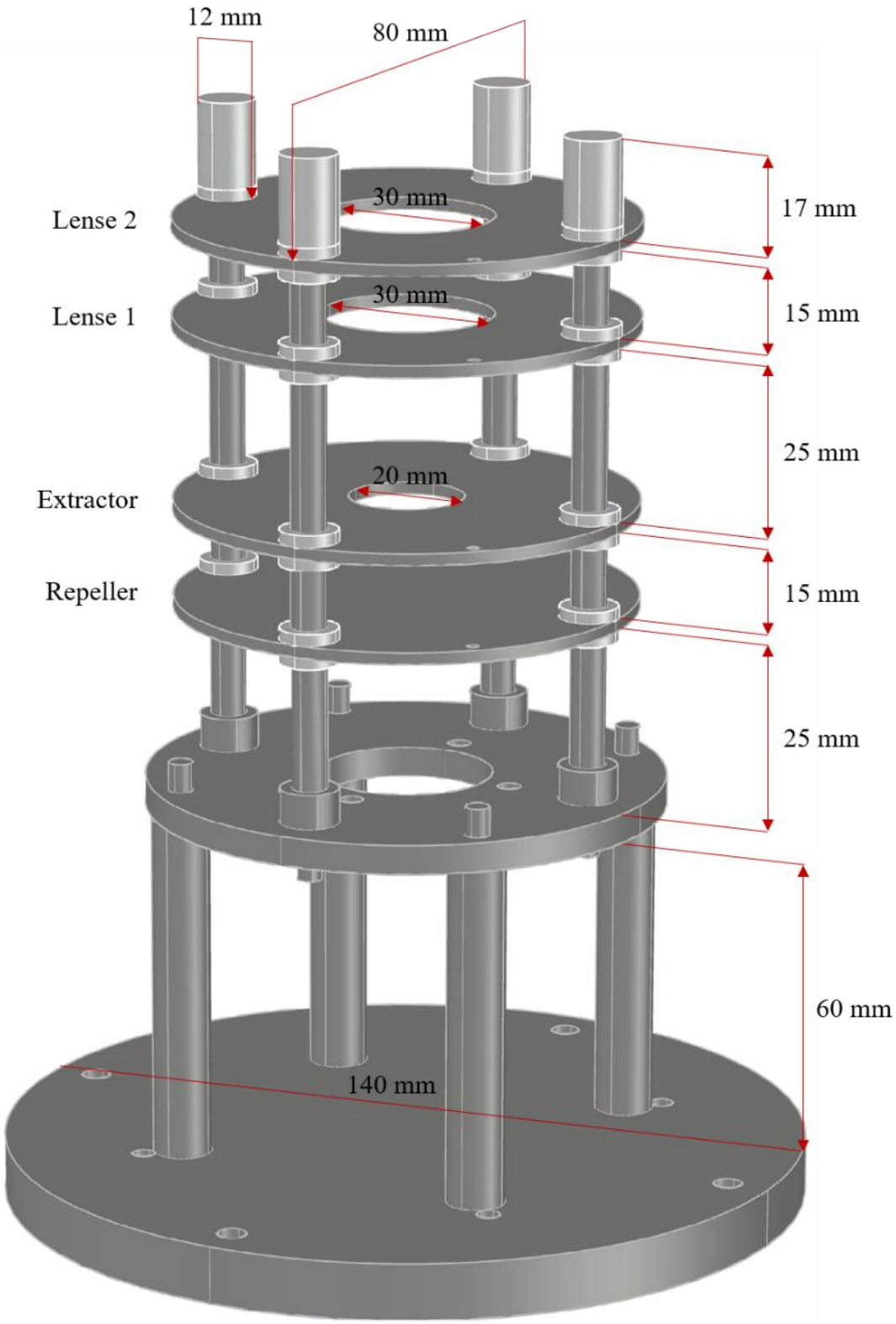

Figure A. 2. *VMI small lenses extraction system not including the deflection plates. The relevant measures are indicated. Each plate, made of stainless steel, is isolated from the adjacent ones employing Teflon separators. This system is supported by a blind CF flange employing rods. The size of these rods is variable to optimize the plates' position in the interaction area.*

VELOCITY MAP IMAGING BIG LENSES EXTRACTION SYSTEM

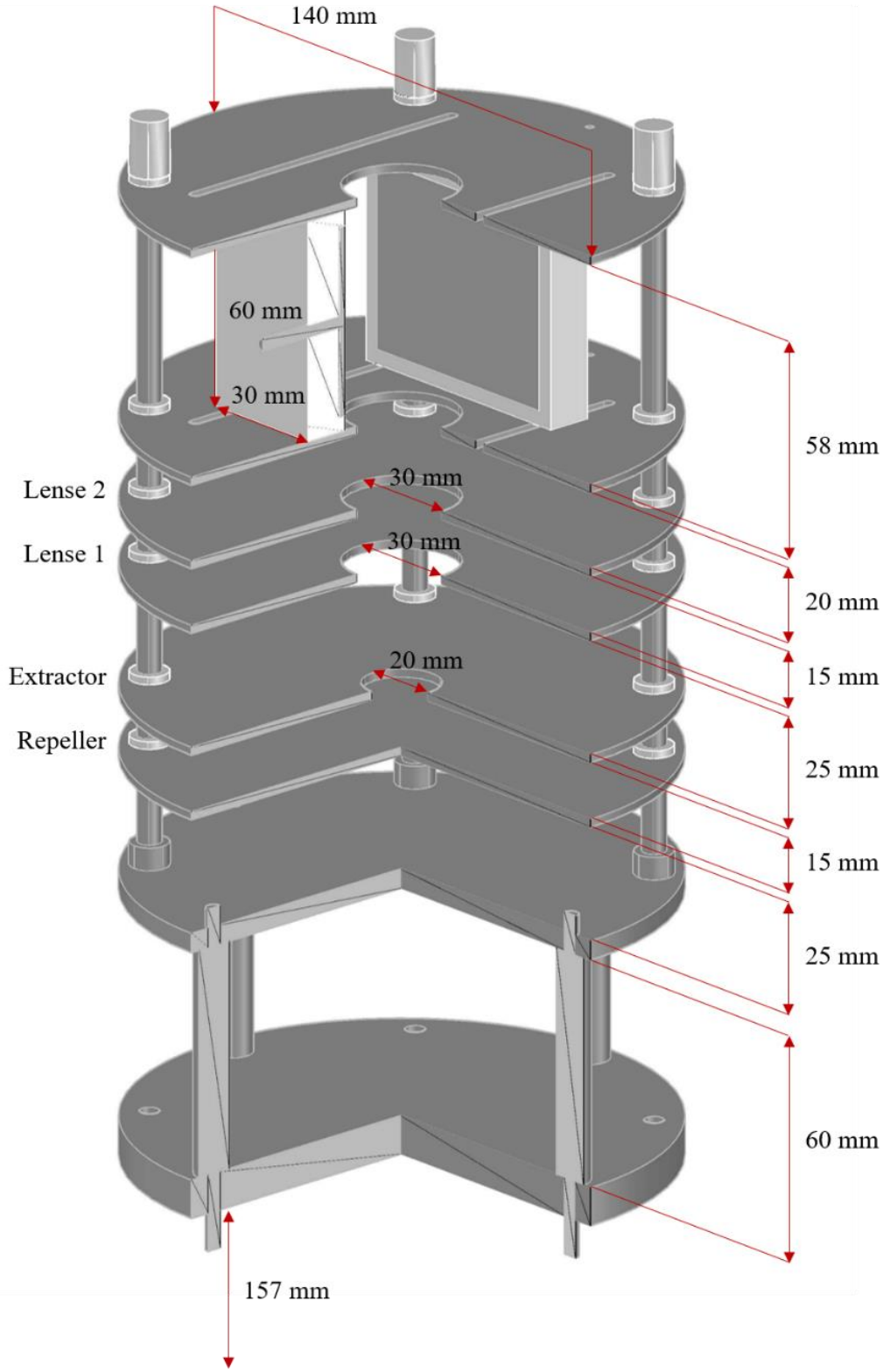

Figure A. 3. *VMI big lenses extraction system including the deflection plates. The relevant measures are indicated. Each plate, made of stainless steel, is isolated from the adjacent ones employing Teflon separators. This system is supported by a blind CF flange by means of rods. The size of these rods is variable to optimize the plates' position in the interaction area.*